CONTENTS

WHISPERING-GALLERY-MODE LASERS IN Er^{3+}-DOPED MICROSPHERES TOWARDS INTEGRATION IN SOI SLOTTED PHOTONIC CRYSTAL WAVEGUIDES 7

Quang Minh Ngo, Van Dai Pham, Thanh Son Pham, Thu Trang Hoang, Van An Nguyen 7

A THEORETICAL STUDY OF THE BAND STRUCTURE AND OPTICAL PROPERTIES OF TWO-DIMENSIONAL MATERIAL Mo_2CF_2 15

Kieu-Anh Thi Doan, Minh Hong Pham, Marilou Cadatal-Raduban, Linh Phan-Thuy Tran and Mui Viet Luong 15

EFFECT OF SILVER LAYER ON INTERMETALLIC COMPOUND FORMATION AT SAC305/METAL PAD INTERFACE 23

Titipa Zunsuwan, Phakkhaphum Lethaisong and Anusara Srisrual 23

OPTIMIZING THE PERFORMANCE OF FLEXIBLE β-GA_2O_3 SOLAR-BLIND PHOTODETECTOR GROWN ON OHP SUBSTRATES BY INSERTING ADHESION LAYERS 31

Vu Thi Kim Oanh and Eun Kyu Kim 31

CHROMATIC DISPERSION CONTROL IN LEAD-BISMUTH-GALLATE GLASS PHOTONIC CRYSTAL FIBERS WITH SELECTIVE HIGH NONLINEAR LIQUID INFILTRATION: APPLICATION TO ULTRA-FLATTENED-NORMAL-DISPERSION 37

Quang Ho Dinh, Nguyen Dang Nguyen, Chin Hoang Van, Ngoc Vo Thi Minh, Trung Le Canh, Thanh Vinh Nguyen, Bien Chu Van, Thao Nguyen Thi and Hieu Van Le 37

APPLICATION OF THE ELECTRICAL RESISTIVITY TOMOGRAPHY AND SEISMIC REFRACTION METHODS FOR GROUNDWATER INVESTIGATION IN SAVANNAKHET PROVINCE, LAOS 45

Viengthong Xayavong, Minh Duc Vu, Duong Anh Nguyen, Tuan Minh Vu, Chung Anh Do 45

THREE-DIMENSIONAL STITCHING METHOD FOR NON-CONTACT ON-MACHINE SURFACE TOPOGRAPHY MEASUREMENT BY USING WHITE LIGHT SCANNING INTERFEROMETRY SYSTEM 54

Vo Quang Sang, Yiting Duan 54

WAVEFORMS CLASSIFICATION OF NORTHERN SUMATRA EARTHQUAKE BASED ON SEISMIC NETWORK STATION USING A RANDOM FOREST MACHINE LEARNING APPROACH 62

Marzuki Sinambela, Pham Hong Minh 62

THERMAL DECOMPOSITION KINETIC ANALYSIS OF THE OCTOGEN-BASED ENERGETIC MATERIALS 67

Toan Nguyen Trung, Huu Hoang Trung 67

INVESTIGATION OF PLASMON RESONANCE IN 2D METAL-DIELECTRIC-METAL NANOSTRUCTURES 78

Thu Trang Hoang, Thanh Son Pham, Xuan Bach Nguyen, Huu Tu Nguyen and Quang Minh Ngo 78

LASER-FABRICATION MECHANISMS OF NANOSTRUCTURES ON Au/Pd THIN FILM 83

Nguyen Thi Huyen Trang, Kudryashov Sergey Ivanovich, Doan Hoai Son 83

SYNTHESIS OF CdSe QUANTUM DOTS AND PHOTOLUMINESCENCE ENHANCEMENT BY ZnO THIN FILM 89

Phan Van Cuong 89

CLOUD REMOVAL FROM LANDSAT IMAGERY USING CLOUD COMPUTING PLATFORM GOOGLE EARTH ENGINE 93

Phu Van Le, Hung Le Trinh, Nguyen Quoc Long, Tien Minh Pham, Hai Van Bui 93

POLYMER BLEND BASED ON POLYAMIDE AND ITS APPLICATIONS 105

Nguyen Trung Thanh, Truong Dinh Tuan 105

SPATIO-TEMPORAL CHANGES IN AQUACULTURE PONDS IN BEN TRE PROVINCE, SOUTHERN VIETNAM 112

Bijeesh Kozhikkodan Veettil, Xuan-Linh Tran and Nhat-Duc Hoang 112

***Bacillus licheniformis* MPC4 - A NOVEL BACTERIAL STRAIN FOR DEGRADATION OF ORGANOPHOSPHORUS PESTICIDES IN TROPICAL SOIL 119**

Chi K. Hoang, Quang H. Tran, Cuong H. Le, Ha T. H. Tran, Huong M. Le and Hang T. N. Tran 119

SILVER MESO-PARTICLES APPLYING IN DETECTION MELAMINE BY SURFACE ENHANCED RAMAN SPECTROSCOPY 127

Nguyen Thi Hang Nga, Nguyen Thi Bich Ngoc, Vu Duong 127

GENERATION OF ENTANGLED STATES IN THREE MODE NONLINEAR KERR-LIKE OSCILLATORS SYSTEM 133

Thi Dung Nguyen, Thi Thao Nguyen 133

EFFECT OF ENDURANCE TRANING IN PATIENT WITH HYPERTENSION ON BICYCLE ERGOMETERS 139

Nguyen The Thuong 139

 ISBN:

CHARACTERIZATION AND EFFECT OF BOUNDARY LAYER IN SEVERE-HAZY POLLUTION EVENT DURING WINTER 2019 IN HANOI 144

Bao Anh Phung Ngoc, Hervé Delbarre, Karine Deboudt, Elsa Dieudonné, Hai Van Bui 144

EFFECTS OF THE γ-POLYOXYMETYLENE FIRE RATARDANT ON THE CHEMICAL STABILITY OF THE DOUBLE BASE ENERGY MATERIALS USING LAVA THERMAL ANALYSIS TECHNIQUE..... 152

Co Ngoc Duong, Toai Pham Van, Tuong Nguyen Manh, Cong Vu Tien, Toan Nguyen Trung, Duong Duc La 152

ENHANCING THE EFFICIENCY INTERPRETATION GROUND PENETRATING RADAR DATA USING TWO-DIMENSIONAL CONTINUOUS WAVELET TRANSFORM 161

Tin Duong Quoc Chanh, Dau Duong Hieu, Van Nguyen Thanh, Thuan Nguyen Van, Phuong Nguyen Le Hoai, Minh Lam Thuy, Nhan Duong Trong, My Tran Diem..... 161

DEEP LERANING FOR WAVEFRONT CODING SYSTEM WITH RADIALLY SYMMETRIC PHASE MASK 168

Van Nhu Le, Van Sang Doan, Quoc Khanh Doan and Thanh Hai Do..... 168

GASES TRANSPORT EQUATION WITH TEMPERATURE INVERSIONS IN THE ATMOSPHERE 173

Vu Ba Dung 173

THE EFFECTS OF Ge GROWTH TEMPERATURE ON THE STRUCTURAL PROPERTIES OF Ge/Mn5Ge3/Ge(111) SYSTEM 179

Le Thi Giang, Nguyen Thi Dung..... 179

MODEL AND RESULTS OF THE GRADIENT METHOD IN GRAVITY DATA PROCESSING 187

Duy Hoang Dang, Nghia Huu Pham 187

CORRELATION OF ELECTRON-ELECTRON SCATTERING IN DIFFERENT SUBBANDS OF QUANTUM WELLS 193

Nguyen Thanh Cong, Doan The Ngo Vinh 193

FABRICATION OF POROUS SILICON USED IN OPTOELECTRONICS AND SENSORS 198

Le Dinh Vi, Tran Quang Dat, Dang Hai Ninh, Ngo Thi Lien, Pham Van Thin, Nguyen Vu Tung 198

DEVELOPMENT OF A DEVICE FOR AUTOMATICALLY MEASURING PARALLELISM OF A PLATE DURING PROCESSING..... 204

Phan Nguyen Nhue, Bui Dinh Bao 204

SYNTHESIS AND MICROWAVE ABSORPTION PERFORMANCE OF $BaFe_{12}O_{19}/NiFe_2O_4$ NANOCOMPOSITE 210

Tran Quang Dat, Nguyen Kim Thanh, Le Dinh Vi, Nguyen Vu Tung, Pham Van Thin 210

MATERIAL CHARACTERIZATION OF BETULIN EXTRACTED FROM BIRCK BARK (BETULA UTILIS) 217

Le Thi Thu Huong, Nguyen Thi Mai Huong, Le Thi Huong, Phan Thi Thuy, Nguyen Thanh Binh, Nguyen Trong Tinh 217

IDENTIFICATION OF *Stephania* spp. COLLECTED IN LAO CAI PROVINCE OF VIETNAM BY MORPHOLOGY, ANATOMY AND DNA BARCODE METHODS 222

Hiep Hoang Phu, Thao Thi Phuong Cao, Danh Thuong Sy, Thi Thanh Nhan Pham .. 222

RESEARCHING THE RETRO-REFLECTION PHENOMENON IN OPTICAL AND OPTOELECTRONIC DEVICES 233

Nguyen Quang Hiep 233

NUMERICAL SIMULATION SUPERCONTINUUM GENERATION IN ALL-NORMAL DISPERSION SUSPENDED-CORE FIBER INFILTRATED WITH ETHANOL AROUND 1064 NM 239

Le Canh Trung, Ha Minh Quan, Dinh Xuan Khoa, Do Thanh Thuy, Nguyen Tien Dung, Nguyen Thi Linh, Le Van Hieu, Ngo Dinh Hong Le, Tran Thi Thanh Huyen, Bui Dinh Thuan 239

PHASE-DEPENDENCE OF OPTICAL PROPERTIES IN A THREE-LEVEL LAMBDA MEDIUM 246

Nguyen Thi Thu Hien, Nguyen Huy Bang, Dinh Xuan Khoa, Hoang Minh Dong, Nguyen Tuan Anh, Thai Doan Thanh, Luong Thi Yen Nga, Le Van Doai, Le Thi Minh Phuong 246

INVESTIGATION OF THE THIRD-ORDER NONLINEAR OPTICAL EFFECT AND THE PHOTODYNAMIC EFFECT OF THE SAFRANIN O ORGANIC MATTER IN WATER AND METHANOL SOLVENTS 254

Nguyen Nang Binh, Duong Chi Tong, Nguyen Thi Thu Hien, Nguyen Hong Giang, Phan Trung Vinh, Nguyen Thanh Lam 254

APPLICATION OF COASTAL BIOSHIELDS FOR SHORELINE PROTECTION IN QUANG NAM, CENTRAL VIETNAM 260

Bijeesh Kozhikkodan Veettil, Xuan-Linh Tran and Nhat-Duc Hoang 260

DETERMINATION OF CAMPHOR CONCENTRATION PROFILE IN 5/7X DETERRED SINGLE BASE PROPELLANT 268

Pham Quang Hieu 268

 ISBN:

RESEARCH TECHNOLOGY FOR CREATION OF ENERGY MATERIALS, REQUIREMENTS TO PHLEGMATIZATION AND USE FOR CHARGES TO THE CARTRIDGE 23 MM AND 30 MM NAVY- PART 1 274

Pham Quang Hieu 274

CONSTRUCTION AND USE OF STUDY FILM IN TEACHING GENERAL PHYSICS EXPERIMENTS 280

Ho Xuan Huy, Nguyen Hong Hai 280

SYNTHESIS OF MoS_2 NANOPARTICLES BY HYDROTHERMAL ROUTE AND ITS CHARACTERIZATIONS 286

Vu Van Thu, Nguyen Dac Dien 286

COMPARISON OF EFFECTIVE MODE AREA OF PHOTONIC CRYSTAL FIBERS WITH DIFFERENT AIR-HOLE DIAMETERS IN THE CLADDING FOR VARIOUS LATTICE TYPES 293

Trong Dang Van, Bao Tran Le Tran, Ngoc Vo Thi Minh, Tan Tran Duy, Lanh Chu Van, Duc Hoang Trong, Thuy Nguyen Thi 293

INVESTIGATING EFFECTIVE REFRACTIVE INDEX AND CONFINEMENT LOSS OF PCFs WITH HETEROGENEOUS RINGS IN THE CLADDING FOR VARIOUS LATTICE TYPES 301

Bao Tran Le Tran, Trong Dang Van, Ngoc Vo Thi Minh, Tan Tran Duy, Lanh Chu Van, Duc Hoang Trong, Thuy Nguyen Thi 301

CHARACTERISTIC ANALYSIS OF HEXAGONAL SILICA-BASED PHOTONIC CRYSTAL FIBERS WITH DIFFERENT RINGS STRUCTURES 309

Thuy Nguyen Thi, Duc Hoang Trong, Trong Dang Van, Bao Tran Le Tran, Hung Dao Van, Lanh Chu Van 309

COMPARISON OF DISPERSION CHARACTERISTICS OF SILICA-BASED PHOTONIC CRYSTAL FIBERS WITH DIFFERENT LATTICES 317

Duc Hoang Trong, Trong Dang Van, Bao Tran Le Tran, Lanh Chu Van, Hung Dao Van, and Thuy Nguyen Thi 317

SYNTHESIS AND THERMAL DEGRADATION OF NITRO-FUNCTIONALIZED HYDROXYL-TERMINATED NATURAL RUBBER 324

Doan Minh Khai, Nguyen Minh Tuan, Phan Duc Nhan, Nguyen Duy Tuan, Nguyen Tuan Anh 324

ANTIOXIDANT CAPACITY AND AQUEOUS SOLUBILITY OF TAXIFOLIN EXTRACTED FROM SIBERIAN LARCH (LARIX SIBIRICA) 332

Son Bach, Thuy Thi Phan, Huong Thi Le and Mai Huong Thi Nguyen 332

GREEN SYNTHESIS ZnO NANOPARTICLEC BY *PIPER CHAUDOCANUM* L. EXTRACT FOR ENHANCED ANTIBACTERIAL ACTIVITY 337

Truong Thi Thao, Le Thi Ngoc Linh, Kieu Thi Van Anh, Nguyen Dieu Linh and Nguyen Van Hao 337

TREATMENT OF PERIARTHRITIS OF THE SHOULDER BY THERAPEUTIC ULTRASOUND 346

Nguyen The Thuong, Vo Thi Anh Tuyet..... 346

POTENTIAL APPLICATION OF SPINAL MOUSE IDIAG M360 FOR EVALUATING SCOLIOSIS IN ADOLESCENTS 351

Nguyen Duc Tri, Huynh Quang Linh and Nguyen The Thuong 351

DEVELOPMENT OF A LOW-TEMPERATURE HYDROGEN PEROXIDE PLASMA STERILIZER..... 357

Chu Thi Minh Hoa, Pham Trung Kien, Nguyen Minh Tan, Doan Thi Thu Thuy, Nguyen Tuan Anh..... 357

DEVELOPMENT OF AN EXTRACORPOREAL SHOCK WAVE THERAPY MODULE USING PNEUMATIC TECHNIQUE 364

Doan Thi Thu Thuy, Chu Thi Minh Hoa, Pham Trung Kien, Nguyen Minh Tan, Nguyen Tuan Anh..... 364

INTERPRETING THE GRAVITY ANOMALY OF THE SOUTHERN VIETNAM USING DERIVATIVE METHOD..... 371

Nguyen Hong Hai 371

MAGNETIC DATA INVERSION FOR 3D GEOMETRY OF THE SHALLOW SOURCES IN THE SOUTHERN VIETNAM..... 380

Nguyen Hong Hai 380

ISOMERIC RATIOS IN INVERSE (γ, n) AND (n,γ) REACTIONSON Ce, Cd, Pd AND Se TARGETS 388

Bui Minh Hue and Tran Duc Thiep 388

OPTIMAL STRUCTURE OF PHOTONIC CRYSTAL FIBER WITH INFILTRATED BENZENE CORE FOR APPLICATION SUPERCONTINUUM GENERATION..... 397

Ngoc Vo Thi Minh, Bao Tran Le Tran, Trong Dang Van, Bao Le Xuan, Thao Tran Ngoc, Long Vu Dinh, Thanh Tran Viet, Oanh Truong Thi Chuyen, Thu Ho Thi Anh, Thuy Nguyen Thi, Vu Tran Quoc, Lanh Chu Van 397

CHEMICAL COMPOSITION OF ESSENTIAL OILS OF *Litsea elongata* (Nees) Benth. & Hook.f. IN PU HOAT NATURE RESERVE, NGHE AN PROVINCE..... 406

Nguyen Tien Cuong, Pham Hong Ban, Mai Van Chung..... 406

AUTHORS INDEX 411

 ISBN:

WHISPERING-GALLERY-MODE LASERS IN Er^{3+}-DOPED MICROSPHERES TOWARDS INTEGRATION IN SOI SLOTTED PHOTONIC CRYSTAL WAVEGUIDES

Quang Minh Ngo[1*], Van Dai Pham[2], Thanh Son Pham[2], Thu Trang Hoang[2], Van An Nguyen[3]

[1]*University of Science and Technology of Hanoi, Vietnam Academy of Science and Technology, 18 Hoang Quoc Viet, Cau Giay, Hanoi, Vietnam*

[2]*Institute of Materials Science, Vietnam Academy of Science and Technology, 18 Hoang Quoc Viet, Cau Giay, Hanoi, Vietnam*

[3]*University of Sciences, Hue University, 77 Nguyen Hue, Hue City, Vietnam*

*E-mail: *ngo-quang.minh@usth.edu.vn*

Abstract. In this work, we review in part of the whispering-gallery-mode (WGM) lasers in Er^{3+}-doped silica microspheres (μS) towards integration in silicon-on-insulator (SOI) slotted photonic crystal (PhC) waveguides. The Er^{3+}-doped silica μS with suitable diameters fabricated by using an electrical discharge method. The single-mode optical tapered fibers were used to guide the pumped laser into the μS surface and collect the resulting lasing emission. The observation of WGM at telecom regime is quantified. The selective single- or multi-emitted modes of the μS laser can be obtained by adjusting the coupling gap between the collection tapered fiber and the μS surface. To overcome the collection tapered fiber's vibration at close range of the coupling gap, the guiding and coupling losses, while being compact enough to fit with complementary metal oxide semiconductor (CMOS) device, the integration of μS with SOI slotted PhC waveguides is proposed and modeled with the help of finite-difference time-domain (FDTD) simulations. The designed structures may find application for the promising photonic devices such as the ultrahigh sensitivity sensors, the lasing sources, and towards advanced quantum communications.

Keywords: *Microspheres, Whispering-gallery-modes, Lasers, Photonic band gaps, Waveguides.*

I. INTRODUCTION

Optical micro-resonators have been the subject of much attention due to their special characteristics and many promising applications for quantum electrodynamics, nonlinear optics, data storages, chemical or bio-sensing, lasers and filters [1-4]. In dielectric microspheres (μS) lights can be confined in the form of the whispering-gallery-modes (WGMs), which have small modal volumes and ultrahigh quality (Q) factors. If μS is composed of an active material, the lasing emission is modulated by the WGM spectrum, therefore the spontaneous emission rate is significant enhanced [3,5]. Numerous materials including polymers, crystalline, or glassy compounds doped with a high enough concentration of rare earth ions have been used to fabricate the μSs and they create active cavities, which act as both the gain media and the resonators for the emitted lasers. In the measurement setup, the tapered single-mode optical fibers were used to guide the pump laser beam coupling into the μS surface and collect the resulting lasing emission. The

achieved μS lasers were emitted by the WGMs with narrowed linewidth multi-mode lines in the telecom wavelength range of ~1550 nm. In addition, by adjusting the coupling gap smaller than the critical length, it is possible to obtain the single-mode of high power with the selected wavelength. As our results shown, there have been wide applications, such as telecom-like spectroscopy, optical switches, high-density wavelength division multiplexing (DWDM) communications and lab-on-a-chip sensors [6]. However, there was a drawback of using a narrow-linewidth emission for spectroscopy and sensors, owing to the low power per emission line and the difficulty of resolving features that are smaller than the emitted mode spacing [7]. In addition, the vibration of the coupling gap, which makes the loss and the instability of the laser and signal coupled into and out the μSs, respectively [8] hinders the practical application of these optical devices.

As the works presented on the progress and infrastructure of integrated photonics for communication and lab-on-chip sensors in terms of complexity, robustness and scalability, silicon photonics can offer almost complete suite with further benefits of miniaturization, cost-effective device manufacture and compatibility with CMOS technology [9,10]. From the general point of view, silicon-on-insulator (SOI) slotted waveguide geometry has been considered for integrated optics due to the high degree of spatial light confinement. It means that light is confined in a narrow-slotted region with low refractive index etched into a high refractive index medium. With the two-dimensional (2D) slotted photonic crystal (PhC) waveguide, which provides the control over the dispersion of light in air, both in the temporal and the spatial domains [11]. It inherits the peculiarity from its geometry that combines two confining mechanisms, such as in slot and in 2D-PhC lattices. Thus, low loss propagation in slotted PhC components is possible and that it is comparable to losses in non-slotted PhC waveguides or in slotted ridge waveguides. Therefore, propagation losses do not restrict the further exploration of high light-matter interaction in slotted waveguides, e.g., for applications of sensing or nonlinear optics [12].

In this paper, based on the fabricated Er^{3+}-doped silica glass μSs with diameters of ~30-40 μm, two tapered optical fibers were used to guide the pumped laser (λ ~1470 nm), restricted to TE polarization (H-field normal to the WGM propagation plane), coupling into the μS surface and collect the resulting signals, respectively. The observed WGM lasing emissions at telecom regime of ~1550 nm are analyzed quantitatively. Depending on the coupling gap between the collections tapered fiber and the μS surface, the WGM single-mode line at given wavelength or multi-mode lines of the μS lasers can be obtained. To visualize the WGMs formed by the μS lasers, the finite-difference time-domain (FDTD) simulations were carried out on the silica glass spherical shapes that closely identical to the real samples fabricated in this work. The electric dipole emitters producing the sinusoidal pulses centered at the lasing emission wavelength were placed in the zone internally near the μS surface. These results in a greater number of observable emission modes, which has good agreement with the analytic model results. Because of using two tapered optical fibers for pumping laser into the μS surface and collecting the lasing emission, the vibration of the fiber due to the close coupling gap induces the coupling losses and instability of the emitted signals. To overcome these limitations and create a

 ISBN:

compatibility with CMOS devices, a large-scale integrated optics configuration between a μS and SOI slotted PhC waveguides is designed and modeled with the help of FDTD simulations [13]. The integrated structure in this work may find applications in the ultrahigh sensitivity sensors, the lasing sources, and the integrated quantum communications.

II. THEORETICAL AND SIMULATION METHODS

Numerous studies have realized the WGMs of the μSs using several analytic models [14]. In here, a simplified 2D model for understanding the physical and optical properties of the 3D optically coupled μS systems was considered. As it is well known that the optical WGM is formed by the repeated total internal reflection of the light on the μS surface as depicted in Fig. 1a. When the phase matching condition is satisfied, standing waves will appear along the corresponding perimeter of the μS shown in Fig. 1b. Three mode numbers describe it: radial (n), angular (l) and azimuthal (m) [15]. The radial number, n, indicates the number of intensity maxima along the radial direction; the angular number, l, represents the number of modal wavelengths that fit into the circumference of the equatorial plane of the μS. It means that $2l$ is the number of maxima in the angular variation of the resonant field around the μS equator. The azimuthal mode number, m, describes the field variation in the polar direction, with the number of intensity maxima along this direction being equal to l-$|m|$+1. In the case of light beams transmitting in a large circle that is inclined at an angle θ to the equatorial plane as shown Fig. 1c, the azimuthal mode number is $m = l\cos\theta$. In practical, we are interested in exciting low-order WGMs with small n and with $m \approx l$ for maximizing the resonant advantages of the μS. These modes have the optical field distributions near the μS surface approximated to the equator and the E-fields are compressed into the smallest modal volume.

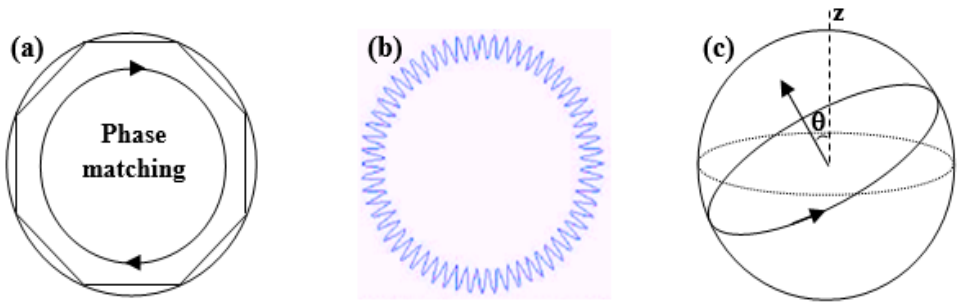

Fig. 1. *μS resonator formed when the phase matching condition is satisfied (a), standing waves appear on the perimeter of the μS (b) and the orbit of the photon along the perimeter of the μS (c).*

In simulation, we used the plane-wave expansion (PWE) method embedded in MIT open-source, called MPB and the commercial Lumerical FDTD software [13,16]. To obtain the spectra, resonant patterns of the μS laser and of the integration between a μS and SOI slotted PhC waveguides, the perfectly matched absorbing boundary conditions were used at the surroundings of these structures [13]. The excitation characteristics: the TE polarized point-source electric dipoles in the vicinity of the μS surface have been taken for the WGM-μS lasers and whereas, the Bloch-mode source located at the input SOI slotted

PhC waveguide after the perfectly matched absorbing layer was used for the μS integrated with SOI slotted PhC waveguide structure.

III. RESULTS AND DISCUSSION

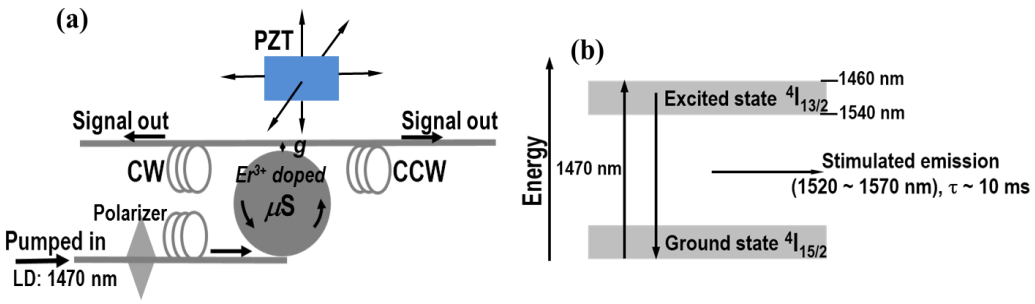

Fig. 2. *a) Schematic illustrations of the (a) fiber-taper-coupled μS optical amplification system and b) two lowest energy-level diagram of Er^{3+} ion.*

The scheme of Lab-made setup for measuring the WGMs of μS is depicted in Fig. 2a. The laser diode at λ = 1470 nm with the minimum output power ~180 mW was polarized at TE mode for excitation of the Er^{3+} ions. The pump laser beam and the resulting lasing emission from the μS are guided by different tapered fibers. This technique has an advantage of flexibility in controlling the coupling gap between the collection fiber and μS surface, while the position of excited fiber was fixed. The spectral characteristics of the lasing emissions were analyzed by the optical spectrum analyzer (OSA)-Advantest Q8384 with the resolution of 0.01 nm. The coupling gap was adjusted by a 3D micro-precision stage with the accuracy of 0.10 μm. Two types of mode corresponding to the two possible directions of propagation (clockwise-CW and counterclockwise-CCW) have been measured.

The arc discharge method has been used for fabrication of Er^{3+}-doped silica glass μS. In our work, the Er^{3+}-doped glass silica μS with diameters of ~40 μm as shown in Fig. 3a has been controlled to (i) fit much larger wavelength of WGM lasing emissions (λ ~1520-1570 nm) as shown in Fig. 2b and (ii) obtain the smaller integrated size scale ~100 μm × 100 μm for miniaturizing the loss. To couple light into the μS efficiently, the evanescent wave mode of the tapered fiber must match with the WGM of the μS. When the Er^{3+}-doped silica glass μS is adequately coupled with the tapered fiber, single-mode emission can be achieved. Otherwise, a multi-mode emission can be observed [17,18]. In the experiment, single- and multi-mode emissions have been measured. As shown in Figs 3b,c, the μS with the diameter of ~38.5 μm and coupling gap of 1.8±0.1 μm produced the multi-mode emissions. As it is shown, these emissions have the CW sense of circulation. It means that there was strong coupling in the CW geometry, which can be known as the in-phase matched coupling [19].

To explore the characteristics of the single WGMs, when the coupling gap is smaller than ~1.0 μm, we have collected its output power by precise adjustment of the coupling gap. In the presented scheme, the diameter of μS and pumped power were kept as same as

 ISBN:

the one shown in Figs. 3b,c, while Fig. 3d presents the single-mode spectra extracting from the CW geometry for coupling gap of 0.5 ± 0.1 μm. This technique has good reproducibility in practice, and we can extract most of the WGMs that can oscillate in the μS with a suitable adjustment of the coupling gap.

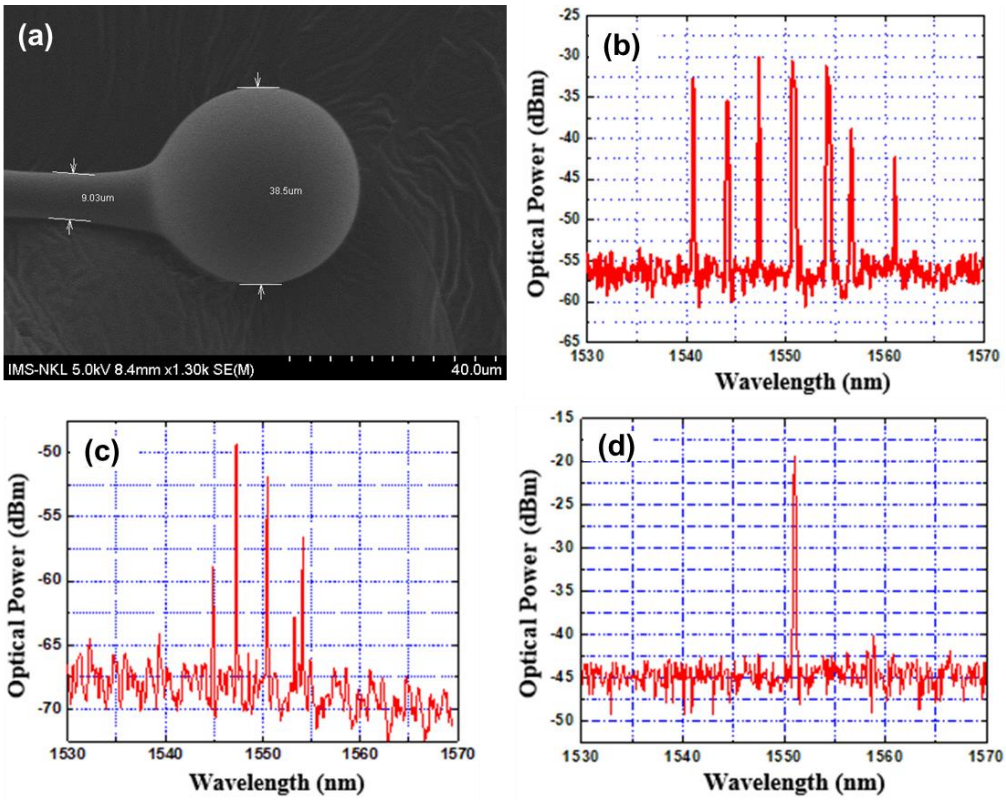

Fig. 3. *a) SEM images of the Er^{3+}-doped silica glass μS with diameters of 38.5 μm. WGM emission spectra extracted from Er^{3+}-μS with diameter of ~38.5 μm and coupling gap of 1.8±0.1 μm for b) CW and c) CCW geometries as shown in Fig. 2a; d) CW geometry when the coupling gap between the tapered fiber and the μS surface ~0.5 μm ± 0.1 μm.*

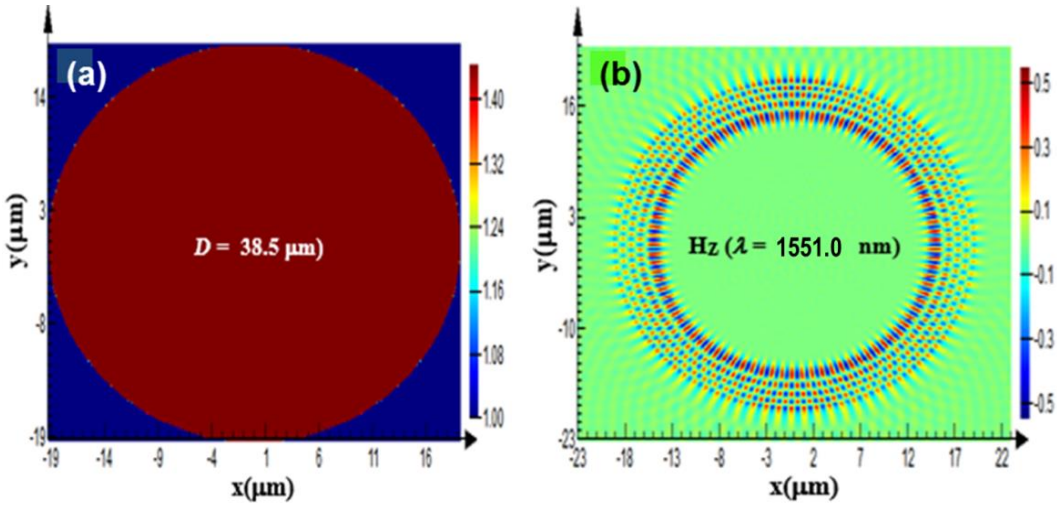

Fig. 4. *a) Refractive index of the silica glass μS with diameter of 38.5 μm and b) Hz component distribution confining inside and on the equatorial plane of the μS for the WGM at λ = 1551.0 nm.*

For visualizing the modes and fields, the 3D-FDTD method combining with perfectly matched layers (PML) were implemented to simulate the radiation patterns of WGMs from μS [13]. As mentioned above, the electric-dipole emitters located near the surface and oriented along the radials of μS, producing the ~20 fs sinusoidal pulses centered at emission wavelengths interact with μS. Figs 4a,b show the refractive index of μS of 1.44 in air and WGM H-field distribution for the μS with the diameter of 38.5 μm at wavelength 1551.0 nm, respectively. The estimated resonance by analytical approach and simulation in our 2D model was found to be a reasonable agreement with that determined by fitting the WGM peaks in the experimental spectra in Fig. 3.

To excite the WGM of the μS, we propose an integration configuration based on the SOI platform. This structure consists of two slotted PhC waveguides coupling to the 38.5 μm diameter μS, one guides the pumped signal into the μS while the other transports the output signal. The schematic view of the proposed configuration is shown in Fig. 5a. For serving the lasing behavior of the Er^{3+}-μS, the input slotted PhC waveguide has the function to guide the TE-polarized light of ~1470 nm and the output slotted PhC waveguide operates at ~1550 nm.

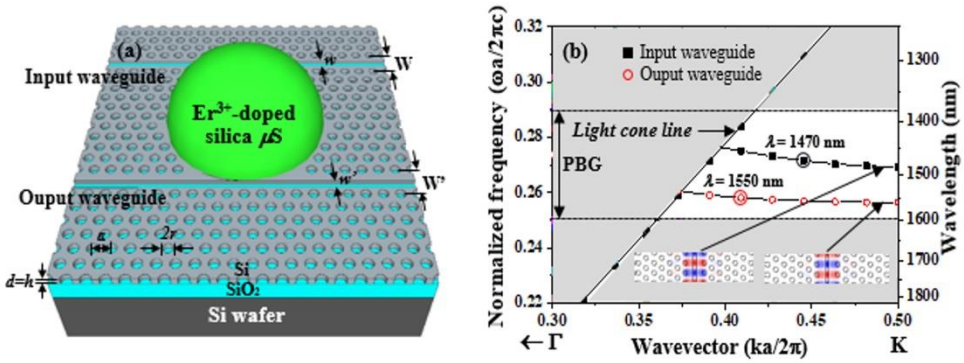

Fig. 5. *a) Schematic diagram of the intergration of the Er^{3+}-μS and the SOI slotted PhC waveguides, b) Projected band diagram for PhC structure and the E-field distribution in the two waveguides at λ = 1470 nm and λ = 1549.01 nm.*

The two slotted PhC waveguide dispersions were calculated by using 3D PWE method [20]. They were both conducted in the lattice constant *a* of 400 nm and the thickness of silicon slab of 220 nm. In this PhC platform, the waveguide width and the slot width were modified to generate the integrated waveguides with different properties on the same SOI chip. The waveguide width was enlarged from the original *W1* ($W1 = a\sqrt{3}$). For the case of the input waveguide, the waveguide width was enlarged to 1.18*W1* according with the slot width of 165 nm, while for the case of the output waveguide, a 1.25*W1* waveguide width and the slot width of 125 nm was considered. Fig. 5b depicts the dispersion diagram of the two input and output waveguides while the insets are E-field profiles at the edge wavelength of these slotted PhC waveguides. The E-fields are strongly localized in the waveguide area with low refractive index. These slotted PhC waveguides were designed considering air cladding to match with the μS mentioned above.

The two slotted PhC waveguides were used to excite the WGMs inside the Er^{3+}-μS and to guide the resulting lasing signal out in the planar SOI PhC platform. The input

 ISBN:

slotted PhC wavegudie can excite the Er^{3+} ions at wavelength ~1470 nm while the output slotted PhC waveguide guides the lasing mode ~1549.01 nm as depicted in Fig. 6, the E-field intensity at wavelength ~1470 nm and ~1549.01 nm at the access regions of input and output slotted PhC waveguides are shown, respectively. Although there is the mismatch between two different kinds of mode: Bloch-mode of the slotted PhC waveguide and the WGM of the μS, this integrated system shows the possibility of coupling the Bloch-mode to the WGM. This configuration offers a compatible and mechanically robust integrated device in the silicon photonic domain, and it can also enrich the diversity of on-chip silicon devices.

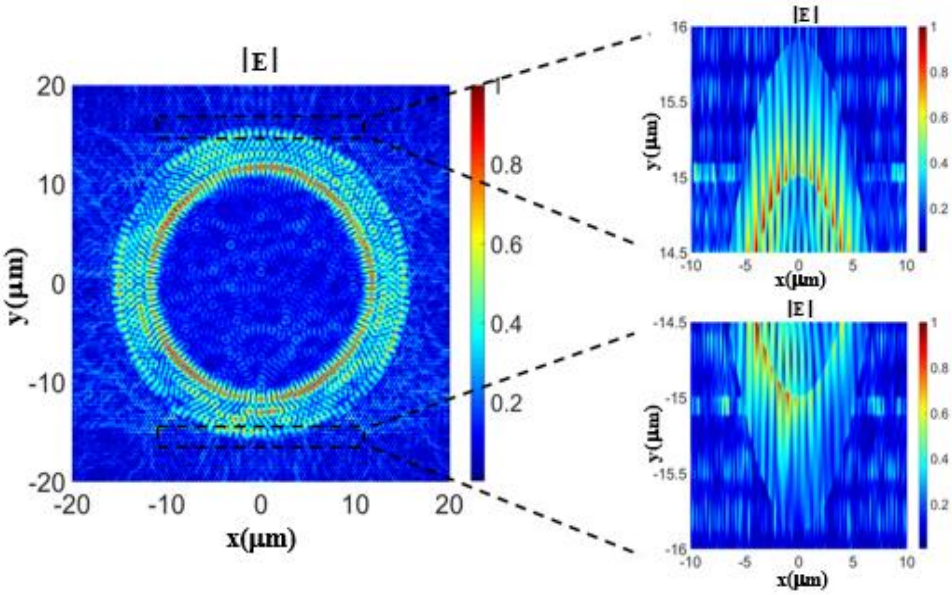

Fig. 6. *E- field profile of the WGM at 1549.01 nm and insets are the access of input waveguide and output waveguide and the μS at 1470 nm and 1549.01 nm, respectively.*

IV. CONCLUSION

In conclusion, based on the fabricated Er^{3+}-μS with diameters of ~30-40 μm, their WGM lasing emissions at telecom regime were quantitatively analyzed. In measurement, the coupling gap between the collection tapered fiber and the μS surface allows us to select the single- or the multi-emitted modes. The integration of a μS with SOI slotted PhC waveguides was proposed and modelled with the help of 3D-FDTD simulations. It was shown that this compact structure works, and further research for applications of ultrahigh sensitivity sensors, lasing sources and towards the advanced quantum communications.

ACKNOWLEDGMENTS. The authors would like to thank the supports of Vietnam Academy of Science and Technology (VAST) under grant number “KHCBVL.06/21-22”.

REFERENCES

[1] K. J. Vahala, Optical microcavities, *Nature*, 2003, **424**, 839.

[2] P. R. Berman, Cavity Quantum Electrodynamics, Academic Press, New York, 1994.

[3] J. U. Fürst, D. V. Strekalov, D. Elser, A. Aiello, U. L. Andersen, C. Marquardt, G. Leuchs, Low-threshold optical parametric oscillations in a whispering gallery mode resonator, *Phys. Rev. Lett*., 2010, **105**, 263904.

[4] T. Asano, Y. Ochi, Y. Takahashi, K. Kishimoto, S. Noda, Ultrahigh-Q photonic crystal nanocavities fabricated by CMOS process technologies, *Opt. Exp*., 2017, **25**, 18165.

[5] A. Toncelli, N. E. Capuj, B. Garrido, M. Sledzinska, C. M. Sotomayor-Torres, A. Tredicucci, D. Navarro-Urrios, Mechanical oscillations in lasing microspheres, *J. Appl. Phys*., 2017, **122**, 053101.

[6] G. C. Righini, S. Soria, Biosensing by WGM microspherical resonators, *Sensors*, 2016, **16**, 905.

[7] P. Del'Haye, O. Arcizet, M. L. Gorodetsky, R. Holzwarth, T. J. Kippenberg, Frequency comb assisted diode laser spectroscopy for measurement of microcavity dispersion, *Nat. Photon*. 2009, **3**, 529.

[8] M. L. Gorodetsky, V. S. Ilchenko, Optical microsphere resonators: optimal coupling to high-Q whispering-gallery modes, *J. Opt. Soc. Am. B*, 1999, **16**, 147.

[9] K. Nozaki, E. Kuramochi, A. Shinya, M. Notomi, 25-channel all-optical gate switches realized by integrating silicon photonic crystal nanocavities, *Opt. Express*, 2014, **22**, 14263.

[10] P. Sibson, J. E. Kennard, S. Stanisic, C. Erven, J. L. O'Brien, M. G. Thompson, Integrated silicon photonics for high-speed quantum key distribution, *Optica*, 2017, **4**, 172.

[11] K. Xu, Integrated silicon directly modulated light source using p-well in standard CMOS technology, *IEEE Sens. J*., 2016, **16**, 6184-6191.

[12] S. Makino, Y. Ishizaka, K. Saitoh, M. Koshiba, Slow-light-enhanced nonlinear characteristics in slot waveguides composed of photonic crystal nanobeam cavities. *IEEE Photon. J*., 2013, **5**, 2700309.

[13] A. Taflove, Computational Electrodynamics, Artech House, Boston, 1995.

[14] B. E. Little, J. -P. Laine, H. A. Haus, Analytic theory of coupling from tapered fibers and half-blocks into microsphere resonators, *J. Lightwave Technol*., 1999, **17**, 704.

[15] S. M. Spillane, T. J. Kippenberg, O. J. Painter, K. J. Vahala, Ideality in a fiber- taper- coupled microresonator system for application to cavity quantum electrodynamics, *Phys. Rev. Lett*., 2003, **91**, 043902.

[16] J. D. Joannopoulos, S. G. Johnson, R. D. Meade, J. N. Winn, Photonic Crystals: Molding the Flow of Light, Second Edition, Princeton Univ. Press, 2008.

[17] V. H. Pham, H. Bui, T. S. Pham, T. A. Nguyen, T. V. Nguyen, H. T. Le, T. N. Bui, V. P. Nguyen, R. Coisson, Control of whispering-gallery-mode spectrum from erbium-doped silica microsphere lasers *J. Opt. Soc. Am. B*, 2013, **30**, 1586.

[18] F. Lissillour, D. Messager, G. Stéphan, P. Féron, Whispering-gallery-mode laser at 1.56 mm excited by a fiber taper, *Opt. Lett*., 2011, **26**, 1051.

[19] C. Dong, Y. Xiao, Y. Yang, Z. Han, G. Guo, L. Yang, Directly mapping whispering gallery modes in a microsphere through modal coupling and directional emission, *Chinese Opt. Lett*., 2008, **6**, 300.

[20] S. G. Johnson and J. D. Joannopoulos, Block-iterative frequency-domain methods for Maxwell's equations in a planewave basis *Opt. Exp*., 2001, **8**, 173.

 ISBN:

A THEORETICAL STUDY OF THE BAND STRUCTURE AND OPTICAL PROPERTIES OF TWO-DIMENSIONAL MATERIAL Mo_2CF_2

Kieu-Anh Thi Doan[1*], Minh Hong Pham[1], Marilou Cadatal-Raduban[2], Linh Phan-Thuy Tran[3] and Mui Viet Luong[4]

[1]*Institute of Physics, Vietnam Academy of Science and Technology, Viet Nam*

[2]*Centre for Theoretical Chemistry and Physics, School of Natural and Computational Sciences, Massey University, New Zealand*

[3]*Department of Physics, Hanoi National University of Education, Viet Nam*

[4]*Graduate School of Engineering, Osaka University, Japan*

*E-mail: *kieuanhdt99@gmail.com*

Abstract. Density Functional Theory (DFT) is implemented in CASTEP of Materials Studio package to calculate the electronic band structure and optical properties of bulk Mo_2CF_2. The Perdew Burke Ernzerhof (PBE) formalism was employed with generalized gradient approximation (GGA) for all calculations. The electronic and optical properties of bulk Mo_2CF_2 were calculated with different layer distances by changing the lattice constant *c* in the unit cell. It is found that two dimensional Mo_2CF_2 is a semiconductor with an indirect band gap of 0.282 eV when c = 7 Å. This band gap increases with increasing lattice constant along the *c* axis. The conduction band minimum is mainly from the Mo-d orbital while the valence band maximum is mainly come from F-p with a minor contribution from the C-p orbitals. The optical properties are calculated for various layer distances in view of potential photoelectronic applications. The effect of layer distance can be extended to other MXene materials.

Keywords: *Two dimensional Mo_2CF_2, Semiconductor, Energy bands, Optical properties.*

I. INTRODUCTION

Two-dimensional MXenes have a large family of materials and their electronic characters can be metallic (e.g. Mo_2CO_2, and Mo_2CS_2) or semiconducting (e.g. Mo_2CF_2 and Mo_2CCl_2) [1], depending on the functionalization group (e.g. X= F, O, OH, Cl,…). MXenes are synthesized by using some acid like hydrofluoric acid (HF) solutions and sonication to exfoliate some members of the MAX phase family into 2D transition metal carbide and nitride layers. The chemical fomular of MXene is $M_{n+1}X_nT_x$, where M is an early transition metal, X is carbon and/or nitrogen and T is a functional group on the surface, typical oxigen (O), hydroxyl (OH) and fluorine (F). These materials also have potential in many experimental and theoretical studies that predict Mxenes possess excellent device applications. For examples, many applications have been proposed for MXenes in electrodes for supercapacitors such as Li-, Na- and K-ion batteries [2,3], promising materials for catalysts [4,5], photocatalytic reactions [6], hydrogen storage media [7], or transparent conductors [8].

From the discovery of MXenes, Mo_2CF_2 indicated significant new potential device applications with many interest researches. This material is attracting much attention as electrode materials due to their excellent energy storage properties and good electrical conductivity. A more recent technology has drawn for bulk Mo_2CF_2 to use in energy storage: Li-ion batteries [9] or promise for thermoelectric material [9,10]. By applying this model, we also can calculate for other 2D material which is promising for electronic applications.

Therefore, in this review, to clear up the electronic structure, and optical properties of bulk Mo_2CF_2, we performed a study using a planar wave Norm conserving pseudopotential technique based on first-principles density functional theory with different layer distances by changing the lattice constant *c* in the unit cell. The rest of this work is organized as follows. The computational method that we used in this work is shown in Section 2. In Section 3, we briefly describe the results and discussion. Firstly, the structure crystal of bulk Mo_2CF_2 is described. Then, the electronic and optical properties using GGA calculations are displayed. Section 4 we give a short summarizes our findings and outlook for future research on Mo_2CF_2.

II. COMPUTATIONAL METHOD

All calculations are performed based on the first-principle density functional theory (DFT) as implemented in CASTEP codes in Material Studios package. The exchange correlation is described in Perdew - Burke - Ernzerhof (PBE) of the generalized gradient approximation (GGA). The cutoff energy and the k reciprocal lattice points for our calculation are 500 eV and 5×5×1, respectively. We carry out our calculations at different layer distances by changing the lattice constant *c* in the unit cell. Atomic structures were visualized with VESTA software. Following the structure, all of the results of bulk M_2CF_2 are calculated with high symmetry points using the G (0,0,0) - M (1/2,0,0) - K (1/3,1/3,0) - G (0,0,0) k - path and also compared to the previous calculation. Additionally, the optical properties such as dielectric function, refractive index, reflectivity, absorption coefficient, and conductivity function are calculated for various layer distances in view of potential photoelectronic applications.

III. RESULTS AND DISCUSSION

3.1. Crystal structure

Figure 1a presents the crystal structure of bulk Mo_2CF_2. Structurally, the crystal structure of Mo_2CF_2 includes two Mo atoms, one C and two F atoms which reside in P1 space group. These atoms are arranged in a triple - layer where C layer is sandwiched between two Mo and F layer. Figure 1b show the 2×2 supercell from top and side views. Khazaei et al [1,9] reported that Mo_2CF_2 has two types of hollow sites exist: the hollow sites without carbon atom (A) and the hollow sites with carbon atom (B).

With the lattice relaxation calculation and using GGA functional, the band gap energy with different layer distances are calculated by changing the lattice constant *c* as

 ISBN:

presented in Table 1. It can be said that the band gap energy calculated for bulk Mo_2CF_2 are increase with increasing lattice constant along the *c* axis. In additional, we also determined the bond length between each atom in the unit cell. These values are consistent with the previous report [11].

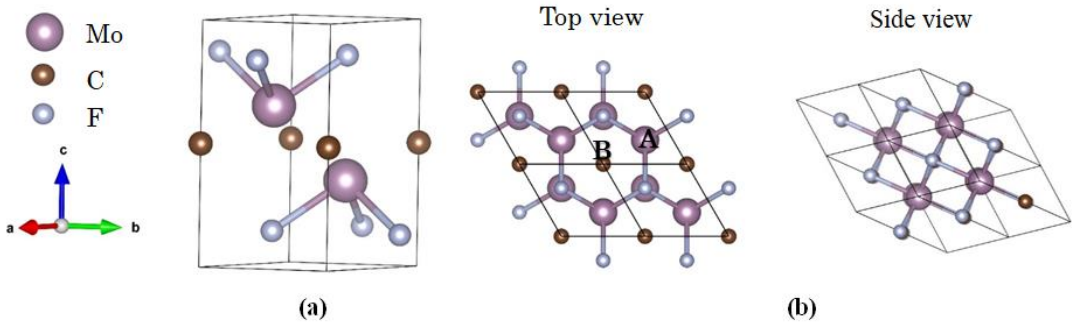

Fig. 1. *Crystal structure of bulk Mo_2CF_2 (a); Top and side views of bulk Mo_2CF_2 with functionalized F at different positions (b).*

Table 1. *Band gap energy corresponding to the lattice parameter.*

Lattice constant c (Å)	Band gap energy (eV)	d_{Mo1-F1} (Å)	d_{Mo1-C1} (Å)
7	0.282	2.28742	2.10653
8	0.304		
9	0.301		
10	0.292		

3.2. Electronic properties

For a detailed, now we turn on the analysis of electronic properties. The electronic band structures and density of states of Mo_2CF_2 are presented in Figure 2. It is seen that the indirect band gap of bulk Mo_2CF_2 has value of 0.282 eV when c = 7 Å. This value in excellent agreement with the previous report value of 0.27 eV [1].

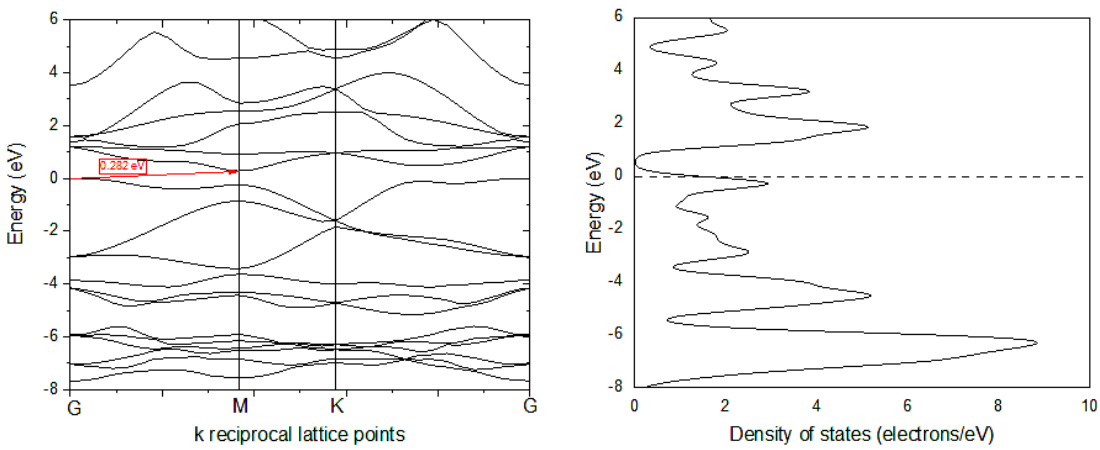

Fig. 2. *Band structure and density of states for bulk Mo_2CF_2.*

The total and partial densities of states are displayed in the Figure 3. An interesting feature arises from the PDOS of the Mo_2CF_2 is that Mo-d states of the Mo_2CF_2 bulk mainly contribute to the conduction band minimum, while valence band maximum is mostly populated by F-p states with a minor contribution from the C-p states. The results are in good agreement with previous report [1].

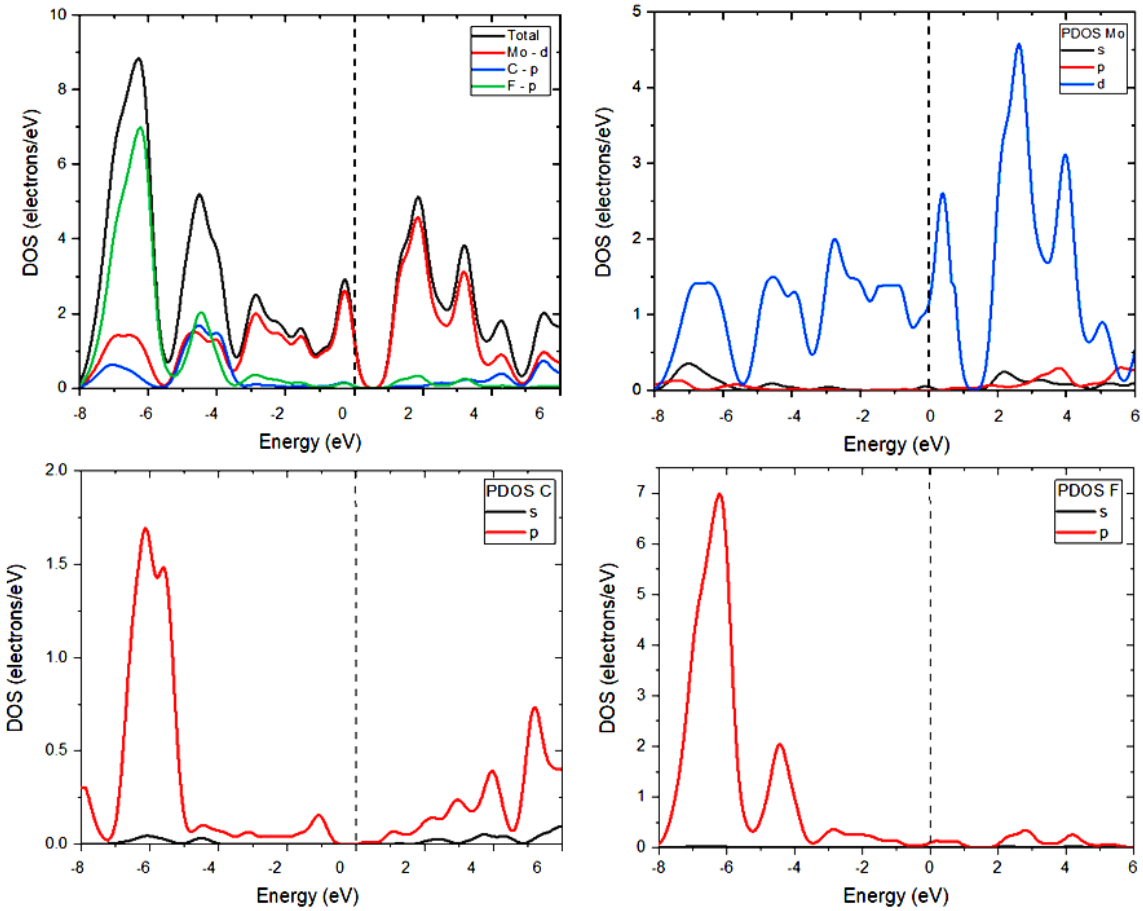

Fig. 3. *Total and projected density of states of Mo_2CF_2 on different atoms and different atomic orbitals.*

3.3. Optical properties

In this section, we have calculated optical properties depend on energy and wavelength. It is noted that all of our results will be compared to the results of another MXenes, $Ti_3C_2X_2$. Figure 4 are displayed the real and imaginary parts of the dielectric function and the refractive index as a function of energy for bulk Mo_2CF_2. It is obvious that both the real and imaginary part of dielectric function slightly increases and then decrease drastically from E = 0 eV. The difference in the dielectric function value between Mo_2CF_2 and $Ti_3C_2X_2$ appears at the location of the energy to obtain the maximum real part of dielectric function. To be more specific, for Mo_2CF_2, we obtained the maximum value for the real part of dielectric function located at the energy equal to 1.3 eV, while this value for the imaginary part is 1.57 eV. This energy is larger than its value for $Ti_3C_2X_2$ [12] (around 0 eV). This may provide a possible way for finding materials with appropriate static dielectric constants. Based on the dielectric function, the other optical properties can be obtained. The real part of dielectric function gives the refractive index, while the imaginary part of dielectric function gives the absorption spectrum of the material.

It is clearly that at low energy, the functionalization with different layer distance c reduces the refractive index (n) and the extinction coefficient (k). We also obtained the maximum refractive index at the energy larger than 0 eV. However, the maximum

 ISBN:

refractive index values between Mo_2CF_2 and $Ti_3C_2X_2$ nearly the same (n_{max} around 5.65) [12].

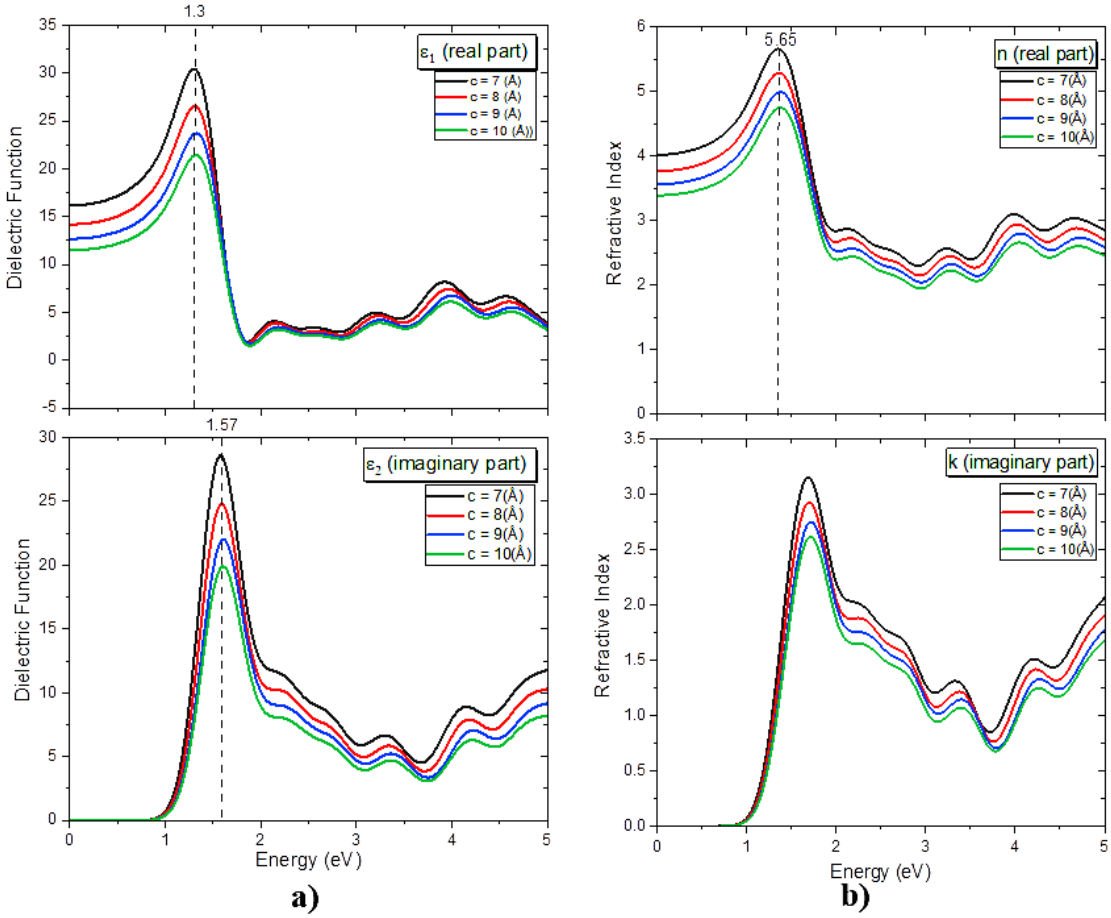

Fig. 4. *The real (ε_1) and imaginary (ε_2) parts of the dielectric function for Mo_2CF_2 (a); Refractive index of the bulk Mo_2CF_2 (b).*

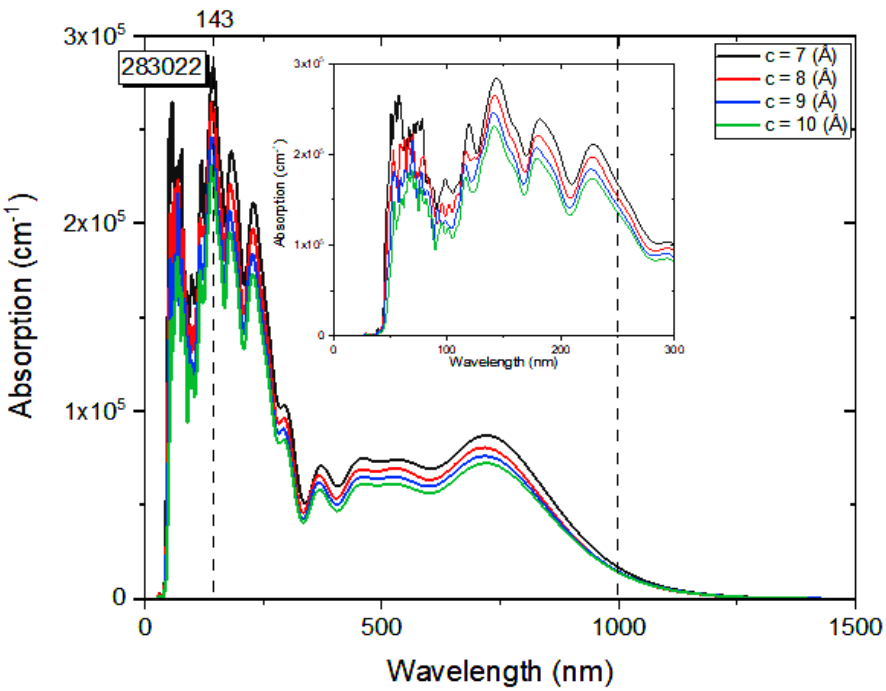

Fig. 5. *Absorption spectrum of the bulk Mo_2CF_2.*

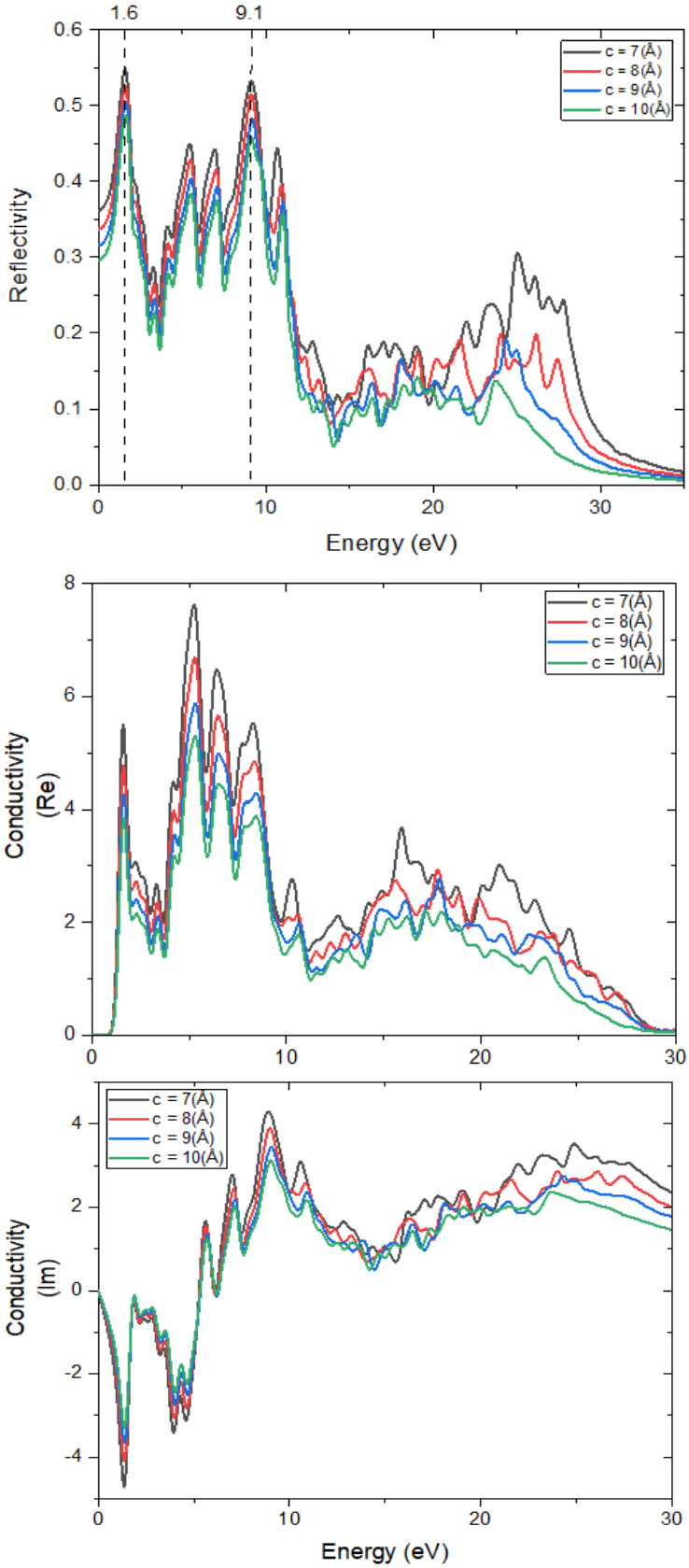

Fig. 6. *Reflectivity and Conductivity of bulk Mo_2CF_2.*

The results of the absorption coefficient as a function of wavelength, shown in Figure 5. In general, when the wavelength increases, the absorption coefficients fluctuate

 ISBN:

drastically. It has been found that bulk Mo_2CF_2 has maximum absorption coefficient at about 143 nm, which is slightly larger than other Mxenes $Ti_3C_2X_2$ [12]. However, the maximum absorption value of Mo_2CF_2 is 283022 cm^{-1} and this value is smaller than $Ti_3C_2X_2$. Additionally, when the wavelength is larger 1000 nm, absorption coefficients of bulk Mo_2CF_2 almost decrease to zero. This indicates that bulk Mo_2CF_2 becomes colorless and transparent when the wavelength is larger 1000 nm. Larger absorption in bulk due to smaller band gap of Mo_2CF_2.

Finally, the reflectivity and conductivity of bulk Mo_2CF_2 is depicted in Fig. 6. First of all, Mo_2CF_2 shows larger reflectivity with two pronounced peaks at 1.6 eV and 9.1 eV. Moreover, the larger reflectivity and conductivity were obtained for all the lattice parameter c in the ultraviolet region (5 eV <E< 10 eV). This makes Mo_2CF_2 as a new potential material for practical applications for anti-ultraviolet ray coating.

IV. CONCLUSIONS

In this work, we calculated the electronic structure and optical properties with different layer distance for bulk Mo_2CF_2 using the DFT is implemented in CASTEP codes. In the electronic properties, it was observed that bulk Mo_2CF_2 has a narrow indirect band gap, is promising for thermoelectric applications. From the total and partial density of state, we obtained the transition between band gap energy from Mo - d orbitals and minor contribution from F-p orbitals. In the optical properties section, our calculations showed that the static dielectric constants flexible, indicated significant new potential of dielectric materials. Additionally, the maximum refractive index for the bulk is promising candidate for penetrating into the materials before being absorped. Moreover, calculations showed that bulk Mo_2CF_2 becomes colorless and transparent when the wavelength is larger than 1000 nm. In the ultraviolet region, the higher reflectivity and conductivity make Mo_2CF_2 as a new potential material for practical applications for anti - ultraviolet ray coating.

ACKNOWLEDGMENTS. This research was funded by the International Center of Physics under the auspices of UNESCO (through project number ICP.2021.07).

REFERENCES

[1] Khazaei M., Arai M., Sasaki T., Estili M. & Sakka Y., Two-dimensional molybdenum carbides: potential thermoelectric materials of the MXene family, *Phys. Chem. Chem. Phys.*, 2014, **16**, 7841-7849.

[2] Naguib M., Halim J., Lu J., Cook K. M., Hultman L., Gogotsi Y. & Barsoum M. W., New two-dimensional niobium and vanadium carbides as promising materials for Li-ion batteries, *Journal of the American Chemical Society*, 2013, **135**, 15966-15969.

[3] Xie Y., Dall'Agnese Y., Naguib M., Gogotsi Y., Barsoum M. W., Zhuang H. L., & Kent P. R. C., Prediction and Characterization of MXene Nanosheet Anodes for non-lithium-ion batteries, *ACS Nano*, 2014, **8**, 9606-9615.

[4] Fan G., Li X., Ma Y., Zhang Y., Wu J., Xu B., et al., Magnetic, recyclable $Pt_yCo_{1-y}/Ti_3C_2X_2$ (X = O, F) catalyst: a facile synthesis and enhanced catalytic activity for hydrogen generation from the hydrolysis of ammonia borane, *New Journal of Chemistry*, 2017, **41**, 2793-2799.

[5] Seh Z. W., Fredrickson K. D., Anasori B., Kibsgaard J., Strickler A. L., Lukatskaya M. R., et al., Two-dimensional molybdenum carbide (MXene) as an efficient electrocatalyst for hydrogen evolution, *ACS Energy Letters*, 2016, **1**, 589-594.

[6] Ling C., Shi L., Ouyang Y., Chen Q., Wang J., Transition metal-promoted V_2CO_2(MXenes): A new and highly active catalyst for hydrogen evolution reaction, *Advanced Science*, 2016, **3**, 1600180.

[7] Hu Q., Sun D., Wu Q., Wang H., Wang L., Liu B., et al., MXene: A new family of promising hydrogen storage medium, *The Journal of Physical Chemistry A*, 2013, **117**, 14253-14260.

[8] Yang Y., Umrao S., Lai S., Lee S., Large-area highly conductive transparent two-dimensional Ti_2CT_x Film, *The Journal of Physical Chemistry Letters*, 2017, **8**, 859-865.

[9] Mehta V., Tankeshwar K., Saini H. S., Prediction of Mo_2CF_2 monolayer as a novel anode material for Li-ion batteries: A first principle study, *Dae Solid State Physics Symposium*, 2019, **2115**(1), 030576.

[10] Bae S., Kang Y. G., Khazaei M., Ohno K., Kim Y. H., Han M. J., et al., Electronic and magnetic properties of carbide Mxenes-the role of electron correlations, *Materials Today Advances*, 2020, **9**, 100118.

[11] Khan S. A., Rehman G., Ahmad I., Maqbool M., Franchini C., Amin B., Intriguing electronic and optical properties of M_2CX_2 (M=Mo, W; X=O, F) MXenes and their van der Waals heterostructures, *Chemical Physics Letters*, 2019, **731**(12), 136614.

[12] Jiang X., Kuklin A. V., Baev A., Ge Y., Ågren H., Zhang H., & Prasad P. N., Two-dimensional MXenes: From morphological to optical, electric, and magnetic properties and applications, *Physics Reports*, 2020, **848**, 1-58.

 ISBN:

EFFECT OF SILVER LAYER ON INTERMETALLIC COMPOUND FORMATION AT SAC305/METAL PAD INTERFACE

Titipa Zunsuwan[1], Phakkhaphum Lethaisong[1,2] and Anusara Srisrual[1*]

[1]*IMI, Faculty of Applied Science, King Mongkut's University of Technology North Bangkok, 1518, Pracharat 1, Wongsawang, Bangsue, Bangkok, Thailand*

[2]*SICC, Faculty of Applied Science, King Mongkut's University of Technology North Bangkok, 1518, Pracharat 1, Wongsawang, Bangsue, Bangkok, Thailand*

*E-mail: *anusara.s@sci.kmutnb.ac.th*

Abstract. Since interconnect between electronic components and printed circuit boards strongly affect to product reliability that plays a key role by intermetallic phase at the interface of interconnect, this work aims to study the effect of silver surface finish on intermetallic compound (IMC) formation at SAC305 lead-free solder/metal pad interface. For this purpose, FR4 printed circuit boards (PCBs) were used and prepared with the metal pad surface finish of bare copper and plated silver that the silver layer was also varied in thickness. SAC305 was pasted on PCB pads, and then soldering is performed in the reflow oven. After that, the thermal aging was performed at 150 °C up to 48 hours. Cross-section technique was applied for interconnect investigation. Morphology was revealed by scanning electron microscope (SEM). Chemical compositions of IMC were analyzed by energy dispersive x-ray spectroscopy (EDS). The results showed the initial formation of Cu_6Sn_5, subsequently with Cu_3Sn intermetallic compound layer in both copper and silver surface finish. The micrographs showed a thicker IMC layer in silver layer conditions, however, a thickness of silver layer does not significantly affect to IMC formation. The higher Cu_3Sn fraction in case of copper pad implies to the faster Cu_3Sn formation, compared to silver pad. Therefore, silver layer shows the effect on IMC growth rate but does not effect on morphology and type of IMC layer.

I. INTRODUCTION

Failures of electronic boards in service can occur when the devices get stresses such as mechanical, electrochemical, or thermal stress. One of the failures, which often found, is the crack at the interconnect between printed circuit board and component [1-3], including the internal package interconnects [4] that usually initial occur and grow at the intermetallic compound layer between solder and metal interfaces. Intermetallic compound phase is formed by two or more metals through atomic diffusion. This phase is typically brittle than the original phases that refers to metal solder and metal substrate in electronic devices.

In printed circuit board assembly process, intermetallic compound layer might form in solder bulk, solder/device interface, and solder/PCBs interface. The formation of intermetallic compound depends on many factors such as process parameters, solder materials, and PCB pad materials. S. Gong et al. [5] showed effect of reflow times on intermetallic compound types and thickness that Cu_6Sn_5 and Cu_3Sn was found, and longer reflow times promoted the thicker layer. V. P. Sharma and N. V. Datla [6] reported the increase intermetallic compound layer thickness with aging time. To improve electronic

ISBN:

joints, solder materials are wildly studied by either commercial solder selection or adding new elements. Q. Guo et al. [7] reported intermetallic compound layer growth of Sn-10Bi solder/Cu was slower than Sn-Ag-Cu solder/Cu, while, types of intermetallic compounds were the same. S.-H. Hu et al. [8] reported the effect of Bi on intermetallic compound growth rate that Bi addition enhanced the growth rate of Cu_6Sn_5 but do not effect on Cu_3Sn. J.-W. Yoon et al. [9] reported intermetallic compound formed at the interface with different surface finishes as electroless nickel immersion gold (ENIG) and electroless nickel-electroless palladium-immersion gold ENEPIG that either $(Cu,Ni)_6Sn_5$ or $(Ni,Cu)_3Sn_4$ intermetallic compound formed both surface finishes but small amount of Pd in both intermetallic compound phases was found in ENEPIG. Pd layer in ENEPIG suppressed the growth of the compound layer, resulting in the superior interfacial stability of the solder joint. C.-L. Kao and T.-C. Chen [10] reported the effect of surface finish on intermetallic compound and strength of joints with Sn-1Ag-0.5Cu solder. $(Cu,Ni)_6Sn_5$ and $(Ni,Cu)_3Sn_4$ formed for Ni/Au surface finish. Cu_6Sn_5 and Cu_3Sn formed for OSP surface finish. Only $(Cu,Ni,Pd)_6Sn_5$ formed for Ni/Pd/Au surface finish. The results showed a higher strength of intermetallic compound for Ni/Pd/Au surface finish, comparing to Ni/Au and OSP (Organic solderability preservative) surface finish. Therefore, intermetallic compound is strongly affected to reliability of products and many factors affected to intermetallic compound formation.

This work aims to study the effect of silver surface finish on intermetallic compound formation at SAC305 lead-free solder/metal pad interface. In addition, thermal process condition as aging time also was studied.

II. EXPERIMENT

The experiments were designed by varied metal surface finish on printed circuit board pad (copper and silver) and thermal process (with and without aging) as shown in Table 1. FR4 printed circuit boards were used and prepared with the metal pad surface finish of bare copper and immersed silver that the silver layer was also varied at 0.6, 0.9, and 1.2 micrometers in thickness. SAC305 lead free solder, which composes of 96.5%Sn 3.0%Ag and 0.5%Cu, was pasted on PCB pads, and then soldering is performed in the reflow oven. In case of samples with aging, the isothermal treatment was performed at 150 °C for 6, 24, and 48 hours. Fig. 1 presents a thermal process conditions of reflow and aging profile.

Table 1. *Experimental designs.*

Metal surface finish	Cu	Ag (0.6, 0.9, 1.2 μm)
Aging condition:		
No aging		
Aging temperature (°C)	150	
Aging time (hrs.)	6, 24, 48	

 ISBN:

The obtained samples were prepared for characterization by cross-sectioning technique that were polished down to 0.3 micrometers and etched by etchant (1 ml HCl, 2.5 ml HNO_3, in ethanol 50 ml) for revealing the interconnect microstructure.

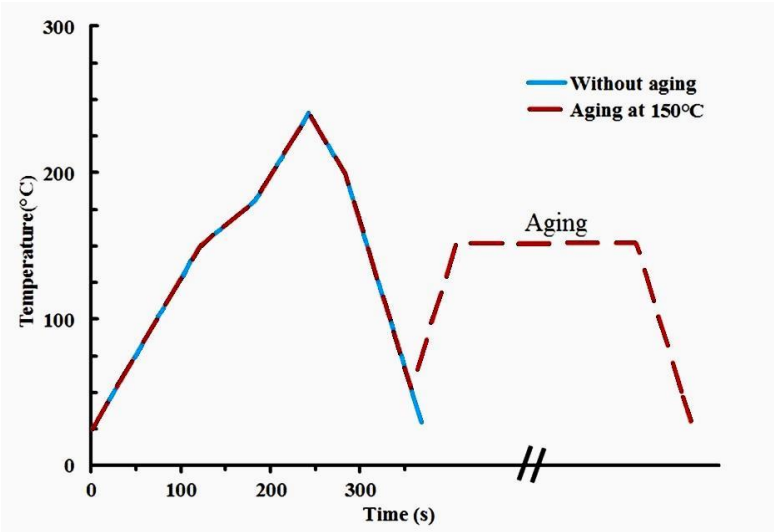

Fig. 2. *Thermal process conditions: reflow profile with and without aging.*

Morphology of intermetallic compound at interconnect was revealed by FEI Quanta 450 scanning electron microscope. Chemical compositions of intermetallic compound were analyzed by EDAX energy dispersive x-ray spectroscopy that could be used for identifying a forming intermetallic compound type. Finally, thickness of each intermetallic compound was consequently evaluated from the obtained micrographs to understand formation and growth of intermetallic compound.

III. RESULTS AND DISCUSSION

Morphology of Intermetallic Compound

Fig. 2 shows the backscattered electron micrographs at the interface between SAC305 lead free solder and PCB pad of the samples with difference in surface finishes and thermal conditions. In all the samples, intermetallic compounds are revealed in between SAC305 solder and copper, even in samples with silver layer. No existence of silver layer at the interface because silver is fast dissolve in solder bulk during soldering process when solder became liquid. Intermetallic compound layer formed in irregular shape and wavy, however, the layer became smoother and seem to be thicker after isothermal aging process. In addition, a thicker intermetallic compound layers are found in silver pad samples (Fig. 2c,e and d,f), comparing to copper pad samples (Fig. 2a and b). Moreover, the micrographs also reveal some intermetallic compound phases precipitated in solder matrix. Therefore, silver layers promote intermetallic compound formation but did not significantly effect on its morphology.

According to backscattered electron micrograph concept, which the backscattered electron yield depends on atomic number of sample, only one intermetallic compound type is revealed at the solder/PCB pad interface in case of no aging samples (Fig. 2a,c,d) but

two different intermetallic compounds are revealed at the interface in case of 48 hours aging samples (Fig. 2b,d,f)). Hence, aging process affected on intermetallic compound type and morphology.

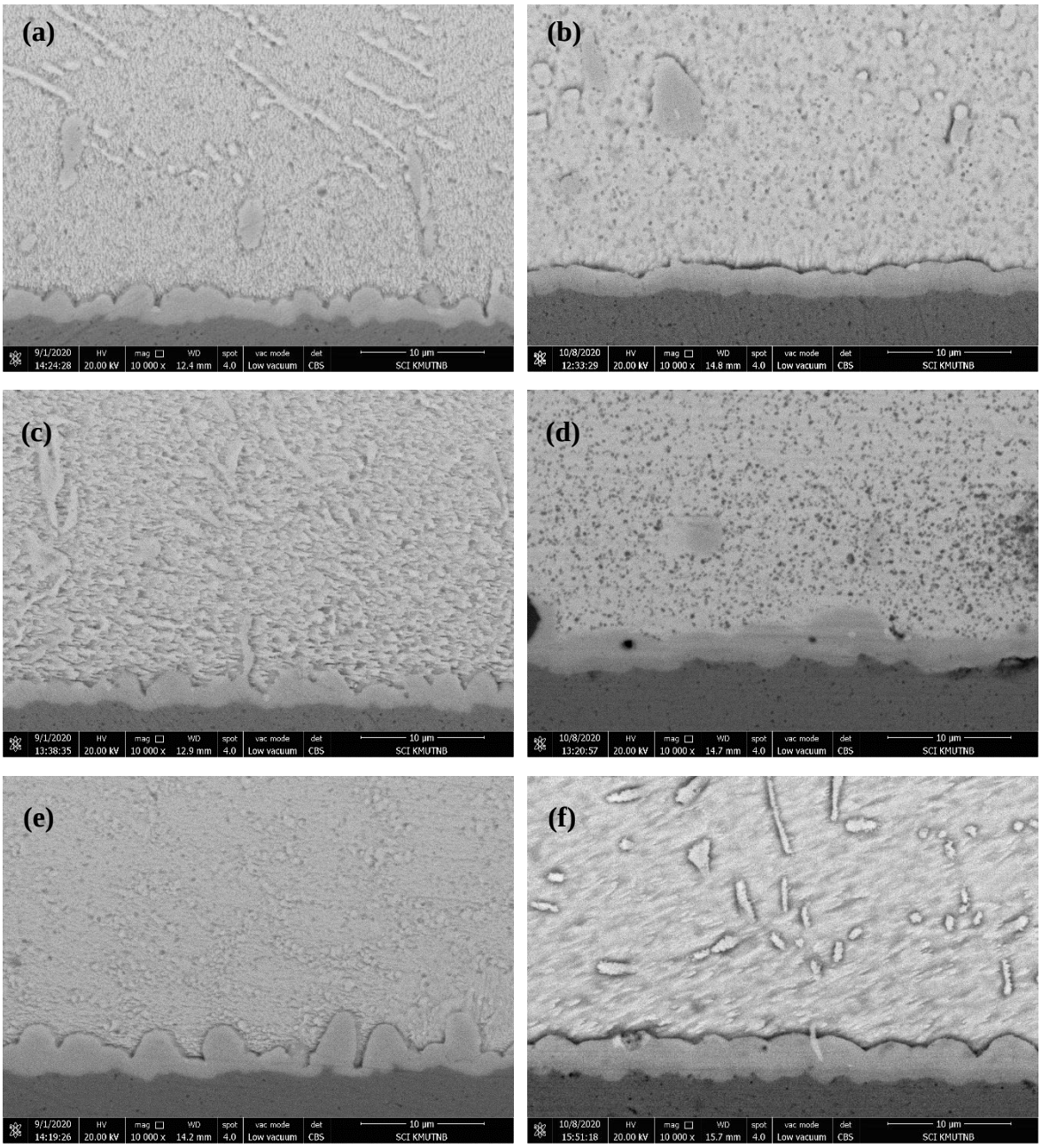

Fig. 2. *The interface between SAC305 lead free solder and PCBs pad of the samples differed in surface finishes and thermal conditions: copper without aging (a) with 48 hours aging time (b), 0.6 μm silver without aging (c) with 48 hours aging time (d), and 1.2 μm silver without aging (e) with 48 hours aging time (f).*

Chemical Composition of Intermetallic Compound

Fig. 3 shows EDS spectra and quantitative analysis tables obtained from intermetallic compound layer of 0.9 μm silver pad sample with aging at 150 °C for 24 hours. Fig. 3a results of the upper light layer report 53.68 at% of copper and 46.32 at% of tin that can imply to be Cu_6Sn_5 intermetallic compound. Fig. 3b results of the lower dark layer report

 ISBN:

74.45 at% of copper and 25.55 at% of tin that can imply to be Cu_3Sn intermetallic compound. The element analysis were performed on all samples that the results reported only two intermetallic compound types on the layers that are either Cu_6Sn_5 or Cu_3Sn similarly to the results in Fig. 3, depending on surface finishes and thermal conditions.

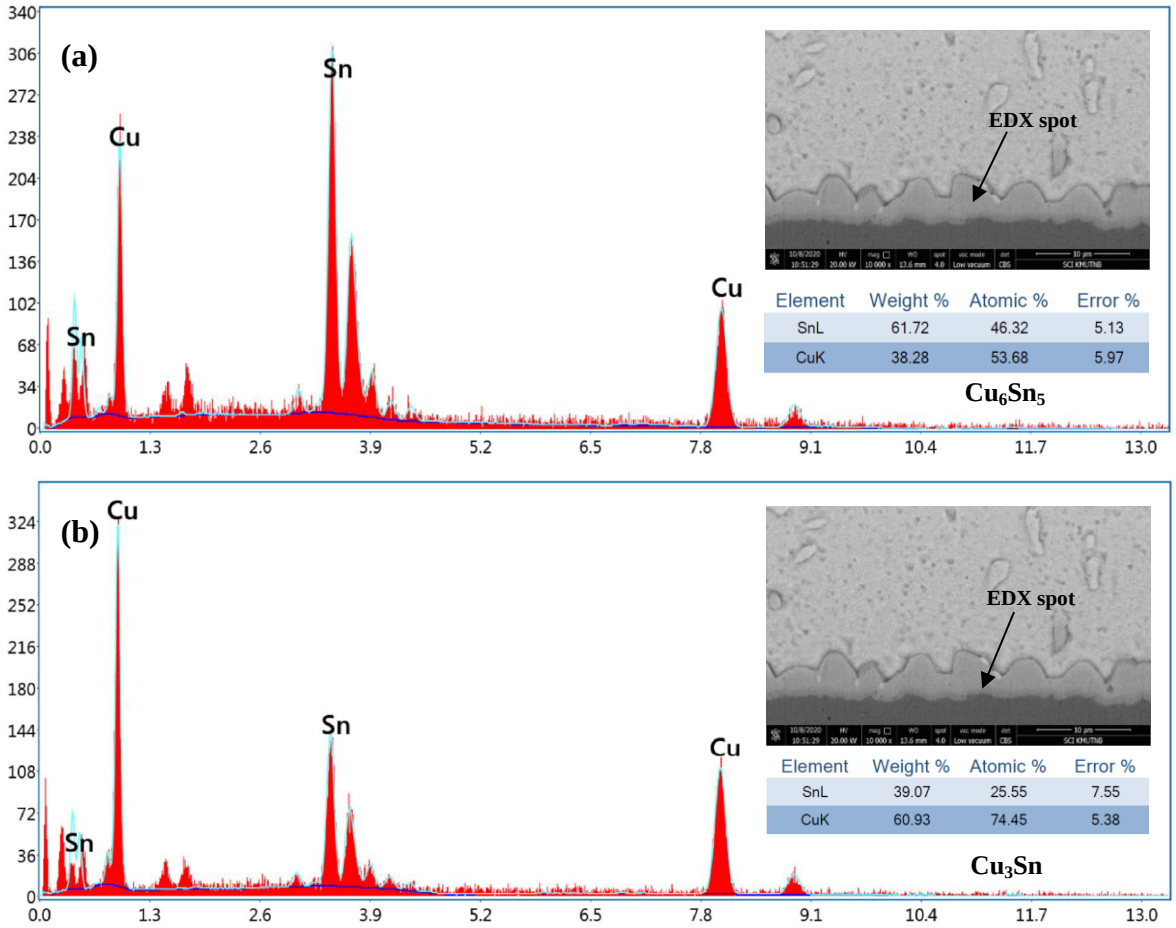

Fig. 3. *EDS spectra and quantitative analysis tables obtained from intermetallic compound layer of 0.9 μm silver pad sample with aging at 150 °C for 24 hours (a) Cu_6Sn_5 and (b) Cu_3Sn.*

Fig. 4 illustrates the examples of intermetallic compound layer identification at the solder/metal pad interface with different surface finishes and thermal conditions. Fig. 4a and 4b represent copper pad samples while Fig. 4c and 4d represent silver pad samples. The results obtained from both copper and silver pad samples coincidently show that only Cu_6Sn_5 layer formed at the interface in case of samples without aging as Fig. 4a and 4c, whereas, Cu_6Sn_5 and Cu_3Sn layer formed in case of samples with aging as Fig. 4b and 4d. Retained silver layer and silver in the intermetallic compound layer did not detected because silver is fast dissolve in solder bulk during soldering process when solder became liquid. Even in copper or silver surface finish, Cu_6Sn_5 is a typical intermetallic compound that initially formed at the solder/metal pad interface. Cu_3Sn subsequently formed in between Cu_6Sn_5 and copper layer because initial Cu_6Sn_5 phase behaved as a barrier and a smaller amounts of tin in Cu_6Sn_5 compared to SAC305. Therefore, a longer aging time conducts a new intermetallic compound phase, whilst, silver layer does not affect to intermetallic compound type even a longer time.

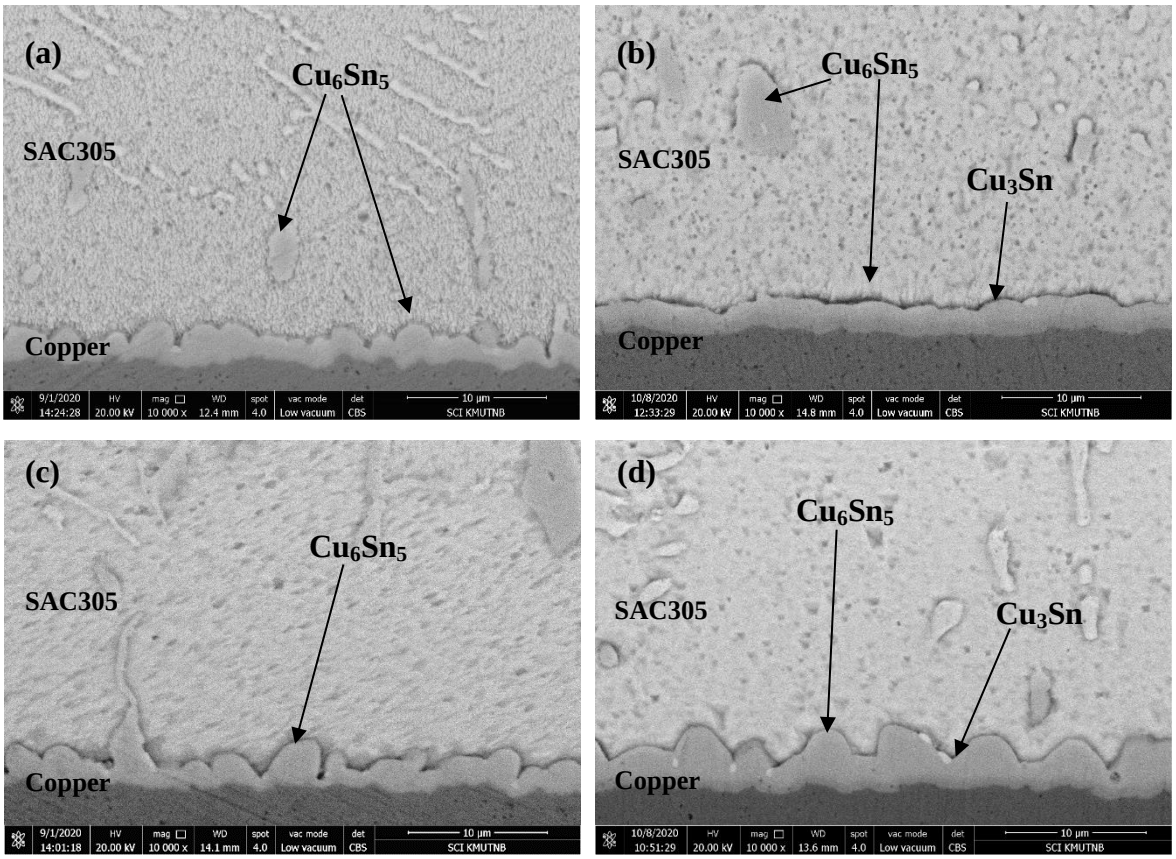

Fig. 4. *Intermetallic compound layer identification at the SAC305/metal pad interface with different surface finishes and thermal conditions: copper pad without aging (a) with 48 hours aging time (b), and 0.9 μm silver pad without aging (c) with 24 hours aging time (d).*

Thickness of Intermetallic Compound

The average total thickness of intermetallic compound layer at SAC305/metal pad interface is reported in Fig. 5. The total intermetallic compound thickness, which is a sum of Cu_6Sn_5 and Cu_3Sn layer thickness, in case of copper and silver surface finish coincidently shows that intermetallic compound layer was thicken when aging time increased. However, growth rate of intermetallic layer slightly decrease in a longer aging time. In addition, intermetallic compound layer is thicker in case of silver pad samples, while, a thickness of silver layer does not significantly affect to intermetallic formation, especially when the layer is thicker than 0.9 μm.

Fig. 6 reports Cu_3Sn fraction, which calculated from the ratio of Cu_3Sn thickness and total intermetallic compound thickness at SAC305/metal pad interface of samples with different surface finishes and thermal conditions. The results show that Cu_3Sn formed after aging and continuously increased according to the increment of aging time, however, the fraction became steady at a time in both copper and silver pad samples. Furthermore, the higher fraction of Cu_3Sn in case of copper pad implies to the faster Cu_3Sn formation, comparing to silver pad. Nevertheless, the fraction of Cu_3Sn of any samples seem to be limited at a similar steady state value that should be caused by the difference of elements mole fraction in Cu_6Sn_5 and copper layer.

 ISBN:

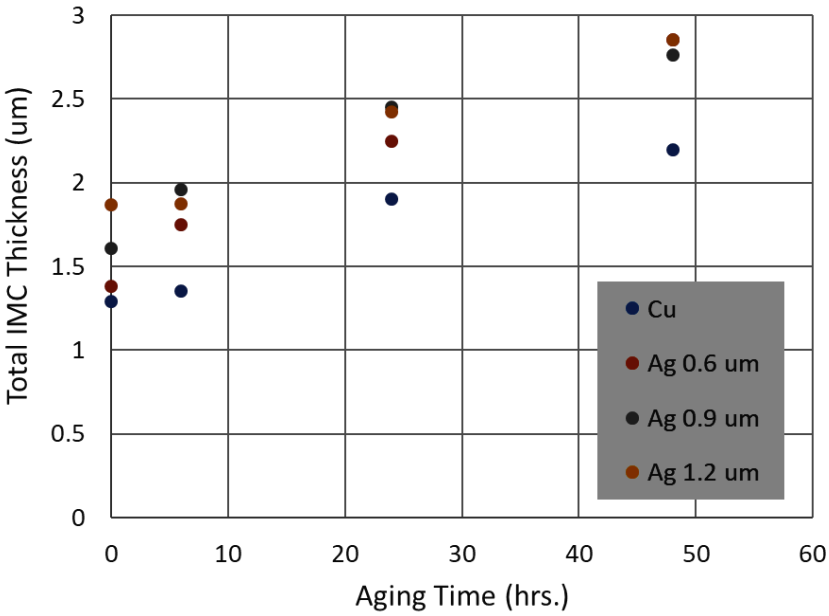

Fig. 5. *The total intermetallic compound layer thickness at SAC305/metal pad interface of samples with different surface finishes and thermal conditions.*

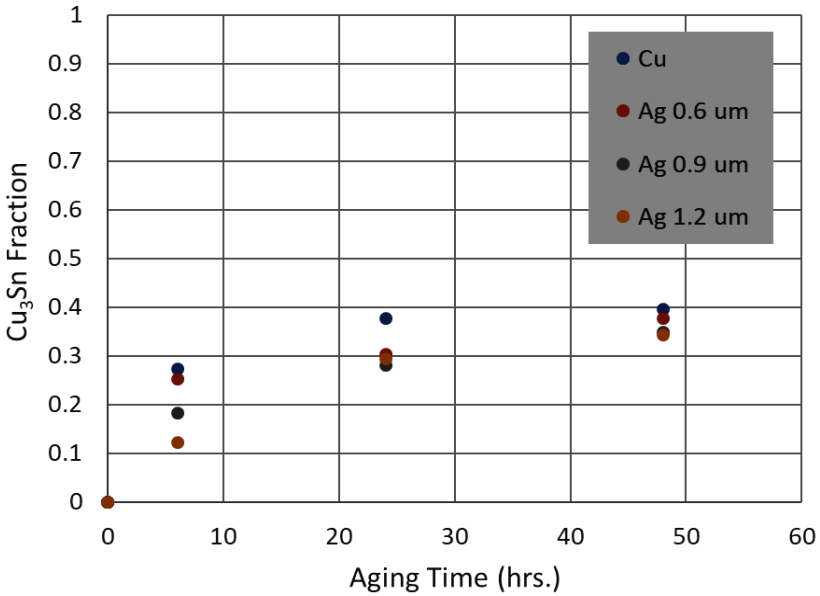

Fig. 6. *The fraction of Cu_3Sn layer thickness in total intermetallic compound layer thickness at SAC305/metal pad interface of samples with different surface finishes and thermal conditions.*

IV. CONCLUSION

All the results about intermetallic compound formation and growth at SAC305/metal pad interface, that were varied in metal surface finish as copper and silver differed in thickness, and thermal aging process, could be summarized as below.

- Aging time affected to thickness and morphology of intermetallic compound layer that gradually thicken and smoothen with the increasing of aging time.

- Silver layer surface finish fast dissolved in molten solder, leading to non-existence of silver layer after soldering.
- In both copper and silver metal pad, Cu_6Sn_5 was an initial intermetallic compound layer formed between solder and copper, subsequently with Cu_3Sn that formed in between Cu_6Sn_5 and metal pad with an increasing of the aging times.
- Silver layer promoted a thicker Cu_6Sn_5 intermetallic compound layer but retarded Cu_3Sn formation and growth. However, silver layer did not affect to morphology and type of intermetallic compound layer.

ACKNOWLEDGMENTS. The authors would like to thank Scientific Instrument and High performance Computing Center, Faculty of Applied Science, King's Mongkut University of Technology North Bangkok for supporting in part of characterization.

REFERENCES

[1] H.W. Zhang, Y. Liu and J. Wang, F.L. Sun, Effect of elevated temperature on PCB responses and solder interconnect reliability under vibration loading, *Microelectron. Reliab.*, 2021, **55**, 2391-2395.

[2] T. An, C. Fang, F. Qin, H. Li, T. Tang, and P. Chen, Failure study of Sn37Pb PBGA solder joints using temperature cycling, random vibration and combined temperature cycling and random vibration tests, *Microelectron. Reliab.*, 2018, **91**, 213-226.

[3] J. Gu, J. Lin, Y. Lei, and H. Fu, Experimental analysis of Sn-3.0Ag-0.5Cu solder joint board-level drop/vibration impact failure models after thermal/isothermal cycling, *Microelectron. Reliab.*, 2018, **80**, 29-36.

[4] K. Pongvittayapanu, A. Srisrual, and K. Fakpan, Effect of thermal cycling and vibration on cracking in Sn-3.0Ag-0.5Cu solder bump, *Mater. Today: Proc.*, 2021, doi: 10.1016/j.matpr.2021.10.222.

[5] S. Gong, G. Chen, S. Qu, A. Ren, V. Duk, Q. Shi, and G. Zhang, Shear strength and fracture analysis of Sn-9Zn-2.5Bi-1.5In and Sn-3.0Ag-0.5Cu paste with Cu-substrate joints under different reflow times, *Microelectron. Reliab.*, 2021, **127**, 114378.

[6] V. P. Sharma and N. V. Datla, Effect of aging time and loading rate on fracture behavior of Cu/Sn-0.7Cu solder joints, *Microelectron. Reliab.*, 2021, **127**, 114381.

[7] Q. Guo, Z. Zhao, and C. Shen, Comparison study on microstructure and mechanical properties of Sn-10Bi and Sn-Ag-Cu solder alloys and joints, *Microelectron. Reliab.*, 2017, **78**, pp.72-79.

[8] S.-H Hu, T.-C. Lin, C.-L. Kao, F.-Y. Huang, S.-C. Hsiao, and J.-C. Kuo, Effects of bismuth additions on mechanical property and microstructure of SAC-Bi solder joint under current stressing, *Microelectron. Reliab.*, 2021, **127**, 114041.

[9] J.-W. Yoon, B.-I Noh, and S.-B. Jung, Comparative study of ENIG and ENEPIG as surface finishes for a Sn-Ag-Cu solder joint, *J. Electron. Mater.*, 2011, **40**(9), 1950-1955.

[10] C.-L. Kao, T.-C. Chen, Ball impact responses of Sn-1Ag-0.5Cu solder joints at different temperatures and surface finishes, *Microelectron. Reliab.*, 2018, **82**, 204-212.

 ISBN:

OPTIMIZING THE PERFORMANCE OF FLEXIBLE β-GA_2O_3 SOLAR-BLIND PHOTODETECTOR GROWN ON OHP SUBSTRATES BY INSERTING ADHESION LAYERS

Vu Thi Kim Oanh[1*] and Eun Kyu Kim[2]

[1]*Institute of Physics, Vietnam Academy of Science and Technology*

[2]*Department of Physics, Hanyang University*

*E-mail: *vuthikimoanh92@gmail.com*

Abstract. Recently, the use of lightweight, cost-effective, easy-to-handle and robust deformable substrates plays a more and more significant role in the development trend of modern optoelectronic technology and our life. Therefore, the photodetectors fabricated on flexible substrates are attracting much interest. In an attempt to improve the quality of the flexible photodetectors, the stability issue still exists. The devices display naturally instability due to poor adhesion of amorphous semiconductor film on the flexible substrate and poor adhesion of metal electrodes on semiconductor film. To enhance chemical reactivity and adhesion of metal-semiconductor-flexible substrate, ultrathin adhesion layers are applied between the semiconductor film and the over metal. In this study, we investigate the influence of the Ti adhesion layer on the performance of Au/β-Ga_2O_3 on OHP substrate based-photodetector fabricated by pulsed laser deposition (PLD). By the presence of the Ti adhesion layer, the fabricated photodetector exhibits more excellent photoelectric performance and stability. Under flat state, the photocurrent obtained by Ti/Au bilayer-device (about 3.1×10^{-8} A) is dramatically higher than that obtained by pure Au-device (about 1.7×10^{-8}) at bias voltage of 10 V. After 250 repeated bending cycles, the photoresponsivity of pure Au-sample dropped about 20 times, while no much degradation in photoresponsivity was observed in Ti/Au bilayer-sample. The results reveal the importance of the adhesion layer in promoting the photodetector area.

I. INTRODUCTION

Recently, Ga_2O_3 based-photodetectors were successfully fabricated on a rigid substrate such as glass [1,2] and sapphire [3,4], however, these rigid substrates are hard and brittle, and thus the fabrication process needs a sophisticated technique. Therefore, instead of using rigid substrates, the use of lightweight, cost-effective, easy-to-handle and robust deformable substrates plays a more and more significant role in the development trend of modern optoelectronic technology and our life. Recently, the photodetectors fabricated on flexible substrates such as polyethylene terephthalate (PET) [5], polyethylene naphthalate (PEN) [6], and polyimide (PI) [7] has been reported. The flexible devices limit the maximum working temperature due to its low glass transition temperature, so their cannot work properly at high temperature. Therefore, exploring a high-withstood-heat substrate for high-performance Ga_2O_3 solar-blind photodetector is essential. The overhead projector (OHP) sheet can be a suitable material in which the glass transition temperature is 30-150 ^oC.

ISBN:

In an attempt to improve the quality of the flexible photodetectors, the stability issue still exists. The devices display naturally instability due to poor adhesion of amorphous semiconductor film on the flexible substrate and poor adhesion of metal electrodes on semiconductor film [1]. To enhance chemical reactivity and adhesion of metal-semiconductor-flexible substrate, ultrathin adhesion layers are applied between the semiconductor film and the over metal. The most used adhesion materials are Cr [8,9] and Ti [10,11], which are known to be more chemically reactive than over metals. However, the effect of these metals as the adhesion layer on the operation of photodetectors has been rarely studied.

In this work, we investigate the influence of the Ti adhesion layer on the performance of Au/β-Ga_2O_3 on OHP substrate based-photodetector fabricated by pulsed laser deposition (PLD). The optoelectronic characteristics of devices designed without and with Ti ultrathin film were investigated by current-voltage (I-V) curves, photoresponsivity, and external quantum efficiency. The difference in surface morphology of Au film before and after the presence of the Ti film was studied by scanning electron microscopy (SEM). By simply inserting the Ti layer and excellent optoelectronic properties are obtained. This demonstrates that the Ti adhesion layer has a great impact on the improvement of PDs quality.

II. EXPERIMENTS

β-Ga_2O_3 thin films were grown on the cost-effective glass and the flexible OHP substrate by PLD from a 99.99% pure 1 in. diameter Ga_2O_3 target. The deposition processes were performed in a vacuum chamber and were pumped down to a base pressure of 5×10^{-7} Torr. The laser ablation was carried out at the density of energy of 95 mT/cm^2 with a repetition rate of 10 Hz using neodymium-doped yttrium aluminum garnet (Nd:YAG) laser (at wavelength of 266 nm). The substrate temperature was kept at room temperature (RT). Each deposition process lasted for 12 min under the oxygen pressure of 50 mTorr. The Ga_2O_3 solar-blind PDs were constructed with a metal-semiconductor-metal structure by evaporation technique. The electrodes Ti/Au (5 nm/50 nm) were deposited at room temperature and a chamber pressure of 5×10^{-6} mTorr.

The surface morphology of the Au electrode film was characterized by field emission scanning electron microscopy (FESEM). For the I-V tests, an LED with a center wavelength of 254 nm was used as a UV light source which intensity level was about 0.32 mW/cm^2 on the film's surface. Responsivity (R) measurements were performed over DUV to visible wavelengths (200-600 nm) using a Xe light source. The incident wavelength of the Xe light was resolved by a monochromator with a wavelength step of 2 nm. The DUV LED at 254 nm was also applied as an excitation source during repetitive on/off measurements, and the I-V curves were obtained by an HP 4155 analyzer. For the detectivity performance under the bending state, the detector was fixed on the cylindrical surface of the plastic bottles with the different radiuses of 25, 20, and 10 mm by using a tape. Then, the devices were separated from the bottles and fixed on a flat glass substrate to represent the flat state performance of the photodetectors.

 ISBN:

III. RESULTS AND DISCUSSION

We have studied the performance of Au/β-Ga_2O_3 based photodetector through an analysis of current-voltage characteristics. Figure 1a depicts the camera image and a diagram of the flexible PD device under a bending test. The device is bent into a circumference of radius r, whose value implies the degree of curvature. To compare the relevance of the Ga_2O_3 thin film on flexible OHP substrate, and on the rigid glass substrate, the photocurrent-voltage curves under DUV illumination (λ = 254 nm) of two these samples were carried out in Fig. 1b. The amorphous device grown on glass substrates obtained the higher photocurrent (about 0.6 μA at a bias voltage of 25 V) than that one grown on OHP substrate (about 0.15 μA at a bias voltage of 25 V). We hypothesized that the slight photocurrent value difference originated from a problem of the contacts. The Au electrodes on the Ga_2O_3 film/flexible substrate could be physically unstable that caused the unstable value of obtained photocurrent. This instability was also observed in the Pt electrode on Ga_2O_3/flexible substrate [1]. This delamination of the electrodes is due to a weak adhesion between Au and Ga_2O_3, and it could enhance by inserted an adhesion layer.

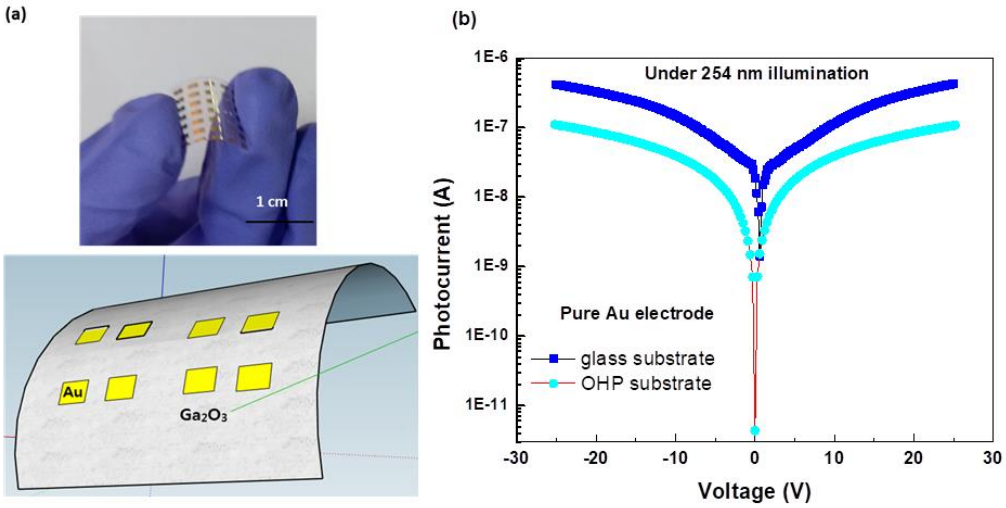

Fig. 1. *a) Photograph of the flexible Au/Ga_2O_3 photodetector (upper part) and schematic of the flexible DUV photodetector (lower part); b) Current-voltage curves of the Au/ Ga_2O_3 photodetector grown on glass and the flexible OHP substrate under 254 nm illumination.*

The bending influence on the photoresponse characteristics of a flexible PD is presented in Fig. 2a. It can be seen that the device exhibits high photosensitivity under every bent state; however, PD on flat state displays a higher performance than that was bent. When the radius of curvature r decreased from 25 to 10 mm, the photocurrent decrease lightly from 0.15 to 0.12 μA (V_{bias} = 25 V), respectively. Fig. 2b shows the on/off repetitive measurements of the device whose bending radius change from a flat to a radius of 10 mm. The PDs exhibit almost stable operation after several on/off cycles; however, the current obtained at ON state also reduces when the bending radius reduces. This degradation of the photodetector's performance might be ascribed to the different contact conditions between Au electrodes and Ga_2O_3 film when PD device is at the different bent states [1]. The bending strain which is perpendicular with the Ga_2O_3 gap could also result

in reducing the photoresponse characteristic of the device. This problem can be overcome by inserting the proper adhesion layer between Au electrodes and Ga_2O_3 film.

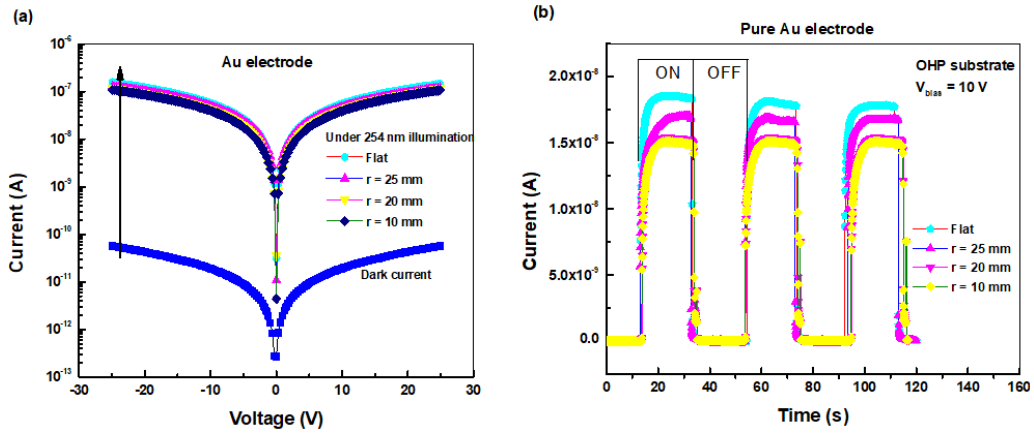

Fig. 2. *(a) Current-voltage curves of the flexible Au/ Ga_2O_3 photodetector before and after DUV illumination and under the various bending conditions r = flat, 25, 20, and 10 mm. (b) The repetitive detection performance of the Au/ Ga_2O_3 photodetector under the same DUV illumination and different bending conditions.*

5 nm-Ti thin film was chosen as an adhesion layer between Au and Ga_2O_3 film. To observe the effect of Ti in Ti/Au bilayer on the performance of Ga_2O_3-based photodetector, the Au thickness was kept the same as the sample with the pure Au electrode. The evolution of structure to obtain the high-performance, cost-effective and flexible photodetector is shown in Fig. 3a. I-V response of the fabricated Au/Ti/Ga_2O_3 device before and after applying UV light illumination (λ = 254 nm) is illustrated in Fig. 3b. Photodetector shows the dark current of 6.7×10^{-11} A which is slightly higher due to the relative higher conductivity of the Ti/Au bilayer than pure Au film. Under UV illumination, the device exhibits the remarkable photocurrent, and the obtained photocurrent are almost stable after being bent at some curvature radiuses.

Fig. 4 illustrated a current-time response that is used to verify the response speed and repeatability of the β-Ga_2O_3 PDs. The current-time response of the device was performed under the different bend states from flat to 10 mm of curvature radius. Time-dependent response tests with 254 nm DUV performed for three cycles at 10 V are shown. It can be seen that all devices demonstrated a good cyclicality to periodic UV illumination. When UV light is turned on, the current rapidly increases to a maximum value and tends to be stable. The current declines dramatically, when illumination is turned off. No significant degradation of the PDs was observed after bending, indicating the good stability and good adhesivity of the Ti layer on Ga_2O_3 film. This suggests a negligible influence of bending strain and satisfying the flexibility of photodetectors. Besides, without bending, the current obtained by Ti/Au bilayer-device (about 3.1×10^{-8} A) is dramatically higher than that obtained by pure Au-device (about 1.7×10^{-8}) at ON state. This indicates that the adhesion layer may play an important impact on reducing electrical resistivity on the film surface which leading to enhance dark and photocurrent [12]. This investigation will be further studied in the next part.

 ISBN:

As reported in previous publish [13], brittle Au film could fracture almost immediately when strained in tension, and not only cracks but also catastrophic failure were formed that result in electrical failure and the optoelectrical properties were impaired. Firstly, under a flat state, Au is grown on a substrate, the well-bonded film is formed, and almost no free-standing, necking or failing can be found. When sample starts bending, small strains are applied then Au grains elongate and grain boundary start opening on the Au film surface. Deformation in the metal film is almost localized at the grain boundary and a little in the grain. Intergranular cracking occurs since the grain boundary opening exceeds critical opening displacement ($\delta_{n,s}$).

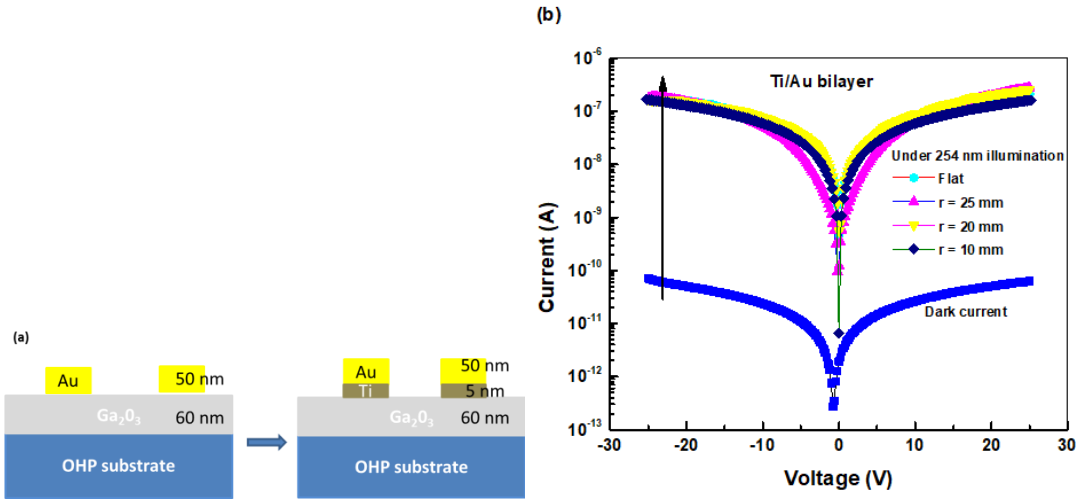

Fig. 3. *a) Schematic of the fabricated MSM-type Ga_2O_3 photodetector with Au electrode (left side) and Ti/Au bilayer electrode (right side); b) Current-voltage curves of the flexible Au/Ti/Ga_2O_3 photodetector before and after DUV illumination and under the various bending conditions r = flat, 25, 20, and 10 mm.*

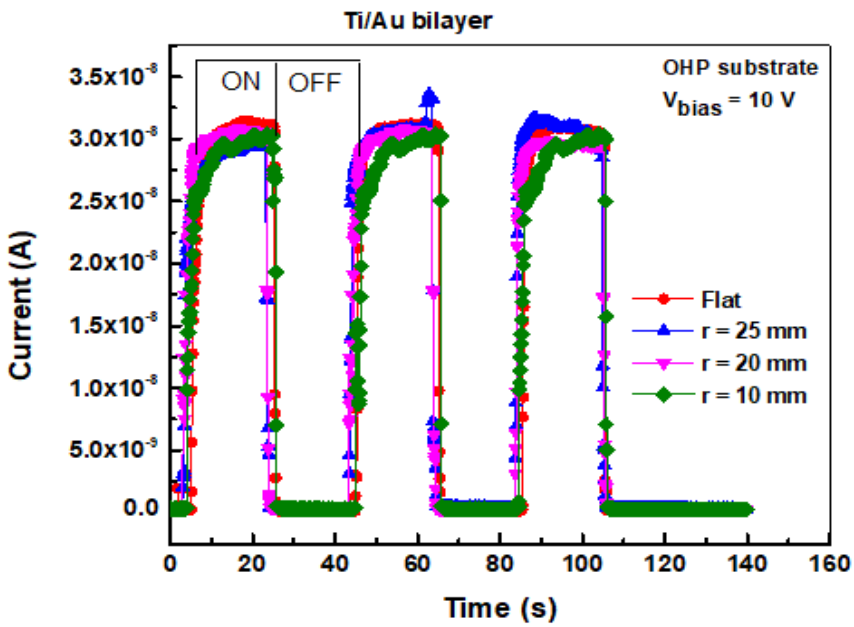

Fig. 4. *The repetitive detection performance of the Au/Ti/ Ga_2O_3 photodetector under the same DUV illumination and different bending conditions.*

IV. CONCLUSION

In this study, we have investigated the influence of Ti/Au bilayer on the performance of β-Ga_2O_3 based-photodetector fabricated by the PLD method. By simply inserting Ti ultrathin film, the photocurrent increased slightly under the flat state, and after being bent at r = 20 mm, responsivity suddenly increased nearly 28 times. We believed that our study herein will provide an economically viable solution for the development of high-performance optoelectronics devices.

REFERENCES

[1] S. H. Lee, S. B. Kim, Y. J. Moon, S. M. Kim. H. J. Jung, M. S. Seo, K. M. Lee, S. K. Kim, S. W. Lee, High-responsivity deep-ultraviolet-selective photodetectos using ultrathin gallium oxide films, *ACS Photonics*, 2017, **27**, 2937-2943.

[2] B. Zhao, F. Wang, H. Chen, L. Zheng, L. X. Su, D. X. Zhao, X. S. Fang, An ultrahigh responsivity (9.7 mA W^{-1}) self-powered solar-blind photodetector based on individual ZnO-Ga_2O_3 heterostructures, *Advanc. Func. Mater.*, 2017, **4**, 1700264.

[3] L. X. Qian, Z. H. Wu, Y. Y. Zhang, P. T. Lai, X. Z. Liu, Y. R. Li, Ultrahigh-responsivity, rapid-recovery, solar-blind photodetector based on highly nonstoichiometric amorphous gallium oxide, *ACS Photonics*, 2017, **4**, 2203-2211.

[4] L. X. Qian, H. F. Zhang, P. T. Lai, Z. H. Wu, X. Z. Liu, High-sensitivity β-Ga_2O_3 solar-blind photodetector on high-temperature pretreated c-plane sapphire substrate, *Opt. Mater*., 2017, **7**, 10.

[5] Z. Lou, L. Li, G. Zhen, High-performance rigid and flexible ultraviolet photodetectors with single-crystalline $ZnGa_2O_4$ nanowires, *Nano Research*, 2015, **8(**7), 2162-2169.

[6] S. Cui, Z. Mei, Y. Zhang, H. Liang, X. Du, Room-temperature fabricated amorphous Ga_2O_3 high-response-speed solar-blind photodetector on rigid and flexible substrates, *Adv. Opt. Mater.*, 2017, **5**(19), 1700454.

[7] S. H Kim, S. W. Na, N. E. Lee, Y. W. Nam, Y. H. Kim, Effect of surface roughness on the adhesion properties of Cu/Cr films on polyimide substrate treated by inductively coupled oxygen plasma, *Surf. Coat. Tech.*, 2005, **200**(7), 2072-2079.

[8] T. G. Habteyes, S. Dhuey, E. Wood, D. Gargas, S. Cabrini, P. J. Schuck, A. P. Alivisatos, S. R. Leone, Metallic adhesion layer induced plasmon damping and molecular linker as a nondamping alternative, *ACS Nano.*, 2012, **6**, 5702-5709.

[9] A. A. Taylor, M. J. Cordill, L. Bowles, J. Schalko, G. Dehm, An elevated temperature study of a Ti adhesion layer on polyimide, *Thin. Solid. Film*, 2013, **531**, 354-361.

[10] F. Ruffino, M. G. Grimaldi, Morphological characteristics of Au films deposited on Ti: A combined SEM-AFM study, *Coatings*, 2018, **8**(4), 121.

[11] M. T.odeschini, A. B. D. S. Fanta, F. Jensen, J. B. Wagner, A. Han, Influence of Ti and Cr adhesion layers on ultrathin Au films, *Appl. Mater. Interf.*, 2017, **9**, 37374-37385.

[12] J. Vancea, G. Reiss, F. Schneider, K. Bauer, H. Hoffmann, Substrate effects on the surface topography of evaporated gold films-a scanng tunnelling microscopy investigation, *Surf. Sci.*, 1989, **218**(1), 108-126.

[13] Z. Zhang, T. Li, Effects of grain boundary adhesion and grain size on ductility of thin metal films on polymer substrates, *Script. Materialia*, 2008, **59**(8), 862-865.

 ISBN:

CHROMATIC DISPERSION CONTROL IN LEAD - BISMUTH - GALLATE GLASS PHOTONIC CRYSTAL FIBERS WITH SELECTIVE HIGH NONLINEAR LIQUID INFILTRATION: APPLICATION TO ULTRA-FLATTENED-NORMAL-DISPERSION

Quang Ho Dinh[1], Nguyen Dang Nguyen[2], Chin Hoang Van[2], Ngoc Vo Thi Minh[3], Trung Le Canh[3], Thanh Vinh Nguyen[3], Bien Chu Van[2], Thao Nguyen Thi[2] and Hieu Van Le[2*]

[1]*School of Chemistry, Biology and Environment, Vinh University, 182 Le Duan Street, Vinh City, Vietnam*

[2]*Faculty of Natural Sciences, Hong Duc University, 565 Quang Trung Street, Thanh Hoa City, Vietnam*

[3]*Department of Physics, Vinh University, 182 Le Duan, Vinh City, Vietnam*

*E-mail: *levanhieu@hdu.edu.vn*

Abstract. We studied numerically the chromatic dispersion of photonic crystal fiber (PCF) made of lead-bismuth-gallate glass with air hole infiltrated with tetrachloroethylene. The dependence of the individual parameters upon dispersion has been presented in detail. The possibility of controlling the lattice constant Λ and the diameter of holes in three subsequent rows allows for precise shaping of dispersion characteristics in a wide range of wavelengths. Especially, by making very small (about tens of nm) changes in the diameter of the liquid-filled holes, we have obtained the PCFs with ultra-flattened dispersion characteristics, fluctuating less than 0.7 ps/nm/km in the wide wavelength range of 820 nm. This is a promise of great applications as a chromatic dispersion controller, nonlinear optical systems.

I. INTRODUCTION

The appearance of photonic crystal fiber (PCF) in 1996 was an important breakthrough in the fiber fabrication technique, it not only had many new unprecedented properties but also overcome many limitations of traditional optical fiber [1]. Therefore, PCFs are widely applied in many fields such as optical communication, nonlinear optical fibers, supercontinuum generation, nanoparticle guidance, and sensors, especially in biomedical applications (bio-imaging, medical diagnostics, glucose monitoring, telemedicine, disease detection) [2]. Recently, PCFs are used in the development of mid-infrared supercontinuum generation laser sources that have attracted great attention due to potential applications in imaging and spectroscopy [3], including hyperspectral imaging, optical coherence tomography (OCT), spectroscopy of human cells and tissue. In order to achieve those goals, many kinds of PCFs are made from different materials and structures (shape and size), but are usually classified into 2 main categories: Index Guiding Fibers, and Photonic Bandgap Fibers. The Index Guiding Fibers are guiding light in a solid core by total internal reflection between a solid core and a cladding region with multiple air-holes. The Photonic Bandgap Fibers are guiding light via the photonic band-gap effect in a low index core-region at the operating wavelength [4].

ISBN:

The index guiding fibers also called holey fibers or micro-structured optical fibers are characterized by a distribution of air holes in the cladding that can provide endless single-mode operation regardless of the wavelength. Simultaneously, the flexible fabrication techniques, great controllability in chromatic dispersion, which can be used to create various PCFs with unique dispersion properties, such as zero-dispersion wavelengths shifted to the visible, near-infrared and mid-infrared wavelengths [5], an ultra-flattened chromatic dispersion [6]. Until now, some methods have been reported to control expected dispersion characteristics. In the conventional PCFs, the chromatic dispersion is controlled by varying the air-hole diameter and lattice constant [7]. The advantage of this technique is easy to implement, but it is difficult to control the dispersion slope and dispersion properties in the wide wavelength range. Another approach is to overcome the limitation of traditional background materials (for example, silica glass or fused silica glass) that is not transparent in the mid-infrared range as well as relatively low nonlinearity. Some highly nonlinear soft glasses such as chalcogenide [8], tellurite glasses [9], lead-bismuth-gallate glass [10] were reported that have a higher nonlinear refractive index than silica and more broadband transmission into the mid-infrared range, opens up many potential applications. Recently, several nonlinear liquids were also used to create expected dispersion characteristics, especially flat or ultra-flat dispersions for application in the development of broad-spectrum sources as ethanol (C_2H_5OH), carbon tetrachloride (CCl_4), carbon disulfide (CS_2), chloroform ($CHCl_3$), toluene (C_7H_8), nitrobenzene ($C_6H_5NO_2$), tetrachloroethylene (C_2Cl_4), 1,2-dibromoethane ($C_2H_4Br_2$) [11]. However, highly nonlinear liquids are usually extremely toxic, volatile, explosive, carcinogenic, requiring safe experimental conditions and complex pumping systems. If these limitations can be overcome, liquids are a potential candidate to expand the applications of PCFs in several fields like medical diagnostics or biomedical technologies [12].

In this paper, in order to control dispersion and dispersion slope, a new controlling technique of ultra-flat normal dispersion in lead-bismuth-gallate (PBG-08) glass photonic crystal fiber is reported. The selected liquid is tetrachloroethylene, because of high nonlinear refractive index $n_2 = 16.75 \times 10^{-20}$ m^2/W at $\lambda = 1.55$ µm (higher than fused silica $n_2 = 2.19 \times 10^{-20}$ m^2/W), super-wide transparent (0.5-3.39 µm), less harmful than CS_2, C_7H_8, CCl_4 [12]. In addition, combined with lead-bismuth-gallate glass exhibits good transparency up to 4.8 µm (transmission window from 500 to 4800 nm), a high refractive index (more than 2.0), and high nonlinear refractive index of $n_2 = 4.3 \times 10^{-19}$ m^2/W at 1240 nm [13], which allows controlling the dispersion slope in the wide wavelength range. It was shown from numerical results that it is possible to control chromatic dispersion characteristic over a wide frequency range by varying the lattice constant Λ and the hole diameter in three subsequent rings. Although, small variations of the diameters of the holes filled with liquid, on the level of tens of nanometers, can lead to a significant change of the dispersion properties.

 ISBN:

II. DESIGN AND SIMULATION

The cross-section of the geometrical structure is schematically illustrated in Fig. 1. The proposed PCF is made of lead-bismuth-gallate glass and consists of eight rings of air holes arranged in regular hexagonal lattice defined by the lattice pitch Λ and the diameter d_1, d_2, d_3 ($d_1 < d_3 < d_2$).

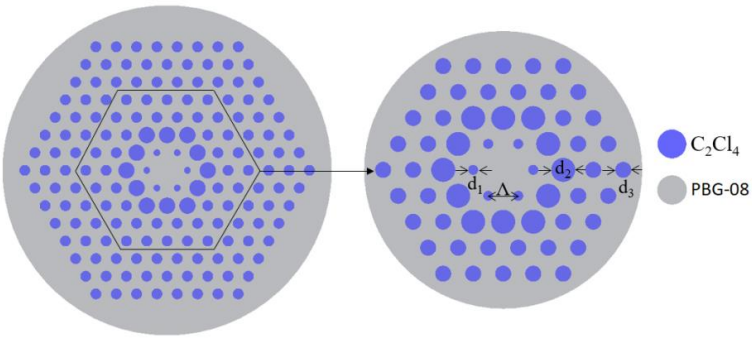

Fig. 1. *Schematic of the proposed PCF, $d_1 < d_3 < d_2$ (μm).*

We assumed that the air-holes are filled with C_2Cl_4. The characteristics of the refractive index of used materials is shown in Fig. 2.

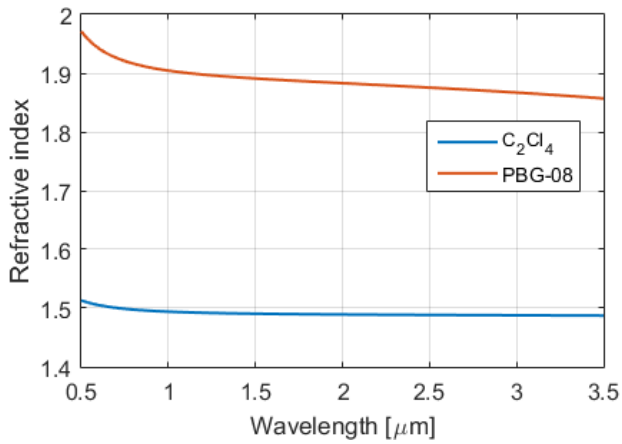

Fig. 2. *The refractive index of used materials for the temperature of 20 °C [13,14].*

The refractive indices of used materials as a function of wavelength are given by the Sellmeier equation as [14]:

$$n(\lambda) = \sqrt{1 + \frac{B_1\lambda^2}{\lambda^2 - C_1} + \frac{B_2\lambda^2}{\lambda^2 - C_2} + \frac{B_3\lambda^2}{\lambda^2 - C_3}} \quad (1)$$

where, the B_i and C_i (μm^2) are Sellmeier's coefficients as given in Table 1.

Table 1. *Sellmeier coefficients of the materials used.*

Materials	Sellmeier coefficients					
	B_1	C_1 [μm^2]	B_2	C_2 [μm^2]	B_3	C_3 [μm^2]
PBG-08 [13]	2.211153	0.01834	0.355174	0.073012	1.16141	127.3884
C_2Cl_4 [14]	1.21453712	0.01456	0.03501419	123.1074	-	-

The numerical analysis was carried out with the use of Lumerical Mode Solution software [15]. Firstly, the simulations were performed using PCFs with all of the same air-hole diameters in the cladding region, which the lattice pitch (Λ) was varied from 1.3 µm to 2.8 µm with a step of 0.5 µm, and the air-hole diameter was 0.8 µm. Each simulation was done for wavelengths in the range of 0.5 µm to 3.5 µm. Next step, the value Λ kept fixed at 1.8 µm, while the air-hole radius was evenly increased from 0.35 to 0.60, in order to control both the dispersion and dispersion slope in the wide wavelength range. However, some parameters in the cladding were constantly changed between the air-hole diameter of d_1, d_2, and d_3 to achieve nearly zero ultra-flattened chromatic dispersion in PCFs.

III. RESULTS AND DISCUSSION

In conventional PCFs, the cladding region with multiple air holes is the same diameter, which is easily varied the hole-to-hole spacing (lattice constant) to achieve the desired chromatic dispersion profile. However, the disadvantage of PCFs is difficult to control the dispersion slope in the wide wavelength range. The results shown in Fig. 3 demonstrated that the chromatic dispersion is affected by varying the lattice pitch. For a certain value of the air-hole radius, increasing the Λ value leads to shifting the chromatic dispersion curves toward the anomalous dispersion regime. In detail, the dispersion characteristics are all-normal dispersion with Λ = 1.3 µm and Λ = 1.8 µm in the considered wavelength. In the opposite direction, the dispersion exist in both normal and anomalous dispersion regimes with Λ = 2.3 µm and Λ = 2.8 µm. Especially, for fiber with Λ = 1.8 µm, the chromatic dispersion curve is near-flat and is changed around 50 ps/nm/km over 1.3-3.2 µm wavelengths. This fiber is chosen to perform the next analyses that can probably give a broad and flat spectrum in supercontinuum generation, and suits the intended purpose.

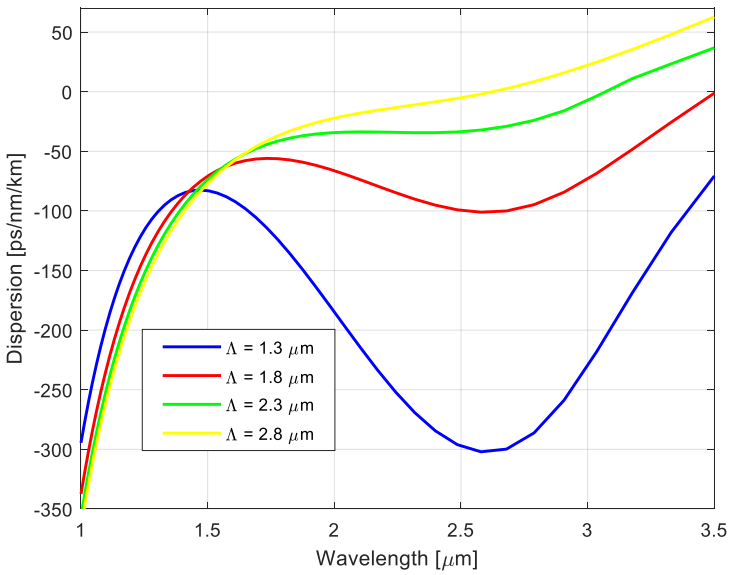

Fig. 3. *Dispersions characteristics of the fundamental mode for various lattices pitch Λ with diameter of air hole d= 0.8 µm.*

 ISBN:

In order to show how the chromatic dispersion is affected by varying the hole diameter, we were performed five simulations as shown in Fig. 4, where the lattice constants Λ is 1.8 µm and the each hole diameter d'_i ($i = 1 \sim 5$) is ranged from 0.7 to 1.1 µm with a step of 0.1 µm. This result indicates that the dispersion profile takes the normal values except for Λ = 1.8 µm and d'_5 = 1.1 µm, where the local maximum in the anomalous dispersion regime (and there are two ZDWs). The chromatic dispersion curves are shifted toward positive value, close to the horizontal axis, and less flattened with increasing the hole diameter. From these results, the hole diameter is selected as 0.8 µm - 1.0 µm for ultra-flattened chromatic dispersion controllability.

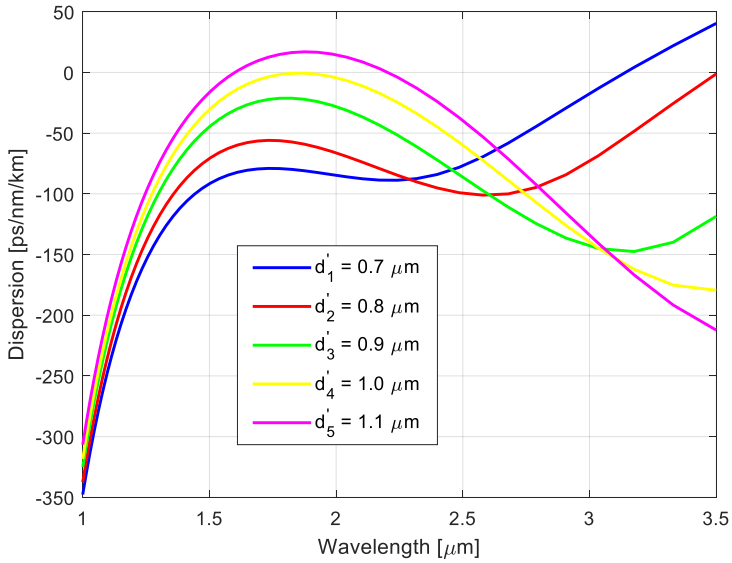

Fig. 4. *Chromatic dispersion curves as a function of wavelength for PCFs with Λ = 1.8 µm and d'_1 = 0.7 µm, d'_2 = 0.8 µm, d'_3 = 0.9 µm, d'_4 = 1.0 µm, d'_5 = 1.1 µm, respectively.*

In PCFs, the guided fundamental mode is almost confined into the core region, and the dispersion characteristics are affected by the inner hole rings at the short wavelength range, while the effective mode area is increased in the long-wavelength range, so the dispersion characteristics are affected not only inner rings but also outer rings, especially when the lattice pitch is small. Therefore, to control both the dispersion and dispersion slope in the wide wavelength range, the diameter of the three inner rings will be varied for optimizing the wish structure. It is also possible to assess the shift of the chromatic dispersion curves to anomalous dispersion regimes such as those given in Fig. 5. The air-hole diameters of the first rings (d_1), second rings (d_2), and third rings (d_3) were changed in turn to select the most appropriate parameters. As can be seen from the plot, the hole diameter, $d_2 = d_3$ = 1.0 µm (constant), while the d_1 values changed from 0.6 µm to 1.0 µm with a step of 0.1 µm, which is in agreement with expectations. The increasing the hole diameter of the first ring makes dispersion flatter, simultaneously the dispersion curve go down the anomalous regime with d_1 > 0.8 µm. At the d_1 = 0.8 µm, the dispersion can also exist all normal-dispersion with the better properties such as low and flatter dispersion (changing around 10 ps/nm/km over 1.69 - 3.5 µm). However, the maximum point in the dispersion curve is far from the horizontal axis, so PCF with parameters Λ = 1.8 µm, d_1 = 0.8 µm was selected to continue investigating the appropriate values of d_2 and d_3.

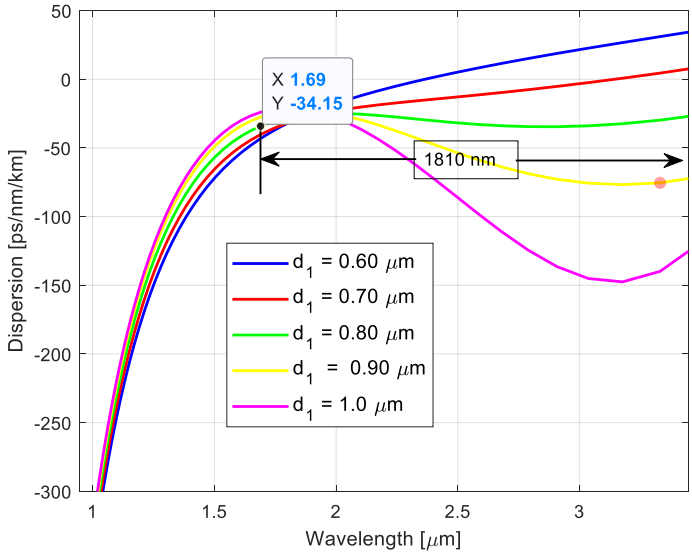

Fig. 5. *Chromatic dispersion curves as a function of wavelength for PCFs with Λ = 1.8 μm and d_1 varied from 0.7 μm to 1.0 μm, d_2 = d_3 = 1.0 μm, respectively.*

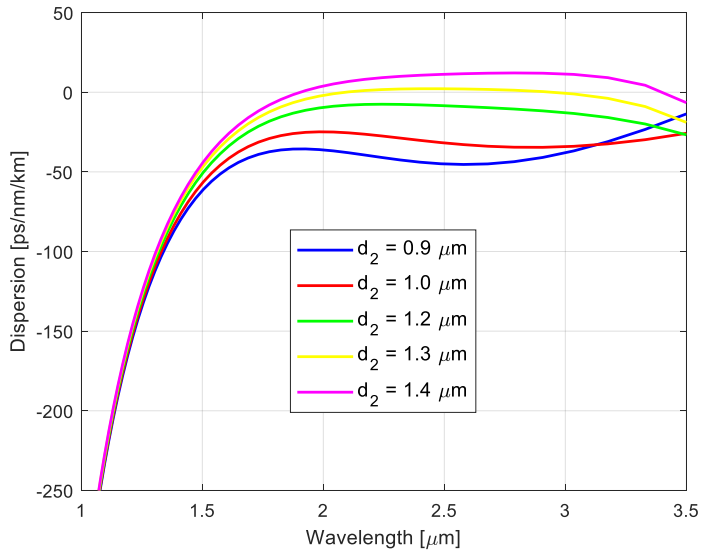

Fig. 6. *Chromatic dispersion curves as a function of wavelength for PCFs with Λ = 1.8 μm, and d_1 =0.8 μm, d_2 varied from 0.9 μm to 1.4 μm, d_3 = 1.0 μm, respectively.*

When the parameters d_1 = 0.8 μm and d_3= 1.0 μm are fixed, changing the d_2 value from 0.9 μm to 1.4 μm, shows a plot of the shift of the chromatic dispersion toward closer to the horizontal axis with increasing the diameter d_2 of the third ring. The slope of the curve is reduced and the closest the horizontal axis at d_2 = 1.2 μm, operates in an all-normal dispersion region (see in Fig. 6), changing small about 10 ps/nm/km, and the maximum point equals -7.5 ps/nm/km for all dispersion characteristics with Λ = 2.2 μm. This value was kept constant, while the hole diameter of the third ring d_3 varied between 0.9 μm and 1.3 μm. This reason makes the desired dispersion curve moves closer to the horizontal axis and becomes flatter. As a result, the dispersion characteristic of PCF with parameter d_3 = 1.1 μm satisfies the requirements, and if the hole diameter d_3 is further increased, it will shift to the anomalous dispersion region.

 ISBN:

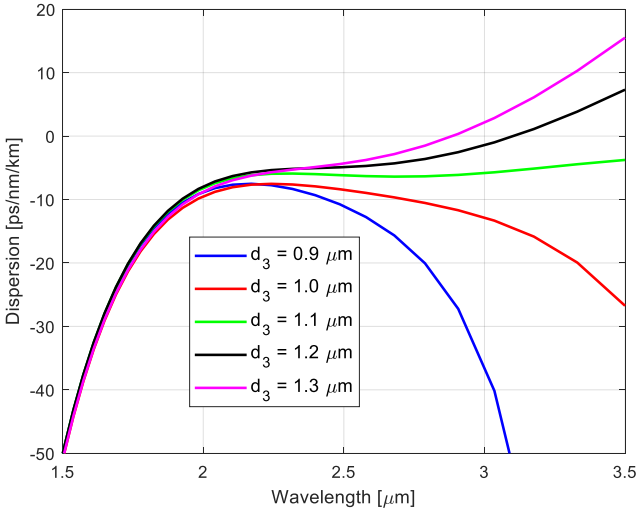

Fig. 7. *Chromatic dispersion curves as a function of wavelength for PCFs with Λ = 1.8 μm, and d_1 =0.8 μm, d_2 = 1.2 μm, d_3 varied from 0.9 μm to 1.3 μm, respectively.*

Finally, the change of d_3 is considered. As shows in Figure 7 that the change of the diameter d_3 has almost no effect on the maximum point of the dispersion curve but influences the dispersion characteristic in the range of 2.2-3.5 μm. In detail that the dispersion curves shift to the anomalous dispersion region, increase the slope, appear the zero-dispersion wavelength points at 2.88 μm (for d_3 = 1.3 μm) and 3.10 μm (for d_3 = 1.2 μm). Meanwhile, the dispersion became more negative when the d_3 values decreasing (for d_3 = 0.9 μm and d_3=1.0 μm). For given value of d_3 = 1.1 μm, the changing dispersion profile is less than 0.7 ps/nm/km in the wavelength range shorter than 3.05 μm (over 820 nm), and ultra-flattened dispersion characteristics. This is a promise of great applications as a chromatic dispersion controller, nonlinear optical systems.

IV. CONCLUSION

A new controlling technique of chromatic dispersion in lead-bismuth-gallate glass photonic crystal fiber infiltrated with C_2Cl_4 was proposed and applied to design PCFs with ultra-flattened dispersion in a wide wavelength range. It was shown from numerical results that it is possible to control chromatic dispersion characteristic over a wide frequency range by varying the lattice constant Λ and the hole diameter in three subsequent rings. Although, small variations of the diameters of the holes filled with liquid, on the level of tens of nanometers, can lead to a significant change of the dispersion properties. The results also that we can obtain the PCF structure with ultra-flattened dispersion characteristics. This is a promise of great applications as a chromatic dispersion controller, nonlinear optical systems.

ACKNOWLEDGMENTS. This research is funded by Vietnam National Foundation for Science and Technology Development (NAFOSTED) under grant number 103.03-2020.19.

REFERENCES

[1] K. T. V. Grattan and T. Sun, Fiber optic sensor technology: an overview, *Sensors and Actuators A*, 2000, **82**, 40-61.

[2] S. Arismar Cerqueira, Recent progress and novel applications of photonic crystal fibers, *Reports on Progress in Physics*, 2010, **73**, pp.024401.

[3] L. Robichaud, S. Duval, L. Pleau, V. Fortin, S. T. Bah, S. Châtigny, R. Vallée, and M.Bernier, High-power supercontinuum generation in the mid-infrared pumped by a soliton self-frequency shifted source, *Opt. Express*, 2020, **28**, 107-115.

[4] K. Saitoh, M. Koshiba, T. Hasegawa, and E. Sasaoka, Chromatic dispersion control in photonic crystal fibers: Application to ultra-flattened dispersion, *Opt. Express*, 2003, **11**, 843-852.

[5] J. M. C. Boggio, A. O. Moñux, D. Modotto, T. Fremberg, D. Bodenmüller, D. Giannone, M. M. Roth, T. Hansson, S. Wabnitz, E. Silvestre, and L. Zimmermann, Dispersion-optimized multicladding silicon nitride waveguides for nonlinear frequency generation from ultraviolet to mid-infrared, *J. Opt. Soc. Am. B*, 2016, **33**, 2402-2413.

[6] K. Saitoh, N. Florous, and M. Koshiba, Ultra-flattened chromatic dispersion controllability using a defected-core photonic crystal fiber with low confinement losses, *Opt. Express*, 2005, **13**, 8365-8371.

[7] C. V. Bien, T. D. Duc, N. M. An, H. D. Quang, N. M. Thang, and L. V. Hieu, Influence of structure parameters on the supercontinuum generation of photonic crystal fiber, *Journal of Military Science and Technology*, 2020, **67**, 161-168.

[8] A. N. Ghosh, M. Meneghetti, C. R. Petersen, O. Bang, L. Brilland, S. Venck, J. Troles, J. M. Dudley, and T. Sylvestre, Chalcogenide-glass polarization-maintaining photonic crystal fiber for mid-infrared supercontinuum generation, *Journal of Physics: Photonics*, 2019, **1**, 1-12.

[9] M. Klimczak, D. Michalik, G. Stępniewski, T. Karpate, J.Cimek, X. Forestier, R. Kasztelanic, D. Pysz, R. Stępień, and R. Buczyński, Coherent supercontinuum generation in tellurite glass regular lattice photonic crystal fibers, *J. Opt. Soc. Am. B*, 2019, **36**, 112-124.

[10] M. Klimczak, B. Siwicki, A. Heidt, and R. Buczyński, Coherent supercontinuum generation in soft glass photonic crystal fibers, *Photon. Res.*, 2017, **5**, 710-727.

[11] H. L. Van, V. T. Hoang, T. L. Canh, Q. H. Dinh, H. T. Nguyen, N. V. T. Minh, M. Klimczak, R. Buczynski, and R. Kasztelanic, Silica-based photonic crystal fiber infiltrated with 1,2-dibromoethane for supercontinuum generation, *Appl. Opt.*, 2021, **60**, 7268-7278.

[12] H. V. Le, V. T. Hoang, H. T. Nguyen, V. C. Long, R. Buczynski, and R. Kasztelanic, Supercontinuum generation in photonic crystal fibers infiltrated with tetrachloroethylene, *Opt. Quant. Electron.*, 2020, **53**, 1-18.

[13] R. Buczynski, H. Bookey, M. Klimczak, D. Pysz, R. Stepien, T. Martynkien, J. E. McCarthy, A. J. Waddie, A. K. Kar, and M. R. Taghizadeh, Two octaves supercontinuum generation in lead-bismuth glass based photonic crystal fiber, *Materials*, 2014, **7**, 4658-4668.

[14] M. Chemnitz, C. Gaida, M. Gebhardt, F. Stutzki, J. Kobelke, A. Tünnermann, J. Limpert, and M. A. Schmidt, Carbon chloride-core fibers for soliton mediated supercontinuum generation, *Opt. Express*, 2018, **26**, 3221-3235.

[15] Mode Solution. Lumerical Solutions, Inc. https://www.lumerical.com/tcad-products/mode/

 ISBN:

APPLICATION OF THE ELECTRICAL RESISTIVITY TOMOGRAPHY AND SEISMIC REFRACTION METHODS FOR GROUNDWATER INVESTIGATION IN SAVANNAKHET PROVINCE, LAOS

Viengthong Xayavong[1,2*], Minh Duc Vu[1], Duong Anh Nguyen[3], Tuan Minh Vu[3], Chung Anh Do[4]

[1]*University of Science, Vietnam National University, 334 Nguyen Trai, Hanoi, Vietnam*

[2]*Physics Department, Faculty of Natural Science, National University of Laos, Dongdok Campus 7322, Vientiane, Laos*

[3]*Institute of Geophysics, Vietnam Academy of Science and Technology, 18 Hoang Quoc Viet, Hanoi, Vietnam.*

[4]*Institute for Ecology and Works Protection, Vietnam Academy for Water Resources, 171 Tay Son, Dong Da, Hanoi, Vietnam.*

*E-mail: *viengthongxv@gmail.com*

Abstract. The hydrogeology information can be revealed from subsurface physical property contrast values through integrated geophysical exploration techniques. The aim of this study is to delineate groundwater potential zones through application of electrical resistivity tomography (ERT) and seismic refraction methods. The results of geophysical exploration methods showed that the moderate resistivity regions vary from 15-60 Ohm.m found at the depth of 16-20 m, is considered as suitable areas for good groundwater potential areas whereas the seismic velocities distribution analysis ranging from 1200-1800 m/s found at the depth of 16-20m, is considered as groundwater table level. These results are compared to ground-truth from boreholes and that agree well with information from two boreholes drilled in the Outhoumphone district, indicated that the location of the water table at 16 to 20 m depth where samples extracted from the drilling samples have been identified as sandstone and siltstone. The geophysical results also demonstrate that the ERT and seismic refraction methods can be an efficient tool for groundwater investigation in Savannakhet province and integrated geophysical techniques can be applied for groundwater investigation in other similar geological areas in Lao PDR.

Keywords: *Electrical resistivity tomography (ERT) and seismic refraction explorations, Groundwater, Aquifers, Laos.*

I. INTRODUCTION

The need for water is strongly ascending and has a diversified function, which is not only important for drinking purposes but is also essential for any developmental activities, which is related either directly or indirectly with water utilization. Both surface and groundwater sources are the main components depending on their quality and availability where surface water is not feasible for the desired activity. Thus, groundwater is an alternative source to supplement water supply for agriculture, irrigation, industry, and household. Whereas, groundwater information is limited for monitoring and evaluation activities regarding quantity and quality of groundwater have not yet been carried out to

any significant degree. In addition, Lao people commonly use shallow hand dug wells at 5 to 10 m depth, which are not biologically safe sources and usually dry out during the dry season, and water-borne diseases caused by infiltrations of domestic waste and from farm animal [1,2]. In Laos, information and programs for the monitoring and evaluation of groundwater quantity and quality are limited. For example, over 100 boreholes were drilled in Savannakhet province, with the success rate of 50-60%, and about 50 boreholes have been selected for production wells, caused by poor water quality [3].

ERT method is currently being very popular with groundwater investigations, which provides depth and thickness of various subsurface layers and their relative water yielding capacities from observed earth electrical resistivity. However, there is ambiguity in interpreting the earth resistivity regions values. Low resistivity values can either indicate higher clay content or higher water content. The results of seismic refraction in term of seismic velocity models may be able to reduce the ambiguity [4]. Therefore, it will be of great benefit if geophysical methods, especially electrical resistivity tomography and seismic refraction explorations to apply for groundwater investigation and management in the study sites. The study area is presently economic actives and population is increasing and associated with trend of increasing demand water has grown, but there are no mechanisms for data collection, compilation and storage, no protocols or entities tasked with the implementation of new groundwater resources.

The aim of this work is to identify groundwater potential zones and depth to aquifers by using ERT and seismic refraction measurements in the research areas. Results of the field studies are compared to ground-truth from boreholes, including the soil samples information.

II. MATERIALS AND METHODS

2.1. Resistivity measurement

The aims of electrical resistivity survey are to measure the resistivity distribution in the subsurface layers by conducting measurements along the ground surface. The electrical resistivity tomography (ERT) or electrical resistivity imaging (ERI) method is an active geophysical exploration method used to obtain a high-resolution image of the earth's electrical resistivity. The earth resistivity values vary greatly due to different subsurface geological information. The various geophysical exploration techniques distinguish subsurface when a contrast exists in their electrical properties. The earth resistivity is function of porosity, permeability, water saturation and the concentration of dissolved solids in pore fluids within the subsurface materials (Table 1) [5]. Rock resistivity of clean sand, saturated aquifer can be explained by Archie's law:

$$\rho_r = a\rho_w\phi^{-m} \tag{1}$$

where, ρ_r , ρ_w are resistivities of rock and water respectively; a is the saturation coefficient $(0.6 < a < 2.0)$; m is the cementation factor $(1.3 < m < 2.2)$; ϕ is fractional porosity.

 ISBN:

Table 1. *Typical electrical resistivity values for various earth materials [5,6].*

Earth materials	Resistivity values (Ohm.m)	
	[5]	[6]
Clay	1-100	1-100
Sand	60-1000	50-1050
Gravel	100-5000	600-10^4
Mudstone	-	-
Siltstone	20-150	-
Shale	20-2000	2-2000
Sandstone	10-5000	
Sandy clay	30-215	
Alluvium	10-800	
Groundwater	10-800	
Fresh groundwater	20-160	
Salt water	0.25	0.2

In 2D electrical resistivity survey, a current is injected into the earth through a pair of current electrodes, and the potential difference is measured between a pair of potential electrodes. The current and potential electrodes are generally arranged in a linear array. The apparent resistivity is the bulk average resistivity of all soils and rock influencing the current. It is calculated by dividing the measured potential difference by the input current and multiplying by a geometric factor specific to the array being used and electrode spacing [6]. In this work, Wenner electrode array (Fig. 1) was selected to use for 2D resistivity data acquisition, where these data were recorded by manually and automatically by using the ABEM Terrameter SAS 1000. The data integrated in these survey areas were interpreted by using EarthImager software in order to provide an inverse resistivity model that approximates the actual subsurface structure, the median depth of investigation is about 0.52 times the electrode spacing for the Wenner electrode configuration [6].

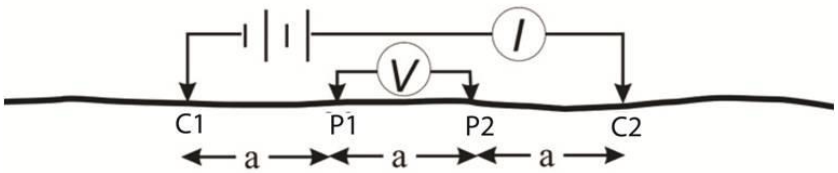

Fig. 1. *The Wenner electrode array.*

2.2. Seismic refraction method

The seismic refraction method utilizes seismic energy that returns to the ground surface after travelling through the earth subsurface layers along refracted ray path, which depends on the seismic velocity variation in difference earth layers. The seismic signal is produced into the subsurface through a shot point using hammer, weight dropped, vibrator and explosives [5]. The first arrival of seismic energy to a seismic detector offset from a seismic source always represents either a direct ray or a refracted ray (Fig. 2).

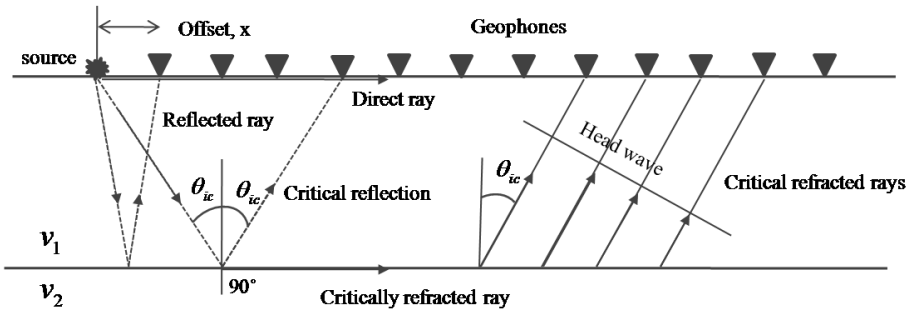

Fig. 2. *Seismic ray path of direct, reflection, and refraction waves.*

The thickness and velocity of subsurface earth upper and beneath an interface can be computed by determining the arrival times for direct and refracted waves from seismic section. The seismic velocities of longitudinal waves, P-wave, V_p and of transverse waves, S-wave, V_s in a homogeneous and isotropic medium are given by the equation (2). The factors affecting seismic velocity depend on their various compositions, textures (i.e., grain shape and degree of sorting), porosities and contained pore fluids, rocks differ in their elastic moduli and densities (Table 2) shows seismic velocity value varies with mineral content, lithology, porosity, density and degree of compaction [7]:

$$V_P = \sqrt{\frac{\lambda + 2\mu}{\rho}} \quad \text{and} \quad V_S = \sqrt{\frac{2\mu}{\rho}} \tag{2}$$

Table 2. *The P-wavevelocity of various earth materials [7].*

Earth materials	P-wave velocity (m/s)
Air	331.5
Water	1400-1600
Sandstone and shale	2000-4500
Limestone	2000-6000
Sand and gravel	500-1500
Shale	2000-4500
Conglomerate	10-800
Alluvium	500-2000
Sand (Unsaturated)	200-1000
Sand (Saturated)	800-2200
Clay	1000- 2500

In the seismic refraction method, the seismic velocity values for the estimation of the depth of the water table or aquifer have ambiguity for interpretation because a wide range of seismic velocity values in connection to the water table level and these values are not uniquely correlated to the aquifer layer. Some authors attribute P-wave velocities around 1500 m/s to represent a saturated layer [8]. Meanwhile, another report proposes seismic velocity values vary from 1200 to 1800 m/s in aquifer layers [9]. Many researchers have been applied the seismic refraction method for the identification of groundwater and structural geology investigations [10 to 15].

The SeisImager software was selected to use for seismic refraction data interpretation in order to map subsurface geology in this work. This software has a system package for

 ISBN:

picking the first arrival time for P-wave known as the PickWin program. All seismic events were picked the first breaks then the arrival times against distance between the shot and geophone positions. The Plotrefa file package was used for the second step of this procedures, which package was used to run the time as inversion in order to generate the seismic velocity model in term of the thickness of the subsurface layers and a seismic velocity value agree with subsurface geological information under the seismic profile [16].

2.3. Survey profiles

The study area was selected in Outhomphone district of Savannakhet province, Laos (Fig. 3) where is situated in the northwestern part of the province with elevation between 175 to 200 m and most areas are covered by rice farm and forests.

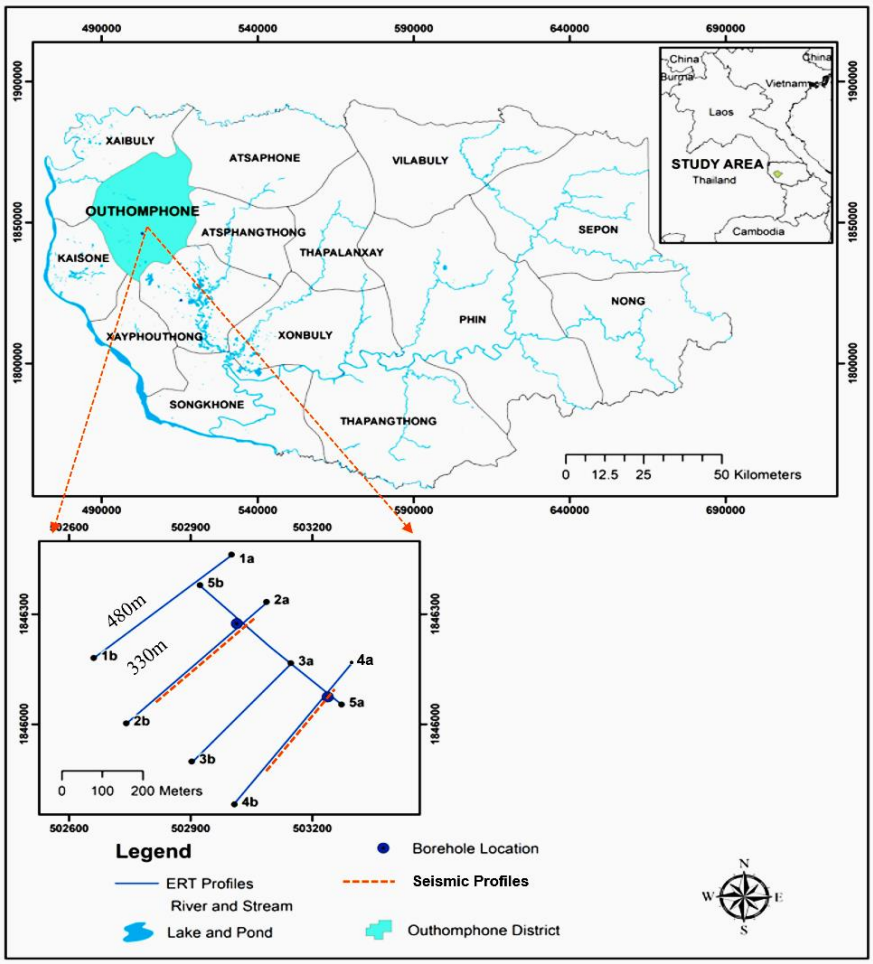

Fig. 3. *Location of the orientation of geophysical survey profiles.*

The average rainfall is about 1780 mm, but it varies regionally [17]. The five ERT profiles were conducted at the study sites, these profiles were oriented in the NE to SW directions, maximum length of profile of 440 to 480m (Fig. 3). The Wenner electrode array was selected to conduct with electrode spacing of a=10 up to 160 m. The data were recorded by manually and automatically in the Terrameter ABEM SAS 1000 (made in Sweden). The two seismic refraction profiles were conducted on overlies on two selected ERT profiles (2 and 4) in the study area, used the SmartSeis ST with 12 channels seismograph (made in USA), seismic profile length of 330 m (Fig. 3), with geophone

interval of 5 m, and consists of 6 spreads for each seismic profile. In this measurement, consisted of laying out 12 geophones in a straight line and recording arrival times from shot points produced by striking a 6.5 kg sledge hammer into a steel plate at 7 shots per spread: one inter-spread shot, three forward and three reverse shots (Fig. 4). The first geophones of spread 1 located at 0 m and the 12th geophone at 55 m; while the first geophone of spread 2 located at 55 m and the 12th geophone at 110 m then move to next spread until reach to the first geophone of spread 6 located at 275 m and the 12th geophone at 330 m. Additionally, two boreholes were drilled at the study area to calibrate, verify and complement the geophysical results.

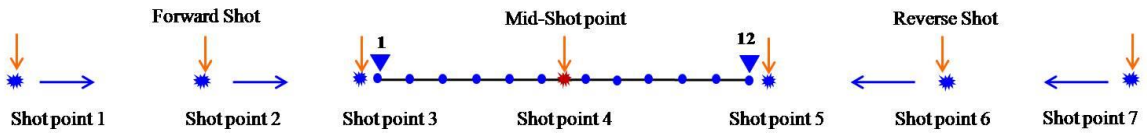

Fig. 4. *A typical seismic refraction data acquisition layout and location of shot points for seismic refraction survey profile.*

III. RESULTS AND DISCUSSION

Four parallel NE to SW oriented profiles (1,2,3 and 4) at the study area showed similar results (Fig. 5).

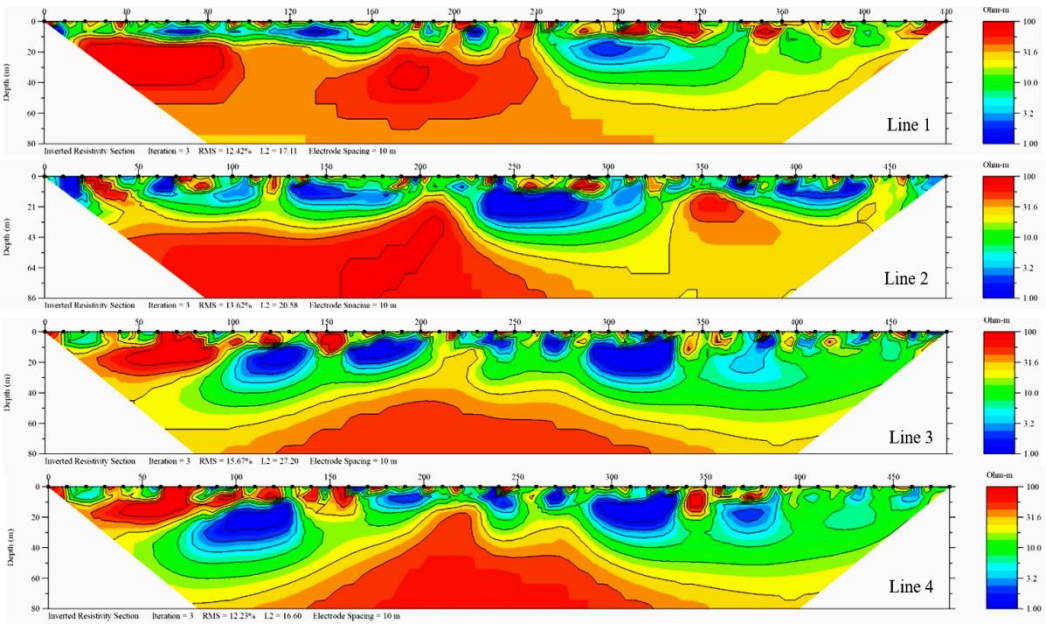

Fig. 5. *2D electrical resistivity tomography (ERT) models under profiles 1,2,3 and 4.*

High resistivity regions greater than 100 Ohm.m found at 15-80m depth along these profiles with unclear thickness are considered as sandstone or bedrocks layers of these profiles. The relative low resistivity regions less than 15 Ohm.m appear at some zones for each profile with unclear thickness are interpreted to be a thick clay zone. However, moderate resistivity regions of 15 to 60 Ohm.m are observed at 16 to 80m depth along these profiles, indicating possibly suitable areas for groundwater potential zones. In order to correlate the existence and positions of the subsurface layers, a fifth profile (profile 5)

 ISBN:

was oriented crossing the two parallel profiles (2 and 4) in an ES to WN direction, with crossing points of profiles 2 and 4 at 60 m and 330 m respectively (Fig. 6). High resistivity values greater than 100 Ohm.m found at 10-80m depth, distances between 0 and 160 m at the depths of unclear, is considered as sandstone or bedrocks layers of the profile. The relative low resistivity regions less than 10 Ohm.m appear at some zones for this profile with unclear thickness are interpreted to be a thick clay zone.

However, moderate resistivity regions of 10 to 60 Ohm.m are observed at 18 to 80 m depth along the profiles, indicating possibly suitable areas for groundwater potential zones.

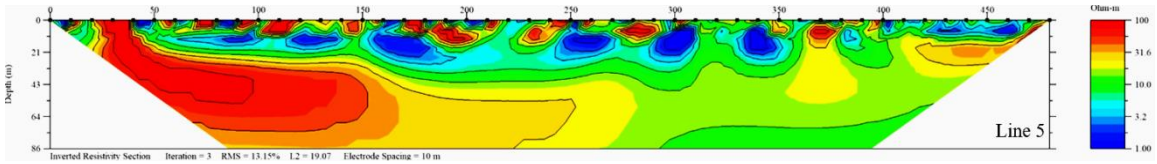

Fig. 6. *D electrical resistivity tomography (ERT) model under profile 5.*

In additionally, two seismic refraction profiles (1 and 2) were conducted at over lied on selected ERT profiles (2 and 4), including two boreholes were drilled at these profiles in order to compare positions of water table or aquifers layers. The obtained results from the borehole 1 and 2 (BH-1 and BH-2) and seismic velocity models results found the water table at about 16 m depth for borehole 1 and 20 m depth for borehole 2 respectively, with soil samples collected from both two boreholes have been identified as sandstone and siltstone at water table interface (Fig. 7c and 8c), which respond well for resistivity models with regions of 15 to 60 Ohm.m (Fig. 7a and 8a) and seismic velocity models with range from 1200 to 1800 m/s were identified for groundwater potential zones (Fig. 7b and 8b).

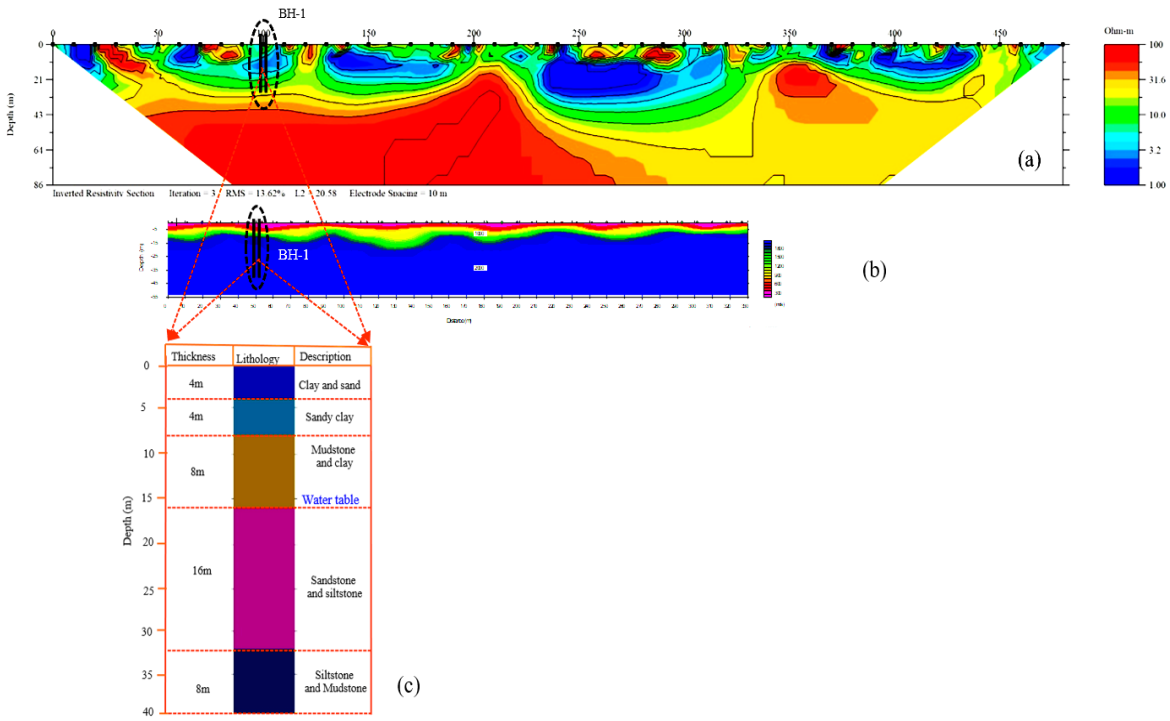

Fig. 7. *a) 2D electrical resistivity tomography (ERT) models under profile 2; b) vertical geological section of borehole 1 (BH-1) at 100 m along ERT profile 2 and 50 m along seismic profile 1; c) The seismic velocity models under profile 1.*

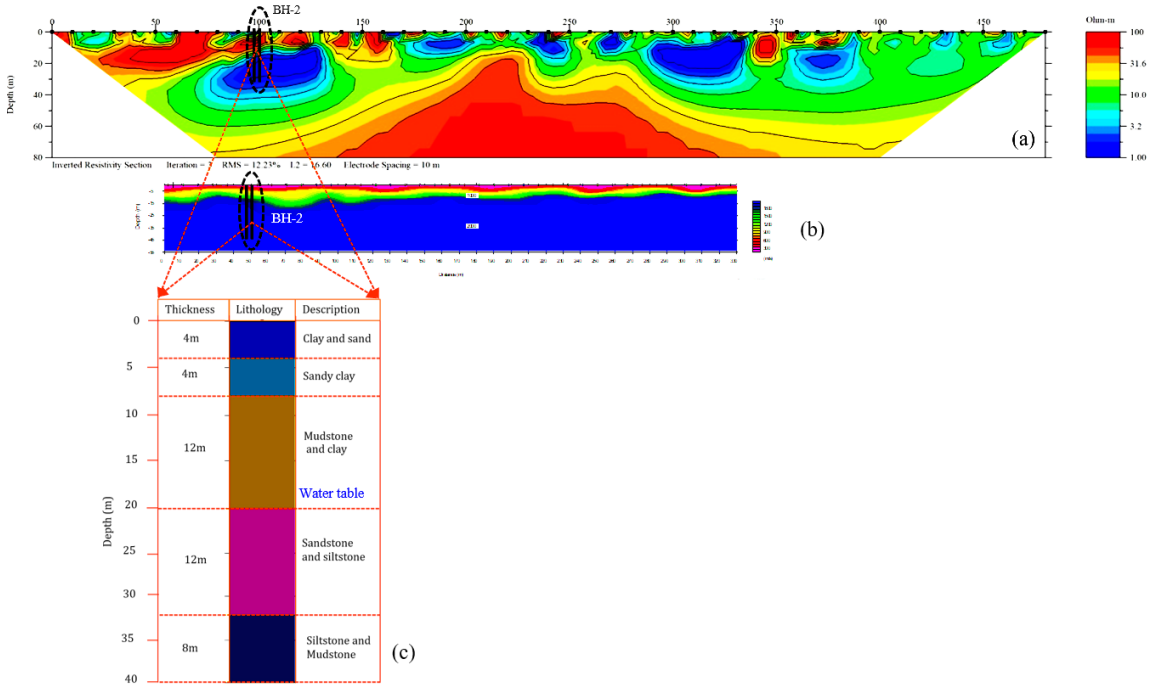

Fig. 8. *a) 2D electrical resistivity tomography (ERT) models under profile 4; b) vertical geological section of borehole 2 (BH-2) at 100 m along ERT profile 2 and 50 m along seismic profile 1; c) The seismic velocity models under profile 2.*

IV. CONCLUSION

The ERT and seismic refraction technique have been proved in mapping the subsurface earth layers. The relative low resistivity regions less than 15 Ohm.m and seismic velocity regions of 300 to 800 m/s are considered as clay layers whereas high resistivity regions greater than 100 Ohm.m and seismic velocity greater than 1800 m/s are interpreted as sandstone or bedrocks layers, and the moderate resistivity regions of 15 and 60 Ohm.m and seismic velocity regions of 1200 to 1800 m/s found at 16 to 20m depth are considered as water table, indicating water table that correlates well with groundwater table from the obtained results from borehole information in the study area. The results of this research work have indicated that the application of the electrical resistivity tomography and seismic refraction exploration methods to identify groundwater in the study areas is feasible and effective. The results of this study will be useful for assessment and groundwater investigation and can be applied for groundwater investigation in other similar geological areas in Lao PDR.

ACKNOWLEDGMENTS. We would like to thanks to the International Science Programme (ISP) of Uppsala University, Sweden and International Center of Physics, Institute of Physics, Vietnam, Grant number ICP.2019.09 for research grant supporting in this research work. The authors would like to express our deepest appreciation to Department of Physics, Faculty of Natural Sciences, National University of Laos for supporting the geophysical equipment and Department of Geology and Mines of Laos for geological information in the study areas. Special thanks to Mr. Thiengsamone

Sounsuandao and BSc. students from Department of Physics, Faculty of Natural Sciences, National University of Laos for the hard fieldwork assistance.

REFERENCES

[1] K. Medlicott, Water sanitation and environemtal health in rural Lao PDR, KAP study for UNICEF, WES Section, August 2001, 20.

[2] K. Takayanagi, Basic design study report on the Project for groundwater development in Vientiane province in Lao PDR, Japan International Cooperation Agency (JICA*)*, 1993.

[3] J. R. Knudsen, The online support and training project for groundwater sector of Lao PDR. 2004, 434-437.

[4] T. Dahlin, V. Leroux, & J. Nissen, Measuring techniques in induced polarisation imaging, *Journal of Applied Geophysics*, 2002, **50**(3), 279-298.

[5] J. M. Reynold, An Introduction to Applied and Environmental Geophysics, Wiley Eds., England, 2002.

[6] M. H. Loke, R. D. Barker, Rapid least-squares inversion of apparent resistivity pseudosections by a quasi-Newton method, *Geophysical Prospecting*, 1996, **44**, 131-152.

[7] P. Kearey, M. Brooks, I. Healy, An introduction to geophysical exploration, The 3rd Ed., Blackwell Science, 2002.

[8] G. Grelle and F. M. Guadagno, Seismic refraction methodology for groundwater level determination: Water seismic index, *Journal of Applied Geophysics*, 2009, **68**, 301-320.

[9] B. Hasselstroem, Water prospecting and rock-investigation by the seismic refraction method, *Geoexploration*, 1969, **7**(2), 213.

[10] G. Amir, M. Ahmed, B. Haydar, B. Khalid, A. Hasan, and M. Saber, The use of seismic refraction and electrical techniques to investigate groundwater aquifer, wadi al-ain, United Arab Emirates (UAE), Conference Proceedings, Tulcea - Romania, 2012, ISBN: 978-606-605-038-8, 94-99.

[11] S. Thomas, W. Benjamin and A. S. Anne, Case study of a geophysical investigation with seismic refraction tomography and the Ohm Mapper to estimate the brine content of a Salar/Salmuera, *Near Surface Geoscience*, 2013, **31**, 85-90.

[12] J. O. Osumeje and E. A. Kudamnya, Hydro-geophysical investigation using seismic refraction tomography to study the groundwater potential of Ahmadu Bello University main campus, within the basement complex of Northern Nigeria, *Journal of Environment and Earth Science*, 2014, **4**(2), 15-22.

[13] Adewoyin, E. O. Joshua and M. L. Akinyemi1, Application of shallow seismic refraction method and geotechnical parameters in site characterization of a Reclaimed Land, *Indian Journal of Science and Technology*, 2016, **9**(45), 17485.

[14] O. Anomohanran, Geophysical interpretation of seismic reflection data obtained from Umureute and Amiynaibo area of delta state. Nigeria, *Nigerian, J. Sci. Environ*., 2012, **11**, 148-153.

[15] Andy A. Bery, High resolution in seismic refraction tomography for environmental study, *International Journal of Geosciences*, 2013, **4**, 792-796.

[16] S. A. Adedibu, C. O. Abimbola, Insight into seismic refraction and electrical resistivity tomography techniques in subsurface investigations, *The Mining-Geology-Petroleum Engineering Bulletin*, 2019, 93-111.

[17] M. Stuart-Fox, D. F. Rooney, Microsoft Encarta, 2006.

THREE-DIMENSIONAL STITCHING METHOD FOR NON-CONTACT ON-MACHINE SURFACE TOPOGRAPHY MEASUREMENT BY USING WHITE LIGHT SCANNING INTERFEROMETRY SYSTEM

Vo Quang Sang[1*], Yiting Duan[2]

[1]*Department of Optical Engineering, Le Quy Don Technical University, Ha Noi, Viet Nam*

[2]*Centre of Micro-nano Manufacturing Technology, Tianjin University, Tianjin, China*

*E-mail: *quangsang88ktq@gmail.com*

Abstract. Non-contact three-dimensional (3D) topography measurements have been widely used in machine vision, automatic processing, rapid prototyping, industrial online detection, product quality control, biomedicine, and other fields. On-machine metrology is playing an increasingly important role in the process chain of manufacturing technologies. However, it is necessary to stitch a small area of images together for large surface analysis while the measurement instrument is used with a limited measurement area. In this work, we describe a novel 3D stitching method for non-contact on-machine measurement by using white light scanning interferometry (WLSI) system. An improved ICP (Iterative Closest Point) algorithm based on an adaptive optimal threshold to align two shape models was proposed to register the point cloud. Hence, the target model and the source model are matched, and all matching point pairs are searched and system errors are calibrated. In addition, we have successfully designed a low-cost, compact size, and high-precision WLSI measurement probe. Experiments show that our proposed stitching method can effectively stitch 3D images of the online machining process with a correlation coefficient above 0.9 for two horizontal overlapping regions after adjustment. Furthermore, we can use the WLSI in-line measurement system to achieve large-scale mosaic measurements. Thus, good mosaic results can still be obtained under general noise conditions.

I. INTRODUCTION

With recent advancements in the fields of ultra-precision machining and high-quality modern optics, engineers from various industries including the manufacturing have increasingly sought a high-accuracy optical surface topography applied to a measurement technique. WLSI has been a well-known and established measurement technique [1,2] and owing to its has high modularity, wide horizontal measurement range, and high vertical resolution, a WLSI measurement system provides a fast, non-contact method for measuring the surface forms. In-line surface metrology can describe by measurement of the workpiece surface carried out on a production line without moving the workpiece outside the production line [3-5]. Consequently, in-line surface metrology can be defined as the workpiece's measurement on the same work floor and in the same manufacturing environment, without isolating the workpiece from the manufacturing environment. In-line measurement refers to the workpiece's measurement without unloading the workpiece on the machine after the completion of processing. Therefore, the main advantage of in-line measurement is that it avoids the positioning of data's errors in off-line detection. The detection results are closer to the real surface. Simultaneously, according to the test results,

 ISBN:

the process can be adjusted in time to reduce the production waste rate. Besides, in-line inspection is an effective method for process control and quality inspection of large and precise workpieces. As mentioned above, in-line measurement technology is an efficient and integrated measurement method. The measurement system is integrated into the processing system, especially suitable for ultra-precision manufacturing of complex surfaces. Besides, the high precision and fast in-line measurement system can improve the processing efficiency and accuracy and effectively avoid the repetitive positioning problem of complex surface micro-workpiece. In recent years, researchers have done in-depth research and developed a large number of in-line measuring instruments. Thus, ultra-precision measurement has been gradually developed from micron to submicron or even nanometer. Fig. 1 shows the flow chart for the in-line measurement of the optical surface.

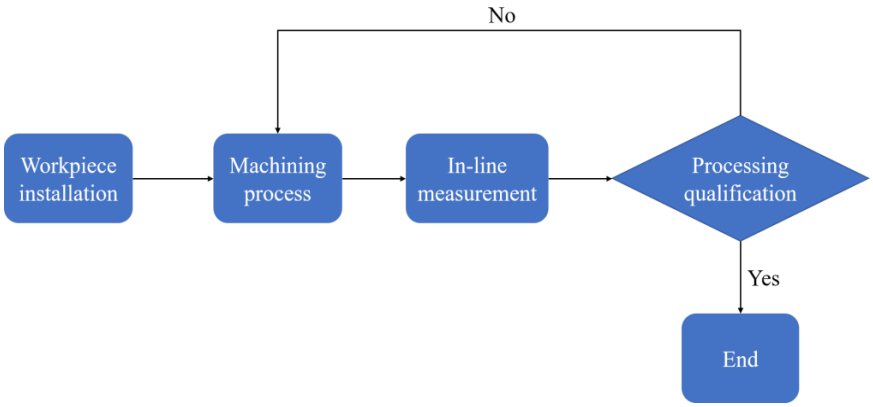

Fig. 1. *Flow chart for in-line measurement of optical surface.*

Currently, the range of the original measurement system is extended by the machine axes, and the measurement path can be controlled using a CNC machine. Hence, point to point scanning is typically used in these current in-line measurements. Moore Nanotech provided a Workpiece Measurement and Error Compensation System (WECS) for on-machine metrology in which an air bearing linear variable differential transformer (LVDT) probe is mounted onto an ultraprecision turning machine [6,7]. This probe moves along the ideal measurement path under control of the X- and Z-axes, whereas the LVDT sensor captures the positional deviation of the probe owing to a shape error of the measured surface. This system provides a compensation of the shape errors through a filtering operation. Therefore, several variants of this approach have been applied. A different way to achieve an ultra-precision in-line measuring is using an AFM system. In 2004, Gao et al. [8] realized aspheric surface morphology detection based on error separation technology using a double probe method. In 2007 [9], they mounted an AFM cantilever tip on a diamond turning machine, and a linear encoder with a resolution of 0.5nm for an accurate measurement of the Z-directional profile height in the presence of noise associated with a diamond turning machine. According to the current development of the micro-nano manufacturing technology, the vertical distribution range of nano-precision microstructures has increased from the micron to millimeter. Due to the limited field of view of a microscope, only a small area can be obtained in a single measurement by WLSI. To achieve an extensive surface measurement range, fast and accurate 3D image stitching technologies have to be used [10,11]. The measurement range of WLSI needs to be

increased from the sub-millimeter level to tens of millimeters to meet the practical application requirements, which is called a large-range surface measurement instrument. In general, the measurement of large-scale transverse microstructures is limited by the size of a single optical field of view. Therefore, one needs to divide the measured surface into a series of single fields of view, measure the microstructures separately, and then mosaic the measured three-dimensional images of a series of surfaces.

In this work, we describe a novel 3D stitching method for non-contact on-machine measurement by using white light scanning interferometry (WLSI) system. An improved ICP (Iterative Closest Point) algorithm based on an adaptive optimal threshold to align two shape models was proposed to register the point cloud. Hence, the target model and the source model are matched, and all matching point pairs are searched and system errors are calibrated. In addition, we have successfully designed a low-cost, compact size, and high-precision WLSI measurement probe. Experiments show that our proposed stitching method can effectively stitch 3D images of the online machining process with a correlation coefficient above 0.9 for two horizontal overlapping regions after adjustment. Furthermore, we can use the WLSI in-line measurement system to achieve large-scale mosaic measurements. Thus, good mosaic results can still be obtained under general noise conditions.

II. EXPERIMENTS

To verify the simulated results by the proposed algorithm, our experimental WLI setup is shown in Fig. 2.

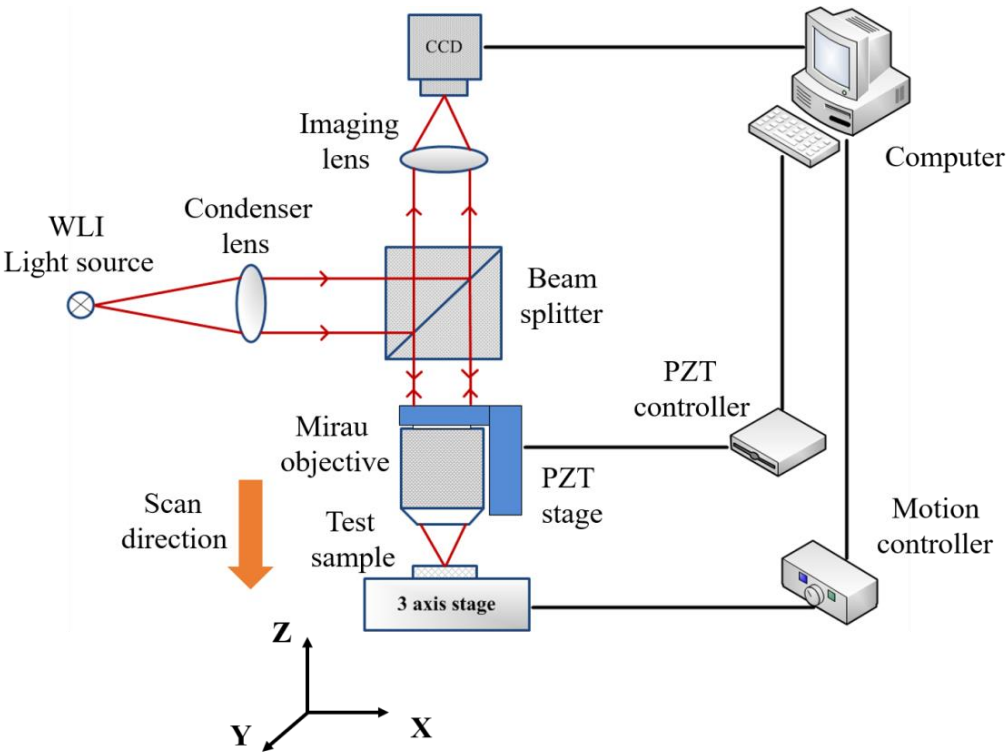

Fig. 2. *Schematic of experimental arrangement for the proposed WLI algorithm.*

 ISBN:

A Mirau type interferometric microscope with an objective lens with magnification of 20× and numerical aperture of 0.4 was used to capture the interferogram, which was recorded by a CCD camera with a resolution of 640×480 pixels and frame rate of 30 Hz, through imaging lens. A PZT nano-position stage (P-841.10, Physic Instrument) and an XY translation stage (Thorlabs, MSC202) controlled by high-precision motion control (BBD202 of Brushless DC Motor Control) was used to move the specimen vertically and horizontally, respectively. The PZT was able to achieve a 0.3nm scanning resolution and was controlled by a servo-controller (E-625.SR, Physic Instrument). A PZT translator for moving the objective vertical scanning in nanometer range, and the CCD camera (SCA1300, Ximea) was used to capture a series of interferograms. The light source was a halogen lamp with a broad continuous spectrum. The object was mounted on a PZT stage, controlled by a computer to move it along the z-direction with a specific interval. For each nanometer scale increment, the CCD recorded one fringe pattern and stored it in a computer. A series of fringe patterns were analyzed and a 3D profile of the test object was obtained. Fig. 3 shows the actual experimental system, which is a miniaturized modified based on the WLSI measurement system. Herein, the probe size is only 11.6 cm × 22 cm, which can simultaneously carry out an off-line measurement and in-line measurement. Its structure is simple, low cost, easy integration, easy adjustment, fast speed, high precision, and strong anti-interference ability.

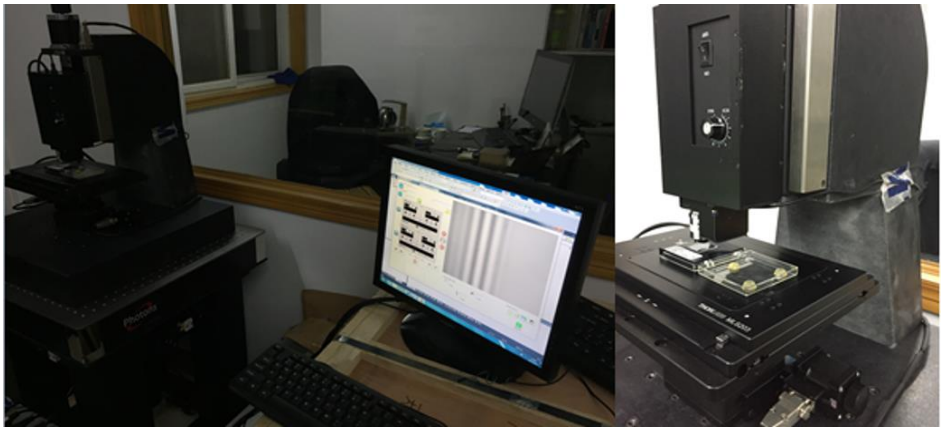

Fig. 3. *WLSI measurement system experimental setup.*

III. RESULTS AND DISCUSSION

The following experiments were performed to verify the in-line measurement of proposed WLSI system. A Moore Nanotech 350 in-line measuring probe was adopted as shown in Fig. 4. First, the standard sphere of 3/8 inch diameter was used to align probe on system coordinate, as shown in Fig. 4a. Further, a test workpiece of copper material are used for in-line measurement experiments, as shown in Fig. 4b. Here, the propose miniaturized WLSI measurement probe was mounted to the Z-axis precision stage, and the optical axis of the probe is perpendicular to the surface of the array plane workpiece. Besides, a linear scanning measurement (the linear movement of the workpiece along the X-direction) was performed on the test workpiece. Fig. 5 show the measurement results acquired by the WLSI measurement probe, respectively.

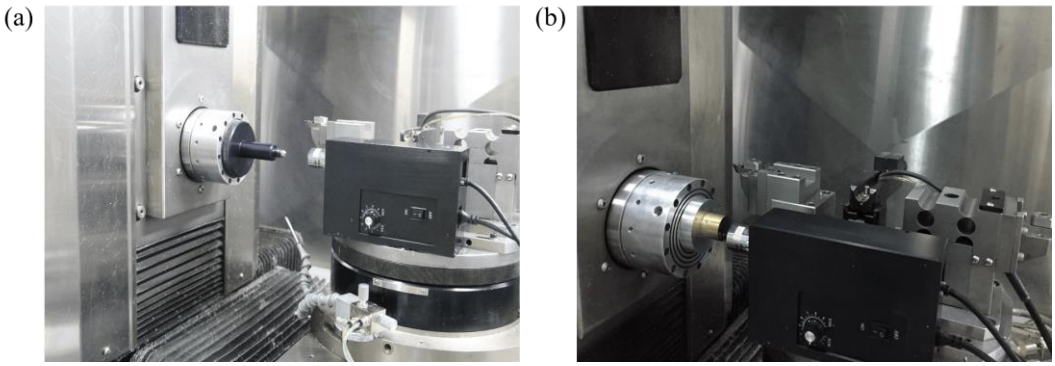

Fig. 4. *In-line measurement device for proposed WLSI system.*
a) Calibration by standard sphere; b) Measuring array plane of copper material.

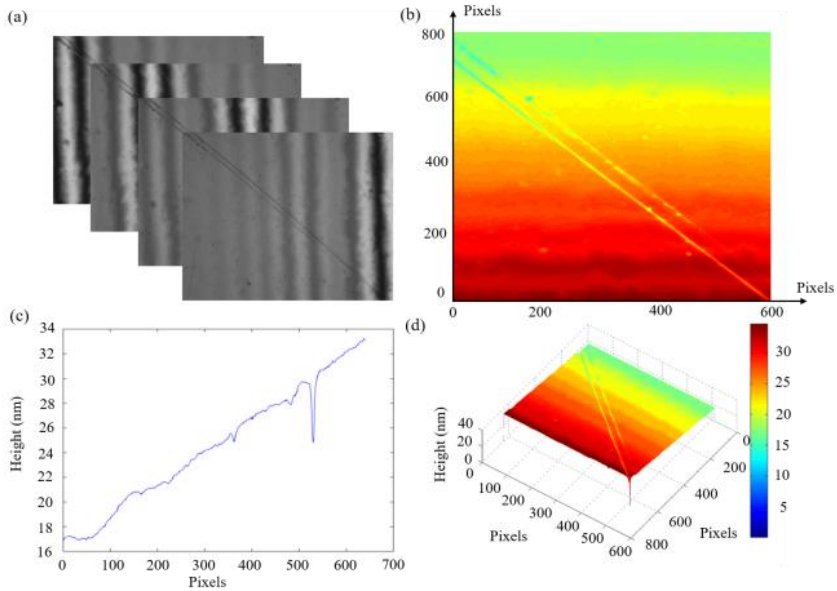

Fig. 5. *Measured surface maps of workpiece by using in-line WLSI system.*

Further, it necessary to implement large-scale measurement and introduce image mosaic in vertical scanning. This method includes two processes: overlapping image-stitching and non-overlapping image stitching. To verify the validity of the stitching algorithm and the WLSI measurement system, the stitching experiment was carried out with a planar workpiece. In this experimental, a 3D stitching method for in-line measurement by the proposed WLSI system was used. An improved Iterative Closest Point (ICP) algorithm based on the optimal adaptive threshold to align two shape models was introduced to register the point cloud. Hence, by matching the target model and the source model are matched, it can obtain all matching point pairs. After that, the calibrate system errors can be achieved. Due to the many numbers of images, in this work, the MATLAB software was used to save us from many complicated calculations. Herein, the stitching process of WLSI in-line measurement can described in Fig. 6.

In the stitching process, the four sub-graphs are 6400×512 pixels in size, and the stitching image size is 1280×1024 pixels. The machine tool moves a certain distance along the horizontal X direction. The magnification of 50X and the scanning step of 50 nm are selected to complete the experiment. Here, the single-step distance value of 10 μm in X

 ISBN:

and Y directions to make the overlap between images 20%. After that, the subgraphs of four regions can be obtained by translational motion, as shown in Fig. 7.

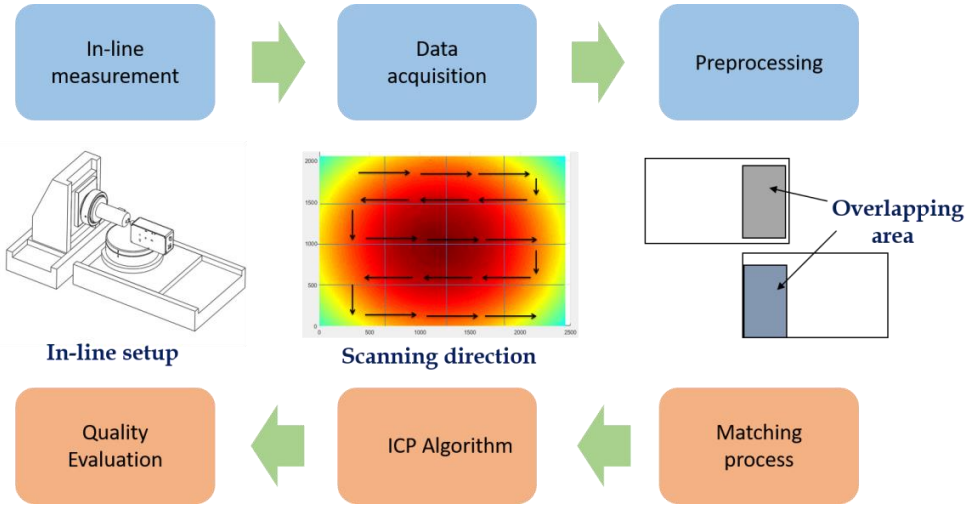

Fig. 6. *WLSI in-line measurement sub-region stitching process.*

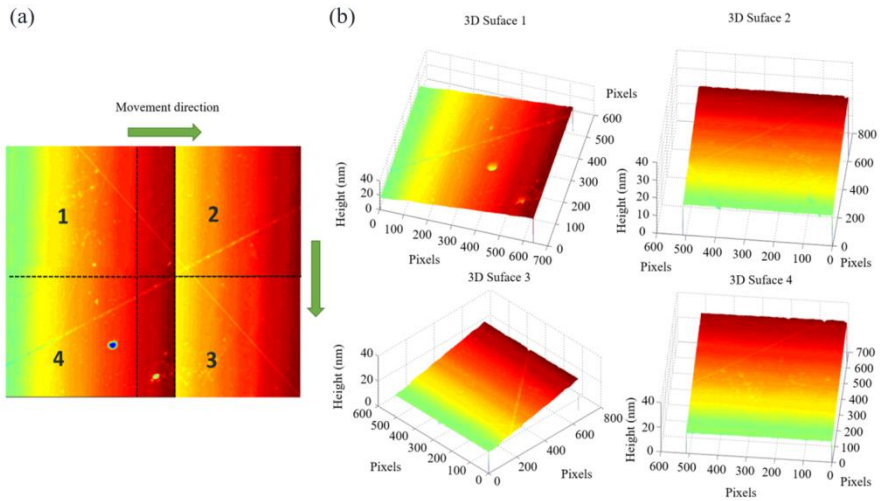

Fig. 7. *a) 3D Surface topography of four sub-graphs Stitching approach; b) 3D surface topography.*

Fig. 7a shows the direction of movement and the position of a stitching sequence of four sub-images. Also, Fig. 7b describes the characterization of three-dimensional surface topography. After the registration and stitching process, the surface profile of these images is merged to form a single image. According to the above-described stitching method, the measurement results of four sub-region 3D topography mosaics can be obtained, as shown in Fig. 8. The above results of the stitching test show that there are horizontal and vertical deviations between adjacent measuring sub-regions due to the movement of the worktable along the horizontal direction and the discontinuous vertical scanning. Consequently, the accuracy of the measurement results is affected. It can be seen that this result has proved that data fusion is good. Furthermore, the WLSI in-line measurement system was used to achieve large-scale mosaic measurements. Thus, good mosaic results can still be obtained under general noise conditions. Besides, the validity and practicability of the WLSI measurement system are verified by mosaic experiments using sub-images.

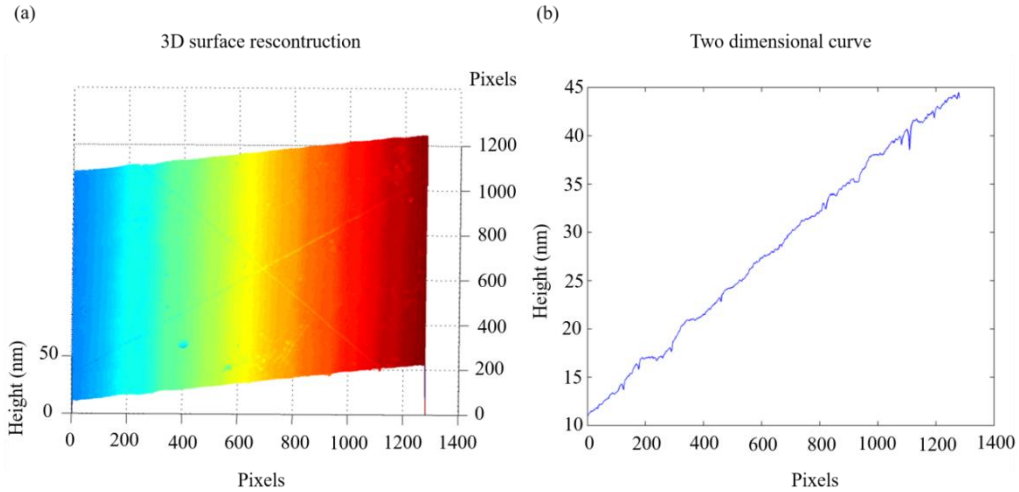

Fig. 8. *Measured results surface topography of four sub-graphs: a) 3D surface reconstruction; b) 2D cross profile.*

IV. CONCLUSION

A high precision and miniaturized WLSI measurement probe was also developed. Through the design and modeling of the WLSI system, including the hardware and software design of the system, the accuracy and stability of the developed system were successfully measured. In the overall software design, a modular design idea is used to improve the stability and scalability of the software system. Finally, the experimental verification results of the off-line and in-line measurement of the miniaturized WLSI system are verified. Also, the actual measurement experiments of standard step and standard spheres are carried out by using the WLSI system, and the errors of the measurement system are analyzed and summarized. Moreover, the stitching in-line measurement is proposed to realize the high accuracy and easy-operating remounting method for miniaturized WLSI system. Thus, the proposed system has great potential for in-line and off-line high precision measurement approach.

ACKNOWLEDGMENTS. The authors would like to express their sincere thanks for the supports of the State Key Laboratory of Precision Measuring Technology & Instruments, Centre of Micro-nano Manufacturing Technology, Tianjin University, Tianjin, China. This work is supported by Funding of Le Quy Don Technical University under Grant Number (21.1.25).

REFERENCES

[1] Mun J. I., Jo T., Kim. T., et al., Residual vibration reduction of white-light scanning interferometry by input shaping, *Optics Express*, 2015, **23**, 464-470.

[2] Pavlicek P., Hybl O., White-light interferometry on rough surfaces-measurement uncertainty caused by noise, *Applied Optics*, 2012, **51**, 465-473.

 ISBN:

[3] Wang D. D., Yang Y. Y., Luo Y. J., et al., In situ measurement technology of piezoelectric micro displacement based on template matching algorithm, *Journal of Instrumentation*, 2010, **31**, 530-535.

[4] Wang L. C., In situ detection method and experimental research of complex curved surface. Huazhong University of Science and Ttechnology, Master Thesis, 2012.

[5] Ohmori H., Watanabe Y., Lin W. M., et al., An ultraprecision on-machine measurement system, *Key Engineering Materials*, 2005, **295**, 375-380.

[6] Pang C. T., Zhang J. M., Luo S. B., et al., Research on LVDT online detection system based on ultra precision machine tool, *Aviation precision Manufacturing Technology*, 2005, **41**, 30-34.

[7] Liu J., Guo Y., Jing H., et al., Non-contacting measurement system design of ultra-precision aspheric surface, International Symposium on Advanced Optical Manufacturing and Testing Technologies: Optical Test and Measurement Technology and Equipment, International Society for Optics and Photonics Conference, 2006.

[8] Gao W., Haitjema H., Fang F. Z., et al., On-machine and in-process surface metrology for precision manufacturing, *CIRP Annals - Manufacturing Technology*, 2019, **68**, 843-866.

[9] Yoshikazu A., Gao W., Hiroki S., et al., On-machine measurement of aspherical surface profile, *Nanotechnology and Precision Engineering*, 2004, **2**, 212-216.

[10] Schtzer K., Stroh C., Schulz H. C., Space based approach for the calculation of toolpaths for freeform surfaces in B-Spline description, *CIRP Annals - Manufacturing Technology*, 2010, **59**, 421-424.

[11] Weckenmann A., Jiang X., Sommer K. D., Multisensor data fusion in dimensional metrology. *CIRP Annals*, 2009, **58**, 701-72.

WAVEFORMS CLASSIFICATION OF NORTHERN SUMATRA EARTHQUAKE BASED ON SEISMIC NETWORK STATION USING A RANDOM FOREST MACHINE LEARNING APPROACH

Marzuki Sinambela[1], Pham Hong Minh[2]

[1]*Agency for Meteorology Climatology and Geophysics (BMKG), Indonesia*

[2]*Institute of Physics, Vietnam Academy of Science and Technology, Vietnam*

*E-mail: *sinambela.m@gmail.com, phminh@iop.vast.vn*

Abstract. Earthquake activity in Northern Sumatra had been continuing to increase in the past year, this condition can be seen from the number of earthquakes that occur, and recorded in regional Center of Meteorology, Climate and Geophysics (BMKG) at more than a thousand events in the 2020 year. The result of the waveform earthquake, describes the variations of earthquakes that occurred in Northern Sumatra, which are quite active, this is due to the potential for seismicity due to subduction sources, and local faults. In this study, the classification of earthquakes that occurred on land and has been recorded by the seismic network at the regional center was carried out using a machine learning approach using random forest. The results of this study illustrate that signal classification with random forest produces an accuracy value of 0.747 and a Receiver operating characteristic (ROC) value of 0.827. This approach with the random forest model shows a good classification of the low signals that have been recorded in the seismic network on a regional scale.

Keywords: *Waveforms, Classification, Earthquake, Machine learning, Random forest.*

I. INTRODUCTION

The seismic waveform is one of the main difficulties to mature automatic detection system for them. In a broad sense, Machine Learning (ML) is not only techniques that extract information directly from the waveform [1,2] but also is a core component in any variance digital signal processing to improve the quality of signal [3,4]. In this case, we use the random forest as a method approach for classification and analyzing signal. The present porpose of this paper to classification of earthquakes that occurred on land and has been recorded by the seismic network at the regional center was carried out using a machine learning approach using random forest. The result of the waveform earthquake, describes the variations of earthquakes that occurred in Northern Sumatra, which are quite active, this is due to the potential for seismicity due to subduction sources, and local faults. The results of this study illustrate that signal classification with random forest produces an accuracy value of 0.747 and a Receiver operating characteristic (ROC) value of 0.827. This approach with the random forest model shows a good classification of the low signals that have been recorded in the seismic network on a regional scale.

II. DATA AND METHDOS

2.1. Data

 ISBN:

The waveforms were employed in Northern Sumatera Region, which recorded from the seismic network. We selected the Mini Region (MiniReg) sensor for more events in the end of year 2019 to April 2020, which recorded from Data Archives. The MiniReg seismic network produced the raw waveform data with component Short Horizontal (North, East and Z component), and located in Sumatera Region (Figure 1).

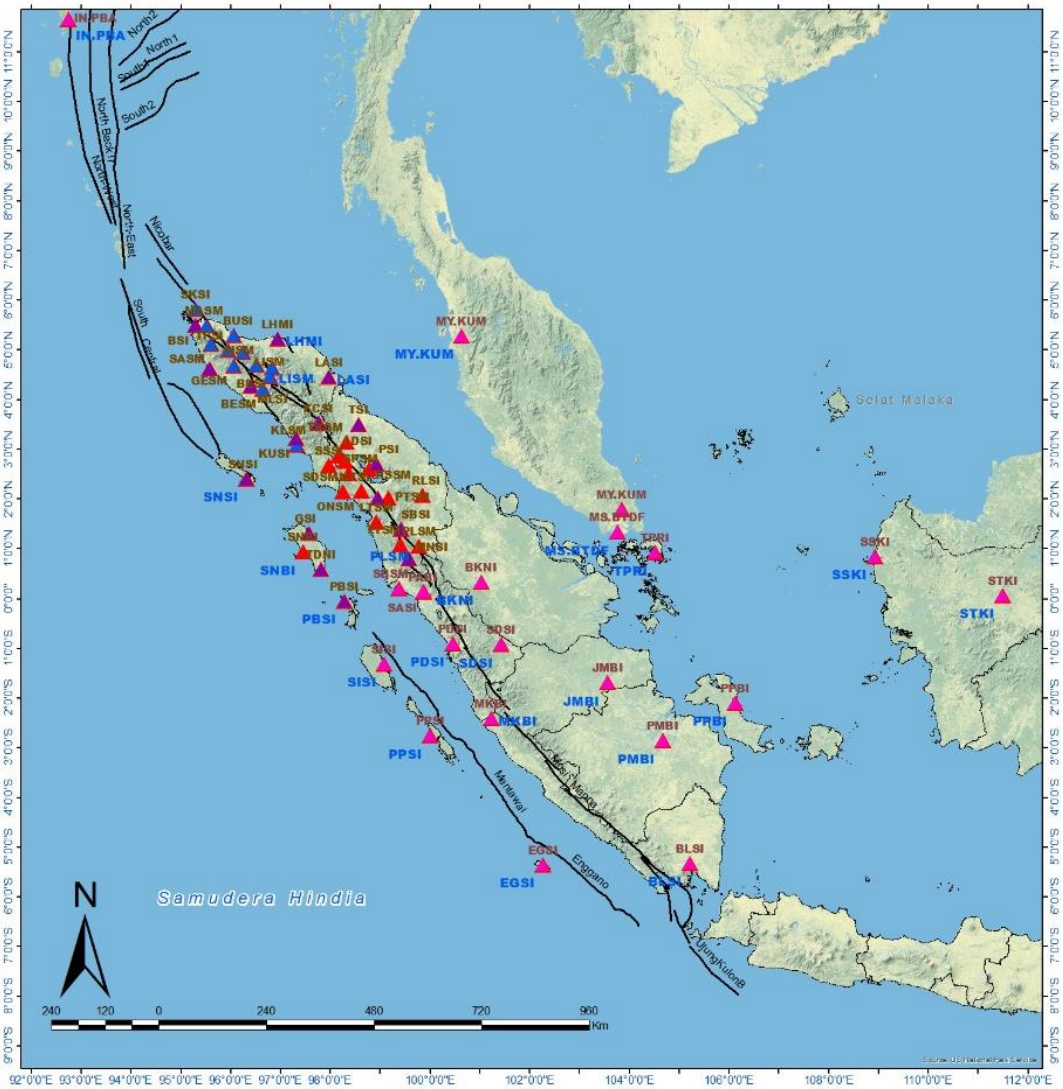

Fig. 1. *Network Seismic Station in Northern Sumatera.*

2.2. Methods

In this paper, we use the random forest machine learning approach to classification of earthquakes that occurred on land and has been recorded by the seismic network at the regional [5]. A random Forest like its identify implies, consists of a massive wide variety of man or woman choice timber that function as an ensemble [6,7]. Each character tree in the random wooded area spits out a category prediction and the type with the most votes becomes our model's prediction. The low correlation between models is the key. Just like how investments with low correlations (like stocks and bonds) come collectively to structure a portfolio that is larger than the sum of its parts, uncorrelated models can produce ensemble predictions that are extra accurate than any of the person predictions.

The reason for this high-quality impact is that the timber defends each other from their character blunders (as long as they don't continuously all err in the same direction). While some timber can also be wrong, many other trees will be right, so as a team the bushes are able to pass in the correct direction [8,9].

III. RESULTS AND DISCUSSION

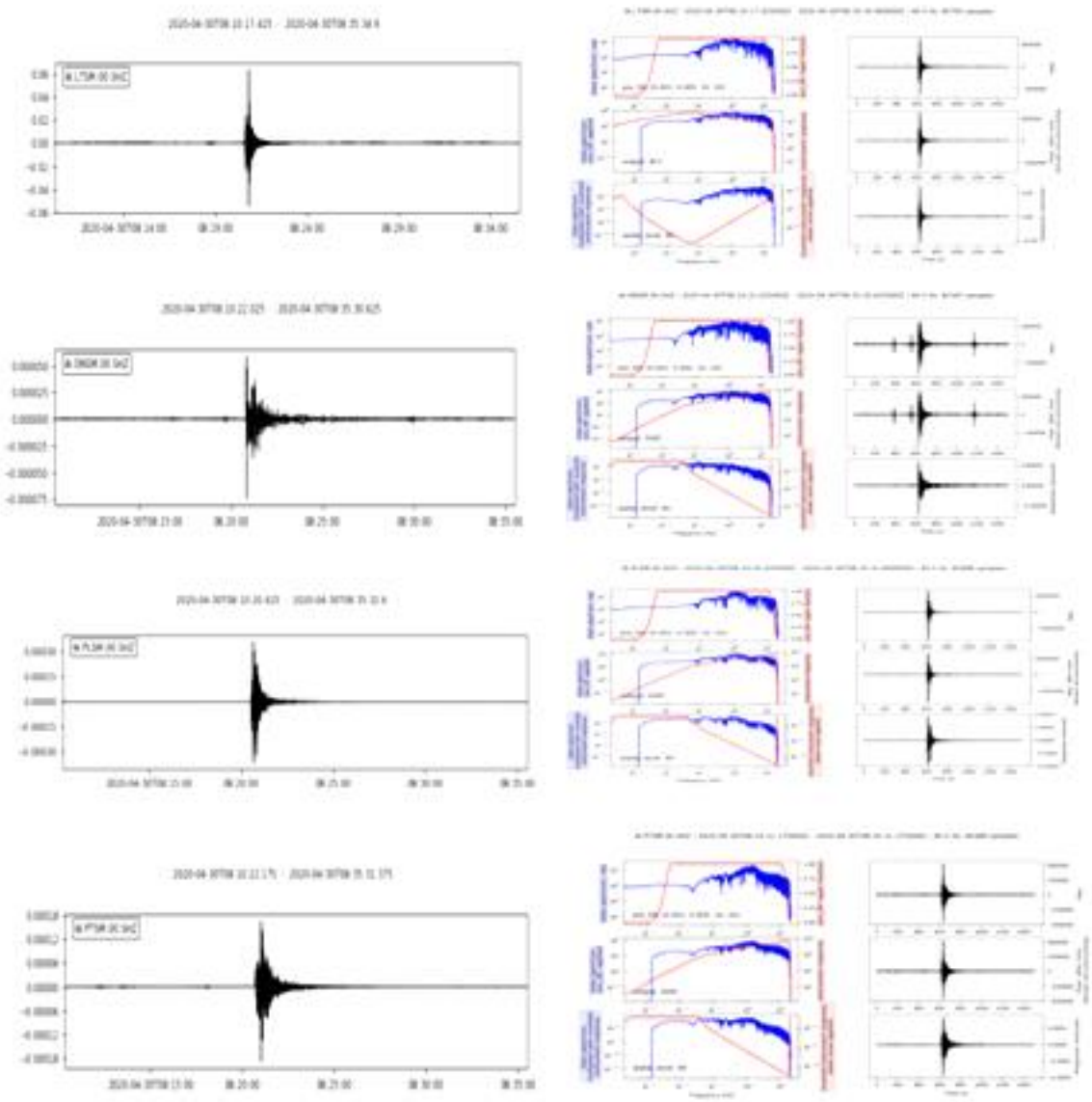

Fig. 2. *Seismograph analysis based on earthquake classification.*

Waveform analysis from the results of earthquake testing in North Sumatra in late 2019 to April 2020, illustrates the very good signal quality in monitoring earthquakes that occur both on land and at sea. In this study, signal analysis is devoted to sensors installed in Northern Sumatra, namely the new sensor mini region. Based on the results of the analysis, the signal characteristics are very local, as can be seen from the very short signal length. It shows a waveform analysis of a displacement seismometer. These results illustrate that the waveform characteristics of the new sensor recordings of the mini region are very effective in detecting earthquakes that occur in Northern Sumatra, especially

 ISBN:

events that are local or local earthquakes. With this, the performance of the new mini-region sensor is optimal for detecting potential earthquake events in North Sumatra [10,11]. Earthquake analysis can be detected by several sensors that have been installed and built in Northern Sumatra.

The results of this study as show in Fig. 2 that a seismograph analysis of the displacement seismometer. These results illustrate that the waveform characteristics of the new sensor recordings of the mini region are very effective in detecting earthquakes that occur in Northern Sumatra, especially events that are local or local earthquakes. With this, the performance of the new mini region sensor is optimal for detecting potential earthquake events in North Sumatra.

Based on the a random forest machine learning approach, the resultof this paper illustrate that signal classification with random forest produces an accuracy value of 0.747 and a Receiver operating characteristic (ROC) value of 0.827. This approach with the random forest model shows a good classification of the low signals that have been recorded in the seismic network on a regional scale.

Methode	Deskription	Accuracy	Pos Recall	Pos F1 score	ROC Score
Benchmark	Random forest	77.04%	0.77	0.77	82..75%

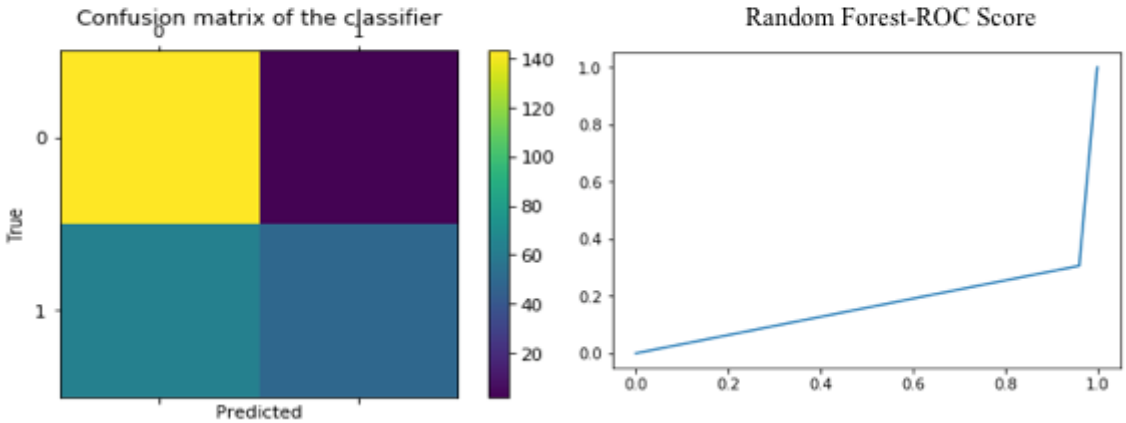

Fig. 3. *Benchmark with random forest machine learning approach.*

IV. CONCLUSION

The performance of the Random Forest model depends on the number and spatial range of recording stations. Classification should be based on several stations located in different azimuth directions around the epicenter. Classification of the seismic signal on the sensor recording that is determined provides detailed frequency information with a wavelet-machine learning approach. The results of this study indicate that signal classification can determine P and S waves in seismic signals originating from tectonic earthquakes. The results of signal classification on data sets sourced from land and sea tectonic earthquakes with Random Forest show an accuracy rate of 77.04 %. The results of extraction and confusion matrix show the dominance of the seismic signal defined by the predominance of positive true values and positive predictions.

ACKNOWLEDGMENTS. We are grateful to all the scientists, scientific personal and Institute of Physics, Vietnam Academy of Science and Technology, Vietnam. We would like thank to BMKG for making the data available.

REFERENCES

[1] J. Qiu, Q. Wu, G. Ding, Y. Xu, and S. Feng, A survey of machine learning for big data processing, *EURASIP J. Adv. Signal Process.*, 2016, Vol. **2016**, No. 1, doi: 10.1186/s13634-016-0355-x.

[2] W. Zhao, A. Bhushan, A. D. Santamaria, M. G. Simon, and C. E. Davis, Machine learning: A crucial tool for sensor design, *Algorithms*, 2008, **1**(2), 130-152, doi: 10.3390/a1020130.

[3] E. Darnila, M. Ula, K. Tarigan, T. Limbong, and M. Sinambela, Waveform analysis of broadband seismic station using machine learning Python based on Morlet wavelet, *IOP Conf. Ser. Mater. Sci. Eng.*, 2018, **420**(1), doi: 10.1088/1757-899X/420/1/012048.

[4] K. Tarigan, M. Sinambela, M. Panjaitan, P. Simangunsong, and H. K. Siburian, Machine learning for waveform spectral analysis on nuclear explosion signal and performance of broadband vertical component, *J. Phys. Conf. Ser.*, 2018, **1120**(1), 1-6,

[5] P. Debnath et al., Analysis of earthquake forecasting in India using supervised machine learning classifiers, *Sustain.*, 2021, **13**(2), 1-13, doi: 10.3390/su13020971.

[6] G. Guo, X. Cui, and B. Du, Random-forest machine learning approach for high-speed railway track slab deformation identification using track-side vibration monitoring, *Appl. Sci.*, 2021, **11**(11), 4756, doi: 10.3390/app11114756.

[7] M. Savargiv, B. Masoumi, and M. R. Keyvanpour, A new random forest algorithm based on learning automata, *Comput. Intell. Neurosci.*, 2021, **2021**, 1-19, doi: 10.1155/2021/5572781.

[8] Y. Kong and T. Yu, A deep neural network model using random forest to extract feature representation for gene expression data classification, *Sci. Rep.*, 2018, **8**(1), 1-9, doi: 10.1038/s41598-018-34833-6.

[9] Y. Kim, R. Hardisty, E. Torres, and K. J. Marfurt, Seismic facies classification using random forest algorithm, *2018 SEG Int. Expo. Annu. Meet. SEG*, 20189, 2161-2165, doi: 10.1190/segam2018-2998553.1.

[10] K. Tarigan, M. Sinambela, M. Panjaitan, P. Simangunsong, and H. K. Siburian, Machine learning for waveform spectral analysis on nuclear explosion signal and performance of broadband vertical component, *J. Phys. Conf. Ser.*, 2018, **1120**, 012083, doi: 10.1088/1742-6596/1120/1/012083.

[11] E. Darnila, M. Ula, K. Tarigan, T. Limbong, and M. Sinambela, Waveform analysis of broadband seismic station using machine learning Python based on Morlet wavelet, *IOP Conf. Ser. Mater. Sci. Eng.*, 2018, **420**, 012048, doi: 10.1088/1757-899X/420/1/012048.

 ISBN:

THERMAL DECOMPOSITION KINETIC ANALYSIS OF THE OCTOGEN-BASED ENERGETIC MATERIALS

Toan Nguyen Trung*, Huu Hoang Trung

Department of Energetic Materials, Le Quy Don Technical University, Vietnam

*E-mail: *trungtoanktqs@gmail.com*

Abstract. In this work, the thermal decomposition processes of Octol and Ocfol formulations were investigated along with single Octogen using non-isothermal thermogravimetry and differential thermal analysis (TG/DTA) and the ignition temperature techniques. The kinetic parameters were determined by Kissinger, Ozawa and the model-free (e.g., modified Kisinger-Akahira-Sunose) methods. It was found that the activation energy values obtained from the model-free method were equivalent to those obtained from other methods. The activation energy values of thermal decomposition processes were 305-320, 234-262, 70-95 and 232-257 kJ.mol^{-1} for Octogen, Ocfol, Octol peak 1 and Octol peak 2, respectively. Besides that, the ignition temperature technique is only used to evaluate the thermal stability of explosives.

I. INTRODUCTION

Cyclotetramethylene-tetranitramine (also known as Octogen, HMX) is a nitramine explosive widely used for military and civilian purposes due to its high energy density and high thermal stability [1-3]. However, HMX is highly sensitive to mechanical pulses (e.g impact and friction) and low compression capacity. To address these drawbacks, HMX is often used in a composite explosive form such as Octol (mixture with trinitrotoluene - an insensitive explosive to melt-cast formulations) [3-5], Ocfol (mixture with ceresin/stearic acid to phlegmatized explosives) [6,7] and polymer-bonded explosives, in which the HMX particles were covered and bonded by an insensitive layer [8-12].

The introduction of trinitrotoluene (TNT)/waxes mixture in Octol/Ocfol formulations not only reduces the sensitivity of explosives to mechanical pulses but also makes the production of explosive charges easier and safer. However, the presence of TNT and/or waxes mixture might negatively affect several characteristics of HMX such as detonation properties and thermal decomposition behaviors.

Compared with other classes of energetic materials (e.g. propellants, rocket fuels, etc.), secondary explosives have significantly higher thermal stability. However, explosive formulations are also thermodynamically unstable materials, and the thermal behavior and thermal decomposition kinetics exert strong influences on the shelf-life and the safety of explosives during its transportation and storage [13]. Therefore, the problems related to the determination of kinetic parameters still attract huge interest. H.R. Pouretedal et.al studied the triplet of the thermal decomposition reaction of Ocfol (95% HMX: 5% wax) using DTA technique with the average activation energy in a range of 214 to 235 kJ.mol^{-1} [14]. On the other hand, A. Singh et. al found that there was no any significant change in the kinetic parameters for 20-aged and fresh Ocfol formulation [15].

This work focused on investigating the thermal decomposition and the kinetic parameters of Octol and Ocfol formulations and compare to single HMX, using several thermal analysis techniques such as thermogravimetry (TG/DTG), differential thermal analysis (DTA) and ignition delay techniques. The thermal decomposition kinetics of explosive samples was calculated by employing Kissinger, Ozawa and the model-free method (i.e. Kissinger-Akahira-Sunose/KAS method). Finally, the results of each method were compared with each other to confirm the accuracy of measurements.

II. EXPERIMENTS

2.1. Materials

The highest purity of cyclotetramethylene-tetranitramine (HMX) and trinitrotoluene (TNT) was used for the preparation of Octol and Ocfol samples. The size of HMX and TNT particles was in the range of 0.1 to 0.2 mm. The ceresin and stearic acid (Sigma-Aldrich) were used as waxes to prepare the phlegmatized agent.

2.2. Experimental techniques and methods

2.2.1. Sample preparation

Ocfol formulation was prepared from a mixture of HMX (96.5 wt.%) and the phlegmatized agents (3.5 wt.% of the mixture of ceresin, stearic acid) [2]. In this process, the HMX powder was added into the water in a reaction vessel, maintaining the explosive/water ratio of 1/5 (w/w), then the suspension was slowly heated up to 90-95 °C under the continuous stirring rate of 500 rpm. The phlegmatized mixtures were melted at 90-95 ºC and added slowly with the stirring rate of 500 rpm to obtain a uniform dispersion of the wax over the explosive particles. When the adding process was completed, the mixture was continuously heated at 90-95 °C at the same stirring rate for 30 min. Finally, the product was cooled to below 30 °C and Ocfol samples were obtained via the vacuum filtration and dried in an oven at 40 °C.

Octol formulation consists of 70% HMX and 30% TNT was prepared by the melt-cast method [4]. TNT was melted in a steam-jacket vessel with a stirrer and heated up to 100 ºC. The wet HMX was added slowly, and stirring was continued until the water was evaporated. The slurry temperature was reduced until the viscosity was satisfactory for casting. The Octol composition was cast onto a continuous belt, as strips or chips.

2.2.2. Experimental techniques

Non-isothermal TG/DTG and DTA curves were obtained using the DTG-60H apparatus (Shimadzu). TG/DTA analyses were carried out at various heating rates of 2, 5, 7, 10 $K.min^{-1}$ (for Octol); and 5, 10, 15, 20 $K.min^{-1}$ (for HMX and Ocfol) under a dynamic argon atmosphere with a flow rate of 50 $mL.min^{-1}$. The explosive samples (7.0 to 8.0 mg) were heated from 25 to 400 ºC in an aluminum oxide crucible.

The ignition delay times were obtained using the Universal Heating Block Thermostat DT-400 apparatus (Reichel & Partner GmbH, Germany). A test tube containing about 0.15 g of explosive sample was inserted into the heating block at a constant temperature to determine the time needed for ignition.

 ISBN:

2.2.3. Kinetics analysis

The kinetic of the thermal decomposition of solid materials is usually described by the following equation:

$$\frac{dx}{dt} = k(T).f(x) \tag{1}$$

where x is a degree of conversion; T is the absolute temperature; $k(T)$ is the rate constant and $f(x)$ is the reaction model. For TG/DTG analysis, the degree of conversion is expressed as follow:

$$x = \frac{m_0 - m_t}{m_0 - m_f} \tag{2}$$

where m_0, m_t and m_f are the initial sample mass, sample mass at any time t and sample mass at the end of the process. The temperature dependence of the rate constant $k(T)$ can be expressed by the Arrhenius equation:

$$k(T) = A.\exp\left(\frac{-E}{RT}\right) \tag{3}$$

and its logarithmic form:

$$\ln k(T) = \ln A - \frac{E}{RT} \tag{4}$$

where R is the universal gas constant; A and E are the pre-exponential factor and the activation energy, respectively. Combining Eq. (1) and Eq. (3) we obtain:

$$\frac{dx}{dt} = A.\exp\left(\frac{-E}{RT}\right).f(x) \tag{5}$$

Kissinger method:

Kinetic parameters of the exothermic decomposition of explosive samples can be evaluated by applying the Kissinger method [16], which is expressed by Eq. (6):

$$\frac{d\left[\ln\left(\frac{\varphi}{T_m^2}\right)\right]}{d\left(\frac{1}{T_m}\right)} = -\frac{E}{R} \tag{6}$$

where T_m is the temperature peak of the DTG curve or DTA curve at linear heating rate $\varphi = dT/dt$. From the straight line obtained by plotting $\ln\left(\frac{\varphi}{T_m^2}\right)$ vs. ($1/T_m$) at different heating rates, the values of activation energy can be determined.

Ozawa method:

At linear heating rate φ Eqn. (5) can be written as:

$$\int_0^x \frac{dx}{f(x)} = \frac{A}{\varphi}\int_{T_0}^{T} \exp\left(\frac{-E}{RT}\right)dT \tag{7}$$

According to the Ozawa method [17], the values of *A*, *f(x)* and *E* are assumed that to be independent of *T*, whereas *A* and *E* are independent on the degree of conversion *x*. Then, Eqn. (7) is represented as integrating form:

$$\lg f(x) = \lg(\frac{AE}{R}) - \lg\varphi - 2.315 - 0.4567\frac{E}{RT_m} \quad (8)$$

and its other form:

$$\lg\varphi = -0.4567\frac{E}{RT_m} + const \quad (9)$$

The *E* values could be determined from the slope *(-0.4567E/R)* of the straight lines obtained by plotting $lg\varphi$ against $(1/T_m)$.

Kisinger - Akahira – Sunose (KAS) method:

The Kissinger and Ozawa methods only give a value of activation energy at maximum decomposition rate, and the entire reaction process has not been mentioned. According to the ICTAC kinetics committee recommendations for performing kinetic computations on thermal analysis data, the Kisinger-Akahira-Sunose method offers a significant improvement in the accuracy of activation energy values [18-21]:

$$\ln\left(\frac{\varphi_j}{T_{x,j}^M}\right) = const - N\left(\frac{E_x}{RT_x}\right) \quad (10)$$

where *M* and *N* are the parameters determined by the temperature integral approximation. Following Starink study [21], the *E* values are more accurate when setting *M=1.92* and *N=1.0008*, so Eqn. (10) turns into:

$$\ln\left(\frac{\varphi_j}{T_{x,j}^{1.92}}\right) = const - 1.0008\left(\frac{E_x}{RT_x}\right) \quad (11)$$

For each degree of conversion *x*, the values of *E* can be determined from the slope and the intercept when plotting $ln(\varphi/T^{1.92})$ vs. *1/T*.

The ignition delay time method:

The relationship between the ignition delay time (t_d) vs. activation energy value is represented by the following equation [13]:

$$t_d = A.\exp\left(\frac{E}{RT}\right) \quad (12)$$

The plots of $ln(t_d)$ vs. *(1/T)* were used to determine the activation energy values.

III. RESULTS AND DISCUSSION

3.1. TG/DTG and DTA results

TG/DTG and DTA analysis were conducted by the DTG-60H (Shimadzu) at the heating rates of 5, 10, 15, 20 $K.min^{-1}$ (for HMX and Ocfol formulations) and 2, 5, 7, 10

 ISBN:

K.min^{-1} (for Octol formulation). TG/DTG and DTA curves of HMX, Ocfol and Octol were recorded and shown in Figure 1.

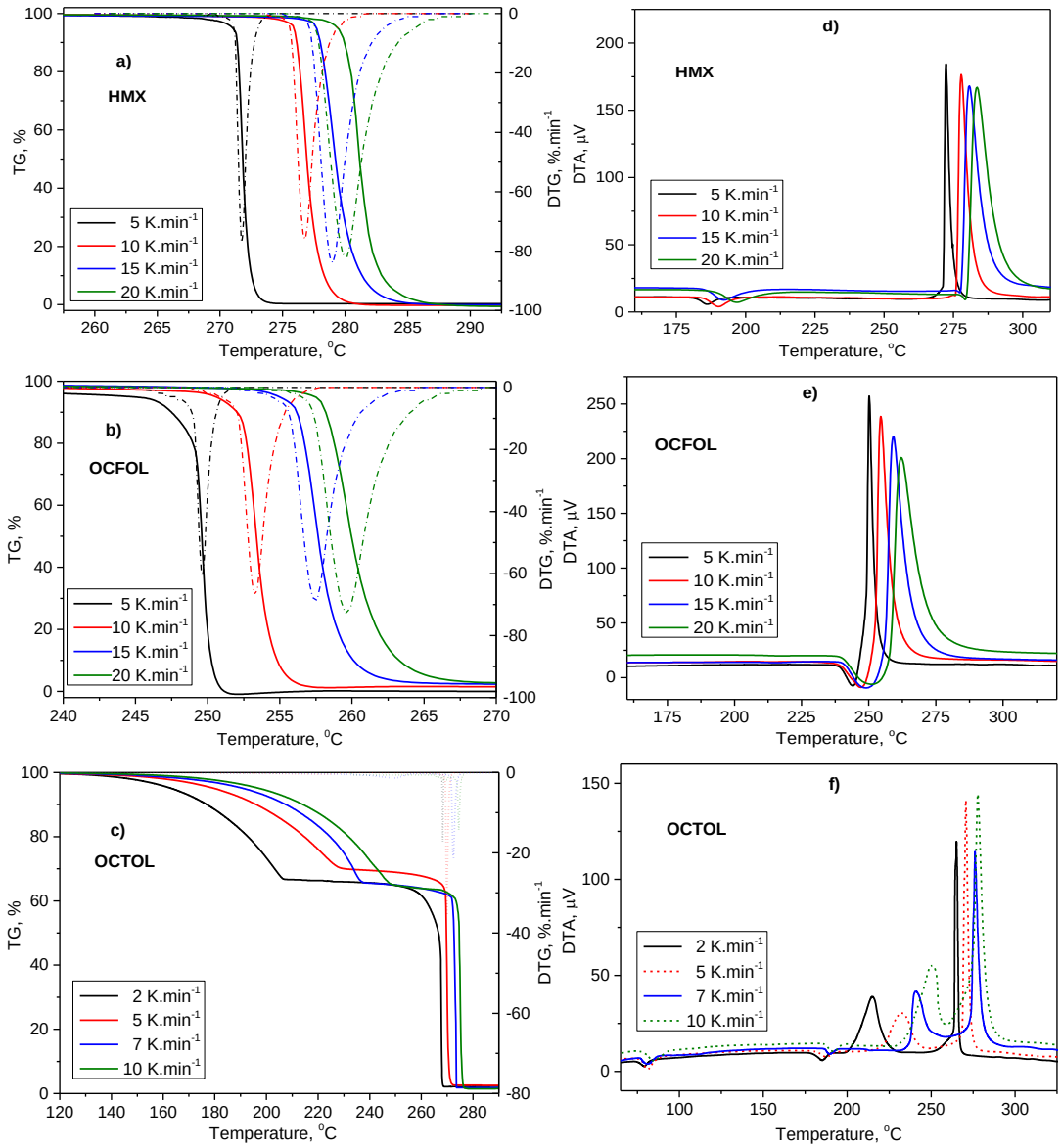

Fig. 1. *TG/DTG and DTA curves of HMX, Ocfol and Octol at different heating rates.*

It can be seen from the TG/DTG curves in Fig. 1(a,b) that the thermal decomposition of HMX and Ocfol formulations took place in one step, relating to the decomposition of a single HMX. The peak temperatures in DTG curves for the thermal decomposition of HMX and Ocfol were observed in a range of 270-280 and 250-260 ºC, respectively. Meanwhile, the TG/DTG curves of Octol shown that its thermal decomposition took place in two steps with a temperature range of 150-280 ºC, corresponding to the decomposition process of TNT and HMX (Fig. 1-c). Thermal analyzes of Octol formulation were performed at lower heating rates (i.e. 2, 5, 7 and 10 K.min^{-1}) to observe the thermal decomposition.

The DTA curves of HMX (Fig. 1-d) show that there has been an endothermic peak in the temperature range of 180-190 ºC for the phase transformation from β-HMX to δ-HMX,

and an exothermic peak appeared after endothermic peak related to the thermal degradation of HMX. For Ocfol, there are an endothermic and exothermic peak occurred consecutively in the temperature range of 240-270 ºC which corresponds to the melting point and the thermal decomposition of HMX (Fig. 1-e). The DTA curves of Octol show two endothermic peaks and two successive exothermic peaks (Fig. 1-f). The first endothermic peak appears at about 80 ºC relative to the melting point of TNT, while the second endothermic peak at about 190 ºC is related to the phase transformation of HMX. Two strong exothermic peaks over the range of 210-250 and 260-280 ºC are related to the degradation of TNT and HMX, respectively. The characteristic parameters of DTA curves of HMX, Ocfol and Octol are summarised in Table 1.

Table 1. *Characteristic parameters of DTA curves of all samples.*

Samples	Heating rate φ ($K.min^{-1}$)	Endothermic peak (ºC)	Exothermic peak (ºC)		
			T_{on}	T_p	T_{oe}
HMX	5	186.2	265.3	272.5	282.2
	10	190.4	275.3	277.7	291.0
	15	191.8	277.4	280.8	296.5
	20	194.0	278.9	283.5	302.1
Ocfol	5	244.2	246.5	249.2	260.0
	10	247.1	250.4	254.4	267.9
	15	249.0	254.5	259.2	273.7
	20	250.6	257.5	262.0	282.8
Octol peak 1	2	79.4	199.2	215.5	230.2
	5	81.6	218.5	232.1	246.0
	7	82.0	226.6	240.2	254.5
	10	83.4	232.0	250.0	259.7
Octol peak 2	2	185.2	253.4	263.5	270.0
	5	188.4	260.3	271.2	279.1
	7	189.6	268.2	275.3	287.4
	10	191.0	273.9	279.8	291.0

T_{on} - decomposition exotherm onset; T_m - the temperature peak of the DTA curve; T_{oe} - onset temperature of the end decomposition.

The thermal decomposition of Ocfol and Octol took place at a lower temperature than a single HMX. This can be explained by the effect of the wax mixture (in Ocfol formulation) and TNT (in Octol formulation) on the thermal behavior of a single HMX. The molten film of the wax mixture or TNT, which appears at about 90 ºC, created an isometric condition for the decomposition of HMX particles. As a result, gaseous decomposition products and increased pressure will accelerate the decomposition of HMX particles in Ocfol and Octol.

3.2. Kinetic analysis

3.2.1. Kissinger and Ozawa method

Base on DTA data in Table 1, the straight lines representing the relationship of $ln(\varphi/T_m^2)$ vs. $10^3/T_m$ (i.e. the Kissinger method) or the $log\varphi$ vs. $10^3/T_m$ (i.e. the Ozawa method) are obtained and shown in Fig. 2, then the kinetic parameters are expressed in Table 2.

 ISBN:

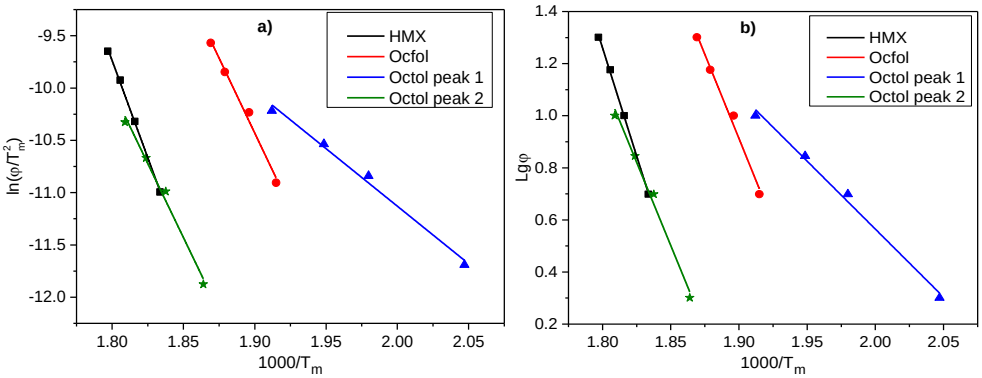

Fig. 2. *a) The $ln(\varphi/T_m^2)$ vs. $10^3/T_m$ plot and b) The $lg\varphi$ vs. $10^3/T_m$ plot.*

As seen, the kinetic parameters of all samples calculated by the Kissinger and Ozawa method are similar. Besides that, the overall activation energy of HMX is higher than that of Ocfol and Octol, which indicates the earlier decomposition of Ocfol and Octol compare to the single HMX. However, the limitation of the Kissinger and Ozawa method is that it cannot evaluate the dependence of the activation energy for each degree of conversion *x*.

Table 2. *Kinetics parameter obtained using Kissinger and Ozawa methods.*

Samples	Kissinger method			Ozawa method		
	E (kJ.mol^{-1})	*lg A* (min^{-1})	R^2	*E* (kJ.mol^{-1})	*lg A* (min^{-1})	R^2
HMX	311.8	29.5	0.9984	305.2	28.9	0.9985
Ocfol	238.2	23.4	0.9847	234.8	23.1	0.9858
Octol 1st peak (TNT)	91.4	8.9	0.9874	94.8	9.3	0.9896
Octol 2nd peak (HMX)	235.3	22.4	0.9835	232.3	22.1	0.9848

3.2.2. Kissinger-Akahira-Sunose method

From the TG curves of all samples, the corresponding curves of the conversion *x* against temperature *T* according to the Eq. 2 were obtained and shown in Fig. 3 (a-c). According to the KAS method, the plot of $ln(\varphi/T^{1.92})$ vs. *1/T* at each degree of conversion *x* can be obtained by linear regression and presented in Fig. 3 (d-f).

The activation energy E_x and the pre-exponential factor *A* were calculated from the slope and the intercept and expressed in Table 3 and the dependence of the activation energy on the degree of the conversion is shown in Fig. 4.

Table 3. *Kinetic parameters of HMX, Ocfol and Octol by the KAS method.*

x	HMX			Ocfol			Octol		
	E_x (kJ.mol^{-1})	*lnA* (min^{-1})	R^2	E_x (kJ.mol^{-1})	*lnA* (min^{-1})	R^2	E_x (kJ.mol^{-1})	*lnA* (min^{-1})	R^2
0.1	332.0	66.7	0.9921	276.0	58.8	0.9992	74.8	11.1	0.9900
0.2	331.5	66.6	0.9946	272.7	56.1	0.9983	73.1	10.0	0.9978
0.3	330.9	66.5	0.9907	272.7	56.2	0.9972	73.9	9.8	0.9918
0.4	327.6	65.7	0.9899	270.2	55.5	0.9966	254.4	49.5	0.9931
0.5	323.7	65.6	0.9894	268.5	55.1	0.9965	256.0	49.9	0.9931
0.6	321.7	64.3	0.9881	264.4	54.0	0.9957	255.3	49.6	0.9938
0.7	314.3	62.7	0.9838	257.7	52.5	0.9954	256.0	49.6	0.9963
0.8	307.6	61.2	0.9850	248.6	50.0	0.9974	259.4	50.4	0.9967
0.9	295.1	58.2	0.9838	230.3	45.9	0.9969	263.5	51.4	0.9979
Mean	**320.5**	**64.1**		**262.3**	**53.8**		**73.9/257.4**	**10.3/50.0**	

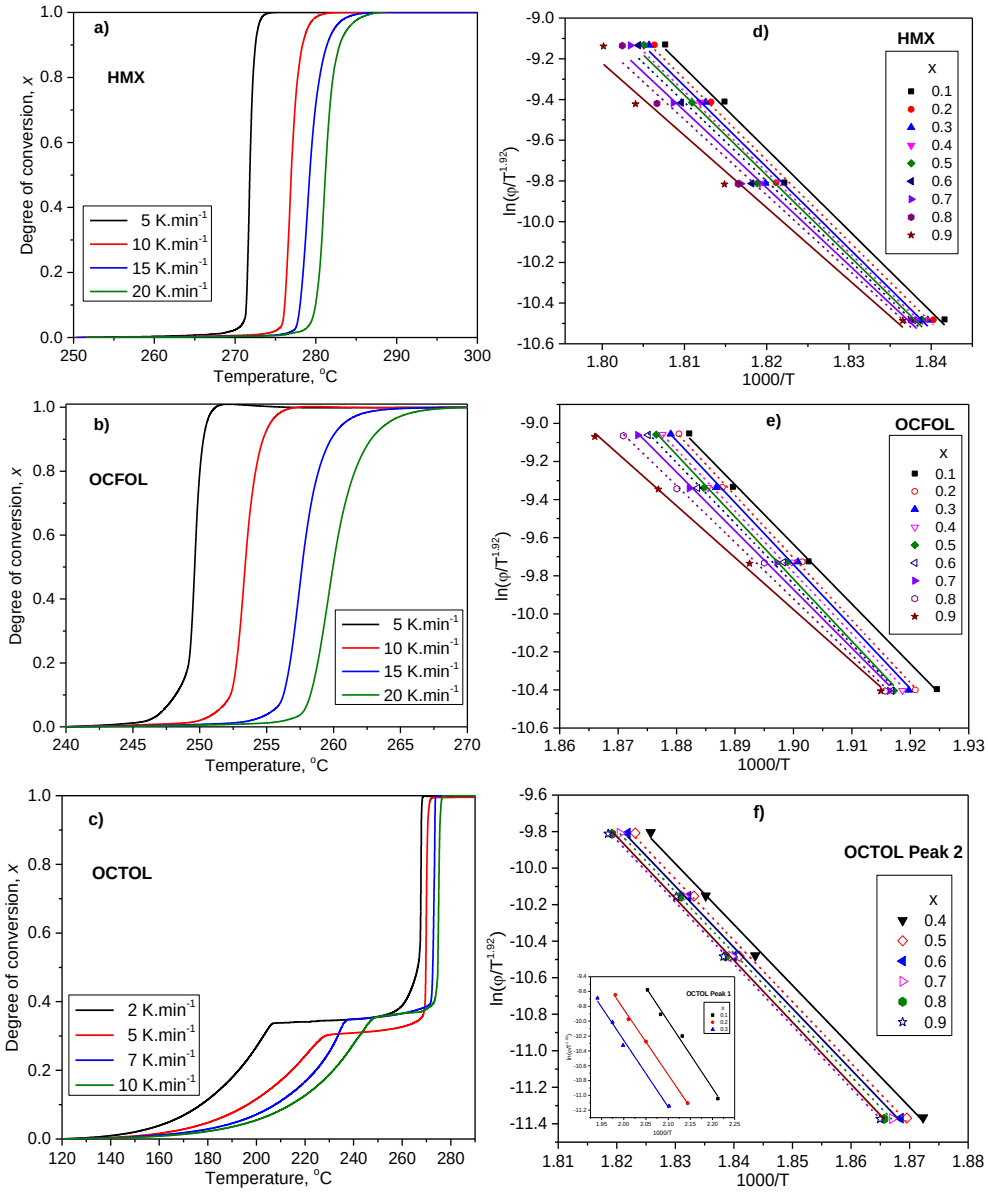

Fig. 3. *The x-T curves at several heating rates and the plot of ln(φ/T$^{1.92}$) vs. 1000/T of HMX, Ocfol and Octol by KAS method.*

The average values of activation energy calculated by the KAS method of HMX, Octol, Octol peak 1 and Octol peak 2 are 320.5, 262.3, 73.9 and 257.4 kJ.mol^{-1}, respectively. Compared to the results obtained by Kissinger and Ozawa method, the activation energy values obtained by the KAS method have an insignificant difference. The kinetic parameters calculated in this study are a little higher than the values reported in the study of A. Singh et al. [15] and H. R. Pouretedal et al. [14].

According to Brill et al. [22], the E_x and the lnA have a compensated relationship, and all of E_x-lnA pairs usually lie on the regression straight line (compensation effect). To evaluate the reliability of the methods, the plots of E_x vs. lnA of all samples were established and represented in Fig. 5. It can be seen that E_x-lnA pairs have a linear relationship, proving the accuracy of the Kissinger, Ozawa as well as KAS method.

 ISBN:

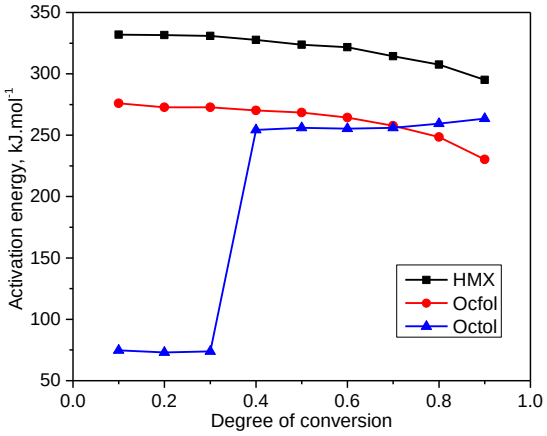

Fig. 4. *Variation of activation energy values of HMX, Ocfol and Octol with the conversion x.*

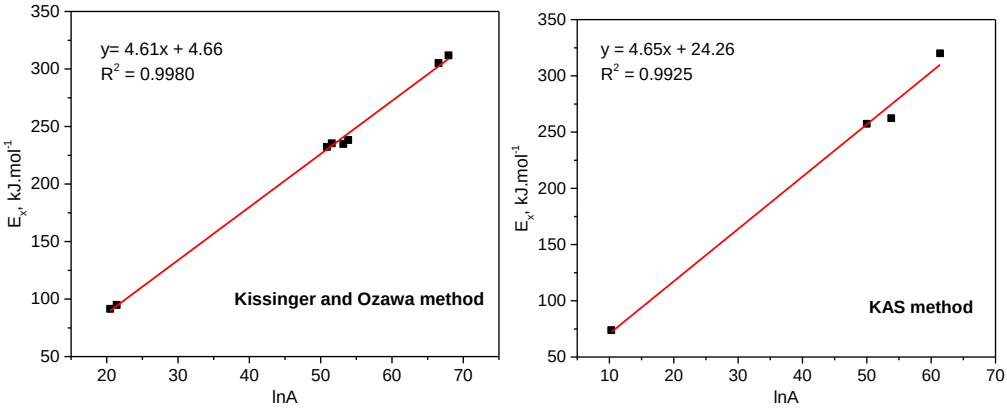

Fig. 5. *The plots of E vs. lnA obtained by the Kissinger-Ozawa and the KAS method.*

3.2.3. Ignition delay time method

The ignition delay time (t_d) of HMX, Ocfol and Octol at several temperatures was determined using DT-400 apparatus. The ignition delay time and the temperature were fitted according to Eqn. (12), and the activation energy was determined by the plot of $ln(t_d)$ vs. $10^3/T$ (Fig. 6). The results are shown in Table 4.

Table 4. *Ignition delay time and the activation values of HMX, Ocfol and Octol.*

Sample	Ignition delay time (s) at temperature (°C)							E (kJ.mol^{-1})	R^2
	280	290	300	310	320	330	340		
HMX	-	-	60	34	17	6	3	225.3	0.9870
Ocfol	68	45	22	11	5	-	-	180.3	0.9856
Octol	75	49	25	13	6	-	-	173.5	0.9870

As can be seen from Table 4, the ignition delay time at different temperatures of HMX is higher than that of Ocfol and Octol. The activation energy of HMX calculated by the ignition delay time method is also higher than that of Ocfol and Octol. However, the activation energy values of all samples obtained by this method are significantly lower than those obtained by the other methods. This might due to the effect of the sample mass, the particle size and the device accuracy on the values of ignition delay time. Therefore, the ignition delay time method is only used for the preliminary assessment of the thermal stability of HMX, Ocfol and Octol.

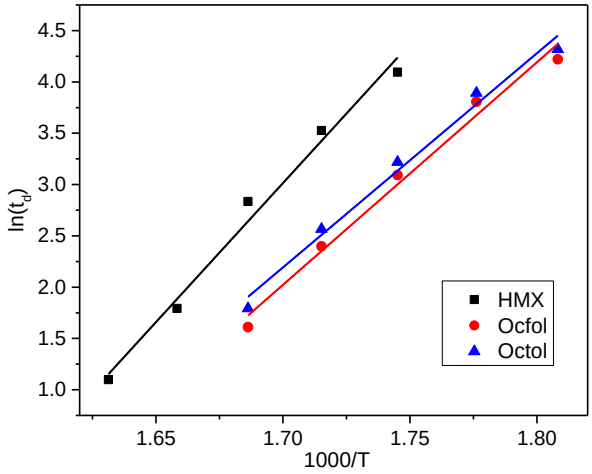

Fig. 6. *The plot of ln(t_d) vs. 10^3/T for HMX, Ocfol and Octol.*

IV. CONCLUSION

The kinetics of the thermal decomposition of Ocfol and Octol formulation were evaluated along with the single HMX using the Kissinger, Ozawa and KAS method. The results demonstrate that the activation energy values of HMX were higher than those of Ocfol and Octol formulation. In particular, the activation values of thermal decomposition of HMX, Ocfol, Octol peak 1 and Octol peak 2 were in the range of approximately 305-320, 234-262, 70-95 and 232-257 kJ.mol^{-1}, respectively. DTA results confirm the negative effect of the binders (i.e. wax mixture or TNT) on the thermal stability of pure HMX, leading to a decrease in the temperature of the exothermic peak. Besides, the activation values obtained by the ignition delay time method were less accurate than those by TG/DTG and DTA method, so the ignition delay time method is only used to assess the thermal stability of explosives.

REFERENCES

[1] J. P. Agrawal, High Eenergy Materials: Propellants, Explosives and Pyrotechnics, John Wiley & Sons, 2010.

[2] T. Urbanski, Chemistry and Technology of Explosives, Vol. III, Pergamon Press New York, 1967.

[3] J. P. Agrawal, and R. D. Hodgson, *Organic Chemistry of Explosives*, Wiley-VCH, 2007.

[4] P. Ravi, D. M. Badgujar, G. M. Gore, S. P. Tewari, and A. K. Sikder, Review on melt cast explosives, *Propellants Explos. Pyrotech.*, 2011, **36**(5), pp. 393-403.

[5] J. C. Lynch, J. M. Brannon, K. Hatfield, and J. J. Delfino, An exploratory approach to modeling explosive compound persistence and flux using dissolution kinetics, *J. Contam. Hydrol.*, 2003, **66**(3-4), 147-159.

[6] N. Akinin, A. Dubovik, and A. Matveev, Complex studies on explosion hazard of metalized Compositions based on powerful explosives, *Russ. J. Phys. Chem. B*, 2019, **13**(5), 748-754.

[7] H. Kemmoukhe, Z. Burzić, S. Savić, S. Terzić, and M. Lisov, Improvement of shaped charge penetration capability and disturbation of the jet by explosive reactive armor, *The Vjesn.*, 2019, **26**(6), 1658-1663.

 ISBN:

[8] A. Elbeih, S. Zeman, M. Jungová, and P. Vávra, Attractive Nitramines and Related PBXs, *Propellants Explos. Pyrotech.*, 2013, **38**(3), 379-385.

[9] A. Elbeih, J. Pachman, S. Zeman, W. A. Trzcinski, and M. Suceska, Study of plastic explosives based on attractive cyclic nitramines, Part II. Detonation characteristics of explosives with polyfluorinated binders, *Propellants Explos. Pyrotech.*, 2013, **38**(2), 238-243.

[10] A. Elbeih, S. Zeman, M. Jungova, and Z. Akstein, Effect of different polymeric matrices on the sensitivity and performance of interesting cyclic nitramines, *Cent. Eur. J. Energ. Mater.* 2012, **9**(2), 131-138.

[11] A. Elbeih, S. Zeman, and J. Pachman, Effect of polar plasticizers on the characteristics of selected cyclic nitramines, *Cent. Eur. J. Energ. Mater.*, 2013, **10**(3), 339-349.

[12] A. Singh, T. C. Sharma, M. Kumar, J. K. Narang, P. Kishore, and A. Srivastava, Thermal decomposition and kinetics of plastic bonded explosives based on mixture of HMX and TATB with polymer matrices, *Def. Technol.* 2017, **13**(1), 22-32.

[13] M. Abd-Elghany, A. Elbeih, and S. Hassanein, Thermal behavior and decomposition kinetics of RDX and RDX/HTPB composition using various techniques and methods, *Cent. Eur. J. Energ. Mater.*, 2016, **13**(3), pp. 714-735.

[14] H. Pouretedal, S. Damiri, H. Sinapour, and A. Malekzadeh, Kinetic study on triplet of thermal decomposition reaction of Ocfol explosive by non-isothermal differential thermal analysis method, *J. Energ. Mater.*, 2016, **11**(1), 11-16.

[15] A. Singh, T. C. Sharma, V. Singh, and N. Mukherjee, Studies on the thermal stability and kinetic parameters of naturally aged Octol formulation, *J. Therm. Anal. Calorim*, 2021, **145**, 411-421.

[16] H. E. Kissinger, Variation of peak temperature with heating rate in differential thermal analysis, *J. Research NBS.*, 1956, **57**(4), 217-221.

[17] T. Ozawa, A new method of analyzing thermogravimetric data, *T. Bull. Chem. Soc. Jpn.*, 1965, **38**(11), 1881-1886.

[18] S. Vyazovkin, and C. A. Wight, Isothermal and non-isothermal kinetics of thermally stimulated reactions of solids, *Int. Rev. Phys. Chem.*, 1998, **17**(3), 407-433.

[19] S. Vyazovkin, A. K. Burnham, J. M. Criado, L. A. Pérez-Maqueda, C. Popescu, and N. Sbirrazzuoli, ICTAC Kinetics Committee recommendations for performing kinetic computations on thermal analysis data, *Thermochim. Acta.*, 2011, **520**(1-2), 1-19.

[20] T. Akahira, and T. Sunose, Method of determining activation deterioration constant of electrical insulating materials, *Res. Rep. Chiba Inst. Technol. (Sci. Technol.)*, 1971, **16**, 22-31.

[21] M. J. Starink, The determination of activation energy from linear heating rate experiments: a comparison of the accuracy of isoconversion methods, *Thermochim. Acta.*, 2003, **404**(1-2), 163-176.

[22] T. Brill, P. Gongwer, and G. Williams, Thermal decomposition of energetic materials. 66. Kinetic compensation effects in HMX, RDX, and NTO, J. Phys. Chem., 1994, 98(47), pp. 12242-12247.

INVESTIGATION OF PLASMON RESONANCE IN 2D METAL-DIELECTRIC-METAL NANOSTRUCTURES

Thu Trang Hoang[1*], Thanh Son Pham[1], Xuan Bach Nguyen[2], Huu Tu Nguyen[3] and Quang Minh Ngo[2]

[1]*Institute of Materials Science, Vietnam Academy of Science and Technology, Vietnam*

[2]*University of Science and Techonology of Hanoi, Vietnam*

[3]*Graduate University of Science and Technology, Vietnam*

*E-mail: *tranght@ims.vast.ac.vn*

Abstract. In this report, we propose the numerical investigation of surface plasmon resonances in 2D metal-dielectric-metal nanostructures. This structure is working in the near-infrared region consists of subwavelength silver (Ag) cylinder arrays positioned on a stack of thin silica (SiO_2) spacer and Ag film on a silicon substrate. Two simulation methods of boundary element method and finite-difference time-domain are used to determine the optical characteristics of the designed structure. At resonance, we numerically observed a strong field localized inside the gap between the Ag nanostructures and the Ag mirror, resulting in a strong confinement of incoming light within the insulator spacer and thus a pronounced absorption at telecommunication wavelengths.

I. INTRODUCTION

The interaction between light and metallic nanostructures possesses unique properties that form the emergent fields called surface plasmons [1]. Surface plasmon resonance (SPR) is a kind of surface plasmon that is the resonant oscillation of conduction electrons at the interface between metallic and dielectric media [2]. Recently, it has attracted intensive research due to its broad scope of applications in different fields from physics, chemistry, and biology [3-4].

Plasmonic metasurfaces based on a metal-dielectric-metal (MDM) platform consisting of a subwavelength resonant elemental array operating in the near-UV to near-infrared regions have been desirable. Their properties can be tuned by reshaping individual resonators, exhibiting functionalities, and expanding the novel applications [5-6]. Using the bottom metallic reflecting layer to prevent the transmission, MDM plasmonic metasurfaces have become rapidly developing research fields, owing to the existing fabrication technologies and unprecedented manipulation over absorption or reflection [7]. When the thickness of the dielectric spacer-layer is thinner than the working wavelength, the light can be strongly localized inside the MDM plasmonic metasurface [8].

In this work, we propose the Ag subwavelength disk array placed on a special substrate that consists of SiO_2/Ag stacked layers on Si substrate. The plasmonic metasurface of Ag disk arrays can couple the incident light in the near-infrared region at an arbitrary angle into the designed structure, creating resonances. At resonance, the light is strongly confined in the SiO_2 spacer layer. Depending on the thickness of the SiO_2 spacer-layer, these coupling changes alter the resonant frequency of the MDM plasmonic

 ISBN:

metasurface. The finite-difference time-domain (FDTD) simulations [9] were demonstrated the dimension dependence and analyzed the surrounding medium's refractive index on the response properties of the sensor, such as resonant wavelength, *Q*-factor, and reflection of the proposed plasmonic metasurface. The results of this work might provide an insight into the interaction between light and metallic nanostructure.

II. DESIGN AND SIMULATION

In Fig. 1a, we show a schematic view of the studied structure. It is composed of an Ag disk (lattice constant, *P*) arrays placed on a special MDM substrate. The diameter and the thickness of the Ag disk at *D* and *h*, respectively. Our study uses a silicon substrate covered by a 100 nm thickness Ag layer, which is thick enough to prevent optical transmission into the silicon, further capped by a continuous SiO_2 film of thickness *t*. A thin chromium layer (5 nm) was sputtered between the substrate and Ag layer for enhancing the adhesion.

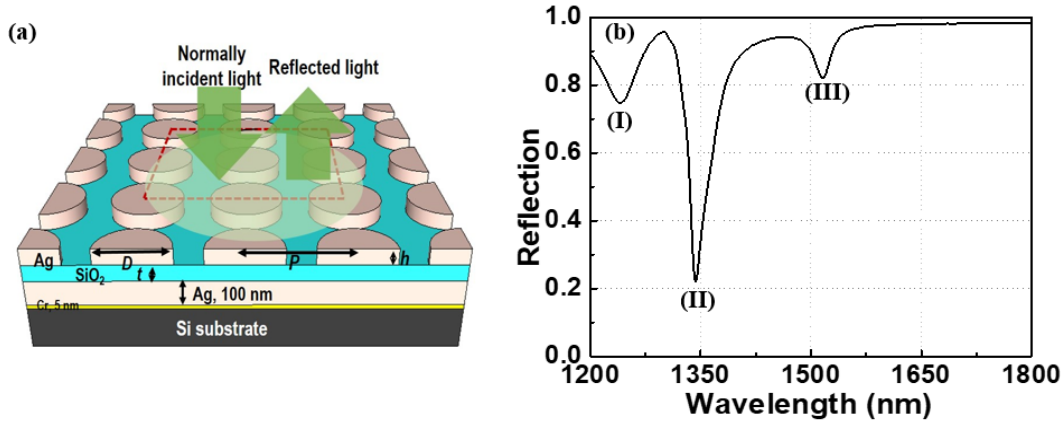

Fig. 1. *a) The designed MDM plamsonic metasurface; b) its reflection spectrum with the structural parameters D = 950 nm, h = 50 nm, and t = 40 nm.*

The reflection and absorption spectrum for MDM plasmonic metasurface having the structural parameters *D* = 950 nm, *h* = 50 nm, and *t* = 40 nm at normal incidence are shown in Fig. 1b. Figures show three reflection dips at (I) ~1235.1 nm, (II) ~1345.5 nm, and (III) ~1511.6 nm. The reflection dip (II) shows the largest contrast and high *Q*-factor compared to the reflection dips (I) and (III); therefore, it is more suitable for sensing applications.

To elucidate the optical properties of the strongly-coupled system, while keeping the lattice and period of the arrays fixed, variable diameter *D* is used to manipulate the plasmonic modes and tunable height *h* is used to manipulate those based on the matching relation between height *h* and incident wavelength λ. Fig. 2 illustrates the dispersion relation of reflection spectra of the designed plasmonic MDM system (*h* = 50 nm) with the various diameters ranging from 500 to 1200 nm. A mode splitting is observed as the diameter larger than 800 nm with the maximum splitting at *D* ~ 1200 nm. This figure clearly shows the coupling conditions changing from uncoupling, weak coupling to strong coupling regime. This change is caused by the radiation field increasing because *D* is rised to the decreasing of lattice constant.

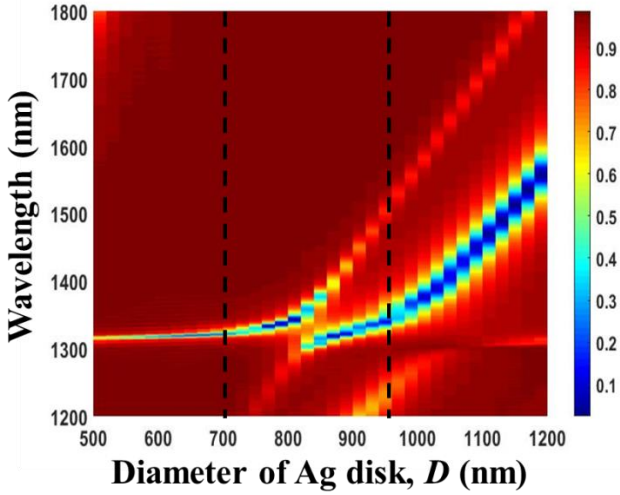

Fig. 2. *Dispersion diagram of the proposed MDM structure with h = 50 nm for diameter D in the range of 500-1200 nm.*

The influence of the SiO_2 spacer-layer thickness on the light confinement is described in Fig. 3.

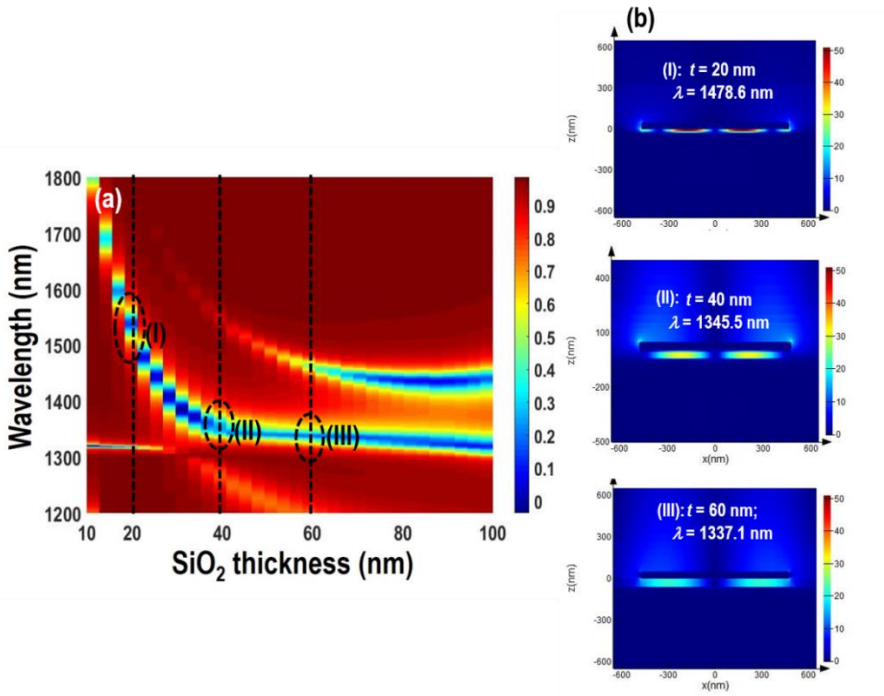

Fig. 3. *(a) The resonant wavelength shifted versus the change of the SiO_2 spacer-layer thickness; (b) side-views of E-field distributions at resonances as noted of the MDM plasmonic metasurface of t = 20, 40, and 60 nm.*

As shown in Fig. 3a, when the SiO_2 spacer-layer thickness is less than 40 nm, the resonant wavelength changes very quickly. Thus, the light confined inside the SiO_2 spacer is dominant in influencing the optical characteristics, making it ideal for sensing applications. Conversely, when the thickness of the SiO_2 spacer-layer increases from 40 to 100 nm, the resonant wavelength changes very slowly. Therefore, we used the SiO_2 thickness of 40 nm for the following investigations. At the thin SiO_2 spacer-layer, the

 ISBN:

coupling is stronger, leading to stronger differences in the resonant shift compared to changes in the SiO_2 thickness. When the SiO_2 spacer-layer is thicker than 40 nm, their coupling gradually stabilizes and the resonant wavelength slowly changes. Fig. 3b presents the side-view of filed distributions at three SiO_2 spacer-layer thicknesses of 20, 40, and 60 nm. As we have seen, the *E*-field at the thin SiO_2 spacer-layer is strongly localized inside the SiO_2 spacer-layer due to strong coupling between two evanescent waves at the Ag disks/SiO_2 and SiO_2/Ag reflecting layer interfaces. When the SiO_2 spacer-layer thickness increases, the *E*-field is spread out and is no longer strongly confined inside the SiO_2 spacer-layer.

Since the MDM plasmonic metasurface is sensitive to the surrounding medium, we investigate its biosensing applications for structural parameters of D = 950 nm, P = 1300 nm, h = 50 nm, t = 40 nm. Figs. 4a and 4b show that when the refractive index changes from 1.0 to 1.1, it corresponds to the vapor medium, and 1.3 to 1.45 relates to the liquid medium. A tiny change in the refractive index results in a significant displacement of the resonant dip, which is useful for highly sensitive sensors.

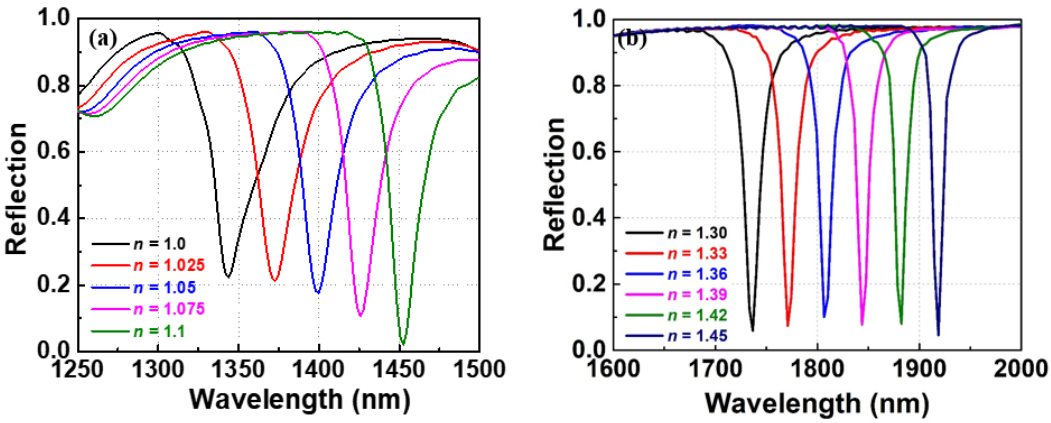

Fig. 4. *FDTD simulated reflection spectra for a variation of the surroungding refractive indices. The structural parameters of D = 950 nm, P = 1300 nm, h = 50 nm, t = 40 nm are chosen for simulations.*

III. CONCLUSION

In conclusion, we have designed and investigated of surface plasmon resonances in 2D metal-dielectric-metal nanostructures. The dependence of resonant wavelengths on the structural parameters such as diameter and SiO_2 spacer-layer thickness has been analyzed. At resonance, we numerically observed a strong confinement of incoming light within the SiO_2 layer, which proves that the plasmon resonance has been enhanced.

ACKNOWLEDGMENTS. This research is funded by Vietnam Academy of Science and Technology (VAST) under grant number “KHCBVL.06/21-22”.

REFERENCES

[1] D. Kotlarek, S. Fossati, P. Venugopalan, N. Gisbert Quilis, J. Slabý, J. Homola, M. Lequeux, F.

Amiard, M. de la Chapelle, U. Jonas, and J. Dostálek, Actuated plasmonic nanohole arrays for sensing and optical spectroscopy applications, *Nanoscale*, 2020, **12**, 9756-9768.

[2] V. Yesudasu, H.S. Pradhan, and R.J. Pandya, Recent progress in surface plasmon resonance based sensors: A comprehensive review, *Heliyon*, 2021, **7**, e06321.

[3] J. Y. Jing, Q. Wang, W. M. Zhao, and B. T. Wang, Long-range surface plasmon resonance and its sensing applications: A review, *Opt. Lasers Eng.*, 2019, **112**, 103-118.

[4] F. V Ramirez, S. Shen, and A. J. H. McGaughey, Near-field radiative heat transfer in graphene plasmonic nanodisk dimers, *Phys. Rev. B*, 2017, **96**, 1-9.

[5] B. Vasić, Semi-analytical approach for refractive index sensors based on reflective metasurfaces, *J. Opt. Soc. Am. B*, 2021, **38**, 1676-1683.

[6] X. Fang, L. Xiong, J. Shi, and G. Li, High-Q quadrupolar plasmonic lattice resonances in horizontal metal-insulator-metal gratings, *Opt. Lett.*, 2021, **46**, 1546-1549.

[7] F. Ding, Y. Yang, R. A. Deshpande, and S. I. Bozhevolnyi, A review of gap-surface plasmon metasurfaces: fundamentals and applications, *Nanophotonics*, 2018, **7**, 1129-1156.

[8] L. Emeric, C. Deeb, F. Pardo, and J. L. Pelouard, Critical coupling and extreme confinement in nanogap antennas, *Opt. Lett.*, 2019, **44**, 4761-4764.

[9] Q. M. Ngo, Y. L.D. Ho, J. R. Pugh, A. Sarua, and M. J. Cryan, Enhanced UV/blue fluorescent sensing using metal-dielectric-metal aperture nanoantenna arrays, *Curr. Appl. Phys.*, 2018, **18**, 793-798.

[10] D. G. Baranov, M. Wersäll, J. Cuadra, T. J. Antosiewicz, and T. Shegai, Novel nanostructures and materials for strong light-matter interactions, *ACS Photonics*, 2018, **5**, 24-42.

[11] Y. Chu, E. Schonbrun, T. Yang, and K.B. Crozier, Experimental observation of narrow surface plasmon resonances in gold nanoparticle arrays, *Appl. Phys. Lett.*, 2008, **93**, 181108.

[12] G. Vecchi, V. Giannini, and J. Gómez Rivas, Surface modes in plasmonic crystals induced by diffractive coupling of nanoantennas, *Phys. Rev. B*, 2009, **80**, 201401.

[13] S. Kasani, K. Curtin, and N. Wu, A review of 2D and 3D plasmonic nanostructure array patterns: fabrication, light management and sensing applications, *Nanophotonics*, 2019, **8**, 2065-2089.

 ISBN:

LASER-FABRICATION MECHANISMS OF NANOSTRUCTURES ON Au/Pd THIN FILM

Nguyen Thi Huyen Trang[1*], Kudryashov Sergey Ivanovich [2], Doan Hoai Son[1]

[1]*Ha Tinh University, N. 447, 26/3 Street, Dai Nai Precinct, Ha Tinh City, Viet Nam*

[2]*Lebedev Physical Institute, Leninskiy Prospect 53, 119991 Moscow, Russia*

*E-mail: *trang.nguyenthihuyen@htu.edu.vn*

Abstract. The theory and the experiment demonstrated the mechanism of formation of a nanotip with a nanoparticle at its top, when femtosecond laser pulse irradiated onto a metal thin film. The melting is responsible for the formation of nanotips and a nanojet formation, which is cooled and solidified. The Kuramoto-Sivashinsky type hydrodynamic equation was used to explain the thermocapillary instability in the melted film in the hydrodynamic model. The simulation shows that the nanojet nucleates in the form of a nanopeak in a pit on the top of a microbump (linear stage) and, then, grows in a nonlinear (explosive) regime of an increase in thermocapillary instability in good agreement with experimental data.

Keywords: *Nanotip, Nanoparticles, Thin film, Microbump, Femtosecond laser pulse.*

I. INTRODUCTION

The metallic nanotips, nanoparticles, microbump are one of the most important nanostructures [1]. They were previously shown that an array of laser-induced nanotips (nanojets) has resonant optical absorption [2] and exhibits an increased photoemission of charged particles under irradiation by an intense ultrashort laser pulse [3]. Today, there are many methods for fabrication nanostructures such as: chemical synthesis, colloidal lithography, electron beam lithography (EBL), ion beam lithography (IBL). However, these methods are complex, not general and require additional processing stages to separate each nano-element or assemble them on highly ordered arrays. In contrast, some nanostructures on metal films with short (nanosecond) and ultrashort (femtosecond) focused laser pulses can fabricate nanostructures cheaper, simpler, more efficient and purer than other methods [4-6].

The formation of laser-induced nanostructures refers to phenomena of the hydrodynamic flow in a melted shell of a microbump [7], pressure of evaporated vapor [5], and thermoelastic and plastic deformation at the expansion of a heated film [8]. At the same time, the effect of the thickness of a metallic film, as well as of focusing of ultrashort laser pulse (width of the melt pool), on the geometric parameters of appearing nanostructures has not yet been systematically studied. Therefore, the physical mechanism of the laserinduced formation of these nanostructures remains unknown.

In this work, the formation of a nanostructures under irradiation by a single femto-second laser pulse with various energies is experimentally studied and a hydrodynamic model of the formation and development of a nanojet with the appearance of a nanoparticle is proposed.

II. EXPERIMENTS

As a sample, we used a film of an 80%/20% Au/Pd alloy with the different thickness deposited in an argon atmosphere on a CaF_2 substrate by magnetron sputtering. A fiber laser facility based on Yb^+ ions was used as a source of ultrashort laser pulses with a wavelength of 515 nm, FWHM of about 200 fs, and a maximum energy in the pulse up to 4 μJ. The spatial distribution of radiation at the output from a single-mode fiber corresponded to the TEM_{00} mode. Laser radiation was focused onto a spot with the radius $R_{1/e} \approx 1.5$ μm on the surface of the sample in air through the objective of a microscope with $NA = 0.25$. The sample was placed on a three dimensional motorized translating stage. The relief of the surface was visualized by scanning electron microscope (SEM).

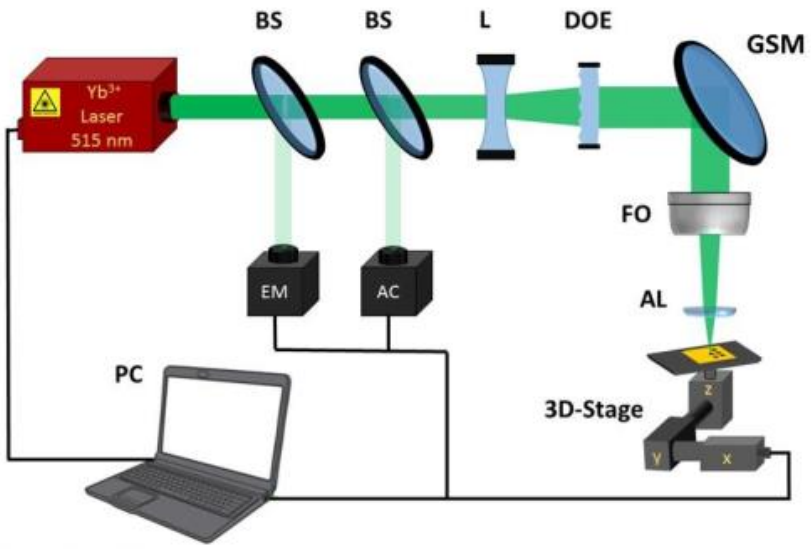

Fig. 1. *The optical scheme of femto-second laser for fabrication of nanostructures on Au/Pd alloy thin films in air (BS - beam-splitter, L - negative lens, DOE - diffractive optical element, GSM - galvano-scanner mirror, FO - focusing objective or AL - aspherical lens, PC - laptop for laser, galvano-scanner and stage control, EM - energy meter, AC - autocorrelator).*

III. RESULTS AND DISCUSSION

The different nanostructures were obtained, when using femto-second laser pulses with various energies (Fig. 2). At the fluence $F \approx 0.11$ J/cm^2, the traces of the melting of the surface and recrystallization of metal nanocrystallite grains (Fig. 2a). It is remarkable that this is not accompanied by visible separation of the film from the substrate. However, the irradiation by an ultrashort laser pulse with the fluence $F \approx 0.13$ J/cm^2 results in not only the melting of the film but also in exfoliation in the form of a microbump (Fig. 2b). A further increase in the fluence leads to the growth of the microbump and the appearance of a nanotip in the pit on the top of the microbump (Fig. 2c). Then (at $F > 0.18$ J/cm^2), the film in its central part (darker region) becomes visibly thinner, and a submicron jet and a nanoparticle are formed immediately at the top of the microbump (Figs. 2d and 2e).

 ISBN:

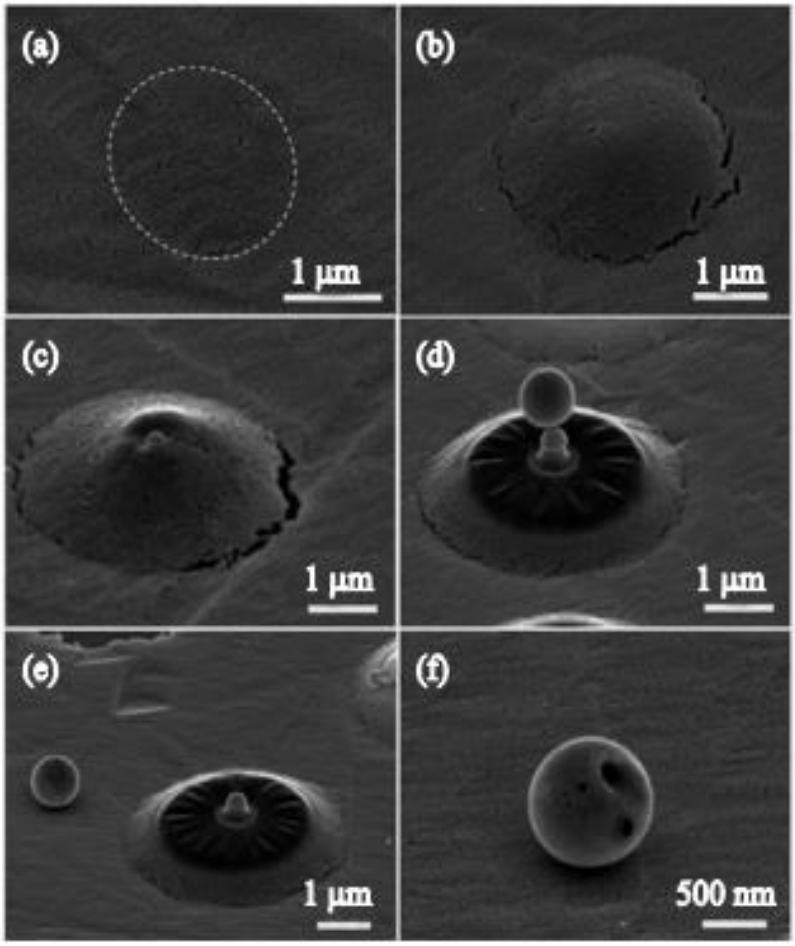

Fig. 2. *Scanning electron microscopy (SEM) images of the surface of the gold film irradiated by single ultrashort laser pulses with the fluence F ≈ 0,11 (a), 0,13 (b), 0,15 (c) and 0,18 (d, f) J/cm²*.

After the irradiation by the ultrashort laser pulse with the fluence $F \approx 0.18$ J/cm^2, a nanotip (a solidified nanojet of metal melt) is observed under the nanoparticle (Fig. 2d); this nanotip ejects the nanoparticle to a certain distance from the microbump until finally total separation (Fig. 2e). However, the formation of nanoparticles with a complex shape, e.g., with a notch (Fig. 2f), has not yet been reported. The notch can appear at the place of separation of the nanoparticle from the nanojet, because the nanojet is solidified owing to the electron heat conduction to the film before the solidification of the nanoparticle connected to the jet through a point contact (Fig. 2d). Because of the later solidification of the nanoparticle, its mechanical contact with the nanotip is weak (Fig. 3c).

The separation of the nanoparticle together with the jet, which is accompanied by the formation of a hole on the top of a hollow microbump, occurs already at the fluence $F \approx 0.23$ J/cm^2 (Fig. 3f). At higher fluences, the diameter of the formed hole increases monotonically, and the nanoparticle together with the nanojet leaves the irradiation region (Fig. 3). In a certain case, the nanoparticle remains on the bottom of the microbump at the center of the hole (Fig. 3a). Under other conditions, the nanoparticle leaves the hole (Fig. 3b).

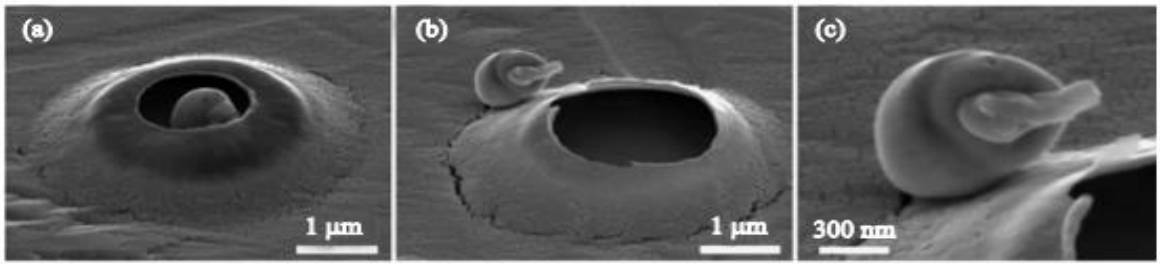

Fig. 3. *Scanning electron microscopy images of the surface of the gold film irradiated by a single ultrashort laser pulse with the fluence F ≈ (a) 0.23 and (b) 0.25 J/cm^2 at an angle of view of 55°. (c) Magnified images of the separated nanoparticle with the nanojet.*

To understand the mechanism of formation of microbumps, nanotips, and nanoparticles, it is important that their formation thresholds slightly above the melting threshold of the film can occur without deformation of the surface (Fig. 1a). This experimental fact cannot be explained by the existing models based either on the molecular dynamics method or on the solution of a continuous problem of the propagation of elastic waves and plastic deformations in a heated film.

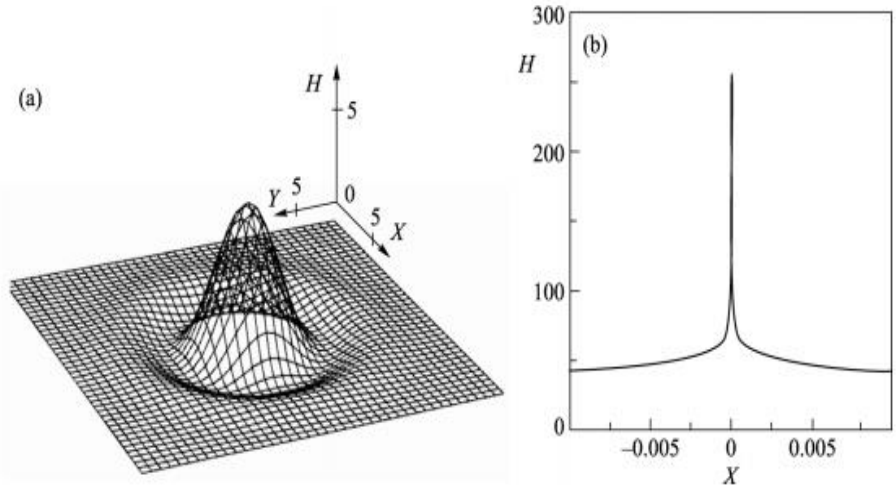

Fig. 4. *Calculated profiles of the nanojet at the (a) quasilinear (solution by Eq. (2) with ε = θ = 1) and (b) nonlinear (numerical solution of one-dimensional equation (1) disregarding the term ~(∇H)^2) stages of its formation.*

We assume that the formation and development of a nanojet and the formation of a nanoparticle are due to the thermocapillary instability of the melted film. Because of a low thermal conductivity of a dielectric substrate under the film with the thickness h, the laser melting of the film results in the appearance of the normal gradient of the temperature T directed from the irradiated surface into the film along the z axis. As a result, the relief of the surface of the melt becomes unstable: at a local increase in the thickness of the melt $h(\mathbf{r}, t) = h_m + h_1(\mathbf{r}, t)$, where h_m = const, $h_1(\mathbf{r}) << h_m$, and $\mathbf{r} = \{x, y\}$, thermocapillary forces generate rising flows enhancing fluctuations. Fluctuation $h_1(\mathbf{r}, t)$ satisfies the two-dimensional Kuramoto-Sivashinskytype hydrodynamic equation obtained in the longwavelength approximation:

$$\frac{\partial H}{\partial \theta} = -\varepsilon \Delta H - \Delta^2 \mathrm{H} - \varepsilon[(\nabla \mathrm{H})^2 + (\Delta \mathrm{H})^2] \quad (1)$$

 ISBN:

where $H = 2h_1/h_m$; $\theta = t(D_1, l^2)$ is the dimensionless time; $\varepsilon = D/D_1 > 0$ is the control parameter; $D = (|\sigma_T| h_m^2 . 2\rho\eta) \left|\frac{\partial T}{\partial Z}\right|_{z=h_m} > 0, D_1 = \frac{\sigma h_m}{3\rho\eta} > 0$, ρ, η and σ are the density, kinematic viscosity, and surface tension coefficient of the melt, respectively; $l_{\|} = h_m/\sqrt{3}$ is the scaling parameter; $\sigma T = \partial\sigma/\partial T < 0$; and Δ and ∇ are the two-dimensional Laplace and gradient operators with respect to the dimensionless coordinates $X = x/l_{\|}$ and $Y = y/l_{\|}$. In the quasilinear regime (at small times) under the phase matching condition for the harmonics of the relief (q_x and q_y), the solution of Eq. (1) is represented in the form of the superposition of harmonics:

$$H(x, y, \theta) = \int_{-\infty}^{+\infty} \int_{-\infty}^{+\infty} exp\{[\varepsilon(q_X^2 + q_Y^2) - (q_X^2 + q_Y^2)^2]\theta\} cos(q_X X + q_Y Y) d\, q_X d q_Y \quad (2)$$

It describes the appearance and growth of an axisymmetric peak (Fig. 4a) with a diameter of about the thickness of the melt *h*m, which is experimentally observed at the initial stage of the formation of the nanojet (Fig. 2c).

In the nonlinear regime (at a quite high laser fluence), the last term of Eq. (1) dominates in the case of strong axisymmetric focusing. The resulting nonlinear equation in the one-dimensional approximation was numerically analyzed, where an "explosive" solution with the subsequent growth of a nanopeak and the formation of a nanotip was demonstrated (Fig. 4b). Upward flows of the cooled melt within the nanojet are responsible for the accumulation of the material at the end of the nanojet with the subsequent formation of a spherical nanoparticle, which minimizes the surface energy. The motion of the melt from the central region of the surface ($x = 0$, Fig. 4b) upward along the nanotip initiates flows of the melt along the surface toward the base of the nanotip, which result in the thinning of the melted film near this base (Figs. 2c-2e).

IV. CONCLUSION

A new principle of the formation of nanoparticles with nanonotches, which are promising for the fabrication of nanoantennas with unique optical properties, has been demonstrated. This instability is manifested in the appearance of a nanojet of the melt at the linear stage and its development at the nonlinear stage of instability with the subsequent decomposition of the nanojet into nanoparticles. The hydrodynamic instability of a thin Au/Pd thin film melted by using femto-second laser pulses has been studied experimentally and theoretically.

ACKNOWLEDGMENTS. This work was supported by the grant of the Ha Tinh University.

REFERENCES

[1] L. Novotny and B. Hecht, Principles of Nano-Optics, Cambridge Univ. Press, Cambridge, 2012.

[2] M. Reininghaus, D. Wortmann, Z. Cao, J. M. Hoffmann, and T. Taubner, *Opt. Express*, 2013, **21**, 32176.

[3] M. A. Gubko, W. Husinsky, A. A. Ionin, S. I. Kudryashov, S. V. Makarov, C. S. R. Nathala, A. A. Rudenko, L. V. Seleznev, D. V. Sinitsyn, and I. V. Treshin, *Laser Phys. Lett.*, 2014, **11**, 065301.

[4] J. P. Moening, S. S. Thanawala, and D. G. Georgiev, *Appl. Phys. A*, 2009, **95**, 635.

[5] Y. Nakata, N. Miyanaga, and T. Okada, *Appl. Surf. Sci.*, 2007, 253, 6555.

[6] F. Korte, J. Koch, and B. N. Chichkov, *Appl. Phys. A*, 2004, **79**, 879.

[7] M. A. Gubko, A. A. Ionin, S. I. Kudryashov, S. V. Makarov, A. A. Rudenko, L. V. Seleznev, and D. V. Sinitsyn, *JETP Lett.*, 2013, **97**, 599.

[8] Y. P. Meshcheryakov and N. M. Bulgakova, *Appl. Phys. A*, 2006, **82**, 363.

 ISBN:

SYNTHESIS OF CdSe QUANTUM DOTS AND PHOTOLUMINESCENCE ENHANCEMENT BY ZnO THIN FILM

Phan Van Cuong*

Department of Physics, Nha Trang University, Vietnam

*E-mail: *cuongpv@ntu.edu.vn*

Abstract. CdSe quantum dots (QDs) were successfully prepared and used for spin coating on glass substrate. Then ZnO thin film was deposited on the CdSe quantum dot coated glass substrate. The enhancement of photoluminescence (PL) of CdSe QDs was studied. The results indicate that CdSe QDs are uniform and the diameter is about 5nm. Notably, with the ZnO thin film deposited on CdSe QDs, the PL intensity was enhanced over two times compared to the CdSe QD layer only.

I. INTRODUCTION

Quantum dots (QDs) have generated tremendous interest both for fundamental research and technical applications such as light emitting diodes (LEDs) [1], bioimaging [2], and solar cells [3]. Because of their size-dependent photoluminescence (PL) related to quantum-size effect tunable across the wide visible spectrum, CdSe QDs have become the most extensively investigated QDs [4]. Since core CdSe QDs usually have low luminescence efficiency, much experimental work has been devoted to surface passivation to improve the luminescence efficiency of QDs. Several methods of organic and inorganic surface modification have been developed to mediate the problems by passivation of the surface defects of QDs. The organic passivation methods such as polymer encapsulation, surface grafting, and ligand exchange [5-7] have usually accompanied a decrease in quantum yield (QY) and an undesirable size increase relative to the original QDs and more QDs being included in the polymer encapsulation. It is well known that shelling of inorganic atomic layers with a wider bandgap on the surface of core QDs effectively reduces nonradioactive recombination which results in the enhancement of PL QY [8,9]. In this report, CdSe QDs were synthesized successfully and the product is used for spin coating on glass substrate. Then ZnO thin film was deposited on the CdSe quantum dot coated glass substrate. The enhancement of photoluminescence (PL) of CdSe QDs was studied.

II. EXPERIMENTS

The CdSe QDs were prepared by TOPO-TOP based organometallic synthesis. A 2M stock solution of trioctylphosphine selenide (TOP:Se) was prepared by dissolving 15.8 g of Se into 100 ml of TOP. The stock solution was filled in 100 ml three-neck round-bottomed flask and fitted with a thermocouple temperature sensor and condenser, with TOPO (10 g), HDA (10 g) and TOP (2.5 ml), and heat to 170 ^{o}C under vacuum for 1-2h and raise the temperature to 340-350 ^{o}C. In a separate vial, mix Cd(acac)2 (620 mg), HDDO (1 g), and TOP (5 ml) and heat under vacuum to 100 ^{o}C; the solution should become homogeneous.

ISBN:

Cool the mixture to approximately 80 ^{o}C and add 5 ml of a 2 M TOP:Se. The solution mixture of cadmium and selenium precursors was rapidly injected into the hot flask containing the coordinating solvent, and then cooled using each solvent. The QDs extracted from same hot batch were divided into different cooling solvents. The synthesized CdSe QDs were spin-coated on glass substrate at a speed of 3000 rpm.

RF sputtering method was used to deposit ZnO thin film layer on CdSe QDs coated on glass substrate which was mentioned above. The ZnO target (99.99%) is used and the pressure is at 7.10^{-3} torr inside chamber, 20 W sputter power, Ar gas is flowed at 15 sccm and the sputtering time is 15 minute at room temperature.

CdSe QDs was characterized by field-emission transmission electron microscope (FE-TEM - Titan G2 ChemiSTEM Cs Probe from FEI Co.). The photoluminescence of the samples is measured under excitation by an iHR320 imaging spectrometer (Horiba Jobin Yvon).

III. RESULTS AND DISCUSSION

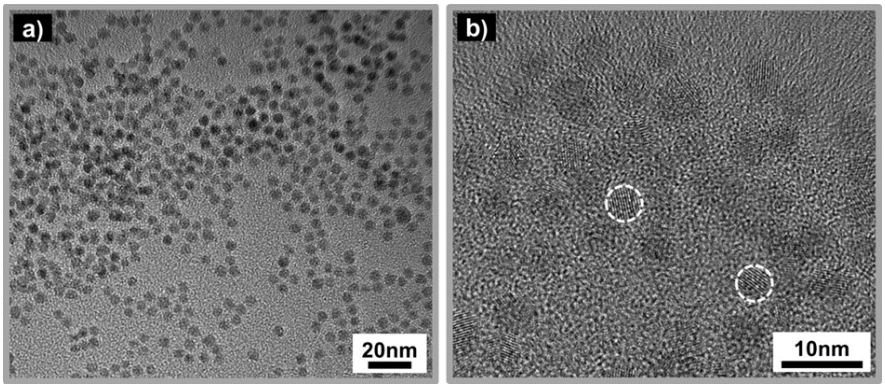

Fig. 1. *TEM images of CdSe quantum dots. (a) The low-magnification image shows the shape and size distribution. (b) The higher resolution image identifies the diameter about 5 nm.*

The TEM images of the CdSe QDs are shown in Figure 1. The black scale bars in the images indicate the lengths of 20 and 10 nm, corresponding to (a) and (b), respectively. The images display the shape and size distribution of the synthesized QDs. Spherical nanostructures are observed, which have an average diameter of about 5 nm.

The enhanced photoluminescence (PL) of CdSe QDs by the ZnO thin film is shown in Figure 2. The inset in this figure is the schematic set up to measure the PL of CdSe QDs with (2) and without ZnO thin film layer (1). The photoluminescence (PL) of all samples is measured under excitation by an iHR320 imaging spectrometer (Horiba Jobin Yvon) with excited wave length of 365 nm at room temperature. The result of the PL spectra shows that the intensity of the CdSe with ZnO film (2) is about two and half times more than that of the CdSe QDs only (1). Meanwhile, the PL wavelength at peak of (1) is almost the same as that of (2).

The enhancement of the PL intensity could be explained by the platform through FRET (Fluorescence Resonance Energy Transfer) to ZnO from CdSe QDs [10,11]. In

 ISBN:

detail, the energy transfer explains FRET from CdSe QD-based donor-excited states to a proximal acceptor (ZnO film) through nonradiative dipole-dipole coupling.

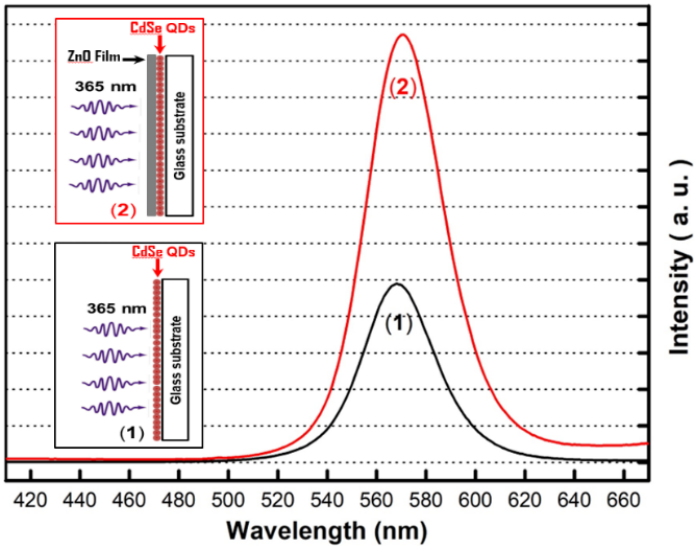

Fig. 2. *The photoluminescence of CdSe QDs coated on glass substrate with (2) and without (1) ZnO thin film.*

IV. CONCLUSION

In this study, CdSe QDs were successfully synthesized and spin coated on glass substrate. ZnO thin film was deposited on the CdSe QDs to enhance the photoluminescence of CdSe QDs. In detail, the diameter of CdSe QDs is about 5 nm, the particles are quite uniform. The PL intensity of the CdSe with coated ZnO film is about two and half times more than that of the CdSe QDs only and the PL wavelength at peak is almost the same for both samples. This PL enhancement of CdSe QDs can be applied for many areas in the future.

ACKNOWLEDGMENTS. This research was supported by Basic Science Research Program through the National Research Foundation of Korea (NRF).

REFERENCES

[1] P. O. Anikeeva, J. E. Halpert, M. G. Bawendi, and V. Bulovic, Electroluminescence from a mixed red-green-blue colloidal quantum dot monolayer, *Nano Lett.*, 2007, **7**, 2196-2200.

[2] H. Tada, H. Higuchi, T. M. Wanatabe, and N. Ohuchi, In vivo real-time tracking of single quantum dots conjugated with monoclonal anti-HER2 antibody in tumors of mice, *Can. Res.*, 2007, **67**, 1138-1144.

[3] B. Farrow and P. V. Kamat, CdSe quantum dot sensitized solar cells. Shuttling electrons through stacked carbon nanocups, *J. Amer. Chem. Soc.*, 2009, **131**, 11124-11131.

[4] M. G. Bawendi, P. J. Carroll, W. L. Wilson, and L. E. Brus, Luminescence properties of CdSe quantum crystallites: resonance between interior and surface localized states, *J. Chem. Phys.*, 1992, **96**, 946-954.

[5] W. T. Al-Jamal, K. T. Al-Jamal, P. H. Bomans, P. M. Frederik, and K. Kostarelos, Functionalized-quantum-dot-liposome hybrids as multimodal nanopartides for cancer, *Small*, 2008, **4**, 1406-141.

[6] J. K. Kim, S. H. Lim, Y. Lee et al., Conjugation of DNA to streptavidin-coated quantum dots for the real-time imaging of gene transfer into live cells, *Proceedings of the NSTI Nanotechnology Conference and Trade Show*, 2004, **3**, 379-382.

[7] X. Ji, J. Zheng, J. Xu et al., (CdSe)ZnS quantum dots and organophosphorus hydrolase bioconjugate as biosensors for detection of paraoxon, *J. Phys. Chem. B*, 2005, **109**, 3793-3799.

[8] D. V. Talapin, I. Mekis, S. Gotzinger, A. Kornowski, O. Benson, and H. Weller, CdSe/CdS/ZnS and CdSe/ZnSe/ZnS core-shell-shell nanocrystals, *J. Phys. Chem. B*, 2004, **108**, 18826-18831.

[9] D. Pan, Q. Wang, S. Jiang, X. Ji, and L. An, Synthesis of extremely small CdSe and highly luminescent CdSe/CdS core-shell nanocrystals via a novel two-phase thermal approach, *Adv. Mater.*, 2005, **17**, 176-179.

[10] Y. Wang, R. Hu, G. Lin, I. Roy, K. T. Yong, Functionalized quantum dots for biosensing and bioimaging and concerns on toxicity, *Acs Appl. Mater. Interfaces*, 2013, **5**, 2786-2799.

[11] E. Jenrette, S.K. Pradhan, G. Rutherford, J. Flowers, D. Ha, A. K. Pradhan, Quantum-dot-conjugated graphene oxide as an optical tool for biosensor, *Opt. Express*, 2015, **23**, 25017-25027.

 ISBN:

CLOUD REMOVAL FROM LANDSAT IMAGERY USING CLOUD COMPUTING PLATFORM GOOGLE EARTH ENGINE

Phu Van Le[1*], Hung Le Trinh[1], Nguyen Quoc Long[2], Tien Minh Pham[3], Hai Van Bui[1]

[1]*Le Quy Don Technical University, Hanoi, Vietnam*

[2]*Hanoi University of Mining and Geology*

[3]*Institute of Applied Informatics and Mechanics, HoChiMinh City, Vietnam*

*E-mail: *phule.ktqs.53@gmail.com*

Abstract. Due to its location in the tropical monsoon area, optical remote sensing images acquired in the territory of Vietnam are often covered by clouds, greatly affecting image quality as well as applicability in practice. This paper presents a method to cloud removal from Landsat optical remote sensing images using cloud computing platform Google Earth Engine (GEE). The proposed method is tested with cloud removal for Landsat images in 03 areas of Vietnam's territory: the Northern Delta, the Central Highlands and the Mekong River Delta. For each test area, Landsat satellite images, including Landsat TM, Landsat ETM+ and Landsat 8 periods from January 2017 to June 2021 were used to create cloudless images. The obtained results show that the proposed method in the study can be effectively used to remove the effect of clouds on optical images such as Landsat. The application of GEE cloud computing platform for cloud removal also saves time and workload in multi-temporal remote sensing data processing.

Keywords: *Optical remote sensing image, Landsat imagery, Cloud removal, Google Earth Engine.*

I. INTRODUCTION

Remote sensing technology is part of a developed space technology that has been rapidly applied in many fields and is available in developed countries. Compared to traditional research methods, remote sensing technology has outstanding advantages such as wide coverage, short update time, wide spectrum, can collect images in remote areas such as primeval forests, islands, areas outside the country,… The application of remote sensing in the study and monitoring of the Earth has become a development trend of every country [1].

Optical remote sensing image allows the classification of manage objects based on their spectral reflection characteristics. Despite this, optical images depend on weather conditions and for areas with tropical monsoon climates such as Vietnam, optical images are often covered by clouds. This greatly affects the accuracy of the results of the interpretation of the objects on the image. The processing of clouds and cloud shadows on optical image is a matter of great practical significance, helping to improve the efficiency of the application of remote sensing data in Earth research.

Many methods of cloud filtering on optical image have been proposed by scientists around the world such as the method of combination optical and radar images [2], the method of using multi-temporal optical image data to create cloudless images [3-6]. The

United States Geological Survey (USGS) has developed a cloud detection method for Landsat images based on the CFMask algorithm and presents the results by quality assessment band (BQA) with necessary information about clouds for each image [7].

Some algorithms process clouds by replacing cloud pixels and cloud shadows on image with other pixels from cloudless images such as automatic cloud removal algorithm (Automated Cloud - Cover Assessment - ACCA), cloud detection algorithm and cloud shadow on satellite imagery (Function of mask - Fmask) [8]. Even so, these algorithms are as limited as being confused between clouds and cloud shadows, which are ineffective with areas with high lighting angles. The research [9] has applied a neural network to identify cloudy and cloudless pixels on optical satellite imagery. This method is more accurate than algorithms such as ACCA, Fmask, but requires a lot of data for machine learning. The collection and storage of large of input satellite images to create cloudless images also causes when using personal computers, time consuming and processing. In addition, there are also some studies on cloud identification and detection from Landsat and Sentinel 2 optical satellite images, thereby improving the accuracy of cloud removal on these images [10-16].

Google Earth Engine (GEE) is a platform built on cloud computing, storing a huge of satellite images, regularly updated and provided for free [17]. GEE is designed so that researchers can share their results with the community. Recently, GEE has provided modern image processing solutions such as machine learning, deep learning, artificial intelligence. GEE is an effective solution that can overcome the data limitations, processing speed and calculation of traditional image processing methods. In particular, GEE provides an interface application, also known as Code Editor, where researchers use JavaScript language to access and analyze data and download results.

For the study, the authors used cloud filtering on a multi-temporal Landsat TM/ETM+/OLI image dataset. Three test areas of Vietnam were selected, including the Northern Delta, the Central Highlands and the Mekong River Delta. For each test area, the study used Landsat TM/ETM+/OLI reference images from January 2017 to June 2021 to create cloudless images. The number of reference image for each test is greater than 100 images to ensure that the cloud effect can be removed as much as possible during the resulting image creation.

II. MATERIALS AND METHODS

Previous cloud filtering methods often used the $NDVI_{max}$ index value to replace cloud-covered pixels or cloud shadows. In general, these methods depend unique on the number and quality of the reference image, so when the mask is created, the value of the replaced pixel will be affected by any difference between the original image and the reference image. The use of the $NDVI_{max}$ method will not change the value of the pixel. However, if the number of selected images is small, the cloud filtering result will likely be disturbed during the replacement of reference pixels. The study used a medium-symity method, which made the image look smoother, especially the overlapping positions between the images. In addition, the study also used Landsat TM, Landsat ETM+ and

 ISBN:

Landsat 8 OLI images to increase the number of input references. The implementation diagram of the cloud filtering process is presented in Figure 1 below. The algorithm is executed in the Java Script programming language.

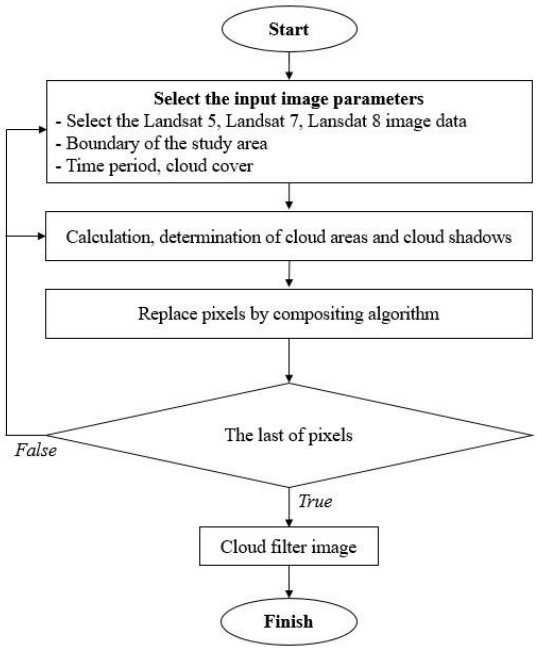

Fig. 1. *Flowchart of the cloud filtering method on platform GEE.*

Step 1: Select the input image parameters

In this step, it is necessary to create a list of Landsat images used for cloud filtering and other related parameters such as the type of image, location, time period, processing level, cloud cover level. Images with cloud cover greater than 80% are not selected because they have little value in cloud filtering, and cloud pixels in the image can create noises that are difficult to control during calculations.

Step 2: Identify cloud areas and cloud shadows

a) Cloud identification: In GEE platform, cloudScore algorithm uses cloud spectral features to identify and remove cloud pixels from satellite imagery. First, cloudScore normalizes the value of image bands on a scale from 0 to 1, according to the following formula:

$$Normalize_X = \frac{Band_X - Threshold_1}{Threshold_2 - Threshold_1} \quad (1)$$

In there, $Threshold_1$, $Threshold_2$ are the threshold values of the image bands, specifically according to the theory in the study [18].

Theoretically, clouds reflect quite strongly on the "blue" band, the cloud threshold applied to this band is in the range from 0.1 to 0.3, applying the normalization function for the "blue" band:

$$Normalize_{blue} = \frac{Band_{blue} - 0.1}{0.3 - 0.1} \quad (2)$$

- For image band in the visible range, on the basis that clouds are also strongly reflected and the cloud threshold applied to this band is in the range from 0.3 to 0.8, so the normalization function with the "visible" bands is calculated according to the formula:

$$Normalize_{visible} = \frac{\left(Band_{red} + Band_{green} + Band_{blue}\right) - 0.3}{0.8 - 0.3} \quad (3)$$

- For infrared bands, the cloud threshold is applied in the range from 0.3 to 0.9. From there, the formula nomalize with "infrared" bands according to the formula:

$$Normalize_{infrared} = \frac{\left(Band_{nir} + Band_{swir1} + Band_{swir2}\right) - 0.3}{0.9 - 0.3} \quad (4)$$

- For thermal infrared bands, clouds have a lower temperature than terrestrial objects. Usually, the temperature of clouds on the thermal infrared bands according to the formula:

$$Normalize_{temperature} = \frac{Band_{temp} - 300}{300 - 290} \quad (5)$$

- Use the Normalized Difference Snow Index (NDSI), then apply the cloud threshold in the range from 0.6 to 0.8. Proceed to average with the "NDSI" bands according to the formula:

$$Normalize_{NDSI} = \frac{Band_{NDSI} - 0.6}{0.8 - 0.6} \quad (6)$$

The NDSI is defined as follows [19]:

$$NDSI = \frac{Band_{GREEN} - Band_{SWIR1}}{Band_{GREEN} + Band_{SWIR1}} \quad (7)$$

Finally synthesizing these bands by the minimum value function, this layer is conducted cloud threshold classification to determine the location of clouds on satellite images according to the following formula:

$$cloudScore_{landsat} = \min\left\{\begin{matrix} 1.0, normalize_{blue}, normalize_{visible}, \\ normalize_{infrared}, normalize_{temperature}, normalize_{NDSI} \end{matrix}\right\} \quad (8)$$

The process of processing to identify clouds on Landsat images using the GEE platform is shown in the following code:

```
var cloudScore = function(img) {
  var rescale = function(img, exp, thresholds) {
    return img.expression(exp, {img: img})
        .subtract(thresholds[0]).divide(thresholds[1] - thresholds[0]);
  };
  var score = ee.Image(1.0);
  score = score.min(rescale(img, 'img.blue', [0.1, 0.3]));
  score = score.min(rescale(img, 'img.red + img.green + img.blue', [0.3, 0.8]));
  score = score.min(rescale(img, 'img.nir + img.swir1 + img.swir2', [0.3, 0.9]));
  score = score.min(rescale(img, 'img.temp', [300, 290]));
  var ndsi = img.normalizedDifference(['green', 'swir1']);
  return score.min(rescale(ndsi, 'img', [0.8, 0.6]));
};
```

b) Cloud shadow identification: The Temporal Dark Outlier Mask (TDOM) method is used to identify cloud shadow pixels [18]. This method is represented by the following formula:

$$z\left(N_b\right) = \frac{N_b - \tilde{N}_b}{\sigma_b} \quad (9)$$

$$darkness = N_{swir1} + N_{nir} \quad (10)$$

 ISBN:

$$cloudShadow = All\left\{z(N_{swir1}) < t_{ZS}, z(N_{nir}) < t_{ZS}, darkness < t_{IR}\right\} \quad (11)$$

where $\breve{N}_b$ and σ_b are the mean value and standard deviation of an image band N_b, t_{zs} is the cloud threshold, t_{IR} is the cloud shadow threshold. In the study, t_{zs} has a value of -0.8 and t_{IR} has a value of 0.35.

The TDOM method calculates the mean value $\breve{N}_b$ and standard deviation σ_b of the near infrared band (NIR) and shortware infrared band (SWIR1) of the input data image. For each image, the algorithm calculates the $z(N_b)$ of the NIR band and the SWIR1 band. Each image has also the dark value (darkness) which calculated as the sum of the NIR band and SWIR1 band. Then, the cloud shadow is determined if a pixel has a *z* score less then -0.8 for both the NIR band and the SWIR1 band. In addition, the value of darkness is less then 0.35. These thresholds are selected after evaluating the TDOM of the input images. In addition, it should be noted that in the process of determining the location of cloud shadows based on darkness, some components such as ridge shadows, other dark objects can be mixed into the set of dark spots just identified above. Therefore, the cloud shadow data needs to remove pixels that are not cloud shadows. The identification of dark areas (cloud shadows, mountain slopes, etc.) is illustrated in the following code:

```
function simpleTDOM2(c,zShadowThresh,irSumThresh,dilatePixels){
  var shadowSumBands = ['nir','swir1'];
  //Lay mot so thong ke ve pixel cho chuoi thoi gian
  var irStdDev = c.select(shadowSumBands).reduce(ee.Reducer.stdDev());
  var irMean = c.select(shadowSumBands).mean();
  //Che dau cac diem ngoai lai toi
  c = c.map(function(img){
    var z = img.select(shadowSumBands).subtract(irMean).divide(irStdDev);
    var irSum = img.select(shadowSumBands).reduce(ee.Reducer.sum());
    var m = z.lt(zShadowThresh).reduce(ee.Reducer.sum()).eq(2).and(irSum.lt(irSumThresh)).not();
    m = m.focal_min(dilatePixels);
    return img.addBands(m.rename('TDOMMask'))});
  return c}
```

After identifying dark areas, the removal of pixels that are not cloud shadows is done based on geometric constraints such as size, direction, distance from cloud (Figure 2). The study used the parameters provided along with the image set of the zenith pole and the azimuth angle in combination with the use of buffer zone techniques to look for cloud shadow areas. The process of identifying areas as cloud shadows is shown in the following code:

```
function projectShadows(cloudMask,TDOMMask,image, meanAzimuth,meanZenith,cloudHeights,dilatePixels){
  var darkPixels = image.select(['nir','swir1','swir2']).reduce(ee.Reducer.sum()).lt(irSumThresh);
  var nominalScale = cloudMask.projection().nominalScale();
  var azR = ee.Number(meanAzimuth).multiply(Math.PI).divide(180.0).add(ee.Number(0.5).multiply(Math.PI ));
  var zenR  = ee.Number(0.5).multiply(Math.PI ).subtract(ee.Number(meanZenith).multiply(Math.PI).divide(180.0));
  var shadows = cloudHeights.map(function(cloudHeight){
    cloudHeight = ee.Number(cloudHeight);
    var shadowCastedDistance = zenR.tan().multiply(cloudHeight);
    var x = azR.cos().multiply(shadowCastedDistance).divide(nominalScale).round();
    var y = azR.sin().multiply(shadowCastedDistance).divide(nominalScale).round();
    return cloudMask.changeProj(cloudMask.projection(), cloudMask.projection().translate(x, y))});
  var shadow = ee.ImageCollection.fromImages(shadows).max();
  shadow = shadow.updateMask(shadow.mask().and(cloudMask.mask().not()));
  shadow = shadow.focal_max(dilatePixels);
  shadow = shadow.updateMask(shadow.mask().and(darkPixels).and(TDOMMask));
  return shadow;
}
```

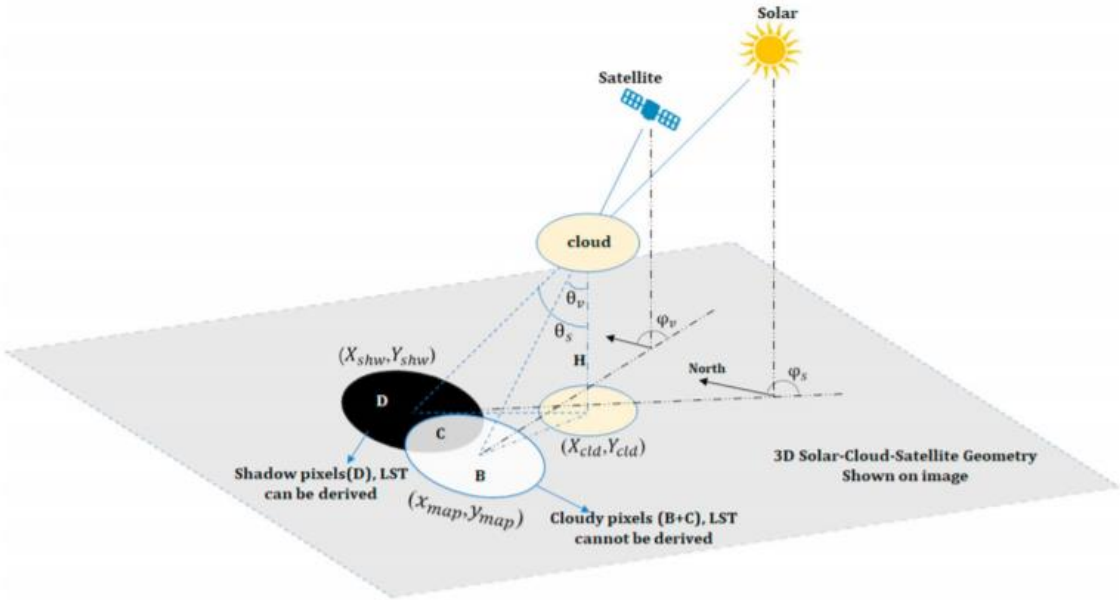

Fig. 2. *Demonstration of the geometric relationship between clouds and clouds.*

Step 3: Replace pixels using compositing algorithm

After determining the location of clouds and clouds, create masks for these locations, where the pixels have value equal by zero. The pixel value at these locations will be replaced by the pixel value from other cloudless images using the medium algorithm.

III. RESULTS AND DISCUSSION

To filter clouds on the GEE platform, in the study, experiment with 03 different areas in Vietnam, including the Northern Delta (Ninh Binh - Nam Dinh), the Central Highlands (Kon Tum) and the South Delta (Mekong River Delta).

Test 1: Test area is located in Kon Tum province (Central Highlands). The Landsat ETM+ and Landsat 8 image datasets for the period 2017 - 2021, including 60 Landsat 7 ETM+ scenes and 79 Landsat 8 image scenes are used to create cloudless images. These images have cloud cover in the range of 10% to 80%. For example, the characteristics of 12 Landsat 8 satellite images in the input dataset are shown in Table 1. The results of creating a cloudless image are presented in Figure 3.

Table 1. *Examples of information on some Landsat 8 image scenes in the reference image dataset for Test 1.*

	Type of image	Image	Image time	Cloud cover (%)
1	Landsat 8 OLI		27/03/2017	76,84
2	Landsat 8 OLI		28/04/2017	40,13

 ISBN:

3	Landsat 8 OLI		15/06/2017	38,89
4	Landsat 8 OLI		01/07/2017	49,17
5	Landsat 8 OLI	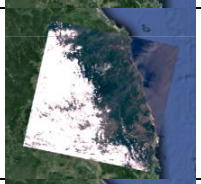	02/8/2017	50,84
6	Landsat 8 OLI		18/8/2017	79,61
7	Landsat 8 OLI		03/9/2017	70,37
8	Landsat 8 OLI	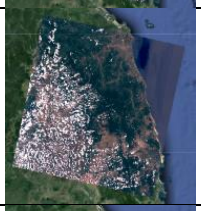	05/10/2017	16,94
9	Landsat 8 OLI	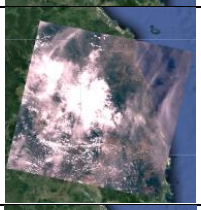	30/03/2018	66,82
10	Landsat 8 OLI	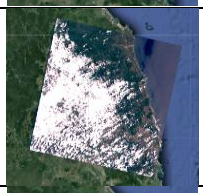	15/04/2018	26,26
11	Landsat 8 OLI		01/05/2018	23,94
12	Landsat 8 OLI		17/05/2018	24,46

Fig. 3. *Results of creating a cloudless image in Kon Tum area.*

Test 2: Similar to test 1, 47 Landsat ETM satellite images and 58 Landsat 8 OLI images for the period 2017 - 2021 in the coastal area of Ninh Binh - Nam Dinh were used as reference images to create cloudless images. The input images also have cloud coverage in the range of 10 to 80%. Examples of some Landsat 8 OLI images in the reference data set are shown in Figure 4. It can be seen that the input images have a fairly large cloud coverage, which greatly affects the usability, practical use if cloud filtering is not carried out. The cloudless imaging results for experiment 2 are shown in Figure 5.

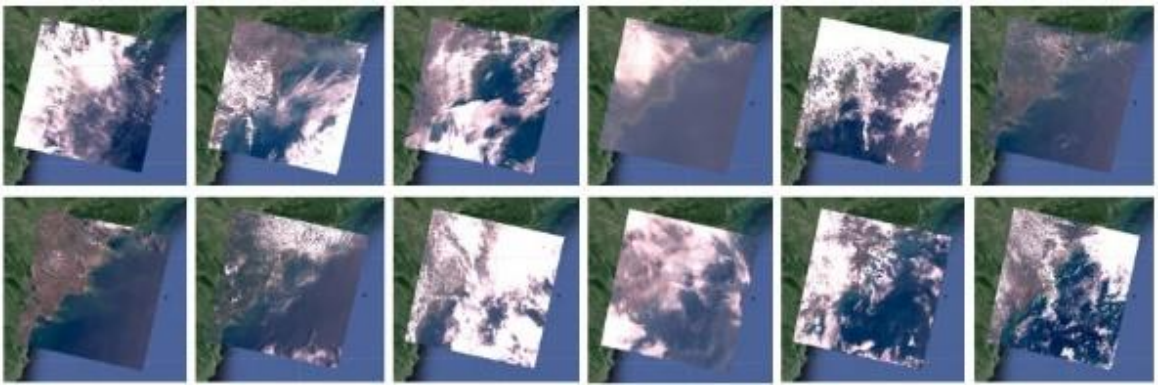

Fig. 4. *The input image data area of Ninh Binh - Nam Dinh.*

Test 3: The selected test area is the Mekong River Delta. This is an area with a sub-equatorial climate, hot and humid, which greatly affects the acquisition ability of optical sensors. With Landsat satellite in particular, optical satellites in general, it is almost difficult to obtain cloudless images in this area.

Similar to the above two test, the Landsat ETM+/OLI image dataset for the period 2017 to 2021 in the Mekong Delta region, includes 51 Landsat ETM+ images and 73 Landsat 8 OLI images with cloud coverage from 10 to 80% is used to create a cloudless

 ISBN:

image. Figure 6 presents images illustrating some Landsat image scenes in the reference dataset. The results of creating a cloudless image from this input data set are shown in Figure 7.

Fig. 5. *Results of creating a cloudless image in Ninh Binh – Nam Dinh area.*

Fig. 6. *The input image data area of Mekong River Delta.*

From the above three tests, it is very difficult to obtain a cloudless Landsat satellite image, especially in the rainy season with weather and climate conditions in Vietnam. In the test areas, clouds appeared at all times of photography during the period from January 2017 to June 2021 with different levels of coverage. The use of multi-temporal Landsat images to create cloudless images is a suitable and effective solution, helping to improve the applicability of optical satellite data in Earth research. Evaluation based on visual interpretation shows that the images after processing (Figures 3, 5, 7) are almost no longer affected by clouds and allow distinguishing basic objects on the Earth's surface such as vegetation cover, water surface, soil. Using the input data set with a relatively large number of images, including Landsat 5 TM, Landsat 7 ETM+ and Landsat 8 OLI_TIRS images, also helps to improve the efficiency of cloud filtering and cloud shadowing. Since there is no need to download and store

input image data to a computer, GEE platform saves time and effort in image processing.

Fig. 7. *Results of creating a cloudless image in Mekong River Delta area.*

IV. CONCLUSION

The study introduced a cloud and cloud shadow filtering solution on Landsat optical satellite imagery using the GEE platform. The input data is a Landsat TM/ETM+/OLI image dataset taken between January 2017 and June 2021, in which each region uses reference images to create cloudless images. During processing, all reference images in the test area are selected with cloud coverage less than 80%. In the process of detecting clouds and cloud shadows, a mask containing objects related to clouds will be created, then, the cloud filter image will be completely clean of clouds. However, in the filtered image, there will be pixels that are not valid during the masking process. These pixels will be selected by the pixels of the same position on the reference images according to the median algorithm. If during the assignment process, the entire reference image has no pixel value at any position, then that pixel in the cloud filter image is also not assigned a value. If this is the case, usually the set of reference images will be reselected through image selection parameters such as period time, cloud coverage.

The study also combined to use the TDOM algorithm to identify cloud-covered areas as well as avoid confusion with other dark spots such as mountain slopes, thereby improving the accuracy of cloud and cloud shadows filtering. From the quality assessment of the images obtained after the cloud filtering process, the proposed algorithm can be used effectively to create cloudless images for areas in Vietnam. In addition, it is necessary to choose the input reference image data set with the right amount and the cloud cover ratio is not too large to ensure that there are cloudless areas to compensate each other, thereby creating cloudless images.

 ISBN:

In particular, the study also shows the great effectiveness of the Google Earth Engine platform in data collection, processing, presentation and storage. Multi-temporal data has been processed quickly, achieving much higher performance than traditional methods.

LỜI CẢM ƠN.

REFERENCES

[1] Trinh L. H., Vu D. T., Application of remote sensing technique fof drought assessment based on normalized difference drought index, a case study of Bac Binh district, Binh Thuan province (Vietnam), *Russian Journal of Earth Sciences*, 2019, **19**(2), ES2003.

[2] Nguyen Thanh Hoan, Tateishi R., Cloud removal of optical image using SAR data for ALOS applications, Experimenting on simulated ALOS data, *Journal of the Remote Sensing Society of Japan*, 2009, **29**(2), 410-417.

[3] Pham V. C., Nguyen V. G., Le V. V. P., Tran A. P. (). A multi-temporal cloud method for detecting cloud and shadow cloud in Landsat 5/8 images on Google Earth Engine, *Journal of Water Resources and Environmental Engineering*, 2019, **67**, 22-31

[4] Tran A. T., Nguyen D. D., Development of Landsat cloud free image data for classification of land cover, case study in Dak Lak province, *Vietnam National University Journal of Science: Earth and Environmental Sciences*, 2019, **35**(4), 80-87.

[5] Song M., Civco D., A knowledge based approach for reducing cload and shadow, *ASPRS-ACSM Annuai Conference and FIG XXII Congress*, April 22-26, 2002.

[6] Martinuzzi S., Gould W., Gonzalez O., Creating cloud-free Landsat ETM+ data sets in tropical landscapes: cload and cloud shadow removal, *General Technical Report IITF-GTR-32*, 2007, 18 pp.

[7] https://www.usgs.gov/, Assessed July 20, 2021.

[8] Zhu Z., Wang S., Woodcock C., Improvement and expansion of the Fmask algorithm: cloud, cloud shadow, and snow detection for Landsat 4-7,8 and Sentinel 2 images, *Remote Sensing of Environment*, 2015, **159**, 269-277.

[9] Mohajerani S., Krammer T., Parvaneh S., A cloud detection algorithm for remote sensing images using fully convolutional Neural Networks, *The IEEE 20th International Workshop on Multimedia Signal Processing*, Vancouver, Canada, 2018, 1-5.

[10] Foga S., Scaramuzza P., Guo S., Zhu Z., Dilley R., Beckmann T., Schmidt G., Dwyer J., Hughes M., Laue B., Cloud detection algorithm comparison and validation for operational Landsat data products, *Remote Sensing of Environment*, 2017, **194**, 379-390.

[11] Jeppesen J., Jacobsen R., Inceoglu F., Toftegaard T., A cloud detection algorithm for satellite imagery based on deep learning, *Remote Sensing of Environment*, 2019, **229**, 247-259.

[12] Oishi Y., Ishida H., Nakamura R., A new Landsat 8 cloud discrimination algorithm thresholding tests, *International Journal of Remote Sensing*, 2018, **39**, 9113-9133.

[13] Skakun S., Vermote E., Roger J., Justice C., Masek J., Validation of the LaSRC cloud detection algorithm for Landsat 8 images, *IEEE Journal of Selected Topics in Applied Earth Observations and Remote Sensing*, 2019, **12**(7), 2439-2446.

[14] Skakun S., Vermote E., Santamaria-Artigas A., Rountree W., Roger J., An experimental sky-image-derived cloud validation dataset for Sentinel-2 and Landsat 8 satellites over NASA GSFC, *International Journal of Applied Earth Observation and Geoinformation*, 2021, **95**, 102253.

[15] Sun L., Mi X., Wei J., Wang J., Tian X., Yu H., Gan P., A cloud detection algorithm generating method for remote sensing data at visible to short-wave infrared wavelengths, *ISPRS Journal of Photogrammetry and Remote Sensing*, 2017, **124**, 70-88.

[16] Wei J., Huang W., Li Z., Sun L., Zhu X., Yuan Q., Liu L.Cribb M., Cloud detection for Landsat imagery by combining the random forest and superpixels extracted via energy-driven sampling segmentation approaches, *Remote Sensing of Environment*, 2020, **248**, 112005.

[17] Gomes V., Queiroz G., Ferreire K., An overview of platforms for big Earth observation data management and analysis, *Remote Sensing*, 2020, **12**, 1253.

[18] Housman. I., Chastain R., Finco M., An evaluation of forest health insect and disease survey data and satellite-based remote sensing forest change detection methods: case studies in the United States, *Remote Sensing*, 2018, **10**, 1184.

[19] Hall D. K., Riggs G. A., Salomonson V. V., Development of methods for mapping global snow cover using moderate resolution imaging spectoradiometer data, *Remote Sensing of Environment*, 1995, **54**, 127-140.

[20] Stromann O., Nascetti A., Yousif O., Ban Y., Dimensionality reduction and feature selection for object-based land cover classification based on Sentinel-1 and Sentinel-2 time series ssing Google Earth Engine, *Remote Sensing*, 2020, **12**, 76.

 ISBN:

POLYMER BLEND BASED ON POLYAMIDE AND ITS APPLICATIONS

Nguyen Trung Thanh*, Truong Dinh Tuan

Institute of Technology, General Department of Defense Industry ,
No. 3 Cau Vong, Duc Thang, Bac Tu Liem, Hanoi, Vietnam

*E-mail: *nguyentrungthanhk42@gmail.com*

Abstract. This article presents effect of metallocene linear low density polyethylene (mLLDPE) on mechanical properties, thermal resistance and morphology of polymer blend polyamide/polypropylene (PA/PP). With mLLDPE of 7 wt.%, mechanical properties were improved. Elongation at break of polymer blend PA/PP/mLLDPE is 306 MPa in compared with 162.30 MPa of PA/PP blend and Tensile strength polymer blend PA/PP/mLLDPE is 63.85 MPa in comparison to that of PA/PP blend is 54.65 MPa. Results of thermal gravimetric analysis (TGA) show that with mLLDPE thermal resistance of polymer blend PA/PP is higher than that of PA/PP blend only. SEM photographs show that phases dispersing of PA and PP into each other better when using mLLDPE. Besides that, the article also introduces the application of polymer blend PA/PP/mLLDPE balls for grinding industrial explosive ammonite (AD1) instead of using gnashing wood balls. The results show that, polymer blend PA/PP/mLLDPE balls are suitable for grinding AD1.

Keywords: *Polyamide blend, Mechanical properties, Compatibilizer, Colymer blend balls, Polymer.*

I. INTRODUCTION

Preparation of polymer blends from commercial polymers is a well-known, easy way and is usually more effective and advantageous than synthesis of new (co)polymers with suitable properties. In the past decades polymer blends of polyamide (PA) and polypropylene (PP) have been studied. This polymer blend can combine outstanding properties two polymers such as good stiffness, strength, heat and solvent resistance, excellent hydrolytic and dimensional stability,… of PP and high chemical, high impact strength, mechanical resistance,… of PA. The differences in structure and polarity of PA and PP prevent them from compatibilizing with each other. In order to favour better compatibility between PA and PP phases as well as improve mechanical and other properties of PA/PP blends, compatibilizers such as block or grafted polyolefin as polypropylene grafted with acrylic acid (PP-g-AA), polypropylene grafted with glycidyl methacrylate (PP-g-GMA),… frequently used with good results [1-3]. Nevertheless, one of the most useful methods is to add a copolymer which is compatible with both phases PA and PP [4-6]. This copolymer migrates at the interface and reduces interfacial tension. Morphology is finer and mechanical properties which are dependent on interfacial adhesion are improved, like elongation at break or impact strength. Generally, block copolymers are more satisfying.

Recently, new random copolymers ethylene-α-olefin (mPE) is obtained using metallocene catalyst. These copolymers have a narrower molecular weight distribution and

a distribution of comonomers more uniform. Numerous studies have been performed about the miscibility or the mechanical properties of PP or PA with these copolymers ethylene-α-olefin, very few publications deal with the compatibilizing effect of these copolymers on PA/PP blends [7-10].

This article showed some results indicating the great compatibility potential of (mLLDPE) for PA/PP blend as mechanical properties, thermal resistance,... Besides that, for application of this polymer blend in industrial scale, the blend is used to manufacturing grinding balls. Now, factories are using gnashing wood balls for grinding industrial explosive ammonite (AD1), but this kind of balls have many disadvantages as low abrasion resistance, expensive, lack of wood in the nature,… The article also showed results of using polymer blend PA/PP/mLLDPE to produce balls for grinding AD1 instead gnashing wood balls. Results showed that, polymer blend PA/PP/mLLDPE balls were better than gnashing balls in grinding AD1.

II. EXPERIMENTS

2.1. Chemicals and materials

Polyamide6 (PA6) is supplied by BASF (Malaysia) SDN BHD-Malaysia, density 1.0-1.2 g/cm^3, melting temperature of approximate 220 ^{o}C.

Polypropylene (PP) is supplied by LyondellBasell (Korea), density 0.91 g/cm^3, melting temperature of 170-175 ^{o}C.

Metallocene linear low density polyethylene (mLLDPE) is supplied by Mitsui Chemical Co., Ltd (Japan), density 0.87 g/cm^3, melting temperature of 93-95 ^{o}C.

2.2. Sample preparation

** Polymer blend preparation*

PA, PP, mLLDPE (scaled as calculated) was prepared in an electric injection molding machine - TH130S. The above components were mixed at temperature of 4 zones as Table 1.

Table 1. *Temperature for polymer blend preparation.*

Zone 1	Zone 2	Zone 3	Zone 4
225 ^{o}C	235 ^{o}C	245 ^{o}C	240 ^{o}C

** Polymer blend ball preparation*

Polymer blend balls with diameter of 60 mm were made in electric injection molding machine - TH130S with conditions in Table 2.

Table 2. *Temperature for polymer blend ball preparation.*

Zone 1	Zone 2	Zone 3	Zone 4	DIE
225 ^{o}C	235 ^{o}C	245 ^{o}C	240 ^{o}C	100 ^{o}C

Pressure: 300 kg/cm^2; Product retention time in mold: 02 minutes.

 ISBN:

2.3. Analysis methods

Mechanical properties: determined according to ASTM-D 638-84 with Universal ZWICK Instrument (Germany).

Thermal resistance: Thermo gravimetric Analysis (TGA) was determined with Shimadzu DTG-60H Instrument (Japan). Working condition: Argon gas at scanning rate of 10 ^{o}C/minute from room temperature to 600 ^{o}C.

Morphology: was observed on the scanning electron micrographs (SEM) with JEOL 5300 (Japan) with magnification of 1000 times.

III. RESULTS AND DISCUSSION

3.1. Mechanical properties of polymer blend PA/PP with and without mLLDPE

3.1.1. Mechanical properties of blend PA/PP

To study on influence of ratio of PA and PP on elongation at break and tensile strength of polymer blend PA/PP, samples were prepared with difference weight percent (wt.%) of PA and PP. Results were shown in Table 3.

Table 3. *Tensile strength and elongation at break of PA, PP, polymer blend PA/PP.*

PA/PP	Tensile strength σ, MPa	Elongation at break ε, %
100/0	63.40	140.50
90/10	59.60	150.20
80/20	54.65	162.30
70/30	33.85	186.15
60/40	30.45	208.40
50/50	29.15	175.80
40/60	30.65	195.75
30/70	33.05	220.60
20/80	34.60	234.20
10/90	32.95	264.15
0/100	31.85	280.55

Table 3 shows that, tensile strength and elongation at break of polymer blend PA/PP were in the range values of PA and PP. The polymer blend could not combine the best elongation at break of PP and the best tensile strength of PA. This can be explained that under conditions of high temperature and spiral worm's movement, PA and PP were melted and mixed each other. There were no chemical reactions or special interactions between macromolecules of PA and PP. So gained material cannot combine or enhance outstanding properties of PA and PP. For enhancing compatibility as well as improve mechanical properties of polymer blend PA/PP, a compatible agent should be used [10].

3.1.2. Mechanical properties of blend PA/PP with mLLDPE

For studying on effect of mLLDPE on elongation at break and tensile strength polymer blend PA/PP with mLLDPE, samples were prepared with ratio of PA/PP as 80/20 and mLLDPE of 1; 3; 5; 7; 9 wt.%. Results were shown in Fig. 1.

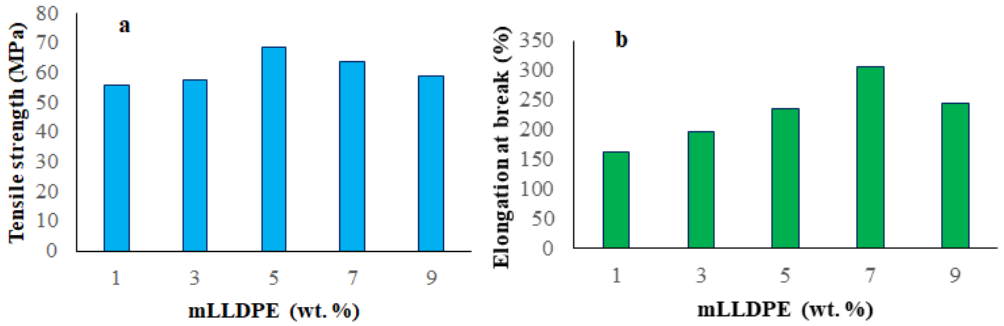

Fig. 1. *Effect of mLLDPE on tensile strength (a) and elongation at break (b) of polymer blend PA/PP.*

Figure 1 shows that, mLLDPE had improved mechanical properties (tensile strength and elongation at break) of polymer blend PA/PP. With mLLDPE of 1; 3; 5; 7 wt.%, mechanical properties of polymer blend were improved but percentage of mLLDPE increased continuously, mechanical properties of polymer blend were low down. This can be explained that, with a suitable percentage of mLLDPE, phase interaction of polymer blend PA/PP was improved. Phase PP was dispersed in continuous PA phase regularly and mLLDPE created physical interactions so PA and PP could be mixed, rolled easily. Therefore, surface tension at interfacial phase was lower, interaction at boundary was higher, which led to distribution of PP phase in PA phase more equally. That might confirm that mLLDPE had enhanced compatibility of PA with PP, improved adhesion of them in polymer blend PA/PP and structure polymer blend PA/PP was more tight-fisted [5-7]. Besides that, may be the interlayer thickness of polymer blend PA/PP/mLLDPE smaller when mLLDPE was under 7 wt.%, when mLLDPE increased the interlayer became thicker and consequently failure occured at PP/mLLDPE interface or PA/mLLDPE or when percentage of mLLDPE was high enough it could agglomerate itself and created the third phase along with PA and PP and resulted in mechanical properties of polymer blend reduced [11].

3.2. Thermal resistance of polymer blend PA/PP with and without mLLDPE

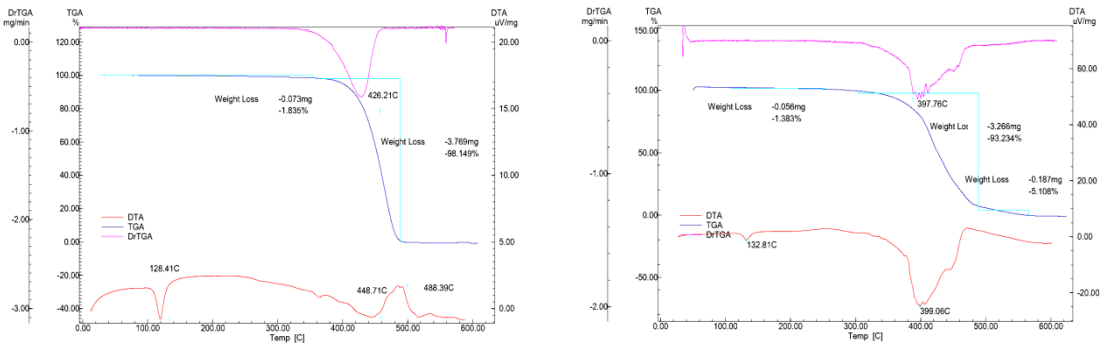

a) **b)**

Fig. 2. *TG diagram of polymer blend PA/PP/mLLDPE: 80/20/7 (a) and PA/PP: 80/20 (b).*

To study on effect of mLLDPE on thermal resistance property of PA/PP blend, thermo- gravimetric analysis (TGA) was used in argon gas at scanning rate of 10 ^{o}C/minute. Samples were prepared with polymer blend PA/PP (80/20) and polymer

 ISBN:

blend PA/PP/mLLDPE (80/20/7). Thermal resistance of samples was determined by weight loss at different temperatures. Results were shown in Fig. 2.

Figure 2 shows that, the slop of TG curve of polymer blend PA/PP/mLLDPE (80/20/7) was lower than that of polymer blend PA/PP (80/20). Figure 2 also shows that, at different temperatures, with the same compatible agent but the weight loss of sample was different. mLLDPE of 7 wt.% had enhanced thermal stability remarkably of polymer blend PA/PP (80/20). This can be explained that, mLLDPE created physical interactions so that phases of polymer blend PA/PP link together closely and more regularly. It prevented thermal decomposing of polymer blend materials based on PA/PP/mLLDPE so thermal resistance of the blend increased. The weight loss at 400 ^{o}C, 450 ^{o}C and 500 ^{o}C were shown in Table 4.

Table 4. *TG data of polymer blend PA/PP with and without mLLDPE.*

Samples	Weight loss (%) at different temprature		
	400 ^{o}C	450 ^{o}C	500 ^{o}C
PA/PP: 80/20	19.50	73.61	96.58
PA/PP/mLLDPE: 80/20/7	6.40	54.35	98.09

3.3. Morphology of polymer blend PA/PP with and without mLLDPE

For studying on effect of mLLDPE on adhesion phases and morphological structure of polymer blend PA/PP, scanning electron micrographs (SEM) was used with polymer blend PA/PP(80/20) and PA/PP/mLLDPE(80/20/7). Results were shown in Fig. 3.

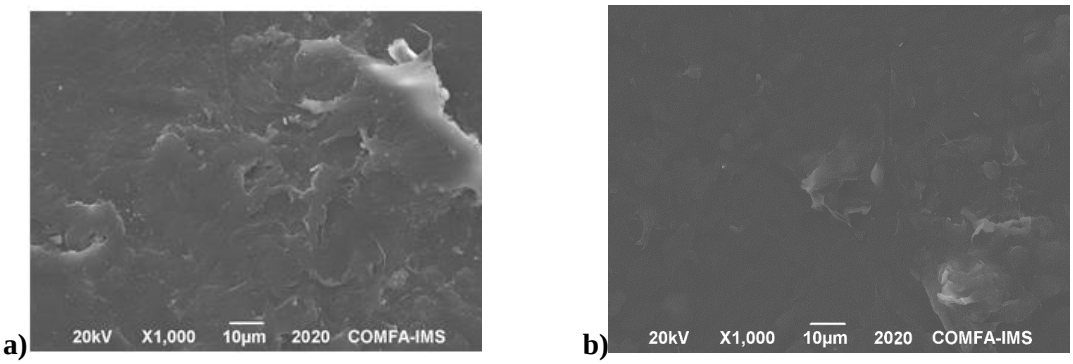

Fig. 3. *SEM of polymer blend a) PA/PP (80/20) and b) PA/PP/mLLDPE (80/20/7).*

Figures 3a and 3b show the big differences in adhesion phases and morphological structure of polymer blend PA/PP with and without mLLDPE. Without compatible agent, PA and PP were mixed mechanically. PP phase was dispersed in continuous PA phase irregularly with large size particles (Fig. 3a). That indicated that adhesion of PA phase and PP phase was bad. When mLLDPE was used (Fig. 3b), the phase interaction of polymer blend PA/PP was improved. Phase PP was dispersed in continuous PA phase regularly with smaller size particles. This can be explained that, mLLDPE created physical interactions so PA and PP can be mixed, rolled easily. Therefore, surface tension at interfacial phase was lower, interaction at this boundary was higher, which led to distribution of PP phase in PA phase more equally. That might confirm that with mLLDPE has enhanced compatibility of PA with PP and improved adhesion in polymer blend PA/PP [12-14].

3.4. Application of polymer blend balls for grinding industrial explosive (AD1)

Fig. 4. *Image of polymer blend balls.*

Currently, AD1 is grinded in tanks by wood balls. AD1 explosive mixture includes: Trinitrotoluene (TNT), ammonia nitrate (NH_4NO_3), wood powder, which is put into the grinding tank as ratio of AD1/balls = 1/1 (200 kgs of AD1 and 200 kgs of balls). Grinding time is 20 minutes, after grinding the AD1 mixture would be sieved by siever number 16 (16 holes/cm^2). To investigate of effective of polymer blend based on PA balls on grinding AD1 instead of wood balls, experiments were done with polymer balls under the conditions for wood balls. Results were shown in Table 5 and Table 6.

Table 5. *Effect of grinding time on polymer blend balls.*

No.	Values	Original value	After 25 hours	After 50 hours	After 116 hours
1	Ball volume (g)	135	134.6	134.3	134.1
2	Dimension (mm)	60- 60.3	60- 60.2	59.9- 60.1	59.8- 60.1
3	Total volume (kg)	200	200	200	199.7

Table 6. *Effective of grinding process of polymer blend balls and gnashing wood balls.*

No.	Technical requirements	Gnashing balls	Polymer blend balls
1	AD1 mixture grinding (20 minutes), Siever No. 16 passed, %	85 - 93	91 - 97
2	Getting products time, Minutes	7 - 9	4 - 5
3	Abrasion resistance (rate of ball losing), kgs of balls/ton of AD1	0.66	0.062

Table 5 and table 6 showed that, abrasion resistance of polymer blend PA/PP/mLLDPE balls was much higher than that of gnashing balls and grinding efficiency was higher. Table 6 shows particle size of AD1 grinded under the current process, results showed that percentage of AD1 powder after grinding passed siever no.16 was over 90% (according to technical requirement the value is over 85%). Thus, it can be confirmed that polymer blend PA/PP/mLLDPE balls are suitable for grinding industrial explosive AD1. Results after 116 hours of grinding AD1 also showed that, absolute safety during grinding, no balls were broken and the most important is that quality of AD1 meets technical requirements.

IV. CONCLUSION

Elongation at break and tensile strength of polymer blend PA/PP/mLLDPE are higher than those of polymer blend PA/PP when percentage of mLLDPE increase to 7 wt.% but more mLLDPE mechanical properties are down. With 7 wt.% of mLLDPE, elongation at break of polymer blend PA/PP/mLLDPE is 306 MPa and tensile strength

 ISBN:

polymer blend PA/PP/mLLDPE is 63.85 MPa, thermal resistance of polymer blend PA/PP is higher than that of samples without mLLDPE. Besides that, mLLDPE has enhanced adhesion phases of PA, PP and morphological structure of polymer blend PA/PP is closer in comparison with polymer blend PA/PP only. Using polymer blend balls instead of gnashing wood balls for grinding industrial explosives (AD1) has great scientific and socio-economic significance as improving labor productivity and working conditions of workers would be improved.

REFERENCES

[1] A. Kmikitev and G., Polymers, Polymer Blends, Polymer Composites and Filled Polymers: Synthesis, properties and applications, Nova publishers, Inc, New York, 2007.

[2] A. Ujhelyiova, Compatibilisation of PP/PA Blends, *Fiber & Textiles in Eastern Europe*, 2012, **93**(4), 30-36.

[3] Coltelli M. B, Passaglia E., One-step functionalization and reactive blending of polyolefin/polyamide mixture (EPM/PA6), *Polymer*, 2006, **47**(1), 85-97.

[4] D. Wang, X. M. Xir, Novel strategy for ternary polymer blend compatibilization, *Polymer*, 2006, **47**(23), 7859-7863.

[5] Ohlsson B., Hassander H., Törnell B, Effect of the Mixing Procedure on the Morphology and Properties of Compatibilized Polypropylene/Polyamide Blends, *Polymer*, 1998, **39**(20), 4715-4721.

[6] L. Utracki, Commercial polymer blends, Chapman & Hall Inc, London, 2010.

[7] B. V. Lingesh, B. N. Ravikumar, B. M. Rudresh, Investigation on the Mechanical Behavior of Polyamide 66/Polypropylene Blends, *Indian Journal of Advances in Chemical Science*, 2016, **4**(2), 168-171.

[8] F. Pa. L. Mantia, M. Ceraulo, M. C. Mistretta, L. Botta, M. Morreale, Compatibilization of Polypropylene/Polyamide 6 Blend Fibers Using Photo-Oxidized Polypropylene, *Materials*, 2019, **12**(1), 81.

[9] B.Y. Shin, M. H. Ha, D. H. Han, Morphological, Rheological, and Mechanical Properties of Polyamide 6/Polypropylene Blends Compatibilized by Electron-Beam Irradiation in the Presence of a Reactive Agent, *Materials*, 2016, **9**(5), 342.

[10] W. S. Chow, Z. A. Mohd Ishak, Polyamide blend-based nanocomposites: A review, *eXPRESS Polymer Letters*, 2015, **9**(3), 211-232.

[11] J. Huitric, J. Ville, P. Mederic, T. Aubry, Solid-state mechanical properties of PE/PA blends filled with organoclay or compatibilized by a graft co-polymer: A comparative study, *Polymer Testing*, 2018, **70**, 208-214.

[12] S. L. Bar, G. T. Wang, Microstructure and Mechanical properties of polypropylene/polyamide6/polyethylene-octene elastomer, *Polymer*, 2004,**45**(9), 3063-3071.

[13] Nguyen Trung Thanh, Effect of mLLDPE on relative melt viscosity, thermal resistance and morpholy of polymer blend PP/PE, *Vietnam Journal of Chemistry*, 2013, **51**(5A), 151-156.

[14] Nguyen Trung Thanh, Effect of Antistatic Agents on Mechanical Properties and Surface Resistivity of Polymer Blend PA/PP, *VNU Journal of Science - Natural Sciences and Technology*, 2016, **32**(3), 118-122.

SPATIO-TEMPORAL CHANGES IN AQUACULTURE PONDS IN BEN TRE PROVINCE, SOUTHERN VIETNAM

Bijeesh Kozhikkodan Veettil[1,2*], Xuan-Linh Tran[2] and Nhat-Duc Hoang[3,4]

[1]*Institute of Fundamental and Applied Sciences, Duy Tan University, Ho Chi Minh City, Vietnam*

[2]*Faculty of Information Technology, Duy Tan University, Da Nang, Vietnam*

[3]*Institute of Research and Development, Duy Tan University, Da Nang, Vietnam*

[4]*Faculty of Civil Engineering, Duy Tan University, Da Nang, Vietnam*

*E-mail: *bijeeshkozhikkodanveettil@duytan.edu.vn*

Abstract. Coastal environments in the low-lying deltas of the world in general and Mekong Delta of Vietnam in particular are highly dynamic and sensitive to natural and anthropogenic perturbations. Climate change, sea level rise, storms and tsunamis are the natural phenomena that affect the Vietnamese Mekong Delta (VMD) and these effects can be exacerbated by human activities, such as mangrove deforestation, aquaculture and infrastructure development. On the other hand, the low-lying coastal areas are important in the economic development of the region. In the present study, we investigated the expansion of aquaculture ponds in the coastal areas of Ben Tre in the VMD during the past two decades (2000-2020) using satellite data. It is recommended that, in addition to hard structures such as rock walls and sea dykes, reforestation of abandoned shrimp ponds in Ben Tre by native mangrove species can be effective as bioshields against coastal hazards, such as shoreline erosion, sea level rise and salt water intrusion.

I. INTRODUCTION

Coastal areas in Southeast Asian countries in general and in Vietnam in Particular are highly dynamic in terms of environmental and socioeconomic aspects. In Vietnam, coastal habitat and biodiversity (e.g. mangrove vegetation) are subjected to the influence of climatic, environmental and anthropogenic factors. Climatic factors (atmospheric warming, sea level rise and tropical storms), environmental factors (salt water intrusion, sea level rise) [1,2] and anthropogenic factors (mangrove deforestation, aquaculture, tourism and pollution) [3] affects the 3250 km long Vietnamese coastline considerably. It is worth noting that the total Vietnamese coastal area accounts for 17% of the total area of the country, which is inhabited by more than 20 million people (267 per km^2). This number is 1.2 times higher than the average population density in the country [4]. Two major deltas in the country, the Red River Delta in the north and the Mekong River Delta in the south, are largely occupied by agricultural activities due to their highly fertile soil [5]. These two deltaic regions in Vietnam have natural mangrove ecosystems, which were undergoing degradation in recent years [6]. The loss of such natural coastal defenses makes the effects of coastal hazards, such as shoreline erosion, severe in recent years [7].

Coastal aquaculture is traditionally practiced along the Vietnamese coastline [8], particularly in the Mekong Delta. Aquaculture offers a lot of economic benefits and GDP growth to Vietnam. However, a large number of negative feedback on the environment, such as the devastation of mangrove forests, occurs during the installation of aquaculture

 ISBN:

ponds [6]. In addition to mangrove deforestation, reduction the water quality due to organic discharges, proliferation of aquaculture structures and changes in regional hydrology also occurs as a result of the rapid aquaculture expansion. In this paper, we investigated recent changes in aquaculture ponds in Ben Tre Province in the Vietnamese Mekong Delta using multispectral satellite data. In addition, we also investigated the changes in mangrove coverage at selected study sites.

II. MATERIALS AND METHODS

Ben Tre Province is located in the downstream of the Mekong River on the coast of South China Sea in Vietnam (Fig. 1). Coastal districts of Ben Tre include Binh Dai, Ba Tri and Thanh Phu. Other districts (Cho Lach, Chau Thanh, Mo Cay, Giong Trom, Binh Dai, Ba Tri and Thanh Phu) and the Ben Tre City is benefited from the natural resources of coastal areas of Ben Tre. There are four estuaries, namely Dai, Ba Lai, Ham Luong and Co Chien, in Ben and the terrain in the coastal area has a low elevation. This makes the population in this area vulnerable to coastal disasters, such as sea level rise, floods and salinity intrusion. Can [9] mentioned that Ben Tre has been potentially affected by climate change in recent years.

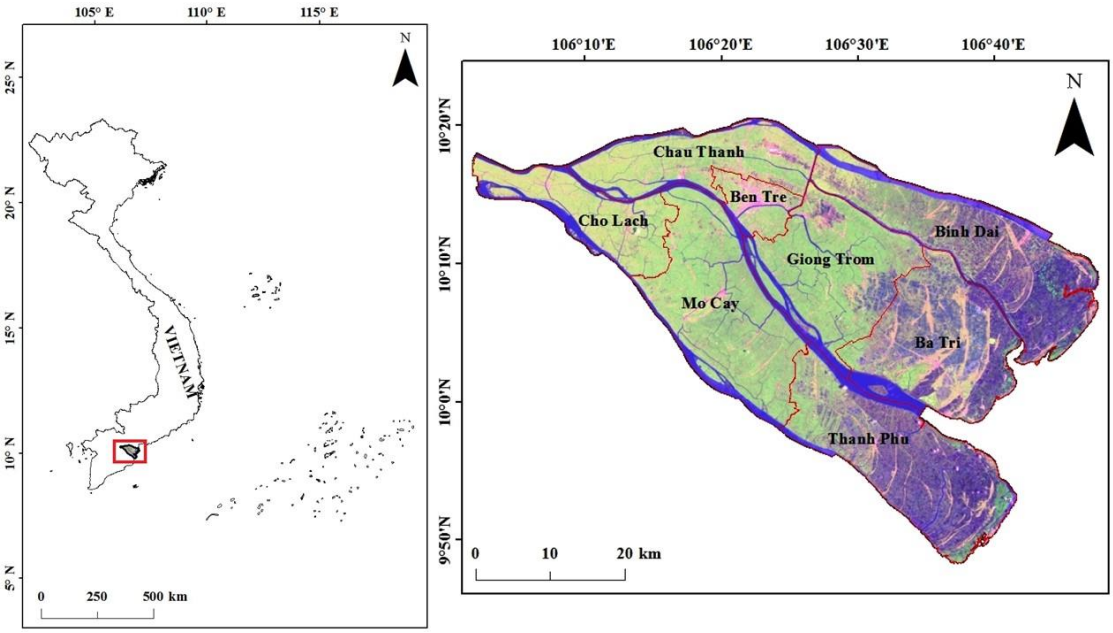

Fig. 1. *Geographical location of Ben Tre and its coastal areas studied (Binh Dai, Ba Tri, and Thanh Phu).*

Aquaculture, fishing, rice, coconut and vegetables are some of the key economic resources in Ben Tre (Fig. 2). Seasonal rainfall dependence of agriculture has become risky in Ben Tre due to salinity intrusion in recent years [10]. In fact, population migration into the coastal areas of Ben Tre started in the 1940s due to its fertile soil and natural resources [7]. During the recent decades, farmers are following a double-income scheme in such a way that planting rice during the wet season and practicing aquaculture during the dry season [10]. According to Phong [7], 44.5% of the land areas in this region is practicing

aquaculture in 2012. A large areas of mangrove forests has been cleared for the expansion of aquaculture in Ben Tre [11].

Fig. 2. *Key economic activities in Ben Tre Province, Vietnamese Mekong Delta*.

For understanding the Spatio-temporal changes in aquaculture ponds and mangrove coverage in the coastal districts of Ben Tre, we used both field investigation and spaceborne multispectral data. Field visits (September 2020 and March 2021) have been conducted with the support from the Institute of Tropical Biology (Ho Chi Minh City). Preliminary analysis for understanding the current status of active and abandoned aquaculture ponds and mangroves (degeneration, regeneration and reforestation) has been done during the field visits. Multispectral satellite imagery has been used for a number of environmental applications, such as mapping Land use land cover (LULC) changes and coastal environmental changes that include spatiotemporal variations in aquaculture ponds [5,11]. In this study, we used Landsat series imagery (TM, ETM+ and OLI), which is freely available from the United States Geological Survey (USGS) EarthExplorer (https://earthexplorer.usgs.gov/). Landsat data used in this study were acquired in January/February, when the cloud cover present, if any, in the data will be the lowest.

The distribution of aquaculture ponds and regeneration of mangrove species in abandoned aquaculture areas have been estimated during the field work along the coast of Ben Tre. Shrimp and fish farming are two key economic resources for coastal community in this region. In addition to the status of aquaculture ponds in Ben Tre, we also estimated the extend of mangrove vegetation along the coastline of Ben Tre.

Image processing algorithms were applied to the satellite data for estimating spatial distribution and areal changes of aquaculture ponds in Ben Tre for the 1988-2021 period. We also estimated abandoned aquaculture ponds/areas in recent years, which can be used

 ISBN:

for mangrove reforestation unless these areas are used for other economic activities (e.g. agriculture, infrastructure development). Aquaculture ponds were mapped by applying normalized difference water index (NDWI) algorithms. The present study also estimated the variations in mangrove vegetation during the study period using vegetation indices, such as the normalized difference vegetation index (NDVI), and GoogleEarth imagery. These algorithms were applied successfully in previous studies conducted in Vietnam [11,12].

III. RESULTS AND DISCUSSION

The present study showed that a serious depletion of mangrove vegetation occurred in Ben Tre, particularly in Ba Tru and Binh Dai districts, in the period between 1988 and 2020. Some areas, such as near the Ba Lai River mouth (Fig. 3), have shown an increase in the area occupied by mangrove vegetation due to reforestation conducted. However, the northern coast of Ben Tre (Mekong River estuary) has witnessed a serious depletion of mangrove forests. Even though mangrove reforestation has been conducted extensively along the coastal communes of Ben Tre, the overall trend in mangrove areal changes in the period between 1988 and 2020 was a decreasing one. For example, in the coastal communes of Binh Dai and Ba Tri districts (Fig. 3), the overall loss of mangrove vegetation was up to 46% in the study period.

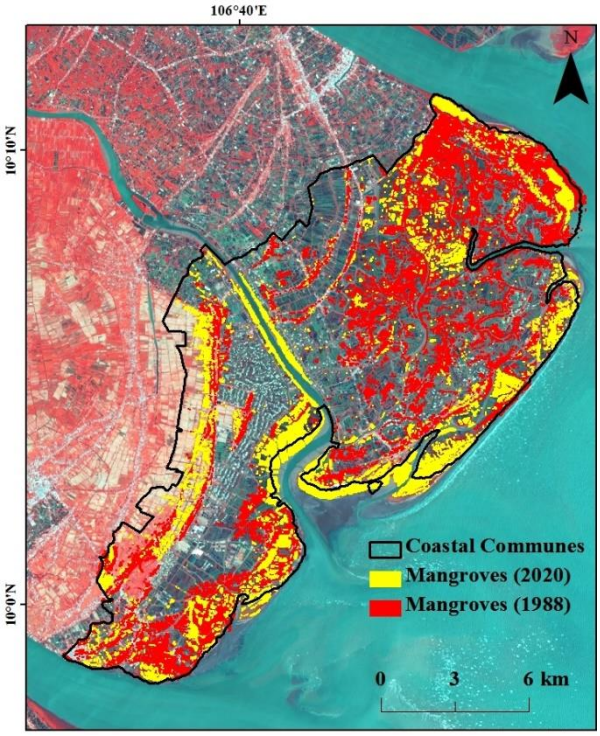

Fig. 3. *Overall area changes in mangroves in the coastal communes of Binh Dai and Ba Tri.*

It was estimated that a number of previously used aquaculture ponds are now unused/abandoned in Ben Tre coastal zones (Fig. 4). During the field survey it was observed that regeneration of Rhizophora mangroves has been occurred in the coastal regions, including the abandoned shrimp pond areas, of Ben Tre. In addition, the mangrove

vegetation developed in the surroundings of abandoned aquaculture areas is healthy, which shows that such sites can be suitable for successful mangrove reforestation (particularly using Rhizophora) unless used for other economic activities. Almost all aquaculture ponds belong to privately owned properties and hence mangrove reforestation in such areas can be complex because the livelihoods of local population depend highly on such economic activities. As an alternative, mixed mangrove-shrimp farming can be implemented instead of complete reforestation of abandoned aquaculture areas.

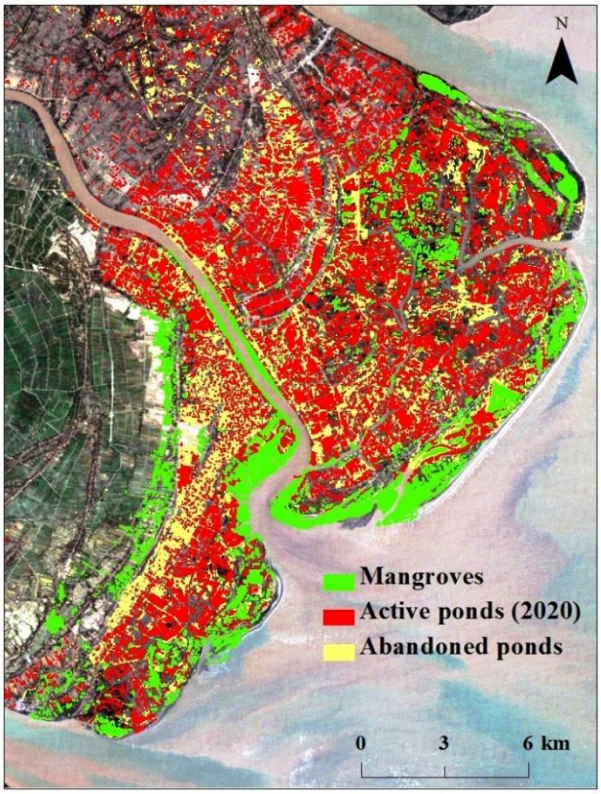

Fig. 4. *Active and abandoned aquaculture ponds and latest mangrove areas (2020).*

Vegetation bioshields are of worldwide usage for long-term coastal protection [13]. In Vietnam also, ecosystem-based coastal protection methods have been a subject of research by various planning agencies and scientists [14]. Compared to the installation hard structures (e.g. seawalls), vegetation bioshields such as mangrove forests, are cost-effective as well as provide several ecosystem services, in addition to the mitigation of coastal hazards. Many ecological benefits are provided by coastal mangrove vegetation, including, but not limited to, shoreline protection, sediment trapping, protection from flash floods, tsunamis and typhoons, post-tsunami regeneration of the coastal environment, and trapping floating debris (e.g. plastic debris). A number of non-mangrove plant species can also be used as a coastal bioshield in Mekong Delta in general and Ben Tre in particular. For example, Casuarina trees have been widely used in Vietnam, including Ben Tre, as a planted vegetation in the coastal areas. Additional benefit from Casuarina trees is dune stabilization, which in turn can be useful in protecting the coasts from erosion and floods. However, it has to be noted that the introduction of non-native species may cause alien plant invasion into the natural ecosystem [15] of the region and detailed studies are needed to avoid such ecological problems in the future.

 ISBN:

Even though abandoned and inactivated aquaculture areas can provide suitable sites for mangrove reforestation, which can be used as a coastal bioshield, it is not an easier task as it seems to be. Firstly, a vast majority of these abandoned aquaculture ponds are located in private properties and acquisition of such areas for mangrove reforestation without proper compensation cannot be not straight forward. Secondly, it is important to restore the natural hydrology of the abandoned shrimp pond areas before planting mangroves, which can be more time consuming and not very cost-effective compared to some hard structures. Thirdly, the success of mangrove reforestation depends on a number of environmental, physical and geomorphological factors [15] and these factors may vary from sites to sites.

IV. CONCLUSION

Despite a number of mangrove plantation projects has been implemented in selected areas, Ben Tre province in the Mekong Delta witnessed a rapid deterioration in coastal vegetation coverage in recent years. However, in some areas, such as the Ba Lai River mouth, planted with mangroves have shown some positive feedback in the environment, including an overall increase in accretion compared to previous decades. However, the reasons behind this increased accretion need to be verified. It is seen that the area covered by shrimp/fish ponds in Ben Tre has been doubled during the 1998-2015 period and a slight decline in the overall area occurred since then. A large area of mangrove vegetation wase cleared for this purpose in the coastal districts of Ben Tre. It is worth noting that the negative environmental issues raised by the rapid expansion of brackish aquaculture can be serious compared to the economic benefits from such activities.

There appeared a large area of abandoned aquaculture ponds in recent years, even though new aquaculture ponds have been created, particularly between 2015 and 2020. Abandoned shrimp ponds, if not used for other economic purposes, are often considered as suitable sites for mangrove reforestation, which can be useful as coastal bioshields. In addition to mangroves, plants such as casuarinas and marsh plants can also be used as coastal bioshields in such areas. It has to be noted that the aquaculture areas are, mostly, private properties and proper compensation needs to be provided when apply mangrove reforestation practices in such areas. In addition, the success of mangrove reforestation depends on a number of environmental and climatic factors as well.

ACKNOWLEDGMENTS. This research is funded by Vietnam National Foundation for Science and Technology Development (NAFOSTED) under grant number 105.99-2019.339.

REFERENCES

[1] A. Smajgl, T. Q. Toan, D. K. Nhan, J. Ward, N. H. Trung, L. Q. Tri, V. P. D. Tri, and P. T. Vu, Responding to rising sea levels in the Mekong Delta, *Nat. Clim. Change*, 2015, **5**, 167-174.

[2] M. W. Strassburg, B. D. Hamlington, R. R. Leben, P. Manurung, J. L. Gaol, B. Nababan, S. Vignudelli, and K. Y. Kim, Sea level trends in Southeast Asian seas, *Clim. Past*, 2015, **11**, 743-750.

[3] D. A. Friess, B. S. Thompson, B. Brown, A. A. Amir, C. Cameron, H. J. Koldewey, S. D. Sasnito, and F. Sidik, Policy challenges and approaches for the conservation of mangrove forests in Southeast Asia, *Conserv. Biol.*, 2016, **30**, pp. 933-949.

[4] N. Q. Cuong, and N. V. Cu, Integrated coastal management in Vietnam: current situation and orientation, *J. Mar. Sci. Technol.*, 2014, **14**, 2014, 89-96.

[5] C. Kuenzer, and F. G. Renaud, Climate and environmental change in river deltas globally: expected impacts, resilience, and adaptation, In: Renaud, F., Kuenzer, C. (Eds.), The Mekong, 2012.

[6] B. K. Veettil, R. D. Ward, N. X. Quang, and N. T. T. Trang, Mangroves of Vietnam: historical development, current state of research and future threats, *Estuarine. Coastal and Shelf Science* 2019, **218**, 212-236.

[7] N. T. Phong, Towards Sustainable Coastal Management and Development in Three Coastal Districts of Ben Tre Province (Binh Dai, Ba Tri and Thanh Phu), IUCN, Gland, Switzerland, 2015, pp. 52.

[8] D. T. T. Vinh, Aquaculture in Vietnam: development perspectives, *Dev. Pract.*, 2016, **16**, 498-503.

[9] N. D. Can, Adaptation to salinity intrusion: an economic assessment of diversified farming systems in saline affected area of coastal Ben Tre province of the Mekong delta, In: Vietnam. International Symposium on Current Agricultural Environmental Issues in Pacific Rim Nations and their Countermeasures - II, March 16 - 18, 2015. Saga University, Saga, Japan, pp. 12.

[10] K. Karila, O. Nevalainen, A. Krooks, M. Karjalainen, S. Kaadalainen, "Monitoring changes in rice cultivated area from SAR and optical satellite images in Ben Tre and Tra Vinh provinces in Mekong delta, Vietnam, *Rem. Sens.*, 2014, **6**, 4090-4108.

[11] B. K. Veettil, N. X. Quang, and N. T. T. Trang, Changes in mangrove vegetation, aquaculture and paddy cultivation in the Mekong Delta: A study from Ben Tre Province, southern Vietnam, *Estuarine. Coastal and Shelf Science*, 2019, **226**, 106273.

[12] B. K. Veettil, J. Costi, W. C. Marques, X. L. Tran, N. X. Quang, D. D. Van, and P. N. Hoai, Coastal environmental changes in Southeast Asia: A study from Quang Nam Province, Central Vietnam, *Regional Studies in Marine Science*, 2020, **39**, 101420.

[13] R. A. Feagin, J. Figlus, J. C. Zinnert, J. Sigren, M. L. Martinez, R. Silva, W. K. Smith, D. Cox, D. R. Young, G. Carter, Going with the flow or against the grain? The promise of vegetation for protecting beaches, dunes, and barrier islands from erosion, *Front. Ecol. Environ.*, 2015, **13**, 203-210.

[14] U. Nehren, H. H. Dac Thai, M. A. Marfai, C. Raedig, S. Alfonso, J. Sartohadi, C. Castro, Ecosystem services of coastal dune systems for hazard mitigation: Case studies from Vietnam, Indonesia, and Chile, In: F. Renaud, K. Sudmeier-Rieux, M. Estrella, U. Nehren (Eds.), *Advances in Natural and Technological Hazards Research*, 2016, 401-433.

[15] B. K. Veettil, R. D. Ward, N. T. K. Dung, D. D. Van, N. X. Quang, P. N. Hoai, N. D. Hoang, The use of bioshields for coastal protection in Vietnam: Current status and potential, *Regional Studies in Marine Science*, 2021, **47**, 101945.

 ISBN:

Bacillus licheniformis MPC4 - A NOVEL BACTERIAL STRAIN FOR DEGRADATION OF ORGANOPHOSPHORUS PESTICIDES IN TROPICAL SOIL

Chi K. Hoang[1], Quang H. Tran[2], Cuong H. Le[1], Ha T. H. Tran[1], Huong M. Le[1] and Hang T. N. Tran[1*]

[1]*Institute of Natural Products Chemistry - Vietnam Academy of Science and Technology, 1H building, 18 Hoang Quoc Viet, Cau Giay, Hanoi, Vietnam*

[2]*Institute of Biotechnology - Vietnam Academy of Science and Technology, A10 block, 18 Hoang Quoc Viet, Cau Giay, Hanoi, Vietnam.*

*E-mail: *hangmy97@yahoo.com*

Abstract. Organophosphates (OPs) represent the most popular chemical compounds used in controlling pests for protection of agricultural crops over the last few decades, yet have been proven to cause serious health and environmental problems concerning their neurotoxicity and genotoxicity characteristics. Since microbial degradation has been considered the most sustainable remediation of OPs, the screening for effective OP degraders is a priority. A bacterial isolate derived from organophosphorus contaminated soil in Northeast region of Vietnam was identified as *Bacillus licheniformis* strain MPC4. The hydrolysis of organophosphorus substrate methyl parathion (MP) by strain MCP4 in terms of colorimetric test was determined. Further investigation uncovered MCP4's ability of utilizing a wide range of organophosphorus substrates including malathion and chlorpyrifos as the sole carbon sources. The bacterial strain was evaluated *in vitro* to be non-toxic to tested cells and animals. Obtained results highlighted application aspect of the bacterium in bioremediation of contaminated areas, particularly in indigenous tropical soils.

Keywords: *Organophosphate, Bioremediation, Biodegradation, Bacillus licheniformis.*

I. INTRODUCTION

Organophosphates (OPs) represent the most intensively used chemical components in controlling pests for protection of agricultural crops in recent decade [1]. The pesticides were assumed to be effective and safer than previously widely used organochlorine counterparts due to higher degradability under natural conditions [2], have albeit been proven to cause serious health and environmental problems concerning their neurotoxicity and genotoxicity characteristics. In general, exposure to OP pesticides and bioaccumulation could generate negative alteration in the nervous system of animals, including human, by inhibiting acetylcholinesterase, an enzyme involved in the metabolism of important neurotransmitter acetylcholine [3]. On the other hand, they cause modification in the genetic properties of exposed flora and fauna, raising severe ecological and environmental impacts [4].

Until 2020, several OP pesticides, including methyl parathion (MP), malathion (MT), fenitrothion, profenofos and chlorpyrifos (CP), were still permitted for agricultural application in many countries [5], leading to the need of effectively removing them from

cropping systems in response to agriculture practices to prevent bioaccumulation and environmental contamination.

The degradation of OPs by microorganisms has been proven to be the most principal factor contributing to the detoxification of such compounds in the environment [6]. Sethunathan and Yoshida (1973) were among the first to describe a bacterial isolate *Flavobacterium* sp. ATCC 27551 capable of utilizing OP substrates parathion and diazinon as the sole carbon source [7]. Bacterial strains belonging to genera *Pseudomonas*, *Acinetobacter*, *Arthrobacter*, *Burkholderia*, *Serratia*, *Sphingobium*, *Bacillus*, *Brevibacterium*, *Ochrobactrum*, *Aspergillus* and *Streptomyce*s have been thereto reported as effective degraders of several OP pesticides [8]. Since application of such bacterial degraders for decontaminating OP residues in soil is considered the most practical strategy, the quest of microbial candidates for efficient bioremediation in particular climate and geographic areas has thus become a study interest.

In our research, OP degrading bacteria were isolated from soil, identified and examined for application prospects. Our work was expected to bring out novel microbial candidate for efficient bioremediation in contaminated agriculture soil in temperate areas.

II. EXPERIMENTS

Isolation of MP-degrading bacteria

Soil samples for bacterial isolation were collected from vegetable cultivating areas in Que Vo, Bac Ninh province (N 21°5’55’’ to N21^{o}5’17’’, E 106°7’18’’ to E 106°8’25’’) with longterm usage of OP pesticides, prevalently CP substrates. The CP amount in soil samples at the time of collection (June 2018) determined by gas chromatography method (US EPA Method 8270D) ranged from 0.018 to 0.032 mg/kg soil. The fate of MP was also detected in slight amounts of 0.005 to 0.008 mg/kg soil in the investigation.

Enriched cultures were prepared as the inoculum of 10 g soil samples in 50 mL sterile minimal salt medium (MSM, composition in g/L: Na_2SO_4 2, $(NH_4)_2SO_4$ 2.7, NH_4Cl 0.5, $KHPO_4$ 14.0, $NaH_2PO_4.H_2O$ 3.6, $(NH_4)_2$-citrate 1.0, pH=7.0±0.2), supplemented with MP as the sole carbon source at gradually increasing concentrations of 50 to 200 ppm for four successive culturing generations (30 °C with agitation (200 rpm). The enriched cultures were then serial diluted in MSM and subcultured on MSM agar plates containing 300 ppm MP. Pure bacterial isolates were obtained after picking colonies and re-streaking.

MP biodegradation studies

Bacterial isolates were selected for further investigation of MP hydrolysis basing on indicative yellow colored product *p*-nitrophenol (PNP) as the method described by Kwak et al. (2013) [9] with modifications. In brief, bacterial isolates were activated in LB broth (16 h, 30 ^{o}C) and transferred to MSM cultures containing 200 ppm MP (150 rpm, 48 h, 30 ^{o}C). Bacterial cells were separated from culture broth by centrifugation (7000 rpm, 15 min) and incubated in Tris-HCl (pH 7.5) containing lysozyme (37 ^{o}C, 30 min) to obtain cell suspension for enzyme assay. The enzyme assay mixture was prepared with 100 µl cell suspension and 100 µl substrate solution (3% methanol) in Tris-HCl buffer (50 mM,

 ISBN:

pH 7.2) and incubated at 30°C for monitoring of 405 nm absorbance increase during 15 minutes by microplate spectrophotometer (Tecan F150, Austria).

Determination of bacterial growth kinetics

Bacteria exhibiting ability to grow in the presence of pesticide substrate MP were inoculated into 100 ml flasks containing 300 ppm of MT or CP in MSM broth. The culture was orbitally shaken at 220 rpm (30 °C) and sampled every 24 hours during the incubation period. The bacterial densities in culture broths were measured at 620 nm using Tecan's infinite spectrophotometer (TECAN, Switzerland).

Identification of microorganism

The 16S rRNA gene of bacteria isolate MPC4 was amplified by PCR with specific primer pair 27F (5′-AGA GTT TGA TCC TGG CTC AG-3′) and 1492R (5′-TAC GGT TAC CTT GTT ACG ACT T-3′) and sequenced on ABI PRISM® 3100 Avant Genetic Analyzer (Applied Biosystems). Using BlastN tool, the obtained 16S rRNA gene sequence was compared with available data at GenBank (*https://blast.ncbi.nlm.nih.gov*). Physiological characteristics of bacterial isolate was determined by API kits 50CH and API20E (bioMerieux, France) following manufacturer's instructions.

Toxic test

Cytotoxicity. Portions of bacterial culture was extracted twice with equal volumes of ethyl acetate, and concentrated microbial crude extract was obtained by vacuum evaporation (EYELA, Japan) with 40 rpm at 40 °C. The extract was subsequently dissolved in dimethyl sulphoxide (DMSO) (Sigma Aldrich, Germany) for assessment of cytotoxicity on Vero cells (*Cercopithecus aethiops* kidney cells, ATCC CCL-81.4) by Sulforhodamine B (SRB) method as described by Likhiwitayawuid et al. [10].

Safety test in animals. Safety test of a bacterium in BALB/c mice was carried out as the procedure mentioned earlier by Carter [11]. Accordingly, BALB/c mice were given either a 0.5 ml intraperitoneal (IP) or 0.2 ml intravenous (IM) injection of brain heart infusion (BHI) broth (Merck, Germany) containing 10^7 CFU/ml of bacterial biomass. Animals were observed daily for health evaluation up to 15 days postinfection.

III. RESULTS AND DISCUSSION

Isolation of bacterial strain

By subculturing on MSM agar plates containing 300 ppm of MP as the sole carbon source, pure bacterial isolates, namely MPC4, MPC7 and MPC9 were obtained. The morphological characteristics of these bacteria on agar plates are demonstrated in Fig. 1.

As shown in Fig. 1, the colonies of three bacterial isolates appeared diversely in size, shape and color, suggesting diverse biological activities, especially in biotransformation of organophosphorus pesticides.

MP degradation

The degradation of MP involves the cleavage of phosphodiester linkage to form DMPA (Dimethylthiophosphoric acid) and yellow colored p-nitrophenol. The higher the

intensity of yellow color, the more effective the MP hydrolysis by bacterium. By monitoring of absorbance increase during incubation time, the MP degrading characteristics of three bacterial isolates were interpolated [9]. Figure 2 and Table 1 present the degradation of MP by these bacteria by enzyme assay.

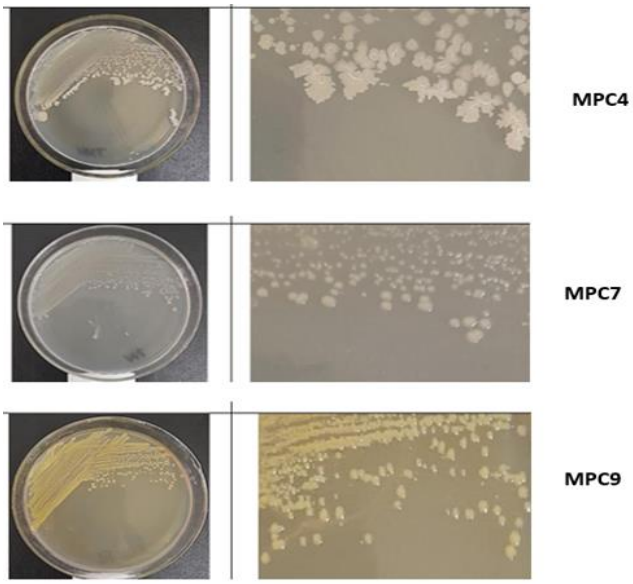

Fig. 1. *Colony morphology of three bacterial isolates MPC4, MPC7 and MPC9 on MSM agar plates (30°C, 3 days).*

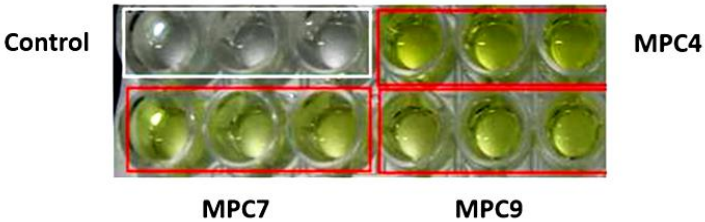

Fig. 2. *The degradation of MP substrate by bacterial isolates MPC4, MPC7 and MPC9 in microplates after 15 minutes of incubation.*

Table 1. *Absorbance of bacterial cell suspensions in MP hydrolase enzyme assay.*

Bacterial cell suspension	**Absorbance at 504 nm** Incubation time (minutes)	
	0	15
MPC4	0.142±0.021	0.575±0.01
MPC7	0.085±0.017	0.227±0.036
MPC9	0.137±0.008	0.451±0.025

The results implied that isolated bacteria MPC4, MPC7 and MPC9 were capable of producing MP-degrading enzyme at different levels. Further investigations were undertaken to characterize biological properties of these bacterial isolates.

Substrate ranges

In general, MP is degraded by enzymatic reaction catalyzed by parathion hydrolase, a broad substrate range enzyme with ability to hydrolyze a number of organophosphorus

 ISBN:

compounds (Brown 1980). For fully understanding the substrate ranges of isolated bacteria, we assessed the ability of three bacterial isolates MPC4, MPC7 and MPC9 to assimilate other OPP substrates, including CP and MT. For the purpose, three isolates were cultured on MSM broth supplemented with CP and MT as the sole carbon sources at increased concentrations of 100 to 500 ppm. The optical density at 620 nm (OD620) of culture reached 0.95. After being incubated on MSM agar plates supplemented with 200 ppm of chlorpyrifos for 48 h, bacterial colonies were observed. The growth of bacterial isolates in terms of cell density in liquid MSM medium in are presented in Fig. 2.

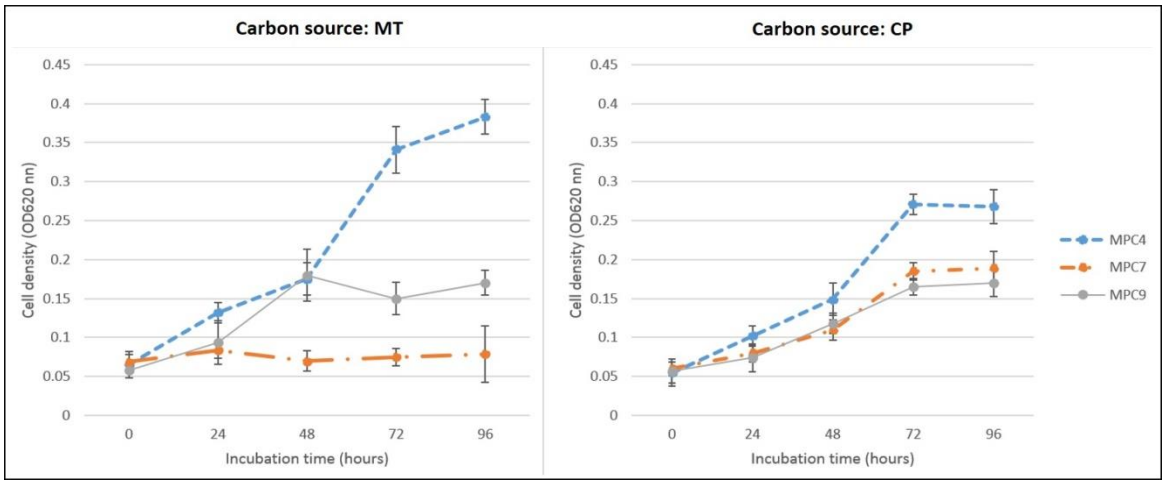

Fig. 3. *Growth kinetics of bacterial isolates in 96 hours of incubation with MT and CP in liquid cultures.*

As indicated in Fig. 2, significant differences in growth kinetics of isolates MPC4, MPC7 and MPC9 in MSM liquid culture supplemented with MT and CP in dependence to incubation time were observed. Within 96 hours, the difference among three bacterial cultures when incubating with MT tended to be more obvious than with CP. While roughly similar growth curves were observed in cultures with substrate CP, an explicit higher growth rate of MPC4 was recorded in cultures with MT. In both substrate conditions, the biomass of MPC4 increased during incubation time and tend to rise continuously.

Among three bacterial isolates obtained from enriched OPP-contaminated soils, isolate MPC4 showed high activity of MP hydrolysis and wide substrate range, thus was chosen for further studies of characterization and toxicity determination.

Characterization of isolate MPC4

Isolate MPC4 was taxonomically determined by analysis of 16S rRNA gene in combination with physiological characterization. The 16S rRNA gene of isolate MPC4 was found similar in sequence with high identity percentage of 97.49% to *Bacillus* sp. strain C72 (Accession: MF184039.1), *B. licheniformis* strain KMDH8 (Accession: KU844050.1) and *B. aerius* strain DX-14 (Accession: KX470406.1). The result suggested that strain MPC4 belonged to bacterial genus *Bacillus*, therefore determination of biochemical and physiological characteristics was required for further identification. API 50CH kit revealed the ability of MCP4 in utilizing wide ranges of carbon sources, including Erythritol, D-ribose, D-xylose, L-xylose, D-glucose, D-fructose, D-mannose, L-sorbose, Dulcitol,

D-mannitol, D-sorbitol, Methyl-α-D-mannopyranoside, N-acetylglucosamine, Amygdalin, Arbutin, Esculin ferric citrate, Salicin, D-cellobiose, D-maltose, D-lactose (bovine origin), D-melibiose, D-saccharose (sucrose), D-trehalose, Inulin, D-melezitose, Amidon (starch), Glycogen and Xylitol. The optimal growth conditions for isolate MCP4 were pH 7-8 at 37 °C (data not shown). Under microscope (magnification x40), MCP4 appeared to be a rod-shaped, Gram-positive, and spore-forming bacterium (Fig. 4). In terms of physiological characteristics determined by tests of API20E kit (Full details are given in Table 2) and interpretation by APIWEB™ databases, MPC4 was identified as a bacterial strain of *B. licheniformis*. The partial 16S rRNA of *B. licheniformis* strain MPC4 was submitted and deposited at GenBank under accession number MW64483.1.

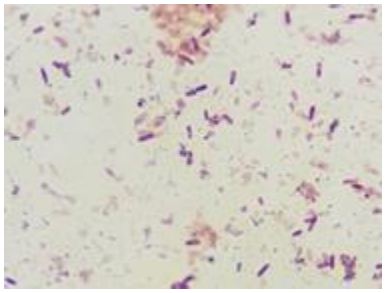

Fig. 4. *Microscopic morphology of bacterial isolate MPC4 (X40 magnification).*

Table 2. *Physiological profiles of isolate MPC4 evaluated by API20E kit.*

No.	Symbol	Substrate	Enzyme/reaction	Result
1	ONPG	2-nitrophenyl-β-D-galactose	β-D-galactosidase	+
2	ADH	L-arginin	Argninine dihydrolase	+
3	LDC	L-lysine	Lysine decarboxylase	-
4	ODC	L-Omithine	Omithine decarboxylase	-
5	CIT	Trisodium citrate	Citrate utilization	+
6	H_2S	Sodium thiosulfate	H_2S production	-
7	URE	Urea	Urease	-
8	TDA	L-trytophane	Tryptophane deaminase	-
9	IND	L-tryptophane	Indole production	-
10	VP	Sodium pyruvate	Acetoin production Voges Proskauer	-
11	GEL	Gelatin	Gelatinase	-
12	GLU	D-glucose	Fermentation	+
13	NIT	potasium nitrate	Nitrate reduction, NO_2 production	±

**Symbols + and – indicate positive and negative for a characteristic, respectively*.

The ability of *B. licheniformis* to degrade OPP residues in soils were reported in several publications, however none of these mentioned the wide spectrum of substrates as revealed in the present study. In 2010, the isolation and application of a CP-degrading *B. licheniformis* strain in China were reported [13]. More recently, a *B. licheniformis* bacterial strain was claimed to be able in degradation of MT via malathion carboxylesterase [14]. To our knowledge, the ability of a *B. licheniformis* in degradation of multi-OPP substrates, i.e. MP, MT and CP, has not been referenced earlier.

 ISBN:

Toxic test

Previous consideration to the database of safety-assessed microorganisms by the German central comittee on biological safety *(https://zag.bvl.bund.de/*, last accessed on 1st Oct. 2021) revealed *B. licheniformis* a non-pathogenesis species, thus in next steps we checked for possibility of toxin production by the bacterial strain belonging to the well known species. At concentration of 100 µg.ml^{-1}, the crude extract of *B. licheniformis* MPC4 exhibited non-cytotoxicity to Vero cells with 98.79±1.32% of cell survival percentage.

In BALB/c mices, no fatal case was recorded when injected with aliquots containing *B. licheniformis* MPC4 cells both intraperitoneally and intravenously. The mortality rates as well as animal's conditions after 15 days of injection were determined presented in Table 3.

Table 3. *Presentations associated with bacterial biomass in BALB/c mice*.

Sample	Number of test animals	Injection route	Mortality rate (%)	Animal's condition	Test result
Control (BHI broth)	6	IM	0	Healthy	Safe
	6	IP	0	Healthy	Safe
BHI broth containing MPC4 biomass	6	IM	0	Healthy	Safe
	6	IP	0	Healthy	Safe

For application in bioremediation, a bacterial inoculant must be safe to living organisms. The fact that *B. licheniformis* strain MPC4's *in vitro* hazard potential in cells and test animals has not been detected therefore could be considered an evidence for application of the bacterium in bioremediation of organophosphorus contaminated soil in field condition.

IV. CONCLUSION

In conclusion, three bacterial isolates with methyl parathion degrading ability were obtained from agricultural soils in Northern Vietnam. Among them, bacterial strain *B. licheniformis* MPC4 showed outstanding degradability, not only in methyl parathion substrate but also in other organophosphorus compounds including malathion and chlorpyrifos. The characteristics of strain MPC4 were investigated with a focus on the taxonomy and toxicity. The present study provides a valuable microbial strain with the potential application in bioremediation of pesticide contaminated soils for development of an environmentally friendly and sustainable agriculture.

ACKNOWLEDGMENTS. This work was funded by the Ministry of Science and Technology of Vietnam (grant NĐT.61.HU/19), and Institute of Natural Products Chemistry for projects of 2021 (project manager: Hoang Kim Chi).

REFERENCES

[1] R. Wang, J. Tang, Z. Xie, W. Mi, Y. Chen, H. Wolschke et al., *Environ. Pollut.*, 2015, **198**, 172-178.

[2] S. Dhas & M. Srivastava, *Asian J. Agric. Sci.*, 2010, **2**(1), 15-17.

[3] G. Muhammad, I. Rashid & S. Firyal, *Matrix Sci. Pharma*., 2017, **1**(1), 10-11.

[4] L. Sun, W. Xu, T. Peng, H. Chen, L. Ren, H. Tan et al., *Neurotoxicology and Teratology*, 2016, **55**, 16-22.

[5] W. Senbua, J. Mearnchu & J. Wichitwechkarn, *Biotechnol. Rep.*, 2020, **27**, e00495.

[6] J. Aislabie, G. Lloyd-Jones, *Soil Res.*, 1995, **33**(6), 925-942.

[7] N. Sethunathan, T. Yoshida, *Can. J. Microbiol.*, 1973, **19**(7), 873-875.

[8] G. K. Sidhu, S. Singh, V. Kumar, D. S. Dhanjal, S. Datta & J. Singh, *Crit. Rev. Environ. Sci. Technol*., 2019, **49**(13), 1135-1187.

[9] Y. Kwak, I. K. Rhee & J. H. Shin, *Appl. Microbiol. Biotechnol.*, 2013, **97**(18), 8097-8105.

[10] K. Likhitayawuid, C. K. Angerhofer, *J. Nat. Prod.*, 1993, **56**(1), 30-38.

[11] G. R. Carter, Diagnostic procedures in veterinary bacteriology and mycology, Academic Press, 1984, 205-209.

[12] K. A., Brown, *Soil Biol. Biochem*., 1980, **12**(2), 105-112.

[13] J. Zhu, Y. Zhao, J. Qiu, *Afr. J. Microbiol. Res.*, 2010, **4**(22), 2410-2413.

[14] S. Khan, H. Zaffar, U. Irshad, R. Ahmad, et al., *Arch. Biol. Sci.*, 2016, **68**(1), 51-59.

 ISBN:

SILVER MESO-PARTICLES APPLYING IN DETECTION MELAMINE BY SURFACE ENHANCED RAMAN SPECTROSCOPY

Nguyen Thi Hang Nga[1*], Nguyen Thi Bich Ngoc[2], Vu Duong[2]

[1]*Thuyloi University, 175 Tay Son, Dong Da, Hanoi, Vietnam*

[2]*Center of Quantum electronics, Institute of Physics, 18 Hoang Quoc Viet Street, Cau Giay, Hanoi, Vietnam*

*E-mail: *nthnga@tlu.edu.vn*

Abstract. Melamine is an organic chemical with high nitrogen concentration which is found in milk, chicken, beef,… and other foods. It is added to commercial products to pass the requirement of protein concentration but it induces kidney stone disease. It was forbidden in some countries for using melamine in foods while a critical standard, i.e. is 2.5 mg/kg in food and animal feeds, is worldwide applied on commercial products. The convenient analytical methods are liqude (or gas) chromatography and mass spectroscopy techniques. These techniques require complex sample pre-treatments. Recently, some methods have been developed for the more direct detection of melamine in products including instrumental analysis, immunoassays, spectroscopy analysis, chemometrics analysis, and Surface-enhanced Raman Scattering (SERS). Surface-enhanced Raman spectroscopy (SERS) is a powerful oscillatory spectroscopy technique that enables highly sensitive structural detection of low-concentration analytes through amplification of the generated electromagnetic fields by excitation of local surface plasmon. The sensitivity of SERS depends on the surface morphology of the metal structures on the SERS substrate, such as nanostructured gold, silver, quantum dots, carbon dots. In this paper, we present the research results on a low concentration of melamine detection using SERS with the silver meso-particles (AgMPs).

Keywords: *Melamine, SERS, Silver meso-particles.*

I. INTRODUCTION

Melamine (1,3,5-triazine-2,4,6-triamine - $C_3H_6N_6$) is nitrogen-rich with 67% content in mass commonly used to produce industrial heat-tolerant polymers, coatings, glues, adhesives, laminates, cleaners, and molding compounds, etc [1-3]. Melamine is illegally added into milk, food, pet food, and animal feeds [3,4] with the amounts exceeding the allowable limit to 0.2 mg/kg body weight per day, 1 mg/kg in infant formula and 2.5 mg/kg for other dairy products [3-5] which is very harmful to our kidneys and even fatal for babies.

Currently, several methods have been established for the detection of melamine in products including instrumental analysis: gas chromatography/mass spectrometry (GC/MS), liquid chromatography-tandem mass spectrometry LC-MS-MS, high-performance liquid chromatography (HPLC), capillary electrophoresis (CE); immunoassays as enzyme-linked immunosorbent assay (ELISA); chemosensors analysis as fluorescence chemosensors, colorimetric chemosensors, electroluminescence chemosensors; biosensor methods such as electrochemical biosensors, optical biosensor, molecularly imprinted polymer-based sensors (MIP) [6-10]. These analytical techniques

have offered good sensitivity in food quality monitoring, they suffer from several disadvantages and can yield reliable results, these analyses often require tedious sample preparation, extensive solvent consumption, complicated operation procedures, and long analysis time [11]. Compared to the aforementioned conventional analytical techniques, the surface enhanced Raman scattering (SERS) is an advanced technique that gives a comparable and reliable or even superior sensitivity, a simple sample preparation, and very short analysis time. Because of the low scattering cross-section, the limit of detection for Melamine is about 10^{-3} M which does not meet the allowance standard [3,11].

For instance, carbon and quantum dots, metal nanoclusters: BSA-stabilized gold nanoclusters (BSA-Au NCs), the tiopronin-stabilized gold nanoclusters (TPN-Au NCs), silver nanoclusters (Ag NCs); nanocomposites: silver nanoparticle-decorated silver/carbon nanospheres (Ag/C/AgNps), CdTe-doped silica nanoparticles (CdTe@SiO_2); nanoparticles: Ag NPs and Au NPs; nanorods and nanotubes [12] suspension-based SERS have been developed to detect melamine in food samples and other products.

The morphology of silver meso-particles (AgMPs) plays an important factor in SERS. Numerous studies have been reported in recent years. These results have developed the anisotropic structures with multi-branched growth with different structures, i.e. sharp spikes, flower-shaped,… by changing the experimental conditions, such as concentrations of chemicals, rotation rate, reaction times, and temperature reaction [13-16]. The branches or spikes in these structures greatly increase the electromagnetic field in the vicinity of the tips, and thus create many hot spots on the surface of the particles, leading to the (SERS) application [17,18]. In this study, we present the research results on the silver meso-particles meatball-like structure used in the detection of melamine with low concentration (10^{-4} to 10^{-8}) by SERS.

II. EXPERIMENTS

Materials

The chemicals used include: silver nitrate ($AgNO_3$, 99%, Sigma-Aldrich), L-Ascorbic acid (L-AA, 99%, China), alcohol (C_2H_5OH, Merk, 99%), chitosan, deionized water, and melamine ($C_3H_6N_6$, 99%, Sigma-Aldrich).

Sample preparation

The AgMPs were fabricated by the wet chemical method with $AgNO_3$ concentrations of 5 mM, L-AA concentration 20 mM, and deionized water. The mixture of the solutions was mixed and magnetically stirred with speed 300 rpm/min in 20 minutes at room temperature. After completed-reaction, the silver mesoparticles were washed in alcohol using a centrifuge to remove the residuals in the solution. The sample was stored in a refrigerator at 4 °C.

For the SERS measurements, we used the marker as the melamine mixed in water with different concentrations 10^{-4} to 10^{-8}. The stored AgMPs were soaked in melamine solution for 5 min. One drop of 3 µl of the mix solution was spread on a silicon plate. After being dried naturally, the sample was analyzed using micro Raman system.

 ISBN:

Characterization

The morphology of the sample was observed by Scanning electron microscopy (SEM). The optical properties were determined by the SHIMADZU-UV-2600 absorption spectrometer. The Raman spectra are obtained using a LabRAM HR Evolution (HORIBA Corp.) spectrometer exciting by 3 mW @ 785 nm diode lasers.

III. RESULTS AND DISCUSSION

Fabrication of AgMPs

The solution synthesis system contains two reagents: $AgNO_3$ with high concentration 5 mM and L-20 mM L-AA, the hierarchical Ag meso-particles were obtained as meatball structures with 700-750 nm in diameter (Fig. 1). The process of forming silver meso-particles occurs according to the reaction equation:

$$C_6H_8O_6 + 2Ag^+ \rightarrow C_6H_6O_6 + 2Ag + 2H^+ \quad (1)$$

The process of formation and growth of meso nanoparticles initially Ag+ ions are reduced to silver atoms by L-AA according to reaction (1). The change in the concentration of the Ag atom is described using the LaMer curve [13]. The forming of AgMPs transfer through four steps:

In the first stage, the concentration of Ag atoms in the solution increases and exceeds the supersaturation point of nucleation, the atoms will clump together to form stable nuclei clusters. Therefore, a large number of Ag nanoparticles are formed in the solution.

In the second stage, when the Ag atom concentration falls below the supersaturation point of nucleation, the nanoparticles will stop being produced. In this process, L-AA not only acts as a reducing agent but also acts as an enveloping agent, adsorbing on the particle surface to stabilize the nanoparticles, L-AA molecules will promote Ag nanoparticles to agglomerate through their glue function.

In the third stage, Ag nanoparticles agglomerate to form spherical mesospheres through a novel and non-classical crystal growth termed seed-mediated growth. Through seed-mediated growth, a polycrystalline or meso-structure is formed depending on the growth conditions [13].

$$r = \frac{kT\rho^{2/3}}{3\pi\eta f_m} \quad (2)$$

where r is the radius of the meso-particle, k is the Boltzmann constant, ρ and f_m are the density and frequency of condensation of the nano-particles, and T and η are the temperature and viscosity of the solution.

In the fourth stage, the remaining Ag ions will be reduced and deposited on the meso particles causing overgrowth of the Ag meso particles. Similar to the dopa molecules, the L-AA molecules will also promote the tips of the silver mesoporous particles to overgrow, thus leading to a hierarchical morphology.

The morphology of the silver mesoporous is shown in Fig. 1. The left image is a standalone particle which has a meat-ball shape. The right image presents a groups of AgMPs which demonstrate a narrow size distribution.

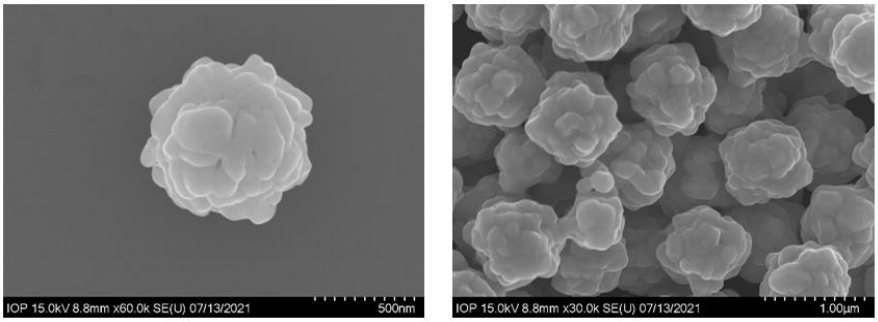

Fig. 5. *SEM imagie of AgMPs.*

The UV-Vis extinction spectrum of Ag meso-particles was measured in a range from 320 to 900 nm and is shown in Fig. 2. The monodispersity of the meso-particles allows the experimental observation of well-defined higher-order multipole plasmon modes in addition to the dipole resonance. The localized surface plasmon resonance (LSPR) was determined by particle size and morphology. With the protrusions on the meso-particle surface becoming longer and sharper, the UV-Vis spectra peaks corresponding to higher-ordered multipole plasmon resonance modes in addition to the dipole resonance [13]. For the meatball-like quadrupole, octa-poles and hexadecapole extinction peaks can be found.

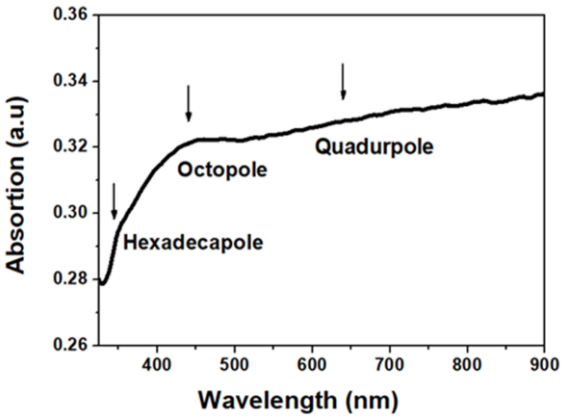

Fig. 6. *The UV-Vis spectra of AgMPs.*

SERS measurement

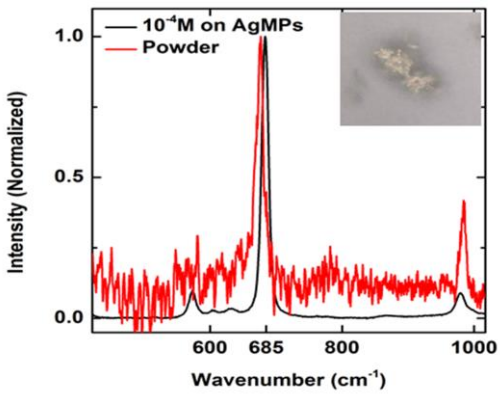

Fig. 7. *Raman spectrum of melamine.*

The Raman spectrum of melamine is shown in Fig. 3. The excitation power is 10 mW at 785 nm. The focus point is about 0.25 µm. At the same condition, the spectrum of melamine powder (red line) and 10^{-4} M solution (solided black line) present the same characteristic peaks at about 680 cm^{-1} and 980 cm^{-1}. The spectrum is normalized to the peak at about 680 cm^{-1} which corresponds for the ring breathing of the melamine molecules. Because of interaction with silver nano the spectrum of melamine molecules in SERS are slightly shifted. The lower energy vibration mode, i.e. 676 cm^{-1}, is shifted to 682 cm^{-1}. In the other way, the higher energy vibration mode at 984 cm^{-1} is reduced to lower energy at 980 cm^{-1}. This energy perturbation is well

 ISBN:

agreed by studies of the SERS effect on silver nanospheres, rods or roughness silver substrate [19]. For the discussion, we consider the characteristic peak of melamine molecules at 682 cm^{-1}. The SERS signals are collected from a silver island shown in the Fig. 3 inset.

The Raman spectra of Melamine solution at different concentrations are shown in Fig. 4. The limit of detection (LOD) is about 10^{-7} *M*, 0.0126 mg/kg, which is about 2 orders of magnitude lower than the allowance of melamine in food, i.e. 2 mg/kg. The LOD for melamine is well known that it is increased under SERS investigation. Advanced techniques have been developed to meet the critical detection level, 10^{-5} M to 10^{-7} M, of melamine using one step sample treatment [20].

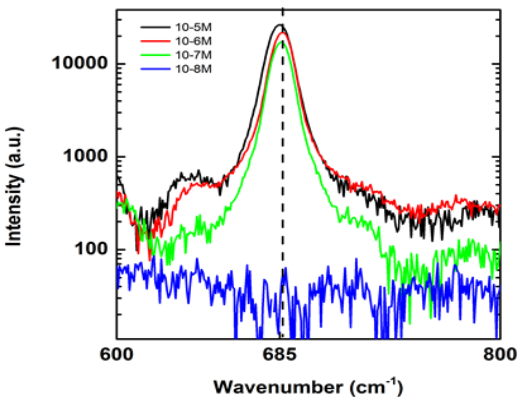

Fig. 8. *The Raman spectra of Melamine solution at different concentration.*

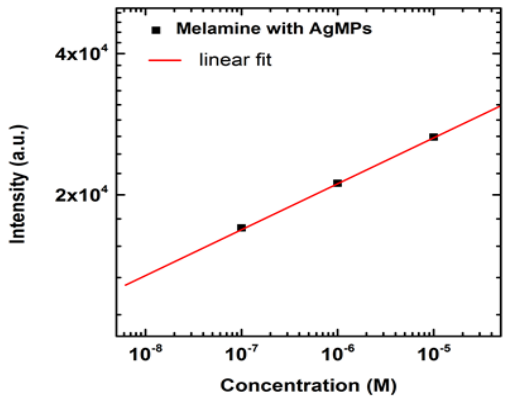

Fig. 9. *The linear fit of different Melamine concentration.*

In our study, not only the sample treatment is simple but also there is no need of preparing a substrate which strongly depends on the quality of the substrate preparation. Since the absorption of the interested molecules on to the AgMPs is proportional to the concentration of the solution. The Raman signal obtained by the microRaman system is expected to present a linear dependence versus the sample concentrations. This prediction is well presented in Fig. 5. Interestingly, within the interested region for applications in food control, the dependence follows a linear function. More data are required to realize the potential of application of qualitatively detection of melamine in food and animal feed.

IV. CONCLUSION

The fabricated silver meso particles with uniform size and good dispersion, which is a suitable object for a simple technique of melamine detection has been realized in this study. Single step, 5 minutes, preparation procedure is required for micro Raman investigation. Because of the enhancement via SERS effect, the LOD approximates to 10^{-7} M which is two orders of magnitude lower than the safety regulation (7 µM, 2 g/kg). The overall signal between 10^{-5} M and 10^{-7} M presents a good linear dependence. These results promote a high application potential on food quality control. A fast and simple sample preparation is the most important for developing handheld or mobile devices.

REFERENCES

[1] J. Cheng, X. O. Su, Y. Yao, C. Han, S. Wang, Y. Zhao, *PLoS One*, 2016, **11**(4), e0154402.

[2] V. Sharma, N. N. Som, S. B. Pillai, P. K. Jha, *Spectrochimica Acta Part A: Molecular and Biomolecular Spectroscopy*, 2020, **224**, 117352.

[3] L. Li, W. S. Chin, *Food Chemistry*, 2021, **357**, 129717.

[4] M. Shellaiah and K. W. Sun, *Chemosensors*, 2019, **7**, 9.

[5] Bates, F.; Busato, M.; Piletska, E.; Whitcombe, M. J.; Karim, K.; Guerreiro, A.; del Valle, M.; Giorgetti, A.; Piletsky, *Separ. Sci. Technol*., 2017, **52**, 1441-1453.

[6] Yang Lu, Yinqiang Xia, Guozhen Liu, Mingfei Pan, Mengjuan Li, Nanju Alice Lee & Shuo Wang, *Critical Reviews in Analytical Chemistry*, 2017, **47**(1), 51-66.

[7] K. Rovina, S. Siddiquee, *Journal of Food Composition and Analysis*, 2015, **43** 25-38.

[8] B. Sharma, R. R. Frontiera, A. I. Henry, E. Ringe, and R. P. V. Duyne, *Material Today*, 2012, **15**(1), 216.

[9] H. Dies, M. Siampani, C. Escobedo and A. Docoslis, *Sensors*, 2018, **18**, 2726.

[10] Y. Liu, E. E. D. Todd, Q. Zhang, J R. Shi, X. J. Liu, *Journal of Zhejiang University Science B*, 2012, **13**(7), 25-32.

[11] L. Jiang, M. M. Hassan, S. Ali, H. Li, R. Sheng, Q. Chen, *Trends in Food Science & Technology*, 2021, **112**, 225-240.

[12] M. Shellaiah and K. W. Sun, *Chemosensors*, 2019, **7**, 9.

[13] H. Wang, N. J. Halas, *Adv. Mater*, 2008, **20**, 820.

[14] T. T. Nhung, S. W. Lee, *ACS Appl. Mater. Interfaces*, 2014, **6**, 21335-21345.

[15] Z. Liu, F. Zhang, Z. Yang, H. You, C. Tian, Z. Li, J. Fang, *J. Mater. Chem. C*, 2013, **1**, 5567.

[16] J. Xiao, L. Qi, *Nanoscale*, 2011, **3**, 1383.

[17] L. Cheng, C.g Ma, G. Yang, H. You and J. Fang, *Journal of Materials Chemistry A*, 2013, **00**, 1-3.

[18] Q. Chang, X. Shi, X. Liu, J. Tong, D.e Liu, Z. Wang, *Nanophotonics*, 2017, **6**(5), 1-10.

[19] An N. T. T., Dao D, Q., Nam P. C., Huy B. T., Nhung Tran H., *Spectrochim Acta Part A Mol Biomol Spectrosc.*, 2016, **169**,230-237.

[20] Cheng J., Su X. O., Yao Y., Han C., Wang S., Zhao Y.,. *PLoS One*, 2016, **11**(4), e0154402.

 ISBN:

GENERATION OF ENTANGLED STATES IN THREE MODE NONLINEAR KERR-LIKE OSCILLATORS SYSTEM

Thi Dung Nguyen*, Thi Thao Nguyen

Hong Duc University, 565 Quang Trung Street, Dong Ve Ward, Thanh Hoa City, Vietnam

*E-mail: *nguyenthidungvatly@hdu.edu.vn*

Abstract. In this paper, we present the techniques of simulation modeling for quantum dynamics of Kerr nonlinear coupler system which consist of three nonlinear Kerr-like oscillators, mutually coupled by continuous linear interaction and excited by the external pulses. We show that by using evolution operator formalism we can model the quantum system, it can behave as a nonlinear quantum scissors and its "truncation" Hilbert space more efficiently. We propose that our model can behave as a 3-qutrit system, and can be dealt with as a source of entangled states.

Keywords: *Entanglement, Qubit, Qutrit, Concurrence, Quantum scissors.*

I. INTRODUCTION

The voyage of Quantum Mechanics began with Planck's idea of energy quantization and the law of radiation to explain the so-called "ultraviolet catastrophe" in the spectrum of matter. Later this idea was extended one step by Einstein when studying the explanation of the photoelectric effect. By the time, Quantum mechanics has been developed, helped us to understand the framework of physics and its principle, it has also become a basis for advancement of many new fields of physics such as quantum information, teleportation, computation and many other branches. The essential features for such advances are known as quantum correlations and can be firmness to transmit, preserve and manipulate information. These led to a considerable development of particular interest in research of quantum correlations in numerous types of quantum systems. The purpose of this paper is to investigate how it is possible to generate time evolution of quantum correlations in terms of the distinctive form - entanglement. Specifically, this system consists of three nonlinear Kerr-type oscillators, they are mutually coupled to each other by continuous linear interaction and excited by the external coherent fields. These oscillators can be expressed by effective Hamiltonians which are alike to those described optical Kerr systems. Quantum Kerr-type nonlinearity systems are commonly discussed in various physical applications. Such models can be put into practice in description of nanomechanical resonators and many optomechanical systems with Bose-Einstein condensate [1]. In addition, Kerr-type oscillatory models were the subject of a large number of papers related to the quantum chaos problems [2]. Thus, the modes of Kerr-type nonlinear couplers proved to be auspicious devices, simple treatment for finding numerical solutions and producing entangled states and hence its quantumness.

II. THE MODEL DESCRIPTION AND DISCUSSIONS

The considered system comprises three nonlinear Kerr-type oscillators, they are mutually coupled to each other by linear interaction and excited by external excitation fields in two boundaries, each oscillator corresponds to a single mode of the field labeled *a, b* and *c*. It is not only the self- coupling term that exists in this system, instead of the so-called cross-Kerr also coupling involves [4] which is different with many systems in previous literature. The Hamiltonian depicting the dynamics of our system can be expressed as (assuming h=1):

$$\hat{H} = \hat{H}_{nl} + \hat{H}_{\text{int}} + \hat{H}_{ext}, \tag{1}$$

where

$$\hat{H}_{nl} = \frac{\chi_a}{2}\hat{n}_a^2 + \frac{\chi_b}{2}\hat{n}_b^2 + \frac{\chi_c}{2}\hat{n}_c^2 + \chi_{ab}\hat{n}_a\hat{n}_b + \chi_{bc}\hat{n}_b\hat{n}_c, \tag{2}$$

describes Kerr-like media (involving cross-Kerr coupling), and:

$$\hat{H}_{\text{int}} = \left(\varepsilon\hat{a}^\dagger + \varepsilon\hat{c}^\dagger\right)\hat{b} + h.c., \tag{3}$$

corresponds to the nonlinear interaction between coupled modes *a-b* and *b-c*,

$$\hat{H}_{ext} = \alpha\hat{a}^\dagger + \gamma\hat{c}^\dagger + h.c, \tag{4}$$

refers to interaction with external fields.

The parameters χ_a, χ_b, χ_c are proportional to the third-order susceptibilities, χ_{ab}, χ_{bc} describes the cross - Kerr coupling processes between a - b, and b - c, whereas ε means the strength of the nonlinear interactions between modes a - b, and b - c. Since Hamiltonian of system is stated in term of bosonic creation and annihilation operators, we can present them as square matrices, in the Hilbert space $\mathcal{H} = \mathcal{H}_a$ Ä $\mathcal{H}_b$ Ä $\mathcal{H}_c$ as:

$$\breve{a} = \hat{a} \otimes \hat{I}_r \otimes \hat{I}_r \quad \text{and} \quad \breve{a}^\dagger = \hat{a}^\dagger \otimes \hat{I}_r \otimes \hat{I}_r \tag{5}$$

$$\breve{b} = \hat{I}_p \otimes \hat{b} \otimes \hat{I}_p \quad \text{and} \quad \breve{b}^\dagger = \hat{I}_p \otimes \hat{b}^\dagger \otimes \hat{I}_p \tag{6}$$

$$\breve{c} = \hat{I}_q \otimes \hat{I}_q \otimes \hat{c} \quad \text{and} \quad \breve{b}^\dagger = \hat{I}_q \otimes \hat{I}_q \otimes \hat{c}^\dagger \tag{7}$$

for the mode *a*, *b* and *c*, respectively. The operators $\hat{I}_{r,p,q}$ are in the form of an identity matrix with *r, p, q* dimensions.

We neglect here damping processes, time-evolution of the tripartite system can be expressed by wave-functions and written in term of the Fock basic as:

$$\left|\psi(t)\right\rangle = \sum_{r,p,q=0}^{\infty} c_{rpq}\left|r\right\rangle\left|p\right\rangle\left|q\right\rangle \tag{8}$$

where the complex probability amplitudes c_{rpq} corresponds to the *r*-, *p*- and *q*- photon Fock states in mode *a*, *b* and c respectively.

 ISBN:

The evolution of the system can be governed by a unitary operator defined from total Hamiltonian.

$$\hat{U} = \exp\left(-i\hat{H}t\right). \tag{9}$$

Assuming that all interactions considered here are weak compared to nonlinearity constants, we are able to interpret that the transition of the state can behave as a resonant case [6, 7]. Since the presence of the resonant coupling by zero-frequency component of external excitation between some eigenstates generated by the Hamiltonian $\hat{H}_{nl}$. The system's evolution is restricted to the limited resonant transition states corresponding to $p, q, r = \{0,1\}$, whereas the others can be neglected. Applying the operator $\hat{U}$ on the initial state, our generated wavefunction can be achieved as:

$$\left|\psi(t)\right\rangle = \sum_{r,p,q=0}^{\infty} c_{rpq} \left|r\right\rangle \left|p\right\rangle \left|q\right\rangle = \hat{U}\left|\psi(0)\right\rangle \tag{10}$$

For our purposes, we define the dimension of each subspace as equal to ten. In addition, we assume that $\chi_a = \chi_b = \chi_c = 1$ are proportional to the third-order susceptibilities, $\chi_{ab} = \chi_{bc} = \tilde{\chi} = 1$.

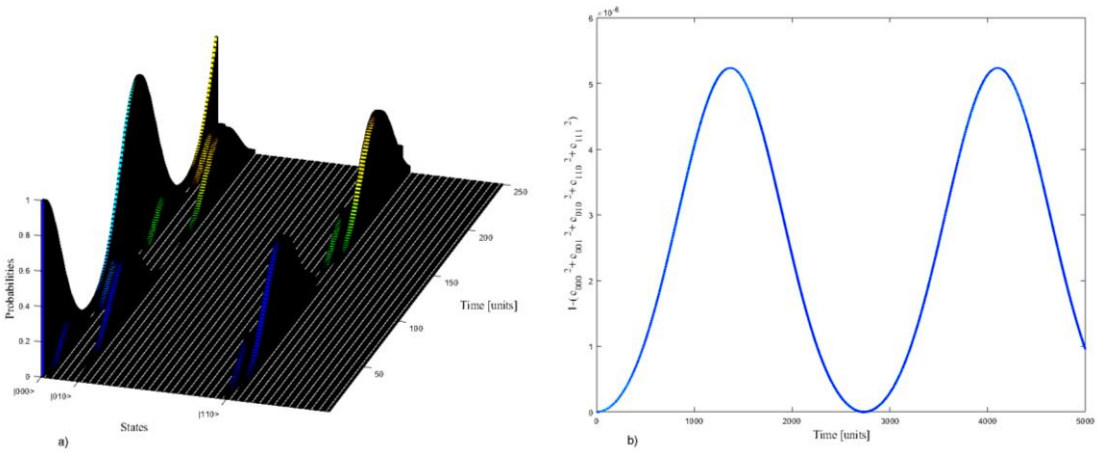

Fig. 1. *a) Time evolution of probabilities of the resonant states* $|0\rangle|0\rangle|0\rangle, |0\rangle|0\rangle|1\rangle$, $|0\rangle|1\rangle|0\rangle$, $|1\rangle|1\rangle|0\rangle$, *and* $|1\rangle|1\rangle|1\rangle$. *b) Deviation from the unity of the sum of probabilities. The parameters are* $\chi_a = \chi_b = \chi_c = 1, \chi_{ab} = \chi_{bc} = \tilde{\chi} = 1$, $\alpha = \gamma = 10^{-3}$, $\varepsilon = 0.8 \times 10^{-3}$.

Fig. 1a shows the time evolution of probabilities of resonant states, when cross-coupling is taken into account. From this, we can recognize that only five states are involved in the system. They are $|0\rangle|0\rangle|0\rangle, |0\rangle|0\rangle|1\rangle, |0\rangle|1\rangle|0\rangle, |1\rangle|1\rangle|0\rangle$, and $|1\rangle|1\rangle|1\rangle$. Fig. 1b shows the deviation of the sum of the probabilities, one can recognize that this maximum deviation is $\sim 10^{-6}$. Then, it is confirmed again that the evolution of wave function is closed within five states with a high precision. Therefore, it can be seen that when the coupling constants are sufficiently smaller than nonlinearity coefficients, this system can be referred to as nonlinear quantum scissors. From the standpoint of quantum information theory, one can say that the discussed system can be considered as a three-qubit one, due to

the fact that only two states (vacuum and one-photon state) for each of the modes are involved in the system's evolution.

Now, it is proposed that a three mode nonlinear coupler may create the bipartite and tripartite entangled state via optical state truncation. As measurement of bipartite entanglement, we apply the bipartite concurrence which was introduced by Wootters [5]. If ρ_{ij} is density matrix of 2-mode system, the concurrence can be obtained by the following:

$$C\left(\rho_{ij}\right) = \max\left\{0, 2\max_{l}\sqrt{\zeta_i} - \sum_{l=1}^{4}\sqrt{\zeta_l}\right\}, \tag{11}$$

here ζ_l (l=1:4) are eigenvalue of matrix R,

$$R = \rho_{ij}\tilde{\rho}_{ij} = \rho_{ij}\left(\sigma_y \otimes \sigma_y\right)\rho_{ij}^{*}\left(\sigma_y \otimes \sigma_y\right) \tag{12}$$

with matrix $\tilde{\rho}_{ij}$ is constructed from ρ_{ij} by applying the spin-flip operations to the density matrix ρ_{ij}:

$$\tilde{\rho}_{ij} = \left(\sigma_y \otimes \sigma_y\right)\rho_{ij}^{*}\left(\sigma_y \otimes \sigma_y\right) \tag{14}$$

ρ_{ij}^{*} is the complex conjugate of ρ_{ij}, whereas σ_y is 2×2 Pauli matrix.

$$\sigma_y = \begin{bmatrix} 0 & -i \\ i & 0 \end{bmatrix}. \tag{15}$$

In order to distinguish many types of tripartite entangled state which can be produced in our system, we use a Sabin's classification [9] to calculate concurrence [10]:

$$C_{\rho_{abc}} = \left(C_{a-bc}C_{b-ac}C_{c-ab}\right)^{1/3}, \tag{16}$$

where C_{i-jk} *(i, j, k=a, b, c)* are I-concurrence are defined as [10]:

$$C_{i-jk}\left(\rho\right) = \sqrt{2\left(1 - Tr\left[\rho_i^2\right]\right)}. \tag{17}$$

$C_{i\text{-}jk}$ are known as the bipartite concurrences for three mode matrix ρ_{abc} where the partial transpose is made for the sub-system i.

Table 1. *The classification of tripartite entanglement.*

Reduced entanglement	Type of tripartite entanglement	Tripartite entangled states
$C_{ij}=C_{jk}=C_{ik}=0$	*2- 0*	GHZ-type states
$C_{ij}\neq 0;\ C_{jk}=C_{ik}=0$	*2- 1*	
$C_{ij}\neq 0;\ C_{jk}\neq 0;\ C_{ik}=0$	*2- 2*	Star shaped-type state
$C_{ij}\neq 0;\ C_{jk}\neq 0;\ C_{ik}\neq 0$	*2- 3*	W -type class

To classify tripartite entanglement Sabin and Garcia [9] have proposed in his paper a classification for both mix and pure states in six entanglement subtypes from fully

 ISBN:

separable state to maximal one. Type 0-0 for fully separability, type 1-1 for biseparable states, and type 2 is for fully entanglement states. In our case we are concerning type 2 with 4 subtypes as follows.

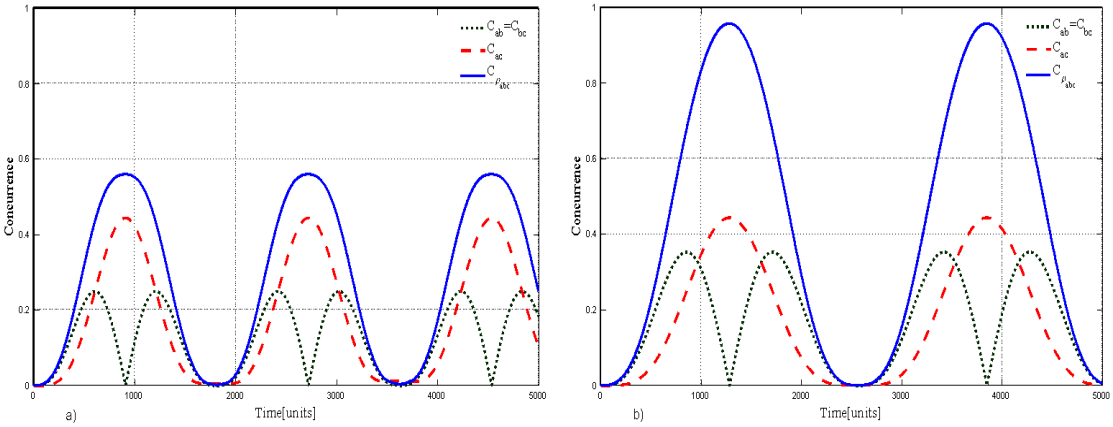

Fig. 2. *a) Time evolution of reduced and tripartite concurrences for a)* $\varepsilon=2.5\times10^{-3}$ *b)* $\varepsilon=0.8\times10^{-3}$ *and* $\chi_a=\chi_b=\chi_c=1,\ \chi_{ab}=\chi_{bc}=\tilde{\chi}=1,\ \alpha=\gamma=10^{-3}$.

Fig. 2a and 2b describe the concurrence of bipartite and tripartite systems with two different values of interaction strength. From these two figures, we can see that bipartite quantum entanglement is generated for the pair a-b, b-c (dotted-line) and also the pair a-c (dashed-line) for both values of interaction strength ε. Thus, the boundary oscillators can form a bipartite entangled state through interaction with the central one. The maximum value of the entanglement between two boundary oscillations does not depend on the magnitude of ε (see both dashed lines in Fig 2a and 2b). In contrast, the entanglement created by two oscillators b-c depends directly on ε. So that, by choosing the value of the magnitude of the linear interaction, we can influence the degree of the neighboring bipartite-, tripartite - entanglement and time of appearance of the entanglement.

During the time evolution, for both values of strength coupling ε, we can obtain different types of tripartite inseparable states. The time is approximately 900, 2650, 4500 (Fig. 2a) and 1300, 3800 (Fig. 2b) we notice the tripartite entangled state being the 2-1 type. At that time, there is not any signal of neighboring entanglement, but our system can generate almost maximally tripartite entangled states. One can recognize that the maxima value of tripartite concurrence is closely to unity (Fig. 2b), this means the maximally tripartite entangled state is created. For other time evolution, inseparable state is produced with smaller probabilities and associated with the W-type class (type 2-3). Thought, the W - type state is not a maximal entangled state however this class has the highest robustness against the loss of one qubit. The present system can be a source of generation of tripartite entangled states, which is a remarkably simple quantum information problem.

III. CONCLUSION

We have dealt with the three-mode system of nonlinear quantum oscillators. When three modes of fields propagate in the Kerr-type medium, not only the self- coupling term

exits but also the so-called cross-Kerr coupling involves. The system is excited by external excitation fields in two boundaries. This discussed system can behave as perfect three - mode nonlinear quantum scissors and evolves within a set of five states under some conditions. In fact, they are able to be treated as a 3-qubit system. We have shown that the system can be a source of entangled 2-qubit and 3-qubit states. In the case of the 2-qubit entanglement, we can observe the entanglement between two boundary oscillators which are not directly coupled together. It has been shown that it is possible to obtain an almost maximally entangled 3-qubit state in W - type class. Physical systems governed by the effective Hamiltonian describing our model can be not only a potential source of various bi- and tri-partite entangled states, but also interesting for finding various types of quantum correlations and relations among them.

REFERENCES

[1] V. Perinova, A. Luks, and J. Krapelka, Dynamics of nonclassical properties of two- and four-mode Bose-Einstein condensates, *J. Phys. B:At. Mol. Opt. Phys.*, 2013, **4**6 195301

[2] A. R. Shahinyan, L. Y. Chew, and G. Y. Kryuchkyan, *Phys. Lett. A*, 2013, **377**, 2743-2748.

[3] J. K. Kalaga, A. Kowalewska-Kudłaszyk, W. Leoński, and A. Barasinski, Quantum correlations and entanglement in a model comprised of a short chain of nonlinear oscillators, *Phys. Rev. A*, 2016, **94**, 032304.

[4] L. Mandel and E. Wolf, Optical Coherence and Quantum optics, Cambridge, New York, 1995.

[5] W. K. Wootters, Entanglement of formation of an arbitrary state of two qubits, *Phys. Rev. Lett.*, 1998, **80**, 2245-2248.

[6] W. Leoński and A. Kowalewska-Kudłaszyk, Progress in Optics, Edited by E. Wolf, Elsevier, 2011, 131-185.

[7] W. Leoński and A. Kowalewska, Kudłaszyk A., Quantum scissors - Finite-dimensional states engineering, 2010, aXiv: 1312(118), 2-9.

[8] W. Dür, G. Vidal & J. I. Cirac, Three qubits can be entangled in two inequivalent ways, *Phys. Rev. A*, 2000, **62**(6). 062314.

[9] C. Sabín, et al., A classification of entanglement in three-qubit systems, *Eur. Phys. J. D*, 2008, **48**, 435-442.

[10] P. Rungta, V. Bužek, C. M. Caves, M. Hillery, G. J. Milburn, Universal state inversion and concurrence in arbitrary dimensions, *Phys. Rev. A*, 2001, **64**, 042315.

[11] C. S. Yu, H. S. Song H. S., A classification of entanglement in three-qubit systems, *Phys. Lett. A*, 2007, **330**, 377.

[12] J. K. Kalaga, M. W. Jarosik, R. Szczęśniak, W. Leoński, Generation of squeezed states in a system of nonlinear quantum oscillator as an indicator of the quantum-chaotic dynamics, *Acta Phys. Pol. A*, 2019, 135.

 ISBN:

EFFECT OF ENDURANCE TRANING IN PATIENT WITH HYPERTENSION ON BICYCLE ERGOMETERS

Nguyen The Thuong*

Institute of Biomedical Physics,
109A Pasteur, Ben Nghe Ward, District 1, Ho Chi Minh City, Vietnam

*E-mail: *thethuong.nguyen@gmail.com*

Abstract. Hypertension or High blood pressure is a common disease that directly leads to cardiovascular diseases. Currently, the main treatment method is still drug treatment, combined with proper nutrition and physical activity. However, specific physical activity for people with high blood pressure in Vietnam is a new issue because of its safety. In the world, exercise for people with high blood pressure in particular and cardiovascular diseases in general is often encouraged by bicycle ergometers. With the advantages of accuracy and safety, this method helps patients decrease in blood pressure values and a significant improvement in their physical and mental condition. This study shows the feasibility of applying this new method in Vietnam, providing an effective method of physical activity for patients in addition to the use of traditional medical therapies.

Keywords: *Hypertension, Endurance training, Bicycle ergometers.*

I. INTRODUCTION

Hypertension (systolic blood pressure and diastolic blood pressure higher than normal ≥ 120/80 mmHg) is a common disease today and tends to be younger. This is a dangerous disease because of the direct risk of cardiovascular disease, even cardiovascular death [1]. This is the reason why many organizations and associations for the prevention of hypertension were established to provide cardiologists and general internists with specific recommendations and guidelines in detection, treatment and prevention. Statistics show that 95% of high blood pressure cases are "idiopathic", meaning no cause for hypertension can be found; is the result of many complex interacting factors that increase intravascular blood pressure, including genetic factors, lifestyle factors (diet, salty diet, sedentary lifestyle, obesity, stress and psychological factors,...) [2]. The remaining 5% of high blood pressure cases are due to secondary causes, which means that hypertension is the result of some primary disease, for example coronary artery disease, hardening of the arteries due to high blood lipids, etc. or due to kidney disease, hormones [2].

Hypertension leads to cardiovascular symptoms such as thickening of the walls of blood vessels, reduced endothelial cell function, and atherosclerosis of medium and large arteries. In addition, it also increases the risk of cardiovascular complications: coronary artery disease, cerebrovascular, kidney disease,… Many studies show that effective treatment of hypertension reduces the risk of cardiovascular disease and death. When blood pressure is reduced by 2 mmHg, the risk of coronary heart disease can be reduced by 7% and the risk of cerebrovascular accident can be reduced by 10% [3]. To treat hypertension, the current popular method is still using drugs, but besides that, people are more interested in the treatment with non-drug methods (lifestyle changes) which is the

diet regimen, nutrition and especially doing exercise. This is also considered the indication for all hypertensive patients. However, how to do exercise properly, enough and suitable for medical conditions is a big problem not only for patients but also for doctors.

In the world, supporting the treatment and prevention of hypertension is often promoted by increasing physical activity. The results showed that the effectiveness of physical exercise improved markedly with the condition of high blood pressure. Study by Hagberg et al., [4] on the effect of exercise on elderly people aged 60-69 years with hypertension, the systolic blood pressure (SBP) decreased by 7 mmHg and diastolic blood pressure (DBP) decreased by 8-9 mmHg after exercise. Whentol et al., [5] studied on 54 control groups to evaluate the effect of aerobic endurance exercise on blood pressure, including patients with hypertension and normal people. The results also showed that when exercising, blood pressure decreased even when body weight did not decrease, with no difference in gender and age. Steffen et al. [6] showed that patients' high blood pressure due to emotional distress and lack of daily physical activity was significantly improved by just 55 minutes of exercise a day. A meta-study by Fang et al. [7] in multiple patients with hypertension for many years and compared with normotensive and pre-hypertensive subjects. The results showed that people regularly exercised, on average, lowered their blood pressure by 2.6-7.4 mmHg.

In Vietnam today, doing exercise to improve high blood pressure is still a very new issue, and faces many difficulties because of the lack of exercise methods as well as measuring and testing equipment to evaluate the effectiveness. In countries with developed sports medicine and medical technology, patients with cardiovascular diseases in general and high blood pressure in particular are often encouraged to do exercise on bicycle ergometers. This is a method of doing exercise, applying the principles of sports training but changing to suit each subject and the patient's condition, to improve strength, endurance and physical condition of the body. Therefore, when the patient exercises with this method, the exercise is planned in very specific detail (load, exercise intensity, time,...) and changes in blood pressure, heart rate , electrocardiogram,... are given direct feedback to help patients exercise moderately, avoid dangerous overload. Accompanying this training method is a complete system of training and assessment equipment for the patient. The application of this method in Vietnam will provide patients with a new, effective and safe method of physical exercise to support health and fitness improvement, helping patients to quickly improve medical condition. The purpose of the study is to show the feasibility of this method to improve the hypertensive index and the patient's medical condition, as a basis for future clinical efficacy evaluations.

II. METHODS

A 63-year-old female patient with above-normal blood pressure (≥150/100 mmHg) and heart rate (≥100 bmp), was diagnosed with idiopathic primary hypertension. Recently, there are often symptoms of fatigue, reduced physical strength, walking and climbing stairs on floors, feeling tired and short of breath, sleeping less, and decreasing sleep quality. The

 ISBN:

patient is not taking blood pressure medication, and is encouraged to practice in the form of medical training to improve health status and maintain normal blood pressure readings.

The bicycle ergometers device used by the patient for endurance training is the Ergoselect 200 (Ergoline GmbH, Bitz, Germany). This is an exercise bike that controls load (W) during exercise, heart rate, and blood pressure automatically due to sensors mounted on the patient's body. Blood pressure measurement mode is activated during exercise. The information related to the patient during exercise is displayed directly, allowing the therapist to monitor the patient's condition during exercise. The patient's exercise record is kept, as a basis for assessing the patient's exercise progress and progress.

The patient's exercise program lasts for 4 weeks, 3 sessions per week, each session lasts for 24 minutes according to the interval training program; including 2 minutes of warm-up exercise, 20 minutes of moderate-intensity exercise (25W), equivalent to a Borg scale of 10/20, and 2 minutes of weightlifting before the end. During exercise, the patient breathes evenly and maintains a steady cycling speed (60 rpm). Blood pressure and heart rate were measured 2 minutes each and 10 minutes after a break.

III. RESULTS AND DISCUSSION

Tables 1 and 2 show details of systolic blood pressure (SBP) and diastolic blood pressure (DBP) of patients during exercise in 12 training sessions (S). The data tables show that the SBP and DBP values during exercise fluctuate and decrease; and at the end of the exercise and 10 minutes after the break, the SBP and DBP have lower values. This result is consistent with studies on exercise that dilates blood vessels, speeds up blood flow, reduces blood resistance and thus lowers blood pressure [8,9].

Table 1. *Systolic blood pressure of the patient during exercise.*

Min	S1	S2	S3	S4	S5	S6	S7	S8	S9	S10	S11	S12
0'	**159**	**148**	**148**	**141**	**142**	**137**	**151**	**136**	**151**	**132**	**154**	**141**
2'	140	129	122	138	119	126	115	129	138	132	125	120
4'	145	144	124	141	126	129	127	138	143	135	140	125
6'	147	145	128	142	144	135	130	139	154	140	148	126
8'	139	148	127	137	134	138	132	143	150	143	146	122
10'	140	138	134	136	132	143	132	136	152	140	141	132
12'	140	145	133	141	135	140	128	144	140	145	143	129
14'	144	145	132	145	128	143	124	139	143	138	146	128
16'	136	146	130	137	143	141	137	142	141	136	144	127
18'	132	141	131	138	140	137	135	145	137	137	142	127
20'	136	139	117	144	126	142	120	147	149	134	144	130
22'	139	148	113	143	136	133	125	136	142	135	143	124
24'	137	140	125	136	132	135	121	137	144	131	140	113
After exercise	**138**	**136**	**129**	**128**	**125**	**136**	**115**	**131**	**122**	**126**	**120**	**109**

Table 2. *Diastolic blood pressure of the patient during exercise.*

Min	S1	S2	S3	S4	S5	S6	S7	S8	S9	S10	S11	S12
0'	**102**	**95**	**88**	**91**	**91**	**89**	**85**	**90**	**93**	**92**	**101**	**86**
2'	82	69	65	70	67	64	51	67	65	69	82	70
4'	76	66	68	68	63	69	64	75	77	67	75	71
6'	77	69	68	63	60	69	59	73	76	65	76	67
8'	73	72	67	69	62	68	60	71	73	65	71	66
10'	70	69	63	67	64	67	60	72	68	64	70	70

12'	71	70	66	66	63	71	65	77	67	61	73	67
14'	74	72	63	69	60	67	56	71	70	61	77	64
16'	72	62	62	66	57	64	60	68	68	67	72	66
18'	74	74	65	69	57	70	57	68	65	62	75	63
20'	72	69	70	69	62	68	63	77	74	66	71	67
22'	72	69	64	64	57	64	65	69	67	60	71	58
24'	78	78	68	71	64	70	68	76	70	63	80	64
After exercise	**95**	**85**	**84**	**87**	**86**	**88**	**79**	**92**	**87**	**85**	**92**	**80**

Figures 1, 2 compare the patient's SBP and DBP values before and after exercise in 12 training sessions. The results also showed that the average curve of the SBP and DBP tended to decrease gradually with the number of training sessions. Thus, before starting the training course and after finishing 12 training sessions, the SBP and DBP tended to decrease. This result proves that exercise has reduced the patient's blood pressure index.

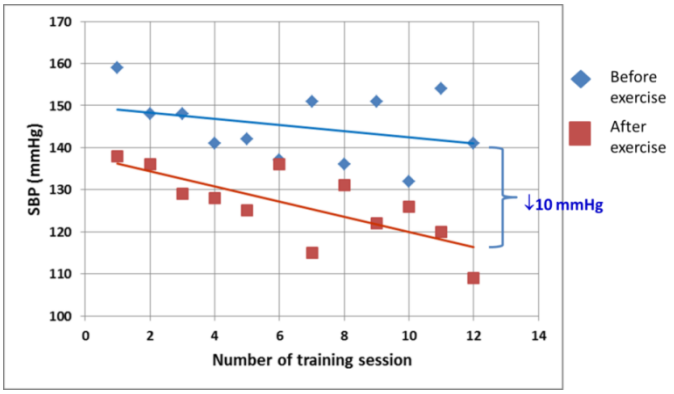

Fig. 1. *Systolic blood pressure (SBP) of the patient before and after exercise.*

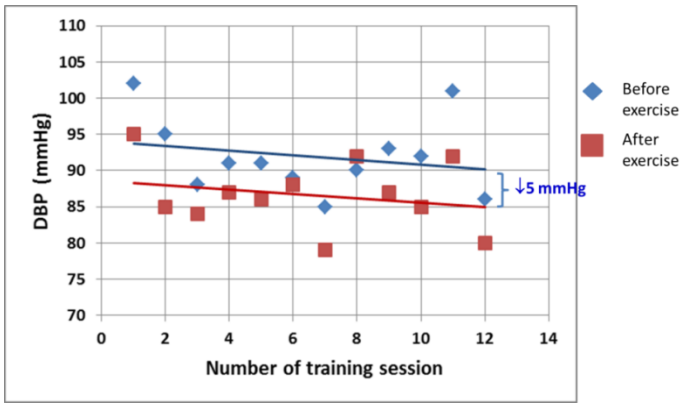

Fig. 2. *Diastolic blood pressure (BP) of the patient before and after exercise.*

In addition, the patient has significantly improved in physical and mental condition. Patients feel that walking and climbing stairs are no longer as tiring as before, and sleep is also improved. Mentally more excited with practice and life. This result is consistent with the patient's work value (kJ) gradually increasing (table 3) during exercise, showed that the patient's condition responded better to training load during exercise. Work value is calculated on the patient's power on the bike multiplied by the time exercises.

Table 3. *Total work value (kJ) of each training session.*

Session	1	2	3	4	5	6	7	8	9	10	11	12
Work value (kJ)	130	130	140	145	145	145	145	160	160	160	160	160

 ISBN:

IV. CONCLUSION

The results of the study showed that the patient had an improvement in the condition of high blood pressure, reflected in the decrease in blood pressure index, especially in systolic blood pressure. In addition, the physical and mental condition has also improved markedly. After each training session, the patient's spirit is very comfortable, there is no worry when exercising, because the exercise is under the supervision of the therapist and the exercise monitoring system. Each exercise has a clear quantification of intensity, training time,... as a method for treatment. Research results have shown the feasibility of applying therapeutic medicine training methods for high blood pressure. In the world, the application of exercise, increasing physical activity to regulate blood pressure has become popular and has become a "guideline" applied even to patients with cardiovascular problems associated with high blood pressure internally medical treatment. However, in Vietnam today, exercise for people with high blood pressure in particular and rehabilitation for cardiovascular patients in general is still limited, because of its safety. The results of this case study may be the premise for future clinical efficacy studies, demonstrating the effectiveness of medical training in improving and preventing diseases related to cardiovascular disease in Vietnam.

REFERENCES

[1] Mancia G., et al., 2007 Guidelines for the management of arterial hypertension, *ESC. J Hypertens*, 2007, **25**, 1105-1087.

[2] Dahlof B., Hypertonihandboken, The Hypertension Handbook, Sollentuna: Merck, Sharp & Dohme, Sweden AB; 2000.

[3] Wolf Meier K., et al., Hypertension treatment and control in five European countries, Canada, and the United States, *Hypertension*, 2004, **43**(1), 10-17.

[4] Hagberg J., et al., Effect of exercise training in 60 to 69-year-old persons with essential hypertension, *Am. J. Cardiol*, 1989, **64**, 348-353.

[5] Whelton S., et al., Effect of Aerobic Exercise on Blood Pressure, *Ann. Intern. Med*., 2002, **136**(7), 493-503.

[6] Steffen P., et al., Effects of exercise and weight loss on blood pressure during daily life, *Med. Sci. Sports Exerc.*, 2001, **33**(10), 1635-1640.

[7] Fang J. et al., Exercise and cardiovascular outcomes by hypertensive status: NHANES I epidemiologic follow-up study, 1971-1992, *Am. J. Hypertens*., 2005, **18**, 751-758.

[8] Duncan J. J., et al., The effects of aerobic exercise on plasma catecholamines and blood pressure in patients with mild hypertension, *JAMA*, 1985, **25**(4), 2069-2013.

[9] Thoren P., et al., Endorphins and exercise. Physiological mechanisms approach, *Med. Sci. Sport Exerc*., 1990, **22**, 17-28.

CHARACTERIZATION AND EFFECT OF BOUNDARY LAYER IN SEVERE-HAZY POLLUTION EVENT DURING WINTER 2019 IN HANOI

Bao Anh Phung Ngoc[1,2*], Hervé Delbarre[1], Karine Deboudt[1], Elsa Dieudonné[1], Hai Van Bui[3]

[1]*Laboratoire de Physique et Chimie Atmosphériques (LPCA), Université du Littoral Côte d'Opale, Dunkerque, France*

[2]*Institute of Human Geography, Vietnam Academy of Social Sciences, Hanoi, Vietnam*

[3]*Le Quy Don Technical University, Hanoi, Vietnam*

*E-mail: *anh-bao.phung-ngoc@univ-littoral.fr*

Abstract. In order to understand and explain variables causing severe pollution events occurring under Northeast monsoon's impact during winter period in Hanoi, a campaign was carried out (11 January to 22 March 2019). The local meteorological parameters such as wind speed and wind direction were investigated, notably using a Doppler Lidar, and the structure of boundary layer was thoroughly studied using elastic Lidar measurements for the first time in Hanoi. Indeed, the elastic Lidar measurements showed that the daily maximum of the hourly boundary layer height varied from 700 m to 1200 m during cloudy days, while it was always below 1000 m during hazy days. Since then, the lower boundary layer on the hazy days tended to weaken the vertical mixing and was directly related to an accumulation of aerosol concentrations at the surface.

Keywords: *Air pollution; Boundary layer; Haze; Lidar; $PM_{2.5}$.*

I. INTRODUCTION

A high level of PM including PM_{10} and $PM_{2.5}$ has been stated to adversely impact human health and life quality [1,2]. Indeed, $PM_{2.5}$ has been considered currently as one of the main issues weakening the air quality in cities in Southeast Asia including Hanoi in which a rapid growth and urbanization over the past two decades has been experienced [3-5]. While higher levels of PM in Hanoi are recorded in winter under impact of cold air intrusion [4,6,7].

Boundary layer height (BLH) and vertical wind profile are parameters that have not been exploited much in studies on air pollution in Vietnam. Concerning the dynamics of boundary layer, it is affected by two main variables including solar radiation and weather conditions. Inland, boundary layer (BL) may undergo a typical daily evolution driven by surface heating, but it is also strongly dependent on local meteorology (haze, sea-breeze) and fronts [8]. Concerning wind profiles, horizontal and vertical wind speeds can change quickly in time as well as in space, thus, monitoring these profiles lead to improve our understanding of atmospheric dynamics as well as the evolution of the BL. Nowadays, Lidar is one of popular method for analyzing the BL structure and determining BLH due to its high spatio-temporal resolution. However, this method requires greater technical resources and it still has some optical limits especially under cloudy weather. In a few

 ISBN:

recent decades, Lidar's application in order to analyze the BLH is widely applied in many regions of the world like Europe and Asia [9-11]

In this study, our goal within is to identify the structure of BL by using the Lidar measurements for the first time in Hanoi. The impact of its evolution during pollution episodes as well as of atmospheric dynamics on hourly PM2.5 concentrations will be explored.

II. FIELD CAMPAIGN FOR A DYNAMICAL STUDY OF AIR POLLUTION IN HANOI

2.1. Devices, location and availability

The campaign was carried out from 11 January to 22 March 2019 in Hanoi. The observation site located at Vietnam Academy of Science and Technology (VAST) (21° 2' N, 105° 47' E) which is a residential and traffic mixed area including a ring road and several busy roads.

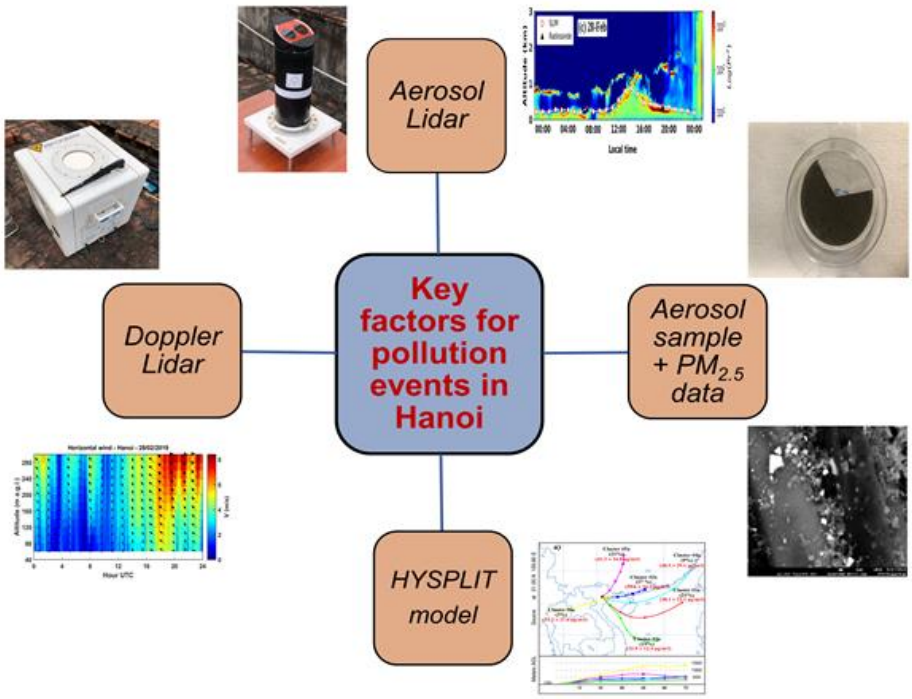

Fig. 1. *The Lidar system at observation site in VAST.*

A Doppler Lidar (Windcube V2 from Leosphere/Vaisala) and a custom-made aerosol micro-pulse Lidar (SLIM) were located at the site OS1 on the rooftop of a 15 m high building (Fig. 1). In addition, an aerosol sampler was set up next to the Lidar devices. A meteorological station (Davis Instruments, Hayward, CA; model Vantage Pro 2) was placed on the rooftop of a second building (50 m above ground level (a.g.l.), around 100 m away from the Lidar location) to minimize the impact of high buildings around the site.

2.2. Remote sensing of boundary layer and wind vertical profile

2.2.1. Doppler Lidar (Windcube V2)

The Windcube V2 from Leosphere/Vaisala is an eye-safe pulsed Doppler Lidar operating in the infrared (1.543 µm) at low power (7 mW laser). It measures the Doppler shift due to the particles motion along the laser beam direction (radial wind speed), which is determined through heterodyne detection followed by fast Fourier transform analysis. The profiles of the three components of the wind are reconstructed using the DBS technique originally proposed for Doppler radars [14], here combining four slanted beams (28° from zenith) pointing in the cardinal directions and a vertical beam. The accumulation time is 1s per bream so that a DBS cycle is repeated every 5 s; then, wind observations are averaged over 10 min periods. The laser pulse duration and shape allow for a 20 m vertical resolution while the optics allow for a minimal/maximal range of 40/280 m a.g.l. During the campaign, this device was set to retrieve the wind every 20m from 60m to 280 m a.g.l. (the 40 m altitude was not used due to the interference of nearby higher buildings). Besides wind speed and wind direction profiles, an upward movement of air, which is known as vertical mixing (σ_w), was also computed by Doppler Lidar. The σ_w is measured by computing the standard deviation of WS from time series with 5 seconds steps during 10 minutes period.

2.2.2. Aerosol micro-pulse Lidar (SLIM)

The SLIM was deployed during the campaign. It is a custom-made micro-pulse Lidar developed at LATMOS in collaboration with CIMEL that operates at the edge of the visible spectrum (808 nm) and at low power (12 mW laser). The device was pointed at the zenith and recorded profiles of elastic signal back-scattered by the atmosphere with a vertical resolution of 15 m, averaged over 10 min, then 1 h. The overlap function was determined using the slope method applied to a 3 h average profile recorded in a well-mixed afternoon BL. Then, the BLH was determined by the 1 h average profiles of the ROCS, noted P(z) with the altitude (z).

In cloud-free conditions, the Lidar signal yields a strong back-scattering from the particles within the BL, then decreases through a transition zone and disperses completely in the free troposphere as back-scattering from the molecules is much weaker, especially at 808nm. Thus, the first derivative of the ROCS exhibits a strong negative peak (P') at the height (z) which is considered to be the BLH. This well-known method for BLH determination is GM [12,13].

$$H_{GM} = \min \frac{d[P\prime(z)]}{d[z]}$$

Some improvement methods for detecting BLH, which are still based on GM method, such as logarithmic gradient method (LGM):

$$H_{LGM} = \min \frac{d[ln(P\prime(z))]}{d[z]}$$

or cubic root gradient method (CRGM):

$$H_{LGM} = \min \frac{d[ln(P\prime(z))]}{d[z]}$$

 ISBN:

III. RESULTS AND DISCUSSION

3.1. BLH evaluation

Radiosonde measurements are considered as the most reliable method for retrieving vertical profiles of meteorological parameters as well as BLH. The height of boundary layer is determined by the height of intersection of the actual potential temperature profile with relative humidity. Unfortunately, soundings are usually released into the atmosphere 2-3 times per day, so this method is not able to monitor continuously the BLH evolution. For example, retrieved BLH from soundings value, which were launched at 07:00 (Fig. 2) on 24 January 2019 indicated around 315 m at that moment.

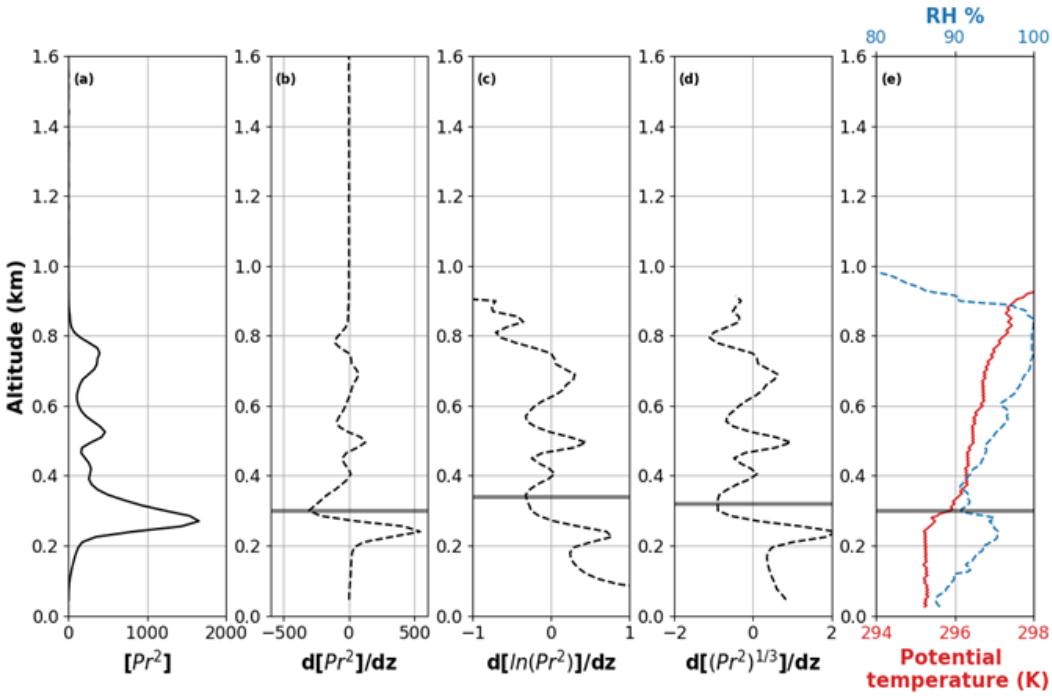

Fig. 2. *Application of derivative methods for retrieval BLH (a) range corrected lidar signal, (b) gradient method, (c) logarithmic gradient, (d) cubic root gradient and (e) potential temperature and relative humidity at 07:00 AM on 24th January.*

Fig. 2 also show the time cross-section of the first derivative of the range corrected signal measured by the SLIM instruments in Hanoi on 24th. GM, LGM and CRGM were applied to evaluate the bias between the methods. As a result, a low bias between retrieval BLH from these methods was indicated. Furthermore, the bias between BLH deriving from Lidar measurement and radiosonde was low. It is stated that Lidar measurement worked properly in this case. However, the result of diurnal variation of the BLH was also classified under haze, cloudy and clear conditions. Unfortunately, there were some days when the height of boundary layer cannot be clearly defined under rainy condition or due to technical problems then these calculations of the BLH were eliminated.

In this study, we use GM method for detecting BLH for all days. The GM is still valid when a thin cloud is capping the BL. Indeed, that type of cloud is included in the BL, and the GM will then detect the strong decrease of signal occurring when the laser beam exits the cloud. When a thick cloud is present just above the BL, it rapidly extinguishes the

laser beam, and the GM will return the extinction height, which is located inside the cloud. This will cause a slight overestimation of the BLH because thick clouds are not included in the BL, so the cloud base should be considered instead as BL top. However, this slight overestimation is not a problem when the main point is to follow the BLH variability and its influence over pollution, so a simple and more reliable algorithm was preferred.

3.2. Role of the boundary layer dynamics on $PM_{2.5}$ levels during pollution events. Case study: Pollution event P1: 18-20/01

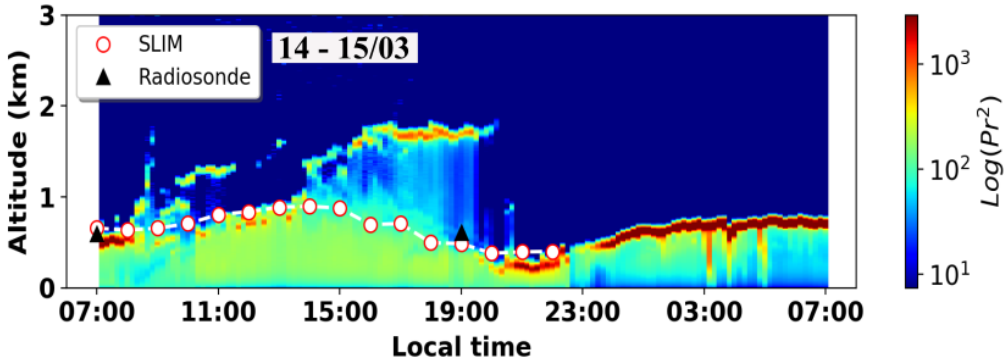

Fig. 3. *Time-height cross-sections of SLIM Lidar range-corrected signal (Pr^2) and time series of boundary-layer height (BLH) on 14/03. The BLH retrieved from SLIM (respectively radiosondes) profiles is represented as red circles (respectively black triangles).*

In general, the evolution of the BL during a day can be described as follows: After the sunrise (recorded at 07:00 LT), the convective boundary layer (CBL) grows steadily and often reaches its maximum height from 14:00 to 16:00 LT. Afterward, the sensible solar radiation decreases and the CBL gradually changes into nocturnal boundary layer (NBL) that has a short-lived state. Around the sunset (recorded at 18:00 LT), the bottom part of the NBL is transformed into stable boundary layer (SBL) driven by weaker and sporadic turbulence under stable conditions [8]. However, the BLH development is strongly impeded under haze conditions because a large part of the incoming solar radiation is either absorbed or scattered by the fog, by clouds or by the pollution layer, thus reducing the solar flux reaching the surface and leading to increased stability. Lower BLH on hazy days weakened the vertical mixing and this condition directly leads to the accumulation of aerosol at the surface, leading to an increase of the aerosol concentration.

Figure 3 shows the time series of BLH measured by the SLIM in Hanoi on 14/03. High back-scattering coefficient values were recorded at altitudes lower than the BLH suggesting that the haze pollution was formed and evolved within the BL. Thus, a fine analysis of the relation between the BLH and $PM_{2.5}$ variations will be performed for the four pollution events that occurred in the campaign.

Day 14/03 was the last day and the most polluted day during the pollution period P4. Concerning the boundary layer, the heights of SBL on this day was commonly higher than these on other cases (with heights ≥ 500 m from 03:00 to 07:00 LT). Furthermore, CBL evolved slowly with a rate ≤40 $m.h^{-1}$ after the sunrise. And BLH reached the highest altitude at 890 m at 14:00 LT (Fig. 4) before decreasing over time as a normal scenario for

 ISBN:

the depletion of the CBL in the late afternoon. After 23:00 LT, the BLH could not be retrieved because of the precipitation. Besides BLH, it is important to take into account the ventilation coefficient (VC) which plays a significant role in the dispersion of aerosols. VC (m^2s^{-1}) was estimated as product of the BLH and the mean wind speed (WS) at 200 m a.g.l as shown in Equation:

$$VC = BLH \times WS$$

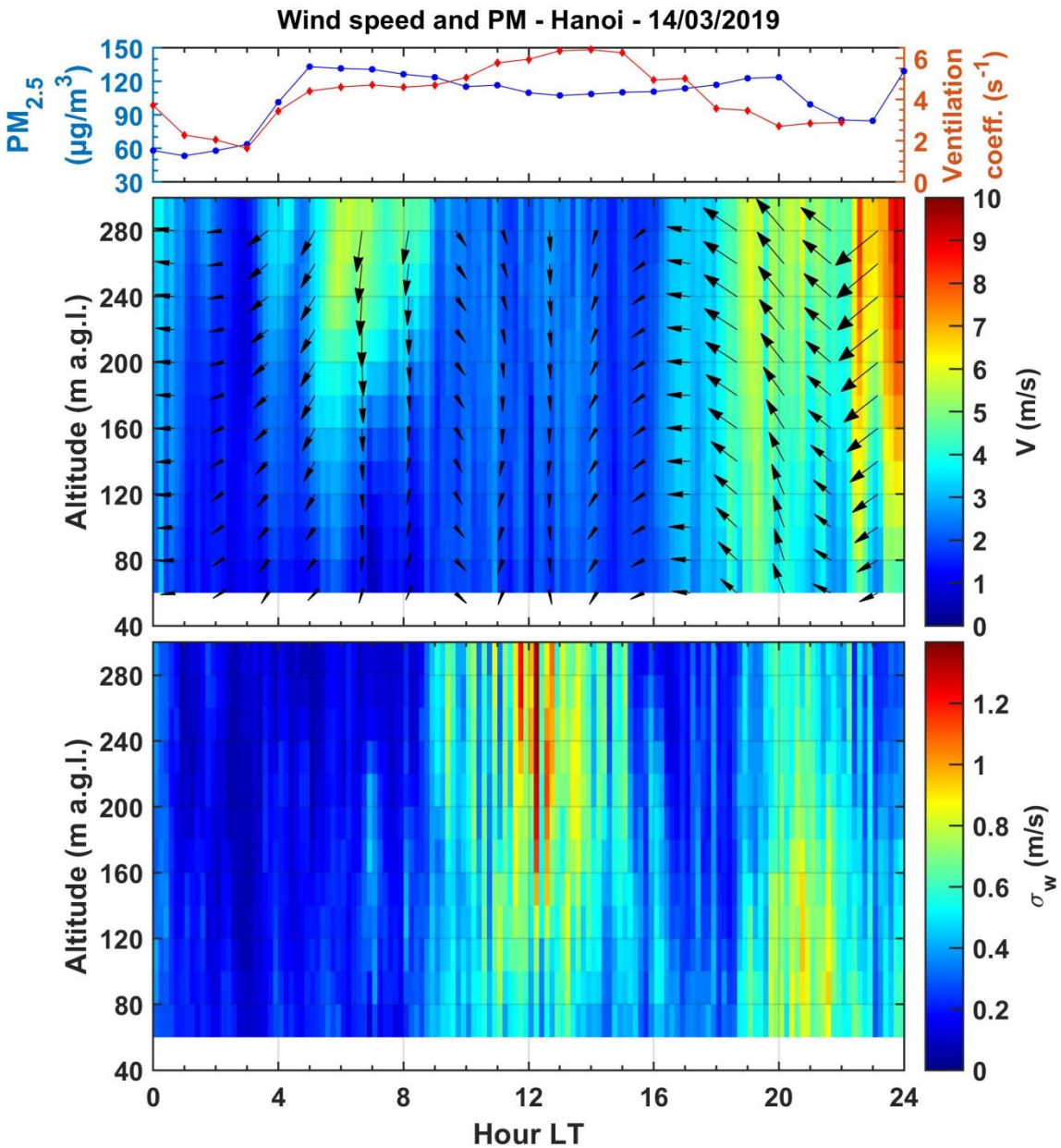

Fig. 4. *Time series of $PM_{2.5}$ concentration (upper) and time-height cross-sections of horizontal wind speeds (middle) and vertical mixing (below) measured by the Doppler Lidar on 14/03.*

At the beginning of the day, $PM_{2.5}$ concentration was lower than the other cases (~60 µg.m^{-3}) but it was still considered as high concentration. This result is expected because of the highest value of VC observed during this day compared to other case studies (Fig. 4). Then, it suddenly increased from 03:00 LT and after two hours, it reached ~130 µg.m^{-3} which was twice as much as its value at the beginning of the day. The Doppler

Lidar shows that a LLJ probably existed from 04:00 to 09:00 LT (Fig. 4), this jet could have carried pollutants from regional sources to Hanoi, leading to the increase of $PM_{2.5}$. Also, the increased wind shear below the jet reinforced the vertical mixing leading to the irruption of pollutants at the surface. Afterward, the $PM_{2.5}$ concentration went down slightly but it maintained at a high polluted level (≥100 $\mu g.m^{-3}$) until 14:00 LT, as the boundary layer only grew moderately after sunrise. After the BLH reached its maximum height of 910 m at 14:00 LT, it tended to decrease gradually and the concentration of $PM_{2.5}$ began to increase until 20:00 LT because of the depletion of the BL. Then, the concentration of $PM_{2.5}$ fell suddenly by the arrival of a new cold surge, which resulted in a significant increase in WS.

IV. CONCLUSION

For the purpose of studying the factors affecting air quality pollution, this study analyzed the relation between multi-scale meteorological conditions and pollution events during 2019. The results of aerosol Lidar showed a large variability in the daytime boundary layer height according to the different weather conditions: the daily maximum of the hourly BLH varied from 700 m up to 1200 m during cloudy days, while it was typically below 1000 m during hazy days. In hazy days, the height of boundary layer was compressed and grow slowly within just a few hundred meters due to strong effect of haze. Because of the lower levels of BLH, the accumulation of pollutants at the surface is reinforced, leading to severe degradations of the air quality in Hanoi.

The methods and results presented in this study can be used to further assess the contents, types and controlling factors of atmospheric dynamics on polluted events in Hanoi under different weather conditions. Our campaign leverages the future field campaigns to better understand the mechanism between meteorological factor, BLH and air quality during winter period in Hanoi.

ACKNOWLEDGMENTS. This work is a contribution to the CPER (Contrat de Plan Etat-Région) research project IRenE (Innovation et Recherche en Environnement) and Climibio. The work is supported by the French Ministère de l'Enseignement Supérieur, de la Recherche et de l'Innovation, the region Hauts-de-France and the European Regional Development Fund. The work is also supported by the CaPPA project. The CaPPA project (Chemical and Physical Properties of the Atmosphere) is funded by the French National Research Agency (ANR) through the PIA (Programme d'Investissement d'Avenir; contract no. ANR-11-LABX-0005-01) and by the regional council of Nord-Pas-de-Calais and the European Regional Development Fund.

We appreciate LPCA, Université du Littoral Côte d'Opale for providing the Doppler Lidar (Windcube V2) and LATMOS, CNRS & Paris Sorbonne University for providing the aerosol micro-pulse Lidar (SLIM). The few anonymous people who provided information in the context of a personal relationship are sincerely acknowledged for their valuable contributions.

 ISBN:

REFERENCES

[1] Kelly F. J., Fussell J. C., Size, source and chemical composition as determinants of toxicity attributable to ambient particulate matter, *Atmos. Environ.*, 2012, **60**, 504-526.

[2] Pope C. A., Coleman N., Pond Z. A., Burnett R. T., Fine particulate air pollution and human mortality: 25+ years of cohort studies, *Environ. Res.*, 2020, **183**, 108924.

[3] Cohen D. D., Crawford J., Stelcer E., Bac V. T., Long range transport of fine particle windblown soils and coal fired power station emissions into Hanoi between 2001 to 2008. *Atmos. Environ.*, 2010, **44**, 3761-3769.

[4] Cohen D. D., Crawford J., Stelcer E., Bac V. T., Characterisation and source apportionment of fine particulate sources at Hanoi from 2001 to 2008, *Atmos. Environ.*, 2010, **44**, 320-328.

[5] Hai C.D., Kim Oanh N. T., Effects of local, regional meteorology and emission sources on mass and compositions of particulate matter in Hanoi, Atmos. Environ., 2013, **78**, 105-112.

[6] Hien P. D., Loc P. D., Dao N. V., Air pollution episodes associated with East Asian winter monsoons, *Sci. Total Environ.*, 2011, **409**, 5063-5068.

[7] Huy L. N., Kim Oanh N. T., Assessment of national emissions of air pollutants and climate forcers from thermal power plants and industrial activities in Vietnam, *Atmospheric Pollut. Res.*, 2017, **8**, 503-513.

[8] Stull R. B. (Ed.), An introduction to boundary layer meteorology, Springer Netherlands, Dordrecht, 1988.

[9] Delbarre H., Augustin P., Saïd F., Campistron B., Bénech B., Lohou F., Puygrenier V., Moppert C., Cousin F., Fréville P., Fréjafon E., Ground-based remote sensing observation of the complex behaviour of the Marseille boundary layer during Escompte, *Atmospheric Res.*, 2005, **74**, 403433.

[10] Liu B., Ma Y., Gong W., Zhang M., Shi Y., The relationship between black carbon and atmospheric boundary layer height., *Atmospheric Pollut. Res.*, 2019, **10**, 65-72.

[11] Menut L., Flamant C., Pelon J., Flamant P. H., Urban boundary-layer height determination from lidar measurements over the Paris area, *Appl. Opt.*, 1999, **38**, 945.

[12] Cohn S. A., Angevine W. M., Boundary layer height and entrainment zone thickness measured by Lidars and wind-profiling radars, *J. Appl. Meteorol*., 2000, **39**, 15.

[13] Flamant C., Pelon J., Flamant P. H., Durand P., Lidar determination of the entrainment zone thickness at the top of the unstable marine atmospheric boundary layer, *Bound. Layer Meteorol.*, 1997, **83**, 247-284.

[14] Koscielny A. J., Doviak R. J., Zrnic D. S., An evaluation of the accuracy of some radar wind profiling techniques, *J. Atmospheric Ocean. Technol*., 1984, **1**, 309-320.

EFFECTS OF THE γ-POLYOXYMETYLENE FIRE RATARDANT ON THE CHEMICAL STABILITY OF THE DOUBLE BASE ENERGY MATERIALS USING LAVA THERMAL ANALYSIS TECHNIQUE

Co Ngoc Duong[1], Toai Pham Van[1], Tuong Nguyen Manh[2,*], Cong Vu Tien[1], Toan Nguyen Trung[3], Duong Duc La[2,*]

[1]*Institute of Propellant and Explosives, 192 Duc Giang, Long Bien, Hanoi, Vietnam*

[2]*Institute of Chemistry and Materials, 17 Hoang Sam, Cau Giay, Hanoi, Vietnam*

[3]*Le Quy Don Technical University, 236 Hoang Quoc Viet, Hanoi, Vietnam*

Abstract. The LAVA instrument has been demonstrated as a relatively quick, reliable and precise technique for the chemical stability testing of energy materials. However, the use of this instrument for testing the energy materials with addition of anti-fire γ-polyoxymetylene (γ-POM) additive has not been reported before. In this work, the LAVA instrument was employed to study the effect of the γ-POM on the chemical stability of the double base propellants at different testing temperatures. The results indicated that the chemical stability of the energy materials decreased upon addition of the γ-POM. When the concentration of γ-POM increased, the chemical stability of the double base propellants decreased. The results also proposed the testing conditions for the chemical stability of γ-POM-contained energy materials using LAVA instrument that are testing temperature of 110 ^{o}C, the gas pressure when stopping the exeriment of 282 mmHg, testing time of less than 13.5 hours with the pressure-raising speed of lower than 28 mmHg.

Keywords: *Energetic materials, Stability, γ-polyoxymethylene, Propellants, Anti-fire additives.*

I. INTRODUCTION

Major role of propellants in the launching part of the weapons and rockets is to direct the warhead to the target. With the complicate flight trajectory of the rockets aiming to the target, there are needs of propellants with different functions such as generation of gasses to lift the rockets' wings after leaving the launching part, generation of gasses for turbine operations, generating the power to operate the control system of the self-led head. The propellants used for these purposes are commonly of long operating time, which require them to have low burning speed and high quantity of the gasses. Thus, these types of propellants are used to have average burning heat, low burning temperature and heat, and generate large volume of gasses [1]. To fabricate the propellants with these properties, many energy-carried polymers with lower burning heat in comparison to nitroglycerine such as diethyelene glycol dinitrate, triethylene glycol dinitrate or nitramine-containing compounds have been widely utilized [2]. Furthermore, energy-maintained additives are also employed in order to decrease the burning speed of the propellants (called fire retardant materials) by the endothermic effect of the additive during the decomposition process [3,4]. Many fire retardant elements have been utilized to slow down the burning speed of the propellant such as γ-polyoxymetylene (γ-POM), polymethylmethacrylate

 ISBN:

(PMMA), fluoroplastic, and 4 ammonium iron phosphate,... [5]. In which, γ-POM is one of the most widely used fire retardant for this purpose.

It is of note that the introduce of the γ-POM in the composition of the propellants could have great effect to the mechanical properties, chemical and energetic stability, and burning process of the propellants. Especially, the interaction or compatibility of the main propellants' compositions (such as nitrocellulose, nitroglycerine) and γ-POM directly affects to the thermal decomposition of the propellants, as a result, affecting the chemical stability of the propellants [6-9]. Many methods have been successfully applied to evaluate the decrease in the chemical stability of the fire retardant-contained propellants [10,11]. One of the most effective approaches is to evaluate the chemical stability of the propellants, which is carried out at the ambient conditions [12-15]. However, the propellant aging experiments at low temperature is a time-consuming process (some experiments could be carried out for more than 10 years) as well as require a large number of samples [16]. To solve this problem, the thermal-accelerating techniques at higher temperature such as vacuum stability test (VST, which measure the gas emitted from the propellant under the vacuum condition), differential scanning calorimetry (DSC, which investigate the continuous heating's effects), thermogravimetric analysis (TGA, which measure the weight loss of the propellant during heating), and others have been employed to significantly reduce the testing time, but still provide the precise results about the chemical stability of the propellants [8-10,17-19]. Another technique, which has been widely used by the Russian for the study of the chemical stability in the propellants, is LAVA method. This technique is to investigate the chemical stability of the propellants by measuring the gas pressure generating during the decomposition process in the isometric and isothermal conditions. Based on the pressure-increasing rate and the pressure value when the experiment is completed, the quality of the propellant is evaluated. The advantages of the LAVA testing technique are relatively quick, reliable and precise. However, to the best of our knowledge, no study has been reported on the investigation of the chemical stability of the propellant upon addition of the γ-POM fire retardant agent using the LAVA technique.

Herein, the effects of the γ-polyoxymetylene fire retardant agents on the chemical stability of the double base propellant (nitrocellulose and nitroglycerine) are investigated using the LAVA thermal analysis technique. Particularly, the work is to study the effects of the contents of γ-POM on the gas generated from the propellant at the different temperature. The optimized γ-POM's content in the propellant composition will be also studied and discussed.

II. EXPERIMENTAL SECTION

Materials

Nitrocellulose (No. 3, N content of 11.94%) and nitroglycerine was manufactured by a Vietnamese company. Centralite (No. 2, Cen2), dibutyl phthalate, trioxane, toluene, hexane, $BF_3O(C_2H_5)_2$, methylene, NaOH, tetrachloromethane and vaseline were obtained from China. All the chemicals were used as received without any further purification.

Synthesis of γ-polyoxymetylene

The γ-POM powder with the molecule formula of CH_3-O-$(CH_2O)_n$-CH_3, melting temperature of 168 ^oC, and n ranging from 99 to 299, was synthesized by polymerizing trioxane in the tetrachloromethane. Typically, toluene, trioxane, tetrachloromethane, hexane, $BF_3O(C_2H_5)_2$ catalyst and methylene were gradually poured into a sealed reactor equipped with an air condenser. The mixture was well-mixed using a mechanical stirrer at temperature of 70- 80 ^oC. At this reacting condition, the trioxane was polymerized to the γ-polyoxymetylene followd the reaction:

$$CH_3OCH_2OCH_3 + 1/3n\ (CH_2O)_3 \xrightarrow{BF_3O(C_2H_5)_2} CH_3O\ (CH_2O)_{n+1}CH_3 \quad (1)$$

The precipitate was filtered and thoroughly washed several times by the diluted NaOH to remove any impurities. The properties of prepared γ-POM were investigated, which meeted the specification of TY 84-841-79 (Russia). The obtained γ-POM with various concentrations was used as fire retardant in the composition of double base propellant.

Propellant preparation

The propellant samples were prepared by the mixing method with the basic components of 58.2% nitrocellulose, 36.4% nitroglycerine; 1.8% centralite, 2.4% dibutyl phthalate, 1.2% vasoline with addition of various γ-POM's contents of 0; 4; 8; 12; 16; and 20% denoted as M0, M1, M2, M3, M4, and M5, respectively. The prepared samples were dyhydraed and gelatinized on the specillzied rolling machine at temperature of 90-95 ^oC. 1 g of the obtained propellant samples with diameter of 2-3 mm was introduced to the heating oven to carry out the LAVA testing.

Propellant testing procedure

The chemical stability of the propellant was carried out using LAVA equipment. Typically, 1 g of samples on the oven was heated to certain temperature. The pressure of generated gas was recorded after every 1 hour with temperature of 90 and 100 ^oC, every 0.5 hour with the testing temperature of 110 ^oC, and 5 minutes with temperature of 120 ^oC. The propellant testing process was experienced by 3 stages. The experiment time was increased when the change in pressure from stage 2 to stage 3 was observed (Figure 1).

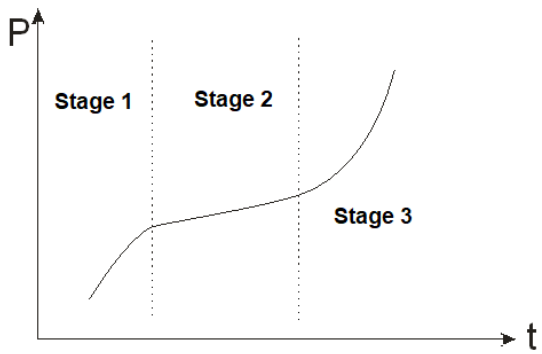

Fig. 1. *Stages of pressure curves tested with LAVA instrument.*

 ISBN:

Stage 1 is the initial stage (volume expansion by heat, and reaction between propellant and gases' components in the reactor), stage 2 is the stable decomposition stage (pressure gradually increase as increase of temperature), and stage 3 is the accelerating decomposition.

The experiment completed when the gas pressure or gas-generating speed is over a certain pressure and speed. The results of pressure and time at this point allowed determining the chemical stability of the propellant.

Result calculation

To remove the effect of the temperature on the volume expansion, the gas pressure was adjusted to the pressure after 1 hour of testing as following formulation:

$$\Delta P_i = P_i - P_{1h} \quad (2)$$

where, ΔP_i is the pressure at the time i (mmHg), P_i is the absolute temperature at the time I (mmHg), P_{1h} is the absolute pressure after 1 hour (mmHg). The plot of ΔP_i *vs.* t was used to determine the stage 2 of heat resisted process and carried out a linear regression step to obtain equation: y=a.x+b (*) with the pressure-increasing speed at the stage 2.

The time interval when stage 2 changed to stage 3 was utilized to assess the chemical stability of propellant. The relative pressure was calculated from linear regression equation (*). If the difference between the calculated relative repressure and the measured pressure is higher than 5%, stage 2-stage 3 changing point is occurred (Figure 3) with the respective t_a and ΔP_a.

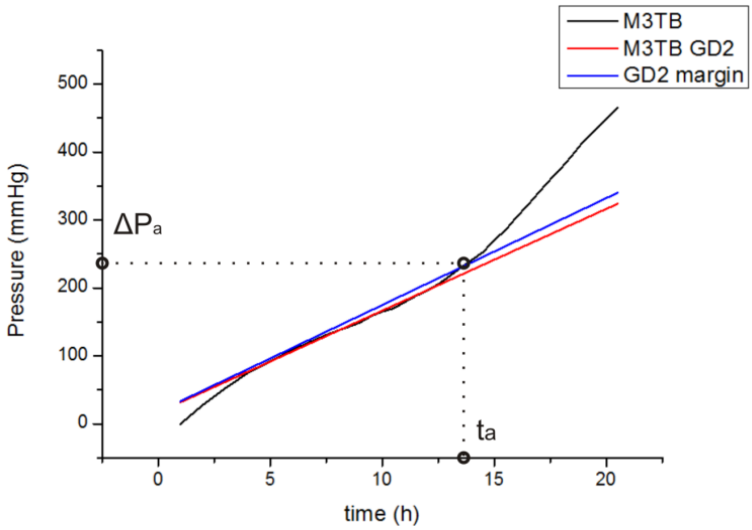

Fig. 2. *Border method to determine the stage2-stage 3 changing point. M3TB is the real pressure line, M3TB GD2is the calculated pressure line via linear regression of stage 3, and GD2 Margin is comparative pressure line with the pressure value of 5 % higher than M3TB GD2.*

Structure of equipment for the LAVA testing technique

The structure of LAVA equipment is shown in Figure 3, which consists of monitoring desktop, block-preparing controller, preparing block, thermostat, compressed air tank, power - gas controller, vacuum pump, and measuring probes. The working

temperature of the LAVA equipment is from 35 to 200 ^{o}C, and the working pressure is from 0 to 249.98 kPa.

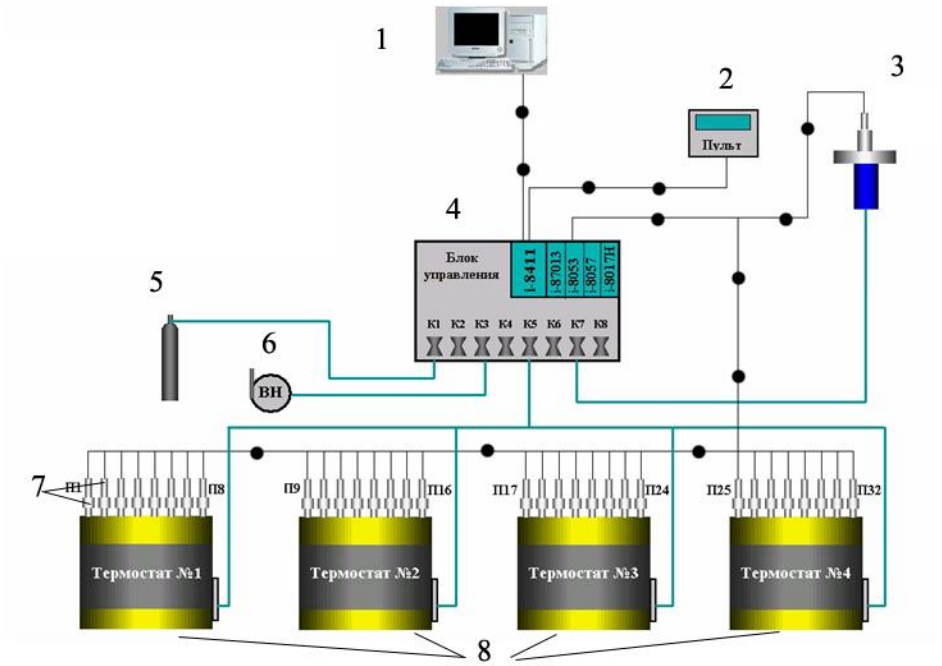

Fig. 3. *Schematic structure of LAVA thermal testing equipment. 1: Monitoring desktop; 2: Block-preparing controller; 3: Preparing block; 4: Power - gas controller; 5: Compressed air tank; 6: Vacuum pump; 7: Measuring probe; 8: Thermostat; -●-●- Power controlling path; ---- Pressure controlling path.*

III. RESULT AND DISCUSSION

The dependence of the gas pressure of the propellant samples generated in the LAVA cup on the temperature is shown in Figure 4. It can be clearly seen that the temperature is of a great effect on the gas pressure, higher temperature results in faster increase of the pressure. At low testing temperature of 90 ^{o}C, 3 stages of the deterioration process of the propellants only completes after approximately 200 hours. This is ascribed to the small change in the pressure at the low testing temperature. Thus, temperature of 90°C should not be recommended for testing the deterioration of propellants using LAVA instrument. When temperature increases to 100 ^{o}C, the propellants are quickly decomposed resulting in the high gas pressure. The 2-3 stage changing point was observed only after less than 50 hours of testing time. Especially, at temperature of 110-120 ^{o}C, these changing points were even observed within few hours, however at these temperatures (especially at 120 ^{o}C), the decomposing speed occurred too quickly and was difficult to control, hence the testing experiment had to be stopped after 3 hours. It is also obvious that at the same testing temperature, the higher contents of γ-POM result in higher and quicker increase of the gas pressure. This might be due to the presence of γ-POM in the propellants' composition helps the gas generating process in the propellants become easier. This will be discussed further in the following sections.

 ISBN:

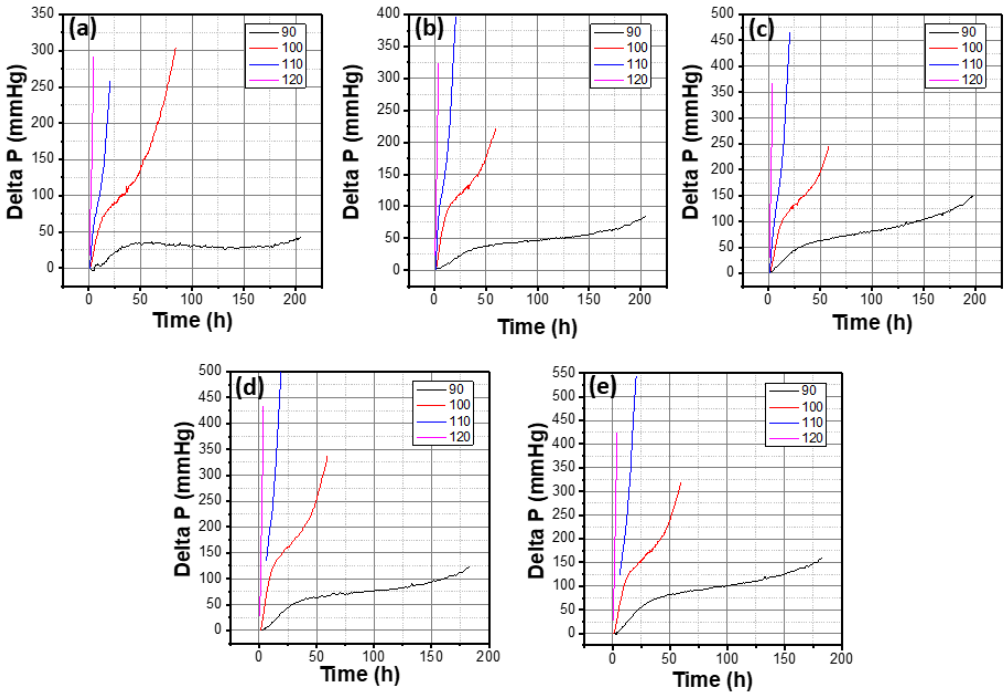

Fig. 4. *P-t curve of γ-POM-contained samples at the various temperatures with different γ-POM contents of (a) 4%; (b) 8%; (c) 12%; (d) 16%; and (e) 20%.*

Effect of γ-POM contents on the gas-generating speed of the propellants

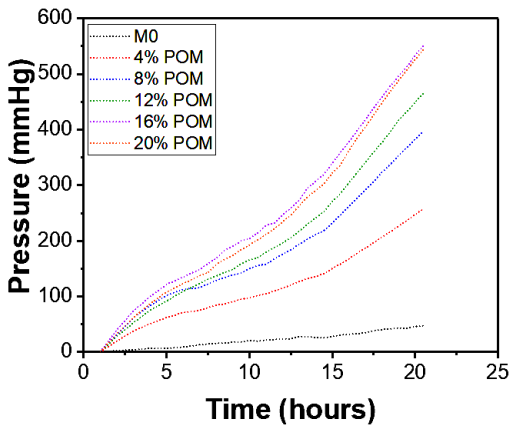

Fig. 5. *Effect of the testing time on the pressure generated by γ-POM-contained energy materials at temperature of 110 °C.*

Illustrated in Figure 5 is the effect of the testing time on the gas pressure of the γ-POM-contained propellant with various γ-POM contents at temperature of 110 °C. It can be clearly seen that the gas pressure increases along with the testing time and upon addition of POM additive. Without the presence of POM in the propellant's composition, the pressure negligibly increases with the pressure value of only 50 mmHg after testing for 20 hours at temperature of 110 °C. When POM anti-fire additive was added to the composition of propellant, the gas pressure significantly increases along with the increases of the POM's contents. The pressure is about 250 mmHg with the POM content of 4% and reaches approximately 500 mmHg with 16 % of POM after 20 hours of testing time at temperature of 110 °C. Further increase of POM's content to 20% witnesses the negligible increase of the pressure in comparison with 16 % POM.

The result of the regression data indicates that the exponential rule is in good agreement with the change in gas-generation speed as shown in Table 1. The "a" parameter (also called limited speed) is employed to determine whether the decomposition of the propellants changed to stage 3. It can be obvious from the table that at the same testing time of 20 hours, the "a" value change significantly at temperature of higher than 110 ^{o}C from 3.22134 at 100°C to 28.0285 mmHg/h at 110 ^{o}C, which is due to the change of deterioration process from stage 2 to stage 3. Thus, when pressure-increasing speed of higher 28 mmHg/h is observed, the testing experiment should be stopped.

Table 1. *The dependence of the gas-generation speed in stage 2 on the γ-POM's concentratrions.*

Regression equation: $y=a-b.c^{x}$	**Parameters**		
Temperature (^{o}C)	a	b	c
90	0.5720	1.6793	0.6404
100	3.22134	2.30563	0.91492
110	28.0285	23.1612	0.92589
120	121.6261	106.1588	0.82982

The dependence of the chemical stability on the POM/Centralite ratios

The presence of γ-POM in the compositions of the energy materials significantly affect to the chemical stability (temperature-resistant time) of the materials. Figure 6 shows the effect of POM/Cen2 ratios on the temperature-resistant time of the energy materials at various temperatures. It can be clearly seen from the figure that the temperature-resisted time of the propellants decreases along with the increase of the γ-POM's contents.

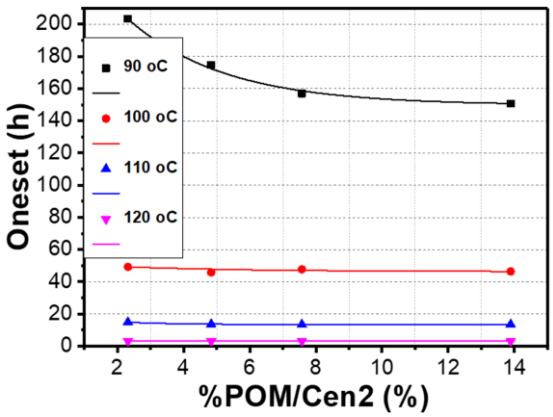

Fig. 6. *The dependence of the temperature-resistant time on the γ-POM/Cen2 ratio at various temperatures.*

The change in the temperature-resisted time is more significant at low testing temperature of 90 ^{o}C, which is from higher than 200 hours with no presence of POM to approximately 150 hours with the POM/Cen2 ratio of around 14. Increasing the testing temperature, the chemical stability of the energy materials significantly decreases. It is also of note that at the high testing temperature, the POM's content does not have much effect on the chemical stability of energy materials. The data obtained from exponential regression is consistent with the decomposing law at temperature of from 90 to 110 ^{o}C. However, at the high temperature of 120 ^{o}C, this regression data is in low agreement, which is attributed to the fast decomposing process at this temperature leading to the close changing point from stage 2 to stage 3 (about few dozens of minutes), while the LAVA instrument only allows to record the data every 5 minutes, as a results, the error is significant. Thus, temperature of 120 ^{o}C is not suitable for the decomposition testing of γ-POM-containing energy materials using LAVA instrument.

 ISBN:

The dependence of the gas pressure on the POM/Cen.2 ratio at the changing point

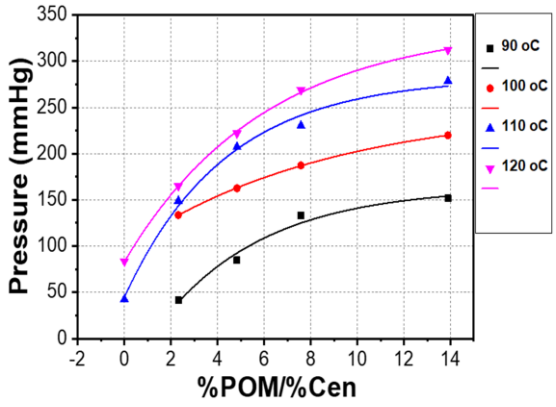

Fig. 7. *The gas-generated pressure of the propellants with various POM/Cen.2 ratio at different testing temperature using LAVA instrument.*

When heating, the energy materials are used to generate and release a large amount of gases, the data from the exponential regression also indicates that the pressure value at the changing point from stage 2 to stage 3 reaches to a constant value. For example, at the testing temperature of 110 ^{o}C, this value is determined to be 282 mmHg, which is the critical pressure of the testing for the γ-POM-contained energy materials using LAVA instrument. This value means that during the chemical stability testing process of the γ-POM-contained energy materials at 110 ^{o}C using LAVA instruments, if the pressure value is higher than 282 mmHg, the experiment should be stopped. Furthermore, it can be also obvious from the Figure 7 that the gas pressure increase significantly with the γ-POM's contents ranging from 0 to 12%. More addition of POM additive witnesses the negligible increase of the gas pressure. This results along with the aforementioned results about the effects of burning speed and gas pressure indicate that the optimized content of γ-POM for the effective gas generation in energy materials is around 12%.

IV. CONCLUSION

In summary, the chemical stability of the γ-POM-contained double-based energy materials has been successfully investigate using LAVA instrument with POM's contents ranging from 0 to 20% at temperature of from 90 to 120 ^{o}C. The results indicate that the presence of the POM anti-fire additive decreases the chemical stability of the energy materials. In the same testing temperature, the increase of the γ-POM's contents resulted in the higher amount of gas generated, which leads to increase of the pressure, as a results, the temperature-resisted time decreased. The suitable testing temperature for the chemical stability of the POM-contained energy materials using LAVA instrument was determined to be 110 ^{o}C. The optimized content of γ-POM for the effective gas generation in energy materials was also estimated to be around 12%. These results indicate that the LAVA instrument could be an effective tool for chemical stability testing of γ-POM the energy materials

REFERENCES

[1] D. Trache, F. Maggi, I. Palmucci, L. T. DeLuca, Thermal behavior and decomposition kinetics of composite solid propellants in the presence of amide burning rate suppressants, *J. Therm. Anal. Calorimetry*, 2018, **132**, 1601-1615.

[2] L. Mendonça-Filho, R. Rodrigues, R. Rosato, E. Galante, J. Nichele, Combined evaluation of nitrocellulose-based propellants: toxicity, performance, and erosivity, *J. Energ. Mater.*, 2019, **37**, 293-308.

[3] A. R. Horrocks, D. Price, D. Price, Fire retardant materials, Woodhead Publishing, 2001.

[4] A. R. Horrocks, D. Price, Advances in fire retardant materials, Elsevier, 2008.

[5] A. Chrisment, Couleur & Colorimétrie, 1998.

[6] L. Reich, Compatibility of polymers with highly energetic materials by DTA, *Thermochimica Acta*, 1973, 5,433-442.

[7] L. Reich, Compatibility of polymers with highly energetic materials by DTA: Part II, *Thermochimica Acta*, 1974, 8, 399-408.

[8] M. A. C. Mazzeu, E. D. C. Mattos, K. Iha, Studies on compatibility of energetic materials by thermal methods, *J. Aerospace Technol. Manag*., 2010, **2**, 53-58.

[9] W. De Klerk, M. Schrader, A. Van der Steen, Compatibility testing of energetic materials, which technique?, J*ournal of Thermal Analysis and Calorimetry*, 1999, 56, 1123-1131.

[10] W. de Klerk, N. van der Meer, R. Eerligh, Microcalorimetric study applied to the comparison of compatibility tests (VST and IST) of polymers and propellants, *Thermochimica Acta*, 1995, 269, 231-243.

[11] D. Trache, A. F. Tarchoun, Analytical methods for stability assessment of nitrate esters-based propellants, *Critical Reviews in Analytical Chemistry*, 2019, **49**, 415-438.

[12] W. P. de Klerk, Assessment of stability of propellants and safe lifetimes, *Propellants, Explosives, Pyrotechnics*, 2015, **40,** 388-393.

[13] L. Druet, M. Asselin, A review of stability test methods for gun and mortar propellants, I: the chemistry of propellant ageing, *Journal of Energetic Materials*, 1988, 6, 27-43.

[14] L. Druet, M. Asselin, A review of stability test methods for gun and mortar propellants, II: Stability testing and surveillance, *Journal of Energetic Materials*, 1988, **6**, 215-254.

[15] S. Elbasuney, A. Fahd, H.E. Mostafa, S.F. Mostafa, R. Sadek, Chemical stability, thermal behavior, and shelf life assessment of extruded modified double-base propellants, *Defence Technology*, 2018, **14,** 70-76.

[16] H. Yıldırım, Ş. Özüpek, Structural assessment of a solid propellant rocket motor: Effects of aging and damage, *Aerospace Sci. Technol.*, 2011, **15,** 635-641.

[17] M. Chovancová, S. Zeman, Study of initiation reactivity of some plastic explosives by vacuum stability test and non-isothermal differential thermal analysis, *Thermochimica Acta*, 2007, **460**, 67-76.

[18] F. May, Australian test procedures for determination of compatibility and stability of military explosives, *J. Hazard. Mater*., 1977, **2**, 127-135.

[19] G. Silva, Estudo cinético da decomposição térmica do α HMX por calorimetria exploratória diferencial, *Anais da Associação Brasileira de Química*, 2003, **1**, 10-12.

 ISBN:

ENHANCING THE EFFICIENCY INTERPRETATION GROUND PENETRATING RADAR DATA USING TWO-DIMENSIONAL CONTINUOUS WAVELET TRANSFORM

Tin Duong Quoc Chanh[1*], Dau Duong Hieu[1], Van Nguyen Thanh[2], Thuan Nguyen Van[2], Phuong Nguyen Le Hoai[3], Minh Lam Thuy[1], Nhan Duong Trong[1] and My Tran Diem[1]

[1]*Can Tho University, Campus 2, 3/2, Ninh Kieu, Can Tho, Viet Nam*

[2]*University of Science, VNU Ho Chi Minh City, 227 Nguyen Van Cu, District 5, Ho Chi Minh, Viet Nam*

[3]*Tay Do University, 68 Tran Chien, Cai Rang, Can Tho, Viet Nam*

*E-mail: *dqctin@ctu.edu.vn*

Abstract. The ground penetrating radar (GPR) data processing takes too much time due to many calculus such as: data format, topographic correction, data filtering, amplification and some others. However, in this process, three crucial parameters including depth, position, and size of the buried objects are needed to determine. In this paper, two-dimensional continuous wavelet transform (2-D CWT) with the appropriate wavelet functions are introduced to determine the position and size of the buried objects by the wavelet transform modulus maxima (WTMM) method, for enhancing the interpretation efficiency of the GPR data. In addition, Kirchhoff migration method is optimized by the minimum entropy and the maximum energy standards, allowing to determine the electromagnetic wave velocity in the material. Thus, the depth from the ground to the top of the buried object is also estimated. After checking the proposed method correctness on the modeling data, a process for the interpretation of the GPR based on combination between the wavelet transform and the optimal algorithm is set up, and then application for analyzing the GPR data in some places of Can Tho city.

Keywords: *Ground penetrating radar (GPR), Electromagnetic wave velocity, Two-dimensional continuous wavelet transform (2-D CWT), Appropriate wavelet functions, Optimal algorithm.*

I. INTRODUCTION

In recent years, GPR has been a kind of rapid developed equipment which is useful tool to detect underground targets with many benefits, for instance, non-destructive, fast data collection, high precision and resolution [1]. It is widely used in shallow structure research such as: forecast landslide, subsidence, mapping urban underground works, traffic design, construction, archaeology and other various fields of environment [2]. Therefore, the method for GPR processing has been developed increasingly.

The wavelet transform is a useful tool in the analysis of nonstationary signals such as that of radar or GPR [3]. Recently, Ouadfeul and his colleagues [4] used the WTMM method in 2-D CWT to interpret geomagnetic, gravity and GPR data with many positive results. Therefore, a new technique to process GPR data using 2-D CWT on GPR signals

was applied, and then combine with Kirchhoff migration method [5] to determine the depth, size and position of the buried pipe.

II. THEORETICAL BACKGROUND

Ground Penetrating Radar

Using radar reflections to detect subsurface objects in the first time was proposed by Cook, in 1960 [6]. Subsequently, Cook and other researchers [7] continued to develop radar systems to discover reflections beneath the ground surface. The fundamental theory of ground penetrating radar was described in detail by Benson [8]. In short, GPR system sends out pulses of electromagnetic wave into the ground, typically in the 10-2000 MHz frequency range, travels away from the source with the velocity depends on material structure of the environment. When the radar wave moves, if it meets anomaly objects or layers with different electromagnetic characteristics, a part of the wave energy will reflect or scatter back to the ground. The remaining energy continues to pass into the ground to be further reflected, until it finally spreads or dissipates with depth. The reflective wave is detected by receiver antenna and saved into memory of the device to analyze and process. The traces along a transect profile are stacked vertically; they can be viewed as two-dimensional vertical reflection profiles of the subsurface stratigraphy or other buried features. When the object is in front of the antenna, it takes more time for the radar waves to bounce back to the antenna. As the antenna passes over the object, the reflection time becomes shorter, and then longer again as it goes past the object. This effect causes the image to take the shape of a curve, called a ‘‘hyperbola”. This hyperbola is actually the image of a smaller object (like a pipe) located at the center of the curve (Figures 1a, 2a).

Two-dimensional continuous wavelet transform and Farshad-Sailhac wavelet function

The 2D-CWT of 2-D signal $f(x,y) \in L^2(R)$ can be given by:

$$W(a,b_x,b_y) = \frac{1}{a}\int_{-\infty}^{+\infty}\int_{-\infty}^{+\infty} f(x,y)\overline{\psi}\left(\frac{x-b_x}{a},\frac{y-b_y}{a}\right)dxdy \tag{1}$$

where, a, b_x, $b_y \in R^+$, $L^2(R)$, $\overline{\psi}(x,y)$, are scale and translation parameters, Hilbert space of 2-D wave functions having finite energy, the complex conjugate function of $\psi(x,y)$, respectively.

To determine the boundary from anomaly objects, and then estimate their size and position, Farshad-Sailhac complex wavelet function is used [9]. It is given by:

$$\psi^{(FS)}(x) = \psi^{(F)}(x) + i\psi^{(S)}(x) \tag{2}$$

where,

$$\psi^{(F)}(x) = \frac{4-2x^2}{\left(x^2+2^2\right)^{\frac{5}{2}}} - \frac{1-2x^2}{\left(x^2+1^2\right)^{\frac{5}{2}}} \tag{3}$$

 ISBN:

$$\psi^{(S)}(x) = Hilbert(\psi^{(F)}(x)) \quad (4)$$

The wavelet transforms modulus maxima (WTMM) method

In image processing, edge determination is a considerable task. According to image processing theory, the edges of image are areas with rapid change sharply of light intensity or colour contrast. For the space signal, like GPR data, the points where the amplitude of the signal quickly or suddenly changed is considered to the boundaries. The edge detection technique using the CWT is based on the locations of the maximum points of the CWT coefficients. Accordingly, the edge detection method using CWT is also called the "wavelet transform modulus maxima" [10]. To analyse GPR data using WTMM is the modern technique for the size and position detection of the buried objects.

The process for GPR data analysis using the wavelet transform and optimal algorithm

Step 1: Determining the position of the buried pipe.

After processing the raw data, a GPR section quite clear and complete was obtained.Performing 2-D CWT for GPR section using Farshad-Sailhac wavelet function.

Plotting the module contours of 2-D CWT coefficients with appropriate scale (a). The maximum point of the wavelet transform coefficients will be found. The horizontal and vertical coordinate of this point will be *bx* and *bt* respectively. The position of the buried pipe in the horizontal direction and the time for the radar waves to bounce back to the antenna will be detected by following equations:

$$x = bx \times \Delta x \quad (5)$$

$$t = bt \times \Delta t \quad (6)$$

Step 2: Determining the size of the buried pipe.

From the GPR section, an optimal data cutting layer (corresponding with *bt* in step 1) is chosen to analyze by the wavelet method.

Performing Farshad - Sailhac wavelet transform with GPR data is selected.

Changing the different scales (a) and repeating the multiscale CWT.

Plotting the phase contours of the CWT coefficients with different scales (a).

The left and right edge coordinates of the buried object will be found on the plot of wavelet phase contours and the size of the buried pipe will be estimated by:

$$D = (right\ edge\ coordinate - left\ edge\ coordinate) \times \Delta x \quad (7)$$

Step 3: Determining the depth of the buried pipe.

The Kirchhoff migration method combined with the minimum entropy and the maximum energy standards was used to determine the electromagnetic wave velocity (v) in the material.

The depth of the buried pipe will be detected by following equations:

$$z = v \times \frac{t}{2} \quad (8)$$

III. RESULTS AND DISCUSSION

Theoretical model

For feasibility test of the proposed method, many different theoretical models has been performed including: the cylinders made from various materials such as plastic, metal and concrete,… These cylinders are also designed in numerous dissimilar sizes and their structures are very close to the actual models buried in the distinct environment (from homogeneous to heterogeneous). The relative errors of size estimation from these models are acceptable from the calculus limits showing that the proposal technique is reliable. However, in this paper, only plastic cylinder model buried in heterogeneous environments is introduced for typical treatment results.

In this model, using antenna frequency 700 MHz, heterogeneous environment including three layers. The first layer, asphalt has thickness 0.2 m, σ = 0.001 mS/m, ε_r = 4.0, μ_r = 1.0, v_1 = 0.15 m/ns. The second layer, breakstone has thickness 0.4 m, σ = 1.0 mS/m, ε_r = 10.0, μ_r = 1.0, v_2 = 0.10 m/ns. The final one, clay soil has thickness 4.4 m, σ = 200 mS/m, ε_r = 16.0, μ_r = 1.0, v_3 = 0.07 m/ns. Underneath anomaly object is the plastic tube: σ = 1 mS/m, ε_r = 3, μ_r = 1.0, v' = 0.17 m/ns, inside contains the air, the center of the object is located at horizontal coordination x = 5.0 m and vertical coordination z = 1.05 m, inside pipe diameter d = 0.30 m, outside pipe diameter D = 0.32 m.

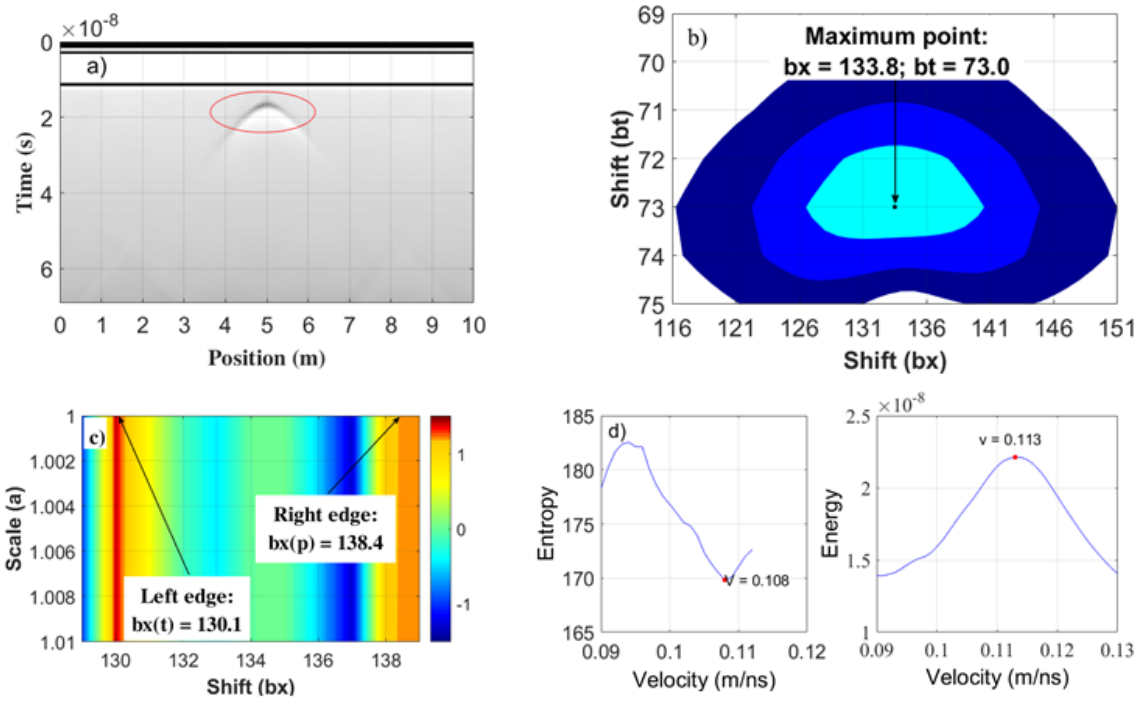

Fig. 1. *The graphs of the theoretical model. a) GPR section of the model, b) The module contour of 2-D CWT, c) The phase contour of the wavelet transform, d) The relation between entropy; energy and velocity.*

According to the results plotting of the module contour of 2-D CWT in the Fig. 1b, the maximum point of the wavelet transform coefficients is easily found at (bx = 133.8; bt = 73.0). In addition, the left and the right edge coordinates of the anomaly object are presented at 130.1; 138.4 respectively in the Fig. 1c. Moreover, the velocity is determined in

 ISBN:

the Fig. 1d. So, the position, size and depth of the pipe are estimated by the equation (5), (6), (7) and (8). The calculative results are represented in Table 1.

Table 1. *Interpretative results of typically theoretical model.*

Position	$x = 133.8 \times 0.03788 = 5.07\ m$	Relative error	*1.4%*
Size	$D = (138.4\text{-}130.1) \times 0.03788 = 0.31\ m$	Relative error	*3.1%*
Depth	$z = 0.11 \times (73.0 \times 0.25)/2 = 1.00\ m$	Relative error	*4.8%*

The calculative results in Table 1 illustrated that the detecting parameters of the pipe in the model buried in the heterogeneous environment having noticeably low error (1.4%, 3.1%, and 4.8% for position, size and depth determination respectively).

The accuracy of the proposed method is confirmed through the data analysis on typically theoretical model. The next job is going to the application of this technique to analyse the actual GPR data in some places of Can Tho City.

Actual data - The underground telecommunication tube

GPR data was recorded by Duo detector (IDS, Italia), using antenna at frequency of 700 MHz. The profile LZZ10032 was done at Mau Than Street, Ninh Kieu District, Can Tho City on Friday, September 21, 2018. Each measurement line on the ground went through anomaly object and the length of the profile was 4.70 m, with the step size of Δx = 0.02784 m. According to the information was provided by VNPT Can Tho, the size of the buried pipe is 0.23 m and it is located at horizontal coordination x = 3.40 m along the survey route and vertical coordination z = 0.32 m.

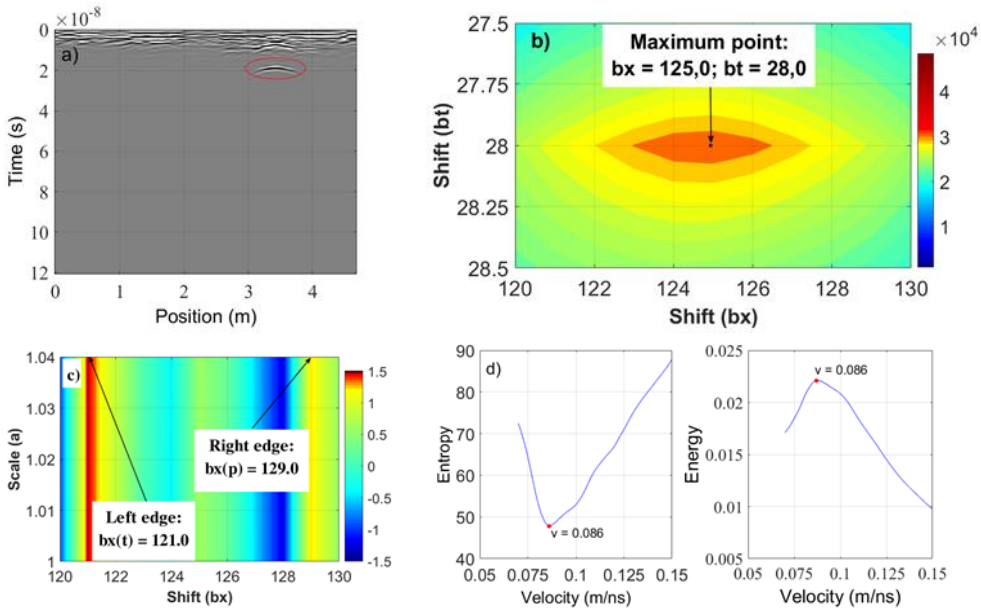

Fig. 2. *The graphs of the actual data. a) GPR section of the underground telecommunication tube data, b) The module contour of 2-D CWT, c) The phase contour of the wavelet transform, d) The relation between entropy; energy and velocity.*

As can be seen in the Fig. 2b and Fig. 2c, the maximum point of the wavelet transform coefficients locating at (bx = 125.0; bt = 28.0), the left and the right edge coordinates of the anomaly object are 121.0, 129.0 in turn. And the velocity is determined in

the figure 2d. Thus, the position, size and depth of the pipe are estimated by the equation (5), (6), (7) and (8). The calculative results are represented in Table 2.

Table 2. *Interpretative results of experimental model.*

Position	$x = 125.0 \times 0.02784 = 3.48\ m$	Relative error	*2.4%*
Size	$D = (129.0\text{-}121.0) \times 0.02784 = 0.22\ m$	Relative error	*4.3%*
Depth	$z = 0.086 \times (28.0 \times 0.25)/2 = 0.30\ m$	Relative error	*6.3%*

The GPR data analysis bases on CWT and optimal algorithm taken a major role for determination of the depth, location and size of the anomaly objects buried shallow in a heterogeneous environment, this could not be done by a radar machine itself. Then, for the next step, we taken out anomalies from the environment or put another pipeline into the ground. It is going to rather easier, saving constructive time and improving the economic efficiency.

From Table 1 and Table 2, it is easy to compare the relative error for computed position with depth and size of the buried pipe using the CWT with Farshad-Sailhac wavelet function and optimal algorithm. Due to the GPR attenuation when penetrating to the environment, depth and size errors is usually larger than error of position.

IV. CONCLUSION

The GPR data interpretation process using 2D-CWT with Farshad-Sailhac wavelet function and optimal algorithm for the determination of depth, position and the size of the anomaly objects has been established and applied successfully. The process to analyze a typically theoretical model and an experimental model have been tested quantily. The theoretical model built in this paper were linked very closely to the objects studied in practice in order to verify the reliability of the proposal method before applying on the real data. There relevant results indicated that using 2D-CWT contributes enhancing the interpretation efficiency for GPR data. If the researchers deeply combine the proposed technique and traditional methods for GPR interpretation, the identification of singularly bodies in shallow geologic study will become more effective.

REFERENCES

[1] Daniels D. J., Ground penetrating radar, The Institution of Electrical Engineers, UK, 2004, 752.

[2] Van N. T., and Giang N. V., Ground penetrating radar - Methods and applications, Vietnam National University Ho Chi Minh City Press, 2013, 222.

[3] Jamal B., Samer L., Mounir H., Imad L., Al-Qadi, and Kmel B., GPR signal de- noising by discrete wavelet transform, *Elsevier, NDT and E. International*, 2009, **42**, 696-703.

[4] Ouadfeul S., Aliouane L., Hamoudi M., Boudella A., and Eladj S., Multiscale analysis of geophysical signals using the 2-D continuous wavelet transform, wavelet transforms and their recent applications in biology and geoscience, Published by InTech, Croatia, 2012, 253-276.

[5] Ozdogan Y., and Stephen M. D., Seismic Data Processing, *Society of Exploration Geophysics*, 1987, 258-260.

 ISBN:

[6] Cook J. C., Proposed monocycle-pulse VHF radar for airborne ice and snow measurements. Journal of the American Institute of Electrical Engineers, *Transactions on Communication and Electronics*, 1960, **79**, 588-594.

[7] Moffatt D. L., Puskar R. J., A subsurface electromagnetic pulse radar, *Geophysics*, 1976, **41**, 506-518.

[8] Benson A. K., Applications of ground penetrating radar in assessing some geological hazards-examples of groundwater contamination, faults, cavities, *Applied Geophys.*, 1995, **33**, 177-193.

[9] Tin, D. Q. C., Dau, D. H., Interpretation of the geomagnetic anomaly sources in the Mekong Delta using the wavelet transform modulus maxima, *Work. on Capacity Build. on Geo. Tech. in Mineral Exp. and Assess. on Land, Sea and Island*, Ha Noi, 2016, 121-128.

[10] Mallat S., Hwang W. L., Singularity detection and Processing with Wavelets, *IEEE Transactions on Information Theory*, 1992, **38**(2), 617-643.

DEEP LERANING FOR WAVEFRONT CODING SYSTEM WITH RADIALLY SYMMETRIC PHASE MASK

Van Nhu Le[1,*], Van Sang Doan[2], Quoc Khanh Doan[1] and Thanh Hai Do[1]

[1]*Le Quy Don Technical University*

[2]*Naval Academy*

*E-mail: *levannhuktq@gmail.com*

Abstract. Wavefront coding system includes the combination of both optical system and digital processing to obtain a high-quality image on the big range of defocus. In this paper, we introduce a deep learning method into a wavefront coding system with a radially symmetric phase mask to obtain a high-quality image. A deep learning model based on U-Net neural network is built to train a set of high- and low-resolution images. Simulation results demonstrated that the proposed method can be used to achieve high-quality images for a wavefront coding system with a radially symmetric phase mask.

I. INTRODUCTION

In traditional optical imaging system design, the purpose is to provide a sharp image at the imaging plane. The image degrades quickly when object deviates from the best focus plane. Wavefront coding technology, which was proposed in [1], serves as an approach to extend the depth of field of incoherent diffraction-limited systems. Meanwhile it can restrain many kinds of aberrations to some extent, including spherical and chromatic aberration. By inserting a phase mask at the pupil plane, the Optical Transfer Function (OTF) and Point Spread Function (PSF) remain nearly invariant over a wide range of defocus. Some types of the PMs to increase the depth of field have been introduced. They can be separated into two kinds including: the radially symmetrical PMs and the asymmetrical PMs [2]. Some types of asymmetrical PMs are suggested to extend the depth of field, such as the cubic phase mask [3], the logarithmic phase mask [4], the root square phase mask [5], the exponential phase mask [6], the sinusoidal phase mask [7], the tangent phase mask [8], the polynomial phase mask [9]. When the asymmetrical PMs are used to place in the pupil plane of the imaging systems the recorded images are blurred. The digital processing should be employed to restore the final high-quality image. However, the image artifacts and SNR are both intrinsic problems in wavefront coding system with the asymmetrical PMs [10-12]. Some kinds of the radially symmetrical PMs to enhance the depth of field have been introduced, such as quartic phase mask (QPM) [13], logarithmic axicon [14], diffraction hybrid lens [15], and logarithmic asphere [16]. The radially symmetrical PMs have symmetrical and sharpness point spread function (PSF). When the radially symmetrical PMs are used to place the pupil plane of the imaging systems, the sharpness image can directly be acquired, while the digital processing should not be used. Additionally, there are not image artifacts over images of the radially symmetrical PMs.

Traditional approaches regard the optical system as a linear position invariant system in which noise is added. The PSF which models the blurred image in turn provides a prior knowledge for image deconvolution. Wiener filtering has been proved to be an effective

 ISBN:

way for retrieving sharp images [17,18]. As a premise, the noise level should be estimated first. In another way, iterative method like LucyRichardson algorithm (LR) improved the image quality on each iteration [19-21]. However, the iteration times and stopping criterion is difficult to determine. For both methods, the noise enhancement is a severe problem to be solved owing to a low spatial bandpass behavior. Attempts have been made to remove the background noise [22] by using a nonlinear processing scheme. The method succeeded in processing gray scale image.

In recent years, Convolutional Neural Networks (CNN) have made substantial advances in many computer tasks, such as image classification [23], object detection [24], and Semantic Segmentation [25]. What's more, Chao et al. [26] established links between an interpolated low resolution image and a super resolution one using a shallow CNN architecture without pooling layers. Zhang et al. [27] proposed CNN architecture for image denoising. For deblurring, [28] showed an improvement compared to other works.

In our work, we exploit the CNN of U-net model for restoring the degraded images in the imaging system with radially symmetric phase mask. By using the U-net model for restoring the degraded images, the imaging quality was improved better.

II. THE WAVEFRONT CODING TECHNIQUE

WFC as an optical-digital hybrid system usually used for increasing the depth of field. By placing an asymmetrical phase mask, the rays of light no longer converge as a point but a speckle. Over a large region of focus, we can obtain focus-insensitive sampled intermediate images. Different kinds of phase mask lead to different modulation effect to intermediate images. In this study, we take the classic QPM as example.

Assuming that the spatial frequency distribution of observed scene can be denoted as $O(u, v)$, the degradation model of a linear position invariant optical system is shown as:

$$G(u,v) = O(u,v) \times H_{\psi}(u,v) + N(u,v)\,, \tag{1}$$

where u and v are the normalized spatial frequencies, G denote the acquired signal, N is the additive noise. And H_{ψ} is the OTF for a given defocus ψ, which is expressed as:

$$\psi = \frac{\pi L^2}{4\lambda}\left(\frac{1}{f} - \frac{1}{d} - \frac{1}{d_0}\right), \tag{2}$$

where L is the radius of the aperture, f is the focal length, d and d_0 denote the object distance and image distance, λ is the light wavelength. Then, the OTF can be described as:

$$H_{\psi}(u,v) = \iint_S P(x+u, y+v) P^*(x-u, y-v)\,dxdy\,, \tag{3}$$

where P denotes the generalized pupil function, as shown in Eq. (4), and S is the area of the aperture.

$$P(x,y) = \begin{cases} \frac{1}{\sqrt{2}} \exp(i[\varphi(x,y) + \psi(x^2+y^2) & \text{if } x^2+y^2 \le 1 \\ 0 & \text{other} \end{cases}, \tag{4}$$

When the QPM is exploited in optical system, the phase function φ can be presented as:

$$\varphi(x,y) = a(x^2+y^2)^2 + b(x^2+y^2), \quad (5)$$

in which *a* and *b* are the phase parameters that determines the magnitude of phase deviation.

III. U-NET MODEL AND SIMULATION RESULTS

The procedure of image dataset generation U-net training is illustrated in Fig. 1. Accordingly, the dataset of blurred images with different defocus positions together with phase masks is generated from high-resolution images. So that the blurred images play a role in observation data and high-resolution images become label ones. The U-net is trained to convert the low-resolution images to reach the appropriate high-resolution ones. In order to update the weight values of the U-net, a root square loss function is applied.

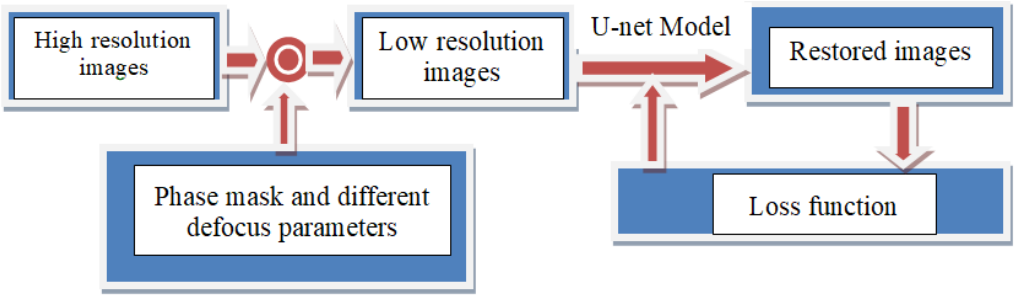

Fig. 1. *The layout for the proposed method. The image processing performs the simulation of image processing of the optical system. The optimal processing will perform the optimization of kernel parameters of U-net model.*

The structure of the U-net model is shown in Fig. 2, where we observe that U-net have many cascades creating two main parts: encoder and decoder. The encoder connects to the decoder by skip connections. The blocks consisting of convolution, ReLu and max pool layers are consecutively connected in the encoder part. The number of filter channels is increased from 64 to 2048. In the decoder part, the blocks have the sample structure; however, they use the opposite procedure. It means that the number of filter channels is decreased from 2048 to 64. It is worth noting that the filter size in convolution layers is designated by 3×3, and the stride in the max pool layers is assigned as (2,2).

In this paper, we use the phase mask parameters with QPM in as Ref. [2], *a*=17.65 and *b* = -14.6. The defocus range is set to ψ =-12 to ψ =12. In this paper, we use 1000 images to respond high-resolution images. Each high image will be generated eight blurred images in eight different positions over on range of defocus [ψ = -12, ψ =12]. As we have 8000 high-resolution images and 8000 low-resolution images. They will be used to optimize the kernel parameters of U-net model. The optimal processing is built by Matlab.

We test the effectiveness of optimal kernels by checking one any image without the optimal data. The images are shown in Fig. 3. The original image is shown in Fig. 3a. The image of the optical system with QPM is indicated in Fig. 3b. It is not difficult to see that

 ISBN:

the image quality of the proposed method is improved in comparison with the image of the optical system with QPM.

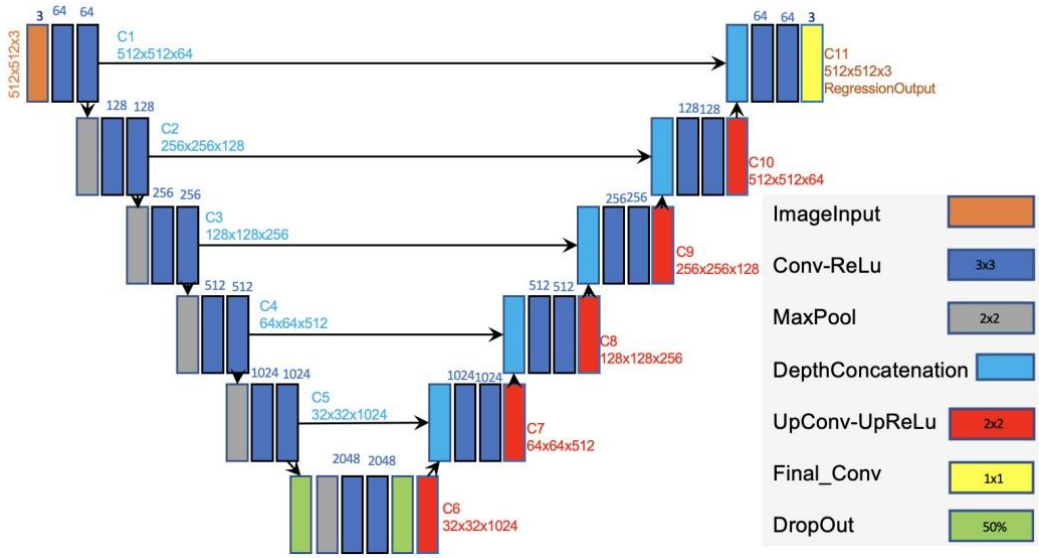

Fig. 2. *The U-net Model.*

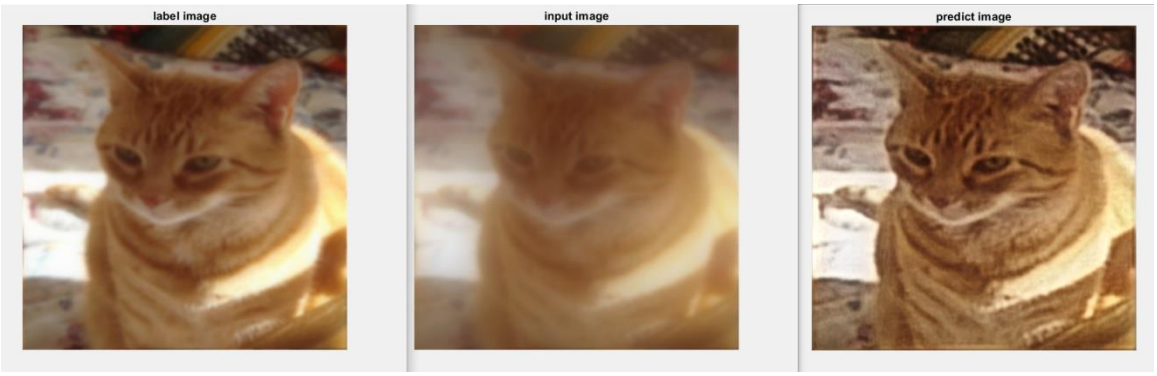

(a) (b) (c)

Fig. 3. *The image results: (a) the high-resolution image (label image), (b) the blurred image and (c) the restored image (predict image).*

IV. CONCLUSION

In this paper, we have been introduced the U-net model to obtain the high image of optical system with radially symmetric phase mask. The kernel parameters of the U-net model are optimized with the data set of high-resolution images and low-resolution images. The effectiveness of the proposed method is tested and shown. The simulation results demonstrated that the proposed method can be used to improve the image quality of optical system with radially symmetric phase mask. In the future, the experimental results will be shown.

ACKNOWLEDGMENTS. This work was supported by Funding of Hanoi Department of Science and Technology number grant: 01C-01/02-2021-3.

REFERENCES

[1] M. Larivere-Bastien, S. Thinault, *Opt. Lett.*, 2013, 38, 3830.

[2] Le X. Hoang, M. Pham, and H. Le, *Eur. Phys. J. D.*, 2019, **73**, 185.

[3] E. R. Dowski, Jr., W.T. Cathey, *Appl. Opt.*, 1995, **34**, 1859.

[4] L. V. Nhu, P. N. Nhue, L. H. Hai, *Commun. Phys.*, 2017, **27**, 45.

[5] V. Le, Z. Fan, N. Minh, S. Chen, *Opt. Eng.*, 2015, **54**, 2630.

[6] Q. Yang, L. Liu, J. Sun, *Opt. Commun.*, 2007, **272**, 56.

[7] H. Zhao, Q. Li, H. Feng, *Opt. Lett.*, 2008, **33**, 1171.

[8] V. Le, S. Chen, Z. Fan, *Opt. Lett.*, 2014, **39**, 2171.

[9] N. Caron, Y. Sheng, *Proc. SPIE*, 2007, **6832**, 68321G.

[10] S. Chen, V. N. Le, Z. Fan, H. C., *Tran, Opt. Eng*., 2015, **51**, 115103.

[11] M. Demennikov, A. R. Harvey, *Opt. Express*, 2010, **18**, 8207.

[12] P. Zammit, A. R. Harvey, G. Carles, *Optica*, 2014, **1**, 209.

[13] M. Xutao, W. Jinjiang, *Proc. SPIE*., 2013, **8907**, 89074H.

[14] J. Sochacki, S. Bara, Z. Jaroszewicz, A. Kolodziejczyk, *Opt. Lett.*, 1992, **17**, 7.

[15] D. Zalvidea, E.E. Sicre, *Appl. Opt*., 1998, **37**, 3623.

[16] W. Chi, N. George, *Opt. Lett.*, 2001, **26**, 875.

[17] Y. Feng, L. Zheng, and X. Zhang, *Optical Engineering*, 2008, **47**(1), 017006.

[18] J. W. Goodman, Introduction to Fourier optics, CA: Roberts and Company Publishers, 2005.

[19] V. N. Boddeti, and B. V. K. V. Kumar, *IEEE Transactions on Systems, Man, and Cybernetics - Part A: Systems and Humans*, 2010, **40**(3), 495-508.

[20] W. H. Richardson, *J. Opt. Soc. Amer*., 1972, **62**(1), 55-59.

[21] L. B. Lucy, *Astron. J.*, 1974, **79**, 745-754.

[22] R. N. Zahreddine, R. H. Cormack, C. J. Cogswell, *Applied Optics*, 2013, **52(**10), pp. D1-D11.

[23] K. Simonyan, and A. Zisserman, arXiv: 1409.1556, 2014.

[24] S. Ren, K. He, R. Girshick R, and J. Sun, *The Advances in Neural Information Processing Systems (NIPS)*, 2015, 91-99.

[25] J. Long, E. Shelhamer, T. Darrell, *IEEE Conference on Computer Vision and Pattern Recognition (CVPR)*, 2015, 3431-3440.

[26] C. Dong, C. C. Loy, K. He, and X. Tang, *IEEE Transactions on Pattern Analysis and Machine Intelligence*, 2016, **38(**2), 295-307.

[27] K. Zhang, W. Zuo, Y. Chen, D. Meng, and L. Zhang, *IEEE Trans. Image Process*., 2017, **26(**7), 3142- 3155.

[28] C. J. Schuler, M. Hirsch, S. Harmeling, and B. Schlkopf, *IEEE Trans. Pattern Anal. Mach. Intell*., 2016, **38**(7), 1439-1451.

 ISBN:

GASES TRANSPORT EQUATION WITH TEMPERATURE INVERSIONS IN THE ATMOSPHERE

Vu Ba Dung*

Hanoi University of Mining and Geology, Vietnam

*E-mail: *vubazung305@gmail.com*

Abstract. Normally, air temperature decreases with an increase in altitude. However, sometimes some layer in the atmosphere can form where the temperature increases with height. This is the temperature inversion. Temperature inversions have a great effect on air pollution. In this paper, based on the thermodynamics theory, gases transport equation with temperature inversions in the atmosphere is presented and discussed. Moreover, the equation are also applied to determine the flux of the carbon dioxide (CO_2) between the temperature inversion layer (IL) and its under layer (UL). The result has shown that in the atmosphere with temperature inversions, the CO_2-flux moves from the temperature inversion layer down to under layers. The reverse transport of carbon dioxide is major cause of the increase pollution of the CO_2 in the UL.

Keywords: *Temperature inversions, Gases transport equation, Mass flux of carbon dioxide.*

I. INTRODUCTION

Under normal conditions air temperature usually decreases with height. Temperature inversions, also called thermal inversion, in which a layer of cool air at the surface is overlain by a layer of warmer air. The temperature inversions play an important role in increasing air pollution. An inversion acts as a cap on the upward movement of air from the layers below. In the temperature inversion, the diffusion of dust, smoke, and other air pollutants (from UL up to IL) is not only limited, but also that can move from the IL down to the UL. Based on the irreversible thermodynamics theory, the equation of gas transport with temperature inversion can find out and apply to determine the carbon dioxide flux that goes from the IL down to the UL.

II. TEMPERATURE INVERSION AND AIR POLLUTION

Usually, in the atmosphere the air near the surface of the Earth is warmer than the air above it. The temperature inversion is the air temperature increases with an increase in altitude [1-4]. The temperature inversion tends to be only at the hundreds of feet height and it can be at a few thousand feet height. The temperature can be from 0.5 ^oC to 8.0 ^oC changed per 100 m changed altitude [2]. Especially, in the Antarctica, the temperature at the height of 10 m can be 25 ^oC greater than that at surface [3,4]. Temperature inversions have a great effect on air pollution because they change the dynamics of air movement, which prevents the convection of gases. Stated differently, the temperature inversion layer like an atmospheric lid or blanket, which traps air pollutants and allows their concentrations to increase. Some of the world's most notable pollution episodes have happened because of temperature inversions [5]: In December 1952, extreme pollution event in London dubbed the Great Smog of 1952 that estimated to have killed up to 12,000

people; 1966 New York City Smog, over Thanksgiving weekend in 1966, the layer of smog killed about 200 people; 2013 Beijing Smog, in January 2013, the pollution levels in north China and Beijing broke all records of the air pollution. The transport gases equation with temperature inversions in the atmosphere and its application is presented in this paper.

III. GASES TRANSPORT EQUATION WITH TEMPERATURE INVERSIONS

The kinetic theory of gases is a simple, historically significant classical model of the thermodynamic behavior of gases, with which many principal concepts of thermodynamics were established. The kinetic theory of gases is simple theory of irreversible thermodynamics, however, it can explain the macroscopic properties of gases, and treat well the transport phenomena in gases such as thermal conduction and mass diffusion.

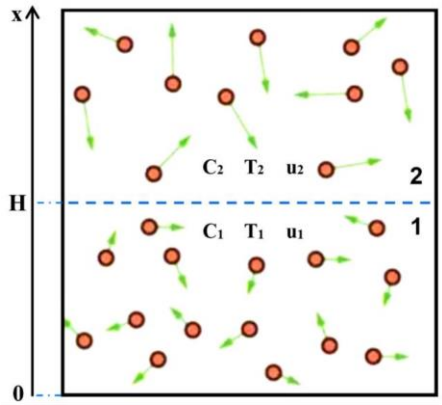

Fig. 1. *The model of gases transport in the atmosphere in which the concentrations and temperatures in 1-layer and 2-layer are different ($C_1 \neq C_2$ and $T_1 \neq T_2$).*

According to the kinetic theory of gases, for macroscopic description, the molecular transport flux between1-layer and 2-layer (Fig. 1) is the sum of two fluxes that oppositely together [6,7]:

$$J = J_1 - J_2 \tag{1}$$

where J_1 and J_2 are given by:

$$J_1 = \frac{C_1}{2} u_1; \quad J_2 = \frac{C_2}{2} u_2 \tag{2}$$

in which C_1 and C_2, u_1 and u_2 are gas concentration, thermal velocities in 1-layer (UL) and 2-layer (IL); J_1 and J_2 are the molecule flux that moves from 1-layer to 2-layer and from 2-layer to 1-layer. Assume the difference of concentrations C_1 and C_2, temperatures T_1 and T_2 (thermal velocities u_1 and u_2) in two areas are determined by the following expressions:

$$C_2 = \beta C_1 = \beta C \tag{3}$$

$$T_2 = \alpha^2 T_1 = \alpha^2 T; \quad u_2 = \alpha u_1 = \alpha u \tag{4}$$

$$C_2 = C_1 + \Delta C; \quad u_2 = u_1 + \Delta u \tag{5}$$

in which the coefficients α, β are positive and β > 1. Combining Eq. (3), (4), (5) we have:

 ISBN:

$$C_1 = \frac{\Delta C}{\beta - 1}; \ \Delta u = (\alpha - 1)u_1 \tag{6}$$

where $\Delta C = C_2 - C_1$ are proportional to the gradient of the concentration [6]:

$$\Delta C = \lambda \frac{\partial C}{\partial x} \tag{7}$$

in which the λ is characteristic length [6]. Combining equations (2) and (6), we have:

$$J = J_1 - J_2 = \left(\frac{C_1}{2} - \frac{\alpha C_1 + \alpha \Delta C}{2} \right) u \tag{8}$$

Substituting C_1 (in Eq. 6) and ΔC (in Eq. 7) into Eq. (8) and it becomes:

$$J = -D \frac{\partial C}{\partial x} \tag{9}$$

where D is the diffusivity which is determined by:

$$D = \frac{\lambda(\alpha\beta - 1)u}{2(\beta - 1)} \tag{10}$$

and thermal velocity u is determined by [7]:

$$u = \left(\frac{8kT}{\pi m} \right)^{1/2} \tag{11}$$

where k is the Boltzmann constant, m is molecular mass. The characteristic length λ equals to the free path in gases [7]:

$$\lambda = \frac{1}{\sqrt{2}\pi n d^2} \tag{12}$$

in which, n is the number density, d is the molecular diameter. Substituting Eq. (11) and (12) into Eq. (9) the gases transport equation becomes:

$$J = -\frac{k^{1/2}(\alpha\beta - 1)T^{1/2}}{\pi^{3/2} m^{1/2} n d^2 (\beta - 1)} \frac{\partial C}{\partial x} \tag{13}$$

Eq. (13) is the form of a diffusion equation with the diffusivity is given:

$$D = \frac{k^{1/2}(\alpha\beta - 1)T^{1/2}}{\pi^{3/2} m^{1/2} n d^2 (\beta - 1)} \tag{14}$$

when $T_2 > T_1$ ($\alpha > 1$), the Eq. (13) becomes the gases diffusion with temperature inversions in the atmosphere.

Eq. (13) and (14) can be applied to classify the CO_2-transport and determine the CO_2-flux with temperature inversions in the atmosphere.

IV. APPLICATION FOR CO_2 WITH TEMPERATURE INVERSIONS

For the CO_2 gas, we have: $m = 7.3\times10^{-26}$ kg; $d = 3.34\times10^{-10}$ m, $n = 2.7\times10^{25}$ m^{-3} [8], the CO_2-diffusivity D is given by:

$$D = 8.3\times10^{-7}\,\frac{(\alpha\beta-1)T^{1/2}}{\beta-1} \tag{15}$$

and CO_2-flux is determined by:

$$J = -8.3\times10^{-7}\,\frac{(\alpha\beta-1)T^{1/2}}{\beta-1}\frac{\partial C}{\partial x} \tag{16}$$

As the $T_2 > T_1$ ($\alpha > 1$), the equation (16) describes the CO_2-diffusion process with temperature inversions in the atmosphere. Based on Eq. (15), the CO_2-diffusion with temperature inversions can be classified into four types: the downhill diffusion, when $D > 0$; the uphill diffusion, when $D < 0$; the diffusion barrier, when $D = 0$ [9].

i) When $C_2 > C_1$ ($\beta > 1$), the diffusivity D is positive ($D > 0$), the CO_2-diffusion is the downhill, it means CO_2-flux moves from IL down to UL.

ii) When $C_2 < C_1$ ($\beta < 1$):

1. If α is large enough ($T_2 >> T_1$) to $\alpha\beta > 1$, the CO_2-diffusivity $D < 0$ and the uphill diffusion occurs for the CO_2, it means CO_2-flux moves from IL down to UL;
2. If α is small enough to $\alpha\beta < 1$, the CO_2-diffusivity $D > 0$ and the CO_2-diffusion is downhill, it means the CO_2-flux moves from UL up to IL;
3. If the α-value makes $\alpha\beta = 1$, the CO_2-diffusivity $D = 0$ and $J = 0$. This is the diffusion barrier of the CO_2.

When $T_1 = T_2$ (the temperature inversions do not occur), it mean $\alpha = 1$, and diffusivity (15) and the diffusion flux (16) become CO_2-diffusivity and CO_2-diffusion flux without the temperature inversion D_N and J_N:

$$D_N = 8.3\times10^{-7}T^{1/2} \tag{17}$$

and

$$J_N = -8.3\times10^{-7}T^{1/2}\frac{\partial C}{\partial x} \tag{18}$$

Applying for the CO_2-transport with temperature inversions over Ho Chi Minh City (HCM city), Vietnam in November, 2006 and Svalbard Fjords, Norway in Spring 2009. Tab. 1 is the value of the H, C_1, C_2, T_1, T_2 [1,11-15]. Substituting the value of the $T = T_1$, T_2, $C = C_1$, C_2, $\partial C/\partial x = (C_2 - C_1)/H$ into Eq. (15) ÷ (17), the CO_2-diffusivities D and D_N, the CO_2-diffusion fluxes J and J_N are determined (Table 2). Results show that:

i) In HCM city, both the CO_2-fluxes J and J_N are negative; it means both CO_2-fluxs move from IL down to UL. However, CO_2-flux J with temperature inversions is about 10 times greater than that J_N without temperature inversions. So, the CO_2-concentration in UL with temperature inversions increases 10 times more than that without temperature inversions.

ii) In Svalbard, the CO_2-fluxes J are negative (the CO_2-fluxs moves from IL down to UL). But, J_N is positive (the CO_2-fluxs moves from UL up to IL). It means the CO_2-concentration in UL increases strongly with temperature inversions, and decreases without temperature inversions.

 ISBN:

Table 1. *The height (H) of IL, the concentrations (C_1 and C_2), the temperatures (T_1 and T_2) in the UL (1-layer) and IL (2-layer) over HCM city and Svalbard.*

Place	**H** (m)	$\mathbf{C_1}$ (mgm^{-3})	$\mathbf{C_2}$ (mgm^{-3})	$\mathbf{T_1}$ (K)	$\mathbf{T_2}$ (K)
HCM City [1,11,12]	2000	688	693	297	303
Svalbard [13-15]	54	696	695.9	258	259

Table 2. *Calculated result of the α and β, the diffusivity D and D_N, the diffusion flux J and J_N of the carbon dioxide over HCM city and Svalbard.*

Place	**D** (m^2m^{-1})	**J**($mgm^{-2}s^{-1}$)	$\mathbf{D_N}$ ($mgm^{-2}s^{-1}$)	$\mathbf{J_N}$ ($mgm^{-2}s^{-1}$)
HCM city	$1.67x10^{-4}$	$-4.18x10^{-7}$	$1.43x10^{-5}$	$-3.56x10^{-8}$
Svalbard	$-1,33x10^{-3}$	$-2.46x10^{-6}$	$1.33x10^{-5}$	$2.46x10^{-8}$

Thus, the CO_2-concentration in the UL with the temperature inversions can increase up to thousands times more than that without the temperature inversions.

V. CONCLUSIONS

The gases transport equation with the temperature inversions can be determined by the irreversible thermodynamics theory. The gases-transport equation with the temperature inversions is the form of the diffusion equation with diffusivity can be positive, negative, and equals zero. Gases transport equation can be applied to calculate the CO_2-flux with the temperature inversions in atmosphere. Calculated result has shown that: in the atmosphere with temperature inversions, the CO_2-flux moves from IL down to UL, which makes CO_2-concentration in UL increase up to hundreds times more than that without the temperature inversions. The gases transport by the diffusion mechanism is the major cause of the increase of air pollution with temperature inversions in atmosphere.

REFERENCES

[1] M. Nodzu, Shin-Ya Ogino, Y. Tachibana, M. Yamanaka, *J. Climate*, 2006, **19**(13), 3307-3319.

[2] S. L. Smith, and P. Philip Bonnaventure, *Arctic, Antarctic, and Alpine Research*, 2017, **49**(1), 173-185.

[3] S. Bourne, U. Bhatt, J. Zhang, R. Thoman, *Atmospheric Research*, 2010, **95**, 353.

[4] P. Baas B. van de Wiel, E. van Meijgaard, E. Vignon, C. Genthon, S. van der Linden, *Q. J. R. Meteorol Soc*., 2019, **145**, 930-946.

[5] D. Smith, Temperature Inversions. *https://learn.kaiterra.com/en/air-academy/temperature-inversions-weather-air-pollution*, 2020.

[6] K. Olah, *Periodica Polytecnica Chem. Eng*., 2005, **49**(2), 91.

[7] A. William, Physical Chemistry of Gas-Liquid Interfaces, Elsevier, 2018, 195-243.

[8] S. Anwar, J. Carroll, Carbon Dioxide Thermodynamic Properties Handbook, New Jersey-USA: John Wiley & Sons, 2016.

[9] V. B. Dung, T. B. Tuan, *Indian J. Phys.*, 2021. Doi: 10.1007/s12648-021-02167-1.

[10] X. Lin, et al, *Atmos. Chem. Phys.*, 2018, **18**, 9475.

[11] L. Cao, et al, *Remote Sens*., 2019, **11**, 94.

[12] https://www.co2.earth/ monthly-co2.

[13] M. Remaud, M. F. Chevallier, A. Cozic, X. Lin, and P. Bousquet, *Geosci. Model Dev*., 2018, **11**, 4489-4513.

[14] L. Cao, X. Chen, C. Zhang, A. Kurban, J. Qian, T. Pan, Z. Yin, X. Qin, F. Ochege, and P. De Maeyer, *Remote Sens*, 2019, **11**, 94.

[15] T. Vihma, T. Kilpelainen, M. Manninen, A. Sjoblom, E. Jakobson, T. Palo, J. Jaagus, and M. Maturilli, *Advances in Meteorology*, 2011, 1-14.

 ISBN:

THE EFFECTS OF Ge GROWTH TEMPERATURE ON THE STRUCTURAL PROPERTIES OF Ge/Mn5Ge3/Ge(111) SYSTEM

Le Thi Giang*, Nguyen Thi Dung

Hong Duc University, 565 Quang Trung Street, Dong Ve Ward, Thanh Hoa City, Vietnam

*E-mail: *lethigiang@hdu.edu.vn*

Abstract. We report on the structural properties of Ge/Mn_5Ge_3/Ge system when epitaxial growing of Ge. The results indicate that a small amount of Mn atoms diffuse into the layer, and another amount of Mn atoms can leave the layers and floats upward during the Ge growth. Mn can then act as a surfactant during Ge growth along the (111) orientation. The Mn segregation length and also the behavior of Mn atoms incorporated in the Ge layers are found to depend on the growth temperature. At a low growth temperature, a short segregation length is observed but the Ge layer and the interface Ge/Mn_5Ge_3 becomes rough. At the intermediate temperature range, the interfaces are little disturbed and also reveal the traces of Mn diffused in the Ge layer. At high temperature, segregated Mn atoms can diffuse into the buffer layer to form the Mn-rich precipitates, and also can react with Ge to form Mn_5Ge_3 which floated at the Ge growth front.

Keywords: *Mn_5Ge_3; Germanium overgrowth; Mn – segregation; GeMn multilayers.*

I. INTRODUCTION

Spintronics technology has been developing rapidly since the giant magnetoresistance effect was discovered in 1988 [1,2]. The application of spintronics is broad and interdisciplinary, from spin-valve structures in hard disk readers to applications in magnetic sensors for molecular detecting in biology and medicine. The realization of such devices requires the combination of materials science and advanced technology. Ferromagnetic semiconductors are promising materials and have been attracting a great deal of research attention [3-8]. The compatibility with CMOS (Complementary Metal-Oxide-Semiconductor) microelectronics technology and the ability to integrate into modern electronic components are extremely valuable properties of these materials.

Among numerous ferromagnetic semiconductors, Diluted Magnetic Semiconductor (DMS) is considered the most ideal material for spintronics applications. However, the successful fabrication of a high Curie temperature (T_C) DMS encounters many obstacles [9,10]. Therefore, recent research efforts have focused on the synthesis of ferromagnetic compounds by epitaxial growth [11,12]. Among these compounds, Mn_5Ge_3 has received special interest because it exhibits ferromagnetic ordering at room temperature [13], has high spin polarization [14], and can grow epitaxially on the Ge(111) substrate [15]. Previous studies have also demonstrated that the Mn_5Ge_3/Ge interface acts as a Schottky junction [16,17]. This opens the way for spin injection into group IV semiconductors via Schottky barrier based on the tunneling effect without depositing an additional oxide barrier as before.

To be able to fabricate Ge/Mn_5Ge_3/Ge multilayer films for applicating in spin valves or in the structures exhibiting GMR effects, the first requirement is to achieve the epitaxial

growth of Ge on the Mn_5Ge_3 film. Meanwhile, the diffusion of Mn atom is a central phenomenon and one of the challenges that must be overcome to ensure the performance and reliability when the material is applied in spintronics devices. Among the parameters that affect this phenomenon, temperature is an important one as the diffusion length is exponentially dependent on temperature. Therefore, in this paper, we focus on studying the influence of Ge overgrowth temperature on the formation of Ge/Mn_5Ge_3/Ge(111) multilayer thin films. From there, it is possible to get an overview of the diffusion and segregation of Mn atom during the Ge deposition on Mn_5Ge_3/Ge heterojunction films. We choose to synthesis samples at three temperatures: 250 ^oC, 350 ^oC and 450 ^oC. This temperature range was chosen because 450 ^oC is the upper limit of the Mn_5Ge_3 compounds formation temperature in the phase diagram and at the temperature below 250 °C, the films often get risk of poor quality Ge layer formation [18].

II. EXPERIMENTS

The films in this study were deposited by molecular beam epitaxy (MBE) with a lower pressure of 1×10^{-10} Torr. The MBE chamber is equipped with high-energy reflected electron diffraction (RHEED) device to monitor the epitaxial growth and substrate surface cleanness. The Mn_5Ge_3/Ge(111) heterostructures were obtained by depositing Mn at room temperature on a Ge(111) substrate followed by annealing up to 450 °C. The thickness of the Mn_5Ge_3 film ranges from 10-30 nm to ensure a good epitaxial layer and smooth surface before depositing the Ge layer. The Ge growth rate determined by the RHEED intensity fluctuations is ~3.3 nm/min. The substrate temperature is measured with a thermocouple in contact with the back of the substrate.

Transmission electron microscopy (TEM) operating at 300 KeV with a resolution of 1.7 Å was used to investigate the structure of the films. Another ultra-high vacuum system equipped with low-energy electron diffraction and Omicron room-temperature scanning tunneling microscope (STM) was also used to monitor the film surface structure during the development first atomic layers of these films.

III. RESULTS AND DISCUSSION

Ge layer growth at 250 °C

In this case, more than 60 nm Ge was deposited at 250 °C. Beyond 6 nm of deposited Ge, the RHEED diagrams evolve from the rods to the diffraction spots which reflect a three-dimensional growth. This means that the surface becomes very rough and the incident electrons are diffracted in transmission through the roughness of the surface. In addition, the RHEED signature of the Mn_5Ge_3 surface has been replaced by another surface whose diffraction pattern can be attributed to that of Ge. Indeed, the same diagram where the double diffraction spots in the direction [1-10] and [11-2] are present has been reported in the growth of Ge nanowires on Ge (111) by the Vapor-Solid Liquid (VSL) mechanism in MBE: this is a diffraction pattern characteristic of a rough surface of Ge(111) orientation [19]. This remark seems to be reasonable because the new deposited

 ISBN:

Ge layer must take the same hexagonal surface structure of Mn_5Ge_3 in order to minimize the energy of the system, which assumes that the direction of Ge growth follows the direction [111].

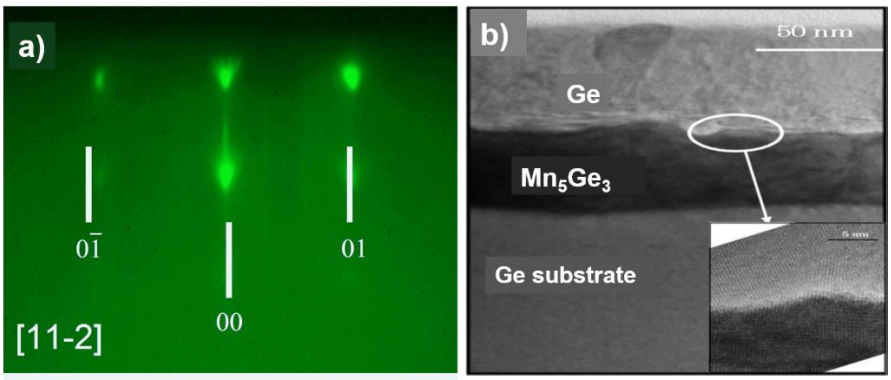

Fig. 1. *The RHEED patterns taken along [11-2] (a) and TEM cross-section (b) of a sample after deposition of Ge on Mn_5Ge_3 at 250 ^oC. The inset is a high resolution TEM image of the interface area.*

The structure of the Ge/Mn_5Ge_3/Ge(111) film shown in Figure 1b exhibits two prominent features related to the Ge layer. First, the Ge layer exhibits relatively many structural defects and contains some clusters. This demonstrates that during Ge deposition, part of Mn migrates upward towards the growth direction and acts as a surfactant, while another part of Mn is incorporated inside Ge layer, leading to the formation of Mn-rich clusters. The incorporation of elements with surfactant properties within the upper growth layers is a common effect and has been observed for most atoms of the surfactant during epitaxial growth. [20,21]. Second, the interface between the Ge coating and the Mn_5Ge_3 film became much rougher than that of the original Mn_5Ge_3 surface (reconfirming the information obtained from the RHEED image in Fig. 1a). Thus, the interface roughness, the presence of defects as well as those of Mn-rich clusters can be seen clearly. These properties are a direct consequence of the segregation of Mn from the Mn_5Ge_3 compound during the evolution of the Ge layer.

Ge layer growth at 350 °C

Growing the Ge coating at an intermediate temperature of 350 °C is also an interesting case to study the dependence of diffusion on temperature. During the deposition to the end, the diffraction plots as shown on the RHEED (Fig. 2a) show the complex evolution of Ge on the film: the main diffraction rods of a Mn_5Ge_3 surface still exist with markedly reduced intensity and additional polycrystalline diffraction rings. It means that the Ge layer still retains the structure of Mn_5Ge_3 and maybe some other GeMn compounds are formed.

The TEM image in Fig. 2b shows that the interface is less disturbed than in the case of deposition at 250 ^oC. In addition, it also shows traces of Mn scattered in the Ge layer. High-resolution TEM image of the interface area between the Mn_5Ge_3 layer and the Ge coating once confirmed the polycrystalline structure of the film. Thus, at this deposition temperature, structural analysis still shows the segregation of Mn from Mn_5Ge_3 and diffusion into the Ge layer.

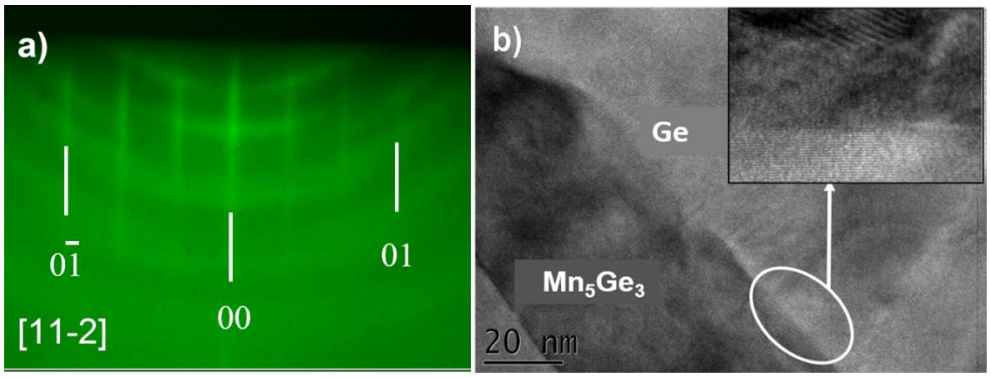

Fig. 2. *RHEED pattern taken along the [11-2] direction (a) and general cross-section TEM image (b) of the film after depositing ~60 nm Ge onto the Mn_5Ge_3/Ge(111) heterostructure at 350 °C. The inset is a high resolution TEM image of the interface area.*

Ge layer growth at 450 °C

Observation of the RHEED images up to the end of the deposition indicates that the growth mode is layer by layer with the presence of the diffraction rods in directions [11-2]. Surface diffraction rods surprisingly persist up to 60nm thickness of deposited Ge.

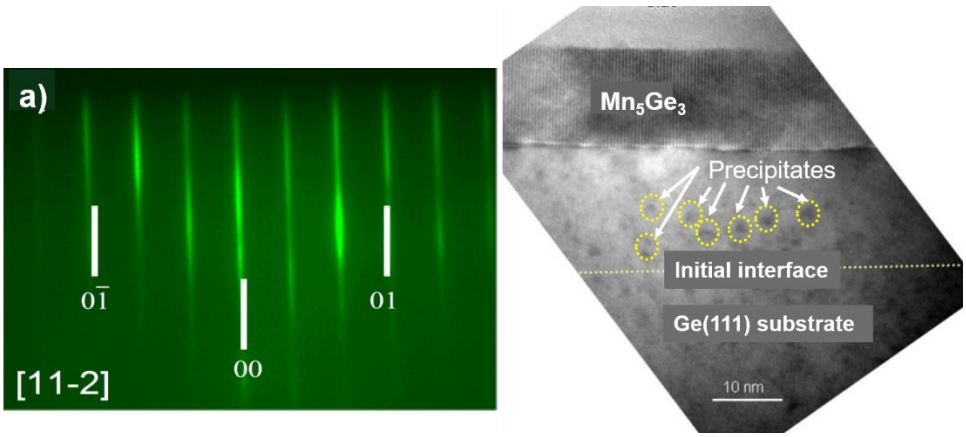

Fig. 3. *RHEED pattern taken along the [11-2] direction (a) and general cross-section TEM image (b) of the film after depositing ~60 nm Ge onto the Mn_5Ge_3/Ge(111) heterostructure at 450 °C.*

Figure 3b shows the cross-section TEM image corresponding to 60 nm Ge deposited on Mn_5Ge_3 at 450 ^oC. It turned out that the 60 nm of deposited Ge is not observed and that the surface layer is the Mn_5Ge_3 phase. Indeed, the transmission diffraction image enabled us to confirm this phase (image not available). Another feature revealed by the TEM image is the presence of precipitates implanted in the Ge layer. These precipitates can be Mn-rich phases and their dispersion is quite large (in the buffer layer and in the substrate). The thickness study also shows that the thickness of the buffer layer has been adjusted (increased) from its initial thickness before the deposition of Ge. All these observations lead to the conclusion that the diffusion and segregation of the entire Mn_5Ge_3 layer towards the surface took place throughout the deposition. More interestingly, the TEM image also evokes the phenomenon of Mn diffusion towards the buffer layer, which forms a layer of Mn doped Ge located under the Mn_5Ge_3 layer. In short, the thickness of the buffer layer

 ISBN:

increases and there are traces of Mn throughout the layer. The mechanism of this diffusion will be discussed in the next section.

STM study of the early stages of Ge adsorption at 450 ^oC and 250 ^oC

In order to understand what happens during the first stage of Ge deposition on the surface and how Mn atoms float upward to the surface, we conducted the STM studies under ultra-high vacuum for Ge growth at these two temperatures. The STM images were acquired every two minutes of Ge deposition, the flux of which is calibrated at about 1-2 monolayers/min. First, the Mn_5Ge_3 surface is characterized by a hexagonal lattice in the shape of a honeycomb, which studies in STM and theoretical simulation have shown previously [22]. Obtaining this surface corresponds to a bias of -0.85V and a tunnel current of 0.6 nA.

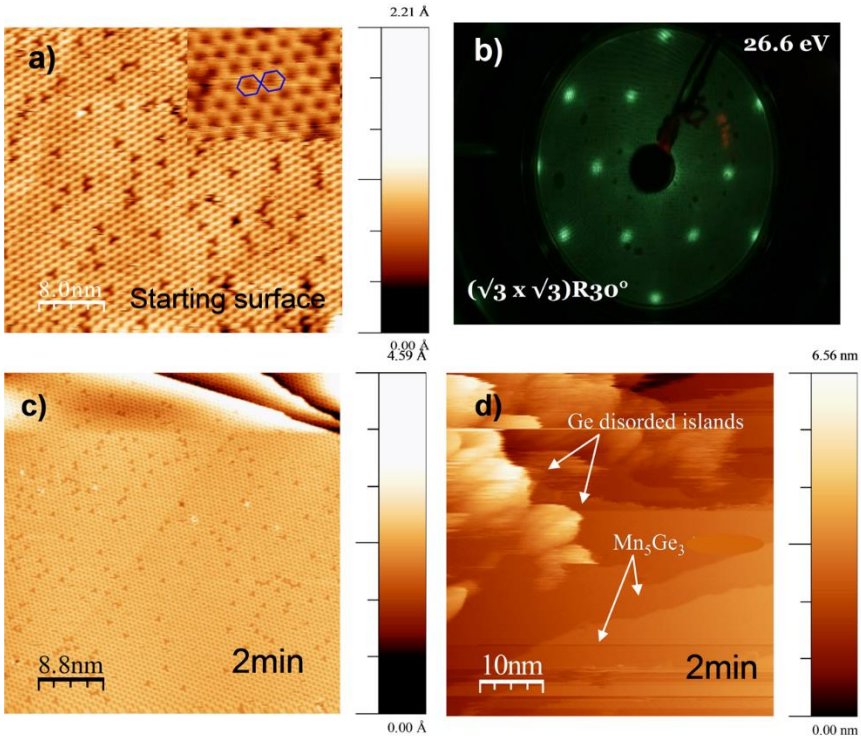

Fig. 4. *STM images of the Mn_5Ge_3 starting surface and its corresponding LEED diffraction pattern (a, b). Figures (c, d) represent the surfaces after 2min deposition of Ge at 450˚C (c) and at 250˚C (d).*

The results show that, at 450 ^oC, the hexagonal structure of the initial surface predominates throughout the Ge deposition up to a fairly large thickness. It seen that the defects due to the lack of Mn atoms are more and more numerous when the quantity of Ge deposited is increased (the defect densities are 6.3×10^{12} cm^{-2} and 8.9×10^{12} cm^{-2} after 0 min and 2 min of Ge deposition respectively). This network of defects seen to be the origin of the step bunching formation for greater thicknesses, compared to the large terraces of a Mn_5Ge_3 surface without Ge deposit that we observe in all our acquisitions. Regarding the Ge deposition at 250 ^oC, STM images indicate a disturbed texture of the surface which exhibits high roughness and Ge-rich areas. It is difficult to form a hexagonal structure of the film at low voltages, because the electron density of the surface decreases and the

material no longer exhibits metallic properties. It is therefore a change from the metallic character of the surface to the semiconductor. In this case, when Ge deposition started about 2 min, the membrane surface no longer showed crystal structure, but instead appeared islands (Figure 4d). Finally, the electronic contribution of the Mn_5Ge_3 layer completely disappeared when the thickness of the deposited Ge layer reached a certain value.

Combining structural and surface analyzes, we can summarize what happens during the deposition of Ge on the Mn_5Ge_3 surface as follows. Starting from the Mn_5Ge_3/Ge(111) surface which is initially characterized by a resurfacing ($\sqrt{3}\times\sqrt{3}$) R30 is rich in Mn [22]. Upon Ge deposition on the surface, one or even several Mn monolayers can leave the Mn_5Ge_3 surface and diffuse towards the surface along the Ge growth direction. This phenomenon, called the surface effect, has been modeled for the Ge-Mn system. Theoretical calculations have shown that the Mn atoms tend to diffuse by the mechanism of jumping over the interstitial sites present in the Ge matrix. The transition phenomenon of Mn atom in the Ge-Mn system has been reported in previous studies [23,24]. Based on the total energy calculation, Zhu et al. [24] predicted that in the Ge [001] orientation, Mn can act as a surfactant, while on Ge(111), it can easily diffuse into the volume. The obtained results show that along the (111) orientation of Ge, part of the Mn atom diffuses deep into the volume to reduce the binding energy [24] and another part moves towards the surface and becomes active as a surfactant.

It is worth noting that in the TEM resolution we did not observe any decrease in the thickness of the Mn_5Ge_3 layer before and after the deposition of the Ge layer. This demonstrates that only excess Mn atoms on the Mn_5Ge_3 surface leave the original Mn_5Ge_3 layer. The reactivity between Mn and Ge depends on the deposition temperature: for a temperature of 250 °C, the Mn atoms are likely to be uniformly distributed across the Ge layer, possibly in both interstitial and alternative positions. At this temperature, Mn_5Ge_3 crystals are not formed inside the Ge layers, as shown in Fig. 1b. For samples deposited at 450 ^{o}C, a layer of Mn_5Ge_3 segregated to the surface as deposition took place and Mn atoms diffused deep into the buffer layer. It shows that the diffusion and separation length of Mn is greatly increased compared to the case of Ge deposition at 250 °C.

IV. CONCLUSION

In summary, from combining structural analysis methods of multilayer films upon depositing of the Ge layer on top of the Mn_5Ge_3/Ge heterostructure, we have provided evidence that Mn atom acts as a surfactant during Ge deposition along the (111) direction. The separation length of Mn is shown to depend on the deposition temperature: at low deposition temperatures, a short separation length is observed but the surface becomes rough. At high temperature, the Mn_5Ge_3 layer is formed and moves towards the surface replacing the Ge layer. Thus, to fabricate Ge/Mn_5Ge_3/Ge multilayer films for spintronics applications, it is necessary to find solutions to suppress or reduce Mn separation to obtain high quality multilayer films.

 ISBN:

ACKNOWLEDGMENTS. The authors thank colleagues at Interdisciplinary Center of Nanoscience of Marseille (CINaM-CNRS), Aix-Marseille University, France for their technical helps and fruitful discussions.

REFERENCES

[1] G. Binasch, P. Grunberg, F. Saurenbach and W. Zinn, Enhanced magnetoresistance in layered magnetic structures with antiferromagnetic interlayer exchange, *Phys. Rev. B*, 1989, **39**, 4828-4838.

[2] M. N. Baibich, J. M. Broto, A. Fert, V. D. Nguyen, F. Petroff, P. Etienne, G. Creuzet, A. Friederich and J. Chazelas, Giant magnetoresistance of Fe(001)/Cr(001) magnetic superlattices, *Phys. Rev. Lett.*, 1988, **61**, 2475-2486.

[3] R. Kalvig, E. Jedryka, M. Wojcik, M. Petit and L. Michez, Selective modification of the unquenched orbital moment of manganese introduced by carbon dopant in epitaxial $Mn_5Ge_3C_{0.2}$/Ge(111) films, *Phys. Rev. B*, 2021, **101**, 094401-094406.

[4] S. F. Olive-Méndez, M. Petit, A. Ranguis, V. Le Thanh, and L. Michez, From the very first stages of Mn deposition on Ge(001) to phase segregation, *Crystal Growth & Design*, 2018, **18**(9), 5124-5132.

[5] S. F. Olive-Méndez, L. A. Ricardo, L. A. Jesús Ponce-Ruiz and T. J. Holguín-Momaca, High anisotropy on epitaxial C-doped Mn_5Ge_3 thin films grown on Ge(001), *Appl. Phys. Lett.*, 2018 **113**, 112408-112416.

[6] T. G. Le and M. T. Dau, Vertical self-organization of $Ge_{1-x}Mn_x$ nanocolumn multilayers grown on Ge(001) substrates, *Mod. Phys. Lett. B*, 2016, **30**, 1650269(1)-1650269(7).

[7] T. G. Le, Direct structural evidences of epitaxial growth $Ge_{1-x}Mn_x$ nanocolumn Bi-layers on Ge(001), *Mat.Sci. and App.*, 2015, **6**, 533-538.

[8] T. G. Le, V. Le Thanh, L. Michez, The effect of carbon on structural and magnetic properties of $Ge_{1-x}Mn_x$ nanocolumns, *Bull. Mater. Sci.*, 2020, **43**, 103.

[9] A. Stroppa, S. Picozzi, and A. Continenza and A. J. Freeman, Electronic structure and ferromagnetism of Mn-doped group-IV semiconductors, *Phys. Rev. B*, 2003, **68**, 155203-155210.

[10] Y. D. Park, A. T. Hanbicki, S. C. Erwin, C. S. Hellberg, J. M. Sullivan, J. E. Mattson, T. F. Ambrose, A. Wilson, G. Spanos, and B. T. Jonker, A group-IV ferromagnetic semiconductor: Mn_xGe_{1-x}, *Science*, 2002, **295**, 651-662.

[11] A. Spiesser, I. Slipukhina, M. T. Dau, E. Arras, V. Le Thanh, L. Michez, P. Pochet, H. Saito, S. Yuasa, M. Jamet and J. Derrien, Control of magnetic properties of epitaxial $Mn_5Ge_3C_x$ films induced by carbon doping, *Phys. Rev. B*, 2011, **84**, 165203-165208.

[12] M. Petit, M. T. Dau, G. Monier, L, Michez, X. Barre, A. Spiesser, V. Le Thanh, A. Glachant, C. Coudreau, L. Bideux, and C. Robert-Goumet, Carbon diffusion and reactivity in Mn_5Ge_3 thin films, *Phys. Status Solidi C*, 2012, **9**, 1374-1380.

[13] Y. Tawara and K. Sato, On the magnetic anisotropy of single crystal of Mn_5Ge_3, *J. Phys. Soc. Japan*, 1963, **18**, 773-778.

[14] P. R. Panguluri, C. Zeng, H. H. Weitering, J. M. Sullivan, S. C. Erwin and B. Nadgorny, Spin polarization and electronic structure of ferromagnetic Mn_5Ge_3 epilayers, *Phys. Status Solidi B*, 2005, **242,** R67.

[15] V. Le Thanh, A. Spiesser, M. T. Dau, S. F. Olive-Mendez, L. A. Michez and M. Petit, Epitaxial growth and magnetic properties of Mn_5Ge_3/Ge and $Mn_5Ge_3C_x$/Ge heterostructures for spintronic applications, *Adv. Nat. Sci.: Nanosci. Nanotechnol*., 2021, **4**, 043002-043010.

[16] A. Sellai, A. Mesli, M. Petit, V. Le Thanh, D. Taylor and M. Henini, Barrier height and interface characteristics of Au/Mn_5Ge_3/Ge (111) Schottky contacts for spin injection, *Semicond. Sci. Technol.*, 2012, **27**, 035014-035020.

[17] T. Nishimura, O. Nakatsuka, S. Akimoto, W. Takeuchi and S. Zaima, Crystalline orientation dependence of electrical properties of Mn Germanide/Ge(111) and (001) Schottky contacts, *Microelectron. Eng.*, 2011, **88**, 605-612.

[18] A. B. Gokhale and R. Abbaschlan, The Ge-Mn (Germanium-Manganese) system, *Bulletin of Alloy Phase Diagrams*, 1990, **11**, 460-468.

[19] M. T. Dau, M. Petit, A. Watanabe, L. Michez, S. Olive Mendez, R. Baghdad, V. Le Thanh, and C. Coudreau, Growth of germanium nanowires on silicon(111) substrates by olecular beam epitaxy, *Journal of Nanoscience and Nanotechnology*, 2011, **11**, 4288-4296.

[20] M. Copel, M. C. Reuter, E. Kaxiras and R.M. Tromp, Surfactants in epitaxial growth, *Phys. Rev. Lett*., 1989, **63**, 632-638.

[21] N. Grandjean, J. Massies and V. H. Etgens, Delayed relaxation by surfactant action in highly strained III-V semiconductor epitaxial layers, *Phys. Rev. Lett.*, 1992, **69**, 796.

[22] C. Zeng, W. Zhu, C. Steven, Z. Zhang, H. H. Weitering, Initial stages of Mn adsorption on Ge(111), *Phys. Rev. B*, 2004, **70**, 205340-205244.

[23] C. Zeng, Z. Zhang, K. van Benthem, M. F. Chisholm, and H. H. Weitering, Optimal doping control of Mmagnetic semiconductors via subsurfactant epitaxy, *Phys. Rev. Lett.*, 2008, **100**, 066101-066106.

[24] W. Zhu, H. H. Weitering, E.G. Wang, E. Kaxiras, and Z. Zhang, Contrasting growth modes of Mn on Ge(100) and Ge(111) surfaces: Subsurface segregation versus Intermixing, *Phys. Rev. Lett.*, 2004, **93**, 126102-126107.

 ISBN:

MODEL AND RESULTS OF THE GRADIENT METHOD IN GRAVITY DATA PROCESSING

Duy Hoang Dang[1,2,3*], Nghia Huu Pham[1,2,4]

[1]*Department of Geophysics, Ho Chi Minh City University of Science, Vietnam*

[2]*Vietnam National University, Ho Chi Minh City, Vietnam*

[3]*Loc Ninh High School, Binh Phuoc Province, Vietnam*

[4]*Long An College, Long An Province, Vietnam*

*E-mail: *duyhoangdang2309@gmail.com*

Abstract. The normalized full gradient method is used in deep structural studies such as oil and ore field identification with relatively high accuracy. This study performs the processing of gravity documents by creating theoretical models combined with algorithms in Matlab software for the purpose of improving the accuracy of the results. Usually, the actual measurement results are discrete values. The generation of the curve from the corresponding Fourier series with attention to the coefficient N plays an important role in determining the normalized gradient and giving the research results. The models are set up to find out the results and verify before putting the actual data in. Actual data is measured in an area of Thailand where the oil field is located.

Keywords: *Gravity method, Gravity gradient*.

I. INTRODUCTION

Today, geophysicists are interested in techniques for processing and interpreting gravity data using the Normalized Full Gradient method [1]. The advantage of this method is that it is fast and efficient to locate anomalies in deep structures, especially when geophysical data is incomplete or document logging is not good. Studies often use the Normalized Full Gradient method according to the line as well as the area to determine the special points that are specific to the foreign bodies causing the local field and then accurately determine the depth and characteristics object.

In this study, we use the Normalized Full Gradient method to apply the verification in gravity data in a small area of Thailand. To make this work, we followed these steps:

• Build theoretical models, write algorithmic programs to link discrete data into continuous curves. Equations with a continuum are created and use the Fourier transform for that continuum. Then find the maximum value of the gravity gradient.

• Apply to real data, draw isometric maps of data and draw conclusions.

II. METHODS

Gradient Method

The gravity anomaly Δg caused by an elongated circular cylinder is described by the equation:

$$\Delta g = V_z(x,0) = 2K\lambda\frac{h}{x^2+h^2}$$

The discrete data of the observed gravity anomaly are approximated by the Fourier series [2], depending on the observed coordinates x along the measuring line and the depth z of this line, here we consider the series with finite order of N:

$$\Delta g(x,z) = \sum_{n=0}^{N}\left[A_n\cos\left(n\frac{\pi}{L}x\right) + B_n\sin\left(n\frac{\pi}{L}x\right)\right]e^{\left(\frac{\pi n}{L}\right)z}$$

Taking the derivative with respect to the variables x and z, respectively, we have the Gradient in the x and z directions: V_{zx} and V_{zz}.

The full gradient method is G(x,z) determined by the formula:

$$G(x,z) = \sqrt{(V_{zx}^2 + V_{zz}^2)^v}$$

where, v is an integer 2, 3, 4,... to improve resolution. Apply this formula to each measuring line with the corresponding depth z. For each certain depth z, we perform the following steps:

(i) Calculate the mean $\overline{G}(x,z)$ of all G(x,z) values on the measuring line at that depth z.
(ii) By dividing each value of G(x,z) at this depth by the average $\overline{G}(x,z)$, we have the normalized Gradient values $G_n(x,z)$ on a line corresponding to this depth.
(iii) Calculating for all other depths, we have a Normalized Full Gradient whose value is distributed in the vertical section along the measuring line.

In this method, finding an appropriate function - with available points will play an important role in analysis, interpretation, finding the relationship between mathematical models and experimental data. We choose the Spline interpolation method to represent the curve. The advantage of the Spline interpolation method is that it is possible to create a new set of values from the existing data due to measurement, while still satisfying that the curve is nearly continuous and passes exactly the points with available there [3]. Next, the exact position of the research object is adjusted by choosing N as the most optimal, then we will have the maximum value of G_{nmax}. Measure the coordinates of that location which is also the location of the research object to be found [4].

Theoretical model

Building a foreign body model with an infinitely long horizontal cylindrical shape typical for each type of mineral: solid minerals λ > 0 (model 1): gold ore, iron ore, ... and liquid minerals λ < 0 (model 2): oil and gas fields, groundwater,... So in this section we have 2 models corresponding to the physical parameters given in Table 1 [5].

Table 1. *Physical parameters of infinitely stretched cylindrical body.*

	L	M	Δx	x_o	h_o	λ
Model 1	50	51	1,0	-10	3,0	0,2
Model 2	50	51	1,0	5	4,0	-0,2

 ISBN:

where, L - Length of measuring line (km); M - Number of measuring points on the route; Δx - Distance of two consecutive measuring points (km); x_o - Location of the object on the measuring line (km); h_o - Depth of object (km); K - Gravitational coefficient K=1 ($dyn.cm^2/g^2$); λ - Long residual density of the cylinder (kg/m).

Table 2. *Table of gravity values Δg of model 1 ($\lambda > 0$) and model 2 ($\lambda < 0$).*

Model 1

	x(km)	Δg(mGal)
1	-2.5000000e+01	-1.7467249e-03
2	-2.4000000e+01	-1.8669778e-03
3	-2.3000000e+01	-2.0000000e-03
4	-2.2000000e+01	-2.1476510e-03
5	-2.1000000e+01	-2.3121387e-03
6	-2.0000000e+01	-2.4960998e-03
7	-1.9000000e+01	-2.7027027e-03
8	-1.8000000e+01	-2.9357798e-03
9	-1.7000000e+01	-3.2000000e-03
10	-1.6000000e+01	-3.5010941e-03
11	-1.5000000e+01	-3.8461538e-03
12	-1.4000000e+01	-4.2440318e-03
13	-1.3000000e+01	-4.7058824e-03
14	-1.2000000e+01	-5.2459016e-03
15	-1.1000000e+01	-5.8823529e-03
16	-1.0000000e+01	-6.6390041e-03
17	-9.0000000e+00	-7.5471698e-03
18	-8.0000000e+00	-8.6486486e-03
19	-7.0000000e+00	-1.0000000e-02
20	-6.0000000e+00	-1.1678832e-02
21	-5.0000000e+00	-1.3793103e-02
22	-4.0000000e+00	-1.6494845e-02
23	-3.0000000e+00	-2.0000000e-02
24	-2.0000000e+00	-2.4615385e-02
25	-1.0000000e+00	-3.0769231e-02
26	0.0000000e+00	-3.9024390e-02
27	1.0000000e+00	-5.0000000e-02
28	2.0000000e+00	-6.4000000e-02
29	3.0000000e+00	-8.0000000e-02
30	4.0000000e+00	-9.4117647e-02
31	5.0000000e+00	-1.0000000e-01
32	6.0000000e+00	-9.4117647e-02
33	7.0000000e+00	-8.0000000e-02
34	8.0000000e+00	-6.4000000e-02
35	9.0000000e+00	-5.0000000e-02
36	1.0000000e+01	-3.9024390e-02
37	1.1000000e+01	-3.0769231e-02
38	1.2000000e+01	-2.4615385e-02
39	1.3000000e+01	-2.0000000e-02
40	1.4000000e+01	-1.6494845e-02
41	1.5000000e+01	-1.3793103e-02
42	1.6000000e+01	-1.1678832e-02
43	1.7000000e+01	-1.0000000e-02
44	1.8000000e+01	-8.6486486e-03
45	1.9000000e+01	-7.5471698e-03
46	2.0000000e+01	-6.6390041e-03
47	2.1000000e+01	-5.8823529e-03
48	2.2000000e+01	-5.2459016e-03
49	2.3000000e+01	-4.7058824e-03
50	2.4000000e+01	-4.2440318e-03
51	2.5000000e+01	-3.8461538e-03

Model 2

	x(km)	Δg(mGal)
1	-2.5000000e+01	5.1282051e-03
2	-2.4000000e+01	5.8536585e-03
3	-2.3000000e+01	6.7415730e-03
4	-2.2000000e+01	7.8431373e-03
5	-2.1000000e+01	9.2307692e-03
6	-2.0000000e+01	1.1009174e-02
7	-1.9000000e+01	1.3333333e-02
8	-1.8000000e+01	1.6438356e-02
9	-1.7000000e+01	2.0689655e-02
10	-1.6000000e+01	2.6666667e-02
11	-1.5000000e+01	3.5294118e-02
12	-1.4000000e+01	4.8000000e-02
13	-1.3000000e+01	6.6666667e-02
14	-1.2000000e+01	9.2307692e-02
15	-1.1000000e+01	1.2000000e-01
16	-1.0000000e+01	1.3333333e-01
17	-9.0000000e+00	1.2000000e-01
18	-8.0000000e+00	9.2307692e-02
19	-7.0000000e+00	6.6666667e-02
20	-6.0000000e+00	4.8000000e-02
21	-5.0000000e+00	3.5294118e-02
22	-4.0000000e+00	2.6666667e-02
23	-3.0000000e+00	2.0689655e-02
24	-2.0000000e+00	1.6438356e-02
25	-1.0000000e+00	1.3333333e-02
26	0.0000000e+00	1.1009174e-02
27	1.0000000e+00	9.2307692e-03
28	2.0000000e+00	7.8431373e-03
29	3.0000000e+00	6.7415730e-03
30	4.0000000e+00	5.8536585e-03
31	5.0000000e+00	5.1282051e-03
32	6.0000000e+00	4.5283019e-03
33	7.0000000e+00	4.0268456e-03
34	8.0000000e+00	3.6036036e-03
35	9.0000000e+00	3.2432432e-03
36	1.0000000e+01	2.9339853e-03
37	1.1000000e+01	2.6666667e-03
38	1.2000000e+01	2.4340771e-03
39	1.3000000e+01	2.2304833e-03
40	1.4000000e+01	2.0512821e-03
41	1.5000000e+01	1.8927445e-03
42	1.6000000e+01	1.7518248e-03
43	1.7000000e+01	1.6260163e-03
44	1.8000000e+01	1.5132409e-03
45	1.9000000e+01	1.4117647e-03
46	2.0000000e+01	1.3201320e-03
47	2.1000000e+01	1.2371134e-03
48	2.2000000e+01	1.1616651e-03
49	2.3000000e+01	1.0928962e-03
50	2.4000000e+01	1.0300429e-03
51	2.5000000e+01	9.7244733e-04

Processing the above models in Matlab software (MathWorks), the results will be mentioned in the section below.

III. RESULTS AND DISCUSSION

Theoretical model processing results

The curve representing discrete values in the survey models according to spline interpolation is shown in Figure 1[5].

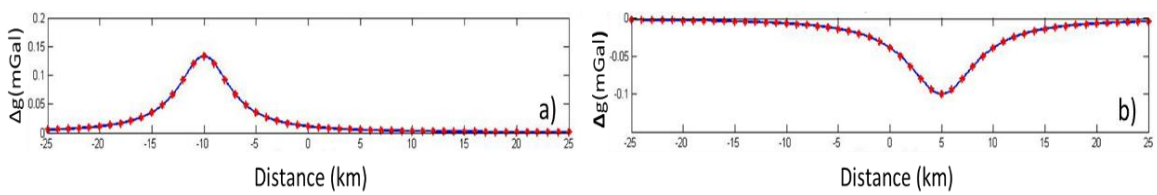

Fig. 1. *a) Model 1: Solid mineral characteristics ($\lambda > 0$);*
b) Model 2: Characteristic for liquid minerals ($\lambda < 0$).

Adjusting the appropriate N value (model 1: N = 22, model 2: N = 17) in the models, we obtain the result in Figure 2 [5].

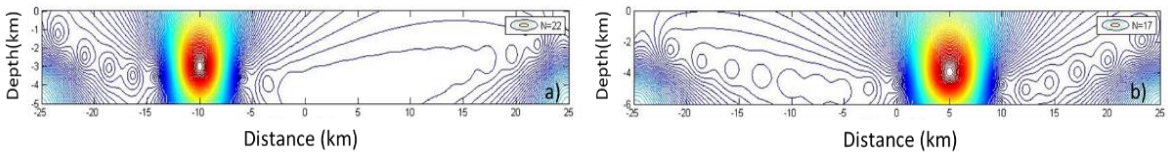

Fig. 2. *a) Gradient graph Model 1(λ > 0); b) Gradient graph Model 1(λ < 0).*

Results:

- Model 1: the center of the object is located at (-10, -3) km
- Model 2: the center of the object is located at (5, -4) km.

General comments about the models:

- The continuous curve shows discrete gravity values through the interpolation Spline reflecting the presence of the research object in the survey measuring line.
- It is possible to apply the theoretical basis and how to use the algorithm in Matlab so that it can serve as a basis for the application of this method in the search for detecting foreign bodies in the deep.

Apply real data: Practical application to the analysis of gravity data measured on an oil and gas survey line in Thailand.

According to the documents we received, the range of the survey line is 50 km long, on this survey line, for each measuring point 2.5 km apart, we can measure 21 gravity values. After processing the measured gravity data on this measuring line, we get the following table of results in Table 3.

Table 3. *Table of gravity values Δg of real data.*

	x(km)	Δg(mGal)
01	-25.00	-0.5293200e+00
02	-22.50	-1.0338350e+00
03	-20.00	-1.8796990e+00
04	-17.50	-2.8665410e+00
05	-15.00	-4.1353380e+00
06	`-12.50	-7.3210530e+00
07	-10.00	-1.1247370e+01
08	-7.50	-1.4137218e+01
09	-5.00	-1.7450752e+01
10	-2.50	-1.9558045e+01
11	0.00	-2.1250704e+01
12	2.50	-1.7812020e+01
13	5.00	-1.4215789e+01
14	7.50	-1.1129301e+01
15	10.00	-8.1296990e+00
16	12.50	-5.5981200e+00
17	15.00	-3.9422450e+00
18	17.50	-2.5375940e+00
19	20.00	-1.9736840e+00
20	22.50	-1.0312350e+00
21	25.00	-0.4513200e+00

 ISBN:

Using the method of Spline interpolation, we can create a new set of values from the existing data due to measurement and still satisfy the curve is almost continuous and pass exactly the existing points.

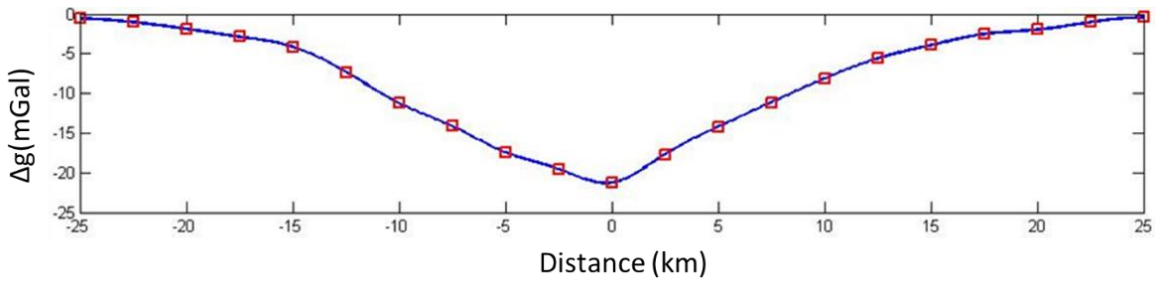

Fig. 3. *Interpolation curve of actual values [5].*

We find that the exact position of the deep foreign body adjusted by choosing N in the Fourier transform is optimal [6]. With a suitable N, the maximum value of G_{nmax} is reached. At that time, we stop and measure the coordinates of that position which is also the location of the object to be found.

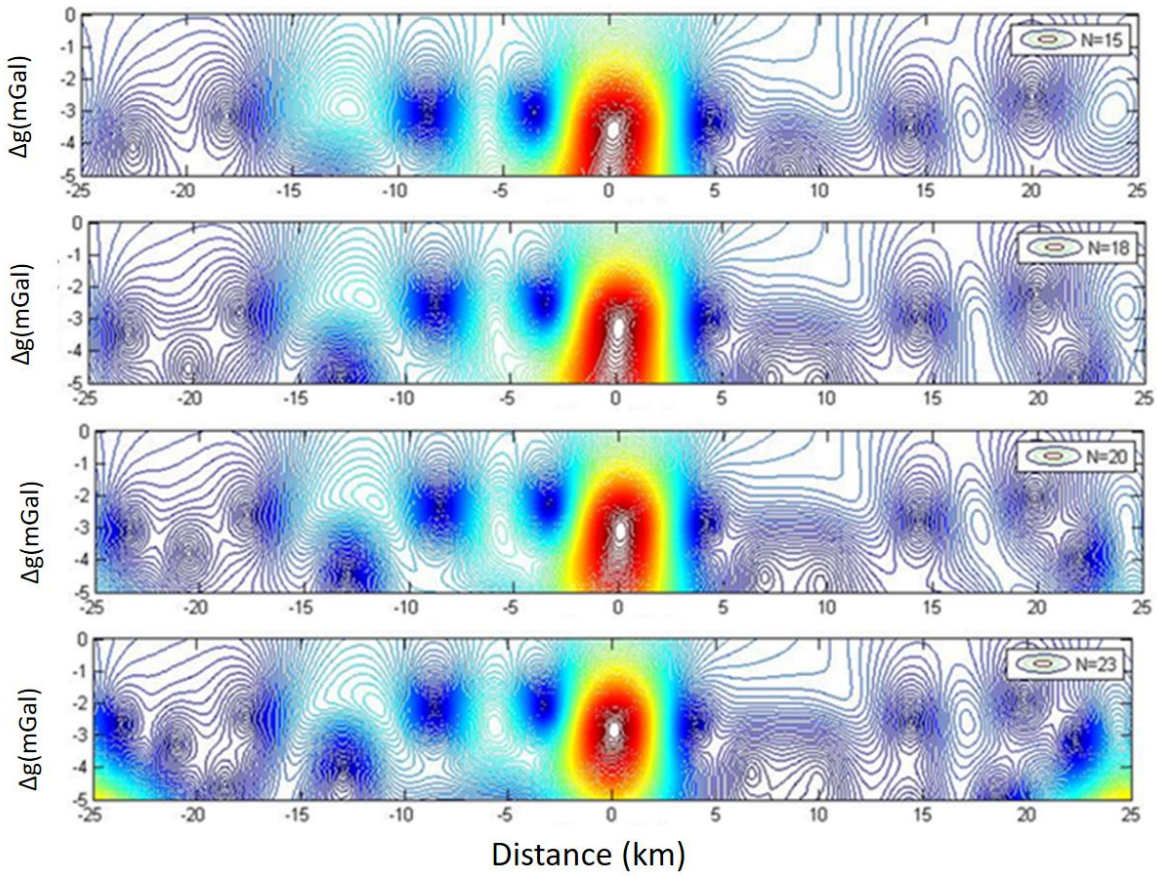

Fig. 4. *Gradient graph with changing values of N, with N = 23, G_{nmax} reaches the maximum value, which is a sign of foreign bodies [5].*

Thus, through the gravity Gradient map, we can see the convergence point characteristic for the foreign body in the survey area. It lies at a depth of about 2.8 km corresponding to N = 23.

IV. CONCLUSION

The Normalized Full Gradient method is a highly effective method in determining the location and depth of underground objects, namely mineral ores, oil and gas fields, etc. This method has many advantages, such as: non-destructive, fast data collection speed, relatively high accuracy. Thanks to the development of science and technology, the combined use of Matlab software has made calculating and processing data faster and more efficient.

In this study, we have accomplished the goal of processing gravity data by using the Gradient method in Matlab algorithms to determine the position of the object (foreign object) to be studied.

ACKNOWLEDGMENTS. The authors would like to thank Associate Professor. Dr. Tran Van Nhac provided the data; Loc Ninh High School and Long An College have created favorable conditions for us to complete this research paper.

REFERENCES

[1] Aydin A., Interpretation of gravity anomalies with the Normalized Full Gradient (NFG) method and an example, *Pure and Applied Geophysics*, 2007, **164**, 2329-2344.

[2] Aghajani H., Moradzadeh A., Hualin Z., Estimation of depth to salt domes from Normalized Full Gradient of gravity anomaly and examples from the USA and Denmark, *Journal of Earth Science*, 2009, **20**(6), 1012-1016.

[3] Berezkin V. M. and Buketov A. P., Application of the harmonical analysis for the interpretation of gravity data (In Russian), *Applied Geophysics*, 1965, **46**, 161-166.

[4] Aydin A., Application of the Normalized Full Gradient (NFG) method to resistivity data, *Turkish Journal of Earth Sciences*, 2010, **19**, 513-526.

[5] Nghia Huu Pham, Master's Thesis, University of Sciences, Ho Chi Minh City, 2020.

[6] Nhac Van Tran, Gravity method in geophysics, Science and Technology Publishing House, Ho Chi Minh City, 2008.

 ISBN:

CORRELATION OF ELECTRON-ELECTRON SCATTERING IN DIFFERENT SUBBANDS OF QUANTUM WELLS

Nguyen Thanh Cong*, Doan The Ngo Vinh

Department of Physics, Vinh University, Nghe An

*E-mail: *nhatancong@gmail.com*

Abstract. The work is devoted to the study of the processes of electron-electron scattering in a quantum well in a quantizing magnetic field. The correlation between intra-subband transitions in different subbands due to electron-electron scattering is considered for the first time. It is shown that this correlation can significantly affect the kinetics of charge carriers.

I. INTRODUCTION

When quantum wells are placed in a quantizing magnetic field, the structure of energy spectrum of the electron changes qualitatively: the subband of dimensional quantization are divided into discrete series of Landau levels [1]. This leads to a qualitative change in the scattering processes. Due to the large distance between the Landau levels (much larger than their width), elastic processes of inter-level scattering (on impurities and roughness of heterograins), as well as quasi-elastic scattering processes on acoustic phonons are significantly suppressed [2]. Therefore, in the system of Landau levels lying below the energy of the optical phonon, the main mechanism for the redistribution of electrons across levels is electron-electron scattering [3]. Since electron-electron scattering is a two-particle process, it leads to a wide variety of transitions of various types. In recent works, electron-electron intersubband scattering has been studied in detail, as well as intrasubband scattering [3-9]. However, another type of transitions is possible (Fig. 1), which was not previously considered. These are scattering acts when the interacting electrons are initially located at the Landau levels of different subbands. Since each of the electrons remains within its own subband, it can be expected that such transitions will be quite intense, and, as a result, affect the kinetics of charge carriers.

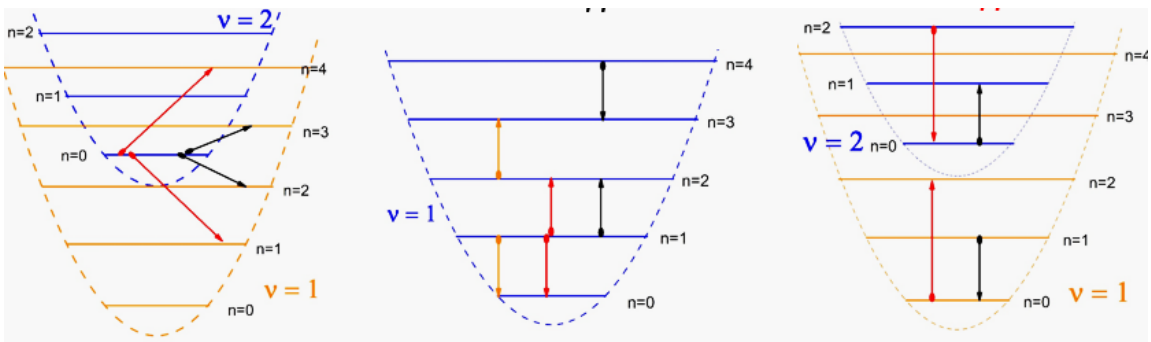

a) b) c)

Fig. 1. *a) Intersubband transitions; b) Intrasubband transitions, which have been studied in detail; c) Intrasubband transitions that were not previously considered.*

In this paper, the probabilities of electron-electron scattering for this type of transitions are calculated. It is found that the rate of such transitions is significant-it is close

in magnitude to the rate of purely intra-band scattering and significantly exceeds the rate of inter-band transitions

II. THEORYTICAL BACKGROUND

The kinetics of electrons in the Landau level system of GaAs/AlGaAs quantum wells at low temperatures (the temperature is significantly less than the width of the levels) can be described by a system of balanced kinetic equations [3].

$$\frac{dN_i}{dt} = \sum_{j,g,f} \mathrm{W}\begin{pmatrix} i & \mathrm{j} \\ \mathrm{f} & \mathrm{g} \end{pmatrix} N_i N_j \left[1-\frac{N_f}{\alpha}\right]\left[1-\frac{N_g}{\alpha}\right] - \sum_{j,g,f} \mathrm{W}\begin{pmatrix} \mathrm{f} & \mathrm{g} \\ \mathrm{i} & \mathrm{j} \end{pmatrix} N_f N_{jg} \left[1-\frac{N_i}{\alpha}\right]\left[1-\frac{N_j}{\alpha}\right] + \sum_f \frac{1}{\tau_{f\to i}^{(LO)}} N_f \left[1-\frac{N_i}{\alpha}\right] \quad (1)$$

here N_i is the population of the Landau level i (the average number of electrons at the level, attributed to the unit of the lateral area S of the sample). The first term in the right hand represents the flow of electrons to the Landau level i due to electron-electron scattering (the average number of electrons arriving at the Landau level from all other levels due to electron-electron scattering attributed to the lateral area S of the sample per unit of time). The second term is the flow of electrons from the Landau level due to electron-electron scattering. $W\begin{pmatrix} i & j \\ f & g \end{pmatrix}$ is element of the electron-electron scattering velocity matrix corresponding to the transition $(i, j) \to (g, f)$, when one electron passes from the Landau level i to the Landau level f, and the other from the Landau level j to the Landau level g. The third term is the flow of electrons to the Landau i level due to the emission of optical phonons from the levels lying above the energy of the optical phonon, $\tau_{i\to f}^{(LO)}$ - the time of scattering of an electron from the Landau level i to the Landau level f due to the emission of an optical phonon.

As can be seen from (1), the electron kinetics in the Landau level system is determined by the electron-electron scattering velocity matrix *W*. Therefore, in order to determine whether a new type of transitions (intra-band transitions of the second type) can contribute to the kinetics, it is necessary, first of all, to evaluate the matrix elements *W* corresponding to such transitions and compare them with the matrices of purely intraband and interband electron-electron scattering.

Using the Fermi golden rule approximation, the element of the electron-electron scattering velocity matrix for the transition (i=(v_i,n_i), j=(v_j,n_j)→(f=(v_f,n_f), j=(v_g,n_g) is given by the expression:

$$W\begin{pmatrix} i & j \\ f & g \end{pmatrix} = \frac{2}{\alpha^2 S} \sum_{k_i,k_j,k_g,k_f} \frac{4\pi}{\mathrm{h}} \left| V_{(f,i)(g,j)}(k_f,k_i,k_g,k_j) \right|^2 F_{(f,i)(g,j)}(k_f,k_i,k_g,k_j) \quad (2)$$

where

$$V_{(f,i)(g,j)}(k_f,k_i,k_g,k_j) = \int d\mathrm{r}_1 \mathrm{d}\mathrm{r}_2 \psi^*_{f,k_f}(\mathbf{r}_1)\psi_{i,k_i}(\mathbf{r}_1) \frac{e^2}{\varepsilon_s |\mathbf{r}_1 - \mathbf{r}_2|} \psi^*_{g,k_g}(\mathbf{r}_2)\psi_{j,k_j}(\mathbf{r}_2) \quad (3)$$

is a matrix element of the electro-electronic interaction. ε_s - static permittivity:

 ISBN:

$$F_{(f,i)(g,j)}(k_f,k_i,k_g,k_j)=\int dE_1dE_2dE_3dE_4\rho_{f,k_f}(E_1)\rho_{i,k_i}(E_2)\rho_{g,k_g}(E_3)\rho_{j,k_j}(E_4)\times\delta(E_1+E_3-E_2-E_4) \quad (4)$$

Eq. 4 is a transition form factor that takes into account the final width of the Landau levels. Since the Landau levels below the energy of the optical phonon are considered, in accordance with the result of [7], we approximate the form factor by the Gaussian:

$$\rho_{i,k_i}(\varepsilon)=\frac{1}{\sqrt{2\pi}\Gamma}\exp\left(-\frac{(\varepsilon-E_i)^2}{2\Gamma^2}\right) \quad (5)$$

with a width of 1 MeV, typical for the structures and magnetic fields under consideration. In this case, the expression for the transition form factor takes the form

$$F_{(f,i)(g,j)}(k_f,k_i,k_g,k_j)=\frac{1}{\sqrt{2\pi}\Gamma_\Sigma}\exp\left(-\frac{(E_i+E_j-E_g-E_f)^2}{2\Gamma_\Sigma^2}\right) \quad (6)$$

where $\Gamma_\Sigma=2\Gamma=2$ meV.

Consider the electron kinetics in GaAs/AlGaAs quantum well structures in quantizing magnetic field $\mathbf{B}=B\mathbf{e}_z$ (axis z is perpendicular to the layers). In Landau gauge the single-electron spectrum is a set of confinement subbands each splitting into a series of Landau levels [10]:

$$E_{(\nu,n)}=\varepsilon_{(\nu,n)}+h\omega_c(n+1/2) \quad (7)$$

with wave function

$$\psi(x,y,z)=\frac{\exp(ikx)}{\sqrt{L}}\varphi_\nu(z)\Phi_n(y-kl_\perp^2) \quad (8)$$

determined by three quantum numbers - subband index ν, Landau level number *n* and *x*-axis momentum component *k*. $l_\perp=\sqrt{\frac{hc}{eB}}$ is the magnetic length. $\Phi_n(y)$ is the wave function of harmonic oscillator with effective mass *m* and cyclotron frequency $\omega_C=\frac{eB}{mc}$. $\varepsilon_{(\nu,n)}$ and $\varphi_\nu(z)$ are the energy and wave function of ν-th subband.

Substitution of wave functions (8) in the expression for the matrix element (3), subsequent integration, we received:

$$W\begin{pmatrix} i & j \\ f & g\end{pmatrix}=\frac{8e^4}{\pi^2\varepsilon_s^2}\frac{l^4}{2^{n_i+n_j+n_g+n_f}n_i!n_j!n_g!n_f!}\Omega_{(f,i)(g,j)}\frac{1}{\sqrt{2\pi}\Gamma_\Sigma}\exp\left(-\frac{(\varepsilon-E_i)^2}{2\Gamma_\Sigma^2}\right) \quad (9)$$

where

$$\Omega_{(f,i)(g,j)}=\iint dk_1dk_2\left|M_{(f,i)(g,j)}(k_1,k_2)\right|^2;$$

$$M_{(f,i)(g,j)}(k_1;k_2)=\int_{-\infty}^{+\infty}\int_{-\infty}^{+\infty}dy_1dz_1\exp\left(-\frac{1}{2}y_1^2\right)\times K_0\left(|k_1|\sqrt{(y_1+k_1-k_2)^2+\frac{4z_1^2}{l^2}}\right)\times R_{\nu_i,\nu_j,\nu_g,\nu_f}(z_1)\Lambda_{n_i,n_j,n_g,n_f}(k_1,y_1)$$

$$\Lambda_{n_i,n_j,n_g,n_f}(k_1,y_1)=\int_{-\infty}^{+\infty}dy_2\exp\left(-\frac{1}{2}y_2^2\right)H_{n_i}\left(\frac{y_2+y_1+k_1}{2}\right)H_{n_f}\left(\frac{y_2+y_1-k_1}{2}\right)\times H_{n_j}\left(\frac{y_2-y_1-k_1}{2}\right)H_{n_g}\left(\frac{y_2-y_1+k_1}{2}\right)$$

$$R_{\nu_i,\nu_j,\nu_g,\nu_f}(z_1) = \int_{-\infty}^{+\infty} dz_2 \varphi_{\nu_i}(z_2)\varphi_{\nu_j}(z_2 - 2z_1)\overset{*}{\varphi}_{\nu_g}(z_2 - 2z_1)\overset{*}{\varphi}_{\nu_f}(z_2).$$

The calculation of the six-fold integral in equation (3) was carried out numerically using the Monte Carlo method.

III. RESULTS AND DISCUSSION

The task of this work was to assess how strongly new type of intrasubband transitions can affect the kinetics. In this paper, the probability of such transitions is calculated and these probabilities are compared with the probabilities of other scattering channels.

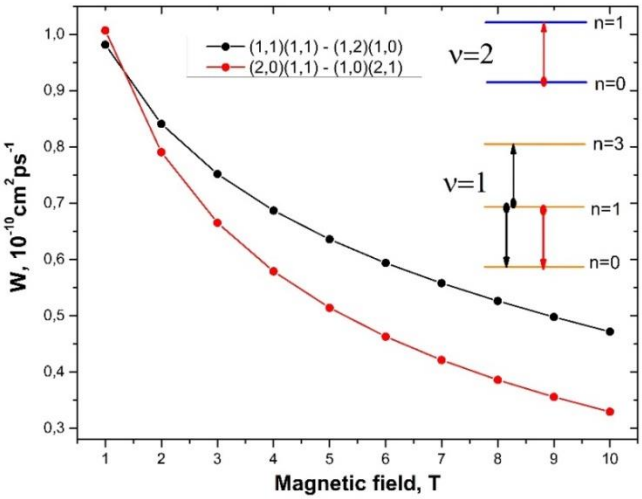

Fig. 2. *The dependence on the magnetic field of the speed of the traditional intrasubband transition type (black curve) and the speed of the intrasubband transition of the new type (red line). The calculation is performed for a quantum well GaAs/$Al_{0.3}Ga_{0.7}$As with a width of 25 nm in a magnetic field B=3.5 T.*

In Fig. 2, the red line shows the speed of the intrasubband transition (1,1)(2,0)→(2,1)(1,0) of the new type, when one electron passes from the ground Landau level of the second subband to the first Landau level of the same subzone, while the second electron passes between the Landau levels of the other lower subband. Here, the black line shows the dependence of the speed of the purely intrasubband transitions (1,1)(1,1)→(1,0)(1,2) on the magnetic field, when both electrons are initially at the first Landau level of the lower subband and, as a result of the scattering act, pass to the main and second excited Landau levels of the same subband.

As can be seen, the speed of the transition of the new type is close in magnitude and may even exceed the speed of a purely intrasubband transition, and, accordingly, significantly exceeds the speed of intersubband transitions. Thus, transitions of a new type should be taken into account when describing the relaxation kinetics. These transitions can play an important role in the situation when the upper subband of dimensional quantization is pumped. As it was shown in [3,9], in such situations, the population of the excited levels of the lower subzone can be quite significant. Accordingly, the intensity of transitions of a

 ISBN:

new type can be quite high. As a result, a relaxation channel may arise, additional to the one traditionally considered.

IV. CONCLUSION

In this paper, the probability of electron-electron scattering is calculated for transitions in which the scattering electrons are initially located at the Landau levels of various subband. It is found that the rate of such transitions is significant - it is close in magnitude to the rate of purely intrasubband scattering and significantly exceeds the rate of intersubband transitions. Thus, it is shown that this scattering channel can play an essential role in the kinetics of charge carriers under conditions of resonant tunneling or optical pumping of the upper subzones of dimensional quantization.

REFERENCES

[1] T. Ando, A.B. Fowler, F. Stern, Electronic properties of two-dimensional systems, *Rev. Mod. Phys.*, 1982, **54**, 437.

[2] M. P, Telenkov, Yu. A. Mityagin, P. F. Kartsev, Carrier kinetics and population inversion in Landau level system in cascade GaAs/AlGaAs quantum well structures, *Opt. Quant. Electron.*, 2014, **46**, 759.

[3] M. P. Telenkov, Yu. A. Mityagin, T. N. V. Doan, K. K. Nagarajad, Kinetics of intrasubband electron energy relaxation in quantum wells in a quantizing magnetic field, *Physica E: Low-dimensional Systems and Nanostructures*, 2018, **104**, 11-15.

[4] K. Kempa, Y. Zhou, J. R. Engelbrecht, Electron-electron scattering in strong magnetic fields in quantum well systems, *Phys. Rev. B*, 2003, **68**, 085302.

[5] I. Savić, Z. Ikonić, V. Milanović, Electron transport in quantum cascade lasers in a magnetic field, *Phys. Rev. B*, 2006, **73**, 075321.

[6] B. Novaković, J. Radovanović, A. Mirčetić, Influence of electron-electron scattering on electron relaxation rates in three and four-level quantum cascade lasers in magnetic fields, *Optics Commun.*, 2007, **279**, 330.

[7] M. P. Telenkov, Yu. A. Mityagin, P. F. Kartsev, Intersubband population inversion and induced transitions between the Landaus levels in resonance-tunneling multiple quantum-well structures, *JETP Letters*, 2010, **92**, 444.

[8] D. Timotijević, J. Radovanović., V. Milanović, The role of electron-electron scattering in gain modulation of a mid-infrared quantum cascade laser in strong magnetic field, *Semicond. Sci. Technol.*, 2012, **27**, 045006.

[9] M. P. Telenkov, Yu. A. Mityagin, A. A. Kutsevol, Intersubband population inversion in landau level system in resonant tunneling quantum well structures with asymmetric double quantum well period, *JETP Letters*, 2014, **100**, 644.

[10] Telenkov M. P., MityaginY. A. & Kartsev P. F., Intersubband terahertz transitions in Landau level system of cascade GaAs/AlGaAs quantum well structures in strong tilted magnetic field. *Nanoscale Res. Lett.*, 2012, **7**, 491.

FABRICATION OF POROUS SILICON USED IN OPTOELECTRONICS AND SENSORS

Le Dinh Vi*, Tran Quang Dat, Dang Hai Ninh, Ngo Thi Lien, Pham Van Thin, Nguyen Vu Tung

Le Quy Don Technical University, 236 Hoang Quoc Viet, Hanoi, Vietnam

*E-mail: *levi.ntv@gmail.com*

Abstract. In this work, the porous silicon (n-Si) was fabricated based on the electrochemical etching method. The porous silicon was anodized on n-Si (111) wafers in an alcohol-containing hydrofluoric acid solution HF by using a constant current regime with various current densities for 15 mins. The structure and surface morphology of porous Si film was characterized by scanning electron microscopy (SEM). The SEM result shows that the structure of the synthesized porous Si is coral-shaped. An additional porous Si film was investigated by photoluminescence (PL) spectrometry. It depicts that the porous Si films fluorescence strongly with luminescence peaks in the region of 650-700 nm. These porous silicon structures have potential applications in the development of luminescent elements, open the prospect of using porous silicon as well as conventional silicon technology in the field of optoelectronics, and will be employed as sensing elements for different types of sensors.

Keywords: *Porous silicon, Electrochemical etching, Optoelectronics, Photoluminescence.*

I. INTRODUCTION

Silicon has been known for years to be the crucial element in the semiconductor technology. It presents in almost all of modern life devices such as computer, phone, spacial mission, etc. In optoelectronics, it seems to be lack of popularity owing to the fact that silicon is of indirect bandgap, which leads to weak luminescence. However, porous silicon is completely different in terms of optical properties thanks to its (i) high value of interior surface area up to ~ 1000 m^2/cm^3 in nanoporous form or ~ 1 m^2/cm^3 in macroporous structure; (ii) ability to promote molecular adsorption effect and surface chemical reaction activity. Therefore the porous silicon can be used as a key component in development of gas and liquid sensing with high sensitivity/resolution [1].

The porous silicon was first successfully synthesised by electrochemically polishing the Si wafer in hydrofluoric acid (HF) solution under the work of Uhlir A. 1956 [2]. At the beginning, porous silicon was not attracted sufficient attention to research and applications, and thus it was not investigating deliberately. In the last few decades, numerous attempts have been paid off to comprehend the properties of porous silicon [1,3-7]. For instance, since the discovery of L. Canham [8] about the effective photoluminescence in the visible regime at room temperature, it is giving rise to prospects of employing porous silicon towards applications, i. e., luminescent elements used in optoelectronics and other fields.

There is a variety of routes to fabricate porous silicon. While stain etching, photochemical etching, vapor etching, spark erosion, and ion implantation, etc [7,9] require critical/expensive conditions (high vacuum) to synthesis the porous silicon,

 ISBN:

electrochemical etching simply involves atmospheric pressure, inexpensive and simple equipment. Hence, it attracts intensive interest from both research and applications.

Though it has been discovered and studied for more than 60 years, the porous silicon materials have been attracting intensively in both research and practical applications. For instance, according to https://www.sciencedirect.com/, the number of scientific publications related to "porous silicon" in the last five years has steadily maintained over 450 articles/year. (Fig. 1). However, in Vietnam, just a few research groups dedicate to this type of material. One of the leading teams is attributed to the group led by Assoc. Prof. Dr. Pham Van Hoi, whose research interests are micro- nanophotonic structure on porous silicon substrate and its applications. The works carried out by the team are highly applicable, and can be used in optoelectronic devices and biochemical sensors [10-12].

However, in order for porous silicon to replace traditional optoelectronic materials and as a sensing element, scientists need to continue to study to improve luminescence, stability, sensitivity and other properties of the material,…

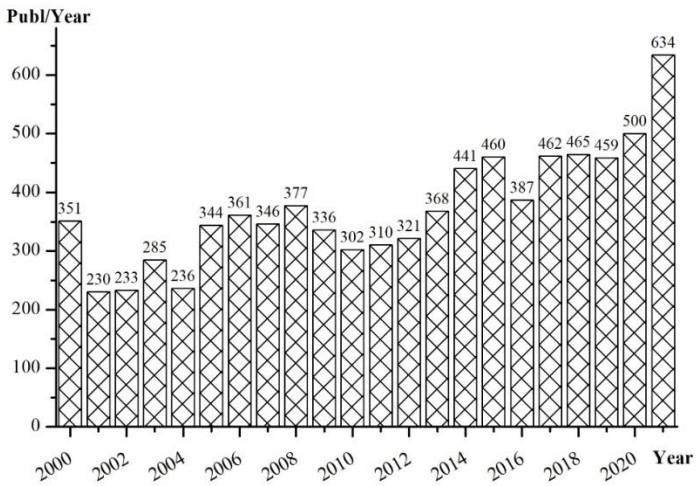

Fig. 1. *Statistics of scientific publications related to porous silicon in the period 2000 - 2021, according to sciencedirect.com, accessed 01/2022.*

In this letter, we present and re-implement the fabrication of porous silicon according to the method that is most commonly used by the scientific community. Accordingly, porous silicon is fabricated by electrochemical etching in an alcohol-containing HF solution at a constant current regime, with various current densities. To evaluate the luminescence, the porous silicon samples after fabrication were excited under ultraviolet light and studied photoluminescence spectroscopy by using HORIBA iHR550 spectrometer. The structure and surface morphology of porous silicon film was characterized by scanning electron microscopy.

II. EXPERIMENTS

Porous silicon was fabricated onto n - doped Si (111) wafers by the electrochemical etching process, for which the resistivity ρ is 3.8 Ω.cm in a standard electrochemical cell [13] consisting of HF acid (40%, Merck, MQ100) and ethanol (96%, Merck, MQ300) (i.e.,

ratio HF: C_2H_5OH = 1:1). Prior to etching, the Si original wafers were applied by the following cleansing procedures [14]: (i) washing in distilled water from 3 to 5 minutes, and then dried at 60 ºC in a furnace; (ii) soaking in H_2SO_4/H_2O_2 solution (ratio of 7:1) 80 ºC during 10 minutes, which allow removing organic impurities accompanied by metallic ions; (iii) Rinsing with distilled water and immersing in H_2O/HF solution (ratio of 100:1) at room temperature to eliminate the native SiO_2 layer; (iv) Following by rinsing with distilled water and drying, the Si substrates were divided into species of 1,5 cm × 1,5 cm, and then treated fairly with an ultrasonic bath in acetone solution for 30 minutes. This process permits removing dust on the sample surface; and (v) finally drying and storing the samples in a desiccator/cabinet.

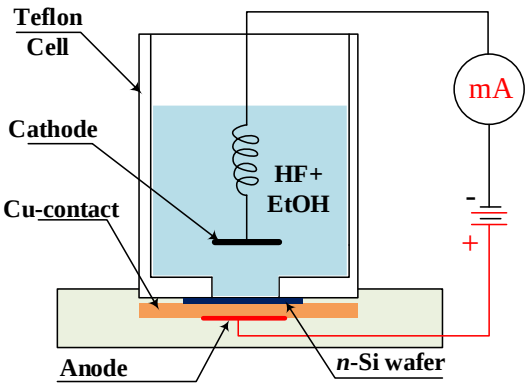

Fig. 2. *Schematic illumination of experimental set-up for fabrication of porous silicon by electrochemical etching method*

The schematic diagram for synthesising porous silicon is illustrated in Fig. 2. It was subjected under constant current densities ranging from 30 mA/cm^2 to 60 mA/cm^2, illuminated with 50 W LED during the etching process at a distance of 15 cm. The source for measuring is supplied by a Keithley 2200-30-5 DC programming. The morphologies of deposited films were performed by optical microscope system (ZST-E745), and scanning electron microscope (SEM - HITACHI S-4800). The optical properties were investigated by imaging spectrometer (HORIBA iHR550).

III. RESULTS AND DISCUSSION

In terms of optical properties, a set of three thick films was deposited at different current densities from 30, 40, and 60 mA/cm^2. The films were later irradiated under 8 W - 365 nm UV lamp. Fig. 3 illustrates the photoluminescence effect of two typical thick films deposited at different current densities. The results show that films fluoresce in the visible regime, for which the strongest intensity appears in the orange-red wavelength range. These results might be attributed by considering the quantum confinement effect due to nanocrystal clusters sizes of porous silicon varying from 2 nm to 5 nm. This observation is in agreement with other studies, in which the luminescence of porous silicon is assigned to the hypothesis of a combination between quantum confinement and surface effects [5,7]. However, by exposing thick films under the air, the photoluminescence intensity of the films is reduced. It is believed that oxidation problem over time is the major cause for such reduction. Thus for practical reasons, there is a must to protect thick films from oxidation

 ISBN:

by introducing a passive layer on the sample.

In order to achieve high performance luminescent porous silicon, the less conventional p-type silicon substrates are frequently employed. The physics behind this can be attributed to the fact that the obtained porous silicon consists of porous microstructure with sizes falling below 5 nm, corresponding the size quantum limitation, for which the porous silicon fluoresce in the visible wavelength region [15]. However, porous silicon based on common n-type silicon (compared to the p-type) is not intensively attracted to the research. The reason is that the fabrication process of porous silicon on these substrates requires irradiation, and the luminescence efficiency is not high. It is therefore successful fabrication of luminescent porous silicon in the visible region, in this work, could be considered as key highlight to enrich the objective literature for this kind of promising material.

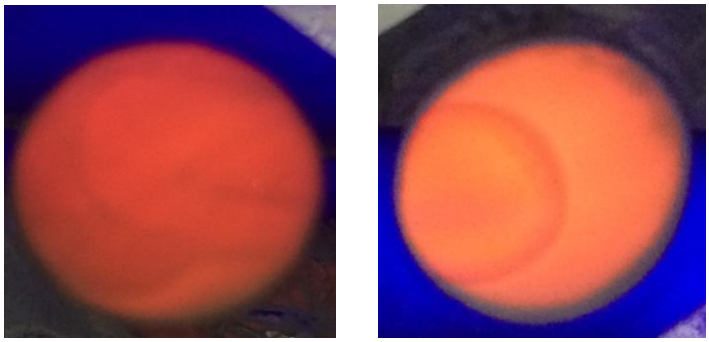

Fig. 3. *Photographs of the porous silicon films with different current densities of 30 mA/cm^2 (left) and 60 mA/cm^2 (right) under excitation of the UV lamp.*

Fig. 4 represents the photoluminescence spectra of the films deposited with current densities of 30, 40, and 60 mA/cm^2 obtained by using a monochromator (Horiba iHR550) and then detected by means of a thermoelectrically-cooled Si-CCD camera (Synapse) with excitation wavelength λ=355 nm, at room temperature.

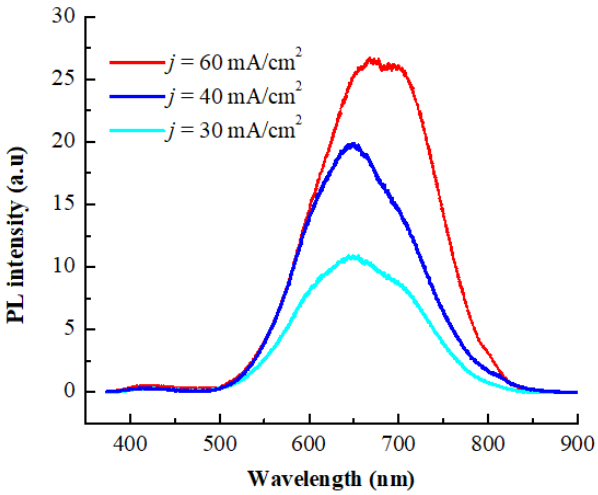

Fig. 4. *The fluorescence spectroscopies of porous silicon films using Horiba iHR550 spectrometer, with λ =355 nm, T=300 K.*

The photoluminescence measurement results demonstrate that the porous silicon samples fluoresce strongly in the wavelength regime from 650 nm - 700 nm, corresponding

to the S-band [7,13]. Similar results also obtained by other authors [16,17]. It is worth to note that the higher the current density is, the higher the value of photoluminescence intensity is obtained. In addition, a red shift is observed by identifying the photoluminescence peaks. This striking observation suggests that it is able to manage the optical properties of the fabricated thick films by adjusting the electrical input parameters during the deposition.

Previous studies on combination of quantum confinement and surface effects [5, 7] allow interpreting the correlation between optical properties and morphologies. Thus, a rigorous investigation on microstructure was made on this set of thick films. Fig. 5 presents plane-view and cross-sectional view (SEM) of the thick films fabricated at current density of 60 mA/cm^2, during 15 minutes, and under excitation of 50 W - LED. Note that the film was cleaved for cross-sectional SEM observation. The film is etched inhomogeneously, with porous sizes fluctuated dramatically (smallest porous size in the range of 50-100 nm), indicated by the SEM plane-view. Moreover, branching microstructures are determined through the film thickness. Both types of top and cross-sectional views indicate that the microstructure of the film is a mixture of meso-(2 nm - 50 nm), macro-porous silicon (>50 nm), at which the diameters of porous parts are varied.

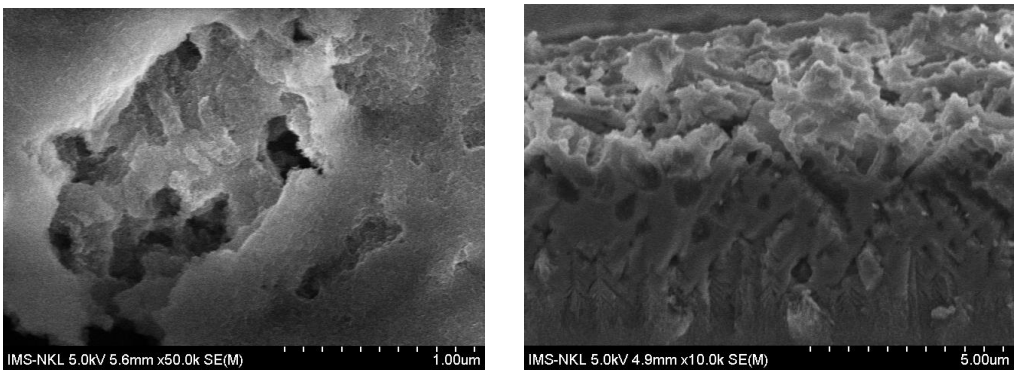

Fig. 4. *SEM images of the porous simples: a) Plane view; b) Cross-sectional view.*

With the various porous microstructures developed in this study, it is possible to synthesize luminescent elements for applications in optoelectronics, and as a buffer layers used as sensing membranes.

IV. CONCLUSION

By using electrochemical etching approach of n-type Si substrates, we have successfully developed porous Si materials, which are capable of luminescence in the visible regime under UV excitation, inducing peaks in the range of 650 - 700 nm. In addition, the morphology and luminescence band of porous Si can be controlled by tuning the etching parameters during fabrication procedure. These films can be applied towards luminescent elements, buffer layers, gas sensors, and optical sensors

ACKNOWLEDGMENTS. The financial support from the grant No. 21.1.02 of Le Quy Don Technical University is gratefully acknowledged.

REFERENCES

[1] P. Granitzer, and K. Rumpf, Porous silicon - a versatile host material, *Materials*, 2010, **3**(2), pp. 943-998.

[2] Jr. A. Uhlir, Electrolytic shaping of germanium and silicon, *Bell System Technical Journal*, 1956, **35**(2), 333-347.

[3] J. L. Gole, and S. E. Lewis, Porous Silicon - Sensors and Future Applications, Nanosilicon, Elsevier, 2008, 149-175.

[4] G. S. Korotcenko, Porous silicon-From formation to application: Biomedical and sensor applications, CRC Press, 2016, **2**, 421p.

[5] G. S. Korotcenko, Porous silicon-From formation to application: Formation and properties. CRC Press, 2016, **1**, 427p.

[6] G. S. Korotcenko, Porous silicon-From formation to applications: Optoelectronics, microelectronics, and energy technology applications, CRC Press, 2016, **3**, 427p.

[7] L. T. Canham, Handbook of porous silicon, Springer, 2018, 1578p.

[8] L. T. Canham, Silicon quantum wire array fabrication by electrochemical and chemical dissolution of wafers, *Applied Physics Letters*, 1990, **57**(10), 1046-1048.

[9] F. Karbassian, Porous silicon, Chapter 1 in Porosity - Process, Technologies and Applications, IntechOpen, 2018, 3-36.

[10] Bui H., et al., Development of nano-porous silicon photonic sensors for pesticide monitoring, *Digest Journal of Nanomaterials & Biostructures (DJNB)*, 2018, **13**(1), 57-65.

[11] Bui H., et al., Determination of low solvent concentration by nano-porous silicon photonic sensors using volatile organic compound method, *Environmental Technology*, 2018, **40**(26), 3403-3411.

[12] Bui H., et al., Progress in the research and development of photonic structure devices, *Advances in Natural Sciences: Nanoscience and Nanotechnology*, 2016, **7**(1), 015003

[13] M. J. Sailor, Porous silicon in practice: Preparation, characterization and applications, John Wiley & Sons, 2012, 254p.

[14] Л. Ануфриев, С. Бордусов, Л. Гурский, и др., Технология изделий интегральной электроники, Интегралполиграф: Минск, 2009, 379с.

[15] Ви Л. Д., Формирование и свойства наноструктурированного кремния в матрице из пористого оксида алюминия и интегральные лавинные светодиоды на его основе, Диссертация к. н. т., Ле Динь Ви, 2020, 52.

[16] В. Трегулов, Пористый кремний: технология, свойства, применение, Рязанский гос. ун-т им. СА Есенина ББК, 2011, 124с.

[17] Huy B., et al., Porous silicon as a promising material for photonics, *International Journal of Nanotechnology*, 2011, **8**(3/4), 360-370.

DEVELOPMENT OF A DEVICE FOR AUTOMATICALLY MEASURING PARALLELISM OF A PLATE DURING PROCESSING

Phan Nguyen Nhue*, Bui Dinh Bao

Department of Optical Devices, Le Quy Don Technical University, Hanoi, Vietnam

*E-mail: *nhue.phan@lqdtu.edu.vn*

Abstract. This paper presents the results of research and fabrication of an electronic autocollimator to quickly measure and evaluate the parallelism error of a flat plate or an optical wedge. The device works on the principle of autocollimation. However, we do not use the eyepiece system to observe the results like a conventional autocollimator; but instead, we use the image sensor to acquire images of laser spots due to the parallelism error of the surfaces. Through image processing, calculating the distance between the two laser spots, we can determine the angular deviation of the two surfaces. The parallelism error of several samples is measured with this instrument and the universal optical bench collimator with a deviation of less than 1%. The good agreement between the two results shows that the device works well and has a high potential for application. We used our device to quickly measure the parallelism of flat plates during processing, greatly improving production efficiency.

I. INTRODUCTION

The angular error of optical components is a parameter that needs to be continuously evaluated during the manufacturing process. Therefore, measuring and evaluating angular error is more important, especially for manufacturing optical components such as parallel plates, prisms, etc.

The methods for determining the angular error can be divided into two categories: contact methods and non-contact optical methods. In the contact method, angle gauges are often used to check the angular error. However, this method is rarely used in the finishing stage because the accuracy is not high and can cause scratches on the working surface of the part. Therefore, at this production stage, people often use non-contact optical methods to determine angular errors, such as interference and autocollimation methods. These methods are highly accurate and do not directly affect the surface of the machined part [1,2]. Compared with the interference method, the autocollimation method is simpler and more suitable for production. In this method, an autocollimator is used to automatically convert the angular deviations of two beams entering the collimator to distance [3]. The autocollimators are well suited for a broad range of applications in metrology and industrial manufacturing, e.g., angle adjustment, measurement of straightness, parallelism and rectangularity of machine tools, etc.

In autocollimation systems that use an eyepiece to get results, these instruments' slow measurement speed is a limitation. Moreover, to use the autocollimator, it is necessary to have experienced technicians to improve the measuring speed. To overcome the limitations of the traditional autocollimator, we have developed a compact model of autocollimator, an

 ISBN:

image processing application to make the results fast and easy to use. The device is used to evaluate the angular error of a parallel plate or measure the wedge angle of an optical wedge when the material's refractive index is known. The instrument was developed to speed up measurement, simplify operation, automatically evaluate and display measurement results. Compared with existing autocollimation devices, the device we built has the advantage of being compact, easy to operate, low cost, and can be used in the process of manufacturing optical components.

II. PRINCIPLE OF AUTOCOLLIMATOR

Figure 1 shows the essential components of the autocollimation system we built. The principle of operation of the device is as follows [3-5]: the light source is emitted from the diode laser, passing through a pinhole to form a point light source. The beam originating from this point light source enters the beamsplitter and is directed towards the objective of the collimator. The point light source position coincides with the focal point of the collimating objective, so the beam after exiting the objective will be parallel. This collimated beam reaches the part's surfaces (e.g., two flat surfaces of a parallel plane) and is reflected back into the objective and creates a spot on the sensor surface, at the focal point of the objective lens. If two surfaces of the optical detail are not parallel, the beams reflected on these surfaces will not be parallel, creating bright spots on the sensor surface at different positions. The distance between the bright spots depends on the angle between the surfaces. By processing the image, we determine the distance between the bright spots and calculate the angle between two surfaces to assess whether the detail has met the requirements quickly. Image processing takes place continuously in real-time and results in digital display on the screen. Therefore, users only need simple operations such as placing measurement samples and reading results. The processes of distance determination and calculation of results are performed automatically by computer software.

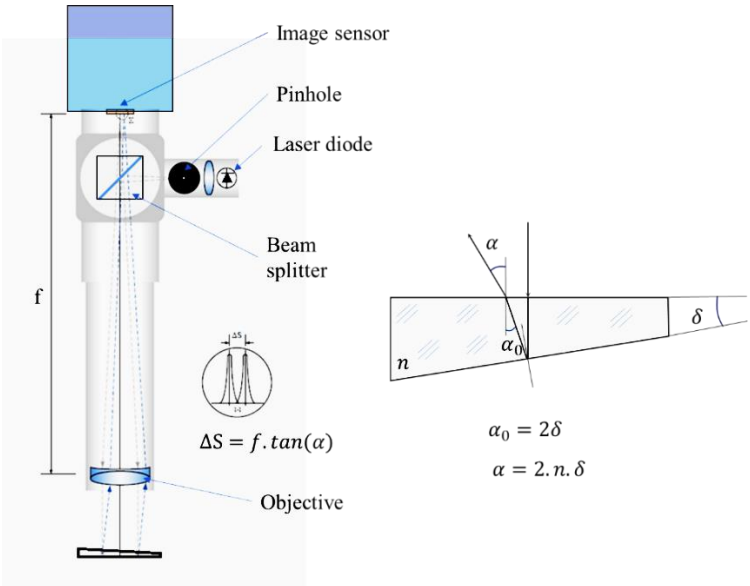

Fig. 1. *The principle of the autocollimator measuring the deflection angle of parallel flat plates.*

The relationship between the distance of two bright spots and the deviation angle of the beams:

$$\Delta S = f.tan(\alpha) \quad (1)$$

If the reflecting surface is perpendicular to the optical axis of the objective, a bright spot at the sensor center is generated. And if a small angle α offsets the reflecting surface and the optical axis, the beam reflected from this surface will form an angle of 2α with the axis. The relationship between the deflection angle between the reflected beams and the parameters of the flat plate is as follows:

$$\alpha_0 = 2\delta \quad (2)$$

$$\alpha = arcsin(nsin\,2\delta) \quad (3)$$

If α is small, we have the following formula for calculating the deflection angle of two reflected beams:

$$\alpha = 2.n.\delta \quad (4)$$

Thus, when determining the deflection angle of the reflected beam between two surfaces and the material's refractive index, we can completely resolve the angle of deviation between the two surfaces.

III. EXPERIMENTS

From the schematic diagram of the autocollimator, as shown in Section 2, we have selected the components to build the experimental device, as shown in Fig. 2. The selected components include:

- Laser diode light source with wavelength 650 nm, hole diameter 30 µm, working voltage 5 V, the maximum output power of 5 mW, the output power can be adjusted;
- A 25.4 mm × 25.4 mm beamsplitter, with a transmission coefficient of 50%, is used to direct the laser beam towards the collimating objective.
- The objective lens (2) with a focal length of 113 mm;
- The image sensor has a size of 3.2 µm × 3.2 µm, a resolution of 2048 × 1036 pixels.

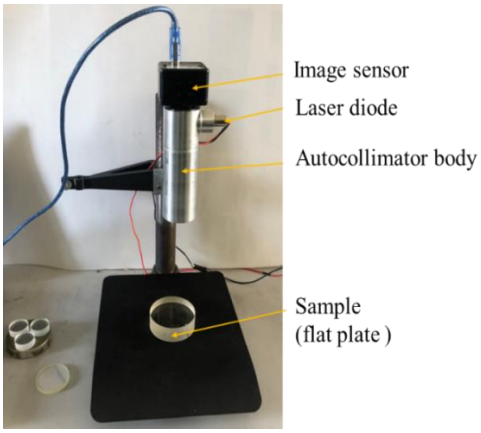

Fig. 2. *Photograph of the autocollimator.*

 ISBN:

Our self-developed specialized software automatically detects and calculates the distance between two light spots, thereby determining the parallelism error of the flat plate. The software has a simple interface and displays the results of measuring the deviation angle of parallel flat plates in real-time (Fig. 3).

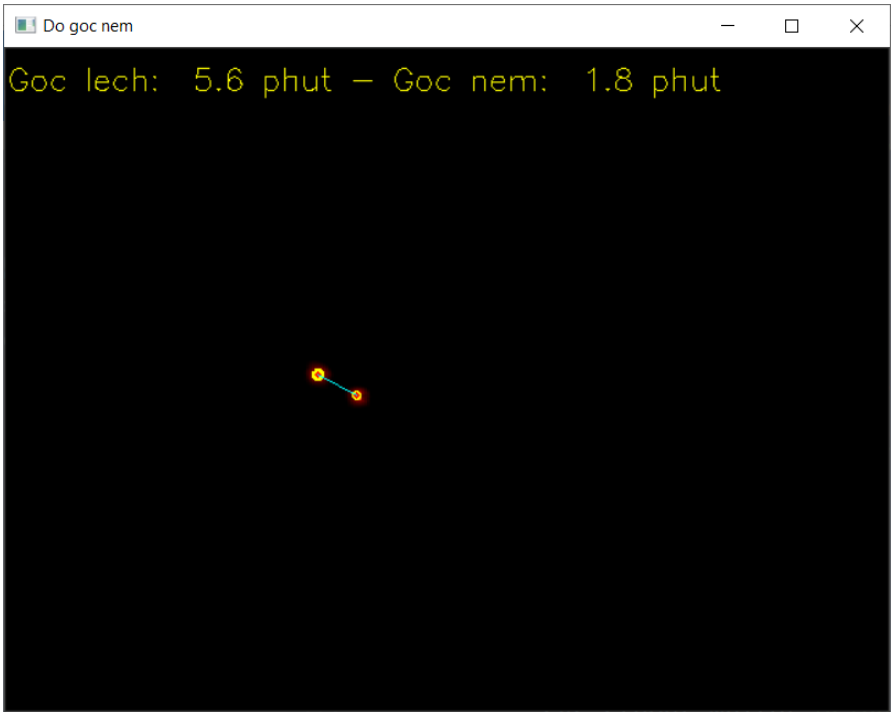

Fig. 3. *Screenshot of real-time wedge angle measurement results.*

IV. RESULTS AND DISCUSSION

Using the built-in device, we measured the wedge angle of parallel flat plates and rotated the measuring sample at various positions. Simultaneously, we measured the deflection angles of the above samples using a universal optical rack autocollimator OCK (Fig. 4) to verify the measurement results from our device. The measurement results summarized in Table 1 show high repeatability in each measurement, and there is a similarity in measurement results when using the two devices.

(a) (b)

Fig. 4. *Arrangement of parallel plane wedge angle meter using autocollimator on universal optical rack OCK. (a) Alignment of measuring device (b) Resulting image when viewed through the eyepiece of the autocollimation.*

Table 1. *Angle measurement results of some parallel flat plates.*

Measurement times	Sample 1		Sample 2		Sample 3	
	Measure with OCK	Measure with built-in device	Measure with OCK	Measure with built-in device	Measure with OCK	Measure with built-in device
1	17	17.2	16.2	15.9	5.6	5.4
2	17	17.5	16.4	16.4	5.4	5.6
3	16.5	17.3	16.2	16.2	6	5.6
Average	16.8	17.3	16.3	16.2	5.7	5.5

The parallel platen samples used in our experiment are fabricated from K8 glass (refractive index n = 1.5141 for 650 nm laser wavelength). According to formula (4), we have determined the actual parallel error of the measured samples according to formula (5) and shown in Table 2.

$$\delta = \frac{\alpha}{2n} \tag{5}$$

Table 2. *Calculation results of wedge angle of some parallel flat plate samples.*

Measurement times	Sample 1		Sample 2		Sample 3	
	Measure with OCK	Measure with built-in device	Measure with OCK	Measure with built-in device	Measure with OCK	Measure with built-in device
1	5.61	5.68	5.34	5.25	1.84	1.78
2	5.61	5.78	5.41	5.41	1.78	1.85
3	5.44	5.71	5.34	5.35	1.97	1.85
Average	5.6	5.7	5.4	5.3	1.9	1.8

The above measurement and comparison results show that the device model achieves high accuracy equivalent to the autocollimation device on the universal optical rack, but the measurement speed is much faster.

Thus, the device for measuring and evaluating the angular error of parallel flat plates has been successfully built and is applicable to quickly evaluate the angular deviation or measure the wedge angles of some optical components.

V. CONCLUSION

The device for measuring and evaluating parallelism error between optical detail surfaces operating on the principle of autocollimation and applying image processing techniques has been successfully built. The main advantage of the device is the ability to give speedy results, simple operation. Compared with the conventional autocollimation system, this instrument does not need an experienced technician in measuring. The results are processed automatically. Through testing and comparing three measuring samples, the results have a good agreement between using the built-in device and the autocollimation device on the universal optical rack OCK. That confirmed, the device has worked well, high reliability. The device is customizable so that the angular error of optical components can be quickly checked during production.

 ISBN:

REFERENCES

[1] Lin K. Y., Burdekin M., Angular Measurement instruments and techniques used in manufacturing engineering, Kochhar A. K. (Eds), Proceedings of the Thirty-First International Matador Conference, Palgrave, London, 1995, doi:10.1007.978-1-349-13796-1_44.

[2] Geckeler R. D., Just A., Krause M. and Yashchuk V. V., Autocollimators for deflectometry: Current status and future progress, *Nucl. Instrum. Meth. A*, 2010, **616**, 140- 146.

[3] *http://www.ifsc.usp.br/~lavfis/images/BDApostilas/ApEspectrRedeDif/autocolimador.pdf*, 8/2021.

[4] Geckeler R. D. and Just A., Distance dependent influences on angle metrology with autocollimators in deflectometry, *Proc. SPIE*, 2008, **7077**, 70770B 1-12.

[5] Tanfer Yandayan (UME, Turkey), Guidelines on the calibration of autocollimators EURAMET e.V, Bundesallee Braunschweig Germany, 2017, **100**, 38116.

SYNTHESIS AND MICROWAVE ABSORPTION PERFORMANCE OF $BaFe_{12}O_{19}/NiFe_2O_4$ NANOCOMPOSITE

Tran Quang Dat*, Nguyen Kim Thanh, Le Dinh Vi, Nguyen Vu Tung, Pham Van Thin

Le Quy Don Technical University, 236 Hoang Quoc Viet Street, Hanoi, Vietnam

*E-mail: *dattq@lqdtu.edu.vn*

Abstract. In this study, the $BaFe_{12}O_{19}/NiFe_2O_4$ nanocomposite has been synthesized by a facile two-step hydrothermal process. The obtained material was characterized by scanning electron microscopy (SEM), X-ray diffraction (XRD), and vibrating sample magnetometer (VSM) to determine the microstructure and magnetic characteristics of the materials. To assess their microwave absorption characteristics, a vector network analyzer (VNA) with a frequency range of 2-18 GHz was used (e.g. complex permittivity, permeability, and reflection loss). The best reflection loss was -48 dB at 12.1 GHz for a sample that was 2.5 mm thick and contained 40% wt%. The effective absorption bandwidths up to 4.4 GHz were successfully achieved with the thickness of only 2.0 mm. The results also show that by controlling the thickness of the absorber, the wideband design in the X-Ku band may be tailored. The combination of $NiFe_2O_4$ and $BaFe_{12}O_{19}$ improves the microwave absorption capabilities of one of the components. The nanostructure of the nanomaterials had a considerable impact on their microwave absorption capabilities. The structure provides a channel for many EM wave reflections. $BaFe_{12}O_{19}/NiFe_2O_4$ nanocomposite can be employed as a potentially efficient microwave absorber due to the features listed above.

Keywords: *$NiFe_2O_4$; $BaFe_{12}O_{19}$; Hydrothermal, Microwave absorber*.

I. INTRODUCTION

Recently, there has been a surge in demand for diverse electromagnetic wave (EMW) absorbers; a single material cannot fulfill these needs, such as a big absorption peak, a wide operating frequency range, and a thin absorption film. To enhance the microwave absorption characteristics of magnetic materials, novel systems based on composite powder including hard and soft magnetic materials have been developed [1]. $NiFe_2O_4$ with a cubic spinel structure is a type of soft magnetic material that has been explored as an EMW absorber at relatively low frequencies [2]. Among hexagonal ferrites, M-type hard ferrites like $BaFe_{12}O_{19}$ (BaM) are notable for their strong magnetocrystalline anisotropic field and natural ferromagnetic resonance frequency. Hexaferrites with high planar magnetic anisotropy are of particular relevance for application in electromagnetic energy dissipation in the GHz region [3].

In this study, $BaFe_{12}O_{19}/NiFe_2O_4$ nanocomposite was synthesized and the microwave absorption properties of obtaining composite significantly improved in the frequency range of 8-18 GHz.

 ISBN:

II. EXPERIMENTS

All the chemicals used in this work are analytical grade. Solutions have been prepared with deionized water (DI). $BaFe_{12}O_{19}$ was synthesized by co-precipitation method and hydrothermal processes. To synthesis $BaFe_{12}O_{19}$, a solution was prepared from 100 mL DI water, 1 mmol $BaCl_2$ and 8 mmol $Fe(NO_3)_3$. The mixture was stirred for 1 h to achieve good uniformity. The prepared mixture was then added drop-wise from 50 ml watery solution containing NaOH 2.5 M. Then, the mixture was accurately stirred for 2 h. The mixture was then subjected to hydrothermal treatment at constant temperature of 220 ^oC for 12 h using 250 ml Teflon-lined autoclave - reactor. Following the hydrothermal treatment, the reactor containing the mixture was allowed to cool to room temperature, and the precipitate was separated from the mixture using a permanent magnet. The precipitate was rinsed with distilled water and ethanol several times before drying at 60 ^oC for 12 hours. The final product is dry synthesized $BaFe_{12}O_{19}$.

$BaFe_{12}O_{19}/NiFe_2O_4$ was synthesized by co-precipitation method and hydrothermal processes. First, a preliminary mixture for hydrothermal synthesis was prepared. It was made up of 2 mmol of $Fe(NO_3)_3.6H_2O$, 1 mmol of $Ni(NO_3)_2.6H_2O$, 100 ml of DI water, and an adequate quantity of $BaFe_{12}O_{19}$. The mixture was precisely stirred for 1 hour to achieve optimum homogeneity. The NaOH solution was then gradually added to the aforementioned solution until the pH reached 11. After stirring for 1 h, the sediments were collected and then subjected to hydrothermal treatment at constant temperature of 170 ^oC for 5 h using 150 ml Teflon-lined autoclave - reactor. The precipitate was then rinsed many times with deionized water and ethanol. The washing process was terminated only when the filtrate became colorless. The collected precipitation was then repeatedly washed with deionized water and ethanol. Washing stopped only when the filtrate became colorless. Finally, the wet collected composite was vacuum dried in a vacuum oven at 60 ^oC for 24 h.

The morphology and crystal structure of obtained composite were determined using scanning electron microscopy (SEM - S4800), X-ray diffraction (XRD, Bruker D5 with Cu Kα1 radiation λ = 1.54056 Å). A vibrating sample magnetometer was used to make magnetic measurements (VSM in magnetic fields up to 10 kOe). In a typical experiment, the homogenous mixture was created by combining the $BaFe_{12}O_{19}/NiFe_2O_4$ material with paraffin wax. The material made about 40% of the total weight in the combination. The final mixes were formed into a toroidal shape with an inner diameter of 3.04 mm and an outside diameter of 7.0 mm. Keysight PNA-X N5242A vector network analyzer was used to assess microwave absorption characteristics. The transmission line approach was used to calculate the microwave absorption characteristics [4].

III. RESULTS AND DISCUSSION

3.1. Morphology and spectral properties

Fig. 1 presents the SEM images of $BaFe_{12}O_{19}/NiFe_2O_4$. The $BaFe_{12}O_{19}$ grains obtained had a typical plate-like shape normal to the crystal plane. These plate-like

$BaFe_{12}O_{19}$ grains have an average diameter of 1.5 - 2 μm. Additionally; $NiFe_2O_4$ particles have a cubic-like shape with a mean particle size of 500 nm.

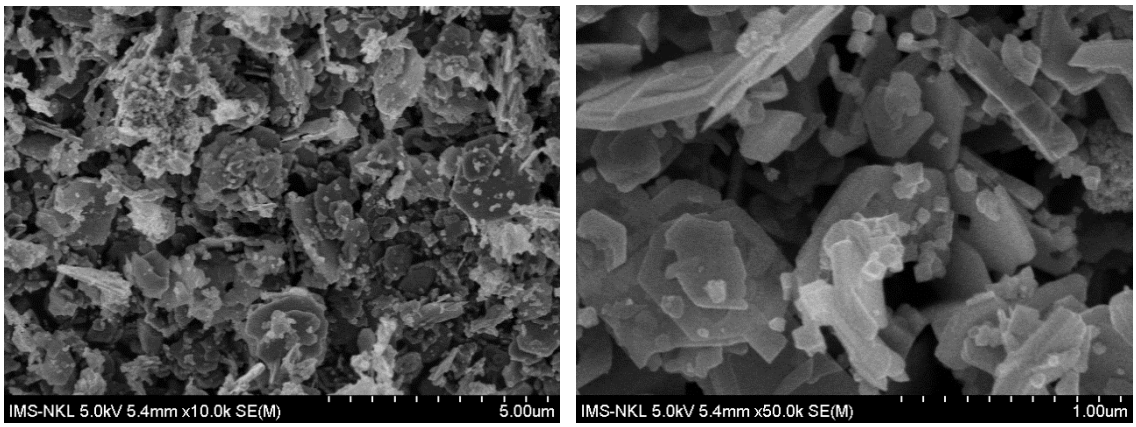

Fig. 1. *SEM images of $BaFe_{12}O_{19}/NiFe_2O_4$.*

The XRD pattern of $BaFe_{12}O_{19}/NiFe_2O_4$ powder is presented in Fig. 2. According to this figure, the characteristic peaks for planes such as (111), (220), (311), (400), (422), (511) and (440) were observed at 18.6°, 30.5°, 35.9°, 43.7°, 54.1°, 57.6° and 63.2° could be indexed in the cubic spinel structure of $NiFe_2O_4$ (JCPDS card No 86-2267) [5]. $BaFe_{12}O_{19}$ particles show a prominent peak at 23.2°, 31.0°, 32.4°, 34.4°, 37.3°, 40.5°, 42.6°, 55.3°, 56.7°and 63.2° corresponding to the (006), (110), (007), (114), (203), (205), (206), (217), (2011) and (220) reflection planes. The hexagonal structure of $BaFe_{12}O_{19}$ can be identified by these peaks (JCPDS card No 84-0757) [6]. The $BaFe_{12}O_{19}/NiFe_2O_4$ composite's XRD pattern shows that it has a high crystallinity and purity phase.

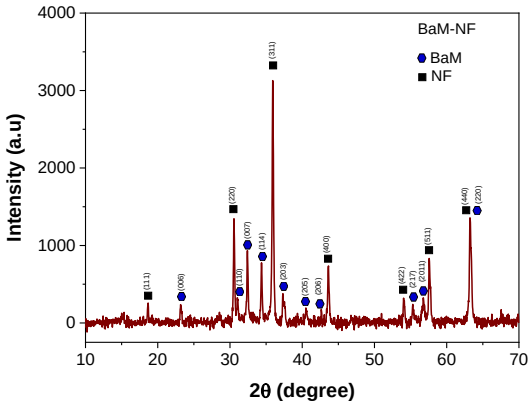

Fig. 2. *XRD pattern of $BaFe_{12}O_{19}/NiFe_2O_4$.*

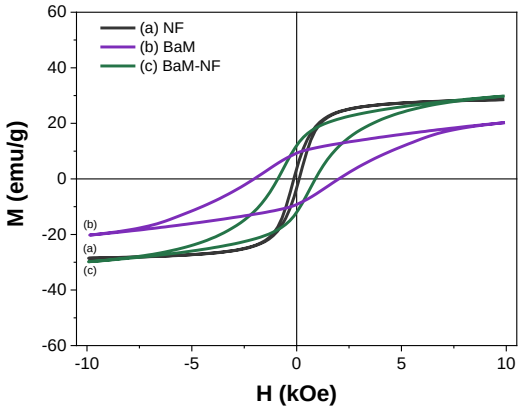

Fig. 3. *Hysteresis loop of $BaFe_{12}O_{19}/NiFe_2O_4$.*

The magnetic hysteresis loop of $BaFe_{12}O_{19}/NiFe_2O_4$ composite sample at room temperature is displayed in Fig. 3. The composite material exhibits a smooth hysteresis loop and single-phase-like magnetization behavior, suggesting that the magnetic hard phase ($BaFe_{12}O_{19}$) and soft phase ($NiFe_2O_4$) are well exchange-coupled [7]. $BaFe_{12}O_{19}/NiFe_2O_4$ composite magnetization is considerably greater (29.8 emu/g) than $NiFe_2O_4$ particles (28.5 emu/g) and $BaFe_{12}O_{19}$ particles (20.2 emu/g). Furthermore, the $BaFe_{12}O_{19}/NiFe_2O_4$ composite mixes the hard magnetic phase of $BaFe_{12}O_{19}$ particles with

 ISBN:

the soft magnetic phase of $NiFe_2O_4$ particles at the same time, resulting in an increase in remanence, which is a property of the exchange coupling interaction [8].

3.2. Microwave absorption properties of material

The real and imaginary frequency dependency curves of complex permitivity and permeability of the sample with a thickness of 2.5 mm are shown in Fig. 4. As can be observed in this figure, the real part (ε') of relative complex permitivity declines in frequency on a regular basis. The range of value of ε' is from 5.37 to 7.11. The imaginary component (ε") of relative complex permitivity has values of from 0.29 to 0.49. The ε' and ε″ denote the storage and loss capacity of electric energy, respectively. The increase of dipolar and interfacial polarization was attributed to the high values of ε' [9].

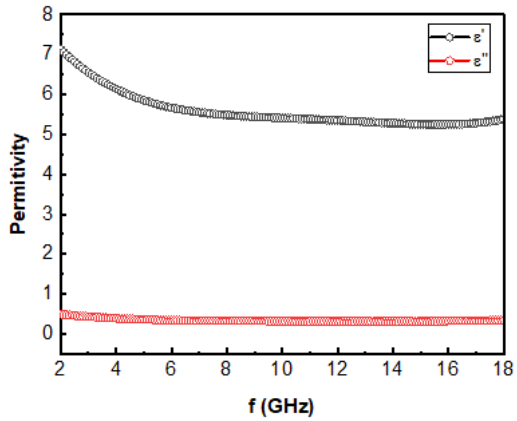

Fig. 4. *The real and imaginary part of complex permittivity.*

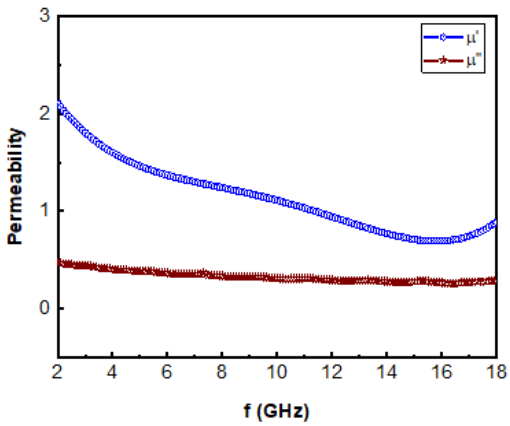

Fig. 5. *The real and imaginary part of complex permeability.*

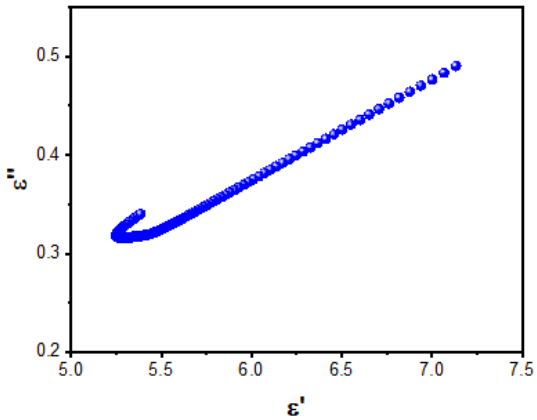

Fig. 6. *The typical Cole-semicircle curve of $BaFe_{12}O_{19}/NiFe_2O_4$.*

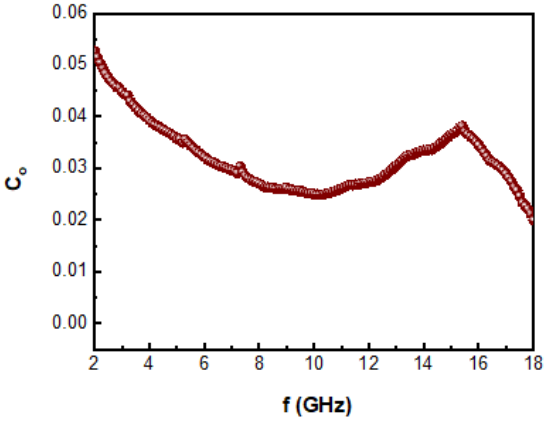

Fig. 7. *The C_0 - f values of $BaFe_{12}O_{19}/NiFe_2O_4$.*

In addition, as shown in Fig. 5, in the frequency range of 2-18 GHz, the curve of real part of relative complex permeability (μ') of $BaFe_{12}O_{19}/NiFe_2O_4$ shows some slight fluctuations. And the imaginary (μ") parts of relative complex permeability remain almost constant with modest modifications. The really high values of μ' and μ" for $BaFe_{12}O_{19}/NiFe_2O_4$ composite are due to the exchange coupling, which is compatible with the above magnetization data [10].

According to Debye theory [3], the relationship between the real and imaginary parts of complex permitivity is used to investigate the material's dielectric characteristics. The single semicircle can be seen in Fig. 6, indicating that the composite material is subjected to the single-dielectric relaxation process. Furthermore, the existence of mechanisms of relaxation dielectric loss, such as defect polarization, interfacial polarization, and conductive loss, could be suggested by the distorted Cole-Cole semicircle [11].

Under the influence of an external electromagnetic field, the heterogeneous interfaces in $BaFe_{12}O_{19}/NiFe_2O_4$ could generate more polarization centers, increasing interfacial polarization and improving associated relaxation. Natural resonance, eddy current loss, and resonance exchange are the most common causes of magnetic loss. The magnetic loss due to eddy currents can be estimated by the coefficient C_0 defined as $C_0 = \mu''/(\mu'^2.f)$, where f is frequency. As shown in Fig. 7, the computed C_0 for the $BaFe_{12}O_{19}/NiFe_2O_4$ sample displays several fluctuations throughout the analyzed frequency range. As a result, the magnetic loss is most likely caused by natural resonance and domain wall resonances [12].

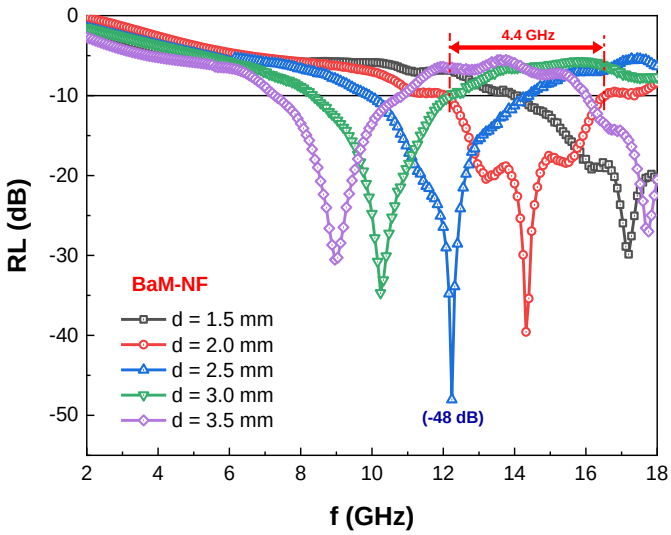

Fig. 8. *Reflection loss of $BaFe_{12}O_{19}/NiFe_2O_4$.*

Fig. 8 shows the microwave reflection loss (RL) at various thicknesses. It can be seen that as the thickness increases, the minimum of reflection loss (RL_{max}) shifts to a lower frequency. The best minimal reflection loss of $BaFe_{12}O_{19}/NiFe_2O_4$ composite is -48 dB at 12.1 GHz with a thin film of 2.5 mm thickness. At a thickness of 2 mm, the highest effective absorption bandwidth (RL - 10 dB) of 4.4 GHz (10.2 - 17.3 GHz) was observed. Furthermore, by varying the thickness of $BaFe_{12}O_{19}/NiFe_2O_4$ composite material, the effective absorption bandwidth may be attained in both the X and Ku bands (8.0 - 18.0 GHz).

The exchange coupling effect between the hard and soft magnetic phases, as well as the improvement in dielectric loss caused by interfacial polarization, dipole orientation polarization, and natural dipole polarization, should be noteworthy for the improved microwave absorption performance of the $BaFe_{12}O_{19}/NiFe_2O_4$ composite [13].

 ISBN:

Table 1 compares the microwave absorption properties of $BaFe_{12}O_{19}/NiFe_2O_4$ composite materials. By comparing these results, it is clear that $BaFe_{12}O_{19}/NiFe_2O_4$ composite material has exceptionally outstanding microwave absorption properties, such as minimal reflection loss, a wide effective absorption bandwidth, and a thin thickness.

Table 1. *Comparison of the microwave absorption properties with other absorbers.*

Absorber	RLmin (dB)	Bandwidth (GHz) (RL ≤ -10 dB)	Thickness (mm) Filled ratio (wt%)	Ref.
$BaFe_{12}O_{19}/NiFe_2O_4$	-23.9	2.2	1.3 (30%)	[7]
$BaFe_{12}O_{19}/ZnFe_2O_4$	-23.1	2.8	3.2 (80%)	[10]
$BaFe_{12}O_{19}/CoFe_2O_4$	-25.0	8.1	2.7 (60%)	[12]
$BaFe_{12}O_{19}/Fe_3O_4$	-33.6	1.3	2.5 (60%)	[13]
$BaFe_{12}O_{19}/NiFe_2O_4$	-48.0	4.4	2.5 (40%) 2.0 (40%)	This work

IV. CONCLUSION

In summary, we synthesized $BaFe_{12}O_{19}/NiFe_2O_4$ composite via a facile two-step hydrothermal process. The homogenous $NiFe_2O_4$ particles are roughly 500 nm in size. The $BaFe_{12}O_{19}$ grains have a plate-like morphology with the average diameter of 1.5 - 2 μm. $BaFe_{12}O_{19}/NiFe_2O_4$ composite material has exhibited a significant microwave absorption performance. The best value of reflection loss of -48 dB was found at 12.1 GHz with the sample which had thicknesses of 2.5 mm. The maximum effective bandwidth stretched 4.4 GHz (10.2 - 17.3 GHz) when thickness was 2.0 mm. The higher magnetic characteristics of the $BaFe_{12}O_{19}/NiFe_2O_4$ composite are mostly due to the sufficient exchange coupling effect between the hard magnetic phase $BaFe_{12}O_{19}$ and the soft magnetic phase $NiFe_2O_4$, which results in improved microwave absorption. As a result, the $BaFe_{12}O_{19}/NiFe_2O_4$ composite developed here has good microwave absorption capabilities in the X-Ku bands.

ACKNOWLEDGMENTS. This work was supported by Le Quy Don Technical University, Vietnam.

REFERENCES

[1] S. A. Mathews, D. R. Babu, P. Saravanan and Y. Hayakawa, Microwave absorption studies of $(Ba_{0.5}Sr_{0.5}Fe_{12}O_{19})_{1-x}(NiFe_2O_4)_x$ hard/soft ferrite nanocomposites, *Mater. Chem. Phys.*, 2020, **252**, 123063.

[2] A. Houbi, Z. A. Aldashevich, Y. Atassi, Z. Bagasharova Telmanovna, M. Saule and K. Kubanych, Microwave absorbing properties of ferrites and their composites: A review, *J. Magn. Magn. Mater.*, 2021, **529**, 167839.

[3] T. T. T. Carol, J. Mohammed, D. Basandrai, S. K. Godara, G. R. Bhadu, S. Mishra, N. Aggarwal, S. B. Narang and A. K. Srivastava, X-band shielding of electromagnetic interference (EMI) by Co_2Y barium hexaferrite, bismuth copper titanate (BCTO), and polyaniline (PANI) composite, *J. Magn. Magn. Mater.*, 2020, **501**, 166433.

[4] T. Q. Dat, N. T. Ha and D. Q. Hung, Reduced graphene oxide-$Cu_{0.5}Ni_{0.5}Fe_2O_4$-polyaniline nanocomposite: Preparation, characterization and microwave absorption properties, *J. Electron. Mater.*, 2017, **46**, 3707-3713.

[5] F. Qiu, Z. Wang, M. Liu, Z. Wang and S. Ding, Synthesis, characterization and microwave absorption of MXene/$NiFe_2O_4$ composites, *Ceram. Int.*, 2021, **47**, 24713-24720.

[6] A. Bahadur, A. Saeed, S. Iqbal, M. Shoaib, I. Ahmad, M. S. Rahman, M. I. Bashir, M. Yaseen and W. Hussain, Morphological and magnetic properties of $BaFe_{12}O_{19}$ nanoferrite: A promising microwave absorbing material, *Ceram. Int.*, 2017, **43**, 7346-7350.

[7] C. Pahwa, S. Mahadevan, S. B. Narang and P. Sharma, Structural, magnetic and microwave properties of exchange coupled and non-exchange coupled $BaFe_{12}O_{19}$/$NiFe_2O_4$ nanocomposites, *J. Alloys Compd.*, 2017, **725**, 1175-1181.

[8] K. S. A. Ali, M. M. Ravikumar, J. Mohammed, N. Farouk, V. Mohanaveland M. Ravichandran, Investigation of Ku band microwave absorption of three-layer $BaFe_{12}O_{19}$, Carbon-fiber@Fe_3O_4, and graphene@$BaFe_{12}O_{19}$@Fe_3O_4 composite, *J. Alloys Compd.*, 2021, **884**, 161045.

[9] S. Acharya, P. Alegaonkar and S. Datar, Effect of formation of heterostructure of $SrAl_4Fe_8O_{19}$/RGO/PVDF on the microwave absorption properties of the composite, *Chem. Eng. J.*, 2019, **374**, 144-154

[10] S. Tyagi, A. Singh, A. K. Paul, R. C. Agarwala and V. Agarwala, Synthesis and characterization of Radar absorbing $BaFe_{12}O_{19}$//$ZnFe_2O_4$, *Mater. Sci. Forum.*, 2015, **830-831**, 452-425.

[11] X. Su, J. Wang, X. Zhang, S. Huo, W. Chen, W. Dai and B. Zhang, Design of controlled-morphology $NiCo_2O_4$ with tunable and excellent microwave absorption performance, *Ceram. Int.*, 2019, **46**, 7833-7841.

[12] X. Huang, J. Zhang, Z. Liu, T. Sang, B. Song, H. Zhu and C. Wong, Facile preparation and microwave absorption properties of porous hollow $BaFe_{12}O_{19}$/$CoFe_2O_4$ composite microrods, *J. Alloys Compd.*, 2021, **648**, 1072-1075.

[13] Y. Lin, Y. Liu, J. Dai, L. Wang and H. Yang, Synthesis and microwave absorption properties of plate-like $BaFe_{12}O_{19}$@Fe_3O_4 core-shell composite, *J. Alloys Compd.*, 2018, **739**, 202-210.

 ISBN:

MATERIAL CHARACTERIZATION OF BETULIN EXTRACTED FROM BIRCK BARK (BETULA UTILIS)

Le Thi Thu Huong*, Nguyen Thi Mai Huong, Le Thi Huong, Phan Thi Thuy, Nguyen Thanh Binh, Nguyen Trong Tinh

Institute of Physics, Vietnam Academy of Science & Technology, Hanoi, Vietnam

*E-mail: *mariotieu@iop.vast.ac.vn*

Abstract. Betulin, a naturally occurring pentacylic triterpene, can be found in several plants such as the Chaga mushroom (Inonotus bolquus) or the red Alder tree (Alnus rubra), especially in many species of birch. Betulin can accounts for around 30% of the dry weight of the birch bark. Betulin, along with its dericative betulinic acid, is widely known for its anti-cancer, antiviral and cytoprotective properties. In this work, the material properties of high-purity betulin (>92%) extracted from the bark of Russian birch (Betula utilis) were investigated through characterization techniques including XRD, SEM, FTIR and UV-Vis spectroscopy. Betulin is practically insoluble in water, therefore, dissolution stability of the extracts in different media with different temperatures and pH has also been conducted in order to develop possible routes of pharmacological formulation.

Keywords: *Betulin, Dissolution stability, Antioxidant activity*.

I. INTRODUCTION

The trend of using herbal products or functional foods to prevent and treat diseases has been increasingly popular in recent years. With the development of modern analytical techniques, many active ingredients are extracted from medicinal herbs, studied to determine the structure and pharmacological effects. Combination of manufacturing technology, research groups as well as many manufacturers have created convenient drug forms for users such as tablets, capsules,… in which the input material is essence or standardized herbal extract with exact active ingredient content. The search and research on new biologically active natural substances for application in the prevention and treatment of diseases has become a direction of great interest in the field of biomedicine.

Betulin, also known as betulinic alcohol, is a naturally occurring pentacyclic triterpene discovered in 1788 by a German-Russian scientist named Johann Tobias Lowitz [1]. Betulin and its derivatives are known to have anticancer, antiviral and hepatoprotective properties [1-3]. Betulin is found in the bark of the birch tree (Betula utilis) and several other plants such as the Chaga mushroom (Inonotus obliquus), the red alder tree (Alnus rubra). Betulin isolated from the bark of the birch tree accounts for up to 30% of the dry weight of the bark, in addition it is also found in the sap of the tree.

Himanshu Joshi (2013), after extracting Betulin from birch bark, conducted a survey and based on some properties of Betulin such as TLC (thin layer chromatography), IR spectroscopy, UV-VIS, mass spectrometry and NMR compares with standards for the qualitative and quantitative determination of Betulin in the extracted product [4]. Liviu Holonec et al evaluated the content of Betulin and Betulinic acid from birch bark grown in

different forestry areas by using High Performance Liquid Chromatography method for comparison [5].

However, the disadvantage of Betulin and many other biologically active compounds is their poor solubility in water, so the research and fabrication of betulin with nanostructures to increase solubility is also being promoted. In order to serve the research of Betulin nano form, as well as to study the structure related to biological activity, the investigation of physical properties to determine the crystal structure, bonding properties,… will be the premise for the next research steps.

II. EXPERIMENTS

Materials

Betulin powder is imported from Russia (95% purity).

Alcohol solvents: methanol, ethanol, isopropanol, provided by Xilong Scientific Co. Ltd., Guangdong firm's n-butane, Guanghua Sci-Tech Co. Ltd, China with 99% purity.

Morphological analysis, characteristics of Betulin powder:

The crystal forms of betulin were determined by XRD spectroscopy measured on a Panalytical Empyrean instrument, belonging to the Hanoi University of Sciences, Vietnam National University, Hanoi.

The morphology of betulin powder was analyzed based on SEM images measured on a Hitachi S-4800 machine, belonging to the Institute of Materials Science, Vietnam Academy of Science and Technology.

FTIR analysis: The chemical bonding of the powder sample was performed on the Carry 630 FTIR machine of Aligent Technologies: The betulin powder sample was pressed into round slabs, 0.01 mm thick, selectable transmittance measurement mode, at room temperature in the range 4000-1200 cm^{-1}.

UV-VIS spectroscopy analysis: The powder sample was dissolved in ethanol and diluted to different concentrations to determine the absorbance value on an AvaSpect Avantes UV-VIS system with an Avalight DHc 200-1150 nm source. A calibration curve that correlates the absorption value and the concentration of the sample was developed for the relative determination of the soluble mass of betulin powder in other experimental measurements.

Evaluation of the solubility of betulin in solvents:

In each beaker, 0.2 g of betulin powder is added and dispersed in 50 ml of individual alcohol solvent. The dispersions are put under constant magnetic stirring at 400 rpm for 30 minutes. After that, the dispersions are left still for 1 hour so the undissolved solid is settled down. The supernatant's UV-Vis absorbance at 240 nm was then taken.

Betulin dispersions in Phosphate Buffer Saline of pH 2.5, 7.0 and 11.0: 0.1g of betulin powder is dispersed in 50 ml of each pH media and kept under magnetic stirring at

 ISBN:

the speed of 400 rpm, temperature 40 ^{o}C for 48 h. The dispersions were then aspirated, filtered through a 450 nm membrane before measurement of absorbance at 210 nm.

III. RESULTS AND DISCUSSION

Characterization of betulin powder

The structure and morphology of the betulin sample

To observe the structural change at the crystal level, firstly, the XRD was measured. Figure 1 shows the XRD spectral structure of the betulin powder sample. We can see some peaks corresponding to 2θ diffraction angles: 7.380; 7.420; 9.040; 10.400; 11.630; 12.370; 14.310; 19.310; 21.680; 31.030 and 38.720, indicating that the sample has a crystalline structure. To compare the crystallinity of different betulin samples through different fabrication methods, one is interested in 2θ=14.310.

Compared with some investigated raw powder samples, the difference between the peaks may be due to the influence of the extraction process, cleanliness, other components mixed in the sample, etc.

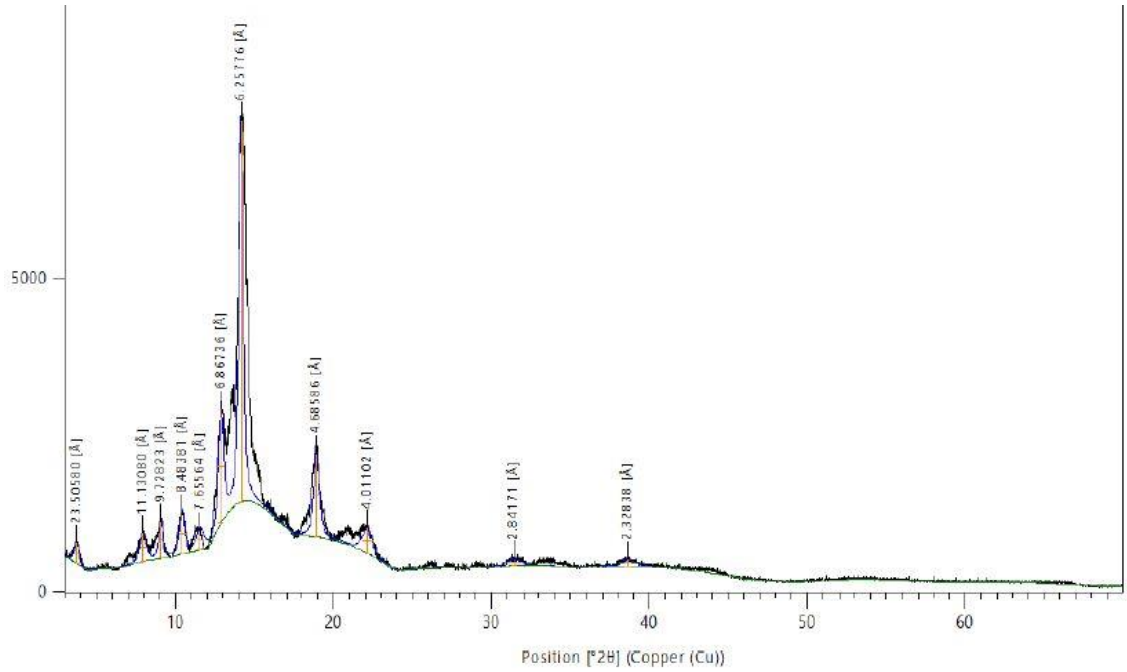

Fig. 1. *XRD spectral structure of betulin powder.*

Figure 2 shows the SEM images of betulin. It can be seen that betulin powders have a cuboidal crystal structure, with the lengths varying from 1 to 6 µm. Particles of different sizes can be seen, uneven, with clumping. Large size, clustering are some of the reasons why betulin is difficult to dissolve in solvents, especially in aqueous media.

Betulin powder was pressed into round, solid pellets before conducting IR spectroscopy to obtain information about the chemical bonding of this compound. The results are shown in Fig. 3 below.

From the figure, we can see the bonds corresponding to the wavenumber as follows: 3434 cm^{-1} (O-H stretching of free -OH group), 1376 cm^{-1} (C-O stretching of –COOH), 2945 cm^{-1} (C-H stretching of C_{sp2}-H bond of $–CH_2$ group), 1217 cm^{-1} (C-H bending of C_{sp2}-H bond of $–CH_2$ group) and 1643 cm^{-1} (C=C stretching vibration).

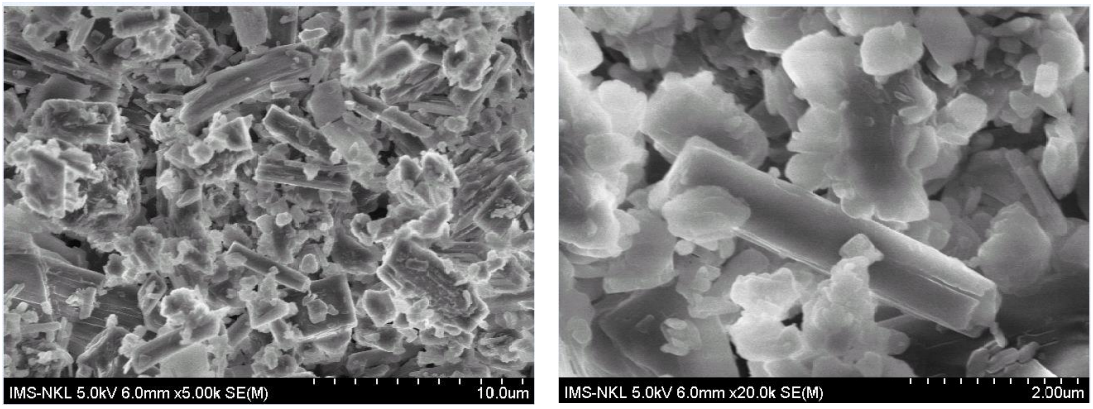

Fig. 2. *SEM images of raw betulin particles.*

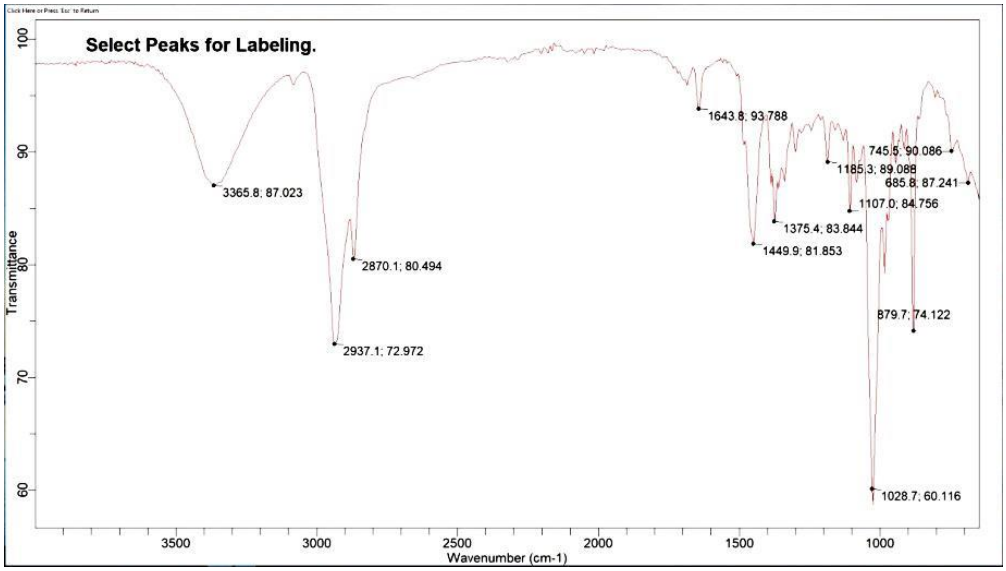

Fig. 3. *FTIR spectrum of betulin powder.*

Result of solubility of betulin powder

The solubilities of betulin in different methanol, ethanol, isopropanol, n-butanol and buffer solutions with pH were measured and the values are shown in Chart 1.

From Chart 1.a it can be seen that betulin powder is quite good soluble in alcohol solvents, above 1.7 mg/ml, and decreases in the order: n-butane > isopropanol > ethanol > methanol. This was also found similar to the results given by Dan Cao et al.

In contrast, the solubility of this compound in water is very poor. Specifically, when mixed with buffer solutions with pH changes: 2.5, 7.0 and 11.0, stirring at 40^0C for 48 hours, a significant difference was observed: the worst solubility was obtained in the neutral medium (pH=7.0), followed by the alkaline (pH=11.0) and finally the acidic medium (pH=2.5).

 ISBN:

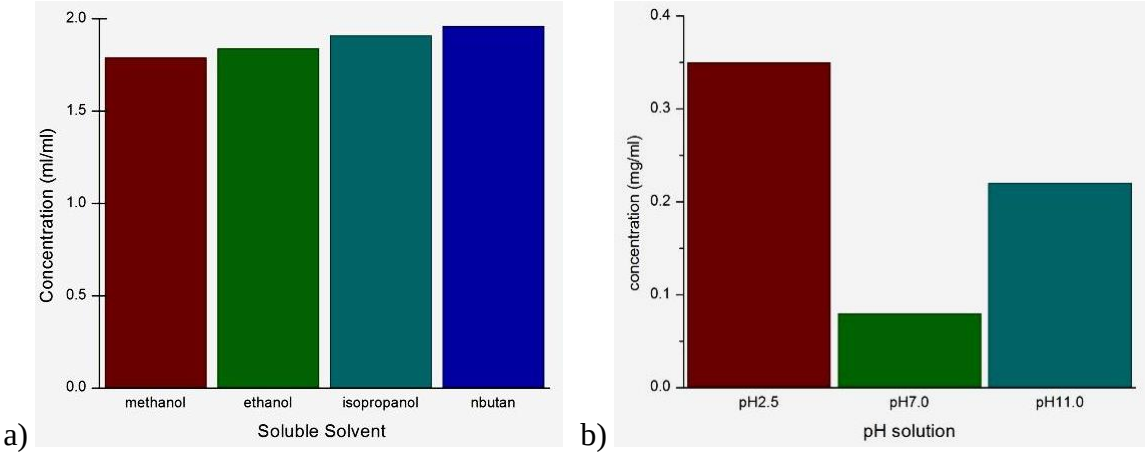

Chart. 1. *The solubility values of betulin in different alcohol (a) and pH (b) solvents.*

The study of solubility in different environments, temperatures, and solvents can provide more information in the evaluation of betulin samples need to be reduced to a smaller size, increased solubility, increased capacity, absorbed during use.

IV. CONCLUSIONS

In this paper, the pine betulin powder sample has a cuboidal, crystalline structure with the size from 1-6 µm. Solubility varies within groups of pH buffered aqueous and alcohol solvents. For the aqueous solvents, the solubility is highest in acidic medium (pH = 2.5) but it is still quite low compared to those of betulin powder dissolved in alcohol solvents.

The survey will serve as a basis for us to conduct nano-chemistry, create nanoscale to increase solubility, increase durability of samples in different environments over time, thereby hopefully opening a new direction of application of this compound in life.

REFERENCES

[1] Lowitz J. T., *Crell's Chem. Ann.*, 1788, **1**, 312-317.

[2] Alakurti S., Makela T., Koskimies S., Yli-Kauhaluoma J., *Eur. J. Pharm. Sci*., 2006, **29**, 1-13.

[3] Tolstikova T. G., Sorokina I. V., Tolstikov G. A., Tolstikov A. G., Flekhter O. B., *Russ. J. Bioorg. Chem*., 2006, **32**, 291-307.

[4] Himanshu Joshi, Phytochemical investigation, isolation and characterization of Betulin from Bark of Betula utilis, *Journal of Pharmacognosy and Phytochemistry*, 2013, **2**(1), 145-151.

[5] Liviu Holonec, Evaluation of Betulin and Betulinic acid content in birch bark from different forestry areas of Western Carpathians, *Not bot horti Agrobo*, 2012, **40**(2), 99-105.

[6] Stanislaw Boryczka, X-ray crystal structure of Betulin-DMSO solvate, *J. Chem Crystallogr*., 2012, **42**, 345-351.

[7] Xiuhua Zhao, Weiguo Wang, Preparation and characterization of betulin nanoparticles for oral hypoglycemic drug by antisolvent precipitation, *Drug Delivery*, 2014, **21**, 6467-479.

IDENTIFICATION OF *Stephania* spp. COLLECTED IN LAO CAI PROVINCE OF VIETNAM BY MORPHOLOGY, ANATOMY AND DNA BARCODE METHODS

Hiep Hoang Phu, Thao Thi Phuong Cao, Danh Thuong Sy, Thi Thanh Nhan Pham*

School of Biology, Thai Nguyen University of Education

*E-mail: *ptnhanbio@tnue.edu.vn*

Abstract. In Vietnam, some species in the genus *Stephania* are being over-exploited and recorded in the Red Data Book of Vietnam. In this article, we present the identification results of *Stephania* spp. collected in Lao Cai province using morphological and anatomical characteristics and the DNA barcode method to contribute to the conservation and exploitation of genetic resources and pharmaceuticals of this species in Vietnam. The *matK* gene and *ITS* region isolated from *Stephania* spp. have a base length of around 900 bp and 500bp, respectively. The sequences of the *matK* gene and *ITS* region obtained in this study have the highest similarity, 98.63% and 99.37%, respectively, to *Stephania brachyandra* species. Based on the combination of the characteristics of morphology, anatomy, and nucleotide sequences of the *matK* gene and *ITS* region, the *Stephania* spp. collected in Lao Cai province of Vietnam were determined as *Stephania brachyandra* Diels.

I. INTRODUCTION

The species *Stephania* spp. belongs to *Stephania*, the largest genus of family Menispermaceae with about 60 species distributed in tropical and subtropical regions of Asia and Africa, some species are also found in Oceania [1,2]. Because their tubers contain a number of important alkaloids such as L-tetrahydropalmatin (rotundin), stepharin, roemerin, cycleanin,... *Stephania* spp. species have long been used in the traditional medicine to treat various diseases such as sedation, blood pressure stabilization, asthma, tuberculosis, dysentery, hyperglycemia, malaria and cancer [3-5]. In Vietnam, this genus comprises 20 species with the similar dioecious flower, including several medicinal species such as *Stephania cepharantha* Hayata, *Stephania rotunada* Lour, *Stephania japonica* Miers,... which are being over-exploited and listed on the Red Data Book of Vietnam [4]. However, the conservation of genetic resources of the species in the genus *Stephania* is still difficult due to the misidentification of species with similar morphological and anatomical characteristics.

Plant species can be identified by many different analytical methods. The current methods such as analysis and comparison of morphological, anatomical, physiological, or biochemical characteristics,... have been reported successfully on a number of crops. However, it is difficult to efficiently identify plants, especially closely related species which are belonging to the same subgenus or their parts are not intact. Recently, DNA barcode data are widely and regularly used to provide additional evidence at the molecular level for plant taxonomic studies. The trend of combination morphological characteristics, chemical and genetic markers into a dataset for species identification becomes very important for systematic studies. In which, DNA barcoding has become one of the most

 ISBN:

efficient tools for species identification of medicinal plants. Several barcoding loci including *matK, rpoC1, trnH-psbA, ITS, rbcL,…* have been studied and applied effectively in the identification of medicinal plants [6]. The *matK* gene found in chloroplasts has been successfully applied to plant identification [7]. The *ITS* gene region located in the cell nucleus, including the *ITS*1-5.8S-*ITS*2 sequence, has achieved high identification rates at the species level. Many other studies demonstrated the role of the *ITS* gene region in plant identification [8,9].

In this study, *Stephania* spp. collected in Lao Cai province were identified using morphological and anatomical characteristics and DNA barcode method. These results have contributed to the conservation and exploitation of genetic resources and pharmaceuticals of this species in Vietnam.

II. EXPERIMENTS

Plant materials

Stephania spp. plants collected in Lao Cai province of Vietnam were sampled to study. These plants were classified at the laboratory of Botany, Genetics and grown in the experimental garden, the faculty of Biology, Thai Nguyen University of Education.

Chemicals used in this study belong to Merck (Darmstadt, Germany) and Invitrogen (ThermoFisher Scientific, USA) such as methylene blue, potassium alum, carmine, chloroform, PCR Master mix,...

Morphological and anatomical analysis

The morphological features of *Stephania* spp. were studied according to Flora of Vietnam by Pham Hoang Ho (1999) and Hu et al. (2008) [10-11]. Key indicators used to analyze include the height of the main stem, the stem color; the number of leaves, leaf shape, and leaf size; the shape, color, and the number of calyx, corolla, stamens, and pistil.

For the anatomical assays, the nutritional organs of *Stephania* spp. such as stem, petiole and leaf blade were analyzed by the methods of making plant specimens for microscopy according to the guidance of Hoang Thi San and Nguyen Thi Phuong Nga (2008) [12].

DNA extraction, PCR amplification, and sequencing

Total genomic DNA was extracted from young fresh leaves material following the protocol of Shaghai-Maroof M. A. et al. (1984) [13]. The sequences of *matK* gene and *ITS* region in *Stephania* spp. plants were amplified by PCR using the primer pairs presented in Table 1.

The PCR amplification was performed using a final volume of 25 µl with 1.5 µl forward (10 pmol.µl^{-1}), 1.5 µl reverse primers (10 pmol.µl^{-1}), 12.5 µl 2x Master mix, 1.0 µl template genomic DNA (500 ng.ml^{-1}), and 8.5 µl deion water. The PCR amplification profiles consisted of 4 min at 94 °C for initial denaturation, 30 cycles of 1 min at 94 °C,

annealing for 1 min at 54 °C, 1 min 30 s at 72 °C for extension, and a final extension step for 10 min at 72 °C. The PCR products were detected by 1.0% agarose gel electrophoresis.

Table 1. *Characteristics of matK, ITS primer pairs for the PCR.*

Primer name	Nucleotide sequence 5'->3'	Theorical length (bp)
matK-F	CGATCTATTCATTCAATATTTC	900
matK-R	TCTAGCACACGAAGTCGAAGT	
ITS-F	ACGAATTCATGGTCCGGTGAAGTGTTCG	500
ITS-R	TAGAATTCCCCGGTTCGCTCGCCGTTAC	

The *matK and ITS* sequences were identified by the machine ABI PRISM® 3100 Avant Genetic Analyzer with Kit BigDye® Terminator v3.1 Cycle Sequencing and a specific primer pair. The data were analyzed by the tool of BLAST (Basic Local Alignment Search Tool), MEGA X.

III. RESULTS AND DISCUSSION

Morphological characteristics of *Stephania* spp.

Perennial, herbaceous climbing vines woody stem base; stem, leaves, flowers are usually hairless. Simple leaf, alternate; petioles about 5-10 cm long, attached to the leaf blade about one-third to one-sixth of the leaf length. The leaf blade is thin, glabrous, and egg-shaped to triangular-rounded, with the entire margins are smooth, base flat or slightly convex. The leaf veins are propeller-shaped, consisting of 8-11 veins originating from the top of the petiole. The leaf tip is pointed or nearly rounded; the leaf base is rounded or heart-shaped. The front side of the leaf blade is dark green while pale green or slightly silver is seen at the backside. Shoots and young stems are usually smooth, dark green, light green, or glossy green. The outer layer of the bark has cracks along the stem or rough warts. Stems ash gray, dark brown, and light brown.

The flowers are unisexual, with the inflorescences compound umbelliform cymes, double canopy, single canopy, or head-shaped. The inflorescences have peduncles, solitary or clustered on the primary inflorescence branches; the terminal branches sometimes irregular or the cymes gather into disc head-shaped [14].

Male inflorescences slightly slender; peduncle 2-4 cm; 6 sepals arranged in 2 rings; 3 yellow-orange petals; disc-shaped anthers. Female inflorescences have shorter stalks than the male inflorescences because of 8-9 small cymes, tightly arranged in headed-shape. Inflorescence peduncle 2-3 cm, apex slightly swollen. Flowers are densely arranged. Therefore, it is hard to see the flower stalk. Female flowers are usually small; sepal 1, pale green; 2 petals arranged on the same side of the flower, yellow-orange, inverted ovate. The ovary is ovate, curved, with a short peduncle; the stigma has 4-5 small spiny lobes. Flowers are cross-pollinated mainly by several insect species [14-15].

The fruit has only one seed, ovate to nearly round, flattened on both sides. The outer skin is usually orange-red, smooth, and shiny when ripe. The ovary has two ovules, but only one develops into the seed whereas the other one degenerates. Seed horseshoe-shaped,

 ISBN:

inverted ovate, amputated head, membranous connected to the semicircular ring; In the middle of the seed, there is an inverted ovoid hole. Along the dorsal and ventral edge of the seed, there are four rows of spines with bulging heads that swell up into the shape of a nail cap.

Tuberous roots are very diverse, usually spherical, lean, and brown. The size and weight of the tuber are very different, ranging from about 1-3 kg, up to 80 kg. The inner part of the tuber is light yellow or lemon yellow, ivory white or reddish-brown. The morphology of *Stephania* spp. collected in Lao Cai province is presented in Figures 1.

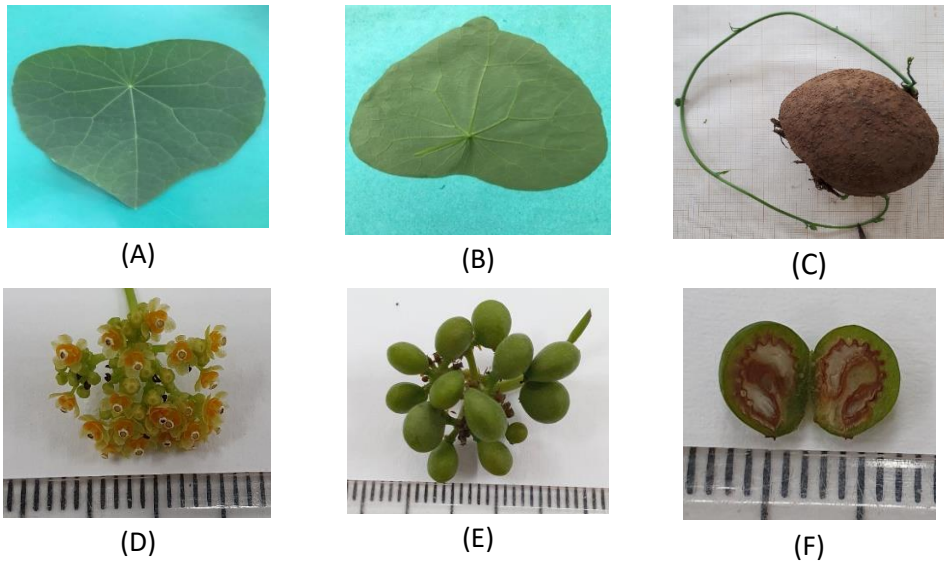

Fig. 1. *Morphology of some parts in the selected Stephania spp., A-Upper-side of leaves; B-under-side of leaves; C-Stem and tuberous tuber root; D-Flowers; E-Fruits; F-cross section of fruit; Scale bar: 1.0 mm.*

The analysis data on morphological characteristics showed that *Stephania* spp. plants collected in Lao Cai province of Vietnam were *Stephania brachyandra* Diels.

Anatomical features of *Stephania* spp. plants

In transection, the stem of *Stephania* spp. collected in Lao Cai province presented a circular shape (Fig. 2A). It consists of three layers: the epidermis, parenchym, and vascular system (xylem and phloem). The epidermis is the outermost layer that protects the inner tissues. Parenchyma is polygonal, round-headed cells with the cells in the outer layer are larger than the ones inside. The stem of this plant has many vascular bundles, composed of xylem and phloem, that are scattered within the parenchyma layer. These vascular bundles present phloem outward and xylem inward.

The cross-section of the petiole has epidermis, parenchyma, collenchyma, and vascular system (Fig. 2B). The petiole epidermis is the thin outermost layer that consists of closely arranged rectangular cells. Beneath the epidermis is cortical parenchyma layer. The parenchyma cells have a slightly rounded shape or polygons shape with rounded corners. The wavy-shaped sclerenchyma ring is observed as the next layer. Sclerenchyma cells have thick walls. The innermost layer is a vascular system consisting of both xylem and phloem. The petioles of the studied plant have around 8 vascular bundles that have xylem and

phloem on the top and bottom, respectively. The xylem tissues have arc-shaped with the concave side facing up. The xylem tissues turned gray while the phloem tissues turned pink when stained in methylene blue and aceto carmine, respectively.

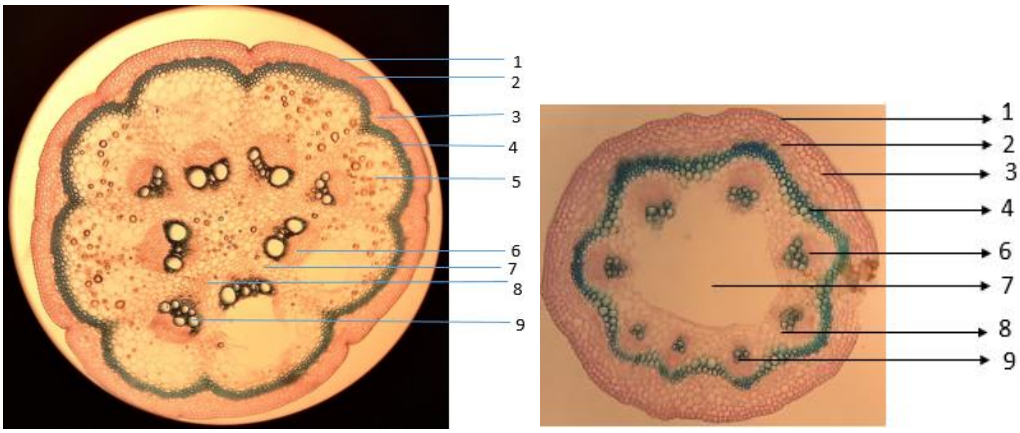

Fig. 2. *The transverse section of the stem (A) and petiole anatomy (B) of Stephania spp.: 1. Epidermis, 2. Collenchyma, 3. Cortical parenchyma, 4. Wavy-shaped sclerenchyma, 5. Parenchyma, 6. Phloem, 7. Pith, 8. Pith parenchyma, 9. Xylem.*

The leaf blade of *Stephania* spp. collected in Lao Cai province consists of epidermal hair, epidermis, collenchyma, parenchyma, and vascular system (Fig. 3). The epidermis is the outermost thin layer that have tiny hairs (trichomes). The epidermal cells are closely arranged rectangular. 4-5 layers of collenchyma cells are seen below epidermis. These cells have a slightly rounded shape or polygons shape with rounded corners.

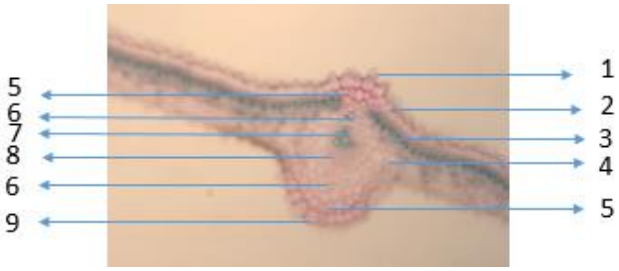

Fig. 3. *Transverse section of the leaf blade of Stephania spp. plants; 1. Trichomes. 2. Upper epidermis, 3. Palisade mesophyll, 4. Spongy mesophyll, 5. Colenchyma, 6. Parenchyma, 7. Xylem, 8. Phloem, 9. Lower epidermis.*

DNA barcodes for the identification of *Stephania* spp.

PCR amplification of the matK gene and ITS region

The purification of total genomic DNA extracted from leaves tissues of *Stephania* spp. was assessed via agarose gel electrophoresis and measured using a spectrophotometer. The result showed the specific band was clean and had no contamination of RNA and protein (data not shown). The *matK* gene and *ITS* region of the genomic DNA were amplified by PCR using primer pairs matK-F/matK-R and ITS-F/ITS-R, respectively. The PCR products detected by 1.0% agarose gel electrophoresis revealed a DNA fragment of the *matK* gene and *ITS* region with the expected size of approximately 900 bp and 500 bp, respectively (Fig. 4).

 ISBN:

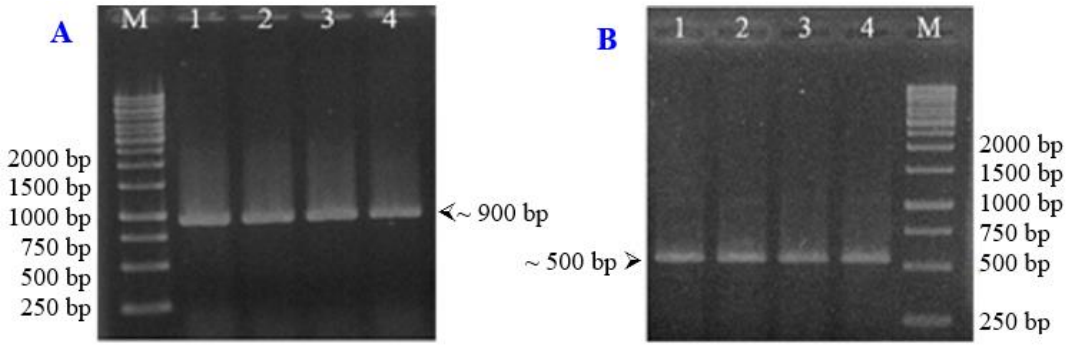

Fig. 4. *PCR amplification of matK gene (A) and ITS region (B).*
M: Marker 1kb; 1-4: PCR products of matK/ITS gene.

The PCR products of the *matK* gene and *ITS* sequence of *Stephania* spp. collected in Lao Cai province were purified and sequenced on an ABI PRISM® 3100 automated sequencer. The sequences were edited and analyzed using BLAST (Basic Local Alignment Search Tool) on NCBI to compare the sequence identity level and identify isolated genes.

Sequences analysis of the matK gene

The nucleotide sequences of the *matK* gene islolated from *Stephania* spp. was compared to 28 sequences of species under the genus *Stephania*on GenBank (full data not shown). The result revealed that gene sequence similarities between them ranged from 94% to 98.63% and our isolated *matK* gene sequence had the highest degree of identity (98.63%) with *Stephania brachyandra*. This result confirmed that the sequence of the *matK* gene in this study was the sequence of the *matK* gene segment of the genus *Stephania*.

In the next step, the nucleotide sequences of the *matK* gene isolated from *Stephania* spp**.** collected in Lao Cai province were compared with the *matK* gene sequence of eight species belong to the *Stephania* genus*: Stephania brachyandra, Stephania succifera, Stephania kwangsiensis, Stephania dielsiana, Stephania delavayi, Stephania chingtungensis, Stephania cephalantha, and Stephania abyssinica* (Table 2). The results revealed in total 51 different single nucleotide polymorphism (SNP) positions between them. In which, the sequence of the *matK* gene isolated from *Stephania* spp**.** has the least difference with that of *Stephania brachyandra*.

Table 2. *The single nucleotide polymorphism (SNP) positions of matK gene segments.*

Position	1	2	3	4	5	6	7	8	9
14	G	G	G	G	C	G	G	G	G
40	C	C	C	C	C	C	C	C	T
74	G	G	G	G	G	G	G	G	T
112	T	T	T	T	T	T	T	T	A
130	A	A	T	T	T	C	C	C	A
131	T	T	T	G	T	T	T	T	T
160	A	A	A	A	C	A	C	A	A
172	T	T	G	G	G	T	T	T	T
187	A	A	A	A	A	A	A	A	T
224	T	T	A	T	T	T	T	T	T
248	G	T	T	T	T	T	G	T	T

251	T	T	C	C	C	T	T	T	T
254	T	T	T	T	T	T	T	C	T
279	C	C	C	C	C	C	C	C	A
325	G	T	G	G	G	G	G	G	G
334	A	A	A	A	A	A	A	A	G
340	T	T	C	C	C	T	T	T	T
353	G	G	T	T	T	T	T	T	T
354	C	C	C	C	C	C	C	A	A
377	G	G	G	G	G	G	G	G	A
378	A	A	A	A	A	A	A	A	G
384	T	T	T	T	T	T	T	T	C
419	G	G	G	G	G	G	G	G	A
436	T	T	T	T	T	T	T	T	C
442	G	G	A	A	A	G	G	G	A
443	G	G	G	G	G	G	G	G	A
450	C	C	A	A	A	G	G	T	G
500	T	T	T	T	T	T	T	T	C
507	C	C	C	C	C	C	C	C	G
538	A	A	A	A	A	A	A	A	T
559	T	T	T	T	T	T	T	T	C
562	T	T	T	T	T	T	T	T	G
564	G	A	G	G	G	G	G	G	C
570	A	A	A	A	A	A	A	A	C
620	A	A	A	A	A	G	A	A	A
627	G	G	G	G	G	T	G	G	G
671	T	T	T	T	T	T	T	T	C
672	A	A	A	C	A	A	A	A	A
731	G	G	G	G	G	G	G	G	A
743	A	A	A	A	A	A	A	A	C
770	G	G	G	G	G	G	G	G	C
779	T	T	T	G	T	T	T	T	T
790	A	A	A	A	A	A	A	A	G
830	T	T	T	T	T	T	T	T	C
848	G	G	G	G	G	A	G	G	G
849	-	A	-	-	-	G	-	-	-
850	-	G	-	-	-	G	-	-	-
851	-	T	-	-	-	G	-	-	-
852	-	T	-	-	-	T	-	-	-
853	-	T	-	-	-	T	-	-	-
854	-	G	-	-	-	G	-	G	-

Note: 1-Stephania brachyandra (EF143871.1); 2-matK_Laocai; 3-Stephania succifera (EF143876.1); 4-Stephania kwangsiensis (NC_048524.1); 5-Stephania dielsiana (NC_054337.1); 6-Stephania delavayi (AF542589.2); 7-Stephania chingtungensis (EF143873); 8-Stephania cephalantha (EF143872.1); 9-Stephania abyssinica(JN051854.1). The capital letters and numbers in parentheses are accesion number of Stephania species published on GenBank.

The genetic relationship between the species of the *Stephania* genus was analyzed based on the nucleotide sequences of the *matK* genes using the MEGAX software. The result showed that the coefficient of difference between the *matK* gene sequence of *Stephania* spp. and eight *Stepphania* species ranged from 0.003 (*Stephania* spp. with

 ISBN:

Stephania brachyandra) to 0.036 (*Stephania spp. with Stephania abyssinica)*. The low divergence of the *matK* gene sequence of the nine species analyzed indicated that the *Stephania spp* is a member of the *Stephania* genus. The genetic relationship between nine different *Stephania* species based on the nucleotide sequences of the *matK* gene was shown in the phylogenetic tree using the Neighbor-Joining method constructed on MEGA X software (Figure 5). The result indicated that the *matK* gene of *Stephania* spp. located in the same branch as *Stephania brachyandra* (EF143871.1).

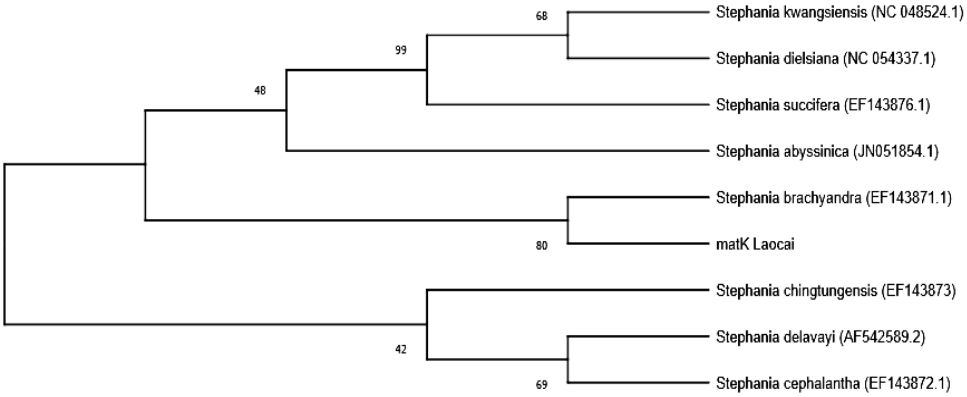

Fig. 5. *Phylogenetic tree of nine Stephania species constructed on the matK gene sequences. Bootstrap values are above the nodes. The capital letters and numbers in parentheses are accesion number of Stephania species published on GenBank.*

Sequences analysis of the ITS region

The nucleotide sequences of the *ITS* region islolated from *Stephania* spp. were compared to one-hundred sequences of species under the *Stephania* genus on GenBank. The result showed that gene sequence similarities between them ranged from 97% to 98.37% (full data not shown). This result confirmed that the sequence of the *ITS* region isolated in this study was the sequence of the *ITS* region of *Stephania*, and the highest similarity, 99.37%, was found between *Stephania* spp. and *Stephania brachyandra* species (EF143871.1).

At the subsequent step, the nucleotide sequence of the *ITS* region isolated from *Stephania* spp**.** collected in Lao Cai province were compared with the *ITS* region of eleven species belong to the *Stephania* genus: *Stephania brachyandra, Stephania viridiflavens, Stephania sinica, Stephania officinarum, Stephania macrantha, Stephania kwangsiensis, Stephania intermedia, Stephania idicentrinifera, Stephania hainanensis, Stephania ebracteata,* and *Stephania dielsiana.* The results revealed in total 24 different single nucleotide polymorphism (SNP) positions between them (Table 3). In which, the sequence of the *ITS* region isolated from *Stephania* spp**.** has only one SNP when comparing with that of *Stephania brachyandra*.

Table 3. *The single nucleotide polymorphism (SNP) positions of ITS gene regions.*

Position	1	2	3	4	5	6	7	8	9	10	11	12
31	A	A	A	A	A	A	A	A	A	A	A	G
60	T	T	T	T	T	T	T	T	T	C	T	T
90	G	G	G	G	G	T	G	G	G	T	G	G
91	A	A	A	A	A	C	A	A	A	C	A	A

93	T	T	T	C	T	T	C	T	T	T	C	C
197	A	A	A	A	A	A	A	A	T	A	A	A
199	G	G	G	G	G	G	G	G	A	G	G	G
200	C	C	C	C	C	C	C	C	G	C	C	C
201	A	A	A	A	A	A	A	A	C	A	A	A
202	T	T	T	T	T	T	T	T	A	T	T	T
203	A	A	A	A	A	A	A	A	T	A	A	A
204	T	T	T	T	T	T	T	T	A	T	T	T
205	C	C	C	C	C	C	C	C	T	C	C	C
206	A	A	A	A	A	A	A	A	C	A	A	A
208	T	T	T	T	T	T	T	T	A	T	T	T
209	A	A	A	A	A	A	A	A	T	A	A	A
231	G	G	G	G	G	G	G	G	A	G	G	G
232	C	C	G	C	C	C	G	C	G	C	-	C
233	G	G	C	C	C	G	C	G	-	G	-	G
235	A	A	G	G	G	A	G	A	G	A	-	A
236	G	G	A	A	G	G	A	G	A	G	-	G
237	G	G	G	G	A	G	G	G	G	G	-	G
238	A	A	G	G	G	A	G	A	G	A	-	A
239	A	A	A	A	G	A	A	A	A	A	-	A

Note: 1-Stephania brachyandra (EF143871.1); 2-matK_Laocai; 3-Stephania viridiflavens (KJ566153.1); 4-Stephania sinica (KJ566150.1);5-Stephania officinarum (KJ566149.1); 6-Stephania macrantha (KJ566147.1); 7-Stephania kwangsiensis (KY189283.1); 8-Stephania intermedia (KJ566141.1); 9-Stephania idicentrinifera (KJ566130.1); 10-Stephania hainanensis (KJ566138.1); 11-Stephania ebracteata (KJ566133.1);12-Stephania dielsiana (KJ566131.1). The capital letters and numbers in parentheses are codes of Stephania species published on GenBank.

The genetic relationship between the species of the *Stephania* genus, was analyzed based on the nucleotide sequences of the *ITS* region using the MEGAX software. The pair-wise distance matrix between *ITS* region sequences of twelve plant species and the phylogenetic tree using the Neighbor-Joining method was shown in Figure 6.

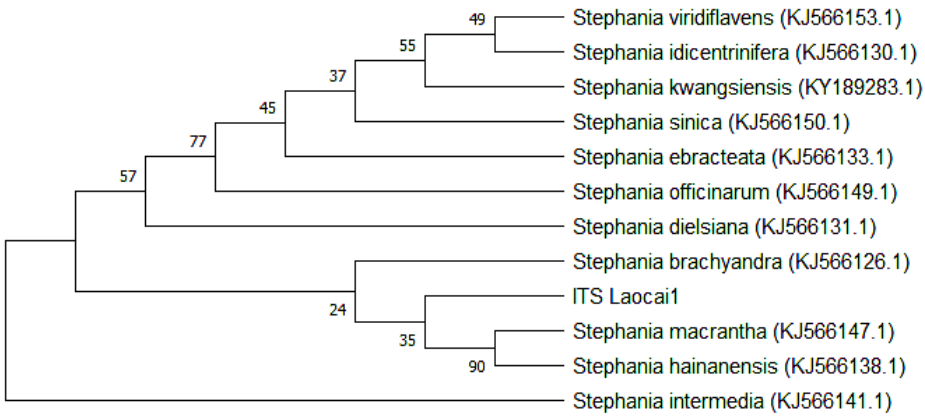

Fig. 6. *Phylogenetic tree of twelve Stephania species constructed on the ITS region sequences. Bootstrap values are above the nodes. The capital letters and numbers in parentheses are accesion number of Stephania species published on GenBank.*

The result indicated that the coefficient of difference between the *ITS* region of *Stephania* spp. and eleven *Stepphania* species ranged from 0.003 (*Stephania* spp. with *Stephania brachyandra)* to 0.058 (*Stephania* spp. with *Stephania idicentrinifera*). Howerver, the *ITS* region has its limitations than *matK*.

 ISBN:

A long with this aproach, Vu Tien Chinh *et al*. (2020) used the chloroplast *rbcL* gene to clarify the relationship between three species of the genus *Stephania* (Menispermaceae) from Vietnam: *S. japonica, S. polygona, S. rotunda* and one subspecies *S. japonica* var. *discolor*. According to these authors, the *rbcL* gene of the chloroplast genome is widely used as an additional data for the study of species origin, molecular evolution and phylogeny. Molecular analysis was performed on 523 bp segment of the *rbcL* genes. The dataset consists of 22 sequences used to reconstruct the evolutionary tree using two methods: Bayesian Infer (BI) and Maximum Likelihood (MP). The results indicated that *S. rotunda* was able to distinguish from *S. japonica* or *S. polygona*, while *S. japonica*, *S. japonica* var. *discolor* and *S. polygona* could not distinguished each another [16]. Howerver, the *rbcL* gene also has its limitations. Previous studies showed that 58.5% of sister species were not identifiable by the *rbcL* gene sequence because of the 100% similarity [6]. Hence, they suggested that should examine furthely other locus such as nuclear *ITS*, chloroplast *trnH - psbA* space or study a combination of multiple gene locus for genus *Stephania*. Wang *et al*. (2007) confirmed that the genus *Stephania* are polyphyly, which have been grouped together but do not share an immediate common ancestor based on phylogeny and morphological evolution of tribe Menispermeae (Menispermaceae) inferred from chloroplast and nuclear sequences [17]. In this study, the morphological and anatomical features of *Stephania* spp. as well as two DNA barcodes were analyzed to identify this species. Our results demonstrate that the *Stephania* spp. collected in Lao Cai province, Vietnam is *Stepphania brachyandra* Diels which was listed in the Red Data Book of Vietnam.

IV. CONCLUSION

The inconsistency between the molecular system and the traditional classification system has been pointed out in the genera of Menispermaceae. Therefore, a combination of morphological and molecular characteristics is needed to rearrange the classification system of the *Stephania* genus. DNA barcodes (or molecular markers) is an effective tool to support for morphology in species identification and rearrangement of the classification system.

ACKNOWLEDGMENTS. This study was funded by the Project of Ministry of Education and Training under grant number *B2019-TNA-09*.

REFERENCES

[1] Vu Tien Chinh, Bui Hong Quang, Ritesh Kumar Choudhary, Nian He Xia, Jongku Lee, Stephania subpeltata H. S. Lo (Menispermaceae): A New recorded species from Vietnam, *Journal Korean Journal Plant Taxon*, 2016, **46**(3), 288-294.

[2] Trinh Thi Phuc, Vu Tien Chinh, Tran Van Tien, Nong Van Duy, The species of the genus stephania Lour. (Menispermaceae) in flora of Vietnam, *Vietnam Journal of Forest Sicences*, 2019, **4**, 22-35.

[3] Nguyen Thu Hang, Nguyen Quoc Huy, Pham Ha Thanh Tung, Hoang Van Thuy, Taxonomy of some species in the genus Stephania Lour. in Vietnam using rADN ITS sequences, *Journal of Pharmacy*, 2014, **54**(9),55-59.

[4] Ministry of Science and Technology, Vietnam Academy of Science and Technology, Red Data Book of Vietnam, Publishing House of Natural Sciences and Technology, 1996, 258-264.

[5] Vu Tien Chinh, Duy Nong Van, Van Tien Tran, Nian He Xia, Stephania polygona (Menispermaceae): A new species from Southern Vietnam, *Phytotaxa*, 2019, **400**(3), 211-214.

[6] Kang Y., Deng Z., Zang R., and Long W., DNA barcoding analysis and phylogenetic relationships of tree species in tropical cloud forests, *Scientific Reports*, 2017, **7**, 12564.

[7] Lahaye R., Van der Bank M., Bogarin D., Warner J., Pupulin F., Gigot G., Maurin O., Duthoit S., Barraclogh T.G. and Savolainen V., DNA barcoding the floras of biodiversity hotspots, *Proc. Natl. Acad. Sci. USA*, 2008, **105**(8), 2923-2928.

[8] Hodkinson, Trevor R., Chase W, Lledo M, Dolores M., Salamin, Nicolas, Renvoize, Stephen A., Phylogenetics of Miscanthus, Saccharum and related genera (*Saccharinae, Andropogoneae, Poaceae*) based on DNA sequences from *ITS* nuclear ribosomal DNA and plastid trnL intron and trnL-F intergenic spacers, *Journal of Plant Research*, 2002, **115**(5), 381-392.

[9] Tao Yang, Tian-lei Zhang, You-Hao Guo, Xing Liu, Identification of hybrids in Potamogeton: Incongruence between plastid and ITS regions solved by a novel barcoding marker PHYB, *PLOS One*, 2016, **11**(11), e0166177.

[10] Pham Hoang Ho, Flora of Vietnam, Youth Publishing House (in Vietnamese), Ho Chi Minh City, 1999, 473-475.

[11] Hu Q., Luo X., Chen T., Gilbert M. G., Menispermaceae, *Flora of China*, 2008, 7, 1166.

[12] Hoang Thi San and Nguyen Phuong Nga, Practices of plant morphological and anatomical, University of Education Publishing House, 2008.

[13] Shaghai-Maroof M. A., Soliman K. M., Jorgensen R. A., Ribosomal DNA sepacer-length polymorphism in barley: mendelian inheritance, chromosomal location, and population dynamics, *Proc. Natl. Acad. Sci. USA*, 1984, **81**, 8014-8019.

[14] Do Tat Loi, Medicinal plants and Drugs from Vietnam, Medical Publising House, Hanoi, 2006, 780-781.

[15] Vu Duc Thang, Collection of *Stephania* spp. tubers in some provinces of Vietnam and quantification of rotundin using TLC-scanning, *Journal of Medicinal Materials*, 2014, **4**, 375-380.

[16] Vu Tien Chinh, Tran Thi Lieu, Duong Van Tang, Using the chloroplast rbcL gene to clarify the relationship between species of the genus Stephania (Menispermaceae) from Vietnam, *Aademia Journal of Biology*, 2020, **42**(2), 109-115.

[17] Wang W., Wang H. C., Chen Z. D., Phylogeny and morphological evolution of tribe Menispermeae (Menispermaceae) inferred from chloroplast and nuclear sequences. Perspectives in Plant Ecology, *Evolution and Systematics*, 2007, **8**, 141-154.

 ISBN:

RESEARCHING THE RETRO-REFLECTION PHENOMENON IN OPTICAL AND OPTOELECTRONIC DEVICES

Nguyen Quang Hiep*

Department of Optical devices, Le Quy Don Technical University, Viet Nam

*E-mail: *quanghiepktq@gmail.com*

Abstract. The retro-reflection effect in optical and optoelectronic devices such as optical sights and cameras is a special phenomenon of reflection that occurs when incoming radiation is reflected at the one of the real image planes of the optical system or on the sensing surface of detectors. The radiant flux of the retro-reflection beam depends on the: i) parameters of incoming beam; ii) parameters of optical and optoelectronic devices and iii) parameters that show the relationship between incoming beam and devices. In order to research this phenomenon the experimental model is used to evaluate the radiant flux of retro-reflection beam is proposed and applied for particular devices. Retro-reflection coefficient of the devices and its dependence on the angle of accident of incoming laser beam can be determined based on the results of the experiments. They are initial data to research and design the optical detection devices.

I. INTRODUCTION

Optical and optoelectronic devices are the devices whose mains functions are performed through the operation of theirs optical system. In optical system, there is always a real image plane that coincides with the detector's surface or reticle's surface. When incoming light beams is focused on this surface, a portion of these beams are reflected backward. Unlike reflections on other surfaces, after leaving the optical system, these reflected beams always will be parallel and in opposite direction with the incident beams. This effect is called retro-reflection or "cat-eye" effect [1-2]. Researching of the "cat-eye" phenomenon has the essential meaning, specially in army. By acquiring and analyzing the retro-reflected beam the information of the optical system in particular and information of the device in generally is received. The retro-reflection effect is the basic ground of the working principle of active optical detecting system [3-4]. This paper will focus on the setting up the experimental model for investigating retro-reflection effect that occurs in the optical systems in PAB-2 device and in night vision device AN/PVS 2. By capturing the radiant flux of retro-reflected beam from tested device and from the reference sample (cube corner) the retro-reflection coefficient of tested device is calculated. The retro-reflection coefficient's dependence on the incident angle of incoming beam is determined by varying the incident angle of interogating laser beam.

II. BACKGROUND

With the use of Fig. 1 we will shortly explain the retro-reflection phenomenon in optical system. Assume that, the optical system is aberration-free and defocus is eliminated. A parallel incoming beam enters the optical system and is focused on the single point on the focal plane of objective. If incoming beam parallel to the optical axis to that

point is the focus of system. If incoming beam is declined to the optical system to that point lies on the focal plane, the position of this point is related to the direction of incident of the beam. Each direction of incident corresponds with one point on the focal plane. Due to the principle of reversibity of the rays the opposite is also the case, namely each point on the focal plane corresponds with one direction of incidence. On this focal plane that coincides with sensitive surface of detector or surface of reticle, not all radiation is absorbed (or is transmitted), so that the part is reflected back toward objective lenses. The reflected radiation is collected by the objective lenses and send into a direction where the original source of the radiation is located. That leads to the fact: if direction of incoming beam is constant, the direction of retro-reflected beam does not vary. It is not dependent on the direction of optical system of the optical and optolectronic devices.

Due to the collection of the objective lenses, the radiation that retro-reflects in optical system could be order of magnitude stronger compared to radiation that scatters at some others surfaces of the optical system. For this reason, the retro-reflection effect can be used for the detection of optical and optoelctronic devices.

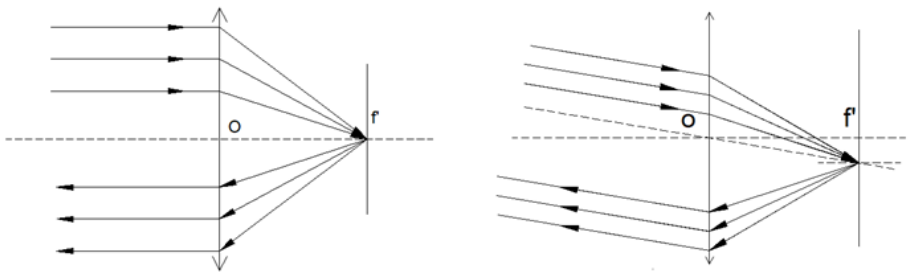

a) b)

Fig. 1. *Retro-reflection effect in the optical and optoelectronic devices*.

Retro-reflection effect in the optical system will be evaluated by intensity of the retro-reflected beam. In what follows we will consider the main factors that influence the power of the retroreflected beam.

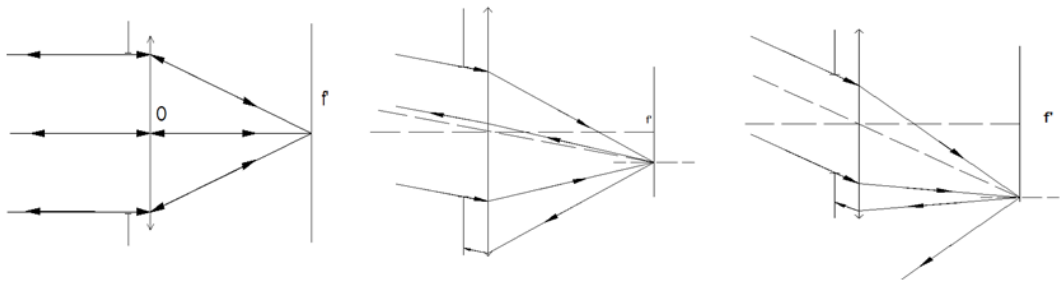

a) b) c)

Fig. 2. *Retro-reflected beam at different incident angle of incoming beam*.

Beside atmospheric absorption and conditions of beam spreading, the radiant flux of retro-reflected beam depends on the following parameters: i) parameters of interrogating laser beam such as: wavelenght, power, angle divergence of the beam, etc; ii) parameters of tested device such as diameter of entrance pupil, vignetting coefficient, coefficient reflection of the retro-reflection surface, etc; iii) parameters that show the relationship

 ISBN:

between the incoming beam and tested device such as distance from the source of laser beam to the tested device, angle incident of laser beam, etc [1-3]. One of the most important parameters is the incident angle of the incoming laser beam.

Fig. 2a shows the case when the incoming beam is parallel to the optical axis, the retro-reflected beam is not cut by any aperture in the optical system of the device. The larger the incident angle created by the incoming beam with the optical axis of the device, the more the retro-reflected beam is cut by the shielding rings in the device's optical system (Fig. 2b), resulting in a decrease in the radiant flux of the retro-reflected beam due to vignetting of the pupil, and there may be no retro-reflected beam out of the optical and optoelectronic device if the incident angle is large enough (Fig. 2c). The influence of vignetting must not be underestimated. A tilt of several degrees could already be sufficient to completely block the retro-reflected signal.

III. THE PROPOSED EXPERIMENTAL DIAGRAM FOR INVESTIGATION RETRO-REFLECTION EFFECT

The proposed experimental model to investigate the retro-reflection phenomenon includes the following main components (Fig. 3): 1 - Laser source, generates laser radiation beam to interrogate the tested device or reference sample; 2 - Collimation system: collimates the laser beam, reduces the angle of divergence of the laser beam before reaching the optical and optoelectronic device to be investigated; 3 - Semi-reflective mirror (or beam splitter): separates the retro-reflected beam of the optical and optoelectronic devices from incoming beam; 4 - Iris aperture: limits the size of the laser beam to the tested devices; 5 - Tested devices or reference sample; 6 - Objective lenses: focus the retro-reflected beam on the sensitive surface of the image sensor; 7 - Filter: reduces the intensity of the retro-reflected beam (if necessary); 8 - Image sensor: captures the image of the retro-reflected beam; 9 - Computer: displays image and performs image processing to calculate the retro-reflection coefficient.

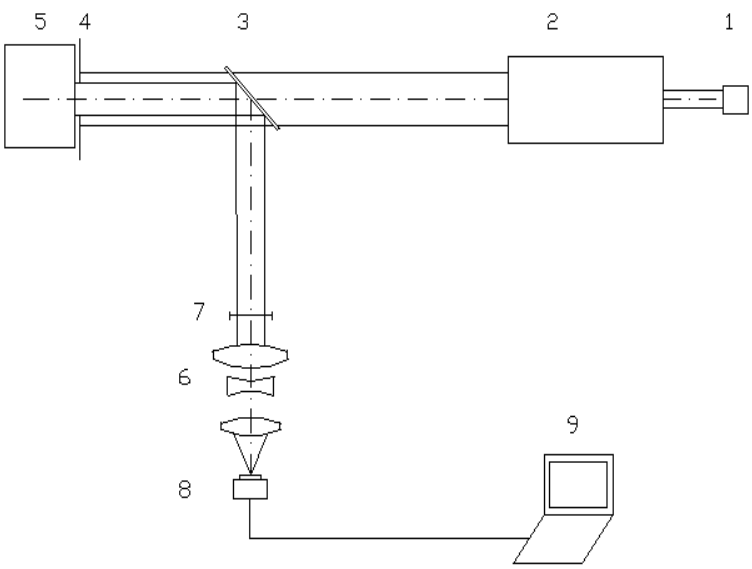

Fig. 3. *The proposed experimental diagram.*

The working principle of the experimental model is as follows: the laser source emits a laser beam. The laser beam, after passing through the collimation system to the semi-reflective mirror (or beam splitter), is divided into two parts, in which one part continues to go straight to the reference sample or to the optical and optoelectronic device that needs to be investigated for the retro-reflection phenomenon. The retro-reflection effect occurs in the optical system of the device. The retro-reflected beam wills propogate backward and when leaving the device it will be parallel but in opposite direction compared with the incident laser beam. When the retro-reflected beam is transmitted to the semi-reflective mirror, then part of it is split and then goes through the filter and then is collected by the objective lenses. Image of retro-reflected beam is created on the image sensor in the form of spot. The signal from the image sensor will be transmitted to the computer and image of retro-reflected beam will be displayed on the screen. Image processing is performed corresponding to the proposed algorithm (Fig. 4) and the retro-reflection coefficient of tested device is calculated.

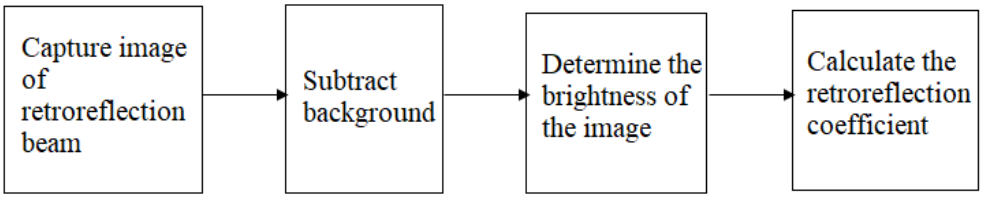

Fig. 4. *The proposed image processing algorithm.*

With this experimental scheme, the retro-reflection coefficient of the investigated devices will be determined through the ratio between the radiant flux of the retro-reflected beam of tested device and the radiation flux of the retro-reflected beam of the reference sample. In order to facilitate the evaluation of the retro-reflection coefficient of tested devices, the reference sample will be selected as a cube corner or plane mirror with a reflectance coefficient of 1. Because the signal received from each pixel of the image sensor is proportional to the radiation flux of incident beam on the detector, so that the brightness level of the image of the retro-reflected beam will be proportional to the radiant flux of the retro-reflected beam. From there, the retro-reflection coefficient of an optical and optoelectronic devices will be determined through the ratio between the brightness of the image caused by the retro-reflection of testes device and the brightness of the image caused by the retro-reflection of the reference sample.

To ensure accuracy, the image created by the retro-reflected beam on the image sensor was acquired with the camera's auto-sensitivity and shutter speed disabled. At the same time, if necessary, an additional filter can be used to ensure that the detector operates within its linear range. The retro-reflection coefficient is determined by using Mathcad software to analyze the image obtained from the detector.

IV. RESULTS AND DISCUSSION

Based on the above proposed experimental scheme, an experimental model is set up to research the retro-reflection effect and determine the retro-reflection coefficient of two

 ISBN:

optical and optoelectronic devices: the PAB-2 (working waveband: 0.4 ÷ 0.78 µm) and the night vision sight AN/PVS2 (working waveband: 0.4 ÷ 0.9 µm) (Fig. 4). The He-Ne laser operating at a wavelength of 0.6328 µm is selected in accordance with the above working waveband of the tested devices.

a) b)

Fig. 4. *Tested devices: a) PAB-2; b) night vision sight AN/PVS2.*

Fig. 5 shows the images of the retro-reflected beam when the retro-reflection efffect occurs in the device PAB-2 with varying the incident angle of the incoming laser beam. In this experiment, the direction of interrogating laser beam does not vary. Optical axis in the tested device is tilted on the vertical and horizontal plane. Fig. 5a represents the situation when incoming beam and optical axis of device are parallel, Fig. 5b - angle between incoming beam and optical system is 20 mil in horizontal plane, Fig. 5c - angle between incoming beam and optical system is 20 mil in vertical plane. Obviously, position of spot does not vary due to the consistancy of the direction of the incoming beam. It is completely corresponds with the above theory.

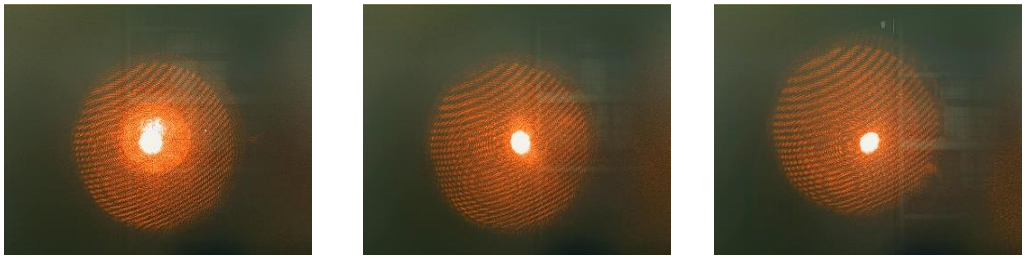

a) b) c)

Fig. 5. *Images of the retroreflected spot at different incident angle of incoming laser beam.*

Fig. 5 also shows that the radiant flux of the retro-reflected beam denpends on the incident angle of interrogating laser beam or angle between incoming beam and optical axis of the tested device. As above statements, the larger incident angle the more radiant flux of the retro-reflected beam is cut by aperture of the optical system. Fig. 6 more clearly shows this conclusion.

Experiments for night vision device AN/PVS2 also were carried out and received results are completely similar. According to the above proposed image processing algorithm, retro-reflection coefficient of the tested devices are evaluated. For PAB-2 it is approximately 0.032 and for AN/PVS2 - 0.131. Notice that the retro-reflection coefficient of AN/PVS2 is 4 times greater than the retro-reflection coefficient of PAB-2. It is due to that reflectivity of the photocathode of image intensifier in the AN/PVS2 significantly greater than the reflectivity of the reticle's surface in the optical system of the PAB-2. Beside that, the night vision devices are typically characterized by a wider aperture. That

leads to the fact that they are also easier to detect by specialized equipment for detecting optical and optoelectronic devices.

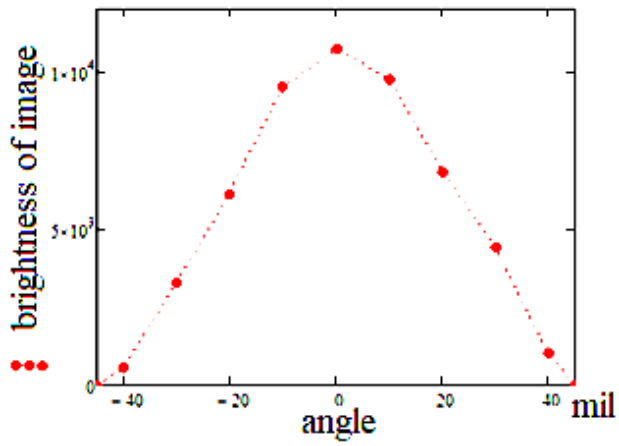

Fig. 6. *Dependence of the radiant flux of retroreflected beam on the incident angle of incoming laser beam.*

V. CONCLUSION

The retro-reflection phenomenon is one of the special phenomena that occur in most optical and opto-electronic devices when a beam of radiation hits them, except those that do not have a real image plane, or do not use reticle. The retro-reflected beam after leaving the device is always parallel but in the opposite direction to the incident beam. The retro-reflection coefficient in each device is different, depending on the parameters of the device itself such as transmittance and reflectivity of the surface where the retro-reflection occurs. The experiments carried out in the content of this paper have confirmed those things. The study and investigation of the retro-reflection phenomenon plays an important role in the researching, designing and manufacturing of active optical detecting devices.

ACKNOWLEDGMENTS. The author would like to acknowledge Department of Optical devices, Le Quy Don Technical University for providing the devices PAB-2, AN/PVS2 and my colleagues for assistance during the fulfilment of this work.

REFERENCES

[1] C. Lecocq, G. Deshors, O. Lado-Bordowsky and J. L. Mayjonnette, Sight laser detection modeling, *Proc. of SPIE.*, 2005, **5806**, 280-286.

[2] Arjan L. Mieremet, Ric M. A. Schleijpen, P. N. Pouchelie, Modeling the detection of optical sight using retroreflection, *Proc. of SPIE.*, 2008, **6950**, 69500E.

[3] Laurel Sadler and Troy A. Alexander, Mobile optical detection system for counter-surveillance, *Proc. of SPIE.*, 2010, **7694**, 76940Y.

[4] Sifeng He, Yuan Meng and Mali Gong, Active laser detection system for recognizing surveillance devices, *Opt. Commun.*, 2018, **426**, 313-324.

 ISBN:

NUMERICAL SIMULATION SUPERCONTINUUM GENERATION IN ALL-NORMAL DISPERSION SUSPENDED-CORE FIBER INFILTRATED WITH ETHANOL AROUND 1064 NM

Le Canh Trung*, Ha Minh Quan, Dinh Xuan Khoa, Do Thanh Thuy, Nguyen Tien Dung, Nguyen Thi Linh, Le Van Hieu, Ngo Dinh Hong Le, Tran Thi Thanh Huyen, Bui Dinh Thuan

Vinh University, 182 Le Duan Street, Vinh City, Viet Nam

*E-mail: *trungch15@gmail.com*

Abstract. In this work, we optimized the structure of suspended-core fiber and filled air holes with ethanol to change the dispersion characteristic to all-normal dispersion for supercontinuum generation. The fiber with a 2.2 µm core diameter filled with ethanol operates in all-normal dispersion region. The SC spectral is formed with the spectrum range from 717 nm to 1700 nm by using a pump pulse with a central wavelength of 1064 nm, pulse width 50 fs, and power of 30 kW.

I. INTRODUCTION

Supercontinuum (SC) generation in all-normal dispersion fiber is studied for its fascinating applications and properties. They have been studied and used in fields such as ultra-short pulse generation [1] and optical coherence tomography [2]. The SC generated in normal dispersion regimen is generated by optical wave breaking (OWB) and self-phase modulation (SPM) [3] mechanisms. Therefore, the SC generation in normal dispersion has the potential for high temporal coherence and flat [4]. For broadband SC generation, numerous efforts have been devoted to extending the spectral width and flatness over wavelength broadband. To achieve this, the initial laser pulse properties should be optimized in terms of pulse duration, pump power, pump wavelength, and input energy [5-6]. Besides, the fiber requires special optical-wave-guiding designs to produce both flat all-normal dispersion and high-nonlinearity properties.

A promising approach is to use suspended core fibers (SCFs) that are fibers composed of small cores, suspended on thin glass bridges [7]. The light is strongly confined in the core of these fibers resulting in high nonlinear coefficient γ [8]. Some articles presenting SCG in silica and soft glasses-based SCFs have been published [9].

In recent years, a promising way to control the dispersion characteristics of SCFs is to infiltrate liquids into the holes of the SCFs. Experimental results of SCFs infiltrated with water have been reported in [4]. In addition, ethanol is also an attractive candidate for SCFs infiltrated with liquids because of its lower refractive index than fused silica, which ensures a modified total internal reflection (M-TIR) mechanism.

In this article, we optimize the dispersion curve of SCFs by infiltrating holes with ethanol. We assume a fiber structure with the core suspended over six thin bridges glass and the background material is fused silica and solved the general nonlinear Schrodinger

equation (GNLSE) to demonstrate the SC generation for our optimized fiber structure. We discuss about this structure.

II. MODELING STRUCTURE AND THE STUDY METHOD

The general structure of the investigated fibers is presented in Fig. 1. The background material of the fiber is made of fused silica and consists of six thin glass bridges.

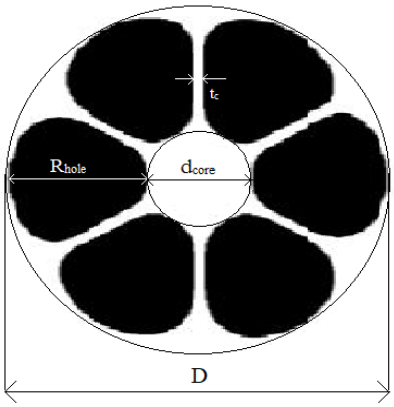

Fig. 1. *The cross-section of simulated SCFs, d_{core} is the core diameter. White area is illustrated fused silica and black area is air or ethanol.*

For modeling, we use the commercial software Lumerical Mode Solution (LMS) on the eigenmode solver method [10]. The refractive indices of the material as a function of wavelength are given by the Sellmeier equation below:

$$n^2(\lambda) = 1 + \frac{B_1\lambda^2}{\lambda^2 - C_1} + \frac{B_2\lambda^2}{\lambda^2 - C_2} + \frac{B_3\lambda^2}{\lambda^2 - C_3} \quad (1)$$

where constant B_i *and* C_i are given in Table 1.

Table 1. *The Sellmeier coefficients of fused silica and ethanol.*

Sellmeier coefficients	Materials	
	Fused silica	Ethanol (C_2H_5OH)
B_1	0.6694226	0.83189
C_1 (μm^2)	4.4801×10^{-3}	0.0093
B_2	0.6694226	-0.15582
C_2 (μm^2)	1.3285×10^{-2}	-49.452
B_3	0.8716947	0
C_3 (μm^2)	95.341482	0

We also numerically modeled SCG in the investigated fibers to analyze the nonlinear processes responsible for spectral broadening. We solved the general nonlinear Schrodinger equation (GNLSE) to achieve these goals [11]:

$$\frac{\partial A}{\partial z} + \frac{\alpha}{2}A - \sum_{k\geq 2}\frac{i^{k+1}}{k!}\beta_k\frac{\partial^k A}{\partial T^k} = i\gamma\left(1 + i\tau_{shock}\frac{\partial}{\partial T}\right)\times\left(A|z,t|\int_{-\infty}^{\infty}R(T')\left|A(z,T-T')\right|^2 dT'\right) \quad (2)$$

 ISBN:

where α is the total fiber loss, z is the spatial coordinate along fiber and β_k is the *k-th* order of dispersion. The GNLSE in our modeling accounts for dispersion terms β_k up to the 9th order. In our simulations, the pump pulse was Gaussian-shaped, the centered wavelength at 1064 nm.

The fiber's mode effective areas were approximated with fixed values of their core areas. The Raman scattering spectra of the fiber were comparable to the fused silica; hence the Raman response function identical to fused silica was used in both simulations, according to:

$$R(T) = (1 - f_R).\delta(T) + f_R \frac{\tau_1^2 + \tau_2^2}{\tau_1 \tau_2^2} \exp(-T/\tau_2) \sin(T/\tau_1) \Theta(T) \quad (3)$$

where f_R =0.18 is the delayed Raman contribution, $\tau_1 = 12.2$ fs, τ_2 =32 fs, $\Theta(T)$ is the Heaviside step function, δ(T) is the Dirac delta function.

In the numerical simulation of SC generation, we used the split-step Fourier method to solve the GNLSE in the frequency domain for input femtosecond pulse. The analysis is simulated with the following parameters: fiber length 15 cm, pulse width 50 fs, and pump wavelength 1064 nm.

III. RESULTS AND DISCUSSION

In our work, we aim at designing a new suspended-core fiber that allows for low chromatic dispersion inside the all-normal regime, which is employed for a commecial pulse laser at central wavelength of 1064 nm.

We analyze how the diameter of the core affects the linear characteristics of the SCFs, especially the effective dispersion for precise shaping and a wide range of wavelengths in the completely normal mode. In all investigated cases, we only consider the SCF's fundamental mode, as shown in Fig. 2.

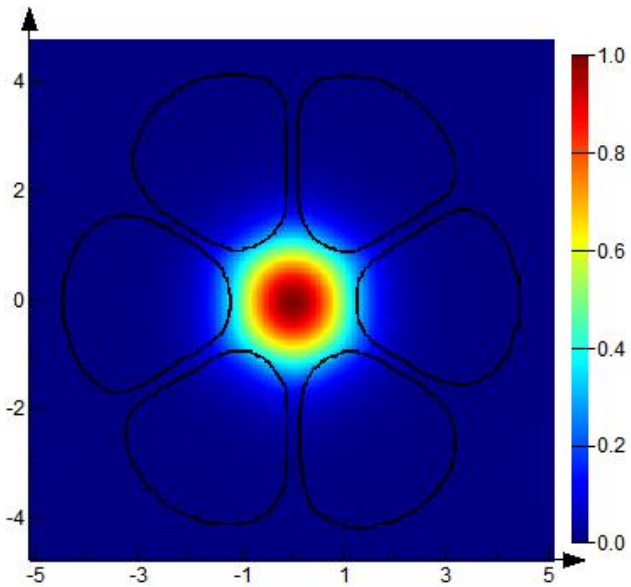

Fig. 2. *Numerically calculated intensity distribution of the fundamental mode of the SCFs.*

To optimize the fiber structure, we first simulate the influence of the diameter core from 4.4 µm to 2.2 µm. The resulting dispersion curves for the fundamental modes are depicted in Fig. 3. Decrease the core diameter leads to increase in dispersion value.

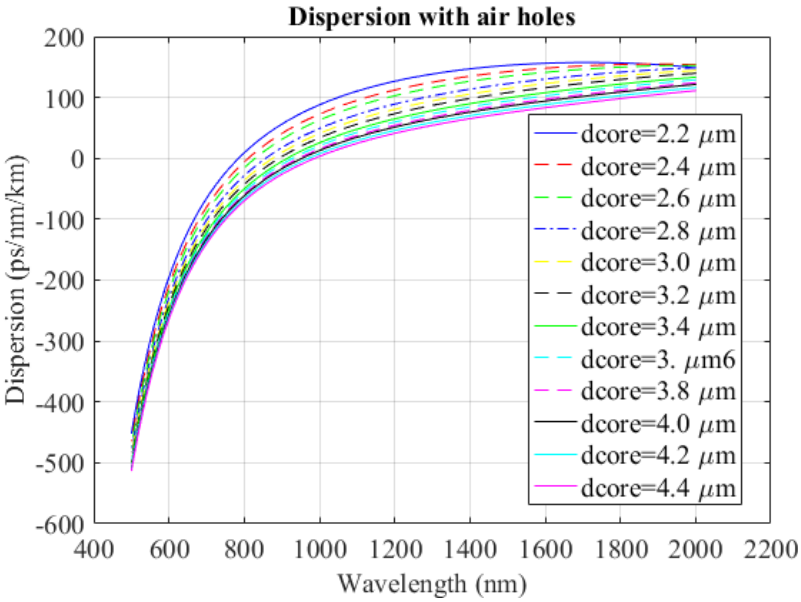

Fig. 3. *Dispersion characteristics of the fundamental mode with air holes.*

In the next step, we filled six air holes with ethanol and Fig. 4 is depicted the dispersion characteristics for different diameters of the core with holes filled ethanol. In the case of fiber filled with ethanol, when the core diameter is reduced from 4.4 microns to 2.2 microns, the dispersion curve changes from anomalous dispersion to normal dispersion.

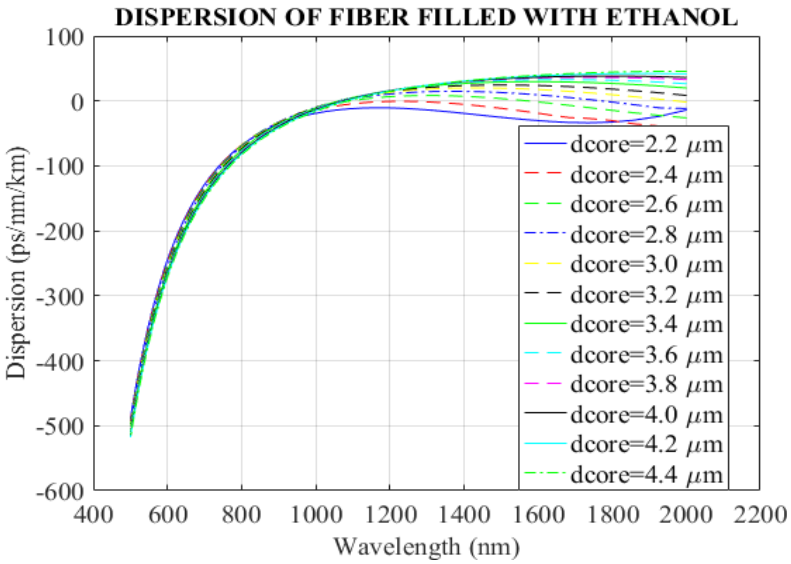

Fig. 4. *Dispersion characteristics of the fundamental mode with ethanol holes.*

Figure 5 shows the different in dispersion characteristics of fiber with 2.2 microns core diameter when the holes filled with ethanol and the air holes. This fiber has optimum dispersion curve for SC generation because it has all-normal dispersion. Where, the dispersion characteristic of fiber with air holes is anomalous dispersion, ZWD is 790 nm, dispersion at 1064 nm is 103.078 ps/nm/km.

 ISBN:

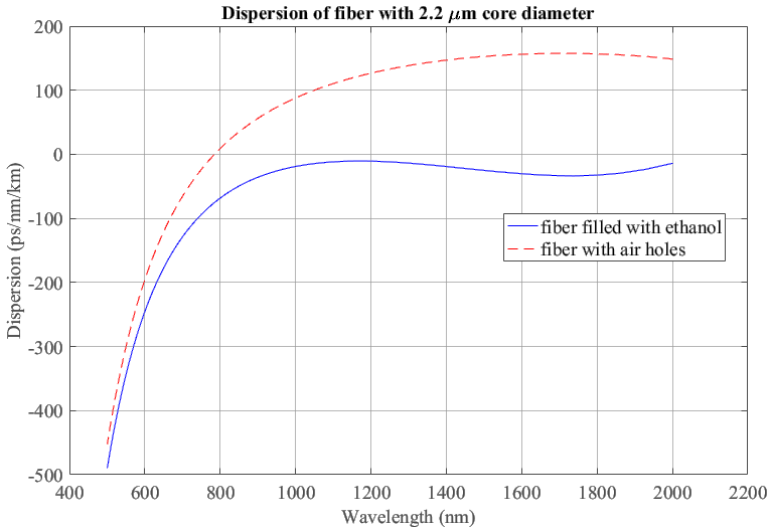

Fig. 5. *Dispersion characteristics of fiber with 2.2 microns core diameter.*

Fig. 6 shows the non-linear coefficient and effective mode area of optimal structure. The non-linear coefficient decrease with wavelength and the effective mode area of fundamental mode increase with wavelength. At wavelength 1064 nm, the non-linear coefficient equal 0.3997 μm^2 and the effective mode area of fundamental mode equal 4.032 $W^{-1}m^{-1}$. Where, the effective mode area is small because the core diameter is small.

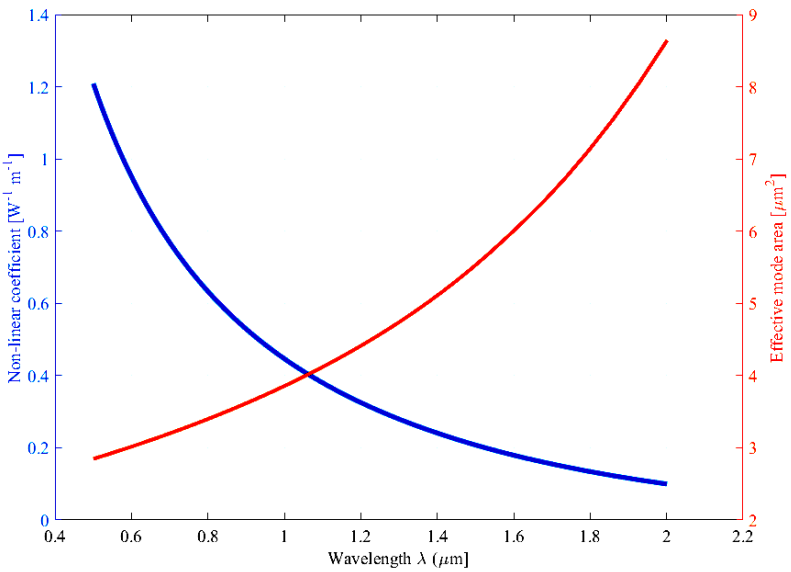

Fig. 6. *Non-linear coefficient and effective mode area of optimal structure SCF.*

In Fig. 7a, the output spectral with difference powers at the *15* cm length of fiber. With pump power of 30 kW, the spectrum range from 717 nm to 1700 nm. Fig. 7b illustrated the spectral of the pulse along the propagation distance with difference powers.

Meanwhile, Fig. 8 shows the spectral and temporal evolution of the pulse along the propagation distance with an input power of 30 kW. The broad spectrum is asymmetric because different frequency components usually have different velocities, the time delay between different frequencies becomes larger with longer propagation.

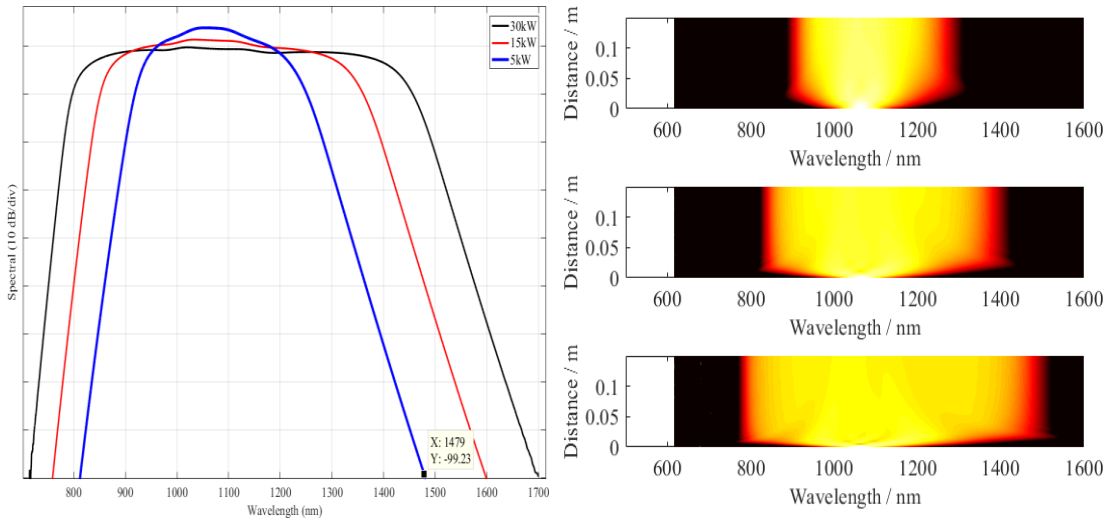

Fig.7. *a) The output spectrum calculated at distance 15 cm with difference powers, b) Numerical calculations of the output spectral of the pulse along the fiber filled with ethanol.*

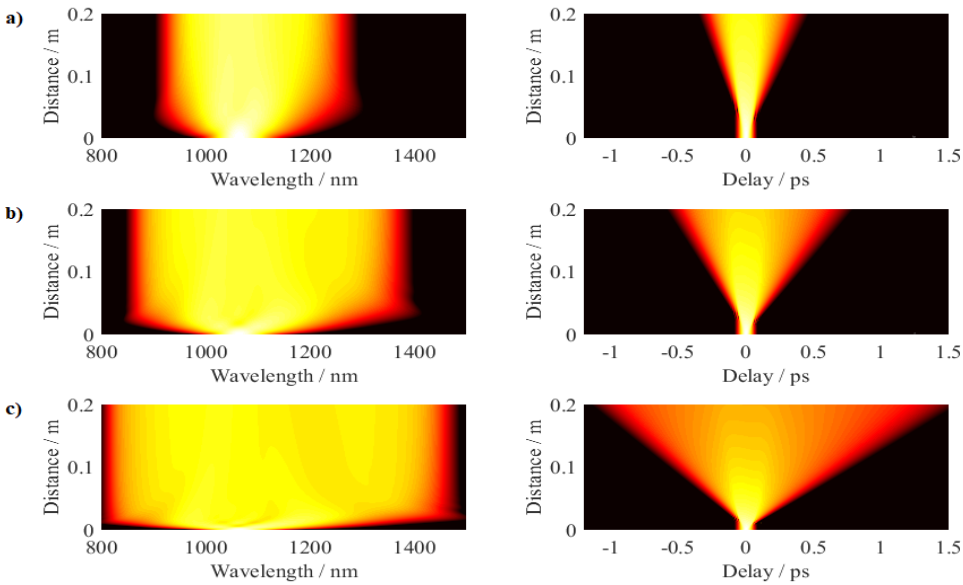

Fig. 8. *Numerical calculations of the spectral and temporal evolution: a) 5 kW; b) 15 kW; c) 30 kW.*

IV. CONCLUSSION

In this paper, we used numerical method on the optimum structure SCFs with background material is fused silica and filled with ethanol. The dispersion characteristic of optimum structure are flat and located in all-normal dispersion for SC generation with pumping at 1064 nm, the optimum structure with 2.2 µm core diameter.

In our result, by using pulses with a central wavelength of 1064 nm, pulse width 50fs and pump power of 30 kW, we obtain output spectrum in the range from 717 nm to 1700 nm. Further increasing the width of the spectral can be expected if we increase input pulse power. The output SC spectral is flat, which has the potential for high temporal coherence.

 ISBN:

REFERENCES

[1] Heidt A. M., Rothhardt J., Hartung A., Bartelt H., Rohwer E. G., Limpert J., et al., High quality sub-two cycle pulses from compression of supercontinuum generated in all-normal dispersion photonic crystal fiber, *Optics Express*, 2011, **19**(15), 13873-13879.

[2] Povazay B., Bizheva K., Unterhuber A., Hermann B., Sattmann H., Fercher A. F., et al., Submicrometer axial resolution optical coherence tomography, *Optics Letters*, 2002, **27**(20), 1800-1802.

[3] Heidt A. M., Hartung A., Bosman G. W., Krok P., Rohwer E. G., Schwoerer H., et al., Coherent octave spanning near-infrared and visible supercontinuum generation in all-normal dispersion photonic crystal fibers, *Optics Express*, 2011, **9**(4), 3775-3787.

[4] Trung Le Canh, Van Thuy Hoang, Hieu Le Van, Dariusz Pysz, Van Cao Long, Thuan Bui Dinh, et al., Supercontinuum generation in all-normal dispersion suspended core fiber infiltrated with water, *Opt. Mater. Express*, 2020, **10**, 1733-1748.

[5] Medjouri A., Abed D., Ziane O., Simohamed L. M., Design and optimization of As_2S_5 chalcogenide channel waveguide for coherent mid-infrared supercontinuum generation, *Optik*, 2018, **154**(2018), 811-820.

[6] Hansen K. P., Dispersion flattened hybrid-core nonlinear photonic crystal fiber, *Optics Express*, 2003, **11**(13), 1503-1509.

[7] P. Kaiser, E. A. J. Marcatili, and S. E. Miller, A new optical fiber, *Bell Syst. Tech. J.*, 1973, **52**(2), 265-269.

[8] S. Afshar V., W. Q. Zhang, H. Ebendorff-Heidepriem, and T. M. Monro, Small core optical waveguides are more nonlinear than expected: experimental confirmation, *Opt. Lett.*, 2009, **34**(22), 3577-3579.

[9] Bo Wu, Zheming Zhao, Xunsi Wang, Youmei Tian, Nan Mi, Peng Chen, Zugang Xue, Zijun Liu, Peiqing Zhang, Xiang Shen, Qiuhua Nie, Shixun Dai, and Rongping Wang, Mid-infrared supercontinuum generation in a suspended-core tellurium-based chalcogenide fiber, *Opt. Mater. Express*, 2018, **8**, 1341-1348.

[10] #x201C; LumericalSolutions, Inc., https://www.lumerical.com/products/mode/.

[11] J. C. Travers, M. H. Frosz, and J. M. Dudley, Nonlinear fiber optics overview, Supercontinuum Generation in Optical Fibers, J. M. Dudley and R. Taylor, Eds., Cambridge University, 2010, 32-51.

PHASE-DEPENDENCE OF OPTICAL PROPERTIES IN A THREE-LEVEL LAMBDA MEDIUM

Nguyen Thi Thu Hien[1,2], Nguyen Huy Bang[2], Dinh Xuan Khoa, Hoang Minh Dong[1,*], Nguyen Tuan Anh[1], Thai Doan Thanh[1], Luong Thi Yen Nga[2], Le Van Doai[2], Le Thi Minh Phuong[3]

[1]*Ho Chi Minh City University of Food Industry, Ho Chi Minh City, Vietnam*

[2]*Vinh University, 182 Le Duan Street, Vinh City, Vietnam*

[3]*Saigon University, 273 An Duong Vuong, Ho Chi Minh City, Vietnam*

*E-mail: *dong.gtvtmt@gmail.com*

Abstract. The absorption (gain) and dispersion behaviors of the probe field are controlled via the relative phase of the applied fields in the closed-loop three-level Λ-type atomic system by numerically solving the density matrix equations in the steady-state. The studied results show that by modulating the relative phase of applied fields we can obtain quite high inversionless gain at different probe detunings with the modulation period is 2π. Our research findings indicate that amplitudes of the microwave field are important factors that can result in different absorption-gain behavior of the probe field. The proposed scheme may have applications in the design of optical switching and optical gain devices in optical communications.

Keywords: *Controlling relative phase, Electromagnetically induced transparency, Absorption-gain, Dispersion.*

I. INTRODUCTION

Over the last few years, the study of quantum coherence and interference in multilevel atomic systems can lead to many interesting optical phenomena [1]. Especially, the discovery of electromagnetically induced transparency (EIT) effect has delivered a new type of material with giant Kerr nonlinearity [2,3]. Such material is expected to promote progress in optical bistability and all-optical switching [4-9], lasing without inversion (LWI) [10]. The EIT effect can also modify the propagation dynamics of light pulses such as the formation and propagation of optical solitons [10-18].

Recently, there has been a growing interest in quantum loop schemes, because closed-loops are sensitive [19] with a relative phase of the interacting fields. The phase can easily modify the linear and nonlinear optical properties dramatically and leads to some interesting phenomena such as phase control of EIT [20,21], amplification without inversion [22], phase-sensitive atom localization [23], enhancement of Kerr nonlinearity associated with self-phase modulation and cross-phase modulation [6,24-26], transient behavior [27,28], optical switching and other phase-dependent coherent properties [29-35], etc., have been reported both theoretically and experimentally in a closed-loop atomic system.

In this paper, we study the effects of the relative phase of the applied fields on the absorption-gain and dispersive behavior of a probe field in the Λ configuration closed by

 ISBN:

an additional microwave field coupling the two lower states. Section 2 describes our theoretical model and present the density matrix equations of a closed-loop three-level Λ-type atomic medium. In Section 3, our discussion is about the absorption-gain and dispersive characteristics of the medium on the probe field under the modulation of the relative phase of applied fields. Finally, a conclusion is given in the last section.

II. MODEL AND BASIC EQUATIONS

We consider a closed-loop three-level lambda-type atomic system coupled by two laser fields and a microwave driving field is shown in Fig. 1. The transition $|3\rangle \leftrightarrow |2\rangle$ is driven by a coupling field with Rabi frequency $2\Omega_c$, initial phase φ_c and angular frequency ω_c. A probe field with Rabi frequency $2\Omega_p$, initial phase φ_p and angular frequency ω_p is applied to the transition $|3\rangle \leftrightarrow |1\rangle$. An assisting microwave driving field with Lamor frequency $2\Omega_m$, initial phase φ_m and angular frequency ω_m is used to couple Zeeman sublevels $|2\rangle$ and $|1\rangle$ through an allowed magnetic-dipole transition and to further form a closed-loop configuration.

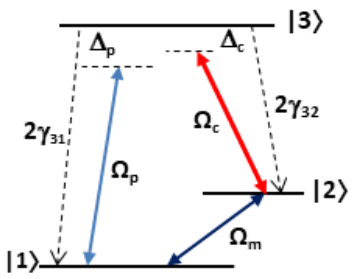

Fig. 1. *The energy scheme of the three-level lambda-type atom driven by the microwave field*.

The leading role of the microwave field is to induce quantum coherence between levels $|2\rangle$ and $|1\rangle$, which is necessary for phase-dependent effects. Another role of the microwave field is to transfer atoms from level $|1\rangle$ to level $|2\rangle$ so that they can be further pumped into level $|3\rangle$ by the coupling field ω_c. The level $|3\rangle$ spontaneously decays to level $|1\rangle$ and $|2\rangle$ are γ_{31} and γ_{32}, respectively. In the interaction picture, with the rotating-wave approximation and the electric-dipole approximation, the semiclassical Hamiltonian describing the atom-field interaction for the system under study can be written as (with the assumption of h=1):

$$H_{\text{int}} = \begin{bmatrix} -\Delta_p & -\Omega_m^* e^{i\phi} & -\Omega_p^* \\ -\Omega_m e^{-i\phi} & -\Delta_c & -\Omega_c^* \\ -\Omega_p & -\Omega_c & 0 \end{bmatrix}, \tag{1}$$

where $\Delta_p = \omega_{31} - \omega_p$, $\Delta_c = \omega_{32} - \omega_c$, and $\phi = (\omega_c + \omega_m - \omega_p)t + (\varphi_c + \varphi_m - \varphi_p)$ are detunings of the probe field and coupling field from the atomic transition frequencies, respectively. The dynamical evolution of the system can be described by the Liouville equation:

$$\frac{\partial \rho}{\partial t} = -i[H_{\text{int}}, \rho] + \Lambda\rho, \tag{2}$$

and the relevant density matrix equations obtained for the closed-loop three-level lambda

system are given as follow:

$$\frac{\partial\rho_{11}}{\partial t} = 2\gamma_{31}\rho_{33} + i\Omega_p^*\rho_{31} - i\Omega_p\rho_{13} + i\Omega_m^* e^{i\phi}\rho_{21} - i\Omega_m e^{-i\phi}\rho_{12}, \tag{3a}$$

$$\frac{\partial\rho_{22}}{\partial t} = 2\gamma_{32}\rho_{33} - i\Omega_m^* e^{i\phi}\rho_{21} + i\Omega_m e^{-i\phi}\rho_{12} + i\Omega_c^*\rho_{32} - i\Omega_c\rho_{23}, \tag{3b}$$

$$\frac{\partial\rho_{33}}{\partial t} = -2(\gamma_{31}+\gamma_{32})\rho_{33} - i\Omega_p^*\rho_{31} + i\Omega_p\rho_{13} - i\Omega_c^*\rho_{32} + i\Omega_c\rho_{23}, \tag{3c}$$

$$\frac{\partial\rho_{21}}{\partial t} = (i(\Delta_c - \Delta_p) - \gamma_{21})\rho_{21} - i\Omega_m e^{-i\phi}(\rho_{22} - \rho_{11}) - i\Omega_p\rho_{23} + i\Omega_c^*\rho_{31}, \tag{3d}$$

$$\frac{\partial\rho_{31}}{\partial t} = -(i\Delta_p + \gamma_{31} + \gamma_{32})\rho_{31} - i\Omega_p(\rho_{33} - \rho_{11}) + i\Omega_c\rho_{21} - i\Omega_m e^{-i\phi}\rho_{32}, \tag{3e}$$

$$\frac{\partial\rho_{32}}{\partial t} = -\left(i\Delta_c + \gamma_{31} + \gamma_{32}\right)\rho_{32} + i\Omega_p\rho_{12} - i\Omega_c(\rho_{33} - \rho_{22}) - i\Omega_m^* e^{i\phi}\rho_{31}, \tag{3f}$$

where the matrix elements obey conjugated and normalized conditions, namely $\rho_{ij}=\rho_{ij}^*$ ($i\neq j$), and $\rho_{11}+\rho_{22}+\rho_{33}=1$, respectively. The absorption (gain) and dispersion of the medium are determined by the imaginary and real parts of ρ_{31}, respectively. In our notation, if Im(ρ_{31})<0, the system exhibits gain for the probe field; if Im(ρ_{31})>0, the probe field is attenuated. When Im(ρ_{31})<0 and $\rho_{33}<\rho_{11}$, gain without inversion can be obtained, then LWI can be realized.

III. RESULTS AND DISCUSSIONS

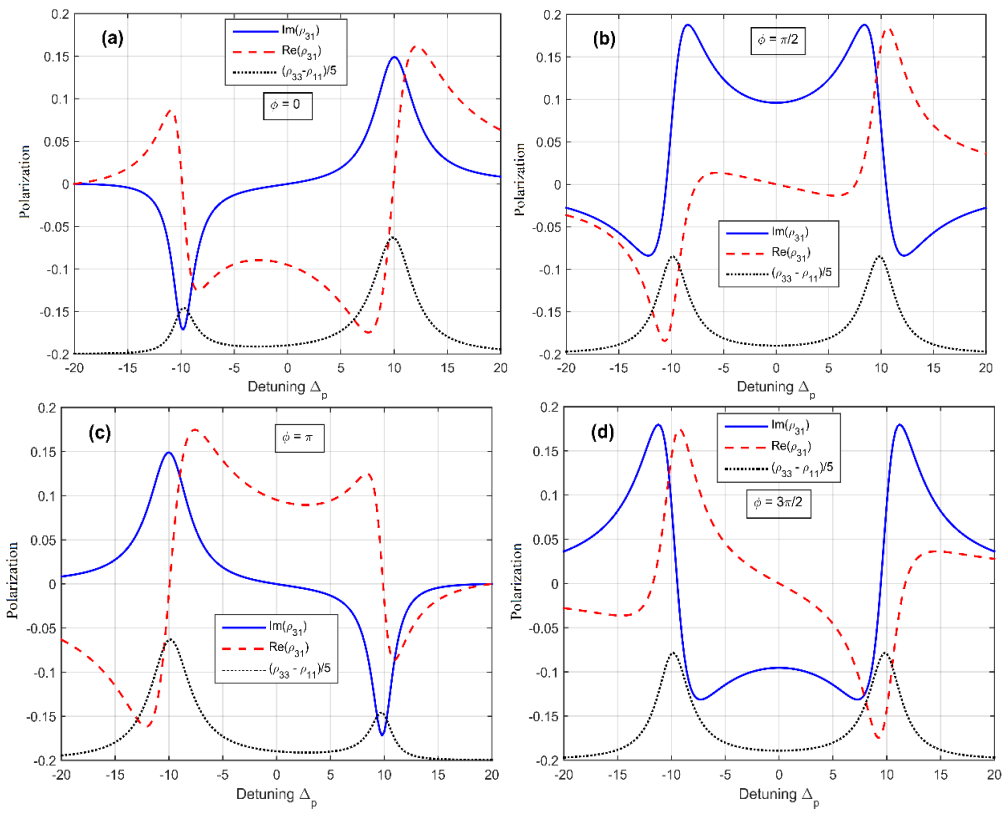

Fig. 2. *Im(ρ_{31}), Re(ρ_{31}) and ($\rho_{33} - \rho_{11}$) versus Δ_p, for different values of the relative phase ϕ: a) $\phi = 0$, b) $\phi = \pi/2$, c) $\phi = \pi$, d) $\phi = 3\pi/2$. The parameters are chosen as $\Omega_p = 0.5\gamma_{31}$, $\Omega_c = 10\gamma_{31}$, $\Omega_m = 1\gamma_{31}$, $\Delta_p = \Delta_c = 0$, and $\gamma_{32} = \gamma_{31}$, respectively.*

 ISBN:

First of all, we consider the influences of the relative phase on the line profiles of the absorption (or gain) and dispersion of the probe field. For simplicity, we assume that each applied field is resonant with the corresponding atomic transition, namely, $\omega_c + \omega_m - \omega_p = 0$ and $\Delta_p = \Delta_c = 0$. Subsequently, that relative phase is only relevant to the initial phase of applied fields $\phi = \varphi_c + \varphi_m - \varphi_p$. In Figure 2, we plot Im(ρ_{31}), Re(ρ_{31}) and ($\rho_{33} - \rho_{11}$) versus the probe detuning Δ_p for different values of ϕ. Comparing Fig. 2a with Fig. 2c, we can see that, the probe absorption-gain Im(ρ_{31}), and dispersive Re(ρ_{31}) with $\phi = 0$ and that with $\phi = \pi$ are exactly symmetric about $\Delta_p = 0$. For $\phi = 0$ ($\phi = \pi$), the probe gain without inversion only can be obtained in the region of $\Delta_p < 0$ ($\Delta_p > 0$), and it increases with the increase of Δ_p. From Figs. 2b and 2d, It can seen that, the probe absorption-gain with $\phi = \pi/2$ and that with $\phi = 3\pi/2$ are exactly symmetric about Im(ρ_{31}) = 0. For $\phi = 3\pi/2$, we can obtain the probe gain without inversion around $\Delta_p = 0$; otherwise, the probe field is absorbed in regions of $\phi = \pi/2$.

In order to have further deeper insight into the influences of the relative phase ϕ on the absorption (gain) and dispersive properties of the probe field, we plot the absorption (gain) Im(ρ_{31}), dispersion Re(ρ_{31}) and population difference ($\rho_{33} - \rho_{11}$) versus relative phase ϕ. From the Fig. 3 we can see that Im(ρ_{31}), Re(ρ_{31}) and ($\rho_{33} - \rho_{11}$) exhibit periodically positive and negative, the period is 2π, as shown in Ref. [36]; by the relative phase controlling, the switching from absorption with inversion to gain without inversion (then LWI) can be realized, increasing of LWI gain and dispersion can be achieved, and the largest index of the refraction corresponding to zero absorption can be obtained always. Thus, the considered three-level closed-loop lambda system can be used for the phase switching of the probe absorption and/or amplification.

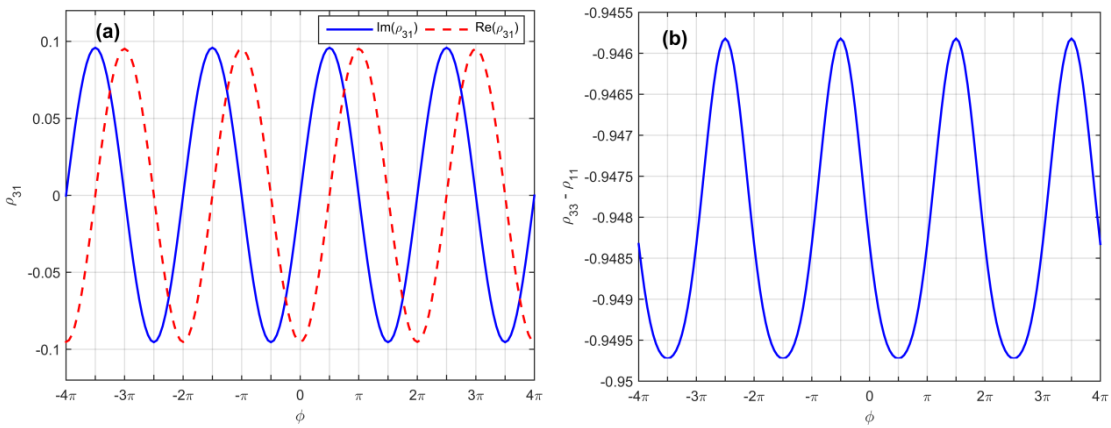

Fig. 3. *(a) Probe absorption Im(ρ_{31}) and dispersion Re(ρ_{31}) coefficients; (b) population difference ($\rho_{33} - \rho_{11}$) versus the relative phase ϕ. Other parameters are the same as in Fig. 2.*

Next, we consider the probe gain Im(ρ_{31}) versus the probe detuning Δ_p for different strengths of the microwave field. In Figure 4, we plot the probe gain Im(ρ_{31}) versus the probe detuning Δp for different values of Ω_m and ϕ. The solid lines in Fig. 4 show that the atomic medium exhibits EIT when $\Omega_m = 0$. However, when $\Omega_m \neq 0$, It is found that the gain behavior of the probe can be raised or reduced by changing Ω_m. For example, when $\Omega_m = 12\gamma_{31}$, can we obtain the probe gain without inversion in a large spectral range around

$\Delta_p = 0$ at the $\phi = \pi/2$. While for $\phi = 3\pi/2$, when the coupling field is not very strong, we can obtain the probe gain in around $\Delta p = 0$. So, in the case of a strong microwave field, in order to obtain a large enough probe gain, we should tune the relative phase into regions of $\phi = \pi/2$ or $\phi = 3\pi/2$.

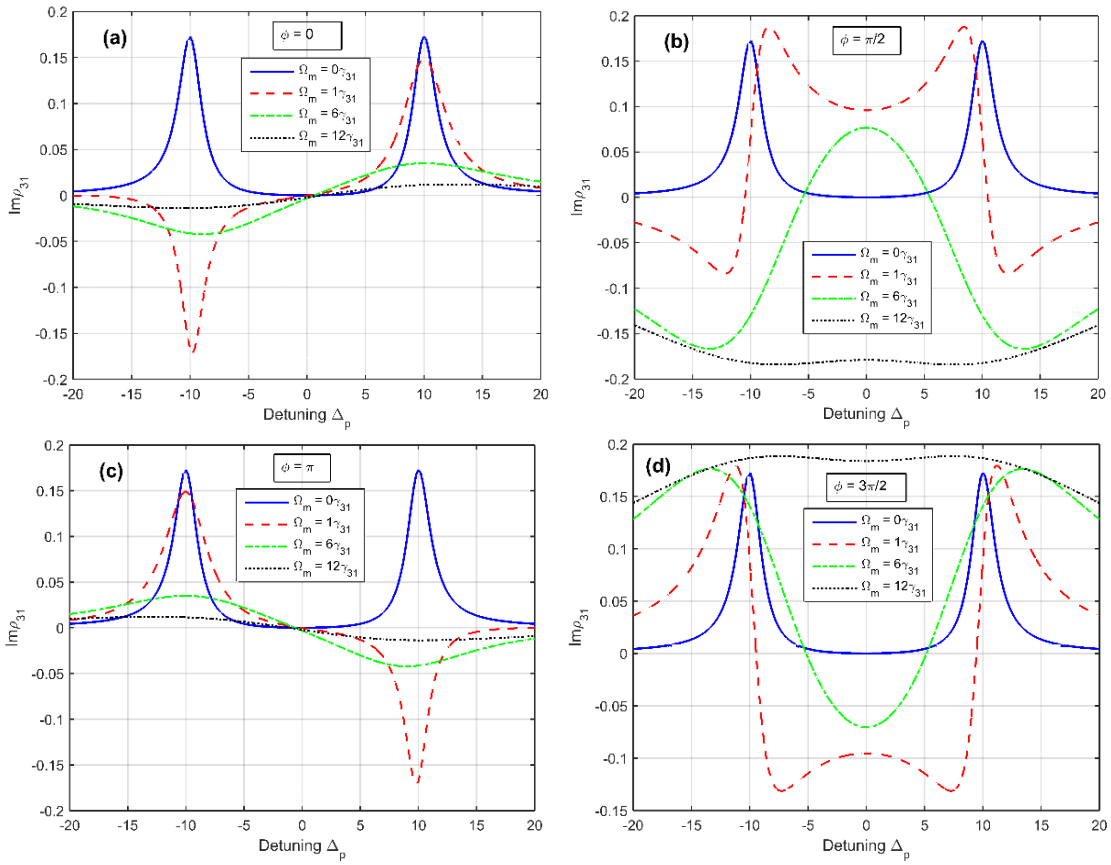

Fig. 4. *The probe gain-absorption Im(ρ_{31}) versus the probe detuning Δ_p for (a) $\phi = 0$; (b) $\phi = \pi/2$; (c) $\phi = \pi$; (d) $\phi = 3\pi/2$ and different values of Ω_m. Other parameters are the same as in Fig. 2.*

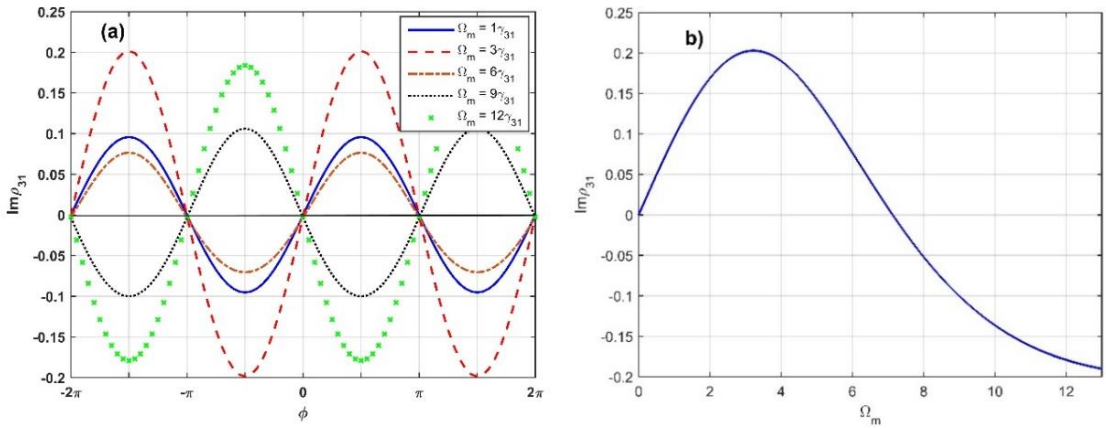

Fig. 5. *a) The probe absorption-gain Im(ρ_{31}) at $\Delta_p = 0$ versus the relative phase ϕ for different values of Ω_m, and b) the probe absorption-gain Im(ρ_{31}) versus the microwave field strength Ω_m. Other parameters are the same as in Fig. 2.*

Finally, we investigate the response of the probe gain to the relative phase ϕ in different cases of the microwave field. We plot the probe absorption (or gain) Im(ρ_{31}) at $\Delta_p = 0$ versus ϕ for different values of Ω_m as in Figure 5. Obviously, the probe absorption (or

 ISBN:

gain) Im(ρ_{31}) is a periodical function of the relative phase ϕ with a period of 2π. From Fig. 5a, we can obtain the probe gain by tuning the relative phase ϕ into proper regions. The probe gains increase with the increasing of Ω_m. However, when the microwave field Ω_m becomes stronger, we only obtained probe absorption (example, the cases $\Omega_m = 9\gamma_{31}$ and $\Omega_m = 12\gamma_{31}$, in Fig. 5a, respectively). It can be seen clearly when we fixed the relative phase at $\phi = \pi/2$ and present the probe absorption (or gain) Im(ρ_{31}) versus Ω_m as shown in Fig. 5b.

IV. CONCLUSION

In this work, we have investigated the absorption (gain), dispersive behavior of the probe field in a microwave-driven closed-loop Λ-type atomic medium. We have shown that due to the quantum coherence between the two lower levels induced by the applied microwave field, the absorption (gain) and dispersive of the probe field are periodical functions of ϕ, the modulation period is always 2π. By modulating the relative phase of the applied fields, the absorption-gain, dispersion properties and population of the probe field can be dramatically changed, the absorption and dispersion can be eliminated just by tuning the relative phase into the proper regions. Our study also shows that the microwave field strength has a considerable effect on the phase-dependent properties of the system. Varying the strength of the microwave field can change the property of the system from absorption to amplification. The properties of phase-controlled probe absorption (gain) provide the possibility of realizing a phase-controlled switching operation, which may have applications in optical switching and optical gain devices in optical communications.

ACKNOWLEDGMENTS. This work has been sponsored and funded by Ho Chi Minh City University of Food Industry under Contract No. 148/HD-DCT.

REFERENCES

[1] M. Fleischhauer, A. Imamoglu, J. P. Marangos, Electromagnetically induced transparency: optics in coherent media, *Rev. Mod. Phys.*, 2005, **77,** 633-673.

[2] K. J. Boller, A. Imamoglu, S. E. Harris, Observation of electromagnetically induced transparency, *Phys. Rev. Lett.*, 1991, **66**, 2593.

[3] Khoa D. X., Doai L. V., Son D. H. and Bang N. H., Enhancement of self-Kerr nonlinearity via electromagnetically induced transparency in a five-level cascade system: an analytical approach, *J. Opt. Soc. Am. B*, 2014, **31,** 1330.

[4] Harris S. E. and Yamamoto Y., Photon switching by quantum interference, *Phys. Rev. Lett*., 1998, **81**, 3611.

[5] H. Schmidt, R. J. Ram, All-optical wavelength converter and switch based on electromagnetically induced transparency, *Appl. Phys. Lett.*, 2000, **76**, 3173.

[6] A. Fountoulakis, A. F. Terzis, E. Paspalakis, All-optical modulation based on electromagnetically induced transparency, *Phys. Lett. A*, 2010, **374**, 3354.

[7] M. A. Antón, O. G. Calderón, S. Melle, I. Gonzalo, F. Carreño, All-optical switching and

storage in a four-level tripod-type atomic system, *Opt. Commun*., 2006, **268**, 146.

[8] H Jafarzadeh, All-optical switching in an open V-type atomic system, *Laser Phys*., 2017, **27**, 025204.

[9] Hoang Minh Dong, Luong Thi Yen Nga, and Nguyen Huy Bang, Optical switching and bistability in a degenerated two-level atomic medium under an external magnetic field, *Applied Optics*, 2019, **58**, 4192.

[10] A. Imamoğlu and S. E. Harris, Lasers without inversion: interference of dressed lifetime broadened states, *Opt. Lett.*, 1989, **14**, 1344-1346.

[11] R. Yu, J. Li, P. Huang, A. Zheng, X. Yang, Dynamic control of light propagation and optical switching through an RF-driven cascade-type atomic medium, *Phys. Lett. A*, 2009, **373**, 2992.

[12] Liu-Gang Si, Xin-You Lu, Xiangying Hao and Jia-Hua Li, Dynamical control of soliton formation and propagation in a Y-type atomic system with dual ladder-type electromagnetically induced transparency, *J. Phys. B: At. Mol. Opt. Phys*., 2010, **43**, 065403.

[13] Rong Yu, Jiahua Li, Chunling Ding, Xiaoxue Yang, Dual-channel all-optical switching with tunable frequency in a five-level double-ladder atomic system, *Opt. Commun.*, 2011**284**, 2930.

[14] Yang Chen, Zhengyang Bai, and Guoxiang Huang, Ultraslow optical solitons and their storage and retrieval in an ultracold ladder-type atomic system, *Phys. Rev. A*, 2014, **89**, 023835.

[15] H. M. Dong, L. V. Doai, V. N. Sau, D. X. Khoa and N. H. Bang, Propagation of laser pulse in a three-level cascade atomic medium under conditions of electromagnetically induced transparency, *Photonics Letter Poland***,** 2016, **3,** 73.

[16] D. X. Khoa, H. M. Dong, L. V. Doai and N. H. Bang, Propagation of laser pulse in a three-level cascade inhomogeneously broadened medium under electromagnetically induced transparency conditions, *Optik*, 2017, **131,** 497.

[17] H. R. Hamedi, Optical switching, bistability and pulse propagation in five-level quantum schemes, *Laser Phys*., 2017, **27**, 066002.

[18] H. M. Dong, L. V. Doai, and N. H. Bang, Pulse propagation in an atomic medium under spontaneously generated coherence, incoherent pumping, and relative laser phase, *Opt. Commun*., 2018, **426,** 553-557.

[19] J. H. Li, R. Yu, X. Yang, Phase-controlled absorption-gain properties and optical switching in nanodiamond nitrogen-vacancy center, *Appl. Phys. B*, 2013, **111,** 65-73.

[20] E. A. Korsunsky, N. Leinfellner, A. Huss, S. Baluschev, L. Windholz, Phase-dependent electromagnetically induced transparency, *Phys. Rev. A*, 1999, **59**, 2302.

[21] D. Bortman-Arbiv, A. D. Wilson-Gordon, H. Friedmann, Phase control of group velocity: From subluminal to superluminal light propagation, *Phys. Rev. A*, 2001, **63**, 043818.

[22] W. H. Xu, J. H. Wu, J. Y. Gao, Phase-dependent properties in a microwave-driven V system: gain without population inversion and narrow resonances, *Opt. Commun*., 2003, **223**, 367-373.

[23] Chengpu Liu, Shangqing Gong, Takashi Nakajima, Zhizhan Xu, Phase-sensitive atom localization in a loop Λ-system, *Journal of Modern Optics*, 2006, **12**, 1791-1802.

[24] Sun H., Niu Y. P., Jin S. Q. and Gong S. Q., Phase control of cross-phase modulation with electromagnetically induced transparency, *J. Phys. B: At. Mol. Opt. Phys.*, 2007, **40**, 3037.

 ISBN:

[25] Sun H., Niu Y. P., Jin S. Q. and Gong S. Q., Phase control of the Kerr nonlinearity in electromagnetically induced transparency media, *J. Phys. B: At. Mol. Opt. Phys*., 2008, **41**, 065504.

[26] Y. Qi, Y. Niu, F. Zhou, Y. Peng and S. Gong, Phase control of coherent pulse propagation and switching based on electromagnetically induced transparency in a four-level atomic system, *J. Phys. B: At. Mol. Opt. Phys*., 2011, **44**, 085502.

[27] W. H. Xu, J. H. Wu, J. Y. Gao, B. Zhang, Elimination of the transient absorption in a microwave-driven Λ-type atomic system, *Phys. Lett. A*, 2003, **314**, 23-28.

[28] Zhi Qiang Zeng, Yu-Ping Wang, and Bang Pin Hou, Amplitude and phase control of transient absorption and dispersion in a microwave-driven atomic system, *Eur. Phys. J. D*, 2013, **67**(4), 76.

[29] G. S. Agarwal, Tarak Nath Dey, Sunish Menon, Knob for changing light propagation from subluminal to superluminal, *Phys. Rev. A*, 2001, **64**, 053809.

[30] Giovanna Morigi, Sonja Franke-Arnold, Gian-Luca Oppo, Phase-dependent interaction in a four-level atomic configuration, *Phys. Rev. A*, 2002, **66**, 053409.

[31] J. H. Wu, J. Y. Gao, Phase and amplitude control of the inversionless gain in a microwave-driven Λ-type atomic system, *Eur. Phys. J. D*, 2003, **23**, 315-319.

[32] Dong-chao Cheng, Cheng-pu Liu, Shang-qing Gong, Optical bistability via amplitude and phase control of a microwave field, *Opt. Commun*., 2006, **263**, 111-115.

[33] Hoonsoo Kang, Gessler Hernandez, Jiepeng Zhang, and Yifu Zhu, Phase-controlled light switching at low light levels, *Phys. Rev. A*, 2006, **73**, 011802(R).

[34] Jiahua Li, Coherent control of optical bistability in a microwave-driven V-type atomic system, *Physica D*, 2007, **228**, 148-152.

[35] J. Kou, R. G. Wan, Z. H. Kang, L. Jiang, L. Wang, Y. Jiang, J. Y. Gao, Phase-dependent coherent population trapping and optical switching, *Phys. Rev. A*, 2011, **84**, 063807.

[36] Hoang Minh Dong, and Nguyen Huy Bang, Controllable optical switching in a closed-loop three-level lambda system, *Phys. Scr.*, 2019, **94**, 115510.

INVESTIGATION OF THE THIRD-ORDER NONLINEAR OPTICAL EFFECT AND THE PHOTODYNAMIC EFFECT OF THE SAFRANIN O ORGANIC MATTER IN WATER AND METHANOL SOLVENTS

Nguyen Nang Binh[1*], Duong Chi Tong[1], Nguyen Thi Thu Hien[2], Nguyen Hong Giang[1], Phan Trung Vinh[1], Nguyen Thanh Lam[1]

[1]*Physics-Engineering Physics Department, University of Science, 227 Nguyen Van Cu Street, Ward 4, District 5, Ho Chi Minh City, Vietnam*

[2]*University of Food Industry, Ho Chi Minh City, Vietnam*

[*]E-mail: *nguyennangbinh1985@gmail.com*

Abstract. We compare nonlinear refractive index and nonlinear absorption coefficient of Safranin O in methanol and in water to evaluate the influence of the solvents on the third-order nonlinear optical parameters of the materials. At the same time, to expand the applicability of Safranin O, we further investigate its photodynamic effect at 532 nm wavelength.

Keywords: *Z-scan methods, Third-order nonlinear optical effect, Nonlinear optics in organic material, Optical limiting effect, Self-divergence effect, Reverse saturation absorption, Photodynamic effect.*

I. INTRODUCTION

The mechanism of nonlinear optical processes is the interaction between photons of light and the outermost electron the atom [1]. Therefore, the mobility of the outermost electrons governs the performance of a nonlinear optical process. The more mobile the outermost electrons are, the stronger the nonlinear optical effect. Organic substances have electrons in orbital with high mobility, currently, it has become a promising material in nonlinear optical applications, especially for optical effect third-order nonlinear and photodynamic effect [2-3].

Photodynamic therapy (PDT) is a form of non-invasive therapy that uses light and a photosensitive chemical to induce molecular oxygen to induce cell death (phototoxicity) [3]. PDT has been shown to kill microbial cells, including bacteria, fungi and viruses. PDT is commonly used in the treatment of skin diseases. It is used clinically to treat many diseases, including age-related macular degeneration, Psoriasis, atherosclerosis and has shown some efficacy in antiviral treatment, including herpes. It also treats malignant cancers of the head and neck, lungs, bladder and especially the skin. The technology has also been tested for the treatment of prostate cancer.

Safranin O is both a third-order nonlinear material and a photosensitizer used in the photodynamic effect. This study will determine the nonlinear refractive index and nonlinear absorption coefficient of Safranin O at three concentrations 0.02 mM, 0.04 mM, and 0.06 mM in methanol and concentrations 0.12 mM in water by Z-scan method of beam radius to determine the nonlinear refractive index and nonlinear absorption coefficient of Safranin O, respectively [4]. Compare and evaluate the influence of solvents on the third-

 ISBN:

order nonlinear optical of the material. At the same time, the group also investigated the photodynamic effect of Safranin O concentrations 0.02 mM, 0.04 mM, 0.06 mM. at 532 nm by observing the change in the absorption spectrum of the mixture of Safranin and Uric Acid with increasing laser irradiation time at 532 nm wavelength.

II. EXPERIMENTS

2.1. Materials

We use Safranin O solute purchased from Sigma-Aldrich Chemical Company. Safranin O is an organic dye with molecular formula $C_{20}H_{19}N_4Cl$, maximum absorption in the region of 532 nm and can dissolve well in water solvents. The molar mass of Safranin O is 350.84 g/mol.

Uric acid was used to evaluate the photodynamic activity of the photosensitizer through consider its absorbance at 293 nm wavelength.

2.2. Transmittance and absorption spectrum

The transmittance and absorption spectrum were measured with a UV-VIS HALO RB-10 spectrometer and shown in Figure 1 and Figure 2. The thickness of the sample cuvette is 1 mm. From the transmittance spectral data, we can derive the transmittance, linear absorption coefficient of Safranin O in methanol is smaller than in water, and effective length of the samples at 532 nm and list them in Table 1. The solutions strongly absorb light at 532 nm with absorption coefficients above 80%. This is also the wavelength of the excitation light source used in this work.

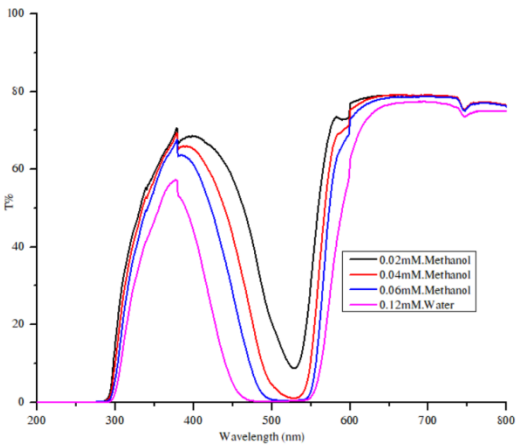

Fig. 1. *Transmission spectrum of Safranin O solution at three concentrations of 0.02 mM, 0.04 mM, 0.06 mM in methanol and 0.12 mM in water.*

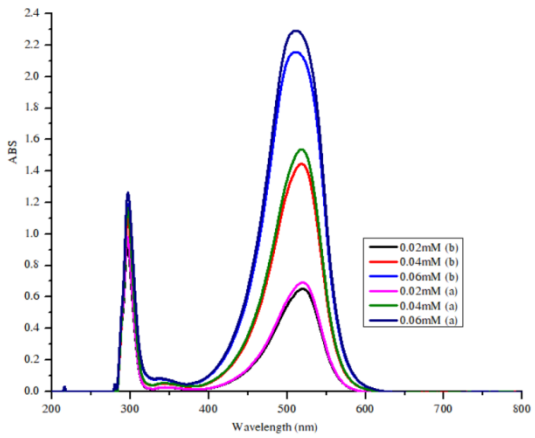

Fig. 2. *Absorption spectrum of Uric Acid solution mixed with Safranin O solution at three concentrations of 0.02 mM, 0.04 mM and 0.06 mM. With a) before laser irradiation, b) after laser irradiation.*

To investigate the photodynamic activity of Safranin O, we added Uric Acid to three concentrations of 0.02 mM, 0.04 mM, 0.06 mM, then observing the change in the absorption spectrum of the mixture of Safranin and Uric Acid with increasing laser irradiation time at 532 nm wavelength.

Uric acid has two absorption peaks at 293 nm and 510 nm. In the from 620 nm to 800 nm wavelengths Uric acid has no absorption phenomenon.

Table 1. *Transmittance, linear absorption coefficient, true length and effective length at wave length 532 nm.*

Solvent	Concentration (mM)	T (%)	α (mm^{-1})	L (mm)	L_{eff} (mm)
Methanol	0.02	9.19	0.239	1	0.89
Methanol	0.04	3.47	0.346	1	0.85
Methanol	0.06	0.51	0.528	1	0.78
Water	0.12	0.4	0.552	1	0.77

To better observe the change of absorption peaks, we plot all spectral values before and after laser irradiation on the same graph as shown in Figure 2. We can observe that values in the wavelength range from 620 nm to 800 nm do not appear on the graph, indicating that in the above wavelength range it is not possible to activate the two-photon absorption effect by the laser 532 nm wavelength. We found that the Safranin solution strongly absorbed at 532 nm wavelength, the absorbance at 293 nm wavelength gradually decreased, showing that this substance has a photodynamic effect. This substance has an absorption peak at 532 nm wavelength, so it can trigger a two-photon absorption effect by laser infrared at wavelength less than 1064 nm.

From the absorption spectral data, we derive the linear, real-length absorption coefficient at 532 nm as shown in Table 2.

Table 2. *Absorption coefficient when irradiating laser with wavelength 532 nm and true length.*

Concentration (mM)	α (mm^{-1})	L (mm)
0.02	5.17	1
0.04	4.37	1
0.06	3.95	1

2.3. Beam radius Z-scan method

Experimental layout of the beam radius Z-scan method is shown in Figure 3. In this method, we will move the sample along the direction of the laser beam around the point where the light is most concentrated (beam neck). The laser beam profiler LBP-1-USB is fixed behind the sample to measure the variation of beam radius with each location. From the location beam radius data, we can determine the nonlinear refractive index and nonlinear absorption coefficient of Safranin O using a Matlab program [5]. Nonlinear refractive index is a parameter that characterizes nonlinear dispersion effects, while nonlinear absorption coefficient is a characteristic parameter for nonlinear absorption effects (saturated absorption, reverse saturation absorption). Reverse saturation absorption can also be the mechanism that produces the optical limiting effect.

III. RESULTS AND DISCUSSTION

Figure 3 shows beam radius data by sample location (beam radius Z-scan curve) of dye solutions at different concentrations in methanol and in solvent water obtained by Z-scan measurement. The actual thickness of the sample is 1 mm. Figure 4 shows the

 ISBN:

nonlinear dispersion (self-divergence) of the negative nonlinear refractive index Safranin O.

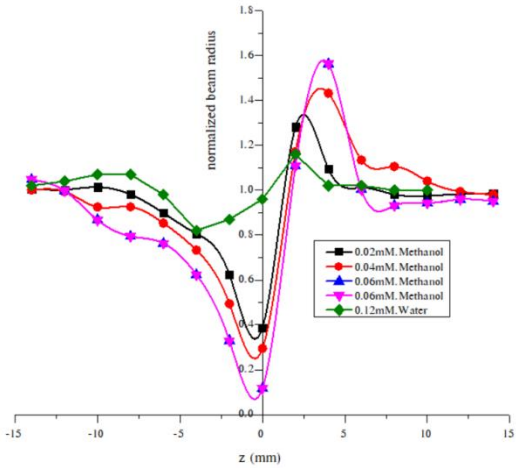

Fig. 3. *Beam radius Z-scan curves of 0.02 mM, 0.04 mM and 0.06 mM dye solutions. The inner radius values on the curve are normalized values, i.e. the radius value measured at a location divided by the beam radius without the nonlinear effect.*

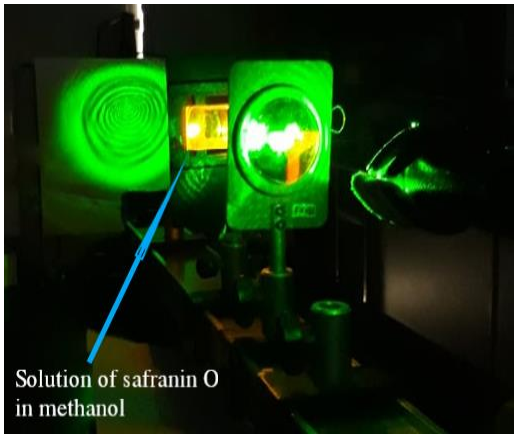

Fig. 4. *The self-divergence effect of negative nonlinear refractive index material (Safranin O).*

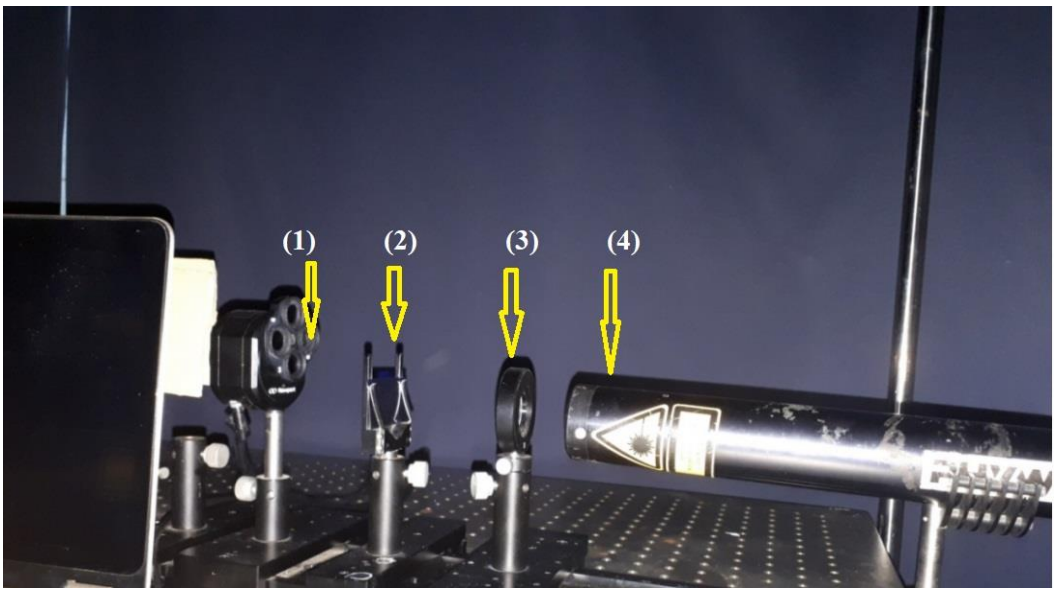

Fig. 5. *An experiment using Laser Beam Profiler to determine the nonlinear parameters of a material sample (1) Laser beam profiler LBP-1-USB features beam radius measurement with error ±2%, (2) Sample need to measure, (3) Lens, (4) Laser.*

The excitation source is a continuous laser with wavelength 532 nm, intensity 63 W/mm^2, about 2 mm Rayleigh length. The actual thickness of the sample is 1 mm. These curves include both nonlinear dispersion and nonlinear absorption. For separate these two effects, we use the method proposed in the work [5]. The result is shown in Figure 6 and Figure 7.

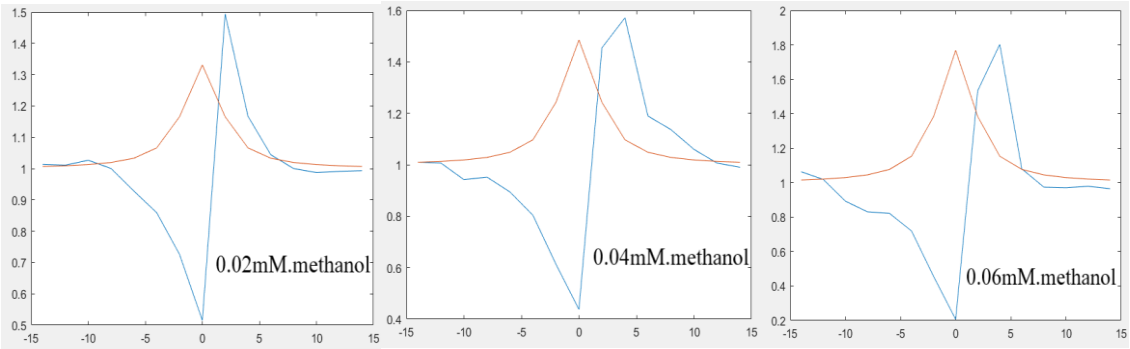

Fig. 6. *The results of separating the nonlinear dispersion and nonlinear absorption curves for the samples with concentrations of 0.02 mM, 0.04 mM, 0.06 mM in methanol by Matlab software.*

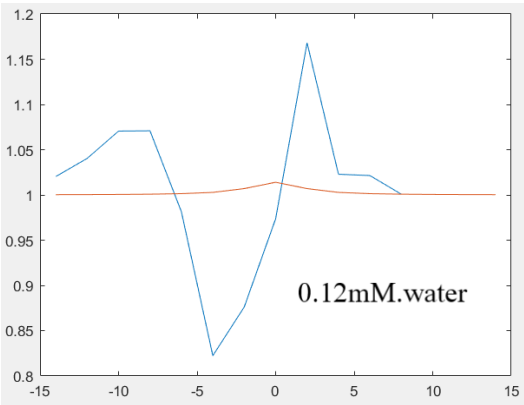

Fig. 7. *The results of separating the nonlinear dispersion and nonlinear absorption curve for the samples with concentration of 0.12 mM, in water by Matlab software.*

Calculation results of nonlinear refractive index n_2 and nonlinear absorption coefficient β are listed in Table 3. We see that Safranin solution in water has almost no nonlinear absorption effect. For comparison purposes, we measured the nonlinear effect at the respective concentrations of 0.02 mM, 0.04 mM, and 0.06 mM of Safranin O in water, but no effect was detected, therefore increased the concentration to twice the maximum concentration, i.e. 0.06 mM. At this concentration the nonlinear effect appears but is very faint.The reason is that because the nonlinear effects here are contributed by thermal nonlinearity, water absorbs heat less than methanol, thus affecting the thermal nonlinear effect.

Table 3. *Nonlinear refractive index n_2 and nonlinear absorption coefficient β were calculated from Matlab program.*

Concentration (mM)	β (mm/w)	n_2 (mm^2/w)
Methanol 0.02 mM	-0.0132	$-3.6399.10^{-6}$
Methanol 0.04 mM	-0.0185	$-4.4142.10^{-6}$
Methanol 0.06 mM	-0.0269	$-6.7748.10^{-6}$
Water 0.12mM	$-4.8398.10^{-4}$	$-1.4869.10^{-6}$

In Fig. 8 and Fig. 9, we can see that n_2, β tends to increase as the concentration increases. This may be because as the concentration increases, the number of dye molecules increases and more participates in nonlinear interactions leading to enhanced synergistic effects. This result is consistent with the results in [6].

 ISBN:

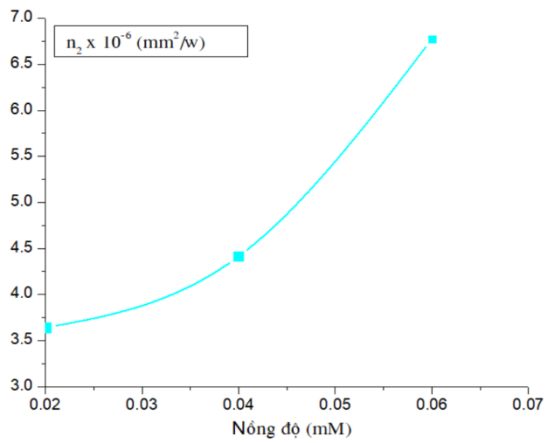

Fig. 8. *Variation n_2 with concentration.*

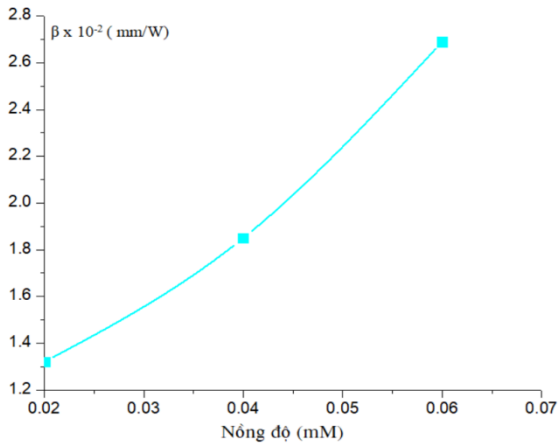

Fig. 9. *Variation β with concentration.*

IV. CONCLUSION

By measuring beam radius Z-scan, we have determined nonlinear refractive index and nonlinear absorption coefficient of Safranin O solution at concentrations of 0.02 mM, 0.04 mM, 0.06 mM in methanol and 0.12 in water, respectively: $-3.6399.10^{-6}$ mm^2/w, -0.0132 mm/w; $4.4142.10^{-6}$ mm^2/w, -0.0185 mm/w; $-6.7748.10^{-6}$ mm^2/w, -0.0269 mm/w; $-1.4869.10^{-6}$ mm^2/w, $-4.8398.10^{-4}$ mm/w. Thereby, we compared the nonlinear refractive index and nonlinear absorption coefficient of Safranin O in methanol and water due to the influence of heat and solvent refraction on the third order nonlinear optical parameters of material. At the same time, by measuring the absorption spectra of Safranin O solution at different concentrations in methanol when irradiating a laser source with a wavelength of 532 nm, we found that the Safranin O solution strongly absorbed at a wavelength of 532 nm. The absorption at 293 nm gradually decreases, indicating that the substance has a photodynamic effect.

REFERENCES

[1] Prasad, P. N., Introduction to biophotonics, John Wiley & Sons, 2004.

[2] Zaira Gadzhimagomedova, Peter Zolotukhin, Oleg Kit, Daria Kirsanova and Alexander Soldatov, Nanocomposites for X-ray photodynamic therapy, *Int. J. Mol. Sci.*, 2020, **21**, 4004.

[3] F. Fischer, G. Graschew, H. J. Sinn, W. Maier-Borst, W.J. Lorenz, P.M. Schlag, A chemical dosimeter for the determination of the photodynamic activity of photosensitizers, *Clinica Chimica Acta*, 1998, **274**, 89-104.

[4] G. Tsigaridas, M. Fakis, I. Polyzos, P. Persephonis, V. Giannetas, Z-scan technique through beam radius measurements, *Appl. Phys. B*, 2003, **76**(1), 83-86.

[5] Lam Thanh Nguyen, Nghia Hong Tran, Cam Tu Bui Thi, Anh Quynh Le, The numerical methods for analyzing the Z-scan data, J. Nonlinear Optic, *Phys. Mat.*, 2014, **23**, 1450020.

[6] G. Balaji, R. K. Rekha, A. Ramalingam, Nonlinear characterization of safranin O dye for application in optical limiting, *Acta Phys. Pol. A*, 2011, **119**, 359-363.

APPLICATION OF COASTAL BIOSHIELDS FOR SHORELINE PROTECTION IN QUANG NAM, CENTRAL VIETNAM

Bijeesh Kozhikkodan Veettil[1,2*], Xuan-Linh Tran[2] and Nhat-Duc Hoang[3,4]

[1]*Institute of Fundamental and Applied Sciences, Duy Tan University, Ho Chi Minh City, Vietnam*

[2]*Faculty of Information Technology, Duy Tan University, Da Nang, Vietnam*

[3]*Institute of Research and Development, Duy Tan University, Da Nang, Vietnam*

[4]*Faculty of Civil Engineering, Duy Tan University, Da Nang, Vietnam*

*E-mail: *bijeeshkozhikkodanveettil@duytan.edu.vn*

Abstract. The Vietnamese coastline faces a number of natural and anthropogenic threats, such as shoreline erosion, flooding, sea level rise, salt water intrusion, typhoons, storms, and pollution. Coastal areas of Central Vietnam are frequently subjected to some of these threats. In this study, we investigated the possibilities, advantages and limitations of using vegetation bioshields for coastal protection in Quang Nam province in Central Vietnam. Special attention has been given to mangrove forests, marshes and other plants. Currently, a number of hard structures have been used for immediate relief from coastal vulnerabilities in Quang Nam. However, an ecosystem-based adaptation using bioshield has been suggested for long-term coastal protection in Central Vietnam. A number of factors, such as coastal geomorphology, degree of vulnerability and biodiversity, influence the applicability of bioshields in Central Vietnam. A combination of hard structures, soft structures and bioshields can be useful for long-term coastal protection in Quang Nam.

I. INTRODUCTION

Coastal areas in Southeast Asia are rich in natural resources; the important economic activities in this region, including fishing, aquaculture, navigation, mining and tourism, have been intensified in recent decades due to population pressure and rapid economic development that led to environmental degradation [1]. Coastal erosion is a major issue threatening human life and environment in Southeast Asia due to a number of natural and anthropogenic factors. Natural factors causing coastal erosion are tides, winds (eolian erosion), storms, waves, near-shore currents, landslides, land subsidence, and sea level rise. Anthropogenic factors triggering coastal erosion are dredging, mangrove deforestation, aquaculture, harbor development, river damming, land reclamation, and mining. Sea level rise is one of the natural phenomena, which is reported to have affected the coastlines in Southeast Asia negatively in recent years [2].

Coastal area of Vietnam is one of the densely populated regions in Southeast Asia [3]. Vietnamese coastline (3260 km in length) is one of the Southeast Asian regions largely influenced by climate change, particularly near the two major river deltas (the Mekong and the Red River) [4]. Coastal areas near other smaller deltas in Vietnam, such as the Cua Dai River mouth in Thu Bon River delta in central region of the country, have been subjected to large magnitude changes in recent years. Some researchers [5] mentioned that the negative impacts of climate change-related sea level rise may have already been happened in Vietnam, which have resulted in accelerated coastal erosion, saltwater intrusion,

 ISBN:

ecosystem degradation and floods in low elevation areas. Nevertheless, anthropogenic activities have increased the unpredictability and severity of coastal hazards such as the ones mentioned previously [6].

Mangrove forests are considered as important agents of coastal area protection from tidal waves and storms [7]. In Vietnam also, particularly in the southern and northeastern coastal regions, mangrove forests play a crucial role in coastal area defense and also in the economic growth of the country [8]. Central coast of Vietnam is, however, has a less fertile soil and is subjected to frequent storms and water currents, which is less favorable for mangrove forests [9]. Furthermore, typhoon-related risks are higher in the north and central coast of Vietnam [10]. In a recent study, Dastgheib et al. [4] mentioned that large changes in net sediment transport rates in Vietnam is expected to occur at the end of the 21st century in the surroundings of Da Nang City, including the central coastal province of Quang Nam. Interestingly, this region (central coast) has the least coverage of mangrove forests in Vietnam [8-9]. Nonetheless, proper mangrove planting programs, if successful, can be helpful in reducing climate change-related coastal environmental hazards in this region to some extent [10].

Before the 2010s, aquaculture, fisheries and tourism were the major source of income in the central coastal region of Vietnam in general and Quang Nam province in particular [11]. However, this situation has been changed recently due to the transition of the regional economy to a successful and modern industrialized one [11-12]. Tourism-related infrastructure development in this province, mainly in the ancient town of Hoi An, has resulted in high erosion rates in recent years [13]. This situation is similar to elsewhere in Southeast Asia, where a fragile coastal environment near river mouths (areas subjected to flash floods) and a booming tourism industry coexists [14].

II. MATERIALS AND METHODS

Quang Nam (Fig. 1) is a central province in Vietnam in the western coast of the South China Sea; the coastal area (100 km in length) of this province is the downstream of Vu Gia-Thu Bon river system, which is a large river basin in the central region of Vietnam. The maximum ground elevation in the province is 2750 m a.s.l. and the coastal areas have a flat topography, which leads to a high flood risk during the rainy season [11,15]. There are 4 coastal districts (Dien Ban, Duy Xuyen, Thang Binh, Nui Thanh) and 2 coastal townships (Hoi An and Tam Ky) in Quang Nam. Quang Nam has an agriculture-dependent population with small farms; extreme weather events have serious consequences on their livelihoods [15]. A number of hard and soft measures were taken by the Quang Nam government to protect its highly eroding coast since the 2010s (Fig. 2). The coastal erosion observed recently was severe along the Cua Dai beach in the Thu Bon River delta [16,17], where the sediment discharges from Thu Bon river has a key role in accretion along the coast. Sea level rise is also reported to have influences on shoreline changes in this area. It is believed that implementation of coastal vegetation bioshields, such as mangrove forests and marsh plants, can protect the ongoing shoreline erosion in Quang Nam [17]. In this

study, we investigated the current status of mangrove vegetation in Quang Nam and its use as a bioshield against shoreline erosion.

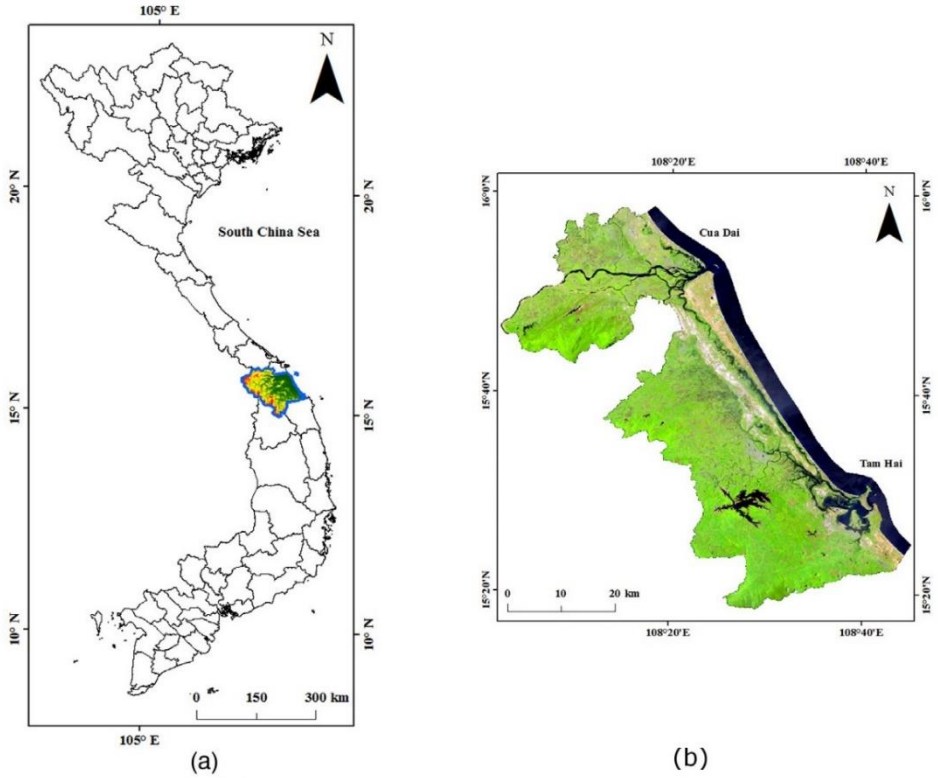

Fig. 1. *a) Geographical location of Quang Nam province, Central Vietnam; b) Coastal area of Quang Nam Province.*

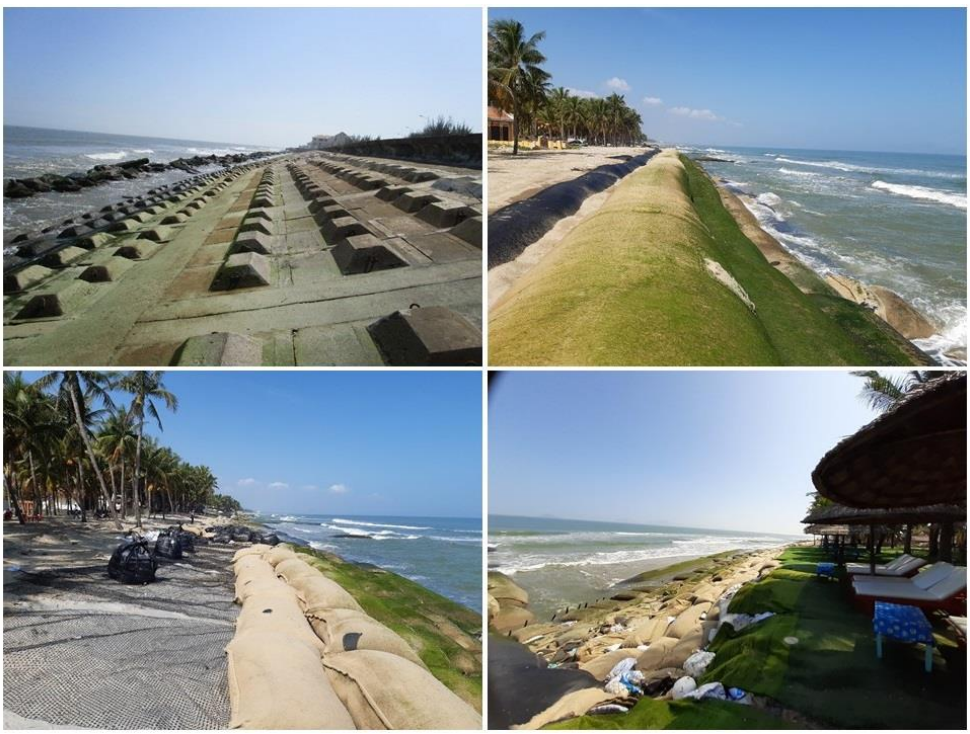

Fig. 2. *Hard structures (concrete and rock) and sand bags for coastal protection in Quang Nam Province. The aesthetic appearance of the beach has been compromised recently.*

 ISBN:

Data used for this study include multispectral satellite data (Landsat series and Sentinel-2A) acquired during the period 1988-2020 and downloaded at no cost from the United States Geological Survey (USGS: https://earthexplorer.usgs.gov), digital elevation models (DEM), and field observation data. Spatial resolution of Landsat and Sentinel-2 data are 30m and 10m (in visible and near-infrared channels), respectively. Field study was conducted (June 2019 and March 2020) for understanding the current status of shoreline, distribution of mangroves, and sediment conditions near the Thu Bon river mouth.

Atmospheric correction algorithm using MODTRAN has been applied to the multispectral data and, afterwards, vegetation indices were calculated for mapping mangrove coverage in the study area. The vegetation index used for mapping mangroves in the present study was the Combined Mangrove Recognition Index (CMRI = NDVI-NDWI) [8, 18], where NDVI and NDWI denote Normalized Difference Vegetation Index and Normalized Difference Water Index, respectively (NDVI = [TM4 − TM3]/[TM4 + TM3]; NDWI = [TM2 − TM4]/[TM2 + TM4]). TM2, TM3 and TM4 denote the Landsat bands 2 (green), 3 (red) and 4 (near-infrared). The CMRI method is based on the higher water content in mangrove vegetation compared to other types of plants [19]. In addition, we applied the Low Elevation Coastal Zone (LECZ) [20] information from DEM, which are the maximum elevation levels habited by mangroves (usually 0-40 m a.s.l.). Mangrove vegetation is, usually, absent beyond this elevation range (i.e. LECZ).

The biogenic coverage, which includes mangrove forests and salt marshes, found along the coastal areas are considered as a vital natural resource in Southeast Asia in general and in Vietnam in particular [21]. In Vietnam, mangrove forests are classified as protection forests [22]. An unprecedented loss of mangroves and other coastal vegetation is alarming because such biogenic coverage has regional importance in protecting coastal areas from natural disasters, such as erosion and coastal floods [22]. Reforestation of mangrove species can be used as an effective tool in reducing such natural disasters in Central Vietnam, depending on the success of such initiatives. In this study, suitable areas for mangrove bioshield installation, such as abandoned shrimp ponds and public sector (with no economic activity) coastal land areas, were estimated using remote sensing data based on the methodology applied in Veettil et al. [23] as well as field investigation. Highly eroding coastal areas were also estimated using satellite data.

III. RESULTS AND DISCUSSION

The estimated changes in shoreline, mangrove areas and possible areas for mangrove reforestation to establish bioshield are given below.

It is seen that shoreline erosion in Cua Dai beach surrounding the Thu Bon river mouth was higher during the study period (Fig. 3a). It is also estimated that there were negligible changes in shoreline along the coastal areas of Tam Hai (Fig. 3b). Similar estimates were shown by Dang and Nguyen [24] and Veettil et al. [23].

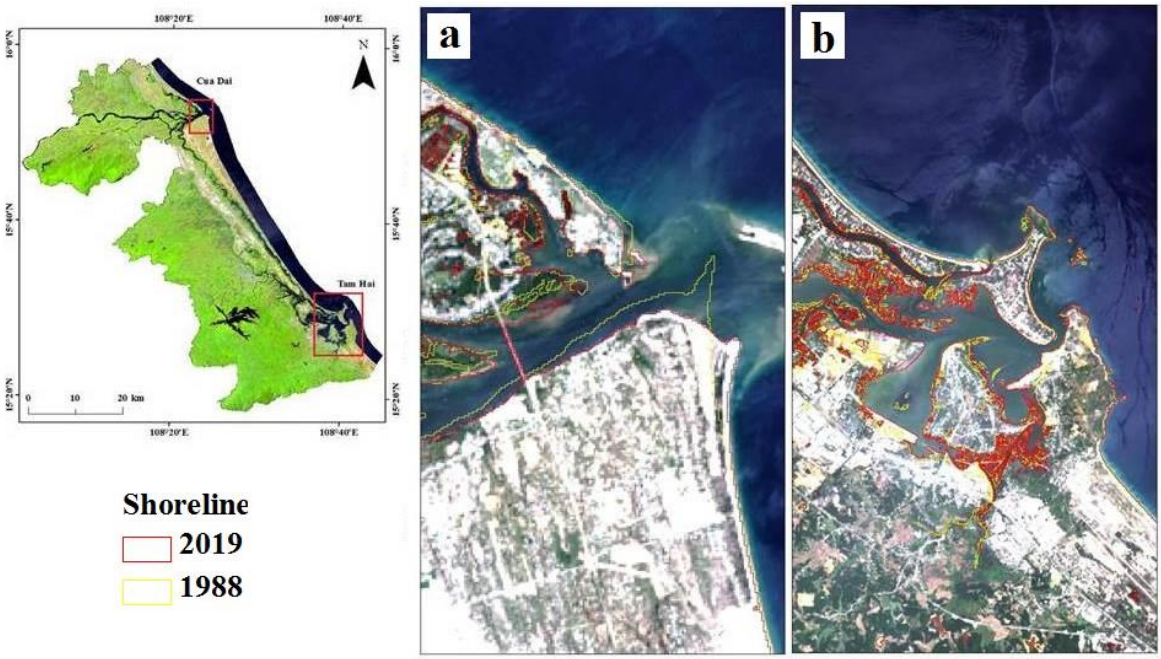

Fig. 3. *Shoreline changes in (a) Cua Dai and (b) Tham Hai.*

Mangrove changes indicated an overall negative trend along the coast of Quang Nam (Fig. 4). The areas showing a decrease in mangrove areas are Hoi An and Nui Thanh. However, mangrove coverage in Tam Ky and Thang Binh has been increased slightly during the study period, probably due to the ongoing reforestation programme in these areas as well as due to the natural regeneration of mangroves.

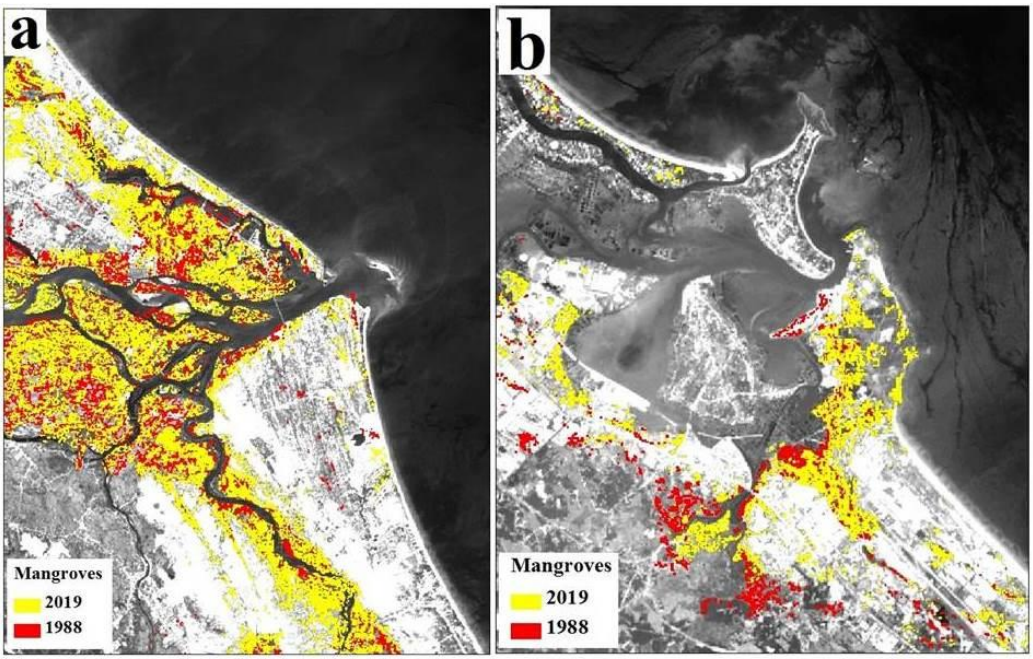

Fig. 4. *Mangrove changes between 1988 and 2019: a) Hoi An, b) Nui Thanh.*

The recent maps of aquaculture ponds (2007-2019) show a small change in spatial coverage, particularly in Hoi An and nearby areas (Fig. 5). It is notable that the changes in

 ISBN:

aquaculture areas are not so higher compared to Mekong Delta provinces, such as in Ben Tre [25]. However, there still exists abandoned aquaculture areas suitable for reforestation.

Fig. 5. *Reduction in recent (2007-2019) aquaculture ponds in Hoi An and nearby areas.*

It was observed that mangrove palm (*Nypa fruticans*) is found natively and naturally in Quang Nam province, particularly along the river banks in coastal areas. Nypa palms are notable for sediment trapping [26] and are one of the options as a bioshield against coastal erosion near river mouths. As observed in the present study, the area of abandoned aquaculture ponds is not as large as the Mekong Delta; reforestation by mangrove vegetation in such areas may not be a suitable solution to implement them as a coastal bioshield. However, coastal areas (with no economic activities) within certain distance (e.g. Rahman and Rahman [27]) can be suitable for this purpose and further research is needed in this direction.

IV. CONCLUSIONS

Shoreline changes observed in Quang Nam province in recent years have been considered as serious. Despite a large number of hard structures, such as concrete seawalls and rock walls, have been installed, the aesthetic appearance of the beaches surrounding the Thu Bon river mouth, particularly the Cua Dai beach, has been compromised to a large extent.

As for mangrove vegetation, coastal areas near Hoi An and Nui Thanh in the north of Quang Nam showed an overall decrease (except Tam Ky and Thang Binh). The areas with rapid expansion of aquaculture ponds to meet seafood requirements in tourism sector were also associated with a decline in mangrove areas.

In addition to building hard structures, such as seawalls, the possibility of reforesting abandoned aquaculture ponds needs to be evaluated in the study area. Coastal bioshields provide an additional protection to hard structures with environmental and ecological benefits. Coastal bioshields using native mangrove species can be installed in abandoned

aquaculture areas and non-economic, nearshore areas. In addition to mangroves, other plant species such as casuarina or marsh plants can also be used as coastal bioshield.

Despite the effectiveness of bioshields against coastal disasters, a number of factors, including sediment dynamics, hydrology and species types, influence the success of reforestation by such plant species. For example, the presence of a hydroelectric dam in Thu Bon River influences the sediment transport, thereby affecting erosion at the river mouth. A large number of resorts were also constructed along the beaches in Hoi An and nearby areas, which also contributes to the changes in natural erosion/accretion characteristics of the region in addition to sea level rise.

Shoreline protection offered by different coastal vegetation species may vary and may also depend on the specific environmental and geomorphological conditions of the coastal areas. Further researches on species-specific characteristics are required for coastal protection in Quang Nam coast using vegetation bioshields.

ACKNOWLEDGMENTS. This research is funded by Vietnam National Foundation for Science and Technology Development (NAFOSTED) under grant number 105.99-2019.339.

REFERENCES

[1] J. N. Paw and C. Thia-Eng, Climate changes and sea level rise: Implications on coastal area utilization and management in South-east Asia, *Ocean Shoreline Manag*., 1991, **15**, 205-232.

[2] M. Strassburg, B. D. Hamlington, et al., Sea level trends in Southeast Asian seas, *Climate Past*., 2015, **11**, 743-750.

[3] N. D. Thao, H. Takagi, and M. Esteban, Economic growth and climate change challenges to Vietnamese ports, In: Thao, N.D., Takagi, H., Esteban, M. (Eds.), *Coastal Disasters and Climate Change in Vietnam*, 2014, 339-354.

[4] S. Dasgupta, B. Laplante, C. Meisner, D. Wheeler, and J. Yan, The impact of sea level rise on developing countries: a comparative analysis, *Clim. Change*, 2009, **93**, 379-388.

[5] P. T. T. Hanh and M. Furukawa, Impact of sea level rise on coastal zone of Vietnam, *Uni. Ryukyus Fac. Sci. Bull*,. 2007, **84**, 45-59.

[6] T.D. Thanh, Y. Saito, D. V. Huy, V. L. Nguyen, T. K. O. Ta, and M. Tateishi, Regimes of human and climate impacts on coastal changes in Vietnam, *Region. Environ. Change*, 2004, **4**, 49-62.

[7] H. L. Koh, S. Y. The, et al., Mangrove forests: Protection against and resilience to coastal disturbances, *J. Trop. Forest Sci.*, 2018, **30**, 446-460.

[8] B. K. Veettil and N. X. Quang, Mangrove forests of Cambodia: Recent changes and future threats, *Ocean Coast. Manag.*, 2019, **181**, 104895.

[9] P. N. Hong and H. T. San, Mangroves of Vietnam, The IUCN Wetlands Programme, Bangkok, 1993.

[10] H. Takagi, M. Esteban, and D. T. Ngyuen, Introduction: coastal disasters and climate change in Vietnam, Thao, N. D., Takagi, J., Esteban, M. (Eds.), Coastal Disasters and Climate Change in Vietnam-Engineering and Planning Perspectives, Elsevier, London, 2014.

[11] V. N. Chau, J. Holland, S. Cassells, and M. Tuohy, Using GIS to map impacts upon agriculture from extreme floods in Vietnam, *Appl. Geogr.*, 2013, **41**, 65-74.

 ISBN:

[12] B. D. Tinh, T. H. Tuan, et al., Local vulnerability and adaptation to extreme climate events along the central coast of Vietnam, Shaw, R., Pulhin, J., Jacqueline, P. J. (Eds.), Bingley, United Kingdom, 2010, 393-416.

[13] N. T. Viet, V. C. Hoang, and H. Tanaka, Morphological change on Cua Dai beach, Vietnam: Part I image analysis, *J. Nat. Disaster Sci.*, 2015, **51**, 81-86.

[14] V. A. Greenwood and L. Dwyer, Reinventing macau tourism: gambling on creativity?, *Curr. Issues Tour.*, 2017, **20**, 580-602.

[15] C. Luu and J. V. Meding, A flood risk assessment of Quang Nam, Vietnam using spatial multicriteria decision analysis, *Water*, 2018, **10**, 461.

[16] A. T. K. Do, S. de Vries, and M. J. F. Stive, The estimation and evaluation of shoreline locations, shoreline-change rates, and coastal volume changes derived from landsat images, *J. Coast. Res*., 2018, **35**, 56-71.

[17] U. Nehren, H. H. D. Thai, N. D. Trung, C. Raedig, and S. Alfonso, Sand dunes and mangroves for disaster risk reduction and climate change adaptation in the coastal zone of Quang Nam Province, Vietnam, In: Nauditt, A., Ribbe, L. (Eds.), Land Use and Climate Change Interactions in Central Vietnam, 2017, 201-222.

[18] K. Gupta, A. Mukhopadhyay, S. Giri, A. Chanda, S. D. Majumdar, D. Mitra, R. N. Samal, A. K. Pattnaik, and S. Hazra, An index for discrimination of mangroves from non-mangroves using Landsat 8 OLI imagery, *MethodsX*, 2018, **5**, 1129-1139.

[19] B. Gao, NDWI-A Normalized difference water index for remote sensing of vegetation liquid water from space, *Remote Sens. Environ.*, 1996, **58**, 257-266.

[20] P. Mondal, S. Trzaska, and A. Sherbinin, Landsat-derived estimates of mangrove extents in the Sierra Leone coastal landscape complex during 1990-2016, *Sensors*, 2018, **18**, 12.

[21] B. K. Veettil, R.W. Ward, N. T. K. Dung, D. D. Van, N. X. Quang, and P. N. Hoai, The use of bioshields for coastal protection in Vietnam: current status and potential, *Regional Studies in Marine Science*, 2021, **47**, 101945.

[22] T. P. Nguyen and K. E. Parnell, Coastal land use planning in Ben Tre, Vietnam: constraints and recommendations, *Heliyon*, 2019, **5**, e01487.

[23] B. K. Veettil, J. Costi, W. C. Marques, X. L. Tran, N. X. Quang, D. D. Van, and P. N. Hoai, Coastal environmental changes in Southeast Asia: A study from Quang Nam Province, Central Vietnam, *Regional Studies in Marine Science*, 2020, **39**, 101420.

[24] A. H. Dang, and T. D. Nguyen, Coastal erosion in Cua Dai beach: Future influence of climate change and sea level rise on coastal protection, *International Conference on Asian and Pacific Coasts*, 2019, 521-528.

[25] B. K. Veettil, N. X. Quang, Changes in mangrove vegetation, aquaculture and paddy cultivation in the Mekong Delta: A study from Ben Tre Province, southern Vietnam, *Estuar. Coast. Shelf Sci.*, 2019, **226**, 106273.

[26] T. P. Nguyen, V. T. Nguyen, P. Q. Le, K. E. Parnell, Community perspectives on an internationally funded mangrove restoration project: Kien Giang province, Vietnam, *Ocean & Coastal Management*, 2016, **119**, 146-154.

[27] M. A. Rahman, M. A. Rahman, Effectiveness of coastal bio-shield for reduction of the energy from storm surges and cyclones, *Procedia Engineering*, 2019, **56**, 676-685.

DETERMINATION OF CAMPHOR CONCENTRATION PROFILE IN 5/7X DETERRED SINGLE BASE PROPELLANT

Pham Quang Hieu*

Institute of Propellants and Explosives, 192, Duc Giang Str., Ha Noi, Viet Nam

*E-mail: *hieuphus@gmail.com*

Abstract. The paper presents the determination of the concentration profile of camphor in a 5/7X deterred single based propellant by using Raman microspectroscopic method. Research results show that camphor content on the external surface of propellant grains is 19%, this value decreases by the depth and reaches a thickness of 100 μm. In addition, unlike immersion technology, there is no deterrent on the inner surface of the perforations of propellant grains when using the spraying method.

Keywords: *Propellant, Deterrent, Camphor, Pirocxilin, Raman spectra*.

I. INTRODUCTION

In order to change interior ballistic characteristics (maximum gaseous pressure, ammunition initial velocity), substances reducing the burning rate of propellants are coated on the surface of propellant grains. This process is call deterrence and substances are call deterrent [1]. The deterrent concentration profile powerfully influences the ballistic characteristics and it is important in the manufacturing process. Raman microspectroscopic technique is one method that could be used to determine the concentration profile of deterrents in propellant grains [2-4]. However, in the above scientific publications, deterrents in propellants were methylcentralite [2,3], dinitrotoluene [4], di-n-butyl phthalate [5]. There is absolutely no study referring to the concentration profile of camphor. In addition, the deterrence was carried on by immerging propellant grains in deterrent solutions. Therefore, the purpose of this study is the determination of the camphor concentration profile in the 5/7X single based propellant containing a total camphor content of 1.51% by using Raman microscopy.

According to the literature [1], the Raman spectrum of camphor indicates that a characteristic peak is at 652 cm^{-1} of wavenumber relative to the C-C bond in the carbon ring. Meanwhile, the Raman spectrum of nitrocellulose (NC) has peaks of 850 cm^{-1} and 1290 cm^{-1}, typical for NO_2 group [2,3]. Therefore, the intensity ratio of peaks at 652 cm^{-1} and 850 cm^{-1} of wavenumber in the Raman spectrum of deterred propellants (I^{652}/I^{850}) can characterize camphor content in propellants. Before we have determined the Raman spectrum of the NC mixture with camphor having different concentrations (Fig. 1). Based on the relationship between the ratio of I^{652}/I^{850} and camphor content (Fig. 2) we have obtained a regression equation [7]:

$$I^{652}/I^{850} = 0.077\,[C] + 0.483 \quad (1)$$

where [C] is concentration of camphor in mixtures with NC, %.

 ISBN:

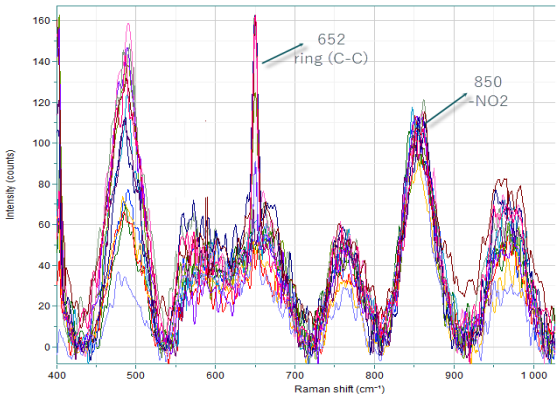

Fig. 1. *Raman spectrum of mixtures with different ratios of camphor and NC.*

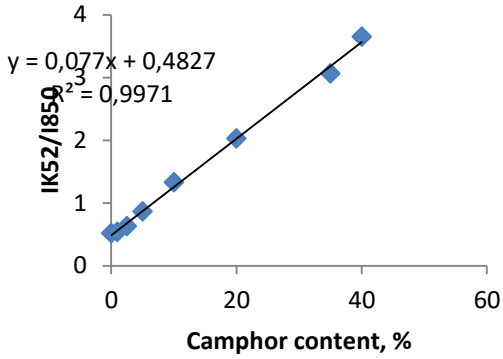

Fig. 2. *Independence of I^{652}/I^{850} on camphor content.*

II. MATERIALS AND METHODS

2.1. Materials

The compositions of the 5/7X seven-perforated single base propellant are nitrocellulose - 92.77%; water - 1.16%; ethyl alcohol - 0.59%; graphite - 0.1%; diphenylamine - 1.46%, cerezin and comphor. The propellant grain has a form of a cylinder with 3.2 mm of length, 2.65 mm in outer diameter, 0.17 mm of perforation diameter, and 0.53 mm of web thickness.

2.2. Characterization

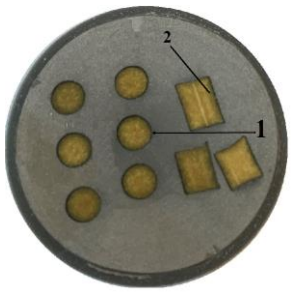

Fig. 3. *Propellant samples for measurement of Raman spectrum:1-cross section; 2-longitudinal section.*

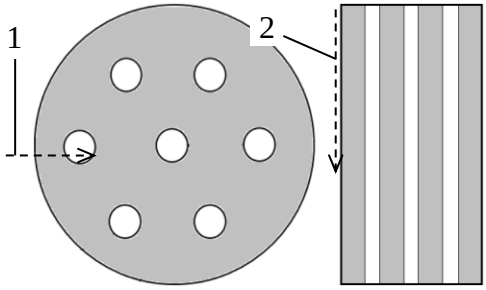

Fig. 4. *Positions of cross (1) and longitudinal (2) sections of the propellant grain where Raman spectrum were taken.*

Propellant grains were cured with epoxy glue in a PVC mold. Then the sample was cut and ground to form cross- and longitudinal sections of propellant grains as shown in Fig. 2. Raman spectrum of the sample at different positions according to the cross-section was recorded by using Labram HR Evolution spectroscope (Horiba, Japan) with 532 nm of laser wavelength. The objective of the spectroscope was x100_VIS. The sample is placed on the spectroscope glass so that the Raman len obtains a clear image of the cross-section. Spectrum was taken at the points from the outer boundary to the deep inside of the propellant grain (by cross-section), and at positions located 20 µm from the inner surface of perforations (by longitudinal section). The distance between two consecutive points is 5 µm (Fig. 4).

Five samples for determination IR spectroscopy were prepared as follows mixing 0.5 g of nitrocellulose (NC) with 0.05; 0.1; 0.125; 0.15 and 0.2 g of camphor, respectively. Thereafter, 10 drops of diethyl ether were added into each sample, mix them together then allow drying under normal conditions. The obtained samples were measured IR spectroscopy by using Spectrum 400 FT-IR Spectrometer (PerkinElmer, USA).

III. RESULTS AND DISCUSSION

3.1. The camphor content profile along cross section of the propellant grain

Raman spectrum at the points along the cross section of 5/7X propellant grains is shown in Fig. 5. From the Raman spectrum in Fig. 5 and equation (1), the camphor content distribution was determined along the cross section of the propellant grains Fig. 6.

It is could be seen that the camphor content gradually decreases from the outer surface to the depths of propellant grains (from 19.01 to 1.51 %), the camphor layer depth is about 100 μm. At a depth of 20 to 80 μm, camphor content does not change significantly (on average 6%). The concentration profile shows that the penetration of camphor occurs by diffusion mechanism with the interaction between deterrent and nitrocellulose [5]. In a study [6], Brodman B. W. and coauthors indicated that there are hydrogen bonds of free hydroxyl groups in nitrocellulose with carbonyl in deterrents such as di-n-butyl phthalate, camphor, N,N'-diethyl-N,N'-diphenylurea, and N,N'-dimethyl-N,N'-diphenylurea. This opinion has been confirmed by us when comparing the infrared spectrum of NC-camphor mixtures at different ratios, which will be show in Section 3.3.

3.2. The camphor content profile along longitudinal section of the propellant grain

Raman spectrum along the longitudinal section of 5/7X propellant at positions located 20 μm from the inner surface of perforations are shown in Fig. 7.

Like the camphor content distribution along the cross section, camphor content is zero at a depth greater than 100 μm from the two ends of the propellant grains. In addition, there is no presence of camphor at any point located around perforations. This is in contrast to previous research results [2,3] confirming the presence of deterrents in perforations of propellant grain using the immersion method. In this study, we applied the spraying method with the short execution time, so the deterrent was unable to diffuse into the perforations of propellant grains.

3.3. The role of hydrogen bond between camphor and NC

IR spectrum of NC mixture with camphor is shown in Fig. 8.

From Fig. 8, the peak in the range of 3200 - 3570 cm^{-1} is typical for the free hydroxyl group as well as the hydrogen bond of this group with the carbonyl group in camphor molecular. The peak of the hydrogen bond is not sharp like the other peaks. Even for NCs, the peak of the free hydroxyl group is curved in the spectral range 3300 - 3400 cm^{-1}. Obviously, when the camphor content is greater than 25% (samples 3,4 and 5), the peak intensity of the free hydroxyl group is very weak and did not differ much,

 ISBN:

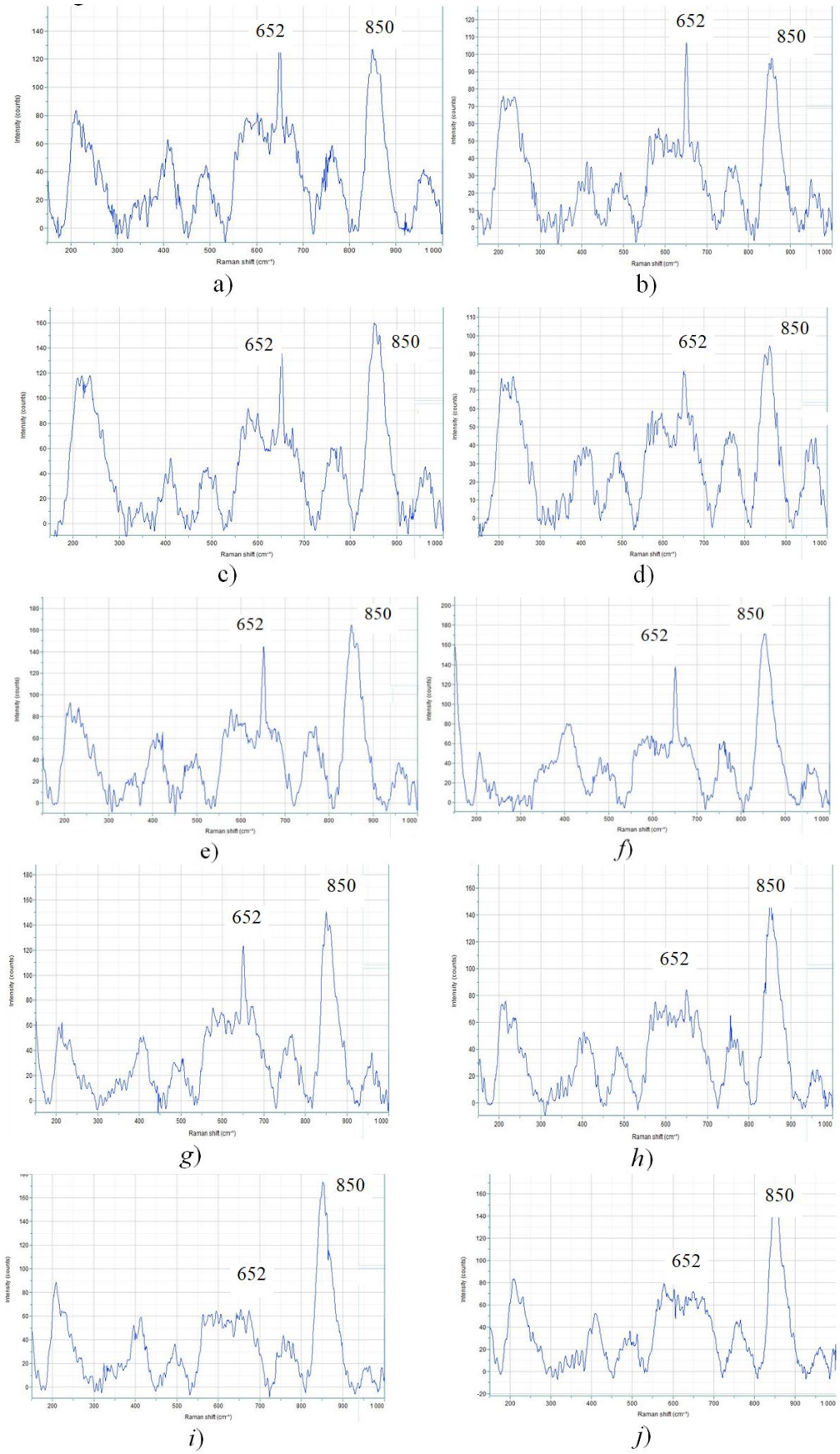

Fig. 5. *Raman spectrum at the different depths from the outer surface of propellant grains: a - 0 µm; b - 10 µm ; c - 20 µm; d - 30 µm; e - 55 µm; f - 60 µm; g - 80 µm; h - 90 µm; i - 95 µm; j - 100 µm.*

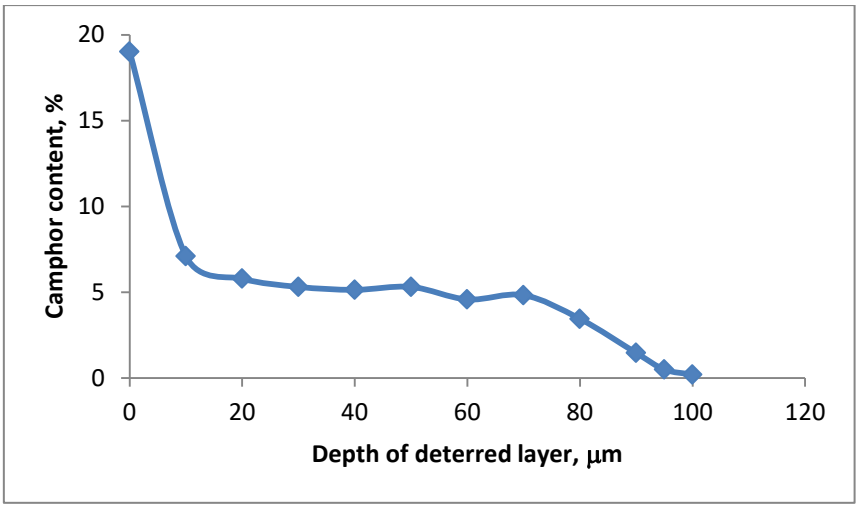

Fig. 6. *Camphor content profile by the cross section of 5/7X propellant.*

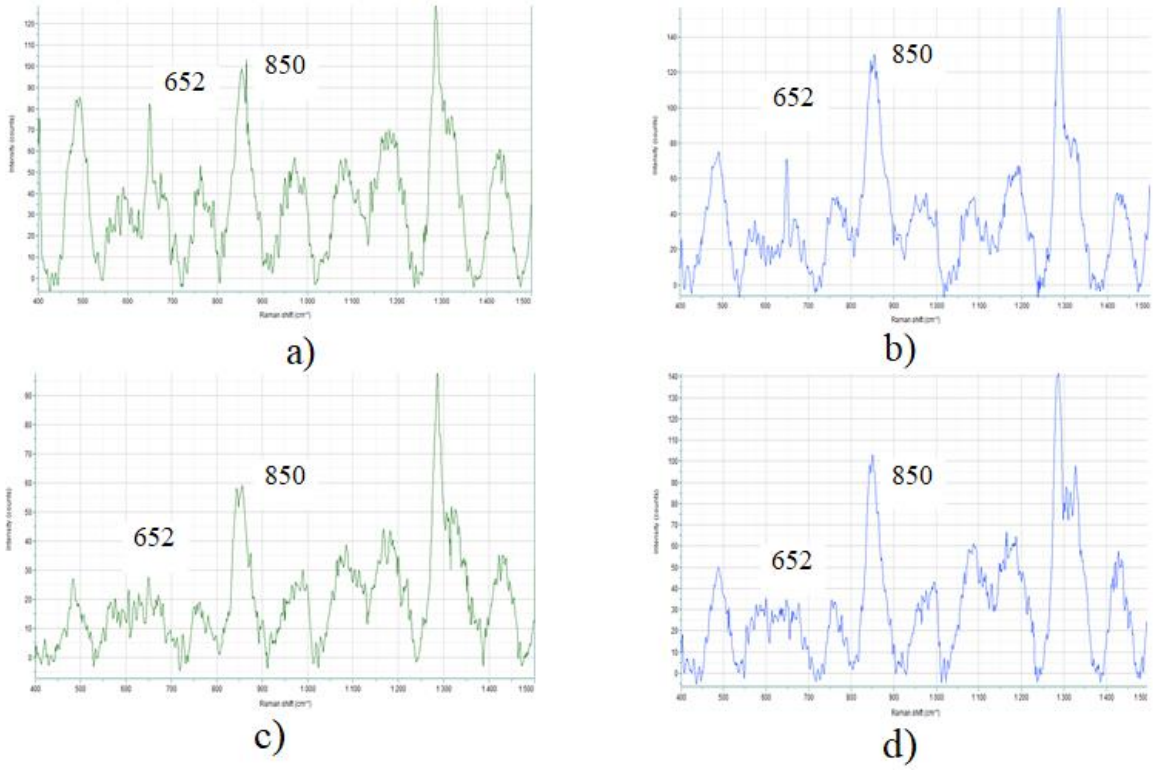

Fig. 7. *Raman spectrum at points along the boundary of the perforations of 5/7X propellant: a - 0 µm; b - 50 µm; c - 90 µm; d - 100 µm.*

while at the content of 20% (sample 2) and 10% (sample 1) the intensity of the peak varies significantly. This is due to the existence of hydrogen bonds between hydroxyl and carbonyl groups. When camphor content is less than 25%, the number of carbonyl groups is not enough to link all the hydroxyl groups in the NC (still observed the presence of the free hydroxyl group on the IR spectrum). When camphor content is greater than 25% (samples 3, 4, and 5), all carbonyl groups in camphor has been linked to hydroxyl groups of NC.

 ISBN:

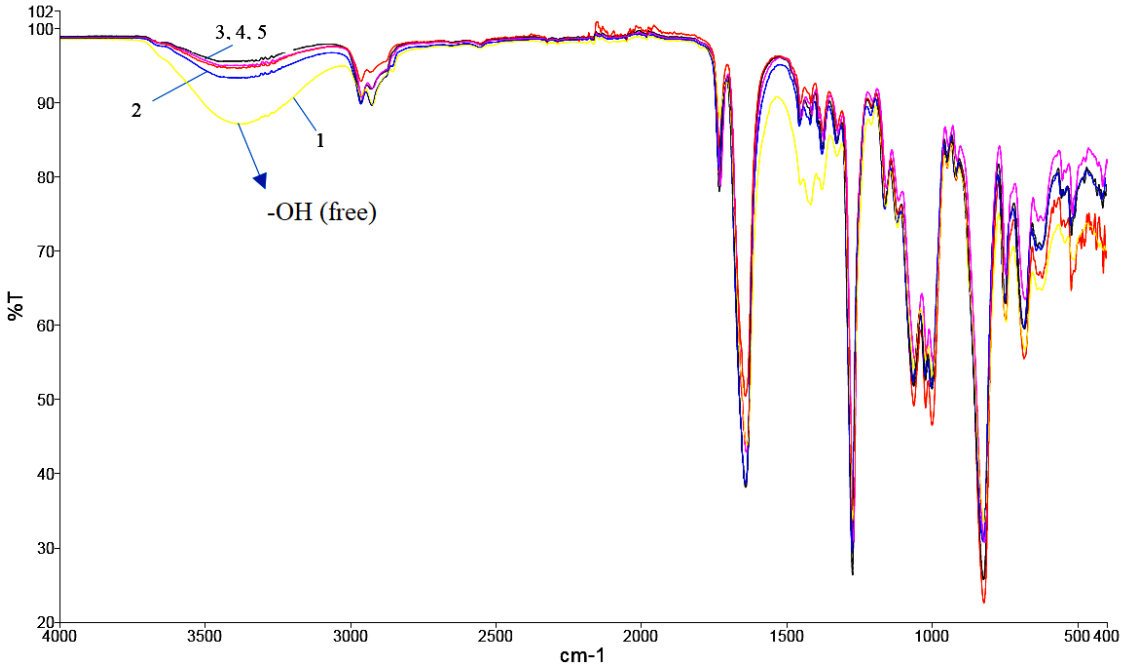

Fig. 8. *IR spectrum of NC mixtures with different contents of camphor.*

IV. CONCLUSION

Thus, Raman microspectroscopic technique allows not only to determine concentration by the depth of the deterrent layer but also to determine the profile of camphor content along with cross- and longitudinal sections of 5/7X propellant. The camphor distribution in 5/7X deterred single base propellant ensures sustainability during storage as well as the use due to the hydrogen bonding.

REFERENCES

[1] Mikhailov, Yu. M., Physical Chemistry of Deterred Propellants, Chernogolovka, 2001, pp. 5.

[2] Louden J. D., Kelly J., Phillipson J., *Journal of Raman Spectroscopy*, 1987, **18**(2), 137-140.

[3] Louden J. D., Kelly J., Phillipson J., *Journal of Applied Polymer Science*, 1989, **37**(11), 3237-3250.

[4] Trewartha S., Shapter J., Gibson C. T., Mikajlo E., Jones A., *Propellants, Explosives, Pyrotechnics*, 2011, **36**(5), 451-458.

[5] Brodman B. W., Devine M. P., Finch R. W., MacClaren M. S., *Journal of Applied Polymer*, 1974, **18(12)**, pp. 3739-3744.

[6] Brodman B. W., Devine M. P., Gurbarg M. T., *Journal of Applied Polymer Science*, 1974, **18**(3), 943-946.

[7] Pham Q. Hieu, Pham V. Toai, Chu C. Huu, Bui A. Thuc, Pham K. Dao, Nguyen Ng. Hai, *Journal of Military Science and Technology*, 2019, **63**, 136-143.

RESEARCH TECHNOLOGY FOR CREATION OF ENERGY MATERIALS, REQUIREMENTS TO PHLEGMATIZATION AND USE FOR CHARGES TO THE CARTRIDGE 23 MM AND 30 MM NAVY- PART 1

Pham Quang Hieu*

Institute of Propellants and Explosives, 192, Duc Giang Str., Ha Noi, Viet Nam

*E-mail: *hieuphus@gmail.com*

Abstract. Energy materials used as a charge in artillery shells are single-based propellant. Single-based propellant is a kind of colloidal structure based on nitrocellulose (NC) and is plastic by volatile solvent as ethanol and diethyl ether. For the cartridge of 23 mm and 30 mm anti-aircraft weapon it is necessary to use phlegmatic propellant to increase the range of fire while maintaining the maximum pressure value. Phlegmatic propellant is special in the group of single-based propellant, the process of creating many differences in comparison with the technology of conventional single-based propellant, in which the most important is the process of phlegmatization of the camphor agent in the discharge particles. This article presents the technology of production of energy carriers (semi-finished products of phlegmatic propellant), the requirements for the possibility of phlegmatization and use as a propellant charge for high ammunition 23 mm and 30 mm Navy.

Keywords: *Single-based propellant, Phlegmatic propellant, Pirocxilin.*

I. INTRODUCTION

Given the urgent need to protect the island's sovereignty, many weapons have been and will continue to strengthen the target group on the island. As for the Coast Guard, in the future it would be possible to equip a 23 mm high-pressure gun with a pyrocxylin (propellant) launcher with 5/7X or 30 mm AK-630 with a 6/7X pyrocxylin. These two types of propellants, which we import from abroad, import very complex and not active in the production of the national launch. Therefore, the study of the phlegmatization of pyroxylin is very necessary and very practical. The most important thing in production is the technology of phlegmatization of pyroxylene. Not only the launcher (or semi-finished product) can be phlegmatized, but only a few types because of their armament requirements that people intervene. Thus, this article will present the technology of production of semi-finished products of pyroxylin, requirements for semi-finished products in order to be able to phlegmatize the best results.

II. MATERIALS AND METHODS

2.1. Research subjects

- Nitrocellulose brand BA;
- Technological regimes investigating the characteristics of imported propellants.

2.2. Materials, chemicals

 ISBN:

- Nitrocellulose brand BA with content NO_x: 208.0÷209.0 ml NO/g;
- Diphenylamine (DPA) China; ethanol, diethyl ether production made in Viet Nam, Cerezin A75 imported from Russia has a melting temperature of 75 ^oC.

2.3. Equipments

Use of equipment and mechanisms in the experiment of the Institute of Propellants and Explosives, technologies in conjunction with equipment on the production line of the factory Z: pyroxylin dehydrator, mixer MZ, HM, pressure measuring equipment P_k, press equipment, grain cutting machine, cooking surface, immersion in the tank, spraying system.

2.4. Research Methods

Based on the materials for the production of single-based propellant, the results of a survey of import propellant from foreign countries are presented, of which the selection of individual components, the design of molds, construction of semi-finished products for phlegamatically. In the course of the study, several methods were used to evaluate the effectiveness of the semi-finished products of propellant.

- Method for determining the shape and size of the shot particle on photographic enlarger V-12A-50123 according to 06 TCV 836:2000;
- Determination of nitroxellulose content (NC) according to 31 TC 120:2001;
- Determination of DPA content according to TQSA 1275: 2006;
- Determination of volatile content according to TQSA 1282: 2006;
- Method of determination of combustion heat according to 06 TCV 889:2001,...

III. RESULTS AND DISCUSSION

3.1. Survey results of foreign propellant imported

The authors collected data, inspected the characteristics of propellants 5/7X and 6/7X made by Secbia. The results are shown in Table 1.

Table 1. *Survey results of importing propellants in Secbia.*

Nº	Name of quantitative norms	Propellant 5/7X	Propellant 6/7X
1	Content of volatile,%	1.15	1.12
2	Content of ethanol and diethyl ether, %	0.45	0.50
3	Content of DPA, %	1.12	1.37
4	Content of cerezin and comphor, %	-	-
5	$2e_1$, mm	0.54	0.71
6	Outside diameter, mm	2.69	3.44
7	Diameter of hole, mm	0.18	0.20
8	Length of grains, mm	3.30	4.30

The results show that in propllents 5/7X and 6/7X in addition to the main components such as ordinary propellant (NC, ethanol, diethyl ether, DPA), here camphor is used as a reflux agent and in propllent 5/7X for high-strength ammunition of 23 mm, cerezin (CE), used in

ammunition to protect the barrel (bulletproof protection) [3]. In addition, geometric dimensions are the basis for a group of authors for designing sets of molds.

3.2. Design of molds

Based on the geometric dimensions of the imported medicine, the authors calculate the design of the injection molding set, in which it is important to calculate the diameter of the hole and the diameter of the needle to create a hole in the powder particles. To achieve the goal, the technology of making the original single-based propellant, the geometric dimensions in general and the average thickness of the fire is important. Therefore, when designing, it is usually desirable to design a mold from the very beginning in order to obtain the desired particle size. The shrinkage coefficient of the initial propellant is in the range of 25-35% [4], the formula for the shrinkage coefficient is shown by the formula:

$$C = 100(1 - \frac{6,3}{E^{1/2}}) \quad (1)$$

where, 6.3 - quality ratio of pyroxylin and fuel production. The coefficient E is the amount of solvent per 100 parts of pyroxylin. If E = 81 parts, shrinkage factor C = 30% (although this is the reference value to initially build mold making, which leads to a reduction in the size of reality will serve as the basis for correcting the shape).

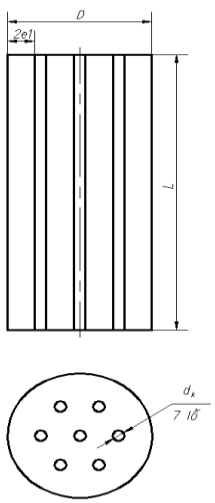

Fig. 1. *The shape of the grain propellant.*

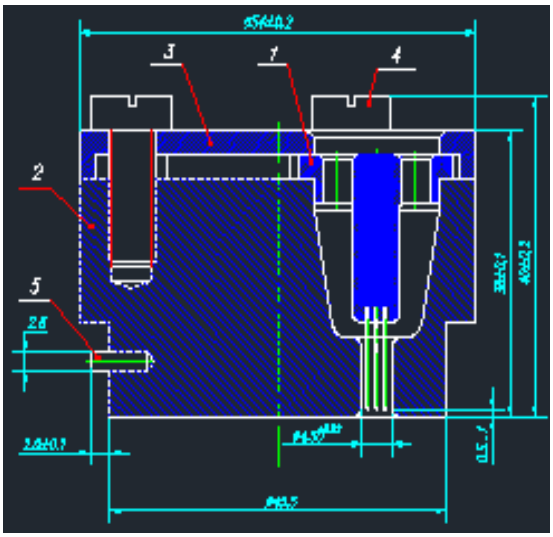

Fig. 2. *Drawings of molds.*

***** For propellant 5/7X with data requiring average fire thickness of $2e_1$ = 0.54 mm, dashed hole diameter = 0.18 mm.

+ Cylinder diameter of the mold outlet is:

$D_{cylinder} = (4\times2e_1+3\times d_{hole})\times(100+C)/100 = (4\times0.55+3\times0.18)\times1.3 = 3.6$ mm;

+ Diameter of needle is: $D_{needle} = (D_{cylinder} - 4x)/3$, where $x = 2e_1\times(100+C_1)/100$ with C_1=C=30%, and x=0.55×(100+30)/100 = 0.715 mm; result D_{needle} = (3.6 - 4×0.715)/3 = 0.24 mm.

***** For propellant 6/7X with data requiring average fire thickness of $2e_1$ = 0.71 mm, dashed hole diameter = 0.20 mm.

+ Cylinder diameter of the mold outlet is:

 ISBN:

$D_{cylinder} = (4\times 2e_1+3\times d_{hole})\times(100+C)/100= (4\times 0.71+3.0\times 0.20)\times 1.3= 4.50$ mm;

+ Diameter of needle is: $D_{needle} =(D_{cylinder} - 4x)/3$, where $x= 2e_1\times(100+C_1)/100$ với $C_1=C=30\%$, and $x= 0.71\times(100+30)/100= 0.92$ m; Result $D_{needle} =(4.50 - 4\times 0.92)/3= 0.27$ mm.

3.3. Construction of single component design for semi-finished fabrication of 5/7X and 6/7X launchers

Calculate the design of single component propellant using dynamical calculation program (Real 3W) fire parameters. Calculate the combustion heat of propellant according to the formula (2):

$$Q_v = \Sigma m_i \times \beta_i \quad (2)$$

Where, m_i - is the concentration of i in the propellant, %; β_i - is the coefficient of heat of i, kcal/kg×%.

The thermal coefficient of the substances given in Table 2.

Table 2. *The thermal coefficient of the substances in propellant*.

Substances	β (kcal/kg × %)	Substances	β (kcal/kg × %)	Substances	β (kcal/kg × %)
NC	5.86N- 33.77	Camphor	-26.84	Graphit	-33.56
DPA	-27.15	Diethyl ether	-22.28		
Cerezin	-32.89	Ethanol	-17.5		

Note: N is the nitrogen content of pirocxilin.

Based on the results of a comprehensive study of the finished product, the authors developed requirements for components of semi-finished products 5/7X and 6/7X, as shown in Table 3, only after the completion of the finished product. Achieving new requirements can be transferred to the phlegmatization of the product.

Table 3. *Quantitative normssemi-finished products 5/7X và 6/7X.*

N°	Name of quantitative norms semi-finished products	Semi-finished propellant 5/7X	Semi-finished propellant 6/7X
1	Content of volatile,%	0.3÷0.6	0.3÷0.6
2	Content of ethanol and diethyl ether, %	< 0.8	< 0.8
3	Content of DPA, %	1.30 ± 0.30	1.6 ± 0.4
4	Content of cerezin, %	2.6 ± 0.6	-
5	Calorie of burning, cal/g	> 850	> 950
6	$2e_1$, mm	0.50÷0.59	0.65÷0.75
7	Diameter of hole, mm	0.13÷0.21	0.15÷0.25
8	Length of grains, mm	3.00÷4.00	4.00 ÷ 4.50

With regard to the requirements for semi-finished products, we must pay attention to the content of volatile matter (water content) and the non-volatile content of the substance (ethanol and diethyl ether). Because the process of phlegmatization is the process of penetration of a phlegmatized substance from a solution into particles of a semi-finished

product. This process is due to the difference in concentration between the outside and inside the particle of the semi-finished product, usually the soluble solvent is alcohol, on the other hand, the phlegmatized material is usually not very soluble in water. Therefore, the content of water-ethanol-diethyl ether should be low in order to simplify phlegmatization.

3.4. Develop the technological process of semi-finished propellant before launching phlegmatization

The semi-finished product is essentially a generic launch single-based propellant, its ingredients include the steps of preparing the material, dehydration Nitroxellulo, mixing nitromass, pressing, pre-drying, cutting grains, drying, fomation a lot, sock and heating. The block diagram is shown in Figure 3.

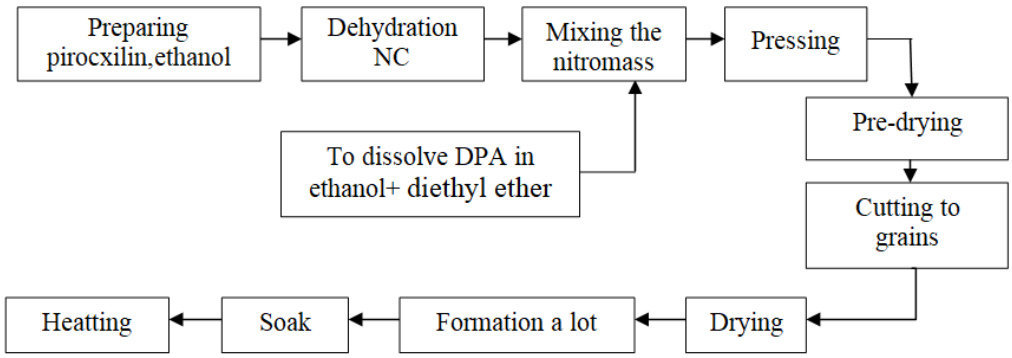

Fig. 3. *Technological process of semi-finished propellant before launching phlegmatization*.

Some requirements in the technology segments are as follows:

- Dehydration stage: water content after dehydration (2.0÷4.0)%; The total content of ethanol and water is (25÷32)%.
- Mixing, plasticization and granulation: Mix pyrroxylin with other ingredients and plasticizer. Check the plasticization through a pressure test, this pressure should reach 100÷120 kg/cm^2.
- Pressing step: to ensure that the required mass is reached, the compression pressure should be 320÷400 kg/cm^2.
- Cutting step: make sure that the length of the particle accelerator is not distorted.
- Pre-drying step: water-ethanol-diethyl ether (10÷15)% is required.
- Soak: Adjust the immersion time, temperature and alcohol concentration in water for soaking, so that the impurity content is less than 0.8%.
- Drying time: drying table temperature and drying time to ensure the content after drying (0.3÷0.6)% (in case of excess drying on the equipment of phlegmatization).

IV. CONCLUSIONS

The manufacturing technique of phlegmatized propellant is basically the same as the technology of making single-based propellant. However, in the production process, there are more cases of phlegmatization. Based on the results of the two importers 5/7X and

 ISBN:

6/7X made by Secbia, the author developed a single component for the production of these two semi-finished products, as well as the molds design to obtain geometry size requirement. In addition, the author has developed a process for the production of semi-finished gunpowder, the main requirements at each stage for obtaining the product after the phlegmatization correspond to the design requirements.

REFERENCES

[1] Ngo Van Giao, Propellant and Rocket Propellant Properties, 2005.

[2] Ю. М. Михайлов, Физикохимия флегматизированных порохов, Черноголовка, Редакционно, 2001.

[3] Фиошина М. А, Основы химии и технологии порохов и твердых ракетных топлив, 2001, 75.

[4] В. И. Гидрич, Технология пироксилиновых порох, 1995, том 2, 176.

CONSTRUCTION AND USE OF STUDY FILM IN TEACHING GENERAL PHYSICS EXPERIMENTS

Ho Xuan Huy[1*], Nguyen Hong Hai[2]

[1]*Faculty of Education, An Giang University, An Giang, Vietnam*

[2]*Experimental - Practical Area, An Giang University, An Giang, Vietnam*

[1,2]*Vietnam National University, Ho Chi Minh City, Vietnam*

*E-mail: *hxhuy@agu.edu.vn*

Abstract. Due to the impact of the Covid-19 pandemic and to achieve the training progress, An Giang University has switched to online teaching. With the experimental part of General Physics, it is very difficult to bring the experimental lectures into online teaching. Study films are one of the teaching means that can be applied in online classrooms that providing good support for learners. The article presents the role of study films, researches and uses study films in the process of online teaching of experimental exercises. The using of study films in teaching will help students follow the lessons, grasp the lesson content more closely, and promote problem solving and self-study.

Keywords: *Study films, Physics, Experiment, Capacity, Teaching means.*

I. INTRODUCTION

The increasingly powerful development of Information and Communication Technology has provided valuable tools in educational institutions. Video and multimedia form a foundational technology for distance and distributed learning as well as for traditional classroom-based courses. With the development of E-learning in the first decade of the 21st century, online approaches have become more commonly used in many educational institutions.

With general physics modules, it usually includes: theory and experimental practice. Study films are used in the traditional classroom as an alternative to other teaching methods. Study films and books provide a large amount of knowledge about structure and layout that makes it easy for students to achieve.

In the process of teaching and researching at An Giang University, we realize that experimental practice plays an important role and it is a characteristic of physics. During the experiment, the lecturer must review the relevant theoretical knowledge as well as guide the students on the usage of measuring instruments and the manipulations and procedures for conducting experiments. Each practice group usually gathers from 25 to 30 students, while small musical instruments are difficult to observe such as: surveying wheatstone bridges, surveying the laws of mechanics, geometric optics and optical instruments,…

Currently, due to the influence of the Covid-19 pandemic and to achieve the training progress, An Giang University has switched to online teaching. With the experimental part

 ISBN:

of general physics, it is very difficult to bring the experimental lectures into online teaching.

If using video - clips in the teaching process in the traditional classroom, the online class will help students follow the scientific lesson more closely and grasp the lesson content more closely. Study films are one of the teaching tools that can be applied in the online classroom - a powerful and engaging educational tool; The film will guide students in detail, specifically from the theoretical background including tools, how to perform, how to assemble experiments, experimental content, and provide good support for learners.

II. OBJECTIVES AND RESEARCH METHODS

2.1. Features of teaching facilities

In the teaching process, teaching facilities help teachers save time in the classroom, help teachers control cognitive activities of learners check and evaluate student's learning results more conveniently profitable and efficient.

With the purpose of use, teaching means can be the ways used directly for teaching and the means used to support and control the teaching process. Based on the structure of the media, it is possible to classify teaching media into two types: traditional teaching media and modern audio-visual media.

Audiovisual media is considered to be highly effective teaching facilities. Using audio-visual media in class creates conditions for learners to better absorb lessons and remember lessons longer by using many sources to stimulate learners' attention (images, sounds, animations,...). Teachers use it in class as an illustrative tool to clarify lesson content. Learners use it for self-study (teaching television, magnetic tapes, computer programs...) [1].

Compared to other teaching facilities, study films have a broader range of possibilities, can convey any amount of information about objects and processes, and are independent of the teaching method because of all that heard and seen can both be recorded on film.

Activity is an important feature of study films: objects, phenomena, processes... are projected onto the screen according to evolving movements. Study films can show the inner workings of static objects. In a study films, learners are like joining a cameraman to consider the subject from different perspectives, compare what is seen, observe the interrelationships between individual elements in a texture general population of the study population. Therefore, study films contribute to training learners in habits and ways of observing the world around them.

2.2. Features and role of study films in the teaching process

Study films contribute to the development of abstract thinking better than other teaching media. Study films help learners to observe processes, things and phenomena that they do not have the conditions to observe directly. Moreover, for the processes that

happen too fast or too slow, or the observed objects are too small, too large,... the study films helps learners slow down, speed up the process or zoom in and out of objects.

Unlike direct observation, the amount of information in the film is built on a theme with a clear goal, so it directs the attention of the learner to the basic aspects of the object, phenomenon or process. With cinematography and film directing, teaching can emphasize the basics, point out the smallest details by shooting close-ups [1].

During experimental practice, observation plays an important role. The skill of observing actual operations has a clear influence on the learners' initial practical activities. Therefore, study films can greatly assist practical teachers in forming these habits for learners.

Study films also play a great role in career guidance. It helps to educate in learners professional pride and sense of responsibility at work.

2.3. Basic principles and steps when creating a study film

Study films are one of the modern teaching means, used with specific activities of teaching. Therefore, the film fully explains the content of the lesson, presents a combination of theory and practice, the implementation process can be easily observed at any time, from any angle and viewed many times on the screen with different purposes, as a basis for training and improving skills, gradually innovating and improving teaching - learning effectiveness.

Based on the teaching goals of capacity development, thinking development, skill development based on the characteristics of cognitive activities, knowledge content to be taught and the role of study films, when building films need to ensure the following basic rules:

Rule 1. Study films must be associated with a specific program content and must show the lesson objectives.

Rule 2. Easy to use, the images in the movie are consistent with the images and phenomena already in the study film and in the lesson.

Rule 3. Study films must be suitable for use by teachers and for student's learning activities.

Rule 4. Orientation to develop learners' problem-solving capacity in the lesson content.

Rule 5. Study films can be used with other teaching forms, methods and media.

Rule 6. Using study films in the teaching process, teacher can evaluate the effectiveness of the film to have appropriate adjustment methods.

III. RESULTS AND DISCUSSION

3.1. The process of building a sdudy films general physics experiment

 ISBN:

With the basic principles when building a study film, we propose the process of building study films of general physics, including the following basic steps:

Step 1. Determine the objectives and content of the study film related to the knowledge identified in the experiments of the course program. This is the first part in the process of building and selecting films to ensure consistency with the principles outlined above.

Step 2: Analyze the experiments: determine the basis for building the learning film; Collect relevant data to build learning movies and collect raw data. Theoretical basis, tools, content and experimental procedure.

Step 3: Write a script: introduction, detailed description of experimental content, details of space, time, location, ideas, preparation of full experimental equipment, preparation steps, scripts play an important role, helping the cameraman, who recognizes the next steps to take.

Step 4: Record and record video. Arrange the experiment, select and arrange the appropriate footage. Set up the timeline according to the script and organize all the available footage.

Step 5: Edit the movies. Arrange videos - clips in the specified order (scenario), add titles first, then music and voiceovers. This step links all videos, titles, music, audio together into a unified (package) so that the movie program can be run on the computer. The film also has certain rules so that when filming does not make viewers uncomfortable due to the image jumping, messy, cumbersome, swaying,…

In this study, we edit movies with software: Adobe Premiere Pro [2], Adobe After Effects [3], Aegisub software [4].

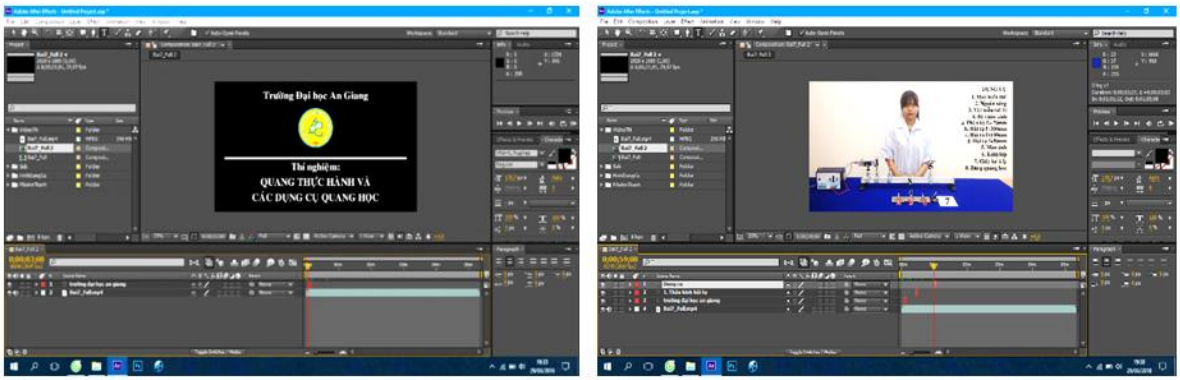

Fig. 1. *Making a movie with Adobe Premiere Pro.*

Step 6: Bring the study films into the lecture

Study films can be incorporated into lectures depending on the form of teaching:

+ Projecting independent videos - clips: during the teaching process, when it comes to the content that needs to be illustrated by video - clips, the teacher just needs to open the video with common movie viewing software (Windows media player, Windows media classic, etc.)

+ Putting video - clips into electronic lectures: when teaching with electronic textbooks (powerpoint, violet,…), teachers can put video - clips into the lecture at the location where you want to show the video - clip. Or right at the position on the electronic lecture that wants to show the video, the teacher can also create a link to the video location to open the video - clip.

- With online teaching, the teacher can create a link to the video - clip location or upload to the school's Online Course.

3.2. Using movies in teaching and practicing general physics experiments

The objective of this topic is to study the basic knowledge of general physics experiments for non-specialized students at An Giang University and make a short film. Since then, we have made a study film to improve the quality of teaching and learning.

Videos can be used to teach physics, as an additional educational tool to prepare students for lab work, and also in online classrooms with physics labs.

Furthermore, video clips can completely or partially replace actual experiments in laboratory physics, in case the necessary equipment is not available, or during online learning. The videos - clips are built and used for the purpose of teaching and learning general physics experiments for first-year students with an average background in physics and high school students. We built the general physics experimental study films with 8 videos - clips. Each video - clip includes information:

+ Introduction to experiments and theoretical basis.

+ Instructions for testing instruments and assembling test kits.

+ The experimental procedure is based on a specific scenario for each experiment.

+ Instructions for recording data and processing data into data tables.

Table 1. *Videos - practice clips of experiments.*

Name practice experiment	The length
Basic measurements of length and mass	09’57’’
Determine the specific heat capacity of the liquid	06’27’’
Determination of melting point of ice	04’31’’
Determine the acceleration due to gravity	04’26’’
Determine the value of the resistor. Survey of Volt – Ampere meter	05’53’’
Wheatstone bridge circuit survey	04’58’’
Practical optics and optical instruments	06’48’’
Investigation of the laws of mechanics	07’43’’

Currently, the COVID-19 pandemic is still taking place and becoming more and more complicated, face-to-face classes at the school's laboratory will not be possible. However, general physics modules that use study films for online classrooms or video-based labs are good options when students are not physically on campus. The content of the activities the instructor assigns to students is based on a video - the clip provides a step-by-step overview of a real lab exercise so that students can visualize the entire experiment and its environment through via a video-clip (Figure 2 is one of the experiments).

 ISBN:

Fig. 2. *Practical Optical Experiments and Optical Instruments.*

3.3. Limitations to the implementation of study films when learning online

The objectives of the experimental part of the curriculum are: develop design, problem-solving and analytical skills; familiarize students with equipment techniques and materials; development of practical skills; development of data recording and analysis skills; develop interpersonal and communication skills; develop technical assessment and professional practice; integration of theory and practice; motivating students to study and research. The online delivery of experimental study films for the online classroom can be effectively designed to achieve most of these approaches except for some elements of real practice exercises.

IV. CONCLUSIONS

Study films include 8 videos - the presented clip of general physics experiments can be easily integrated into a lecture in traditional classroom activities or online classes. Students can use the video-clips to get a first-hand feel of the actual experiment and become familiar with the tasks and corresponding calculations involved in performing the experiment. Study film of experimental physics is fully explains the content of the curriculum, presents the combination of theory and experiment, follows and promotes the optimal functions of the instruments and equipment of the experiment, helping many students to knowledge and content to do experiments. Experimental processes can be easily observed at any time, from any angle and viewed many times on the screen for different purposes, serving as a basis for training and improving practical skills.

REFERENCES

[1] Phan Gia Anh Vu, Lectures teaching means, Hue University of Education, 1998.

[2] Jerron Smith & AGL Creative Group, Post-processing with adobe premiere pro - adobe after effects CS6 digital classroom, Hanoi University of Technology, 2015.

[3] Jerron Smith and AGL Creative Group, Handle with Adobe after effects- Adobe after effects CS6 digital classroom, Hanoi University of Technology, 2015.

[4] Tyler Peterson and Rolando Coto, Step-by-step guide to subtitling in Aegisub, http://www.public.asu.edu/~trpete13/materials/Step-by-step-guide-to-subtitling-in-Aegisub.pdf

SYNTHESIS OF MoS_2 NANOPARTICLES BY HYDROTHERMAL ROUTE AND ITS CHARACTERIZATIONS

Vu Van Thu*, Nguyen Dac Dien

Faculty of Occupational Safety and Health, Vietnam Trade Union University

*E-mail: *thuvv@dhcd.edu.vn*

Abstract. In this paper, we synthesized molybdenum disulfide (MoS_2) nanoparticles via a simple hydrothermal method using ammonium molybdate $(NH_4)_2MoO_4$ as molybdenum source and thioacetamide (CH_3CSNH_2) as sulfur source. In which, MoS_2 was obtained by treating the solution of $(NH_4)_2MoO_4$ and CH_3CSNH_2 mixture at 120 °C for 24 h under assistance of hydrochloric acid (HCl). Most importantly, this procedure allows the formation of MoS_2 nanoparticles with enhanced homogeneity and dispersity. The size and shape of as-prepared MoS_2 nanoparticles were characterized by scanning electron microscopy (SEM). SEM image revealed that the MoS_2 nanoparticles had irregular sizes with diameter ranging from 3 to 10 nm. It was found that the addition of HCl played a crucial role in the formation of the particle-like MoS_2 in this experiment. The structural characterization was obtained from X-ray diffraction pattern (XRD), energy dispersive X-ray spectroscopy (EDS) and Raman spectrum. XRD result indicated that the as-prepared sample can be indexed to the hexagonal phase of MoS_2. EDS showed that the nanoparticles were only composed of S and Mo with atomic ratio of 2.12. The results from this work demonstrated that MoS_2 can be easily prepared by the solution-phase chemical reaction. The possible formation mechanism of MoS_2 nanoparticles is also discussed.

Keywords: *Molybdenum disulfide, Hydrothermal method, Characterization, Nanoparticles.*

I. INTRODUCTION

Nanomaterials possess large surface area, unique electrical properties, remarkable physical and chemical properties such as high strength, excellent chemical reaction rate, so they have attracted heightened attention because of their potential applications in nanodevices, functional materials used in industry and biotechnology [1]. Transition metal dichalcogenides (MX_2 with M = Mo, W, Ti, Zr, Hf, V, Nb, Ta, Tc, Re, Co, Rh, Ir, Ni, Pd, Pt and X = S, Se, Te) with unusual crystal structure have been attracting a wide range of research interests because their electronic characters could be semiconducting, metallic or superconducting [2]. Molybdenum disulfide (MoS_2) is a representative member of the transition metal dichalcogenide family of materials as well as the transition metal disulfide family which belongs to a direct band gap semiconductor [3]. MoS_2 has been one of the most studied transition metal dichalcogenides because they are widespread in nature as molybdenite. MoS_2 is constructed of three atom layers (Mo^{4+} layer is sandwiched between two S^{2-} layers by covalent bonds in a sequence of S - Mo - S) stacked together through weak Van der Waals interaction [4,5]. It has attracted lots of interest because of its outstanding properties such as unusual optical property, robust mechanical property, oxidative resistance and superior electrical performance which make it scientific and industrial importance [6]. MoS_2 has been the subject of significant research in many fields including photovoltaics, photocatalysis for energy conversion, nanoelectronics, energy

 ISBN:

storage in nonaqueous lithium batteries, electrochemical hydrogen storage, switching device, capacitors, sensing, catalytic hydride sulfurization of petroleum and hydrogen evolution reaction, solid lubricant for wear resistance, intercalation host, bioelectronics and biology [7-11]. MoS_2 nanostructures exhibit the optical and electronic properties vastly different from the bulk material [12]. The emerging applications of MoS_2 contain field-effect transistor (FET), memory device, photodetector, solar cell, electrocatalyst and so on [13]. For all of these applications, the important processes occur either at the surface or at the exposed edges of the MoS_2 layers [14]. MoS_2 nanomaterials have been prepared in practice via various methods [3,4,6,10,12,15-26]. Various morphologies of MoS_2 nanomaterials have been successfully fabricated, including two-dimensional (2D) graphene-like MoS_2, one-dimensional MoS_2 (nanorods, nanowires, nanotubes, nanofibers, nanobelts) [13,14,27-29]. Hydrothermal synthesis is becoming popular due to its simplicity, high efficiency, low cost and environmental reason since reaction solvent used is water instead of organics [30]. Hydrothermal approach has been applied to generate several types of MoS_2 nanostructures such as nanowalls, nanoplates, nanorods, flower-like microspheres, nanosheets, nanocapsules, nanoflakes etc. [31]. To our best knowledge, synthesis of zero-dimensional (0D) MoS_2 nanoparticles by hydrothermal route using $(NH_4)_2MoO_4$ as Mo starting agent and thioacetamide as reductant has not yet been reported. Since the preparation of MoS_2 nanomaterials are quite difficult, it is valuable to search for a simpler routine.

In this contribution, the MoS_2 nanoparticles were fabricated by a simple low temperature hydrothermal treatment using ammonium molybdate, thioacetamide as precursors and hydrochloric acid as pH controller. This procedure allows the formation of MoS_2 nanoparticles with the priority in simplicity and cost. Synthesis of MoS_2 nanoparticles was confirmed by scanning electron microscopy (SEM), X-ray diffraction (XRD), energy dispersive X-ray spectroscopy (EDS) and Raman spectrum.

II. EXPERIMENTS

Diammonium molybdate $(NH_4)_2MoO_4$ as molybdenum source, thioacetamide (CH_3CSNH_2) as sulfur source and hydrochloric acid (HCl) were acquired from Shanghai Chemical Reagent Corporation (China) and used as received without further purification. All chemicals were of analytical purity, aqueous solutions were prepared with ultrapure water. Double-distilled water was used throughout the experiments.

The preparation of MoS_2 nanoparticles was carried out via a simple hydrothermal route. In a typical procedure, 0.2 g of $(NH_4)_2MoO_4$ was dissolved in 25 ml of deionized water in a glass baker equipped with a magnetic bar. Under vigorous stirring for 10 min, a homogenous solution of $(NH_4)_2MoO_4$ was formed with the concentration of 0.04 M. 0.5 g CH_3CSNH_2 was added into the above solution, the mixture was kept stirring for 10 min. Then, 0.1 M HCl was dropped on the above solution under continuously stirring for 5 min to adjust the pH of the solution to 6.5. Subsequently, the mixture was transferred into a 50 ml Teflon-lined stainless steel autoclave, it was sealed tightly and heated at 120 °C for 24 h. After the autoclave was allowed to cool to room temperature naturally, the dark

precipitate was isolated by filtration and rinsed extensively with double-distilled water for several times to remove the ions possibly remaining in the end product. The final product, MoS_2 nanoparticles, were collected and dried in an electric oven at 80 °C in air overnight.

The resulting MoS_2 was characterized by scanning electron microscopy (SEM, Hitachi S4800, Japan) operated at an accelerating voltage of 20 kV for examining surface morphology. X-ray diffraction measurement was performed on a Bruker D8 Advance X-ray diffractometer (Germany) using Cu-K_α radiation (wavelength of 0.15406 nm) at a scanning rate of 5°/min within 2θ Bragg angle range of 10°-70°. Field-emission transmission electron microscope (JEOL JEM 1010) equipped with an energy dispersive spectrometer (EDS) was used to obtain the information of the chemical composition of the sample. Raman experiment was performed in a confocal Raman microscopic spectrometer (Renishaw) using a 473 nm excitation laser with 60 mW power.

III. RESULTS AND DISCUSSION

The surface morphology of MoS_2 was observed by SEM analysis. SEM micrograph of synthesized MoS_2 nanoparticles (Fig. 1) reveals its morphological and nanostructural details. The size of MoS_2 nanoparticles is irregular with the diameter in the range of 3-10 nm. The larger nanoparticles are the combinations of the smaller nanoparticles.

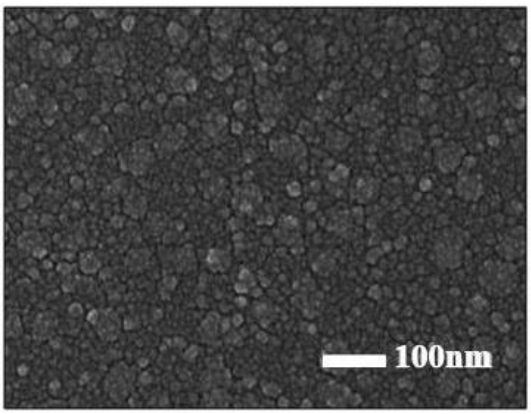

Fig. 10. *SEM image of prepared MoS_2 nanoparticles synthesized by hydrothermal route.*

Hydrochloric acid (HCl) is an inorganic acid which plays an important role in the formation of MoS_2 nanoparticles. According to Lin's group, if HCl was replaced with silicotungstic aicd $H_4Si(W_3O_{10})_4$, nanoparticles were not obtained, the products were turned to nanorods [14]. Molybdic compound reduction chemistry is quite complex and the nature of the product strongly depends on the reaction conditions [28]. The Mo (VI) can be easily reduced with H_2S reductant provided by thioacetamide decomposition in solution. The oxidation-reduction process between ammonium molybdate and hydrogen sulfide should be responsible for the formation of MoS_2. The reaction for the formation of MoS_2 can be expressed as follows:

$$CH_3CSNH_2 + 2H_2O \rightarrow H_2S + CH_3COOH + NH_3 \quad (1)$$

$$4(NH_4)_2MoO_4 + 9H_2S \rightarrow 4MoS_2 + 6NH_3 + (NH_4)_2SO_4 + 12H_2O \quad (2)$$

 ISBN:

$$HCl + NH_3 \rightarrow NH_4Cl \quad (3)$$

Step 1 is a sulfureted reaction, in which an intermediate phase H_2S is produced. The intermediate product H_2S could serve as a reductant for the subsequent growth of MoS_2 nanoparticles. Step 2 is a reduction reaction under hydrothermal conditions to reduce Mo^{6+} to Mo^{4+}. HCl reacts with NH_3 to form NH_4Cl, so promotes the reactions (1) and (2) that produce NH_3. Without hydrochloric acid, sulfureted reaction does not react completely. Therefore during the formation of MoS_2 nanoparticles, hydrochloric acid plays a prominent role. Combining equations (1) and (2) gives the possible reaction mechanism as:

$$4(NH_4)_2MoO_4 + 9CH_3CSNH_2 + 6H_2O \rightarrow 4MoS_2 + 15NH_3 + (NH_4)_2SO_4 + 9CH_3COOH \quad (4)$$

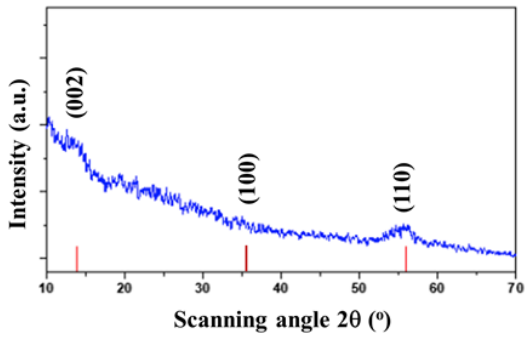

Fig. 11. *XRD pattern of the MoS_2 NPs.*

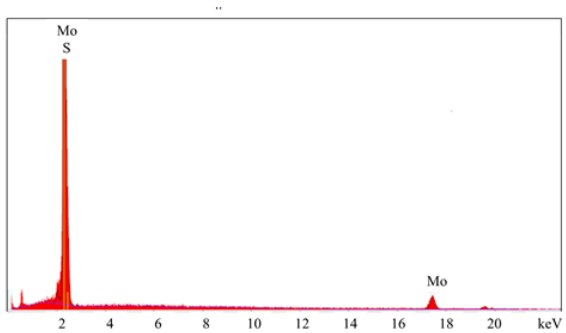

Fig. 12. *EDS spectrum of MoS_2 nanoparticles.*

The crystallinity of the as-prepared MoS_2 nanoparticles was characterized using a XRD diffractometer. It can be seen from Figure 2 that the powder XRD pattern displays only three very weak and broad diffraction peaks located at 2θ values of 12-16°, 35-38° and 55-58° which can be assigned to the (002), (100) and (110) crystal planes, respectively, corresponding to the hexagonal phase of MoS_2 nanoparticles (JCPDS 37-1492) [16, 18] with space group P63/mmc and lattice constants $a = 3.16116$ Å and $c = 12.2985$ Å [28]. No sharp peaks are present in the XRD pattern indicating the poor crystallinity of MoS_2 nanoparticles. Thus, the overall spectrum is typical of amorphous nature of MoS_2 [17]. Energy dispersive X-ray spectroscopy (EDS) determined the elements contained in the sample. The result in Figure 3 showed that the sample contains Mo and S with calculated S to Mo atomic ratio of 2.12, and no other elements existed indicating that the product was stoichiometric MoS_2.

Raman spectroscopy is an effective tool to provide nondestructive structural information about nanomaterials [32]. Figure 4 is the Raman scattering spectrum of the as-prepared MoS_2 nanoparticles (NPs) showing the anisotropic character of the vibrational modes. Subjecting MoS_2 to IR scattering would result in two Raman-active modes which are characteristic signatures of the MoS_2 structure. These modes are originated from the E^1_{2g} and A_{1g} Raman modes observed at 380 cm^{-1}, 410 cm^{-1} corresponding to in-plane (E^1_{2g}) and out-of-plane (A_{1g}) vibrational modes of S atoms, respectively [25]. The E^1_{2g} mode is assigned to in-plane (S-Mo-S) atomic vibrations involving the opposite vibration of two S atoms with respect to the Mo atom between them. The A_{1g} mode is attributed to the out-of-plane vibration of S atoms in opposite directions (Figure 5). The intensity ratio for E^1_{2g} and

A_{1g} is ~0.45 and the peak spacing between E^1_{2g} and A_{1g} is 30 cm^{-1}. These two peaks are two typical Raman-active phonon modes which reflect the crystal structure of MoS_2. The peak at 525 cm^{-1} originates from the Si substrate. The intensity ratio between E^1_{2g} and Si peaks depends on the layer thickness [33]. This result agrees well with the observation for deposited MoS_2 layer [24]. These observations confirm the successful preparation of the MoS_2 nanoparticles.

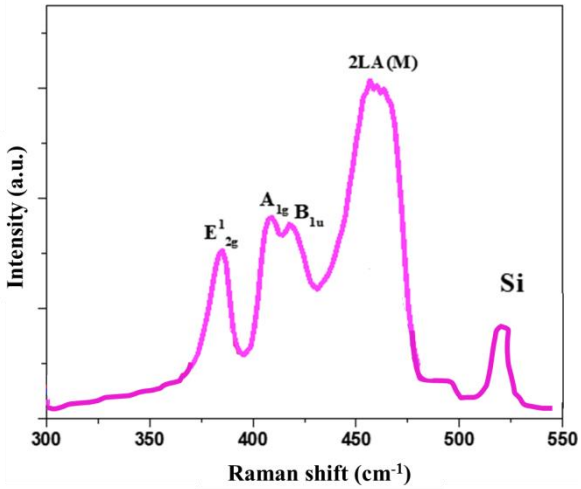

Fig. 13. *Raman scattering spectrum of the MoS_2 nanoparticles.*

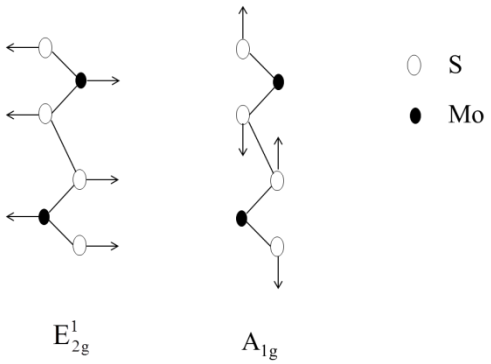

Fig. 14. *Atomic vibration of the two Raman modes in the unit cell of the MoS_2 crystal [34].*

IV. CONCLUSION

In summary, the obtained results demonstrate a simple low temperature hydrothermal route can be used with some benefits for preparation MoS_2 nanoparticles with diameter of 3-10 nm. Synthesis of MoS_2 nanoparticles was verified by SEM, XRD, EDS and Raman spectroscopy. XRD patterns indicated the amorphous MoS_2. It can be demonstrated that the optimum conditions for preparing MoS_2 nanoparticles are 120 °C for 24 h in HCl solution. This energy-saving and less pollution approach can be further used to grow other transition metal dichalcogenides. The as-synthesized MoS_2 can be effectively used in a wide variety of electrical and opto-electronic devices based on transition metal dichalcogenides.

ACKNOWLEDGEMENT. The authors gratefully acknowledge the financial support of this study by Vietnam Trade Union University.

REFERENCES

[1] J. A. Hubbell, A. Chilkoti, Nanomaterials for drug delivery, *Science*, 2012, **337**, 303-305.

[2] A. K. Geim, I. V. Grigorieva, Van der Waals heterostructures, *Nature*, 2013, **499**, 419-425.

[3] J. Kibsgaard, Z. Chen, B. N. Reinecke, T. F. Jaramillo, Engineering the surface structure of MoS_2 to preferentially expose active edge sites for electrocatalysis, *Nat. Mater.*, 2012, **11**, 963-969.

 ISBN:

[4] X. Wang, F. Nan, J. Zhao, T. Yang, T. Ge, K. Jiao, A label-free ultrasensitive electrochemical DNA sensor based on thin-layer MoS_2 nanosheets with high electrochemical activity, *Biosens. Bioelectron.*, 2015, **64**, 386-391.

[5] D. Jariwala, V. K. Sangwan, L. J. Lauhon, T. J. Marks, M. C. Hersam, Emerging device applications for semiconducting two-dimensional transition metal dichalcogenides, *ACS Nano*, 2014, **8**, 1102-1120.

[6] N. Goswami, A. Giri, S. K. Pal, MoS_2 nanocrystals confined in a DNA matrix exhibiting energy transfer, *Langmuir*, 2013, **29**, 11471-11478.

[7] S. Z. Butler, S. M. Hollen, L. Cao, Y. Cui, J. A. Gupta, H. R. Gutierrez, T. F. Heinz, S. S. Hong, J. Huang, A. F. Ismach, E. Johnston-Halperin, M. Kuno, V. V. Plashnitsa, R. D. Robinson, R. S. Ruoff, S. Salahuddin, J. Shan, L. Shi, M. G. Spencer, M. Terrones, W. Windl, J. E. Goldberger, Progress, challenges, and opportunities in two-dimensional materials beyond graphene, *ACS Nano*, 2013, **7**, 2898-2926.

[8] J. S. Ross, S. Wu, H. Yu, N. J. Ghimire, A. M. Jones, G. Aivazian, J. Yan, D. G. Mandrus, D. Xiao, W. Yao, X. Xu, Electrical control of neutral and charged excitons in a monolayer semiconductor, *Nat. Commun.*, 2013, **4**, 1-6.

[9] M. Chhowalla, H. S. Shin, G. Eda, L. J. Li, K. P. Loh, H. Zhang, The chemistry of two-dimensional layered transition metal dichalcogenide nanosheets, *Nat. Chem.*, 2013, **5**, 263-275.

[10] S. Ding, D. Zhang, J.S. Chen, X.W.D. Lou, Facile synthesis of hierarchical MoS_2 microspheres composed of few-layered nanosheets and their lithium storage properties, *Nanoscale*, 2012, **4**, 95-98.

[11] S. Wi, H. Kim, M. Chen, H. Nam, L.J. Guo, E. Meyhofer, X. Liang, Enhancement of photovoltaic response in multilayer MoS_2 induced by plasma doping, *ACS Nano*, 2014, **8**, 5270-5281.

[12] L. A. King, W. Zhao, M. Chhowalla, D. J. Riley, G. Eda, Photoelectrochemical properties of chemically exfoliated MoS_2, *J. Mater. Chem. A*, 2013, **1**, 8935-8941.

[13] X. Li, H. Zhu, Two-dimensional MoS_2: Properties, preparation, and applications, *J. Mater.*, 2015, **1**, 33-44.

[14] H. Lin, X. Chen, H. Li, M. Yang, Y. Qi, Hydrothermal synthesis and characterization of MoS_2 nanorods, *Mater. Lett.* 2010, **64**, 1748-1750.

[15] T. Yang, H. Chen, T. Ge, J. Wang, W. Li, K. Jiao, Highly sensitive determination of chloramphenicol based on thin-layered MoS_2/polyaniline nanocomposite, *Talanta* 2015, **144**, 1324-1328.

[16] K. J. Huang, L. Wang, J. Li, Y. M. Liu, Electrochemical sensing based on layered MoS_2-graphene composites, *Sens. Actuators B*, 2013, **178**, 671-677.

[17] J. Yoon, T. Lee, B.B. G., J. Jo, B.-K. Oh, J. W. Choi, Electrochemical H_2O_2 biosensor composed of myoglobin on MoS_2 nanoparticle-graphene oxide hybrid structure, *Biosens. Bioelectron.*, 2017, **93**, 14-20.

[18] X. Lin, Y. Ni, S. Kokot, Electrochemical cholesterol sensor based on cholesterol oxidase and MoS_2-AuNPs modified glassy carbon electrode, *Sens. Actuators B*, 2016, **233**, 100-106.

[19] S. Su, H. Sun, F. Xu, L. Yuwen, C. Fan, L. Wang, Direct electrochemistry of glucose oxidase and a biosensor for glucose based on a glass carbon electrode modified with MoS_2 nanosheets decorated with gold nanoparticles, *Microchim Acta*, 2014, **181**, 1497-1503.

[20] H. S. S. R. Matte, A. Gomathi, A. K. Mannan, D. J. Late, R. Datta, S. K. Pati, C. N. R. Rao, MoS_2 and WS_2 analogues of graphene, *Angew. Chem. Int. Ed.*, 2010, **49**, 4059-4062.

[21] K. S. Novoselov, D. Jiang, F. Schedin, T. J. Booth, V. V. Khotkevich, S. V. Morozov, A. K. Geim, Two-dimensional atomic crystals, *Proc. Natl. Acad. Sci. USA*, 2005, **102**, 10451-10453.

[22] B. Radisavljevic, A. Radenovic, J. Brivio, V. Giacometti, A. Kis, Single-layer MoS_2 transistors, *Nat. Nanotechnol.*, 2011, **6**, 147-150.

[23] J. V. Lauritsen, J. Kibsgaard, S. Helveg, H. Topsoe, B. S. Clausen, E. Laegsgaard, F. Besenbacher, Size-dependent structure of MoS_2 nanocrystals, *Nat. Nanotechnol.*, 2007, **2**, 53-58.

[24] Y. H. Lee, X. Q. Zhang, W. Zhang, M. T. Chang, C. T. Lin, K. D. Chang, Y. C. Yu, J. T.-W. Wang, C.-S. Chang, L.-J. Li, T.-W. Lin, Synthesis of large-area MoS_2 atomic layers with chemical vapor deposition, *Adv. Mater.*, 2012, **24**, 2320-2325.

[25] M. R. Laskar, D.N. Nath, L. Ma, E. W. L. Il, C. H. Lee, T. Kent, Z. Yang, R. Mishra, M. A. Roldan, J. C. Idrobo, S. T. Pantelides, S. J. Pennycook, R. C. Myers, Y. Wu, S. Rajan, p-type doping of MoS_2 thin films using Nb, *Appl. Phys. Lett.*, 2014, **104**, 1-4.

[26] Q. Li, J. T. Newberg, E. C. Walter, J. C. Hemminger, R. M. Penner, Polycrystalline molybdenum disulfide (2H-MoS_2) nano- and microribbons by electrochemical/chemical synthesis, *Nano Lett.*, 2004, **4**, 277-281.

[27] J. N. Coleman, M. Lotya, A. O'Neill, S. D. Bergin, P. J. King, U. Khan, K. Young, A. Gaucher, S. De, R. J. Smith, I. V. Shvets, S. K. Arora, G. Stanton, H. Y. Kim, K. Lee, G. T. Kim, G. S. Duesberg, T. Hallam, J. J. Boland, J. J. Wang, J. F. Donegan, J. C. Grunlan, G. Moriarty, A. Shmeliov, R. J. Nicholls, J. M. Perkins, E. M. Grieveson, K. Theuwissen, D. W. McComb, P. D. Nellist, V. Nicolosi, Two-dimensional nanosheets produced by liquid exfoliation of layered materials, *Science*, 2011, **331**, 568-571.

[28] G. Nagaraju, C. N. Tharamani, G. T. Chandrappa, J. Livage, Hydrothermal synthesis of amorphous MoS_2 nanofiber bundles via acidification of ammonium heptamolybdate tetrahydrate, *Nanoscale Res. Lett.*, 2007, **2**, 461-468.

[29] C. Jun, L. Suolong, G. Feng, X. Qiang, K. Tanaka, Low-temperature catalytic preparation of multi-wall MoS_2 nanotubes, *Sci. China*, 2003, **46**, 191-195.

[30] R. Kumar, S. Sahoo, E. Joanni, R. K. Singh, R. M. Yadav, R. K. Verma, D. P. Singh, W. K. Tan, A. P. d. Pino, S. A. Moshkalev, A. Matsuda, A review on synthesis of graphene, h-BN and MoS_2 for energy storage applications: Recent progress and perspectives, *Nano Res.*, 2019, **12**, 2655-2694.

[31] H. Gong, F. Zheng, Z. Li, Y. Li, P. Hu, Y. Gong, S. Song, F. Zhan, Q. Zhen, Hydrothermal preparation of MoS_2 nanoflake arrays on Cu foil with enhanced supercapacitive property, *Electrochim. Acta*, 2017, **227**, 101-109.

[32] X. Gan, H. Zhao, X. Quan, Two-dimensional MoS_2: A promising building block for biosensors, *Biosens. Bioelectron.*, 2017, **89**, 56-71.

[33] Y. Zhan, Z. Liu, S. Najmaei, P. M. Ajayan, J. Lou, Large area vapor phase growth and characterization of MoS_2 atomic layers on a SiO_2 substrate, *Small*, 2012, **8**, 966-971.

[34] U. Krishnan, M. Kaur, K. Singh, M. Kumar, A. Kumar, A synoptic review of MoS_2: Synthesis to applications, *Superlattices Microstruct.*, 2019, **128**, 274-297.

 ISBN:

COMPARISON OF EFFECTIVE MODE AREA OF PHOTONIC CRYSTAL FIBERS WITH DIFFERENT AIR-HOLE DIAMETERS IN THE CLADDING FOR VARIOUS LATTICE TYPES

Trong Dang Van[1], Bao Tran Le Tran[1], Ngoc Vo Thi Minh[1], Tan Tran Duy[2], Lanh Chu Van[1], Duc Hoang Trong[3], Thuy Nguyen Thi[3*]

[1]*Department of Physics, Vinh University, 182 Le Duan, Vinh City, Viet Nam*

[2]*Truong Xuan High School, Thap Muoi district, Thap Muoi Province, Viet Nam*

[3]*University of Education, Hue University, 34 Le Loi Street - Hue City, Viet Nam*

*****E-mail: *ntthuy@hueuni.edu.vn*

Abstract. A novel small effective mode area silica-based photonic crystal fibers (PCFs) is proposed in this paper. The small effective mode areas are achieved by the selection of PCFs in which the air-hole diameter of the first ring is different from the others in the cladding. It offers a new design for all three selected types including circular, square, and hexagonal lattice. We numerically analyze and compare the effective area of PCFs with these three types of lattice, in which the influence of lattice constant and filling factor on the nonlinear properties of PCFs is noted. PCF with hexagonal structure possesses the highest nonlinear coefficient because of its smallest effective mode area at 1.55 µm wavelength. This opens up good application opportunities for PCFs in supercontinuum generation.

Keywords: *Photonic crystal fibers (PCFs), Small effective mode area, High nonlinear coefficient, Various lattice types.*

I. INTRODUCTION

The introduction of photonic crystal fiber (PCF) in 1996 was a breakthrough event in fiber technology [1]. With design flexibility through changing geometrical and structural parameters such as lattice type, size of core or air-holes, lattice constant, background material, and permeable material,... PCFs exhibit outstanding advantages over conventional optical fibers. Therefore, PCFs not only have the same applications as conventional optical fibers but also have special applications in the field of high-sensitivity sensors or supercontinuum generation [2-12]. The effective refractive index, effective mode area, dispersion, and loss confinement were the main characteristics affecting the efficiency of PCF in supercontinuum generation.

In the past decades, many publications have often focused on the three main types of PCF lattice including circular lattice [13-14], square lattice [15-16], hexagonal lattice [17]. In which, PCF characteristics can be easily controlled by the variation of the filling factor and lattice constant. The flat dispersion, high nonlinearity, low loss confinement,... can be achieved in these PCFs. However, these works have not evaluated the optimization of PCF features for each type of lattice. Recently, the work [18] has investigated the influence of structural parameters on the PCF characteristics for each type of lattice, but the authors have not emphasized the role of differences in air-hore diameter in the rings to properties of PCF.

In our study, the PCFs are designed with different types of lattices, the difference in air-hole diameters in the rings is noticed to control the effective mode areas and nonlinear coefficients of PCFs. Furthermore, these two quantities are also analyzed and compared to the most optimal structure.

II. NUMERICAL MODELLING OF PCFs

Lumerical Mode Solutions [19] software was used to design three silica-based PCFs with a lattice of eight air hole rings arranged in different lattice types including square, circular and hexagonal structures. The cross-section of silica-based PCF with different lattices is presented in Fig.1. Silica was selected as the substrate material to create a difference in the refractive index between the core and the cladding. The lattice constant (Λ) has values of 0.7, 0.8, 1.0, and 1.5 µm. The diameter of the air hole of the first ring is d_1, corresponding to the filling factor d_1/Λ, which varies from 0.3 to 0.8 with a step of 0.05. Meanwhile, the filling factor of the other rings d/Λ is kept constant at 0.95, with d is the air hole diameter of the second and subsequent rings. The core diameter (D_{core}) depends on d_1 and Λ and is determined by the formula $D_{core} = 2\Lambda - 1.1d_1$. The effective mode area and nonlinear coefficients of PCF are controlled by the filling factor in the first ring.

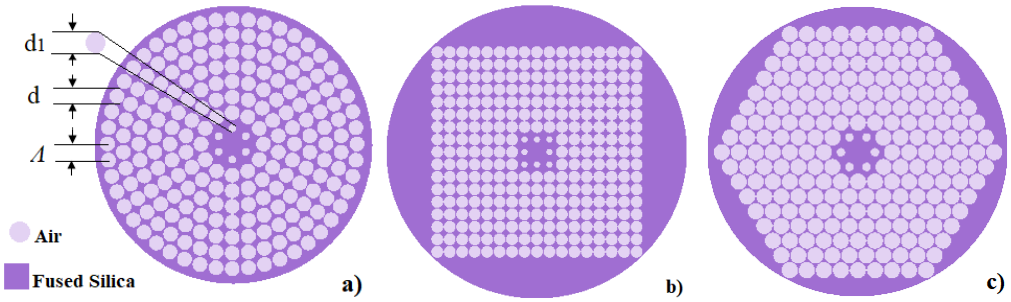

Fig. 1. *Cross-section of silica-based PCF with different lattices*
(a) Circular Lattice, (b) Square Lattice, and (c) Hexagonal Lattice.

Since the refractive index is dependent on wavelength, the refractive index of fused silica can be obtained using Sellmeier's equation (Eq. 1):

$$n^2_{\text{Fused silica}}(\lambda) = 1 + \frac{0.6694226\lambda^2}{\lambda^2 - 4.4801\times10^{-3}} + \frac{0.4345839\lambda^2}{\lambda^2 - 1.3285\times10^{-2}} + \frac{0.8716947\lambda^2}{\lambda^2 - 95.341482} \quad (1)$$

where the wavelength λ has dimensions of micrometers.

The effective mode area is one of the important parameters characterize the PCF nonlinearity. The effective mode area (A_{eff}) is determined as follows [5, 20]:

$$A_{eff} = \frac{\left(\int_{-\infty}^{\infty}\int_{-\infty}^{\infty} |E(x,y)|^2\, dxdy\right)^2}{\int_{-\infty}^{\infty}\int_{-\infty}^{\infty} |E(x,y)|^4\, dxdy} \quad (2)$$

where E is the electric field amplitude.

 ISBN:

The nonlinear coefficient is inversely proportional to the effective mode area, determined according to the following formula [21]:

$$\gamma = \frac{\omega}{c}\left(\frac{n_2}{A_{eff}}\right) = \frac{2\pi}{\lambda}\left(\frac{n_2}{A_{eff}}\right) \tag{3}$$

where, the unit of gamma is ($W^{-1}.km^{-1}$). ω is the angular frequency, n_2 is the nonlinear refractive index, and (n_2/A_{eff}) is the nonlinear constant.

III. RESULTS AND DISCUSSION

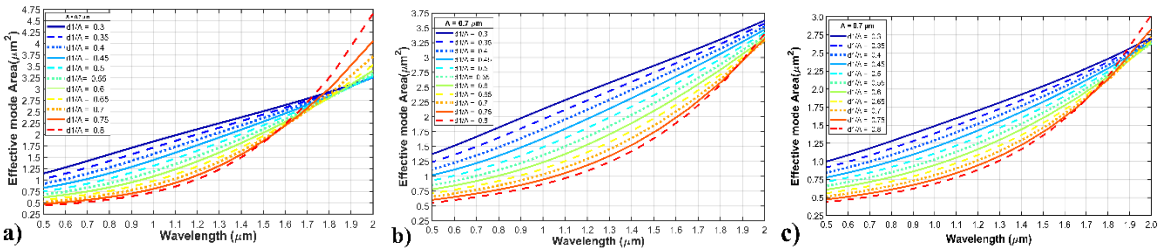

Fig. 2. *The effective mode areas characteristics of silica-based PCFs with Λ = 0.7 µm, d_1/Λ = 0.3 ÷ 0.8 for lattices: a) Circular Lattice, b) Square Lattice, and c) Hexagonal Lattice.*

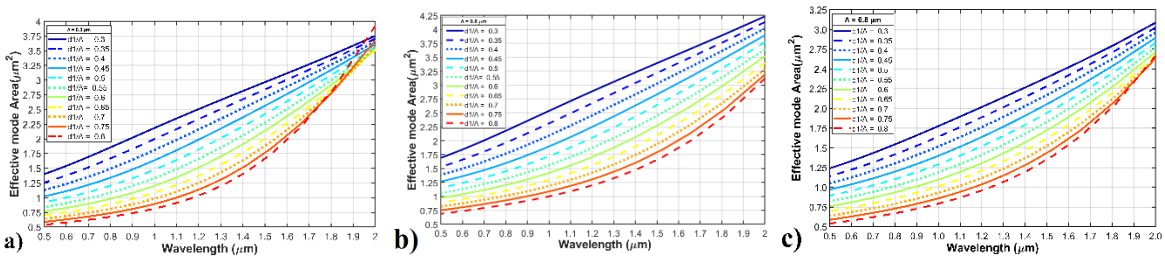

Fig. 3. *The effective mode areas characteristics of silica-based PCFs with Λ = 0.8 µm, d_1/Λ = 0.3 ÷ 0.8 for lattices: a) Circular Lattice, b) Square Lattice, and c) Hexagonal Lattice.*

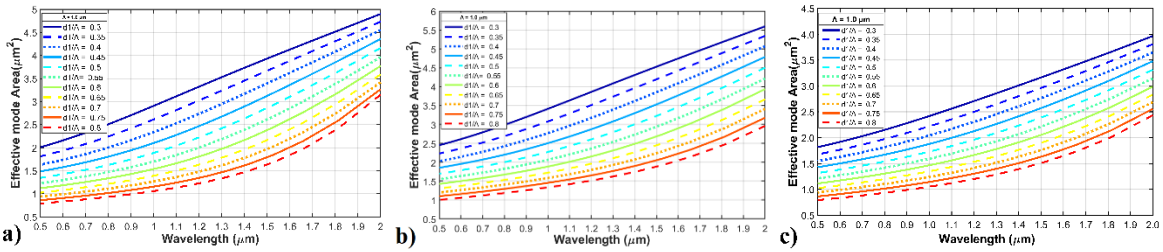

Fig.4. *The effective mode areas characteristics of silica-based PCFs with Λ = 1.0 µm, d_1/Λ = 0.3 ÷ 0.8 for lattices: a) Circular Lattice, b) Square Lattice, and c) Hexagonal Lattice.*

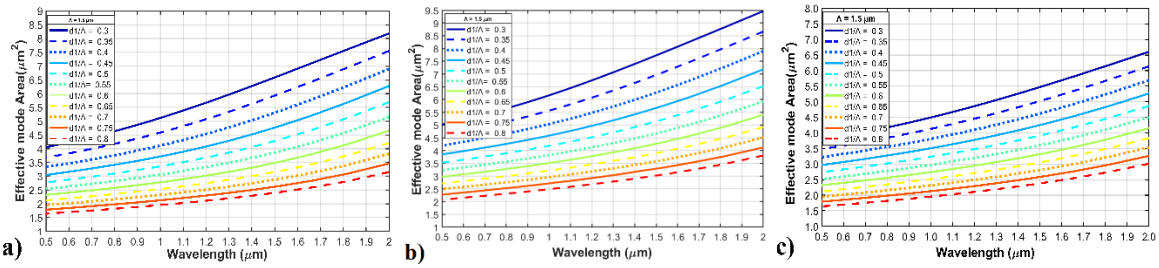

Fig. 5. *The effective mode areas characteristics of silica-based PCFs with Λ = 1.5 µm, d_1/Λ = 0.3 ÷ 0.8 for lattices: a) Circular Lattice, b) Square Lattice, and c) Hexagonal Lattice.*

Fig. 2, 3, 4, and 5 show the dependence of the effective mode area on a wavelength with various d_1/Λ and Λ for all three structures including circular, square and hexagonal lattice,... At the same structural parameters, the effective mode area varies with wavelength and has the same shape. Specifically, as the wavelength increases, the effective mode area rises. For PCF structures with the same lattice constant, the effective mode area increases rapidly with wavelength with a large filling factor (d_1/Λ) and slowly increases with a small filling factor (d_1/Λ). Furthermore, the effective mode area increases with increasing lattice constant. With large core PCFs, the effective mode area curves tend to separate more clearly in the wavelength region from 1.8 to 2.0 µm, i.e. the increase in effective mode area with wavelength is more uniform.

Table 1 shows the value of the effective mode area of PCF with various filling factors and lattices constant for three lattices at wavelength 1.55 µm. For each type of structure, an increase of d_1/Λ causes the value of the effective mode area to reduce, and this value increases with the increasing of lattice constant. Compared with the other two structures, the hexagonal structure gives the value of the smallest effective mode area. With $\Lambda = 0.7$µm and $d_1/\Lambda = 0.8$, the effective mode area values of circular, square and hexagonal lattice are 2.021 (µm^2), 1.761 (µm^2), and 1.467 (µm^2), respectively.

Benefiting from tight mode confinement due to PCFs design, high nonlinearity is another feature of these PCF. Fig. 6, 7, 8, and 9 display the influence of the filing factor d_1/Λ and lattice constant Λ on the nonlinear coefficients. In contrast to the effective mode area analyzed above, the nonlinear coefficient decreases with increasing wavelength. At the same time, the small values of d_1/Λ make the nonlinear coefficient smaller than others. With the same type of lattice and parameter d_1/Λ, the value of the nonlinear coefficient goes down as the lattice constant rises up.

Table 1. *The effective mode area values of silica-based PCF at 1.55 µm with lattice constant $\Lambda = 0.7$ µm, $\Lambda = 0.8$ µm, $\Lambda = 1.0$ µm,* and *$\Lambda = 1.5$ µm the filling factor d_1/Λ varies from 0.3 to 0.8. The effective mode area (A_{eff}) is in µm^2.*

λ (µm)	d_1/Λ	Λ = 0.7 (µm)			Λ = 0.8 (µm)		
		Circular	**Square**	**Hexagonal**	**Circular**	**Square**	**Hexagonal**
1.55	0.3	2.578	2.933	2.1	3.041	3.476	2.456
	0.35	2.515	2.825	2.033	2.924	3.307	2.35
	0.4	2.445	2.71	1.966	2.797	3.122	2.243
	0.45	2.373	2.588	1.895	2.663	2.934	2.13
	0.5	2.3	2.462	1.822	2.529	2.746	2.02
	0.55	2.226	2.334	1.753	2.392	2.557	1.911
	0.6	2.158	2.208	1.685	2.26	2.379	1.805
	0.65	2.096	2.086	1.621	2.132	2.206	1.705
	0.7	2.047	1.97	1.559	2.014	2.046	1.609
	0.75	2.019	1.861	1.508	1.906	1.896	1.523
	0.8	2.021	1.761	1.467	1.816	1.76	1.442
λ (µm)	**d_1/Λ**	**Λ = 1.0 (µm)**			**Λ = 1.5 (µm)**		
		Circular	**Square**	**Hexagonal**	**Circular**	**Square**	**Hexagonal**
1.55	0.3	4.032	4.637	3.242	6.744	7.9	5.579
	0.35	3.777	4.31	3.042	6.08	7.123	5.124
	0.4	3.509	3.972	2.848	5.448	6.421	4.716
	0.45	3.242	3.648	2.653	4.896	5.802	4.34
	0.5	2.984	3.341	2.47	4.397	5.265	3.996

 ISBN:

	0.55	2.733	3.052	2.295	3.962	4.778	3.68
	0.6	2.498	2.788	2.13	3.576	4.363	3.387
	0.65	2.279	2.546	1.975	3.235	3.985	3.117
	0.7	2.079	2.331	1.833	2.945	3.657	2.869
	0.75	1.897	2.137	1.7	2.682	3.358	2.642
	0.8	1.734	1.963	1.576	2.455	3.085	2.431

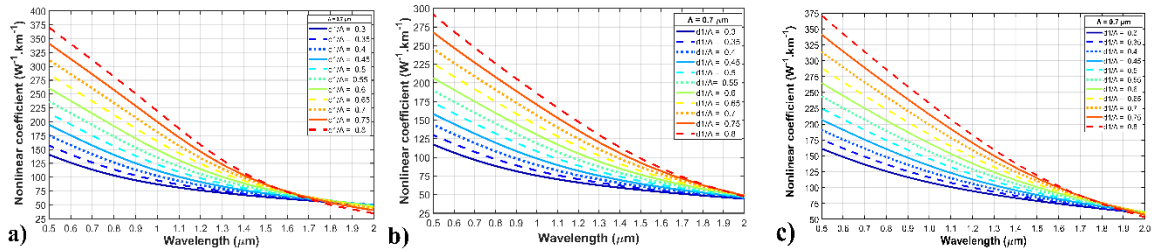

Fig. 6. *The nonlinear coefficient of silica-based PCFs with Λ = 0.7 μm, d_1/Λ = 0.3 ÷ 0.8 for lattices: a) Circular Lattice, b) Square Lattice, and c) Hexagonal Lattice.*

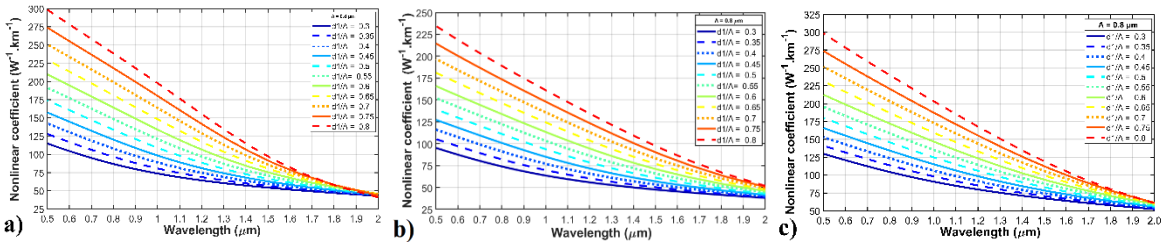

Fig. 7. *The nonlinear coefficient of silica-based PCFs with Λ = 0.8 μm, d_1/Λ = 0.3 ÷ 0.8 for lattices: a) Circular Lattice, b) Square Lattice, and c) Hexagonal Lattice.*

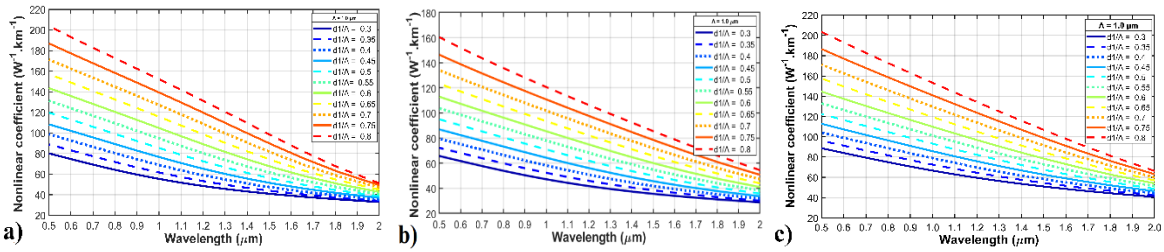

Fig. 8. *The nonlinear coefficient of silica-based PCFs with Λ = 1.0 μm, d_1/Λ = 0.3 ÷ 0.8 for lattices: a) Circular Lattice, b) Square Lattice, and c) Hexagonal Lattice.*

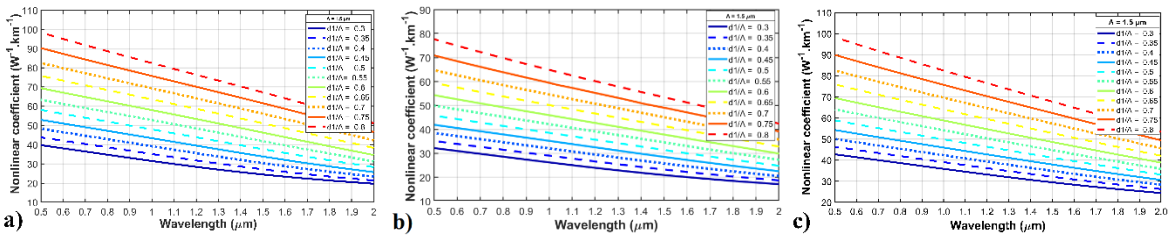

Fig.9. *The nonlinear coefficient of silica-based PCFs with Λ = 1.5 μm, d_1/Λ = 0.3 ÷ 0.8 for lattices: a) Circular Lattice, b) Square Lattice, and c) Hexagonal Lattice.*

Table 2 exposes the values of the nonlinear coefficients calculated at 1.55 μm of the wavelength. The difference in the values of the nonlinear coefficients of the proposed PCFs with the same set of structural parameters is the purpose of this calculation. For all variable values of d_1/Λ and Λ, PCF with hexagonal lattice structure always possesses the largest nonlinear coefficient. For example, a wavelength of 1.55 μm of a structure with the

lattice constant of 0.8, the nonlinear coefficients in circular, square and hexagonal lattice are 89,417 ($W^{-1}.km^{-1}$), 91,878 ($W^{-1}.km^{-1}$), and 112.211 ($W^{-1}.km^{-1}$), respectively. With the properly chosen parameter, the maximum nonlinear coefficient can be achieved in the proposed PCF to be as high as 112.211 ($W^{-1}.km^{-1}$) with Λ = 0.8 µm and d_1/Λ = 0.8.

Table 2. *The nonlinear coefficient values of silica-based PCF at wavelength 1.55 µm with lattice constant Λ = 0.7 µm, Λ = 0.8 µm, Λ = 1.0 µm, and Λ = 1.5 µm and the filling factor d_1/Λ varies from 0.3 to 0.8. The nonlinear coefficient γ is in ($W^{-1}.km^{-1}$).*

λ (µm)	d_1/Λ	Λ = 0.7 (µm)			Λ = 0.8 (µm)		
		Circular	**Square**	**Hexagonal**	**Circular**	**Square**	**Hexagonal**
1.55	0.3	62.535	54.965	76.8	53.019	46.384	65.651
	0.35	64.114	57.071	79.316	55.149	48.756	68.627
	0.4	65.968	59.51	82.048	57.669	51.665	71.925
	0.45	68	62.333	85.158	60.593	54.981	75.758
	0.5	70.191	65.551	88.566	63.828	58.763	79.9
	0.55	72.539	69.155	92.117	67.507	63.114	84.483
	0.6	74.89	73.146	95.879	71.505	67.868	89.464
	0.65	77.159	77.454	99.743	75.854	73.212	94.767
	0.7	79.116	82.096	103.732	80.354	78.983	100.439
	0.75	80.324	86.97	107.367	85.006	85.273	106.173
	0.8	80.478	91.96	110.472	89.417	91.878	112.211
λ (µm)	**d_1/Λ**	**Λ = 1.0 (µm)**			**Λ = 1.5 (µm)**		
		Circular	**Square**	**Hexagonal**	**Circular**	**Square**	**Hexagonal**
1.55	0.3	39.989	34.764	49.734	23.906	20.406	28.894
	0.35	42.697	37.41	53.008	26.518	22.631	31.457
	0.4	45.963	40.601	56.63	29.599	25.109	34.184
	0.45	49.759	44.214	60.786	32.938	27.787	37.143
	0.5	54.089	48.282	65.298	36.677	30.621	40.341
	0.55	59.069	52.874	70.294	40.697	33.739	43.803
	0.6	64.638	57.881	75.758	45.095	36.951	47.588
	0.65	70.899	63.386	81.697	49.847	40.458	51.712
	0.7	77.725	69.246	88.045	54.75	44.085	56.182
	0.75	85.23	75.51	94.94	60.11	48.012	61.013
	0.8	93.271	82.234	102.434	65.681	52.248	66.305

IV. CONCLUSION

In this work, we have analyzed the effect of the filling factor and lattice constant on the value of effective mode area and nonlinear coefficient. The values of these properties in different types of lattices have been also compared. The obtained results show that the filling factor and lattice constant strongly influence the effective mode area and the nonlinear coefficient. Moreover, in the hexagonal lattice, the value of the effective mode area is the smallest and the nonlinear coefficient is the highest among the three types of studied lattices. This makes our proposed PCF fibers valuable in supercontinuum generation.

ACKNOWLEDGMENTS. This research is funded by Vietnam National Foundation for Science and Technology Development (NAFOSTED) under grant number 103.03-2020.03 and Vietnam's Ministry of Education and Training (B2021-DHH-08).

REFERENCES

[1] J. C. Knight, T. A. Birks, P. St. J. Russell, and D. M. Atkin, All-silica single-mode optical fiber with photonic crystal cladding, *Opt. Lett.*, 1996, **21**, 1547-1549.

[2] T. A. Birks. J. C. Knight and P. S. J. Russell, Endlessly single-mode photonic crystal fiber, *Opt. Lett.*, 1997, **22**, 961-963.

[3] R. F. Cregan, B. J. Mangan, J. C. Knight, T. A. Birks, P. S. J. Russell, P. J. Roberts and D. C. Allan, Single-mode photonic band gap guidance of light in air, *Science*, 1999, **285**, 1537-1539.

[4] P. Russell, Photonic crystal fibers, *Science*, 2003, **299**, 358-362.

[5] R. Buczyński. Photonic crystal fibers, *Acta Physica Polonica Series A*, 2004, **106**, 141-168.

[6] I. M. Nascimento, G. Chesini, M. Sousa, J. H. Osório. J. M. Baptista, Cristiano M. B. Cordeiro, P. A. S. Jorge, Application of a photonic crystal fiber LPG for vibration monitoring, *Proc. of SPIE*, 2013, **8794**. 87941L-1.

[7] K. Barczak, Application of photonic crystal fiber in optical fiber current sensors, *Acta Physica Polonica A*, 2012, **122**(5), 793-795.

[8] Ana M. R. Pinto and Manuel Lopez-Amo, Photonic crystal fibers for sensing applications, *Journal of Sensors*, 2014, **21**. doi:10.1155/2012/598178.

[9] K. M. Hilligsoe, H. N. Paulsen, J. Thogersen, S. R. Keiding, and J. J. Larsen, Initial steps of supercontinuum generation in photonic crystal fibers, *J. Opt. Soc. Am. B*, 2003, **20**, 1887-1893,.

[10] Lanh Chu Van, Van Thuy Hoang, Van Cao Long, Krzysztof Borzycki, Khoa Dinh Xuan, Vu Tran Quoc, Marek Trippenbach, Ryszard Buczyński and Jacek Pniewski, Supercontinuum generation in photonic crystal fibers infiltrated with nitrobenzene, Laser Phys., 2020, **30,** 035105.

[11] Chu Van Lanh, Van Thuy Hoang, Van Cao Long, Krzysztof Borzycki, Khoa Dinh Xuan, Vu Tran Quoc, Marek Trippenbach, Ryszard Buczyński and Jacek Pniewski, Optimization of optical properties of photonic crystal fibers infiltrated with chloroform for supercontinuum generation, *Laser Phys*., 2019, **29**(7), 075107.

[12] Lanh Chu Van, A. Anuszkiewicz, A. Ramaniuk, R. Kasztelanic, Khoa Xuan Dinh, M Trippenbach, Ryszard R Buczynski, Supercontinuum generation in photonic crystal fibres with core filled with toluene, *Journal of Optics*, 2017, **19,** 125604.

[13] Abdelkader Medjouri, Lotfy Mokhtar Simohamed, Omar Ziane, Azzedine Boudrioua, Analysis of a new circular photonic crystal fiber with large mode area, *Optik*, 2015, 126(24), 5718-5724. doi:10.1016/j.ijleo.2015.09.035.

[14] Sanat Kumar Pandey, Yogendra Kumar Prajapati, J.B. Maur, Design of simple circular photonic crystal fiber having high negative dispersion and ultra-low confinement loss, *Results in Optics*, 2020, **1**, 100024.

[15] Shuvo Sen, Md. Abdullah-Al-Shafi, Muhammad Ashad Kabir, Hexagonal photonic crystal Fiber (H-PCF) based optical sensor with high relative sensitivity and low confinement loss for terahertz (THz) regime, *Sensing and Bio-Sensing Research*, 2020, **30**, 100377.

[16] Y. E. Monfared, A. R. M. Javan, A. R. M. Kashani, Confinement loss in hexagonal lattice photonic crystal fibers, *Optik*, 2013, **124,** 7049-7052.

[17] Yujun Wang, Shuguang Li, Junjun Wu, Pengtao Yu, Zenghui Li, Design of an ultrabroadband and compact filter based on square-lattice photonic crystal fiber with two large gold-coated air holes., *Photonics and Nanostructures - Fundamentals and Applications*, 2020, **41,** 100816.

[18] Bao Tran Le Tran, Thuy Nguyen Thi, Ngoc Vo Thi Minh, Trung Le Canh, Minh Le Van, Van Cao Long, Khoa Dinh Xuan, Lanh Chu Van, Analysis of dispersion characteristics of solid-core PCFs with different types of lattice in the claddings, infiltrated with ethanol, *Photonics Letters of Poland*, 2020, **12**(4), 106-108. doi:10.4302/plp.v12i4.1054.

[19] *https://www.lumerical.com/products/mode.*

[20] S. Kedenburg, M. Vieweg, T. Gissibl, and H. Giessen, Linear refractive index and absorption measurements of nonlinear optical liquids in the visible and near-infrared spectral region, *Opt. Mat. Express*, 2012, **2**, 1588.

[21] J. C. Knight, T. A. Birks, R. F. Cregan, and P. S. J. Russell, Large Mode area photonic crystal fiber, *Opt. Photonics News*, 1998, **9**(12), 34-35.

[22] Mario F.S. Ferreira, Nonlinear effects in optical fibers, John Wiley & Sons, Inc. All rights reserved, 2011.

 ISBN:

INVESTIGATING EFFECTIVE REFRACTIVE INDEX AND CONFINEMENT LOSS OF PCFs WITH HETEROGENEOUS RINGS IN THE CLADDING FOR VARIOUS LATTICE TYPES

Bao Tran Le Tran[1], Trong Dang Van[1], Ngoc Vo Thi Minh[1], Tan Tran Duy[2], Lanh Chu Van[1], Duc Hoang Trong[3], Thuy Nguyen Thi[3*]

[1]*Department of Physics, Vinh University, 182 Le Duan, Vinh City, Viet Nam*

[2]*Truong Xuan High School, Thap Muoi district, Thap Muoi Province, Viet Nam*

[3]*University of Education, Hue University, 34 Le Loi Street - Hue City, Viet Nam*

*****E-mail: *ntthuy@hueuni.edu.vn*

Abstract. Silica-based photonic crystal fibers (PCFs) structure with the difference in air-hole diameters of the first and subsequent rings in the cladding has been creatively proposed. We present a comparative numerical analysis to determine the effective refractive index of PCFs by using various lattices such as circular, square, and hexagonal with the influence of the lattice constant and the filling factor of the first ring. On increasing the wavelength, the real part of the effective refractive index reduces resulting in the increase in confinement losses. In particular, the low confinement loss of PCFs decreases rapidly in the 0.5 ÷ 0.8 µm wavelength, then it rises slowly in the remaining wavelength region. At 1.55 µm wavelength, the effective refractive index of PCFs with square lattice has the largest value. The proposed PCF structure will have great application value in the field of optical communication.

Keywords: S*ilica-based PCFs, The difference in air-hole diameters, Various lattice types, Effective refractive index, Low confinement loss.*

I. INTRODUCTION

In recent years, photonic crystal fibers (PCFs) have attracted a great deal of attention from scientists around the world and have brought tremendous development in fiber optic technology. Contrary to conventional optical fibers, PCFs have more freedom in design and fabrication including guide mechanism, size and shape of air-holes, lattice constant, and lattice types,... Changing the geometrical parameters together with the right choice of materials allows controlling dispersion, transmission, and even nonlinear properties of the fibers as well. Nowadays, PCFs have been intensively studied and have had a very wide range of applications in fiber lasers, optical amplifiers, nonlinear devices, high-power transmissions lines, highly sensitive gas sensors [1-3], and especially the application for supercontinuum generation (SC) [4-8].

On the other hand, the great variety in the size and spacing of the air-holes (lattice constant) in the cladding leads to the modification of the optical properties of the PCF. The effective cladding refractive index of PCF which plays an important role in the transmission mechanism of the PCF can be controlled by adjusting the hole diameter (d) and the lattice constant (Λ) of their air-hole arrays in the cladding. The difference of refractive index between the core and shell regions not only determines the light

confinement mechanism but also affects the confinement loss value, which is an important factor in improving the efficiency of SC.

Up to now, there is a lot of theoretical and experimental works investigated the characteristics of PCFs with common lattice types such as circular, square, hexagonal lattices and reached many outstanding achievements comprising low confinement loss [9], high negative dispersion [10], large effective mode area [11], high nonlinearity and birefringence [12],... Especially in the recent publication [13], the authors have analyzed the effect of structural parameters on the PCF properties for all the above lattices. However, most of these works use the same diameter parameters of the air-holes rings in the photonic cladding, and at the same time, they have not evaluated the optimal level of the survey quantities for each specific type of lattice. These have enormous importance for their applied research.

In this paper, we present a new design with the difference between the structural parameters in the first and other rings of three solid-core photonic crystal fibers based on silica, with circular, hexagonal, and square lattices as a cladding. The influence of these parameters on the guiding properties in terms of effective refractive index and confinement loss of the fundamental mode was also numerically studied. As a result, we optimized structures for use in applications in fiber optic technology.

II. NUMERICAL MODELLING

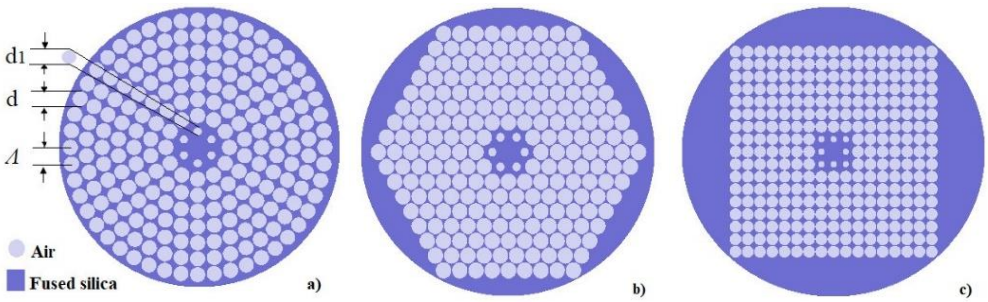

Fig. 1. *Geometric structure of three solid-core PCFs with circular (a), hexagonal (b), and square (c) lattice in the cladding.*

The schematic of the geometrical structure of the modelled solid-core PCFs with different lattice types (cross-section) is shown in Fig. 1. Each structure with empty air-holes consists of eight rings of air-holes ordered in the circular, square, and hexagonal lattices with lattice constant Λ. The background material is fused silica which helps to create a disparity between the core and the shell refractive index to improve light confinement in the core. In the numerical simulation, we chose the following lattice constants: 0.7 µm, 0.8 µm, 1.0 µm, and 1.5 µm. The first row of holes has a linear filling factor varying from 0.3; 0.35; 0.4, 0.45; 0.5; 0.55; 0.6; 0.65; 0.7; 0.75; 0.8; while that of the second and subsequent rings is kept constant at 0.95 with d_1 and d are the diameter of the first and other rings, respectively. The purpose of this alteration is to optimize the characteristic quantities for SC, since the first round near the core mainly defines the dispersion properties of the guided modes even the displacement of zero-dispersion

 ISBN:

wavelength (ZDW) while the mode attenuation is decided by the remaining rings, particularly for higher modes [14], therefore we go up the value of the linear filling factor of the outer rings to the maximum. The commercial Lumerical Mode Solution software [15] based on the finite difference method [FEM] was used for the simulations.

The refractive index of fused silica glass is described using the following Sellmeier relation [16]:

$$\varepsilon = n^2(\lambda) = 1 + \frac{A_1\lambda^2}{\lambda^2 - C_1} + \frac{A_2\lambda^2}{\lambda^2 - C_2} + \frac{A_3\lambda^2}{\lambda^2 - C_3} \quad (1)$$

with coefficients: A_1=0.6694226; A_2=0.4345839; A_3=0.8716947; C_1=4.4801×10^{-3} µm^2; C_2=1.3285×10^{-2} µm^2; C_3=95.341482 µm^2; λ is the wavelength whose in micrometers. Refractive index of the air hole is one.

Another important measure of the PCF is confinement loss (L_c) arose due to the leakage of the modes and the finite width of the cladding structure [17]. The relationship between confinement loss and the imaginary part of effective refractive index is given by [18-20]:

$$L_c = 8.686 k_0 \,\mathrm{Im}[\mathrm{n}_{eff}] \;\; (dB/m) \quad (2)$$

where Im[n_{eff}] represents the imaginary part of the effective refractive index [21], k_0 is the number of waves in free space. The confinement loss decreases exponentially when the number of air-holes gets rose and the selection of lattice type and lattice constant is appropriate. Besides, increasing the diameter of air-holes leads to an increase in the air filling part, thereby falling confinement loss.

III. RESULTS AND DISCUSSION

3.1. Effective refractive index

In Fig. 2 to 5, the effective index of refraction n_{eff} of fundamental modes in the proposed PCFs is calculated for the structures with the first ring filling factor varying from 0.3 to 0.8, and lattice constants are taken as 0.7 µm, 0.8 µm, 1.0 µm, and 1.5 µm. As seen in these graphs, the effective refractive index of the circular, square, and hexagonal PCFs changes with the change of wavelength, lattice constant Λ, filling factor d_1/Λ and have a similar shape. Pointedly, when the wavelength is increased, the effective refractive index considerably reduces. The reason is that the longer wavelength has a stronger ability to penetrate within the PCF cladding region than that of the shorter wavelength [22]. It is also observed that the n_{eff} curves rise with the lattice constant in the structure increasing, as opposed to their decrease in slope as d_1/Λ goes down in the available wavelength. This result is completely the same for all three fiber structures.

However, with the same set of structural parameters (Λ and d_1/Λ), the magnitude of the effective refractive index of the circular, square, and hexagonal PCFs at each particular value of the wavelength is different. To clearly see this difference, we determined the value of the real part of the effective refractive index of the fibers with different Λ and d_1/Λ at the

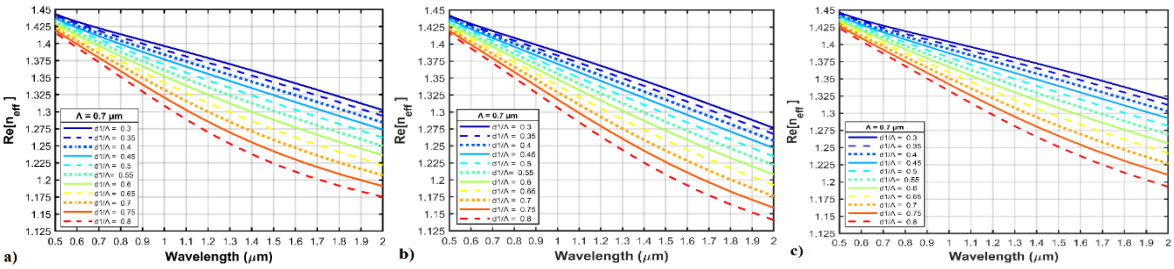

Fig. 2. *Real part of effective refraction index as a function of wavelength with Λ = 0.7 μm, d_1/Λ = 0.3 ÷ 0.8 for three PCFs: a) circular, b) hexagonal, and c) square lattices.*

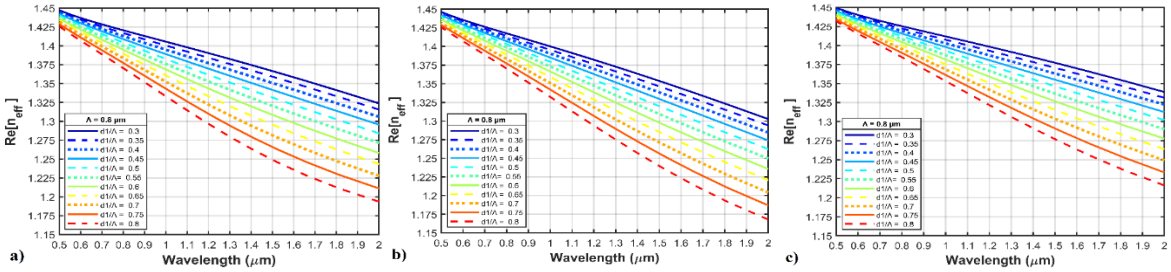

Fig. 3. *Real part of effective refraction index as a function of wavelength with Λ = 0.8 μm, d_1/Λ = 0.3 ÷ 0.8 for three PCFs: a) circular, b) hexagonal, and c) square lattices.*

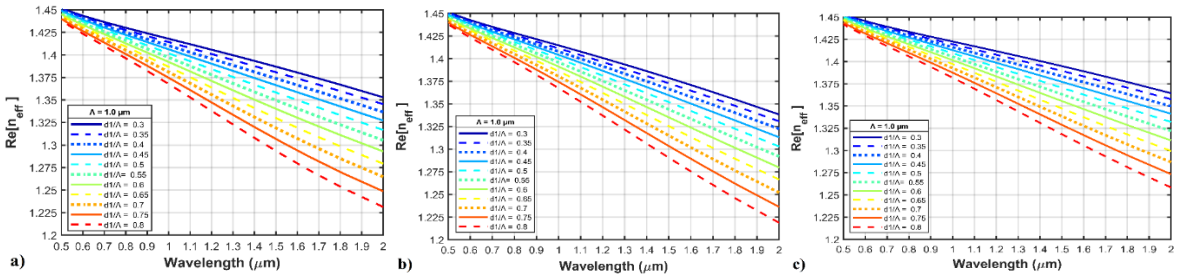

Fig. 4. *Real part of effective refraction index as a function of wavelength with Λ = 1.0 μm, d_1/Λ = 0.3 ÷ 0.8 for three PCFs: a) circular, b) hexagonal, and c) square lattices.*

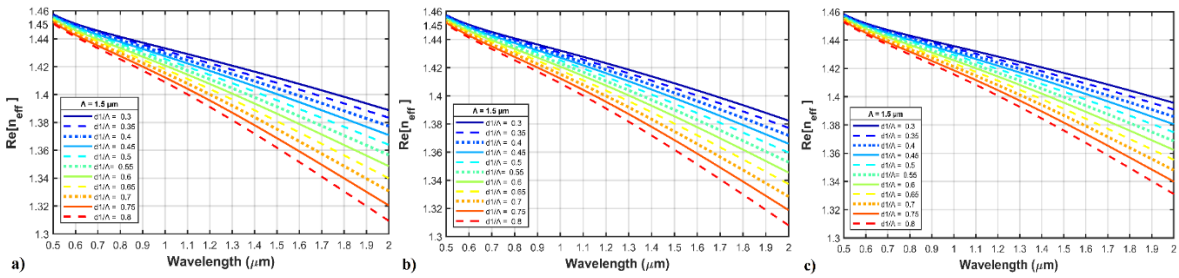

Fig. 5. *Real part of effective refraction index as a function of wavelength with Λ = 1.5 μm, d_1/Λ = 0.3 ÷ 0.8 for three PCFs: a) circular, b) hexagonal, and c) square lattices.*

wavelength of 1.55 μm. The results show that the effective refractive index of all three PCFs reaches the maximum value at d_1/Λ = 0.3 and the minimum one at d_1/Λ = 0.8. In all simulation cases, PCF with square lattice has the largest effective refractive index, with 1.415, corresponding to Λ = 1.5 μm, d_1/Λ = 0.3. That number is followed by the circular lattice, with the value of 1.41 while ne_{ff} of hexagonal lattice is the lowest (equal to 1.406) at the same set of parameters. Those results are displayed in Table 1. Alternatively, changing the structure of the lattice cladding brings about a difference in the number of air-holes in the shell resulting in a different density of SiO_2 and air in the cladding. Moreover,

 ISBN:

the mode area at the core is also not the same, so the refractive index of different lattice structures will be different. This provides flexibility in design and is suitable for various applications of PCF.

Table 1. *The value of the effective refractive index of the fibers at 1.55µm wavelength with various lattices constant and the linear filling factor of the first ring.*

λ(µm)	d_1/Λ	$Re[n_{eff}]$					
		Λ = 0.7 (µm)			Λ = 0.8 (µm)		
		Circular	Hexagonal	Square	Circular	Hexagonal	Square
1.55	0.3	1.347	1.329	1.36	1.362	1.349	1.374
	0.35	1.339	1.321	1.352	1.355	1.341	1.367
	0.4	1.329	1.312	1.344	1.346	1.333	1.359
	0.45	1.319	1.302	1.335	1.337	1.324	1.351
	0.5	1.308	1.291	1.325	1.327	1.314	1.342
	0.55	1.296	1.279	1.314	1.315	1.303	1.332
	0.6	1.283	1.266	1.302	1.303	1.291	1.322
	0.65	1.268	1.251	1.289	1.29	1.278	1.31
	0.7	1.253	1.236	1.275	1.275	1.264	1.298
	0.75	1.236	1.219	1.26	1.26	1.249	1.285
	0.8	1.218	1.2	1.244	1.242	1.232	1.27
λ(µm)	d_1/Λ	Λ = 1.0 (µm)			Λ = 1.5 (µm)		
		Circular	Hexagonal	Square	Circular	Hexagonal	Square
1.55	0.3	1.384	1.375	1.392	1.41	1.406	1.415
	0.35	1.377	1.369	1.386	1.406	1.403	1.412
	0.4	1.37	1.362	1.38	1.402	1.399	1.408
	0.45	1.362	1.355	1.374	1.397	1.395	1.405
	0.5	1.354	1.347	1.367	1.393	1.391	1.401
	0.55	1.345	1.339	1.359	1.388	1.387	1.397
	0.6	1.335	1.33	1.351	1.383	1.382	1.393
	0.65	1.325	1.319	1.342	1.377	1.376	1.388
	0.7	1.313	1.309	1.333	1.371	1.37	1.383
	0.75	1.3	1.296	1.323	1.364	1.364	1.378
	0.8	1.287	1.283	1.312	1.357	1.357	1.372

3.2. Confinement loss

The next step of this study is the analysis of confinement loss of three fibers with different lattice constants and the linear filling factor of the first ring indicated in Fig. 6 to 9. As observed, although decreasing significantly in the 0.5 ÷ 0.8 µm wavelength, the low confinement loss slightly goes up in the remaining wavelength range. Furthermore, the confinement loss curves have almost the same shape, especially the longer wavelength is, the more separated the curves are. At Λ = 1.5 µm, the curves almost coincide.

Table 2 illustrates the value of confinement loss for the above-proposed design at 1.55µm wavelength. The L_c value declines in the case of increasing Λ due to a large difference in the refractive index of core and cladding regions and dependence on the imaginary part of the effective refractive index according to formula (2). In general, the largest and lowest confinement loss for hexagonal and circular PCFs is 249.132 dB/m and 176.042 dB/m at Λ = 1.5 µm, d_1/Λ = 0.3 và Λ = 0.7 µm, d_1/Λ = 0.8, correspondingly. The minimal confinement loss is one of the important contributors to supercontinuum generation.

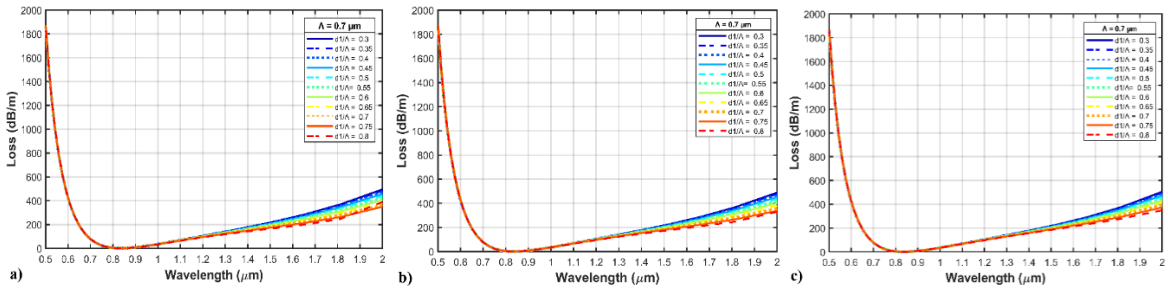

Fig. 6. *The confinement loss characteristics of three solid-core PCFs with Λ = 0.7 μm, d_1/Λ = 0.3 ÷ 0.8 for lattices: a) circular, b) hexagonal, and c) square lattices.*

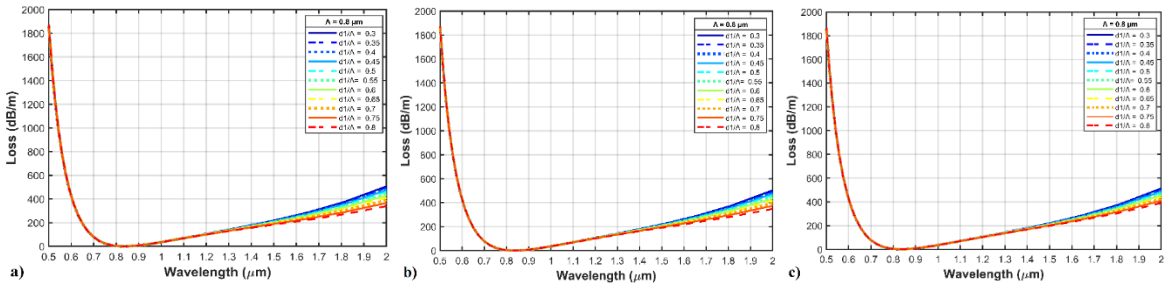

Fig. 7. *The confinement loss characteristics of three solid-core PCFs with Λ = 0.8 μm, d_1/Λ = 0.3 ÷ 0.8 for lattices: a) circular, b) hexagonal, and c) square lattices.*

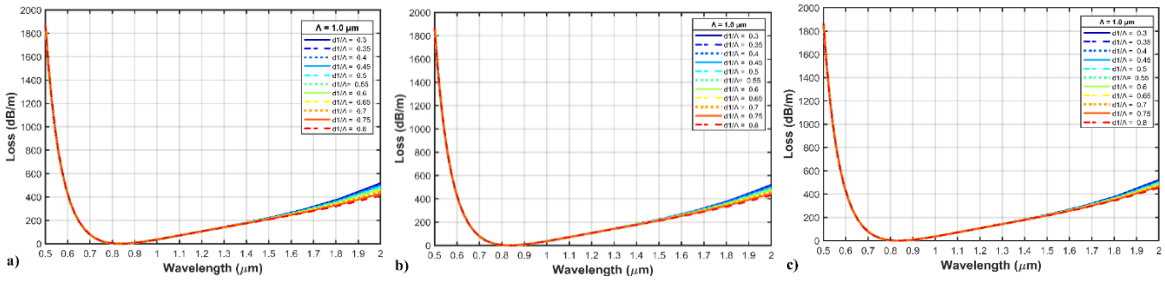

Fig. 8. *The confinement loss characteristics of three solid-core PCFs with Λ = 1.0 μm, d_1/Λ = 0.3 ÷ 0.8 for lattices: a) circular, b) hexagonal, and c) square lattices.*

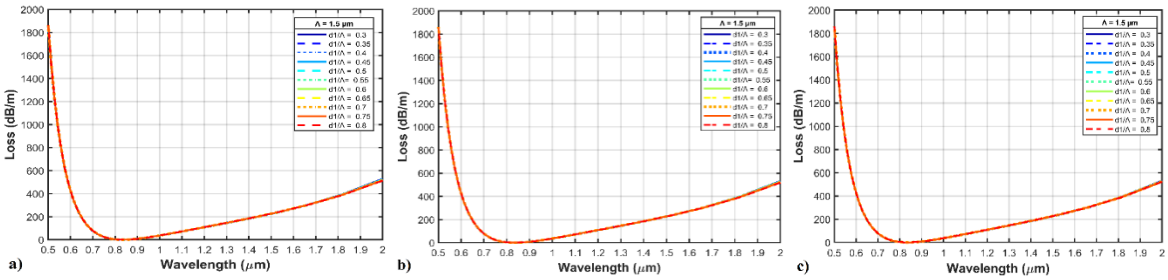

Fig. 9. *The confinement loss characteristics of three solid-core PCFs with Λ = 1.5 μm, d_1/Λ = 0.3 ÷ 0.8 for lattices: a) circular, b) hexagonal, and c) square lattices.*

Table 2. *The value of the confinement loss of the fibers at 1.55 μm with various lattice constant and the linear filling factor of the first ring.*

λ(μm)	d_1/Λ	L_c (dB/m)					
		Λ = 0.7 (μm)			Λ = 0.8 (μm)		
		Circular	Hexagonal	Square	Circular	Hexagonal	Square
	0.3	238.338	238.257	240.631	240.861	241.616	242.554
	0.35	234.63	234.843	237.67	237.895	239.043	240.293

 ISBN:

1.55	0.4	230.392	231.302	234.362	234.656	236.45	237.831
	0.45	226.018	227.381	230.956	231.381	233.734	235.42
	0.5	221.012	223.165	227.407	227.683	230.824	233.005
	0.55	215.716	218.544	223.501	223.869	227.72	230.395
	0.6	209.689	213.393	219.579	219.664	224.331	227.873
	0.65	202.867	207.497	214.96	214.914	220.45	224.918
	0.7	195.379	200.778	210.187	209.721	216.021	222.022
	0.75	186.253	193.162	204.74	203.505	210.998	218.712
	0.8	176.042	183.879	198.502	196.251	204.819	214.799
λ(µm)	**d_1/Λ**	**Λ = 1.0 (µm)**			**Λ = 1.5 (µm)**		
		Circular	Hexagonal	Square	Circular	Hexagonal	Square
1.55	0.3	243.894	245.3387	245.041	247.873	249.132	248.374
	0.35	242.177	244.0048	243.854	247.757	249.11	248.426
	0.4	240.426	242.7907	242.658	247.744	249.176	248.492
	0.45	238.906	241.6499	241.651	247.877	249.245	248.665
	0.5	237.184	240.4654	240.739	247.97	249.329	248.824
	0.55	235.624	239.259	239.791	248.164	249.35	248.945
	0.6	233.969	237.9882	239.018	248.302	249.407	249.118
	0.65	232.115	236.4647	238.007	248.396	249.317	249.106
	0.7	230.305	234.7865	237.084	248.517	249.273	249.15
	0.75	228.041	232.7668	235.931	248.46	249.139	249.024
	0.8	225.492	230.2676	234.426	248.425	248.871	248.828

IV. CONCLUSION

The effective refractive index and confinement loss characteristics of solid-core photonic crystal fibers with different types of photonic lattice in the cladding have been numerically investigated considering the influence of new design parameters, the linear filling factor and lattice constant. Obviously, modification of the air-holes diameter in the first ring to be different from the others has remarkably affected the characteristic properties of PCF. Compared with the fibers with hexagonal and circular lattices, the effective refractive index of square PCF is the highest, its value is 1.415 at 1.55 µm. Simultaneously, the minimum confinement loss value is found for circular lattice (equal to 176,042 dB/m) at the same survey wavelength. Our results are promising and open up many possibilities for applications in the field of optical communication.

ACKNOWLEDGMENTS. This research is funded by Vietnam National Foundation for Science and Technology Development (NAFOSTED) under grant number 103.03-2020.03 and Vietnam's Ministry of Education and Training (B2021-DHH-08).

REFERENCES

[1] J. C. Knight, T. A. Birks, P. St. J. Russell, D. M. Atkin, All-silica single-mode optical fiber with photonic crystal cladding, *Optics Letters*, 1996, **21**, 1547.

[2] J. C. Knight, J. Broeng, T. A. Birks, P. St. J. Russell, Photonic band gap guidance in optical fibers, *Science*, 1998, **282**, 1476-1478.

[3] P. St. J. Russell, Photonic crystal fibers, *Science*, 2003, **299**, 358 362.

[4] C. V. Lanh, H. V. Thuy, Cao L. Van, K. Borzycki, D. X. Khoa, T. Q. Vu, M. Trippenbach, R. Buczyński and J. Pniewski, Supercontinuum generation in photonic crystal fibers infiltrated with nitrobenzene, *Laser Phys.*, 2020, **30,** 035105.

[5] C. V. Lanh, H. V. Thuy, V. C. Long, K. Borzycki, D. X. Khoa, T. Q. Vu, M. Trippenbach, R. Buczyński and J. Pniewski, Optimization of optical properties of photonic crystal fibers infiltrated with chloroform for supercontinuum generation, *Laser Phys.*, 2019, **29**(7), 075107.

[6] D. X. Khoa, C. V. Lanh, H. D. Quang, L. V. Xuan, M. Trippenbach, R. Buczynski, Dispersion characteristics of a suspended-core optical fiber infiltrated with water, *Applied Optics*, 2017, **56**(4), 1012-1019.

[7] D. X. Khoa, C. V. Lanh, C. L. Van, Quang Ho Dinh, Luu Van Mai, Marek Trippenbach, Ryszard Buczyński, Influence of temperature on dispersion properties of photonic crystal fibers infiltrated with water, *Optical and Quantum Electronics*, 2017, **49**(2), 87.

[8] H. Q. Quy, C. V. Lanh, Spectrum broadening of supercontinuum generation by fill styrene in core of photonic crystal fibers, *Indian Journal of Pure & Applied Physics*, 2021, **59**, 522-527.

[9] S. Sen, Md. A. Al-Shafi, M. A. Kabir, Hexagonal photonic crystal Fiber (H-PCF) based optical sensor with high relative sensitivity and low confinement loss for terahertz (THz) regime, *Sensing and Bio-Sensing Research*, 2020, **30**, 100377.

[10] S. K. Pandey, Y. K. Prajapati, J. B. Maur, Design of simple circular photonic crystal fiber having high negative dispersion and ultra-low confinement loss, *Results in Optics*, 2020, **1**, 100024.

[11] A. Medjouri, L. M. Simohamed, O. Ziane, A. Boudrioua, Analysis of a new circular photonic crystal fiber with large mode area, *Optik*, 2015, **126(**24), 5718-5724.

[12] Md. Faizul Huq Arif, and Md. Jaminul Haque Biddut, Photonic crystal fiber based sensor for detecting binary liquid mixture, *Sens. Bio-Sens. Res.*, 2017, **12**, 8.

[13] L. T. B. Tran, N. T. Thuy, V. T. M. Ngoc, L. C. Trung, L. V. Minh, C. L. Van, D. X. Khoa, C. V. Lanh, Analysis of dispersion characteristics of solid-core PCFs with different types of lattice in the claddings, infiltrated with ethanol, *Photonics Letters of Poland*, 2020, **12**(4), 106-108.

[14] K. Saitoh, M. Koshiba, T. Hasegawa, and E. Sasaoka, Chromatic dispersion control in photonic crystal fibers: application to ultra-flattened dispersion, *Opt. Express*, 2003, **11**, 843.

[15] Lumerical Solutions, *http://www.lumerical.com/tcad-products/mode/*

[16] G. Stepniewski, R. Kasztelanic, D. Pysz, R. Stepien, M. Klimczak, R. Buczynski, Temperature sensitivity of chromatic dispersion in nonlinear silica and heavy metal oxide glass photonic crystal fibers, *Optical Materials Express*, 2016, **6**(8), 2689-2703.

[17] T. P. White, R. C. McPhedran, C. M. de Sterke, L. C. Botten, and M. J. Steel, Confinement losses in microstructured optical fibers, *Opt. Lett.*, 2001, **26**, 1660.

[18] Monfared, Yashar E, Maleki Javan, A. R, Monajati Kashani, A. R, Confinement loss in hexagonal lattice photonic crystal fibers, *Optik - International Journal for Light and Electron Optics*, 2013, **124**(24), 7049-7052.

[19] V. Finazzi, T. M. Monro, and D. J. Richardson, The role of confinement loss in highly nonlinear silica holey fibers, *Photonics Technology Letters*, IEEE, 2003, **15**, 1246-1248.

[20] J. Vijay and M. Sabir, Low-flattened dispersion hexagonal photonic crystal fiber with low confinement loss, *International Journal of Emerging Technology and Advanced Engineering*, 2013, **3**, 153-158.

[21] S. Fatema, R. Absar, M. Istiaque Reja, and J. Akhtar, Detection of harmful food additives using highly sensitive photonic crystal fiber, *J. Opt. Commun.*, 2018, **410**, 396.

[22] Papiya Dhara, Vinod Kumar Singh, Investigation of rectangular solid-core photonic crystal fiber as temperature sensor, *Microsystem Technologies*, 2021, **27**, 127-132.

 ISBN:

CHARACTERISTIC ANALYSIS OF HEXAGONAL SILICA-BASED PHOTONIC CRYSTAL FIBERS WITH DIFFERENT RINGS STRUCTURES

Thuy Nguyen Thi[1], Duc Hoang Trong[1], Trong Dang Van[2], Bao Tran Le Tran[2], Hung Dao Van[3], Lanh Chu Van[2*]

[1]*University of Education, Hue University, 34 Le Loi Street, Hue City, Viet Nam*

[2]*Department of Physics, Vinh University, 182 Le Duan, Vinh City, Viet Nam*

[3]*Naval Academy, 30 Tran Phu Street, Nha Trang City, Viet Nam*

*****E-mail: *chuvanlanh@vinhuni.edu.vn*

Abstract. In this paper, we present a new design of silica-based solid-core photonic crystal fibers (PCFs) with a hexagonal structure. The variation of air-hole diameter in the first ring near the core and its fixation for the second and other rings in numerical simulations has significantly improved the nonlinear properties of the fibers. The dependence of effective refractive index, dispersion characteristic, nonlinear coefficient, and attenuation on lattice parameters such as the filling factor (d_1/Λ) and lattice constant (Λ) is investigated. The flat all-normal dispersion, high nonlinearity, and low attenuation are the outstanding advantages of these PCFs. From there, three optimal structures with Λ = 0.7 µm, d_1/Λ = 0.4, 0.45 and Λ = 1.0 µm, d_1/Λ = 0.4 are selected and analyzed in detail for guiding the application in supercontinuum generation.

Keywords: *Photonic crystal fibers (PCFs), All-normal dispersion, Nonlinear coefficient, Attenuation*.

I. INTRODUCTION

In recent years photonic crystal fibers (PCFs) have been studied extensively in all theories, simulattions, and experiments because their optical properties can be flexibly controlled through the selection of structural parameters. The change of the cross-section [1,2], fiber core diameter, air-hole diameter, lattice constant [3,4], substrate material in the whole fiber, material used to filled air-holes or hollow cores [5-7],… causes the optical characteristics of PCFs to change drastically, which also makes the application of PCFs more and more abundant. In optical communication and sensing, PCFs present many advantages over conventional optical fibers [8-11]. Particularly, PCFs with high nonlinearity and flat dispersion are good platforms for supercontinuum (SC) generation [4-7,12,13].

The improvement of PCF characteristics such as effective refractive index, dispersion, effective mode area, nonlinear coefficient, and attenuation to make it more and more useful in supercontinuum generation is always a hot topic that attracts many researchers. Among them, dispersion is a significant factor in the design of PCF, because it is responsible for SC efficiency. PCFs with flat dispersion [14], multiple zero dispersion wavelengths (ZDWs) [15,16], high negative dispersion [17],... dominates the nonlinear effects in SC generation such as four-wave mixing effect, self-phase modulation, Raman

scattering, soliton,... In addition, PCF with all-normal dispersion and low attenuation is used to generate a broader coherent SC spectrum [18,19].

In this paper, we present a hexagonal PCF in which the difference in air-hole diameters of the first ring near the core and the other rings of the cladding are designed to improve the optical features of PCF. The filling factor ($d1/\Lambda$) for the first ring is made variable while it is kept constant for the others. This difference together with the change of the lattice constant has a strong influence on the characteristics of PCF such as effective refractive index, dispersion characteristic, nonlinear coefficient, and attenuation. Three optimal structures (Λ = 0.7 µm, d_1/Λ = 0.4, 0.45 and Λ = 1.0 µm, d_1/Λ = 0.4) with all-normal and anomalous dispersion are suggested to analyze the effective mode area, nonlinearity properties, and attenuation which makes a lot of sense for using these PCFs for SC generation.

II. NUMERICAL MODELLING OF PCFs

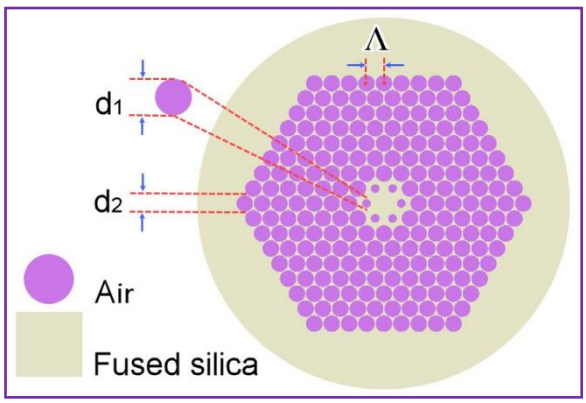

Fig. 1. *The cross-section of the hexagonal PCF.*

The cross-section view of the hexagonal PCF, designed in our study, has been displayed in Fig. 1. The PCF consists of eight rings of air holes, arranged in an orderly arrangement in the cladding region, the air holes in the first ring near the core are of different sizes from the other air holes. The diameter of these holes is d_1 while the other holes have a diameter of d_2, and Λ is the hole-to-hole spacing. In work [20], dispersion properties and the shift of ZDW are dominated mainly by the size of the first ring, while the other rings are responsible for the mode attenuation. Thus, we pay attention to the variation of the filling factor (d_1/Λ) of the first ring, d_1/Λ changes from 0.3 to 0.8 respectively with a step of 0.05, and d_2/Λ is kept constant of 0.95 for the next rings. The values of Λ are 0.7 µm, 0.8 µm, 1.0 µm, and 1.5 µm. The small core of PCFs helps the electromagnetic modes propagate over a wide range of wavelengths, its diameter is defined by the formula $D_{core} = 2\Lambda - d_1$.

In this paper, we used the commercial software Lumerical Model Solution multiphysics [21] with finite difference eigenmode method to calculate the PCF nonlinear optical parameters including effective index, chromatic dispersion, effective mode area, and confinement loss of the fundamental mode with different values of Λ and the d_1/Λ in the 0.5-2 µm wavelength region.

 ISBN:

III. SIMULATION RESULTS AND ANALYSIS

The effective refractive index can be calculated via the Sellmeier equation [22] about wavelength (λ) with coefficients: B_0 = 1; B_1 = 0.6694226, B_2 = 0.4345839, B_3 = 0.8716947, C_1 = 4.4801×10^{-3}µm^2, C_2 = 1.3285×10^{-2} µm^2, C_3 = 95.341482 µm^2. The real part of the effective refractive indices corresponding to the fundamental mode over the wavelength range from 0.5 µm to 2.0 µm have been found out and shown in Fig. 2.

$$n^2_{\text{Fused silica}}(\lambda) = B_0 + \frac{B_1\lambda^2}{\lambda^2 - C_1} + \frac{B_2\lambda^2}{\lambda^2 - C_2} + \frac{B_3\lambda^2}{\lambda^2 - C_3} \quad (1)$$

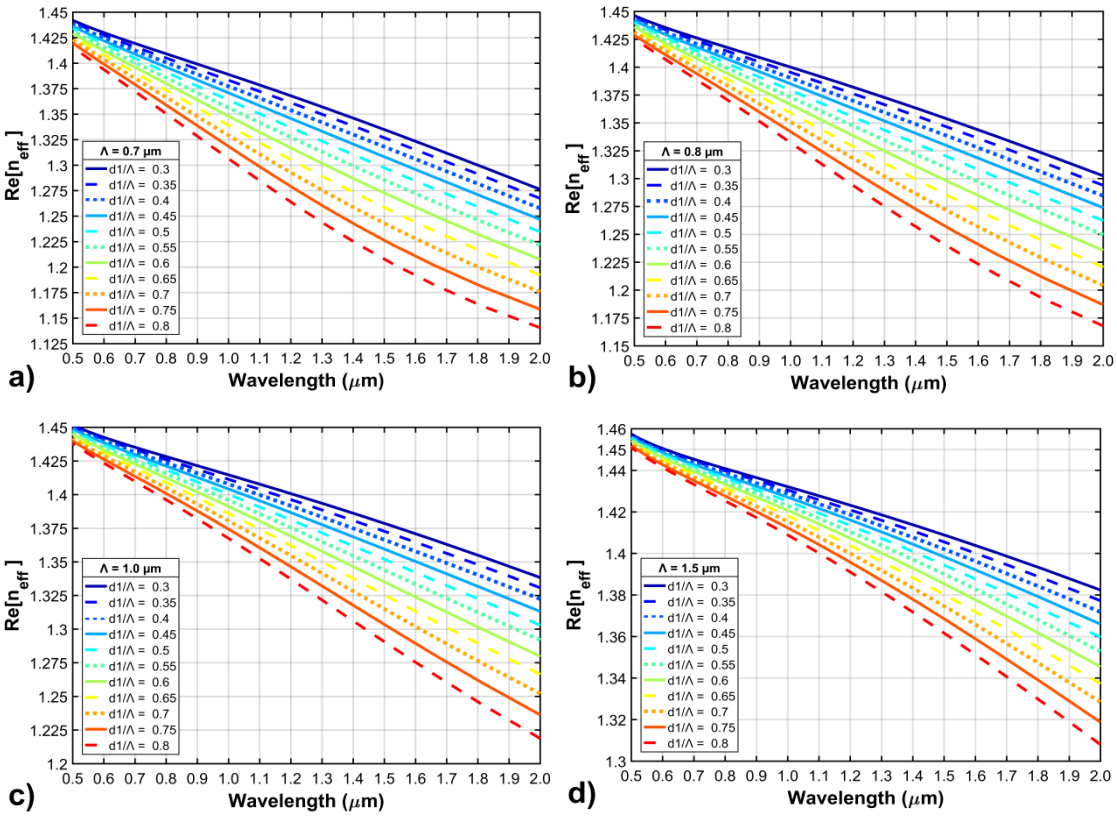

Fig. 2. *The real part of effective refractive index as a function of wavelength of PCFs with various d_1/Λ for (a) Λ =0.7 µm, (b) Λ = 0.8 µm (c) Λ =1.0 µm, (d) Λ = 1.5 µm.*

For all cases, the effective refractive index decreases monotonically with the increase of wavelength due to the stronger penetration of long wavelengths into the cladding region of PCF. The variation of lattice constant Λ and filling factor d_1/Λ also significantly changes the value of the effective refraction index. An increase of d_1/Λ at a particular wavelength for PCFs reduces this value, but an increase of Λ causes the effective index to increase. As can be seen, the change of effective refractive index is mainly influenced by two lattice structure parameters d_1/Λ and Λ.

The dispersion parameters of the fundamental mode are one of the important factors in generating SC, because they are mainly concerned with waveguide propagation of different wavelength components, traveling at different speeds in the medium. The fiber materials and structures often govern the value, the number of ZDWs, the flatness of dispersion. Total dispersion coefficient $D(\lambda)$ is calculated as the combined effect of

waveguide dispersion (D_w) and material dispersion (D_m) which is given as $D = -\frac{\lambda}{c}\frac{d^2(\mathrm{Re}[n_{\mathrm{eff}}])}{d\lambda^2}$, where Re[$n_{\mathrm{eff}}$] is the real part of the mode index [23].

Fig. 3 shows the dependence of dispersion with wavelength and the variation of d_1/Λ and Λ of PCFs. These figures show that the dispersion characteristics significantly depend upon the diameter of the air holes the lattice constant. PCFs with small core diameters (Λ = 0.7), dispersion properties are quite diverse with all-normal, anomalous dispersion with one ZDW, and two ZDWs (Fig. 3a). This is because with a smaller core, the waveguide dispersion is more pronounced, and thus the total dispersion curve varies more drastically [24]. With d_1/Λ is less than 0.45, the dispersion curves intersect the zero-dispersion line at a point i.e. the anomalous dispersions with one ZDW are achieved in the investigated wavelength region, the all-normal-dispersions are found when d_1/Λ = 0.45-0.55, while the remaining PCFs exhibit anomalous dispersion with two ZDWs. In particular, we observe that the dispersion is flat in the case of d_1/Λ = 0.45, this curve is closest to the horizontal axis in the wavelength range of 0.9-1.3 µm, the flat and all-normal dispersion is very beneficial for the efficiency of SC generation in extending the output pulses.

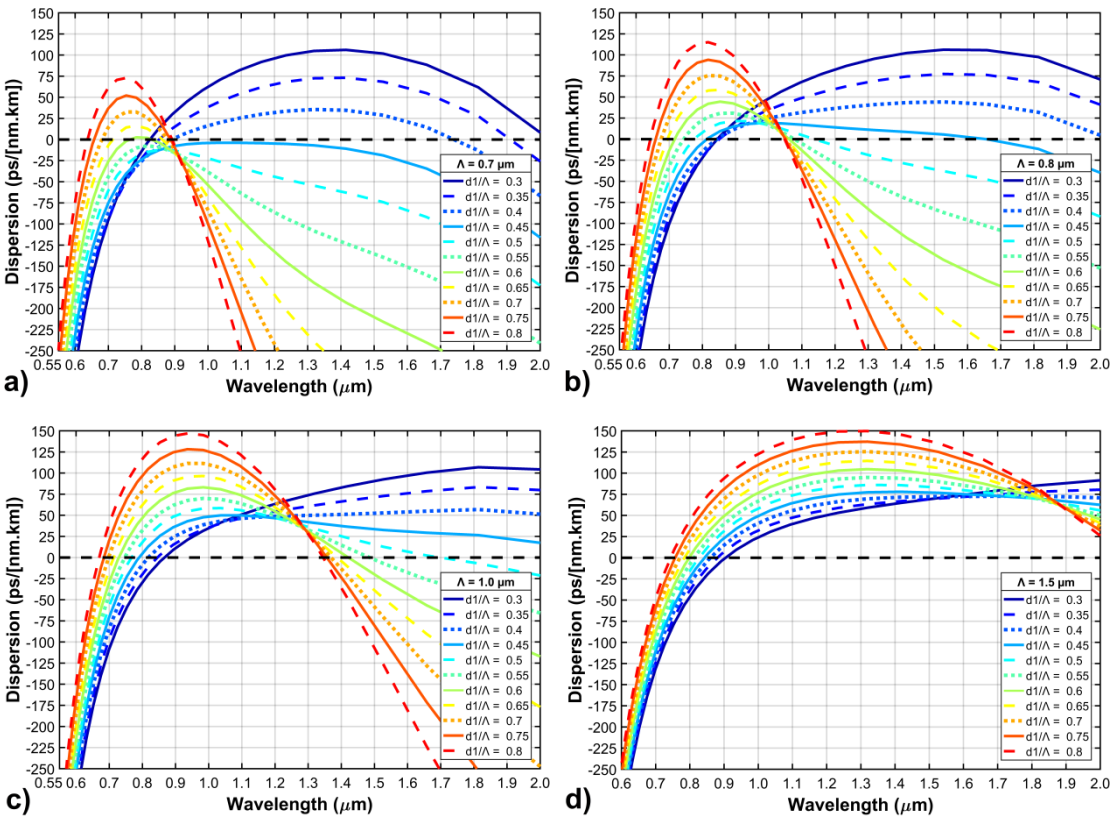

Fig. 3. *The dispersion as a function of wavelength of PCFs with various d_1/Λ and Λ.*

The characteristic properties of the dispersion, including the shift of ZDW, are not only strongly influenced by the filling factor, but also by the value of the lattice constant. Specifically, when increasing the lattice constant (Λ = 0.8, 1.0), the all-normal dispersion properties disappear in the investigated wavelength region, leaving only anomalous dispersions with one or two ZDWs. Especially, fibers with d_1/Λ = 0.4 have a very flat

 ISBN:

dispersion over a wide wavelength range from 1.1 µm to 1.9 µm (Fig. 3b and c). With the larger core fiber (Λ = 1.5), there are only the anomalous dispersion curves with one ZDW over the entire wavelength range, the anomalous dispersion curves tend to be flat due to the combined effect of material dispersion and waveguide dispersion [24]. Although the dispersion curve (d_1/Λ = 0.45) has a transition from all-normal to anomalous dispersion, the flatness is still maintained in the range of 1.2-1.6 µm of the wavelength (Fig. 3d).

The difference between the size of the air-holes in the rings of the cladding as our design makes the ability to confine light in the core stronger i.e. the structural parameters play a major role in tuning the dispersion parameter. From the above results, we propose three structures with possible optimal dispersion with Λ = 1.0, d_1/Λ = 0.4; Λ = 0.7, d_1/Λ = 0.4; and Λ = 0.7, d_1/Λ = 0.45 which called #F_1, #F_2 and #F_3, respectively. Their structural parameters are exposed in Table 1.

Tab. 1. *The structure parameters of proposed PCFs.*

#	Λ (µm)	d_1/Λ	D_{core} (µm)
#F_1	1.0	0.4	1.560
#F_2	0.7	0.4	1.092
#F_3	0.7	0.45	1.054

Fig. 4 displays the dispersion characteristics of the proposed PCFs. #F_1 fiber possesses a flat anomalous dispersion curve, the value of ZDW is 0.818 µm, while fiber #F_2 has an anomalous dispersion curve with two ZDWs at 0.891 µm and 1,741 µm, the flat normal dispersion is required to generate to a broad SC spectrum is observed in #F_3 fiber. The selected PCFs with diversity in the dispersion can be suitable for SC generation with the desire to observe more nonlinear effects such as four-wave mixing, phase self-modulation, and soliton,… with the appropriate input pulse. The center wavelength of the input pulse (the pump wavelength) are chosen for #F_2, and #F_3 fibers are 1.03 µm, respectively, with #F_1 fiber it is 0.85 µm.

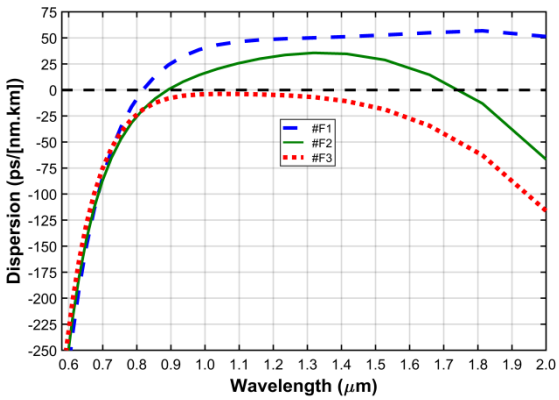

Fig. 4. *The dispersion properties of proposed PCFs.*

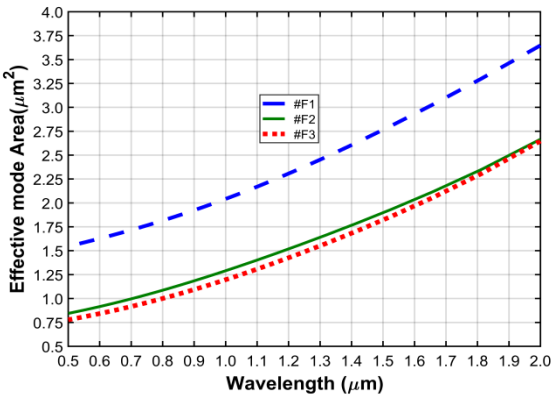

Fig. 5. *The effective mode area properties of proposed PCFs.*

The effects of variation in wavelength, d_1/Λ, and Λ on the effective mode area (A_{eff}) of proposed PCFs are evinced in Fig. 5. The increase in wavelength causes the value of the effective mode area to increase quite linearly. Fibers #F_2 and #F_3 have this value quite

close to each other, in which the effective mode area of the #F_2 fiber is slightly higher than that of the #F_3 fiber. The highest value of the effective mode area in the studied wavelength belongs to the #F_1 fiber, that is, the nonlinear coefficient (γ) of this fiber is the lowest in comparison with other fibers because the nonlinear coefficient is inversely proportional to the effective mode area (Fig. 6) while fiber #F_3 owns the highest value of the nonlinear coefficient. High nonlinear PCFs are the most desirable for SC generation with input energies as low as picojoules. The attenuation (L_k) characteristics of the fundamental mode for #F_1, #F_2, and #F_3 fiber are specified in Fig. 7. In the 0.5 µm to 1.7 µm of wavelength region, there is not much difference in this value of all three fibers. The attenuation of the #F_3 fiber increases dramatically when the wavelength is greater than 1.7 µm, while the #F_2 fiber has a lower attenuation value. Especially, the attenuation value of #F_1 fiber is the lowest, this curve is almost coincident with the horizontal axis.

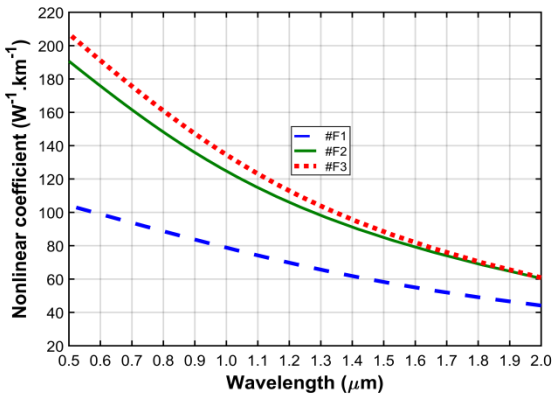

Fig. 6. *The nonlinear coefficients of proposed PCFs.*

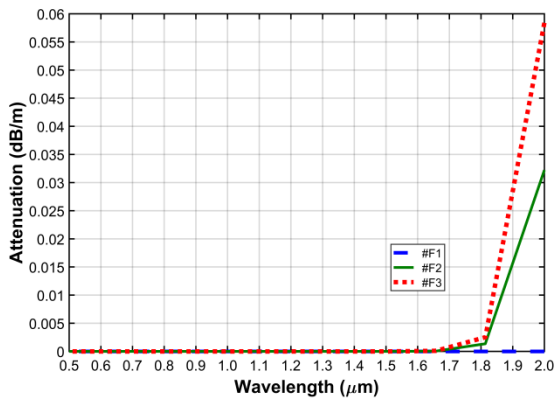

Fig. 7. *The attenuation properties of proposed PCFs.*

Table 2. *The value of quantities characterizing calculated at the pump wavelength of the proposed PCFs.*

#	*The pump wavelength* (µm)	*D* (ps.[nm.km]$^{-1}$)	A_{eff} (µm^2)	γ (W^{-1}.km^{-1})	L_k (dB/m)
#F_1	0.85	11.998	1.869	86.231	-1.299E-19
#F_2	1.03	19.566	1.324	121.738	2.517E-14
#F_3	1.03	-3.809	1.23	131.069	4.035E-14

The values of the quantities characterizing the nonlinearity of the proposed PCFs are calculated at the pump wavelength, quoted in Tab. 2. Among them, the dispersion value of #F_3 fiber is the smallest because of the closest to the zero-dispersion line, its value is -3.809 ps.nm^{-1}.km^{-1} at the pump wavelength of 1.03 µm. While the dispersion values at the pump wavelength of #F_1 and #F_2 fibers are 11.998 ps.nm^{-1}.km^{-1} and 19.566 ps.nm^{-1}.km^{-1}, respectively. The larger the core diameter designs, the larger the effective mode area is provided, so the nonlinear coefficient drops in the studied wavelength region. The maximum and minimum values of A_{eff} are 1.869 µm^2 and 1.23 µm^2 corresponding to the #F_1 and #F_3 fibers. Besides, the largest core fiber #F_1 has the smallest nonlinear coefficient of 86.231 W^{-1}.km^{-1}, and this value of the smaller core fiber #F_2 and #F_3 are 121.738 W^{-1}.km^{-1} and 121.738 W^{-1}.km^{-1}, respectively. A very small value of the attenuation is the

 ISBN:

advantage of these selected PCFs, the values of L_k are around 10^{-14} dB/m for #F_2, #F_3, and 10^{-19} dB/m for #F_1. Thus, with flat all-normal and anomalous dispersion properties, the characteristic quantity values such as dispersion, effective mode area, nonlinear coefficient, and attenuation are as acceptable as possible, this makes the selected PCFs suitable for SC generation.

IV. CONCLUSIONS

With a new design that emphasizes the difference in air hole diameters in the cladding, the characteristic properties of PCFs with hexagonal structures have been dynamically controlled. The flat all-normal and anomalous dispersion are achieved by varying the filling factor and lattice constant. Other characteristics of the proposed PCFs including effective mode area, nonlinear coefficient, attenuation are also analyzed in detail, the optimal dispersion, high nonlinearity, and low attenuation are the advantages of this work. The obtained values can be considered for SC generation.

ACKNOWLEDGEMENTS. This research is funded by Vietnam National Foundation for Science and Technology Development (NAFOSTED) under grant number 103.03-2020.03 and Vietnam's Ministry of Education and Training (B2021-DHH-08).

REFERENCES

[1] Z. Rahman, M. A. Rahman, M. A. Islam, and M. S. Alam, Design of an elliptical air-hole dual-core photonic crystal fiber for over two octaves spanning supercontinuum generation, *J. of Nanophotonics*, 2019, **13**, 046013.

[2] Bao Tran Le Tran, Thuy Nguyen Thi, Ngoc Vo Thi Minh, Trung Le Canh, Minh Le Van, Van Cao Long, Khoa Dinh Xuan, and Lanh Chu Van, Analysis of dispersion characteristics of solid-core PCFs with different types of lattice in the claddings, infiltrated with ethanol, *Photon. Lett. of Poland*, 2020, **12**, 106-108.

[3] R. Ahmad, M. Komanec, and S. Zvanovec, Circular lattice photonic crystal fiber for mid-IR supercontinuum generation, *IEEE Photon. Technol. Lett.*, 2016, **28**, 2736-2739.

[4] Ho Quang Quy, and Chu Van Lanh, Spectrum broadening of supercontinuum generation by fill styrene in core of photonic crystal fibers, *Indian J. of Pure & Appl. Phys.*, 2021, **59**, 522-527.

[5] Khoa Dinh Xuan, Lanh Chu Van, Van Cao Long, Quang Ho Dinh, Luu Van Mai, Marek Trippenbach, and Ryszard Buczyński, Influence of temperature on dispersion properties of photonic crystal fibers infiltrated with water, *Opt. and Quantum Electron.*, 2017, **49**, 87.

[6] Chu Van Lanh, Van Thuy Hoang, Van Cao Long, Krzysztof Borzycki, Khoa Dinh Xuan, Vu Tran Quoc, Marek Trippenbach, Ryszard Buczyński, and Jacek Pniewski, Optimization of optical properties of photonic crystal fibers infiltrated with chloroform for supercontinuum generation, *Laser Phys.*, 2019, **29**, 075107.

[7] Lanh Chu Van, Van Thuy Hoang, Van Cao Long, Krzysztof Borzycki, Khoa Dinh Xuan, Vu Tran Quoc, M. Trippenbach, R. Buczyński, and Jacek Pniewski, Supercontinuum generation in photonic crystal fibers infiltrated with nitrobenzene, *Laser Phys.*, 2020, **30**, 035105.

[8] F. Tani, J. C. Travers, and P. St. J. Russell, Multimode ultrafast nonlinear optics in optical waveguides: numerical modeling and experiments in kagomé photonic-crystal fiber, *J. Opt. Soc. Am. B*, 2014, **31**, 311-320.

[9] R. Otupiri, E. K. Akowuah, S. Haxha, H. Ademgil, F. AbdelMalek, and A. Aggoun, A novel birefrigent photonic crystal fiber surface plasmon resonance biosensor, *IEEE Photon. J.*, 2014, **6**, 1-11.

[10] H. Ademgil, and S. Haxha, Highly birefringent nonlinear PCF for optical sensing of analytes in aqueous solutions, *Optik - Int. J. Light Electron. Opt*., 2016, **127**, 6653-6660.

[11] X. Yang, A. S. P. Chang, B. Chen, C. Gu, and T. C. Bond, High sensitivity gas sensing by Raman spectroscopy in photonic crystal fiber, *Sens. Actuat. B: Chem*., 2013, **176**, 64-68.

[12] Khoa Dinh Xuan, Lanh Chu Van, Quang Ho Dinh, Luu Van Xuan, Marek Trippenbach, and Ryszard Buczynski, Dispersion characteristics of a suspended-core optical fiber infiltrated with water, *Appl. Opt.*, 2017, **56**, 1012-1019.

[13] J. Pniewski, T. Stefaniuk, Hieu Le Van, Van Cao Long, Lanh Chu Van, Rafał Kasztelanic, Grzegorz Stępniewski, Aleksandr Ramaniuk, Marek Trippenbach, and Ryszard Buczyński, Dispersion engineering in nonlinear soft glass photonic crystal fibers infiltrated with liquids, *Appl. Opt.*, 2016, **55**, 5033-5040.

[14] K. M. Gundu, M. Kolesik, J. V. Moloney, and K. S. Lee, Ultra-flattened-dispersion selectively liquid-filled photonic crystal fibers, *Opt. Express*, 2006, **14**, 6870-6878.

[15] K. M. Hilligsøe, T. V. Andersen, H. N. Paulsen, C. K. Nielsen, K. Mølmer, S. Keiding, et al., Supercontinuum generation in a photonic crystal fiber with two zero dispersion wavelengths, *Opt. Express*, 2004, **12**, 1045-1054.

[16] S. Zhao, H. Yang, N. Chen, X. Fu, and C. Zhao, Soliton trapping of dispersive waves in photonic crystal fiber with three zero-dispersive wavelengths, *IEEE Photon. J.*, 2013, **7**, 7102709.

[17] M. S. Habib, and E. Khandker, Highly birefringent photonic crystal fiber with ultra-flattened negative dispersion over S + C + L + U bands, *Appl. Opt.*, 2015, **54**, 2786-2789.

[18] M. R. Karim, H. Ahmad, and B. M. A. Rahman, All-normal dispersion chalcogenide PCF for ultraflat mid-infrared supercontinuum generation, *IEEE Photon. Technol. Lett.*, 2017, **29**, 1792-1795.

[19] K. Tarnowski, T. Martynkien, P. Mergo, K. Poturaj, G. Soboń, and W. Urbańczyk, Coherent supercontinuum generation up to 2.2 μm in an all-normal dispersion microstructured silica fiber, *Opt. Express*, 2016, **24**, 30523-30536.

[20] K. Saitoh, M. Koshiba, T. Hasegawa, and E. Sasaoka, Chromatic dispersion control in photonic crystal fibers: application to ultra-flattened dispersion, *Opt. Express*, 2003, **11**, 843-852.

[21] https://www.lumerical.com/products/mode.

[22] K. Moutzouris, M. Papamichael, S. C. Betsis, I. Stavrakas, G. Hloupis, and D. Triantis, Refractive, dispersive and thermo-optic properties of twelve organic solvents in the visible and near-infrared, *Appl. Phys. B.* 2014, **116**, 617-622.

[23] R. Buczyński, Photonic crystal fibers, *Acta. Phys. Pol. A*, 2004, **106**, 141-168.

[24] T. Huanga, P. Huanga, Z. Chenga, J. Liao, X. Wua, and J. Pan, Design and analysis of a hexagonal tellurite photonic crystal fiber with broadband ultra-flattened dispersion in mid-IR, *Optik*, 2018, **167**, 144-149.

 ISBN:

COMPARISON OF DISPERSION CHARACTERISTICS OF SILICA-BASED PHOTONIC CRYSTAL FIBERS WITH DIFFERENT LATTICES

Duc Hoang Trong[1], Trong Dang Van[2], Bao Tran Le Tran[2], Lanh Chu Van[2], Hung Dao Van[3], and Thuy Nguyen Thi[1*]

[1]*University of Education, Hue University, 34 Le Loi Street, Hue City, Viet Nam*

[2]*Department of Physics, Vinh University, 182 Le Duan, Vinh City, Viet Nam*

[3]*Naval Academy, 30 Tran Phu Street, Nha Trang City, Viet Nam*

*E-mail: *ntthuy@hueuni.edu.vn*

Abstract. We punctuate the ability to improve the dispersion characteristics of silica-based photonic crystal fibers (PCFs) with three types as circular, hexagonal, and square lattice with a new design in which the filling factor (d_1/Λ) of the first ring near the core is controlled differently from the others. When the lattice constant (Λ) varies from 0.7 to 1.5 µm, both all-normal and anomalous dispersion is achieved depending on d_1/Λ. The all-normal dispersions are found for PCFs with small lattice constants of 0.7 and 0.8 µm, the increase of Λ makes the anomalous dispersion more dominant in the investigated wavelength region. PCF with hexagonal structure owns all-normal dispersion which is flatter and closer to zero than others. Based on analysis of numerical simulation results, we have proposed structures with optimal dispersion characteristics and pump wavelength that is suitable for supercontinuum generation application.

Keywords: *Photonic crystal fibers (PCFs), All-normal dispersion, Anomalous dispersion, Optimal dispersion characteristics.*

I. INTRODUCTION

Photonic-crystal fiber (PCF) is a class of optical fiber-based on the properties of photonic crystals which has attracted the attention of many researchers over the past decades due to outstanding properties in light propagation compared to conventional optical fibers [1-4]. Its cladding consists of air holes as minuscule channels in a certain regular ordering that run through the whole length of the PCF. Propagation of light in PCF is governed by two principles namely total internal reflection in which refractive index (RI) of the core is higher as compared to RI of cladding while in photonic bandgap cladding RI is higher than that of core [5]. Numerous research and investigation of PCF suggest that the characteristics and guiding properties of the PCF can be flexibly adjusted by changing its geometrical configuration such as the shape and size of the core, cladding, air-holes, substrate material, or infiltration of liquid. Diversity in characteristics of PCFs makes it possible for people to find its application in wider domains like sensors fabrication, polarization sustaining devices, and biomedical fields of applications [6-9], supercontinuum generation [10-15]. Control of dispersion in PCFs has been an interesting challenge because it plays an important role in determining the spectral expansion efficiency of supercontinuum. To get desirable dispersion property, the dimension variables such as lattice constant (Λ) and diameter (d) of air-holes are tailored flexibly. In

this way, the dispersion properties like flatness, dispersion slopes, zero-dispersion wavelength (ZDW) can be easily controlled [16]. Recently, various unique geometries structures of the PCF have been introduced such as triangular, circular, rectangular, square, elliptical, and hexagonal lattice [10-12,14,17-20]. Through the adjustment of the lattice parameters Λ and d, the dispersion characteristics of these structures have significant improvements include the flat dispersion, flat and near-zero dispersion, all-normal or anomalous dispersion, the shift of ZDW towards the longer wavelength. However, determining which structure gives the most optimal dispersion has not been mentioned by the researchers. Furthermore, the difference in the air-holes diameter of the rings in the cladding also strongly governs the dispersion properties of PCF [21].

In this paper, we present a new structural design of PCFs in which the difference in air-holes diameters between the first ring and the other rings in the cladding is emphasized to improve dispersion characteristics, one of the important factors of PCFs for SC application. Additionally, a comparison of dispersion characteristics has been made among circular, square, and hexagonal-lattice PCFs to find the structure giving the most optimal dispersion. The obtained all-normal and anomalous dispersions strongly depend on the variation of the lattice constant Λ and the filling factor d_1/Λ and the all-normal dispersions are achieved for PCFs with small lattice constants of 0.7 and 0.8 µm.

II. NUMERICAL MODELLING OF PCFs

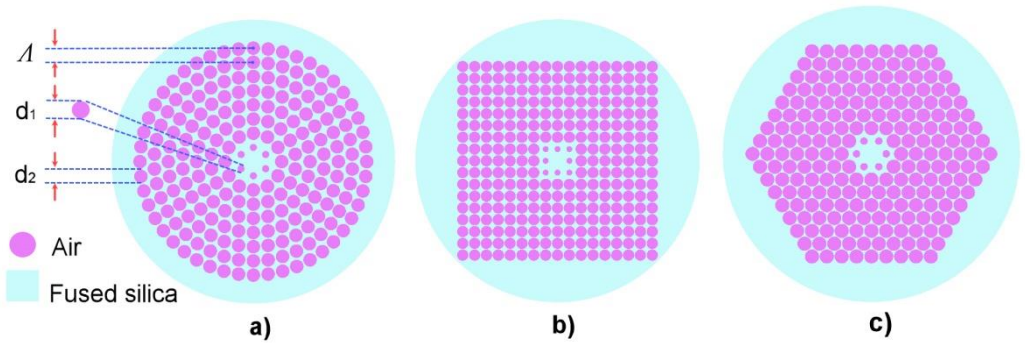

Fig. 1. *The cross-section of silica-based PCFs with different lattices a) CL, b) SL, and c) HL.*

The cross-sectional view of the designed silica-based PCFs has been presented in Fig. 1. The PCFs used in our study are circular (CL), square (SL), and hexagonal-lattice (HL) with eight rings of air-holes of a diameter d, the lattice constant Λ, and the linear filling factor d/Λ is in the photonic cladding. This way of designing creates a large difference in refractive index between the core and the cladding causes the light to be strongly confined in the core. We pay attention to the dissimilarity in the diameters of the air-holes in the first ring near the core and the other rings, as this has a strong effect on the characteristic quantities of the fibers. In which, the flatness, all-normal or anomalous properties of dispersions even the shift of ZDW are dominated mainly by the size of the first ring, while the other rings are responsible for the mode attenuation [21]. So we design the first ring with the d_1/Λ changing from 0.3 to 0.8 respectively with a step of 0.05, where

 ISBN:

d_1 is the diameter of the air holes of the first ring. The values of Λ are 0.7 µm, 0.8 µm, 1.0 µm, and 1.5 µm. The filling factor d_2/Λ = 0.95 of the second and subsequent rings is kept a constant.

In this paper, the finite difference eigenmode method is used to design and calculate the dispersion curve over a wavelength range of 0.5-2.0 µm. The total dispersion (D) is a function of wavelength which depends on the effective indices of propagating mode and can be computed as follows [22]:

$$D = -\frac{\lambda}{c}\frac{d^2\left(\mathrm{Re}\left[n_{\mathrm{eff}}\right]\right)}{d\lambda^2}$$

here Re[n_{eff}] stands for the real part of the effective indices obtained from simulations and c is the velocity of light in a vacuum.

III. SIMULATION RESULTS AND ANALYS

The dispersion properties of fiber demonstrate a dominant role in the propagation of short optical pulses that help expand the spectrum in SC generation. The dispersion curves corresponding to the effect of variation of Λ and d_1/Λ on fibers are exposed from Fig. 2 to Fig. 5. For the three structures, the shape of the dispersion curves is quite similar but the change of D with wavelength is diverse, the all-normal and anomalous dispersion with one or two ZDWs have been achieved in the studied wavelength region. Furthermore, the variation of the filling factor d_1/Λ and lattice constant Λ significantly dominates the dispersion characteristic of fibers and causes the ZDW to shift towards longer wavelengths. For small cores (Λ = 0.7 µm and 0.8 µm), the all-normal and anomalous dispersion with one or two ZDWs are found, and D tends to get smaller values as the filling factor rises, that means there are many parabolic dispersion curves in the narrow wavelength region. Fig. 2a (Λ = 0.7 µm) shows that, for the circular lattice structure, only fiber with d_1/Λ = 0.3 has the anomalous dispersion with one ZDW, when the filling factor increases the all-normal dispersion curves appears (d_1/Λ = 0.45-0.75), but PCFs with d_1/Λ is greater than 0.75 exhibits the anomalous dispersion with two ZDWs. While we get the all-normal dispersions in the range of 0.5-0.7 of d_1/Λ, and PCFs own the anomalous dispersion with one ZDW when $d_1/\Lambda \leq 0.4$ for the square lattice (Fig. 2b). The PCFs with hexagonal lattice structures operate in all-normal dispersion regions with the filling factor equals 0.45; 0.5; and 0.55; no anomalous dispersion with one ZDW is detected in this case. In particular, the fiber with d_1/Λ = 0.45, possesses very flatness dispersion and is close to the zero-dispersion curve (Fig.2c). When the lattice constant has a value of 0.8, the number of all-normal dispersions curves reduces for each lattice type. The circular lattice has four all-normal dispersion curves corresponding to 0.45-0.6 of the filling factor, while the square one shows only two structures with all-normal dispersions for d_1/Λ = 0.5 and 0.55. In contrast, no all-normal dispersion curves are received in the hexagonal lattice (Fig. 3). Therefore, we can conclude that dispersion features can be controlled more effectively in smaller core PCFs because of their strong light confinement ability.

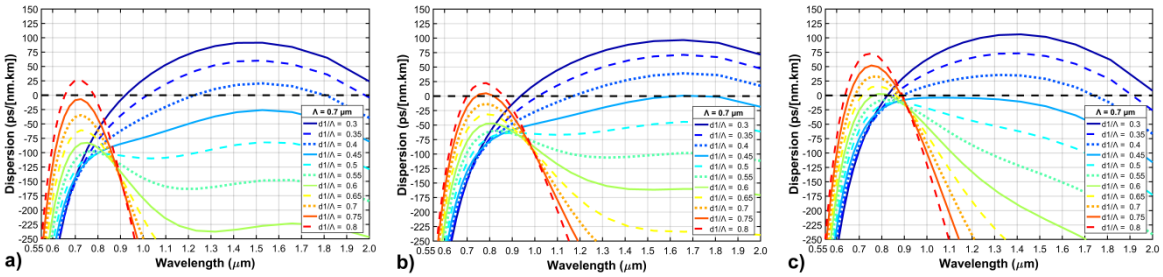

Fig. 2. *The dispersion properties of PCFs with various d_1/Λ and Λ = 0.7 μm for a) CL, b) SL, and c) HL.*

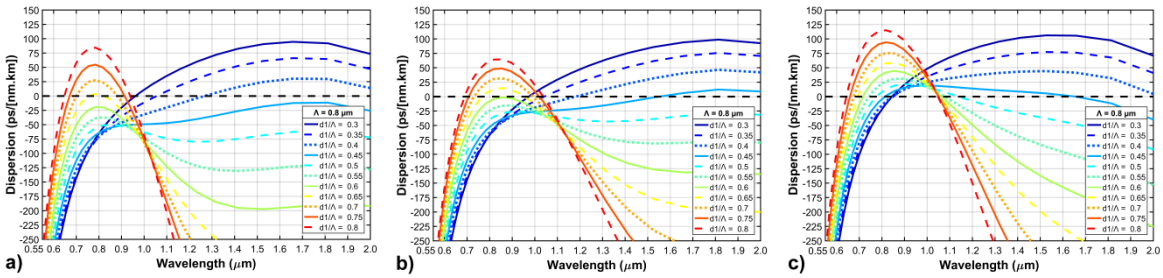

Fig. 3. *The dispersion properties of PCFs with various d_1/Λ and Λ = 0.8 μm for a) CL, b) SL, and c) HL.*

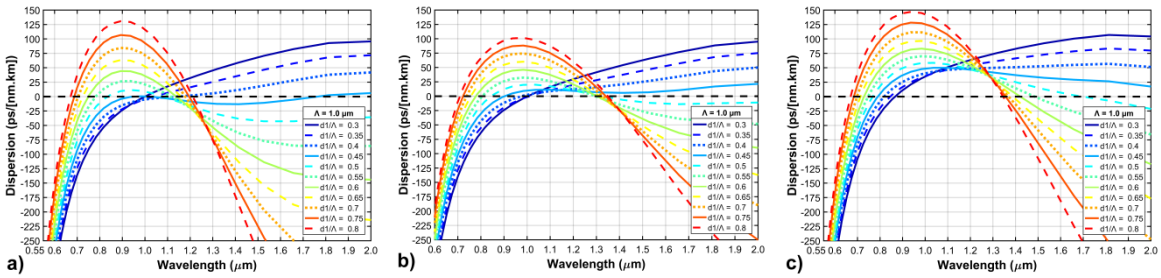

Fig. 4. *The dispersion properties of PCFs with various d_1/Λ and Λ = 1.0 μm for a) CL, b) SL, and c) HL.*

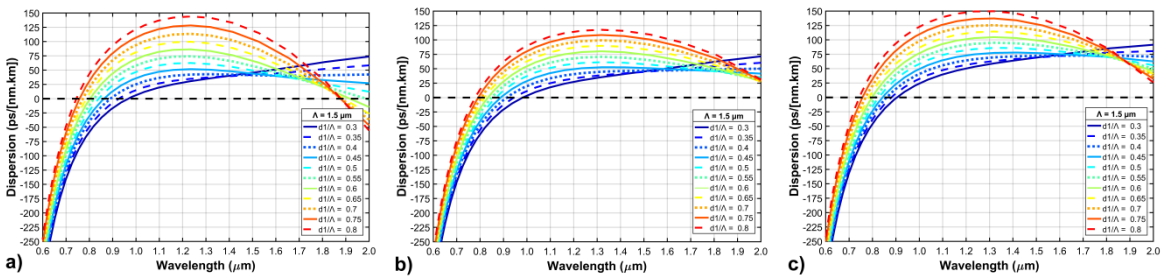

Fig. 5. *The dispersion properties of PCFs with various d_1/Λ and Λ = 1.5 μm for a) CL, b) SL, and c) HL.*

Obviously, the structure parameter Λ also strongly influences the properties of dispersion, a huge change in the nature of the dispersion profile has been observed with a larger lattice constant. As Λ is lifted, the all-normal dispersion does not appear anymore, the fibers exhibit anomalous dispersion with one and two ZDWs (Λ = 1.0 μm). When Λ = 1.5 μm, the anomalous dispersion with one ZDW completely dominates in the surveyed wavelength range for SL and HL structures (Fig. 4 and Fig. 5).

The difference between the size of the air-holes in the rings of the cladding, the

 ISBN:

geometrical structure, and the variation of the lattice structure parameters like our design are the important keys affecting the ability to confine light in the core, i.e. the value of effective indices that plays a major role in tuning the dispersion parameter. The flat, all-normal, and near-zero dispersion of fiber are the determining factors for the generation of an ultra-broadband SC. Because, the SC generation with all-normal dispersion PCF makes output pulses coherent, single, expansive, and flat when the fiber is pumped at the wavelength closest to that of the maximum dispersion or the flat dispersion point. Therefore, the three proposed structures satisfy the above features to analyze and compare their suitability in SC generation applications. Based on the numerical simulation results, we introduce three PCFs corresponding to CL, SL, and HL with Λ = 0.8 µm, d_1/Λ = 0.6 (CL), Λ = 0.8 µm, d_1/Λ = 0.55 (SL), and Λ = 0.7 µm, d_1/Λ = 0.45 (HL), they are named #F_1, #F_2 and #F_3, respectively. Their structural parameters are indicated in Table 1.

Table 1. *The structure parameters of proposed PCFs.*

#	Type	Λ (µm)	d_1/Λ	*Core diameter* (µm)
#F_1	CL	0.8	0.6	1.120
#F_2	SL	0.8	0.55	1.160
#F_3	HL	0.7	0.45	1.085

Fig. 6 evinces the all-normal dispersion characteristics of the proposed PCFs. Clearly, the dispersion curve (#F_3) of the hexagonal structure is flattest and closest to the horizontal axis, its flatness stretches from 0.9 to 1.3 µm, which is very valuable for SC. Fiber #F_2 has a lower dispersion curve and #F_1 shows an almost parabolic dispersion curve with maximum dispersion at 0.8 µm wavelength. The central wavelength of the laser pump source of these fibers is selected to be 0.8, 0.85, and 1.03 µm respectively.

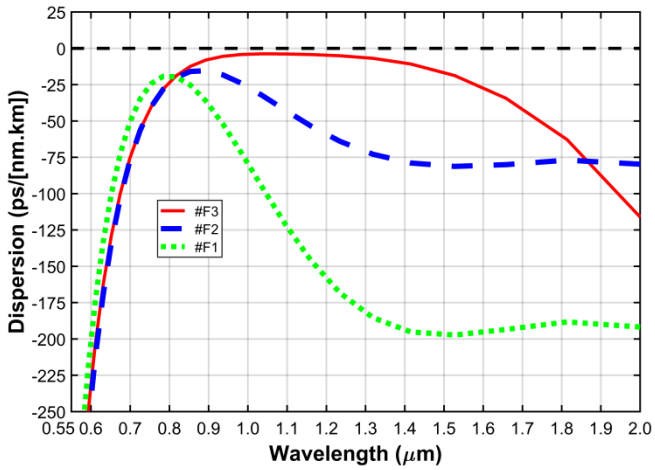

Fig. 6. *The dispersion properties of proposed PCFs.*

The value of dispersion calculated at the pump wavelength is quoted in Table 2. Among them, the dispersion value of #F_3 fiber with hexagonal lattice is the smallest because of the closest to the zero-dispersion line, its value is -3.809 ps.nm^{-1}.km^{-1} at the pump wavelength of 1.03 µm. While the dispersion values at the pump wavelength of #F_1 and #F_2 fibers are -19.407 ps.nm^{-1}.km^{-1} and -16.294 ps.nm^{-1}.km^{-1}, respectively.

Table 2. *The value of dispersion calculated at the pump wavelength of the proposed PCFs.*

#	Type	*The pump wavelength* (µm)	*D* (ps.(nm.km)$^{-1}$)
#F_1	CL	0.80	-19.407
#F_2	SL	0.85	-16.294
#F_3	HL	1.03	-3.809

IV. CONCLUSIONS

The dispersion characteristics of silica-based PCFs with three types such as circular, hexagonal, and square lattice with a new design have been evaluated and compared. The difference in the geometric structure of fibers makes the dispersion properties diverse, and the flexibility in controlling the dispersion parameters is fully achieved by the variation of the filling factor of the first ring near the core and the lattice constant. Although hexagonal lattice owns less all-normal dispersion curves than others they are very flat and near zero, which is very beneficial for SC generation. Among three fibers with optimal dispersion, the PCF with hexagonal structure gives the smallest value -3,809 ps.nm^{-1}.km^{-1} of dispersion at the pump wavelength of 1.03 µm in comparison with the other two structures. Our simulation results are valuable for fabricating optical fibers as an SC generation source with a wide, flat, and smooth spectrum.

ACKNOWLEDGEMENTS. This research is funded by Vietnam National Foundation for Science and Technology Development (NAFOSTED) under grant number 103.03-2020.03 and Vietnam's Ministry of Education and Training (B2021-DHH-08).

REFERENCES

[1] John M. Dudley, Goëry Genty, and Stéphane Coen, Supercontinuum generation in photonic crystal fiber, *Rev. Mod. Phys.*, 2006, **78**, 1135.

[2] Stuart D. Jackson, Towards high-power mid-infrared emission from a fibre laser, *Nat. Photo.*, 2012, **6**, 423-431.

[3] R. R. Alfano, The ultimate white light, *Sci. Am.*, 2006, **295**, 86-93.

[4] J. Broeng, D. Mogilevstev, S. E. Barkou, and A. Bjarklev, Photonic crystal fibers: A new class of optical waveguides, *Opt. Fiber Technol.*, 1999, **5**, 305-330.

[5] Anurag Upadhyay, Shivam Singh, Y. K.Prajapati, Rajeev Tripathi, Numerical analysis of large negative dispersion and highly birefringent photonic crystal fiber, *Optik*, 2020, **218**, 164997.

[6] J. Park, S. Lee, S. Kim, K. Oh, Enhancement of chemical sensing capability in a photonic crystal fiber with a hollow high index ring defect at the center, *Opt. Express*, 2011, **19**, 1921-1929.

[7] Ahmmed A. Rifat, Kawsar Ahmed, Sayed Asaduzzaman, Bikash Kumar Paul, and Rajib Ahmed, Development of Photonic Crystal Fiber Based Gas/Chemical Sensors, *Computational Photonic Sensors*, Springer International Publishing AG 2018,

[8] Abinash Panda, Pushpa Devi Pukhrambam, Photonic crystal biosensor for refractive index based cancerous cell detection, *Opt. Fiber Tech.*, 2020, **54**, 102123.

[9] Sumaiya Akhtar Mitu, Dipak Kumar Dey, Kawsar Ahmed, Bikash Kumar Paul, Yanhua Luo,

 ISBN:

R. Zakaria, and Vigneswaran Dhasarathan, Fe_3O_4 nanofluid injected photonic crystal fiber for magnetic field sensing applications, *J. of Mag. and Mag. Mater*., 2020, **494**, 165831.

[10] Lanh Chu Van, Van Thuy Hoang, Van Cao Long, Krzysztof Borzycki, Khoa Dinh Xuan, Vu Tran Quoc, Marek Trippenbach, Ryszard Buczyński, and Jacek Pniewski, Optimization of optical properties of photonic crystal fibers infiltrated with chloroform for supercontinuum generation, *Laser Phys*., 2019, **29**, 075107.

[11] Khoa Dinh Xuan, Lanh Chu Van, Van Cao Long, Quang Ho Dinh, Luu Van Xuan, Marek Trippenbach, and Ryszard Buczynski, Dispersion characteristics of a suspended-core optical fiber infiltrated with water, *Appl. Opt*., 2017, **56**, 1012-1019.

[12] Lanh Chu Van, Alicja Anuszkiewicz, Aliaksandr Ramaniuk, Rafal Kasztelanic, Khoa Dinh Xuan, Van Cao Long, Marek Trippenbach, and Ryszard Buczyński, Supercontinuum generation in photonic crystal fibres with core filled with toluene, *J. Opt*., 2017, **19**, 125604.

[13] Van Thuy Hoang, Rafal Kasztelanic, Alicja Anuszkiewicz, Grzegorz Stepniewski, Adam Filipkowski, Slawomir Ertman, Dariusz Pysz, Tomasz Wolinski, Khoa Dinh Xuan, Mariusz Klimczak, and Ryszard Buczynski, All-normal dispersion supercontinuum generation in photonic crystal fibers with large hollow cores infiltrated with toluene, *Opt. Mast. Express*, 2018, 8, 3568-3582.

[14] Lanh Chu Van, Van Thuy Hoang, Van Cao Long, Krzysztof Borzycki, Dinh Xuan Khoa, Vu Tran Quoc, Marek Trippenbach, Ryszard Buczynski, and Jacek Pniewski, Supercontinuum generation in photonic crystal fibers infiltrated with nitrobenzene, *Laser Phys*., 2020, **30**, 035105.

[15] Ho Quang Quy, and Chu Van Lanh, Spectrum broadening of supercontinuum generation by fill styrene in core of photonic crystal fibers, *Indian Journal of Pure & Applied Physics (IJPAP)*, 2021, **59**, 522-527.

[16] Pranaw Kumar, Vikash Kumar, and Jibendu Sekhar Roya, Design of quad core photonic crystal fibers with flattened zero dispersion, *AEU - International Journal of Electronics and Communications*, 2019, **98**, 265-272.

[17] P. Morin, B. Kibler, J. Fatome, C. Finot, and G. Millot, Group birefringence cancellation in highly birefringent photonic crystal fibre at telecommunication wavelengths, *Electron. Lett*., 2010, **46**, 525-526.

[18] D. Lu, X. Zhang, M. Chang, A. Kamagara, and S. Zhuang, Single-polarization single-mode photonic crystal fibers with rectangular-lattice and elliptical-hole arranged perpendicular to each other, *Optik*, 2003, **124**, 3026-3028.

[19] P. R. Chaudhuri, V. Paulose, C. Zhao, and C. Lu, Near-elliptic core polarization-maintaining photonic crystal fiber: Modeling birefringence characteristics and realization, *IEEE Photon. Technol. Lett*., 2004, **16**, 1301-1303.

[20] M. S. Islam, J. Sultana, Md. Faisal, Md.R. Islam, A. Dinovister, B.W.H. Ng, D. Abbott, A modified hexagonal photonic crystal fiber for terahertz applications, *Opt. Mater*., 2018, **79**, 336-339.

[21] K. Saitoh, M. Koshiba, T. Hasegawa and E. Sasaoka, Chromatic dispersion control in photonic crystal fibers: application to ultra-flattened dispersion, *Opt. Express*, 2003, **11**, 843-852.

[22] R. Buczyński, Photonic crystal fibers, *Acta Physica Polonica Series A*, 2004, **106**, 141-168.

SYNTHESIS AND THERMAL DEGRADATION OF NITRO-FUNCTIONALIZED HYDROXYL-TERMINATED NATURAL RUBBER

Doan Minh Khai*, Nguyen Minh Tuan, Phan Duc Nhan, Nguyen Duy Tuan, Nguyen Tuan Anh

Le Quy Don Technical University, 236 Hoang Quoc Viet, Hanoi, Vietnam

*E-mail: *khaihv@lqdtu.edu.vn*

Abstract. The article reports the C-nitro functionalization of hydroxyl-terminated natural rubber (HTNR) by nitration with nitryl-iodide agent over the HTNR backbone, resulting in the formation of a conjugated nitro-alkene derivative of HNTR (N-HTNR). The reaction was carried out with sodium nitrite and iodine. The structure of N-HTNR was approved by FTIR, ^{1}H-NMR, and ^{13}C-NMR. The thermal degradation was determined by TGA. The spectral methods show the presence of nitro-alkene groups in the chain of N-HNNR and no change of the other structure of the HTNR chain. The N-HTNR has good thermal stability for practical applications. The kinetic parameters for the degradation of N-HTNR were obtained from non-isothermal TGA.

Keywords: *Hydroxyl-terminated natural rubber, Nitration, Thermal degradion, N-HTNR.*

I. INTRODUCTION

The hydroxyl-terminated natural rubber (HTNR), which is a liquid olefin polymer, is prepared from natural rubber. The main chain of HTNR is similar to polyisoprene including hydroxyl-terminated groups and a few epoxy [1,2]. The HTNR is used as a binder (10 to 15% mass) for the composite solid propellants [3-6] or plastic-bonded explosives [7]. The use of energitic polymers as a binder for the materials helps improving performance [8-10]. Energy polymers often contain nitro, nitrate or nitramine groups in the macromolecule. In particular, the content of functional groups in the polymer does not have much influence on the physical and mechanical properties of the polymer. Thus, the inclusion of nitro groups in the HTNR improves the energitic efficiency of the HTNR-based materials.

The synthesis of nitro-functionalized olefins can be caried out by several methods. It is possible that initial attack by the NO_2^+ ion is followed by elimination.

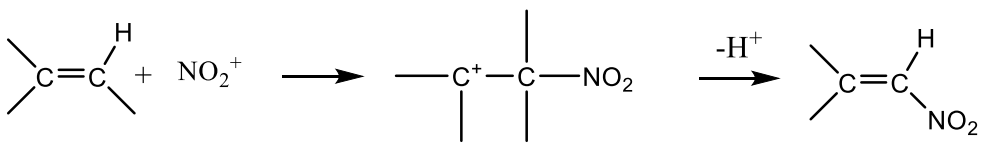

The nitration of lower olefin with concentrated HNO_3 was considered to take place through an addition-elimination process [11]. By this method, the reaction of diphenyl ethylene, cinnamic acid, and unsaturated steroids with nitric acid were carried out [12]. The nitration of highly flourinated olefins was studied with strong nitrating acid mixtures, such as HNO_3/H_2SO_4 and HNO_3/HF [11]. Many olefins were also nitrated by acetyl nitrate (HNO_3/Ac_2O) such as cyclohexene, stiibenes and styrenes. The nitryl halides (NO_2X, X: F,

 ISBN:

Cl, Br, or I) were also used as agents for nitration of alkenes. The product of this reaction was nitro-halogenated compounds followed by alkaline medium to transform the conjugated nitro-alkene derivative. So, the alkenes can be functionalized C-nitro at double bond by nitration. Up to now, there has been no published work on the C-nitro functionalization of hydroxyl-terminated natural rubber which is an alkene.

Thermal degradation is an important characteristic that determines the use of energy materials. The thermal degradation characteristics of energy polymers can be investigated by several different methods and models. Experimental investigation of thermal degradation can be done through TGA or DSC techniques [13-16]. Calculating kinetic parameters and evaluating thermal degradation of materials can use Kissinger's model [17-20].

In this paper, the C-nitro functionalization of HTNR by nitration over the HTNR backbone is carried out. The structrure of the sample is examined and the thermal characteristics of N-HTNR are investigated.

II. EXPERIMENTS

2.1. Materials

HTNR, which was used for this experimental, was prepared by photo-chemical degradation. The structure of HTNR is similar to the structure of natural rubber. In addition, the HTNR has an average molecular weight of 10.000 g/mol, a hydroxyl degree of 2.83 and about unit 4% of epoxy.

Sodium nitrite, iodine, ethyl aceate, ethylene glycol, sodium thiosulphate, sodium bicarbonate; sodium sulfate were purchased. Distilled water and ice-salt water was prepared in our laboratory.

2.2. Method of nitration

HTNR (5 g) was dissolved in ethyl acetate (50 ml) in a round-bottomed flask. A solution of sodium nitrite (3.5 g) in ethylene glycol (2.5 ml) and water (5.5 ml) was added to the above HTNR solution. Reaction content was stirred and cooled to 0 ^{o}C by a ice salt bath. Iodine (4.75 g) was now added to the reaction flask and stirring continued for 72 hours at room temperature. The organic layer was separated and washed with 10% hypo solution (sodium thiosulphate) until it was decolorized, followed by washing with saturated aqueous $NaHCO_3$ and brine, dried with anhydrous Na_2SO_4 and finally evaporated to get the crude product. A washing with methanol was given to remove soluble impurities to obtain a reddish brown viscous liquid.

2.3. Spectrum methods

FTIR method: The samples were dried at temperature of 65 ^{o}C for 24 hours in vacuum. Then, the samples were cooled down for 30 minutes at room temperature in desiccator. A solution was prepared by dissolving 0.3 g of sample in 50 ml of tetrahydrofuran. Rinse and fill a cell with the solution of sample, using a 1 ml syringe. The measure of the samples was carried out at room temperature of 25 ^{o}C and the humidity of 35%. FTIR spectra of the

samples were recorded on a Perkin Elmer Spectrum 400. A total of 32 cumulative scans were taken with a resolution of 4 cm^{-1}, in the frequency range from 4000 to 450 cm^{-1}.

NMR method. ^{1}H-NMR and ^{13}C-NMR spectra were recorded on an EvanceNEO at 600 MHz and 298.8 K. Chemical shifts are reported in ppm downfield from the tetramethylsilane (TMS) reference. The $CDCl_3$ solvent was used for dissolving N-HNTR.

2.4. Thermal analysis

The TGA curves of sample were examined by Perkin Elmer Pyris in the range of temperature from 40 to 300 ^{o}C with heating rates from 5 to 15 ^{o}C/min. The degradation peak of sample was determined by the differential curve of the mass loss with temperature. The Arrhenius parameters viz. activation energy (E) and pre-exponential factor (A) for the degradation of N-HTNR were obtained using the Kissinger method. This method allows to obtain the value of E and A from a plot of $\ln(\beta/T^2)$ against 1000/T for a series of experiments at different heating rates (β), where T is the peak temperature of the degradation in differential TGA curve. The equation is as follows.

$$\ln\left(\frac{\beta}{T^2}\right) = \ln\left(\frac{A \times R}{E}\right) - \frac{E}{R \times T}$$

III. RESULTS AND DISCUSSION

3.1. Structure of N-HTNR

It was confirmed that the main chain of HTNR is almost unchanged in comparision with natural rubber, additionally, there is hydroxyl- terminal groups and a small amount of epoxy group [2]. In order to approve the presence of conjugated nitro-alkene derivative, the structure of N-HTNR is investigated by FTIR, ^{1}H-NMR and ^{13}C-NMR spectra. The results are shown in Figs. 1-3.

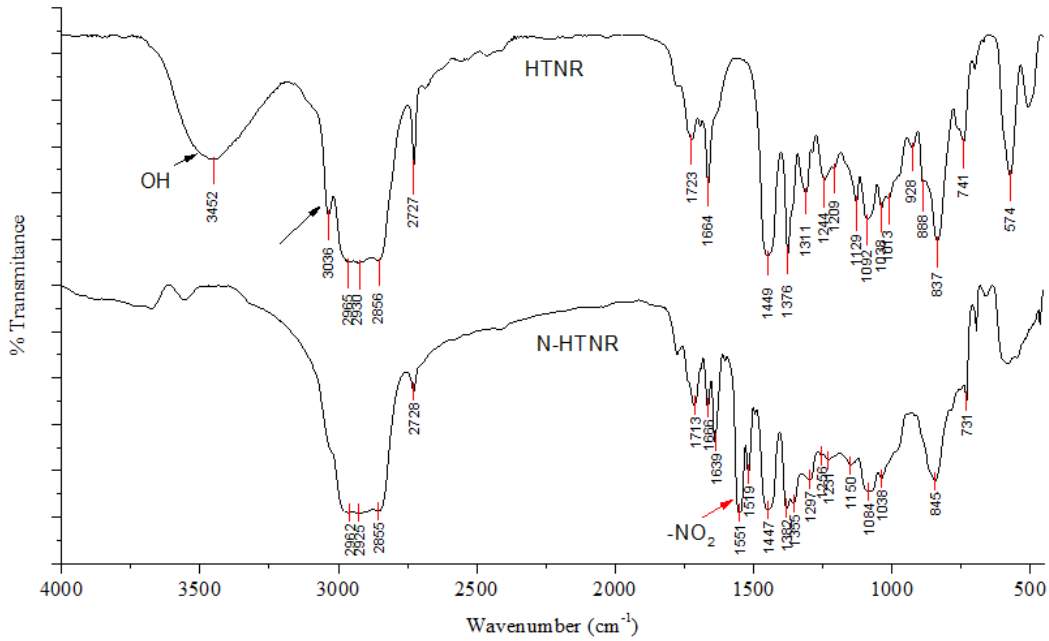

Fig. 1. *FTIR spectra of HTNR and N-HTNR.*

 ISBN:

As shown in Figure 1, the spectrum of N-HTNR is almost similar to that of the spectrum of HTNR and has some different peaks from HTNR. In which, the same absorption peaks include: 2965-2855 cm^{-1} of CH_3 and CH_2 groups; 1664 cm^{-1} vibrations of C=C bond, 1447-1449 cm^{-1} vibrations of CH_2 group, 1382-1376 cm^{-1} corresponding to vibrations of CH_3 group and 837-845 cm^{-1} vibrations of =C-H,... Besides, the peaks at 1551 cm^{-1} and 1519 cm^{-1} indicate the appearance of the -NO_2 group of N-HTNR in comparison with HTNR. The separation of the C=C peak at 1639 cm^{-1}, 1664 cm^{-1} and the NO_2 group at 1551 cm^{-1}, 1519 cm^{-1}shows that the nitro group resonates with the double bond. Thus, the infrared spectrum confirms the presence of the NO_2 group in the N-HTNR.

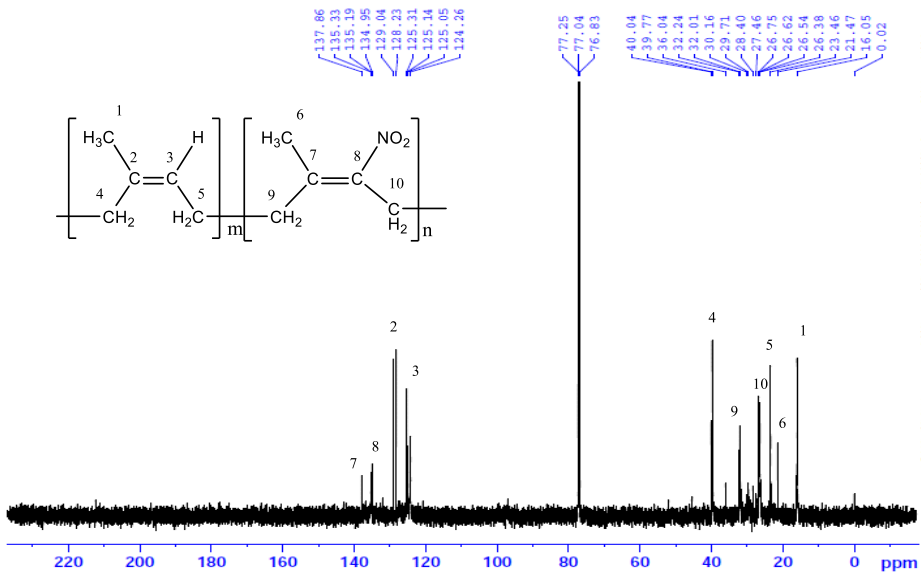

Fig. 2. *^{13}C-NMR spectrum of N-HTNR.*

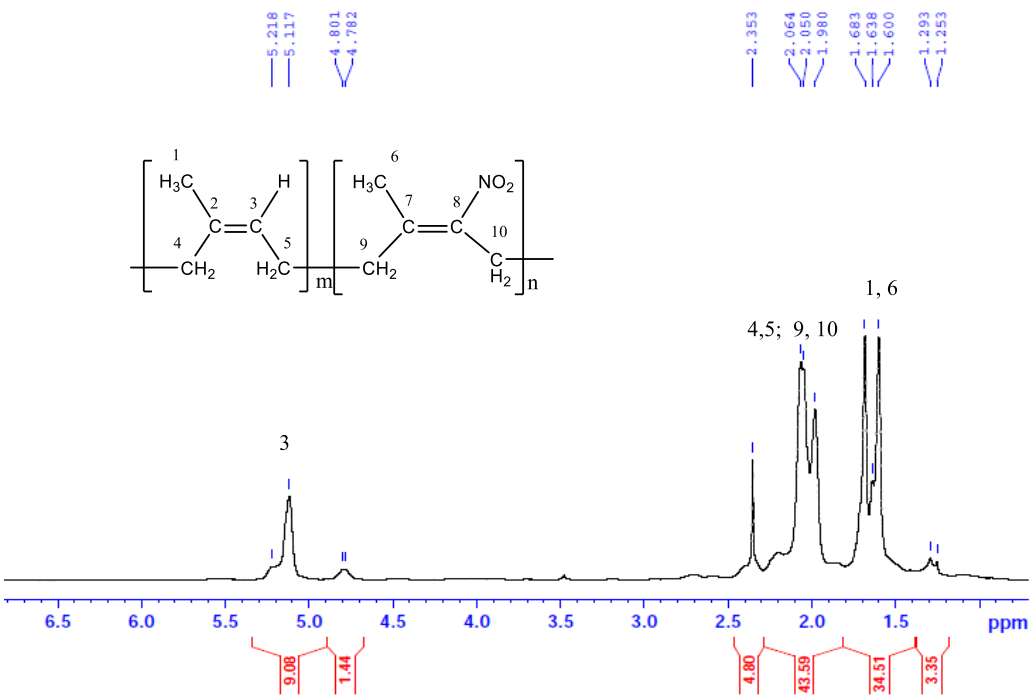

Fig. 3. *^{1}H-NMR spectrum of N-HTNR.*

The ^{13}C-NMR spectrum in Fig. 2 shows shifts corresponding to the structure of the isoprene units and nitrated units in chain of N-HTNR. The shifts at 16.05 ppm and 21.47 ppm is due to carbons of methyl (-CH_3). Additionally, methylenes (-CH_2-) have the shifts from 23.46 ppm to 40.04 ppm. Furthermore, the shifts from 124.26 ppm to 137.86 ppm is of vinylene (>C=C<) in the isoprene units. The nitrated units can be shown by separation of the above shifts. So, ^{13}C-NMR of N-HTNR also shows the presence of nitro functional groups in the chain.

The ^{1}H-NMR spectrum of N-HTNR indicated the shifts corresponding to the structure of the isoprene units and the appearance of some new shifts. The peaks have $\Delta\delta$ = 1.6 ppm of proton in the methyl group (-C**H**$_3$), 1.9-2.0 ppm of proton in the methylene group (-C**H**$_2$-) and 5.1 ppm of proton in the cis-vinylene group (>C=C**H**-) of the cis-1,4-isoprene unit. Especially, the occurrence of new peaks with $\Delta\delta$ = 4.8 ppm and 5.2 ppm corresponds to the propton of the methylene group next to the nitro group. A quantification of nitro groups is possible through the protons at the 4.8-5.2 ppm shift of C=C**H** relative to the protons of the methylene group (-C**H**$_2$-). The result is a nitro group content of 13.04 % mol.

3.2. Thermal characteristics

The thermal characteristics of an energetic material is important for understanding of degradation mechanism and also for the assessment the long term stability, hazards involved in handling, storage and processing of such substance. In this experiment, the sample was examined by TGA method at heating rates of 5; 7; 10; 15 ^{o}C in the range from 40 to 300 ^{o}C. The TGA curve is shown in Fig. 4.

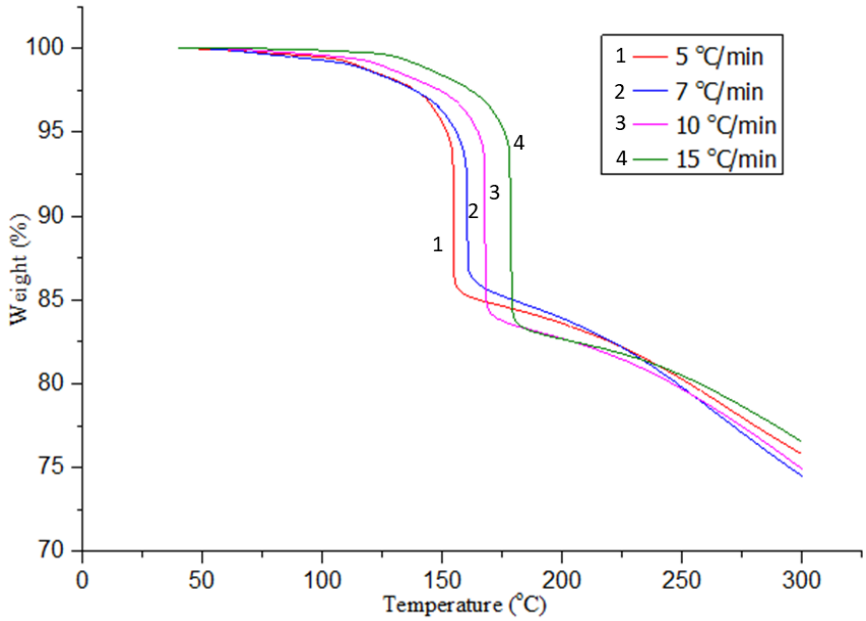

Fig. 4. *TGA curves of N-HTNR degradation at several rate of heating.*

As shown in Figure 4, the N-HTNR curve shows a distinct degradation in range from 153.5 to 177.5 ^{o}C corresponding to about 15% of weight loss, which represents loss of NO_2 groups in the form of HNO_2. Further weight loss at higher temperature represents the degradation of hydrocarbon backbone.

 ISBN:

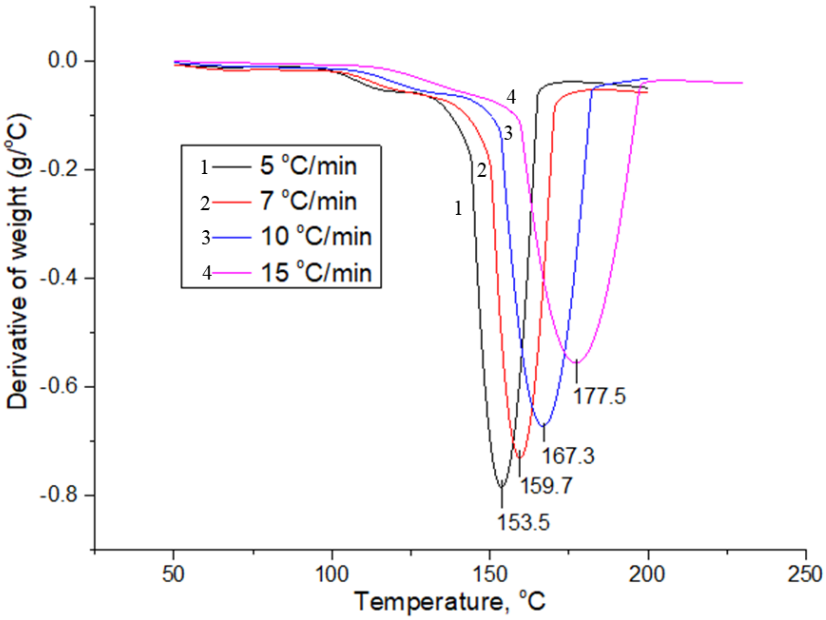

Fig. 5. *Derivative of TGA curves of N-HTNR degradation.*

Figure 5 shows the derivative of TGA curves of N-HTNR degradation obtains at various heating rates. As a result, a straight line (R-square = 0.994) is obtained from the plot of $\ln(\beta/T^2)$ against 1000/T (Fig. 6). This obtained result indicates that the mechanism of thermal degradation of N-HTNR do not vary during the degradation under different heating rates. The activation energy (E) and preexponential factor (A) of the degradtion are derived from the slope and intercept of plotting regression line, respectively. In order to calculate the pre-exponential factor, it is assumed that the degradation of N-HTNR followed first-order kinetics. The results obtain for activation energy and pre-exponential factor by the Kissinger method are listed in Table 1.

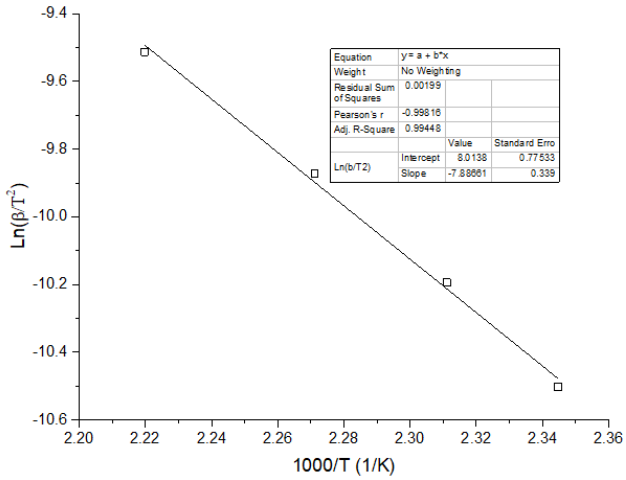

Fig. 6. *The plot of ln (β/T^2) vs. 1000/T for the N-HTNR sample.*

Table 1. *Kinetic parameters of N-HTNR.*

Activation energy, E/kJ.mol^{-1}	Pre-exponential factor, A/min^{-1}	Square of the correlation coefficient, R^2
65.57	23.84x10^6	0.994

IV. CONCLUSION

The nitro-alkene derivative is synthesized by nitration of HTNR with nitryl iodide (NO_2I). The nitro group ($-NO_2$) is added to isoprene units at the proton of vinylene group (>C=C**NO_2**-). The structure of N-HTNR is not much different from the HTNR and has 13.04% mol of nitro groups in a chain. The strongly thermal degradation of N-HTNR is in the range of temperature from 153.5 to 177.5 ^oC with a heating rate from 5 to 15 ^oC/min, respectively. The kinetic parameters for the degradation of N-HTNR were estimated to be 65.57 kJ/mol of activation energy and 23.84×10^6 of pre-exponential factor.

REFERENCES

[1] H. M. Nor and J. R. Ebdon, Telechelic liquid natural rubber: A review, *Progress in Polymer Science*, 1998, **23**(2), 143-177.

[2] D. M. Khai and P. D. Nhan, Effect of some experimental factors on preparation of liquid natural rubber, *Vietnam Journal of Science and Technology*, 2016, **54**(4), 563.

[3] M. Onn, H. M. Nor, and W. K. W. Ali, Development of solid rocket propellant based on isophorone diisocyanate-hydroxyl terminated natural rubber binder, *Jurnal Teknologi*, 2014, **69**(2), 53-58.

[4] W. K. W. Ali, K. L. Ang, and M. N. M. Jaafar, Experimental Solid and Liquid Propellant Rocket Development in Universiti Teknologi Malaysia: 1992-2011, *Jurnal Teknologi*, 2015, **73**(1), 35-52.

[5] N. Baharulrazi, H. M. Nor, W. K. W. Ali, Hydroxyl Terminated Natural Rubber (HTNR) as a Binder in Solid Rocket Propellant, *Applied Mechanics and Materials*, 2015, **695**, 174-178.

[6] Solomon Thomas, et al., Natural Rubber Based Fuel Rich Propellant for Ramjet Rocket, *Defence Science Journal*, 1992, **42**(3), 141-146.

[7] D. M. Khai, Evaluation of the characteristics of plastic explosive adhered by liquid natural rubber, *Vietnam Journal of Science and Technology*, 2020, **58**(5), 557-564.

[8] M. E. Colclough and N. C. Paul, Nitrated hydroxy-terminated polybutadiene: Synthesis and properties, ACS Publications, 1996.

[9] M. Eamon Colclough, et al., Energetic polymers as binders in composite propellants and explosives, *Polymers for Advanced Technologies*, 1994, **5**(9), 554-560.

[10] Colclough M. E., Golding P. and Paul N., Nitrated hydroxy-terminated polybutadiene (NHTPB) a new energetic binder, Proc. 14th Int. Pyrotechnics Seminar, 1989, Henry Ling Press, Dorset, UK, 105-111.

[11] G. A. Olah, R. Malhotra, and S. C. Narang, Nitration Methods and Mechanisms, Wiley-VCH, 1988.

[12] J. V. der Lee, The action of nitric acid on derivatives of ethylene. II. Nitration of some styrene derivatives, *Recueil des Travaux Chimiques des Pays-Bas,* 1928, **47**(11), 920-933.

[13] S. M. Pourmortazavi, et al., Non-isothermal kinetic studies on thermal degradation of energetic materials: KNF and NTO, *Journal of Thermal Analysis and Calorimetry*, 2012, **110**(2), 857-863.

 ISBN:

[14] M. R. Sovizi, S. S. Hajimirsadeghia, and B. Naderizadehb, Effect of particle size on thermal degradation of nitrocellulose, *Journal of Hazardous Materials*, 2009, **168**, 1134-1139.

[15] S. Pisharath and H. G. Ang, Thermal degradation kinetics of a mixture of energetic polymer and nitramine oxidizer, *Thermochimica Acta*, 2007, **459**(1-2), 26-33.

[16] S. Löbbecke, H. H. Krause, and A. Pfeil, Thermal analysis of ammonium dinitramide degradation, *Propellants, Explosives, Pyrotechnics*, 1997, **22**(3), 184-188.

[17] R. L. Blaine and H. E. Kissinger, Homer Kissinger and the Kissinger equation, *Thermochimica Acta*, 2012, **540,** 1-6.

[18] K. Kishore, S. Sankaralingam, and A. S. Begum, Studies on the ageing behaviour of Polyvinylchloride/ammonium perchlorate composite solid propellant, *Fuel*, 1989, **68**(11), 1476-1479.

[19] H. E. Kissinger, Reaction kinetics in differential thermal analysis, *Analytical chemistry*, 1957, **29**(11), 1702-1706.

[20] H. E. Kissinger, Variation of peak temperature with heating rate in differential thermal analysis, *Journal of Research of the National Bureau of Standards*, 1956, **57**(4), 217-221.

ANTIOXIDANT CAPACITY AND AQUEOUS SOLUBILITY OF TAXIFOLIN EXTRACTED FROM SIBERIAN LARCH (LARIX SIBIRICA)

Son Bach*, Thuy Thi Phan, Huong Thi Le and Mai Huong Thi Nguyen

Institute of Physics, Vietnam Academy of Science & Technology, Hanoi, Vietnam

*E-mail: *btson@iop.vast.vn*

Abstract. Taxifolin (3,5,7,3,4-pentahydroxy flavanone or dihydroquercetin) is a flavonoid-class substance commonly found in various plant sources and possesses many promising therapeutic effects. In this study, the antioxidant potential and aqueous solubility of high-purity taxifolin extract powder (> 92% taxifolin) from Siberian larch are evaluated using the Cupric-ion Reducing Antioxidant Capacity assay (CUPRAC) and shake-flask equilibrium solubility method. The taxifolin-rich product demonstrates a Trolox-equivalent cupric reducing capacity of 2.85, which is almost three times higher than the reported value of vitamin C/ascorbic acid. On the other hand, the powder is only slightly soluble in water (2.6 mg/ml at 38°C). It is concluded that the taxifolin extract requires further formulations to improve its solubility and achieve satisfactory oral bioavailability.

I. INTRODUCTION

Taxifolin (3,5,7,3,4-pentahydroxy flavanone or dihydroquercetin) is a flavonoid commonly found in many plant sources including milk thistle, onions and the bark of trees in the pine family [1]. Although it is rarely used as a single compound, taxifolin is present in several medicinal products like silymarin, Pycnogenol® and Venoruton® [2]. It was first isolated from the bark of Douglas fir (*Pseudotsuga taxifolia* (Lindl.) Britton), followed by the Siberian and Dahurian larch (*Larix sibirica* Ledeb. and *Larix gmelinii* (Rupr.) Kuzen.) [3]. In the last thirty years, numerous research works on the pharmacological effects of taxifolin have been published, among which antioxidant, anti-inflammatory, anticancer, antimicrobial, anti-Alzheimer, hepatoprotective and cardioprotective are the most notable. It is also considered to be fairly safe for oral consumption since it is not embryotoxic and does not lead to malformations, hypersusceptibility or mutations [4].

The present study aims to quantitatively determine the antioxidant potential and aqueous solubility of taxifolin-rich extract of Siberian larch (*Larix sibirica*), which is marketed as a natural antioxidant food additive and dietary supplement. The Cupric-ion Reducing Antioxidant Capacity assay (CUPRAC) is chosen to measure its antioxidant efficiency. In comparison to other antioxidant assays, the CUPRAC is more favorable given its realistic pH, accessibility and stability of required chemical reagents, along with the applicability to both lipophilic and hydrophilic antioxidants [5]. For measuring the aqueous solubility of the taxifolin extract, the low-throughput traditional saturation shake-flask method is employed to provide more accurate information, which is relevant to further formulation strategies [6].

 ISBN:

II. MATERIALS AND METHODS

Chemicals

Powder extract from the bark of Siberian larch (*Larix Sibirica*) of 92% minimum dihydroquercetin/taxifolin purity (by HPLC), which is marketed under the trade name Flavitol, is purchased from Russia. Neocuproine (2,9-dimethyl-1,10-phenanthroline), trolox (6-hydroxy-2,5,7,8-tetramethylchroman-2-carboxylic acid) and taxifolin standards (> 99%) are obtained from Sigma-Aldrich. Ammonium acetate ($NH_4CH_3CO_2$/NH_4Ac) and copper (II) chloride dihydrate ($CuCl_2.2H_2O$) are purchased from Guangdong Guanghua Sci-Tech Co. Ltd. All chemicals used are of analytical grade.

Preparation of sample and reagent solutions for antioxidant capacity evaluation

The $CuCl_2$, NH_4Ac and neocuproine reagent solutions are prepared by following the instructions from the original paper [7]. 12.5 mg of trolox is added into a 50 ml volumetric flask and dissolved to the mark in ethanol 96% in order to obtain 1 mM (= 0.25 mg/ml) trolox standard solution.

16 mg of the taxifolin-rich powder is added into a 50 ml volumetric flask and dissolved to the mark in ethanol 96% in order to obtain a stock taxifolin extract sample solution. An aliquot of the stock solution is diluted in ethanol 96% to the final concentration C_f of 0.0128 mg/ml (dilution factor D = 25) before it is used in the actual experiment described just below.

Measurement of antioxidant capacity by the CUPRAC assay

Evaluation of the taxifolin extract's antioxidant capacity is performed according to the CUPRAC assay originally described by Apak et al. with some minor changes [7]. 1 ml of 0.01 M $CuCl_2$ + 1 ml of 1 M NH_4Ac buffer + 1 ml of 7.5×10^{-3}M neocuproine + 1 ml of diluted taxifolin extract sample solutions are added to a test tube, respectively. The test tube is then stoppered and gently shaken for a few seconds to ensure that the total liquid content inside is well-mixed. After 30 minutes of incubation at the ambient temperature, absorbance against a reagent blank A_{452nm} is measured at 452 nm by an UV-Vis spectrophotometer (Avantes's AvaSpec ULS2048x16). The same procedure is repeated for a dilution series of the trolox standard solution to plot a standard curve of absorbance vs concentration which is linear in the concentration range of 0.04 - 0.25 mM (r^2 > 0.995). The antioxidant capacity of the taxifolin sample is expressed as the dimensionless Trolox-equivalent antioxidant coefficient (TEAC), which is calculated from the slope a and y-intercept b of the trolox standard curve using linear regression:

$$\text{TEAC} = [(A_{452nm} - b)/a]\times0.25/C_f$$

Measurement of aqueous solubility by the saturation shake-flask method

An amount of excess taxifolin powder extract is added into a 50 ml beaker and dispersed in 15-20 ml of double distilled water. The beaker is then sealed to prevent evaporation of the solvent and kept in isothermal condition and under constant magnetic stirring for at least 24 hours so that the suspension reaches thermodynamic equilibrium. After that, a small aliquot of the suspension is extracted by a clean plastic syringe and

filtered through a 0.45 µm nylon membrane. An exact volume of the filtrate is further diluted in ethanol 96% before its UV-Vis absorbance A_{289nm} at 289 nm is measured. Thus, the solubility of the taxifolin-rich extract in water is interpolated from A_{289nm} using the taxifolin standard calibration curve's equation of linear regression.

III. RESULTS AND DISCUSSION

Antioxidant capacity determined by CUPRAC assay

Mechanism of the CUPRAC assay is based on the ability of antioxidants to donate electrons, which reduces Cu^{2+} ions to Cu^{+}. The Cu^{+} ions are then bonded with the chelating agent neocuproine (Nc) to form a stable chromophore, Cu(I)-Nc. Formation of the Cu(I)-Nc complex is signified by the development of orange-yellow color which gives rise to the absorbance peak at 450 nm. Intensity of the peak is thus dependent on the amount of antioxidant taking part in the redox reaction, as it can be seen in Fig. 1.

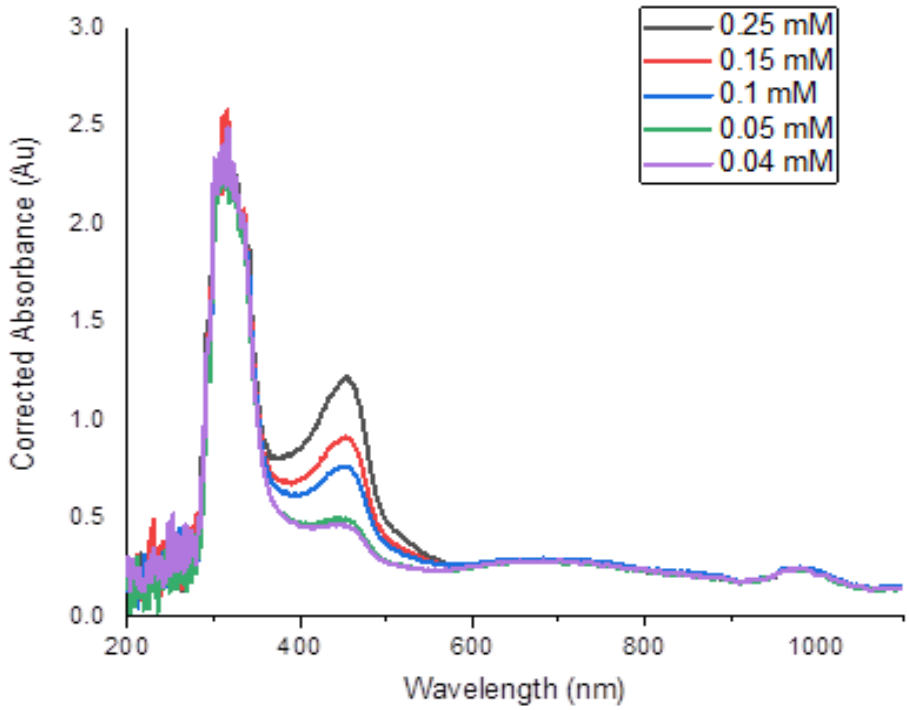

Fig. 1. *UV-Vis spectra of Cu(I)-Nc complex formed as a product of CUPRAC redox reaction with different concentrations of Trolox .*

The standard curve of CUPRAC absorbance response to trolox concentration in Fig. 2 is fitted with a linear equation (y = 3.469x + 0.024). The TEAC coefficient of the taxifolin extract sample calculated from this equation is 2.85, which means the antioxidant capacity of a 1 mg/ml solution of taxifolin extract is equal to that of trolox standard solution at the concentration of 2.85 mg/ml. The reported TEAC values of some common antioxidants such as vitamin C/ascorbic acid and vitamin E/α-tocopherol are 0.96 and 1.11, respectively [7]. It is obvious that the taxifolin extract is a highly potent antioxidant supplement.

 ISBN:

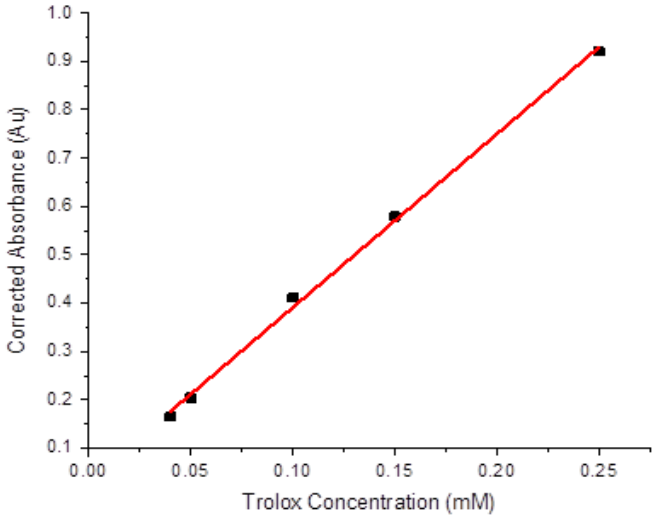

Fig. 2. *Trolox standard UV-Vis response curve used for determination of antioxidant capacity according to the CUPRAC assay. The curve is fitted with a linear equation* $y = 3.469x + 0.024$ *(*$r^2 > 0.99$*).*

Evaluation of solubility in water

A calibration curve of absorbance vs concentration is constructed by preparing a series of taxifolin standard dissolved in ethanol 96% at known concentrations (see Fig. 3). The saturation solubility in double distilled water of the taxifolin extract powder at different temperatures are displayed in Table 1**,** each solubility value is the average of three consecutive measurements. As expected, solubility of the larch extract increases with temperature. The increased average kinetic energy of particles within the solution at higher temperatures makes seperating the solute molecules which are held together by intermolecular attractions easier. Nevertheless, the extract is considered to be sparingly soluble according to the standard laid out by the U.S. Pharmacopeia [8]. This result suggests that drug formulation strategies are necessary to further enhance the extract's oral bioavailability.

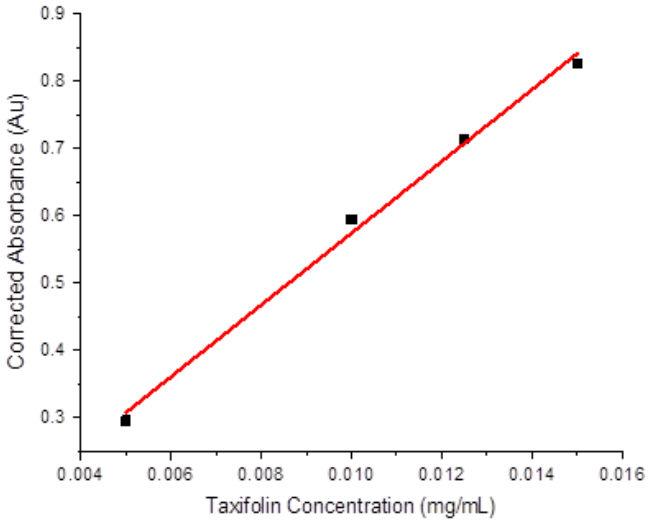

Fig. 3. *Calibration curve of taxifolin standard solution in ethanol 96%, which is used to calculate the taxifolin-rich larch extract's solubility in water. The curve is fitted with a linear equation* $y = 55.291x + 0.035$ *(*$r^2 > 0.99$*).*

Table 4. *Saturation solubility values of taxifolin-rich larch extract in double distilled water.*

Temperature (^oC)	Solubility (mg/ml)
38	2.60
43	4.51
54	12.66

IV. CONCLUSION

Quantification of antioxidant capacity using the CUPRAC assay confirms the taxifolin-rich extract's excellent antioxidant ability in comparison to other common dietary substances such as vitamin C & E. On the other hand, the product's solubility in water measured by the traditional shake-flask method is rather limited, which prompts drug formulations in the future to improve its oral availability and reduce the daily dosage.

REFERENCES

[1] Sunil C. and B. Xu, An insight into the health-promoting effects of taxifolin (dihydroquercetin), *Phytochemistry*, 2019, **166**, 112066.

[2] Nathan M. and R. Scholten, The complete German commission E monographs: Therapeutic guide to herbal medicines, *Annals of Internal Medicine*, 1999, **130**(5), 459.

[3] Pew J. C., A flavonone from douglas-fir heartwood2, *Journal of the American Chemical Society*, 1948, **70**(9), 3031-3034.

[4] Wang Y., et al., Enzymatic water extraction of taxifolin from wood sawdust of Larix gmelini (Rupr.) Rupr. and evaluation of its antioxidant activity, *Food Chemistry*, 2011, **126**(3), 1178-1185.

[5] Apak R., et al., Total antioxidant capacity assay of human serum using copper(II)-neocuproine as chromogenic oxidant: the CUPRAC method, *Free Radical Research*, 2005, **39**(9), 949-61.

[6] Veseli A., S. Žakelj, and A. Kristl, A review of methods for solubility determination in biopharmaceutical drug characterization, *Drug Development and Industrial Pharmacy*, 2019. **45**(11), 1717-1724.

[7] Apak R., et al., Novel total antioxidant capacity index for dietary polyphenols and vitamins C and E, using their cupric ion reducing capability in the presence of neocuproine: CUPRAC method, *Journal of Agricultural and Food Chemistry*, 2005, **52**(26), 7970-81.

[8] Censi R. and P. Di Martino, Polymorph impact on the bioavailability and stability of poorly soluble drugs, *Molecules*, 2015, **20**(10), 18759-18776.

 ISBN:

GREEN SYNTHESIS ZnO NANOPARTICLEC BY *PIPER CHAUDOCANUM* L. EXTRACT FOR ENHANCED ANTIBACTERIAL ACTIVITY

Truong Thi Thao[1], Le Thi Ngoc Linh[2], Kieu Thi Van Anh[2], Nguyen Dieu Linh[2] and Nguyen Van Hao[1*]

[1]*TNU- University of Sciences, Tan Thinh Ward, Thai Nguyen Province, Vietnam*

[2]*Luu Nhan Chu High school, Dai Tu District, Thai Nguyen Province, Vietnam*

*E-mail: *haonv@tnus.edu.vn*

Abstract. *Piper Chaudocanum* L. is a medicinal plant in Vietnamese traditional medicine, which has detoxifying and anti-inflammatory effects. In this study, ZnO nanoparticles (ZnO NPs) synthesized by sol-gel method (ZnO S) and co-precipitation method (ZnO CP) in the presence of aqueous extract or extract of ethanol-water mixtures of *Piper chaudocanum* L. leaf. Extracts was preliminary screened to determine the presence of major components in the leaf extracts using standard methods. The prepared ZnO NPs were characterized by using X-ray diffraction (XRD), Fourier-transform infrared spectroscopy (FTIR), field emission scanning electron microscopy (FESEM) and Transmission electron microscope (TEM). The antibacterial activity of synthesized ZnO NPs was preliminary investigated by using agar well diffusion method against Gram-negative *Pseudomonas aeruginosa* (PA) and Gram-positive *Staphylococcus aureus* (SA) bacterial in vitro. The experiment results shown that ZnO CP is better against *PA* and *SA* than ZnO S. IC_{50} values of ZnO CO NPs against *PA*, *SA*, *Citrobacter freundii* (*Citro*), *Eschericha. Coli* (*E. coli*) and *Serratia marcescens* (*SM*) is 61.77 to 96.71 μg/ml.

Keywords: *ZnO nanoparticles, Piper chaudocanum, Antibacterial activity, Sol-gel method, Co-precipitation method.*

I. INTRODUCTION

ZnO is a multifunctional material, is one of the materials that is attracting the attention of scientists today. That is because ZnO has unique physical and chemical properties as quite chemical stable, good UV radiation absorption, high electrochemical coupling coefficient, high photostabilty [1]. ZnO is applied research in memory devices, electronics, optoelectronics, spintronic, laser technology, sensor, converter, energy generator, solar cells, catalysis, photocatalyst, ceramics industry, biomedicine and in pro-ecological systems, biomedicine and in pro-ecological systems [1,2]. ZnO nanoparticles (NPs) was synthesized following many differences fabrication techniques: hydro-/solvo-thermal technique (i), solution-based technique (ii), ultrasonic and microwave-assisted methods (iii), in situ self-assembly (iv), electrospinning method (v), thermal decomposition (vi), and chemical co-precipitation technique (vii). Prepared ZnO NPs are in many other structures (1D, 2D, 3D), in many differences morphologies and dimensions [1-3].

With application in medical science like nanomedicine, nanoantibiotics, antioxidant, antimicrobial activities and drug delivery, one of the most interested ZnO synthesis methods is green synthesis (or biosynthesis). Green synthesis is using some biomaterials

such as bacteria, fungi, yeasts, algae, plant and including agricultural waste as one of the precursors of ZnO synthesis [4,5], replace a part or a whole traditional chemicals. Green synthesis is an eco-friendly, cost-effective, that is considers a trending alternative to the conventional physical and chemical synthesis processes. In which, plant extract (the extracts of a part such as charcoal, roots, leaves or a whole plant [6]) is the first choice due to its popularity, diversity and ease of regeneration. *Piper chaudocanum* is one of many medicinal plants of Vietnamese traditional medicine. *Piper chaudocanum* belongs to Piper genus, Piper genus contains a variety chemical composition such as alkaloids, flavonoids, steroids, terpenoids,… [7-12]. Although there have been no systematic studies on the chemical composition and biochemical activity of *Piper chaudocanum*, but in folklore, it is used as an effective antidote to a variety of poisons, and cure weather diseases. The closest to the *Piper chaudocanum* is the *Piper betle*, which is very famous for its cure for dental caries or gynecological infections.

This study focuses on the preparation of ZnO NPs using *Piper chaudocanum* leaf extract, the physico-chemical characteristics and evaluation of the antibacterial ability of the fabrication material against five bacterial pathogens including *Staphylococcus aureus (SA), Citrobacter freundii (CF), Serratia marcescens (SM), Escherichia Coli (E. Coli)* and *Pseudomonas aeruginosa (PA)* are investigated.

II. EXPERIMENTS

2.1. Materials

Zinc acetate dihydrate ($Zn(CH_3COO)_2{\cdot}2H_2O$), sodium hydroxide and ethanol of analytical grade, HNO_3, H_2SO_4, $FeCl_3$, NaOH, $CHCl_3$, dimethyl sulfoxide (DMSO) nutrient broth and Mueller Hinton agar mediums were purchased from Merck, Germany. Distilled water (DW) was utilized in all experiments. *Piper chaudocanum* leaves were collected from Son La province, Vietnam. All the strains of bacteria were isolated at Microbiology Department, Thai Nguyen University of Medicine and Pharmacy.

2.2. Preparation of *Piper chaudocanum* leaves extract

Piper chaudocanum leaves were thoroughly washed with tap water, dried in an oven at 50 ^oC, and then grinded into powder. To prepare the extract, 10 g of *Piper chaudocanum* L. leaf powder was ultrasound extracted by 100 ml of distilled water or mixture of 50 ml distilled water and 50 ml ethanol for 1 hour at 60 ^oC. The extracts were centrifuged, filtered and then stored at 4 °C for further experiments, and denoted AE (aqueous extract) and ME (mixed solvent extract, ethanol-distilled water), respectively.

2.3. Phytochemical screening test

The screening carried out to investigate the qualitative chemical compositions of the AE and ME by using the standard methods [9]. Chemical reactions and color change were used as an indicator to identify the presence of major chemical groups such as phenolic, flavonoids, terpenoids, alkaloids, proteins and steroids in the leaf extracts.

2.4. Green synthesis of ZnO NPs

 ISBN:

The green synthesis was done in sol-gel method and co-precipitation method. The details of two processes were shown below.

Co-precipitation method. 10 ml of extract (acts as a surfactant) were added in 30 ml of 2.2 g acetate dihydrate solution under vigorous stirring. Then, 1 M of NaOH was added dropwise into the zinc acetate solution until it reached pH 12 for 1 h at a constant temperature of 70 °C. The precipitates obtained were centrifuged at 5000 rpm, 4 °C, washed with alcohol and then washed with DW to neutral. Then precipitates were dried at 80 °C overnight to acquire a dry powder. The corresponding product symbol are ZnO (without extract); ZnO_AE; ZnO_ME.

Sol-gel method. 15 ml of extract (or solution of 1.2 g oxalic acid) were added drop by drop into 30 ml of 2.2 g acetate dihydrate solution under vigorous stirring at 70 ^{o}C until they have a pasty consistency. They were then dried at 80 °C overnight to acquire a dry powder (xerogel). They were then finely ground and calcinated at 450 °C for 60 minutes, heating rate 150 ^{o}C/h. The corresponding product symbol are ZnOS, ZnOS_AE; ZnOS_ME. The extract acts as a reaction precursor, in order to form complexes with Zn(II), and support the sintering process.

2.5. Characterization of ZnO NPs

The synthesis of ZnO NPs was studied by various techniques: X-Ray Diffraction (XRD) was used to understand the crystal structure of the samples at the wavelength of 1.5406 Å in the range of 20-80° at 40 kV; Scanning Electron Microscopy (SEM) and Transmission electron microscope (TEM) were used to study their morphology; Fourier-Transform Infrared Spectroscopy (FTIR) was used to study the functional groups present in the samples in the spectral range of 4000-400 cm^{-1} with the resolution of 4 cm^{-1}.

2.6. Bactericidal activity of ZnO NPs

The bactericidal activity of synthesized ZnO NPs was assessed by agar well diffusion test against both Gram-positive (*SA*) and Gram-negative (*PA)* bacterial pathogens. The samples were dissolved in DMSO and then diluted 2 steps to obtain 100 μg/ml stock solutions. 100 μl of each samples were put on each well on the LB agar plate, then the LB agar plates were incubated for 18-24 hours at 30 ^{o}C, and then observed and recorded the inhibition zones. The best sample was evaluated for the minimal concentration of 50% inhibition of bactericidal activity (IC_{50}) against *SA*, *CF*, *SM*, *E. Coli* and *PA* bacteria. The stock solution was incorporated into 0.5 ml of sterilized nutrient broth for bacteria and serially diluted to achieve 75; 50; 25; 12.5; and 6.25 μg/ml, respectively. A 300 μl standardized suspension of the test bacteria (10^5 CFU/ml) was transferred to the Falcon tube containing 3 ml of liquid LB. Then, another 300 μl of diluted samples were added to each Falcon tube, shaked well and the Falcon tubes were incubated at 37 ^{o}C for 24 h. After 24 h of incubation, the bacterial concentration was measured by photometric method. The data was presented in term of % inhibition of microorganism growth. To control correctness, all experiments were executed in triplicates and the average value was reported. IC_{50} determination was analyzed using Raw data.

III. RESULT AND DISCUSSION

3.1. Phytochemical screening

The results of qualitative phytochemical screening of extracts of *Piper chaudocanum* leaf (shown of Fig. 1) revealed the presence of proteins, flavonoids, phenolds, alkaloids and terpenoids in AE. The ME consists of flavonoids, phenolds, alkaloids, teroids and terpenoids.

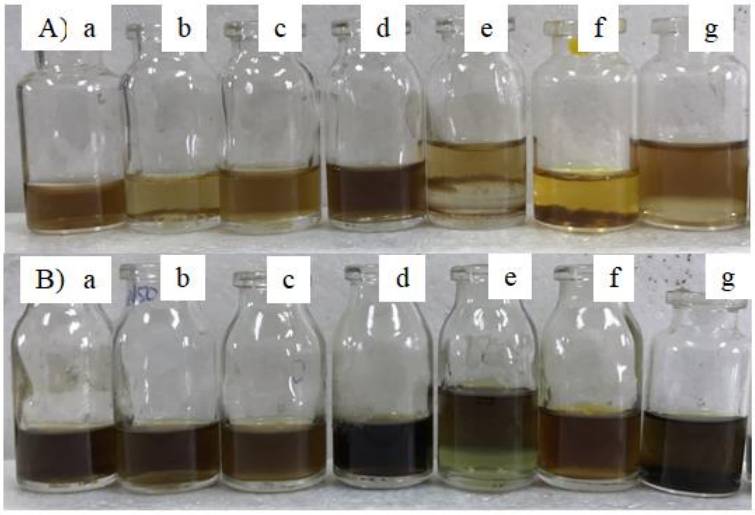

Fig. 1. *Phytochemical screening extract of Piper chaudocanum leaf in DW (A) and mixture of ethanol and DW (1:1), showing the qualitative determination (b) proteins, (c) flavonoids, (d) phenols, (e) steroids, (f) ankaloids, (g) terpenoids and (a): blank.*

3.2. Characterization of green synthesized ZnO NPs

XRD analysis

The crystal structure and phase purity of as-prepared samples were determined by powder XRD on Fig. 2. All diffraction peaks in the pattern are well matched to (100); (002); (101); (102); (110); (103); (200); (112); (201) and (004) crystal plane and were indexed to the hexagonal wurtzite structure of ZnO (JCPDS card No.36-1451) with the presence of strong diffraction peaks. The differences in the crystallinity of the samples can be distinguished from the differences in peak intensities. The crystallite size (D_{hkl}) of prepared ZnO NPs was calculated follows Scherrer's equation. The determined average crystallite sizes for the ZnO, ZnO_ME, ZnO_AE, ZnOS, ZnOS_ME and ZnOS_AE are 26; 27.8; 29.7; 31.7; 22.4 and 22.4 nm, respectively. ZnO NPs size obtained by co-precipitation method in the presence of extract was slightly increased compared to that in the absence of extract, it is due to the formation of ZnO particle coating by organic compounds in the extract; while synthesizing by sol-gel method, the ZnO particle size is significantly reduced compared to use oxalic acid. It indicated that the complexes formed between Zn^{2+} ions with the extract composition has reduced the aggregation of particles together, and when the ligands were burned, the smaller ZnO particles were obtained.

 ISBN:

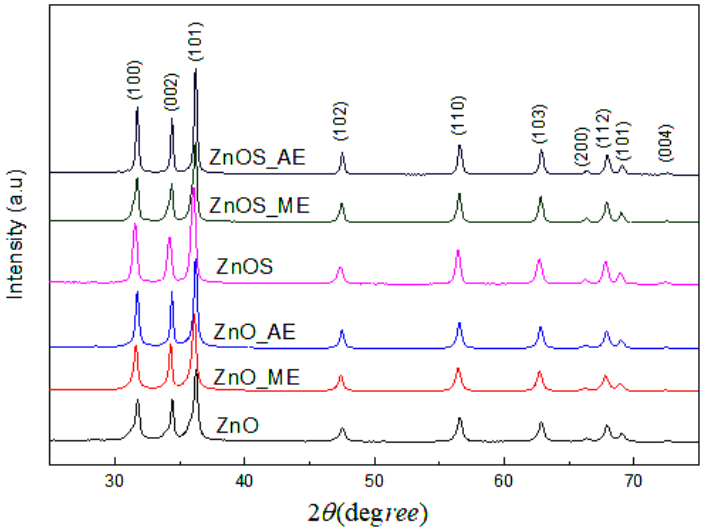

Fig. 2. *X-ray diffraction (XRD) analysis of synthesized ZnO samples*.

Surface chemical groups study using FTIR

The FTIR spectrum of ZnO NPs and extracts of *Piper chaudocanum* leaves are shown in Fig. 3. In Fig. 3a, the broad absorption peaks from 3700 to 3000 cm^{-1}, event much extended towards 2000 cm^{-1} that is referred to O-H stretching (of moisture) and associated with the stretching mode of the C-H bond on the ME and AE spectrums. The consecutive appearance of peaks in the 1700 ÷ 1000 cm^{-1} (at 1037; 1077; 1123 cm^{-1}; 1245; 1261 cm^{-1}; 1384.6; 1442; 1489; 1513 and broad absorption peak at 1645 cm^{-1}) on the ME patter or phenomenon of superimposed spectral peaks appearing in this region of AE (the similar in the region below 1000 cm^{-1}) showed the complexity in the chemical composition of extracts. May be the presence of esters, ethers, carboxylic acid, proteins, phenolic group, alkaloid, steroid and carbohydrates in the *Piper chaudocanum* leaves extract.

In Fig. 3b, the IR spectrum of all samples occurred the peaks in the range of 400-800 cm^{-1} is related to the Zn-O bond. The broad absorption peaks at around 3500 cm^{-1} on the spectrum of ZnO was extended towards 2700 cm^{-1} on the spectrum of other ZnO samples belong to the stretching bands of H-O of moisture and associated with the C-H stretching vibrations. This is the result of the interaction between the extract and Zn^{2+} to form complexes or absorption or coating ZnO particles. This is also observed on the 1700 ÷ 700 cm^{-1} region. On the ZnO_ME and ZnO_AE spectra, the absorption peaks at 1640; 1563; 1414; 1085; 1038; 928;855; 772 and 718 cm^{-1} corresponding to aromatic C-O bonds, N-H bonds stretching[5], the stretching bands of C-O of amide group, carbonyl C-C stretching vibration, symmetric or asymmetric stretching of carboxylate and C-O group or to Zn-OH bending vibrations, respectively [4]. The presence of carboxyl and amino functional groups existed in the extract could act as reducing and stabilizing agents for the biosynthesis of ZnO NPs. But, on the ZnOS_ME and ZnOS_AE spectra, several peaks were dramatically reduced or disappeared (at 1085; 1038; 928; 855; 772 and 718 cm^{-1}) and new peaks (at 2300-2400 cm^{-1}) were formed compare with ZnO_ME and ZnO_AE; the characteristic absorption peaks are at 1416; 1558 and 1646 cm^{-1} belong to

C=C stretching or N-H bending or COO^- stretching. In the process of preparing ZnO by sol-gel method, Zn^{2+} ion interacts with the extract to form a metal-organic complex, and then calcined to 450 ^oC for 1 hour. The calcination has only partially burned the organic substances to form products which consists of ZnO and some organic substances.

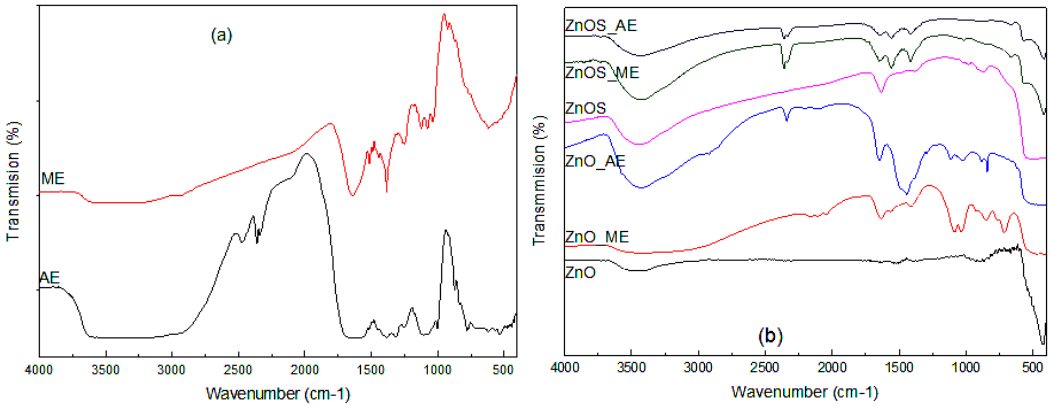

Fig. 3. *FTIR spectrums of xerogel of Piper chaudocanum leaves extract (a) and synthesized ZnO NPs (b).*

Morphology study

Figure 4 shows FESEM and TEM images of ZnO NPs. The results showed that ZnO in the absence of extract were not uniform in size and adhered together to form a tree (Fig. 4a).

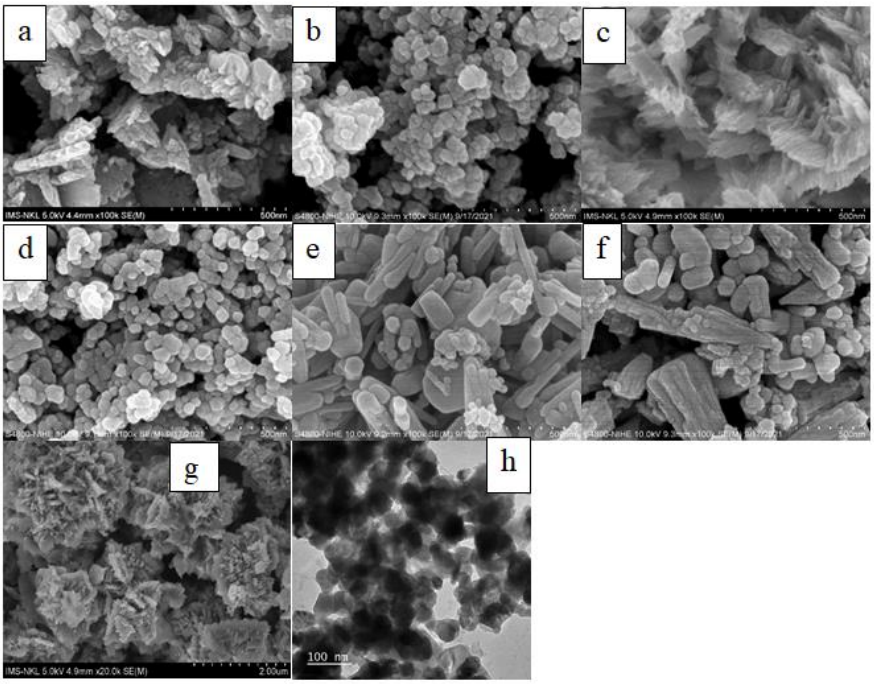

Fig. 4. *FESEM and TEM images of synthesized ZnO NPs. a) ZnO; b) ZnO_ME; c) ZnO_AE; d) ZnOS; e)ZnOS_ME; f) ZnOS_AE at 100K magnification; g) ZnO_ME at 20K magnification and h) TEM image of ZnO_ME.*

In the presence of the mixed extract (Fig. 4b), the ZnO_ME NPs adhesion was significantly reduced, and the particles had more uniform size and shape. However, in the

 ISBN:

presence of the aqueous extract (Fig. 4c, 4g), the ZnO_AE NPs did not clearly see the grain boundaries, but rather adhered to thin, narrow foliage and arranged in the form of flowers. While the ZnOS NPs synthesized by the sol-gel method in the presence of oxalic acid (Fig. 4d) are quite homogeneous, the hexagonal structure and size are larger than that of the ZnO. However, in the presence of the extract, the individual ZnOS_ME NPs sizes decreased, but there was a fairly uniform stick formation (mixed extract, Fig. 4e) or alternating rod and granular forms (aqueous extract, Fig. 4f). The TEM image of the ZnO_ME sample (Fig. 4h) shows that, when dispersed in water, the particles are surrounded by a translucent shell with nuclei around 20-25 nm. This coating is the organic compounds in the extract that adsorb or form complexes with ZnO NPs.

3.3. Antibacterial ability

The antibacterial activity of prepared ZnO NPs was examined with agar well diffusion method against *SA* and *PA* bacterials. The results are shown in Figure 5 and Table 1.

Table 1. *The zones of inhibition produced by 100 μg/ml ZnO NPs in SA and PA bacterial strains by using agar well diffusion assay.*

Name of bacterial	Zone of inhibition (mm)*					
	ZnO	ZnO_ME	ZnO-AE	ZnOS	ZnOS-ME	ZnOS-AE
SA	28	30	31	16	6	20
PA	27	30	35	15	8	22

**Inhibition zone excludes diameter of the disc (8 mm).*

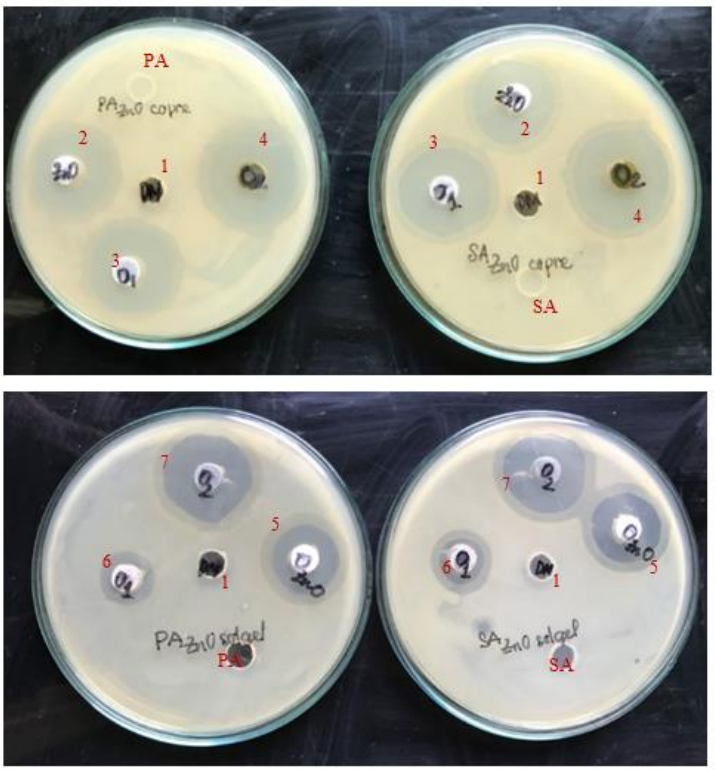

Fig. 5. *Antibacterial activity of 100 μg/ml ZnO NPs against Pseudomonas aeruginosa and Staphylococcus aureus. (1. DMSO; 2. ZnO; 3. ZnO_ME; 4. ZnO_AE; 5. ZnO_S; 6. ZnO_S-ME; 7. ZnO_AE).*

The results show that ZnO NPs synthesized by sol-gel method have generally lower antibacterial effect than ZnO NPs synthesized by co-precipitation method. Antibacterial activity of ZnO NPs depends directly on shape, size and surface-to-mass ratio [13], and ZnO CP were coated or complexed by many organic components from the extract to enhance the antibacterial ability of the material. On the basis of this result, ZnO_ME and ZnO_AE NPs were evaluated the IC_{50} on five types of bacteria (including Gram positive bacteria *Staphylococcus aureus (SA)*, Gram negative bacteria*: Citrobacter freundii (CF), Serratia marcescens (SM), Escherichia Coli (E. Coli)* and *Pseudomonas aeruginosa* (*PA*)). The results are presented in Table 2.

Table 2. *IC_{50} value of ZnO_AE and ZnO_ME.*

Materials	IC_{50} (μg/ml)				
	SA	**CF**	**SM**	**E.Coli**	**PA**
ZnO_AE	61.77	78.03	67.34	67.17	78.93
ZnO_ME	91.66	96.72	83.64	85.68	91.10

Similar to the agar well diffusion method, ZnO_AE's inhibitory effect on all five bacteria were slightly higher than that of ZnO_ME. This in addition to measuring the morphological characteristics of the material, is due to the organic components present in the material. As the results of the study on the chemical composition of the extracts were slightly different, the compounds entering the product structure ZnO_ME and ZnO_AE were slightly different, and created a significant difference in the material morphology. The results of this study show that the antibacterial effect of green synthesized ZnO NPs from *Piper chaudocanum* leaf extract is quite high compared to green synthetic ZnO NPs from some other plants [7,14,15].

IV. CONCLUSION

In this study, we have synthesized the first time the biosynthesis of ZnO nanoparticles using *Piper chaudocanum* leaf extract by co-precipitation and sol-gen methods. We confirmed the formation of ZnO nanoparticles from XRD, SEM, TEM and FTIR. The synthesized ZnO NPs were found to have a crystalline structure; the particle size ranges from 20 to 25 nm. The biosynthesized nanoparticles have strong antibacterial activity against Gram-negative *Pseudomonas aeruginosa* (PA) and Gram-positive *Staphylococcus aureus* (SA), in which ZnO CP NPs is better against PA and SA than ZnO S NPs; ZnO_AE NPs exhibited a better antibacterial inhibition than those of that ZnO_ME NPs. Finally, green synthesis of ZnO nanoparticles using plant materials is considered as a conventional and environmentally friendly method, compared with chemical and physical synthesis methods.

REFERENCES

[1] Kolodziejczak-Radzimska et al., Zinc oxide-from synthesis to application: A review, *Materials Basel*, 2014, **7**, 2833-2881.

 ISBN:

[2] Goktas S. & Goktas A., A comparative study on recent progress in efficient ZnO based nanocomposite and heterojunction photocatalysts: A review, *J. Alloys Compd.*, 2021, **863**, 158734.

[3] Boon C., et al., A review of ZnO nanoparticles as solar photocatalysts : Synthesis , mechanisms and applications, *Renew. Sustain. Energy Rev.*, 2018, **81**, 536-551.

[4] Motazedi R., Rahaiee S. & Zare M., Efficient biogenesis of ZnO nanoparticles using extracellular extract of Saccharomyces cerevisiae: Evaluation of photocatalytic, cytotoxic and other biological activities, *Bioorg. Chem.*, 2020, **101**, 103998.

[5] Jevapatarakul D., et al., Utilization of Cratoxylum formosum crude extract for synthesis of ZnO nanosheets: Characterization, biological activities and effects on gene expression of nonmelanoma skin cancer cell, *Biomed. Pharmacother.*, 2020, **130**, 110552.

[6] Bayrami A., Haghgooie S., Rahim P. S., Mohammadi A. F. & Habibi-Yangjeh A., Synergistic antidiabetic activity of ZnO nanoparticles encompassed by Urtica dioica extract, *Adv. Powder Technol.*, 2020, **31**, 2110-2118.

[7] Noohpisheh Z., Amiri H., Farhadi S. & Mohammadi-Gholami A., Green synthesis of Ag-ZnO nanocomposites using Trigonella foenum-graecum leaf extract and their antibacterial, antifungal, antioxidant and photocatalytic properties, *Spectrochim. Acta - Part A Mol. Biomol. Spectrosc.*, 2020, **240**, 118595.

[8] Soto-Robles C. A., et al., Study on the effect of the concentration of Hibiscus sabdariffa extract on the green synthesis of ZnO nanoparticles, *Results Phys.*, 2019, **15**, 102807.

[9] Ahmad W. & Kalra D., Green synthesis, characterization and anti microbial activities of ZnO nanoparticles using Euphorbia hirta leaf extract, *J. King Saud Univ. Sci.*, 2020, **32**, 2358-2364.

[10] Salehi B.. et al., Piper species: A comprehensive review on their phytochemistry, biological activities and applications, *Molecules*, 2019, **24**, 1364.

[11] Ali M., et al., Green synthesis and evaluation of n-type ZnO nanoparticles doped with plant extract for use as alternative antibacterials, *Appl. Nanosci.*, 2020, **10**, 3787-3803.

[12] Ruangtong J., T-Thienprasert J. & T-Thienprasert N. P., Green synthesized ZnO nanosheets from banana peel extract possess anti-bacterial activity and anti-cancer activity, *Mater. Today Commun.*, 2020, **24**, 101224.

[13] Muthuvel A., Jothibas M. & Manoharan C., Effect of chemically synthesis compared to biosynthesized ZnO-NPs using Solanum nigrum leaf extract and their photocatalytic, antibacterial and in-vitro antioxidant activity, *J. Environ. Chem. Eng.*, 2020, **8**(2), 103705 (2020).

[14] M. Khatami, et al., Applications of green synthesized Ag, ZnO and Ag/ZnO nanoparticles for making clinical antimicrobial wound-healing bandages, *Sustain. Chem. Pharm.*, 2018, **10**, 9-15.

[15] R. Alvarez-Chimal, V. I. García-Pérez, M. A. Álvarez-Pérez & J. A. Arenas-Alatorre, Green synthesis of ZnO nanoparticles using a Dysphania ambrosioides extract. Structural characterization and antibacterial properties, *Mater. Sci. Eng. C*, 2021, **118**, 111540.

TREATMENT OF PERIARTHRITIS OF THE SHOULDER BY THERAPEUTIC ULTRASOUND

Nguyen The Thuong[1*], Vo Thi Anh Tuyet[2]

[1]*Institute of Biomedical Physics, 109A Pasteur, Ben Nghe Ward, District 1, Ho Chi Minh City*

[2]*Faculty of Applied Science, Ho Chi Minh City University of Technology (HCMUT), 268 Ly Thuong Kiet Street, District 10, Ho Chi Minh City, Viet Nam*

*E-mail: *thethuong.nguyen@gmail.com*

Abstract. The periarthritis of the shoulder is a common disease that manifests as pain and limitation of movement of the shoulder joint. Due to damage to soft structures such as tendons, muscles, ligament, this disease greatly affects the activities and quality of life. Currently, the treatment of periarthritis of the shoulder often uses anti-inflammatory drugs, pain relievers mainly. However, this therapy often has side effects such as decreased body resistance, osteoporosis, stomach ulcers, making patients unable to use it regularly for a long time. In recent years, conservative treatment methods, in which physical therapy methods are increasingly interested, especially therapeutic ultrasound because of its effectiveness. The results of the study on patients with ultrasound showed that the pain was reduced, the range of motion of the shoulder joint and the patient's muscle strength were significantly improved.

Keywords: *Periarthritis of the shoulder, Pain, Ultrasound therapy.*

I. INTRODUCTION

The periarthritis of the shoulder is a very common disease that manifests as pain and limitation of movement of the shoulder joint. Due to damage to the soft structures surrounding the joint such as tendons, muscles, ligaments, and joint capsule, this disease has many important impacts to the functioning of the upper extremities [1]. The upper limb is the limb that performs most of the necessary movement, greatly affecting the quality of daily life, in which the shoulder joint is the joint with the widest range of motion compared to other joints in the body [2]. Due to this flexible, frequent, and continuous activity, the shoulder joint is often injured leading to inflammation that in medical terms or commonly known as periarthritis of the shoulder, tends to progress to the condition of the shoulder joint. Chronic shoulder pain is very persistent and difficult to treat. The detection and effective treatment of periarthritis of the shoulder joint is a matter of great practical significance.

Currently, the main method of the treatment of periarthritis of the shoulder is the use of anti-inflammatory drugs, pain relievers [3]. Therefore, there are often side effects such as decreased resistance of the body, osteoporosis, stomach ulcers, making patients unable to use it for a long time. Physiotherapy has the advantage of no side effects, direct pain relief, so it is very suitable for the treatment of shoulder periarthritis, in which ultrasound becomes the most common agent [4,5]. Ultrasound is defined as sound with a frequency of greater than 20 kHz. Generally, therapeutic ultrasound has a frequency of 0.7 and 3.3 MHz in order to maximize energy absorption at a depth of 2 to 5 cm. Ultrasound has a variety of biological effect. It increases the temperature of deep and superficial tissues and has a

 ISBN:

range of non-thermal effects. The thermal effect includes metabolic rate, reduction and control of pain and muscle spasm, alteration of nerve conduction velocity, increase circulation and increased soft tissue extensibility. The non-thermal effect is result of the mechanical events, including cavitation, microstreaming, and acoustic streaming. These both effects have been considered separately, and are used as component of the treatment of periarthritis of the shoulder. Many studies have shown that ultrasound can be more effective in controlling pain than treatment with other thermal agent [6,7]. Moreover, for people with shoulder arthritis, physical therapy combined with exercise, coordinated movement against muscle atrophy, and increased local circulation, reduces shoulder pain very well [8].

With the advantages of therapeutic ultrasound and exercise therapy, the combination of both therapies in the treatment of shoulder periarthritis is a work of great scientific and practical significance. Our study was to investigate the efficacy of both therapies for the treatment of patients with the periarthritis of the shoulder.

II. METHODS

This study was conducted at the Institute of Biomedical Physics in Ho Chi Minh City, consisted of 32 patients between 40-70 years of age. The criteria for inclusion in the study were: Shoulder pain of varying degrees; Limiting shoulder joint movement from little to much; Muscle atrophy, muscle spasticity or not. X-ray of the shoulder joint: Normal or with bone spurs, joint space narrowing, osteoporosis, bone thickening, calcium deposition. The criteria for exclusion were: tuberculosis progression, cancer, hemophilia, pregnancy, heart attack. The patients were questioned about their demographic characteristics and medical history. Documenting the initial pain scale, assessing muscle strength of shoulder and arm muscle groups, is critical in determining the efficacy of the treatment plan.

Pain: assessed according to VAS score, divided into 10 lines corresponding to 10 points, 0 line means no pain = 0 points. Line 10 most intense pain = 10 points (Patient has constant pain that makes it difficult to sleep at night).

Pain	Point	Grade
No	0	0
Mild	1-4	1
Average	5-7	2
Severe	8-10	3

Assess muscle strength of shoulder the on the 5 grades:

- Grade 0: when stimulated without any trace of muscle contraction, the muscle is completely paralyzed.
- Grade 1: muscle contraction is very weak, can feel the contraction of muscle tendons, but cannot perform the movement.

- Grade 2: muscle contraction realizes the full range of motion of the joint after removing all the weight of the limb.
- Grade 3: muscle contraction can perform the full range of activities and overcome the gravity of the limb.
- Grade 4: muscle contraction to perform the full range of activity, overcome the body's gravity and overcome moderate external resistance.
- Grade 5: muscle contraction to perform the full range of activities, overcome the body's gravity and overcome the strong resistance from the outside.

Overall assessment after treatment"

	Good	**Rather**	**Medium**	**Poor**
Muscle strength	Grade 4,5	Grade 2,3,4	Grade 2,3,4	Grade 0,1
Pain	Grade 0,1	Grade 1	Grade 2	Grade 3

The ultrasound was applied for 10 min per session with the continuous mode at 800 Hz frequency and 2.3 W/cm^2 intensity. After coating the skin with an aquasonic gel, US was delivered by moving the applicator over the anterior, superior, and posterior regions of the target joint in slow, overlapping strokes. The exercise program in 30 min consisted of split joint, slip joint, soft tissue massage, stretching, exercise resistance to movements with elastic bands, pulley.

III. RESULTS AND DISCUSSION

Demographic features of the patients are given in Tables 1, 2, 3, and 4. In our study, thirty-two patients were enrolled. Women often suffer from arthritis around the shoulder joint more than men. Elderly people are more likely to get arthritis around the shoulder joint more than young people. Patients often come for treatment when they have passed the chronic inflammatory stage. There is not much difference in the location of left or right lesions of shoulder periarthritis, and patients usually have one joint. Patients with shoulder periarthritis usually do not have lesions such as calcium deposits on conventional radiographs of the shoulder joint.

Table 1. *Classification by sex.*

Sex	No. Patient
Male	12
Female	20
Total	32

Table 2. *Classification by age.*

Age	Patient
41 – 50	2
51 – 60	17
> 60	13
Total	32

Table 3. *Classification by disease duration.*

Duration of disease	Patient
< 1 (months)	8
1 – 3 (months)	12
> 3(months)	12

Table 4. *Classification by shoulder position disease.*

Position of disease	Patient
Right shoulder	13
Left shoulder	14
Both	5

ISBN:

The effectiveness of treatment on patients is given in Table 5, 6, 7, and 8. In Table 5, the pain relief effect before and after the treatment is shown. Before the treatment, the patients at pain grande 2 and 3 are the majority, but after treatment, most patients only had mild pain symptoms (grade 1 and 0). The therapeutic effect is also shown in muscle strength. Table 6 shows that before treatment, the patient's muscle strength is weak and moderate (grade 2 and 3) but after the end of treatment, muscle strength is at rather and good level (grade 4 and 5). Most patients regain normal muscle strength. Table 7 shows specific values of changes in pain and muscle strength. The efficiency index for treatment is 81.14% for pain and 46.81% for muscle strength. Finally, Table 8 classifies the overall clinical efficacy; all patients are good level after treatment.

Table 5. *Pain classification table before and after treatment.*

Pain grade	Pre-treatment		Post-treatment		P- value
	Frequency (n =32)	%	Frequency (n = 32)	%	
0	0	0	4	12.5	<0.05
1	4	12.5	28	87.5	
2	12	37.5	0	0	
3	16	50	0	0	
Total	32	100	32	100	

Table 6. *Muscle strength classification before and after treatment.*

Muscle strength grade	Pre-treatment		Post-treatment		P- value
	Frequency (n =32)	%	Frequency (n =32)	%	
0	0	0	0	0	<0.05
1	0	0	0	0	
2	5	15.6	0	0	
3	20	62.5	0	0	
4	7	21.9	17	53.1	
5	0	0	15	46.9	
Total	32	100	32	100	

Table 7. *Comparison of pain and muscle strength values before and after treatment.*

	Pre-treatment		Post-treatment		P- value	Efficiency index (%)
	Mean	SD	Mean	SD		
Pain	7.13	1.88	1.34	0.83	0.000	81.14
Muscle strength	3.06	0.62	4.47	0.51	0.000	46.08

Table 8. *Overall assessment before and after treatment.*

Overall	Pre-treatment		Post-treatment		P- value
	Frequency (n =32)	%	Frequency (n =32)	%	
Good	1	3.1	32	100.0	<0.05
Rather	3	9.4	0	0	
Medium	13	40.6	0	0	
Poor	15	46.9	0	0	
Total	32	100	32	100	

IV. CONCLUSION

Ultrasound therapy combined with exercise therapy for patients with shoulder periarthritis is an effective treatment method, the patient's pain symptoms are reduced, the shoulder joint's range of motion and muscle strength are improved. The sooner the patient arrives for treatment, the shorter the treatment time will be and the better the treatment results will be compared to the late patient, the longer the treatment time, and often the more pain during the treatment, especially when it has reached the chronic stage. The duration of treatment for patients usually lasts only a maximum of one month. Patients with shoulder arthritis are quite common, including many professions, from self-employed workers, traders, to office workers, etc. Elderly people often have shoulder arthritis rather than the elderly. Young people; and often with muscle pain and weakness; this may be due to the aging of the musculoskeletal system is reduced; low mobility and prone to shoulder joint damage. This result shows that to effectively prevent shoulder arthritis, it is important to exercise to increase the range of motion of the shoulder joint every day, while also increasing flexibility and strength. Strength and endurance of the muscles around the shoulder.

ACKNOWLEDGMENTS. Thanks to Dr. Lai Hai Binh and medical assistants in the Institute of Biomedical Physics for their help in this study.

REFERENCES

[1] Dalton S. E., The shoulder Rheumatology, 3rd Ed. Toronto: Mosby, 2003, 615-630.

[2] Dias R., Cutts S., Massoud S., Frozen shoulder, *BMJ*, 2005, **331**, 1453-1456.

[3] Pajareya K., Chadchavalpanichaya N., Painmanakit S., et al., Effectiveness of physical therapy for patients with adhesive capsulitis: A randomized controlled trial, *J. Med. Assoc. Thai*, 2004, **87**, 473-480.

[4] Mao C. Y., Jaw W. C., Cheng H. C., Frozen shoulder: correlation between the response to physical therapy and follow-up shoulder arthrography. *Arch. Phys. Med. Rehabil*, 1997, **78**, 857-859.

[5] Gursel Y. K., Ulus Y., Bilgic A., et al., Adding ultrasound in the management of soft tissue disorders of the shoulder: A randomized placebo-controlled trial, *Phys. Ther.*, 2004, **84**, 336-343.

[6] Robertson V. J., Baker K. G., A review of therapeutic ultrasound: Effectiveness studies, *Phys. Ther.*, 2001, **81**, 1339-1350.

[7] Basford J. R., Therapeutic physical agents. In: Physical medicine and rehabilitation, Principles and practice, Philadelphia: Lippincott Williams & Wilkins, 2005, 251-270.

[8] Safoora E., Bijan F., Ehsan F., Arash B. G., Does ultrasound therapy add to the effects of exercise and mobilization in frozen shoulder? A pilot randomized double-blind clinical trial, *J. Bodyw. Mov. Ther.*, 2017, **21**, 781-787.

 ISBN:

POTENTIAL APPLICATION OF SPINAL MOUSE IDIAG M360 FOR EVALUATING SCOLIOSIS IN ADOLESCENTS

Nguyen Duc Tri[1], Huynh Quang Linh[1] and Nguyen The Thuong[2*]

[1]*Faculty of Applied Science, Ho Chi Minh City University of Technology (HCMUT), 268 Ly Thuong Kiet Street, District 10, Ho Chi Minh City, Viet Nam*

[2]*Institute of Biomedical Physics, 109A Pasteur, Ben Nghe Ward, District 1, Ho Chi Minh City, Viet Nam*

*E-mail: *thethuong.nguyen@gmail.com*

Abstract. Scoliosis is one of the most common spine disorders. Scoliosis usually causes back pain and muscular imbalance that affect the movement of the patient. The main diagnosis of scoliosis is using X-rays, but with the radiation exposure this method has a risk of causing cancer and shouldn't be used often on the same patient. This study aimed to introduce potential application of Spinal Mouse IDIAG M360 which is a radiation-free back scan device for evaluating scoliosis in adolescents. Spinal Mouse IDIAG M360 quantifies the curvature and mobility of the spine by gliding the device manually down the spine. In this study, 4 volunteered students had their backs scanned with scoliometer, Spinal Mouse IDIAG M360 and DIERS formetric 4D. The result showed that Spinal Mouse IDIAG M360 could be used as a potential device for evaluating scoliosis.

Keywords: *Scoliosis, Scoliometer, Spinal mouse, IDIAG M360, DIERS formetric 4D.*

I. INTRODUCTION

The spine is formed by 7 cervical vertebrae (C1 to C7), 12 thoracic vertebrae (T1 to T12), 5 lumbar vertebrae (L1 to L5), 5 fused sacral vertebrae which form the sacrum (S1 to S5) and 3 to 5 coccygeal vertebrae. Between 2 vertebrae is the intervertebral disc acting like a shock-absorbing system. The spine connects the head and the body, a signal from brain is transmitted to nerves in limbs through spinal cord which lies along the spine so that we can stand, lie down, run and do more motions. The spine plays an important role in the movements of our body and any deformity of the spine will affect our movements.

Scoliosis is one of the most common spine disorders. In frontal plane, patient with scoliosis has a spine that curves to the side, it usually has "S" or "C" shape. The cause of scoliosis can be genetic factors, some diseases like Duchenne muscular dystrophy (DMD), Marfan syndrome or it can be from lifestyle. Scoliosis usually causes back pain and muscular imbalance that affect the movement of the patient [1,2]. It can affect the respiratory system if patient with scoliosis has a large curve in thoracic spine [3]. Due to the constant back pain, patient's life quality will also be reduced.

The main diagnosis of scoliosis is using X-rays. By using X-rays method, we can see the shape of the curve to point out the vertebra which roles the apex of the curve, the upper-lower most tilted vertebrae and from that we can calculate the Cobb angle. Cobb angle is a measurement used to quantify the magnitude of the spinal curvature of scoliosis patient. Cobb angle below around 20° is considered to be mild while above around 45° can

be considered to be severe. Although X-rays method is mainly used to diagnose scoliosis, the radiation exposure of this method has a risk of causing cancer [4,5]. Children and adolescents have chance to have idiopathic scoliosis so X-rays method shouldn't be used often on the same patient to monitor scoliosis treatment.

This study aimed to introduce potential application of Spinal Mouse IDIAG M360 for evaluating scoliosis, especially in adolescents. Spinal Mouse IDIAG M360 is a radiation-free back scan device made in Switzerland. By gliding the device manually down the spine, the result will be generated, including the shape and the mobility of the spine, in frontal plane or sagittal plane. The device has 2 wheels which track the spine on the surface of the back. The sensors inside will record the shape and generate the result. Because Spinal Mouse IDIAG M360 is small and doesn't have radiation exposure, it can be used often and conveniently in scoliosis treatment to monitor the progress of patient's spine.

Fig. 1. *Spinal Mouse IDIAG M360 [6].*

II. METHODS

The measurements in this study were conducted in MTT REHA Clinic in Ho Chi Minh City. Four students volunteered to have their backs scanned. All the volunteers were male (between the ages of 21 and 22). Four subjects participated in the measurements didn't have any spine injury and were in good health condition. Subject's back was scanned with a scoliometer, Spinal Mouse IDIAG M360 and DIERS formetric 4D. The scoliometer used in this study was ScolioLife™ - a scoliometer app on Android [7]. DIERS formetric 4D (Germany) is an optical back scanning method using line grid light. DIERS formetric 4D used light projector to cast line grid on the surface of the back which was recorded by a camera, the software analyzed the curvature and generated a 3D model of the spine [8].

Each subject's back was scanned with scoliometer, Spinal Mouse IDIAG M360 and DIERS formetric 4D. In preparation for the measurements, all subjects were asked to remove upper clothes and shoes. With scoliometer, patient had to be in Adam's forward bend test position. We recorded the apical values of scoliometer in the thoracic and lumbar spine area and used these values to calculate predicted Cobb angles using Ma et al. formulas [9]:

$$TC = 2.6\ TI - 1.4\ LI\ (r = 0.931) \quad (1)$$

 ISBN:

$$LC = -1.5\ TI + 2.0\ LI\ (r = 0.874) \quad (2)$$

where, TC: predicted thoracic Cobb angle; LC: predicted lumbar Cobb angle; TI: apical thoracic scoliometer value; LI: apical lumbar scoliometer value; r: correlation value.

With Spinal Mouse IDIAG M360, the spine was recorded in sagittal plane and frontal plane by gliding down the device from cervical vertebra C7 to sacral vertebra S1 along the line of the spine. In sagittal plane, subject stood in 3 positions: upright, flexed, extended. Each position was measured 1 time. In frontal plane, subject had to stand upright, incline to the left and incline to the right. Each position was measured 1 time.

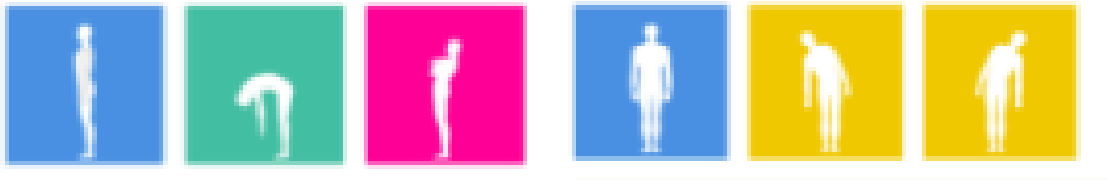

Fig. 2. *Six positions for measuring using Spinal Mouse IDIAG M360 [6].*

With DIERS formetric 4D, all subjects had to remove all clothes except underwear and only stood upright. The software analyzed the images recorded by camera and generated result. In this study, we only took 2 parameters from DIERS formetric 4D: thoracic kyphosis angle and lumbar lordosis angle. We compared Cobb angles between scoliometer (using formulas (1) and (2)) and Spinal Mouse IDIAG M360 and compared thoracic kyphosis angle, lumbar lordosis angle between Spinal Mouse IDIAG M360 and DIERS formetric 4D. Statistical analysis included t-Test: Two-Sample Assuming Unequal Variances and t-Test: Two-Sample Assuming Equal Variances provided by Microsoft Excel 2013.

III. RESULTS AND DISCUSSION

In the result of Spinal Mouse IDIAG M360, values showed in degree. Black colored values were in normative reference range while red colored values were out of normative range. The reference data matching each gender and age group was from the Institute for Learning in Motion - Health Promotion in Vienna, Austria and the Ludwig Maximilian University in Munich, Germany [6]. In sagittal plane, the result had 3 positions of the spine; each had 3 parameters (in regional angle view mode): thoracic kyphosis angle (from T1 to T12), lumbar lordosis angle (from T12 to S1) and sacral angle. In frontal plane, the result also had 3 positions of the spine, each had 3 parameters (in regional angle view mode): thoracic Cobb angle (T1 to T12), lumbar Cobb angle (T12 to S1) and inclination angle of sacrum.

We compared the Cobb angles between scoliometer and Spinal Mouse IDIAG M360. By using t-Test: Two-Sample Assuming Unequal Variances, we had the following Table 1.

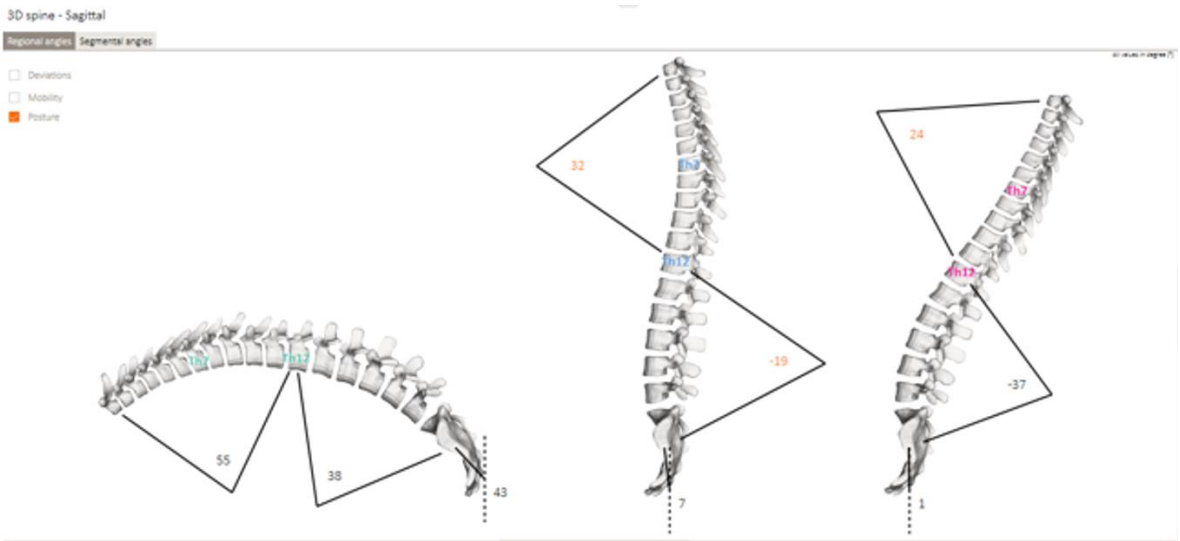

Fig. 3. *The result of Spinal Mouse IDIAG M360 in sagittal plane.*

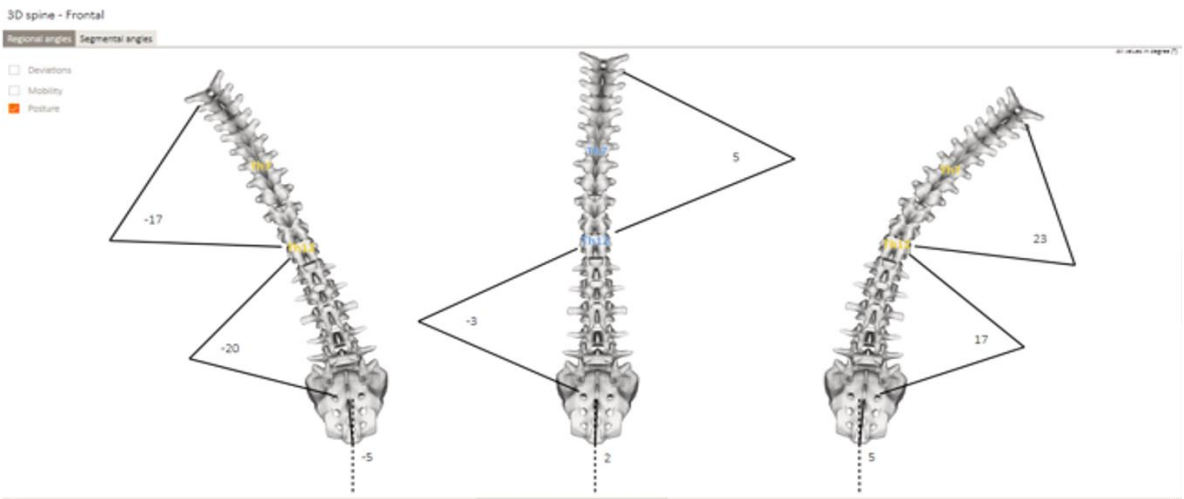

Fig. 4. *The result of Spinal Mouse IDIAG M360 in frontal plane.*

Table 1. *Comparison between scoliometer and Spinal Mouse IDIAG M360.*

Cobb angles between Scoliometer and IDIAG M360				
	Scoliometer Mean (SD)	IDIAG M360 Mean (SD)	p value	Confidence interval 95% alpha = 0.05
Thoracic Cobb angle (°)	12.9 (10.46)	3 (1.83)	0.1591 > 0.05	
Lumbar Cobb angle (°)	9.5 (13.42)	3.75 (1.71)	0.4578 > 0.05	

The means of scoliometer were greater than the means of IDIAG M360 because there was 1 subject who had trunk asymmetry on the surface of the back (vertebral rotation around 4° using DIERS formetric 4D result) that made the scoliometer value high. This led to greater predicted Cobb angle compared to other 3 subjects. But using Spinal Mouse IDIAG M360 result, there was no sign of high Cobb angle. Both p values > 0.05 so we said that there was no difference in Cobb angles between scoliometer and Spinal Mouse IDIAG M360.

 ISBN:

In the following Table 2, we had the comparison of thoracic kyphosis angle, lumbar lordosis angle between DIERS formetric 4D and Spinal Mouse IDIAG M360.

Table 2. *Comparison between DIERS formetric 4D and Spinal Mouse IDIAG M360.*

Thoracic kyphosis and lumbar lordosis angles between DIERS formetric 4D and IDIAG M360				
	DIERS 4D Mean (SD)	IDIAG M360 Mean (SD)	p value	Confidence interval 95% alpha = 0.05
Thoracic kyphosis angle (°)	53 (6.16)	40.25 (5.68)	0.0227 < 0.05	
Lumbar lordosis angle (°)	31.75 (9.43)	25.25 (5.19)	0.2725 > 0.05	

By using t-Test: Two-Sample Assuming Equal Variances, we saw that in thoracic kyphosis angle, p value < 0.05 and in lumbar lordosis angle, p value > 0.05. We said that there was no difference in lumbar lordosis angle measured between DIERS formetric 4D and Spinal Mouse IDIAG M360 but there was a difference in thoracic kyphosis angle measured between 2 methods.

In this study, the number of subjects was small (4 subjects) so the statistical significance might be weak. While measuring with scoliometer and Spinal Mouse IDIAG M360, any factors (shaking hand, false landmarks,…) coming from the experimenters could cause errors.

IV. CONCLUSION

The results in this study might show weak statistical significance due to the small number of subjects but we can see the potential application of Spinal Mouse IDIAG M360 in evaluating Cobb angle and posture of the spine in different positions. Beside posture of the spine, it can also provide information about mobility of the spine when changing position. Spinal Mouse IDIAG M360 will have advantages in clinical use as it has no radiation exposure and can be used often on the same patient, especially children and adolescents with scoliosis who are under treatment.

REFERENCES

[1] McIntire K. L., Asher M. A., Burton D. C., & Liu W., Trunk rotational strength asymmetry in adolescents with idiopathic scoliosis: an observational study, *Scoliosis*, 2007, **2**, 9.

[2] Park J. H., Noh S. C., Jang H. S., Yu W. J., Park M. K., Choi H. H., The Study of Correlation between Foot-pressure Distribution and Scoliosis. In: Lim C.T., Goh J. C. H. (Eds.), *13th International Conference on Biomedical Engineering. IFMBE Proceedings*, Vol. **23**, Springer, Berlin, Heidelberg, 2009.

[3] Koumbourlis Anastassios, Scoliosis and the respiratory system, *Paediatric Respiratory Reviews*, 2006, **7**, 152-160.

[4] Linet M. S., Slovis T. L., Miller D. L., Kleinerman R., Lee C., Rajaraman P., & Berrington de Gonzalez A., Cancer risks associated with external radiation from diagnostic imaging procedures, *CA: A Cancer Journal for Clinicians*, 2012, **62**(2), 75-100.

[5] Ron E., Cancer risks from medical radiation, *Health physics*, 2003, **85**(1), 47-59.

[6] IDIAG M360 - Radiation-free analysis of the spine. *https://www.idiag.ch/en/idiag-m360-en/*

[7] Scoliometer App by ScolioLife™. *https://scoliolife.com/en_IN/scoliometer/*

[8] DIERS formetric 4D - Spine & Posture Analysis. *https://diers.eu/en/products/spine-posture-analysis/diers-formetric-4d/*

[9] Ma, H. H., Tai, C. L., Chen, L. H., Niu, C. C., Chen, W. J., & Lai, P. L., Application of two-parameter scoliometer values for predicting scoliotic Cobb angle, *Biomedical engineering online*, 2017, **16**(1), 136.

 ISBN:

DEVELOPMENT OF A LOW-TEMPERATURE HYDROGEN PEROXIDE PLASMA STERILIZER

Chu Thi Minh Hoa*, Pham Trung Kien, Nguyen Minh Tan, Doan Thi Thu Thuy, Nguyen Tuan Anh

Center of Laser Technology, National Centre for Technological Progress, C6 Thanh Xuan Bac, Thanh Xuan, Hanoi, Vietnam

*E-mail: *ctminhhoa@gmail.com*

Abstract. Most medical and surgical devices used in healthcare facilities are required to sterilize before use. Among medical devices, many devices are not suitable for heat, moisture, or chemical sterilizations, then low-temperature sterilizations are considered. Recently, hydrogen-peroxide gas plasma technologies are developed and used to sterilize medical devices. The sterilization almost destroys all microorganisms on the surface of an article or in a fluid to prevent disease transmission, based on the effect of the high oxidation of H_2O_2, UV radiation appearing during the plasma process, and the complex biological chain reaction in tissues activated by plasma. This paper presents the research and development of a low-temperature hydrogen peroxide plasma sterilizer. The device is programmed with a cycle sterilizing process that includes four fundamental steps: (i) Vacuum pumping; (ii) Pre-plasma; (iii) Diffuse; (iv) Venting and end of the cycle. Once the program is called, the cycle sterilizing process is activated. The H_2O_2 gas pressure inside sterilizing chamber is changed in the range of 600 Pa to 108000 Pa according to the sterilizing steps. Some medical articles such as rigid endoscopes, flexible endoscopes, endoscopic instruments, metal instruments,… are used as samples to be sterilized. Self-contained biological indicators (SCBIs) model VH_2O_2 of gke Steri-Record, GmbH company are used to monitor the sterilizing process. The obtained results show that the final visual of the spore growth is recorded in 24 hours (incubation temperature is in the range 55 to 60 ^oC) and that the articles are totally sterilized: the purple color of the indicators is unchanged.

Keywords: *Low-temperature plasma sterilizations, Self-contained biological indicators.*

I. INTRODUCTION

In many health care facilities, surgical procedures including invasive medical procedures such as endoscopic surgeries are performed almost every day. The failure to properly sterilize equipment leads to infection or the risk of pathogen transmission. Thus, medical devices that have contact with sterile body tissues should be sterilized before use because any microbial contamination could result in disease transmission.

Generally speaking, sterilization is a process of destroying or eliminating all forms of microbial life by physical or chemical methods. Steam under pressure and dry heat are the usual sterilizing agents. If medical devices are heat or moisture resistant, these agents are recommended because it has the largest margin of safety due to their high reliability and consistency. However, heat or moisture-sensitive medical devices require the use of low-temperature sterilization technology. As a result, the agents such as EtO gas, liquid chemicals, peracetic acid, hydrogen peroxide gas plasma are used. EtO Gas, liquid chemicals, or peracetic acid have high effectiveness with chemical-resistant devices but

they are not suitable with chemical-sensitive devices. In these cases, hydrogen peroxide gas plasma is the solution. In other words, hydrogen peroxide (H_2O_2) sterilizations (also called plasma sterilization processes) are the low-temperature sterilization process that is alternatively used to ethylene oxide, formaldehyde, and radiation sterilization processes.

Hydrogen peroxide gas plasma sterilization has many advantages in comparison with other methods [1]: (i) safe for the environment; (ii) easy disposal of the sterilizing agent hydrogen peroxide at the end of the sterilization process and leaves no toxic residuals; (iii) short sterilization time (cycle time varies in 28 - 75 minutes) and no aeration necessary; (iv) can be used for heat and moisture-sensitive items; (v) low temperature (<60 °C) in the sterilization chamber, thus there is no heat effect to the sterilized items; (vi) simple to operate. In brief, it is compatible with most medical devices. Nevertheless, this process also has disadvantages: (i) the limitation of the penetration characteristics of hollow devices, thus is less suitable to sterilize long plastic tubes; (ii) cellulose (paper), linens, and liquids cannot be processed; (iii) requires synthetic packaging (polypropylene wraps, polyolefin pouches) and special container tray.

In the late 1980s, the first hydrogen peroxide gas plasma system for sterilization of medical devices was developed. An electrical field activated by radio frequencies created gas plasma.

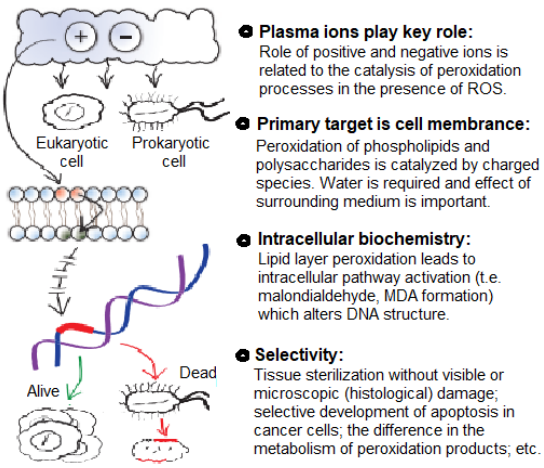

a) The key role in plasma-cell interaction [2].

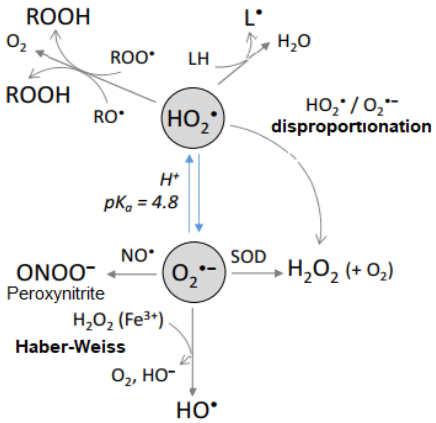

b) Chemical reactions of the superoxide and the perhydroxyl radicals [3].

Fig. 1. *The key role and chemical reactions on plasma interaction with biological organisms.*

The key role in plasma-cell interaction is played by both positive and negative ions and is a chemical rather than a physical phenomenon. Ions catalyze peroxidation processes both inside and outside of the biological organism with the presence of oxygen where Reactive Oxygen Species (ROS) play a crucial intermediate role [2].

In hydrogen peroxide gas plasma, the gas molecule is excited to produce charged particles. As a result, many free radicals such as superoxide anion (O_2•-), hydroxyl radical (HO•), and hydroperoxyl also called hydrogen superoxide (HO_2•) are created. These free radicals are ROS that interacts with essential cell components (e.g., enzymes, nucleic acids) and disrupts the metabolism of microorganisms. Moreover, gas plasma also produces UV light that contributes to the antimicrobial effects [3].

 ISBN:

II. DEVELOPMENT OF THE DEVICE

The Blog diagram of the low-temperature hydrogen peroxide plasma sterilizer is shown in Fig. 2.

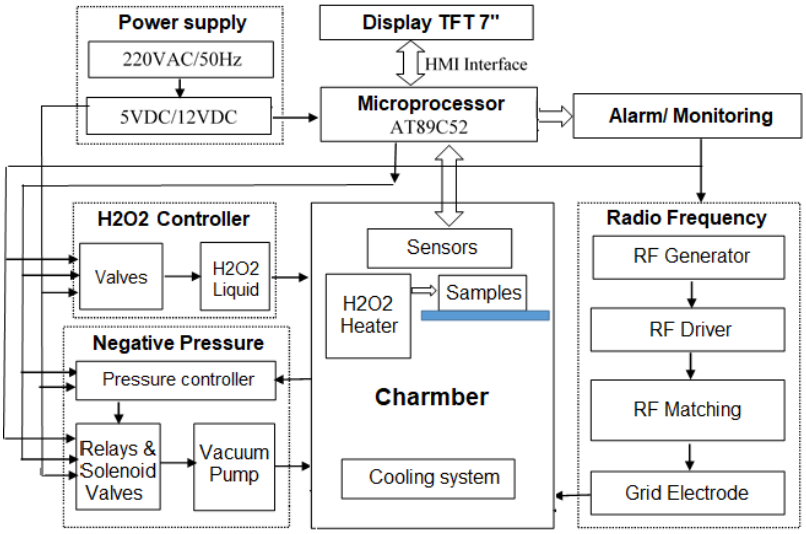

Fig. 2. *Blog diagram of the low-temperature hydrogen peroxide plasma sterilizer.*

The H_2O_2 vapor is created from H_2O_2 liquid (60%) by the H_2O_2 Heater, then is sent to the chamber, where it is converted into a plasma state under the effect of an electrical field activated by radio frequencies.

A cycle sterilizing process includes four basic steps:

- Vacuum pumping: The inside of the sterilizing chamber is pumped to a low vacuum by the Negative Pressure module.
- Pre-plasma: Before sterilizing, the inside of the chamber and the samples that are needed to sterilize must be cleaned, thus, the pre-plasma is required.
- Diffuse: In order to deeply sterilize all the items, the H_2O_2 gas is distributed anywhere in the chamber. In other words, the pressure inside the sterilizing chamber is pumped to negative pressure.
- Venting and end of the cycle: After completing the sterilizing process, the inside of the chamber should return to atmospheric pressure, be ready for the next sterilization.

III. RESULTS AND DISCUSSION

The low-temperature hydrogen peroxide plasma sterilizer is designed and developed following the standards and functionalities of the sterilizing device Model 4050T, Hanshin Medical Co. Ltd, Korea. The image of the system is shown in Fig. 3.

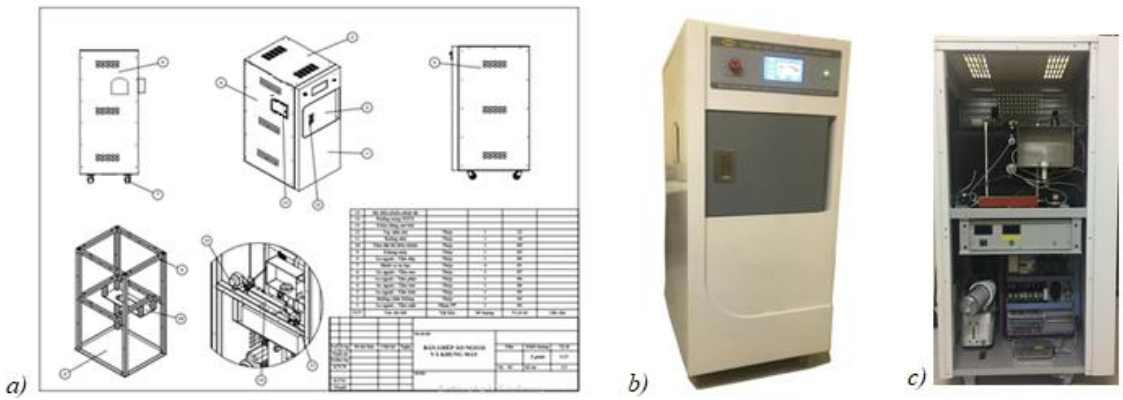

Fig. 3. *Images of the developed low-temperature hydrogen peroxide plasma sterilizer: a) Mechanical drawings; b) The outside image; c) The arrangement inside the device.*

After starting sterilizing procedure, parameters such as the pressure, the running time of each running step, the workflow of the sterilizing process are automatically displayed on the screen.

- **RF signals and the plasma created inside the chamber:**

Plasma inside the chamber is created by the effect of an electrical field activated by radio frequencies 13.56 MHz (300 Vpp, 50% Duty Cycle - Fig. 4).

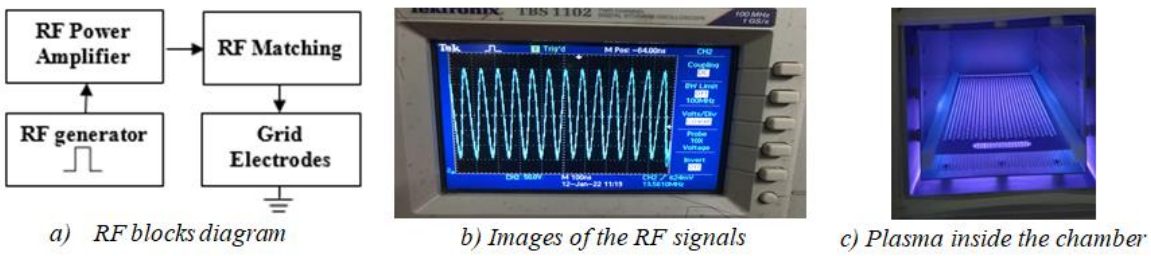

Fig. 4. *H_2O_2 gas plasma created by RF signals.*

The obtained results show that the plasma is rather evenly distributed inside the sterilization chamber.

- **Pressure measurement inside the chamber:**

The pressure inside the chamber is monitored by the pressure sensor (sensor BFY-1103). Moreover, the pressure of each running step is correspondingly converted into voltage signals. Thus, the pressure inside the chamber can be measured by a multimeter via voltages. The obtained pressure measurement is shown in Table 1.

Table 1. *Sensor output voltages according to the pressure of the Oxygen Tank.*

No.	Time (min)	Pressure (Pa)	Voltage (V)	No.	Time (min)	Pressure (Pa)	Voltage (V)
1	1	107832	5.38	21	35	33769	1.69
2	3	107832	5.39	19	37	107915	5.39
3	5	107832	5.38	23	39	5966	0.29
4	7	107832	5.38	24	41	758	0.04

 ISBN:

5	9	107832	5.39	25	43	808	0.04
6	11	107832	5.38	26	45	624	0.03
7	13	107832	5.38	27	47	703	0.03
8	15	107832	5.38	28	49	32771	1.64
9	17	49014	2.45	29	51	107923	5.39
10	19	24018	1.2	30	53	39670	1.98
11	21	107812	5.39	31	55	960	0.04
12	23	36655	1.8	32	57	602	0.03
13	25	1152	0.06	33	59	718	0.03
14	27	656	0,03	34	61	671	0.03
15	29	750	0.04	35	63	768	0.04
16	31	29656	1.48	36	65	49016	2.45
17	33	31472	1,57	37	67	108013	5.39

The obtained results show that the H_2O_2 gas pressure inside sterilizing chamber is changed in the range of 600 bar to 108000 bar according to the sterilizing steps (Fig. 5).

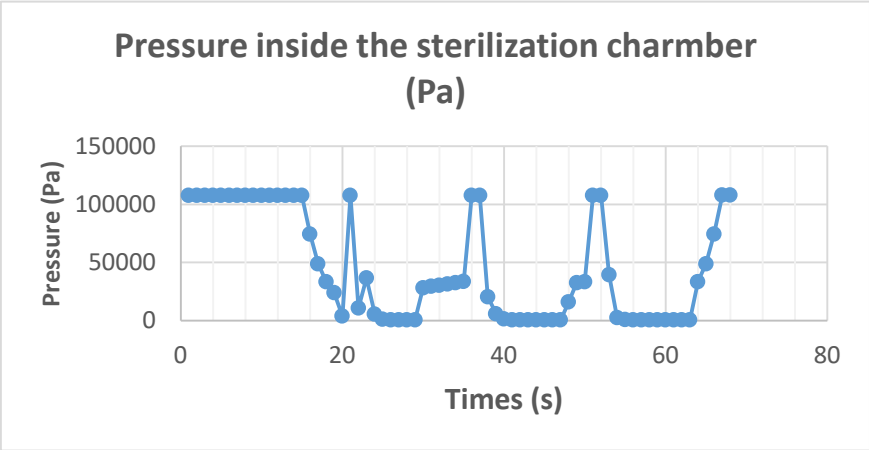

Fig. 5. *Changing of the H_2O_2 gas pressure inside the sterilization chamber.*

- **Measurement of the efficacy of H_2O_2 sterilization processes:**

  - **Preparation:**

The experiment was carried out by five steps: (1) sample cleaning; (2) sample wrapping with Self-Contained Biological Indicators (SCBIs); (3) sample sterilization; (4) SCBIs incubation; (5) result evaluation.

In order to evaluate the efficacy of the H_2O_2 sterilization processes, SCBIs are usually used. SCBIs contain bacterial spores sealed in a glass ampoule within a vented plastic vial with a pH indicator. The color-changing of the pH indicator indicates the presence of the spore growth: unchanged color means no spore growth and there is the spore growth when the color changed.

SCBI model VH_2O_2 of gke Steri-Record GmbH, Germany (purple color) was used to monitor the sterilizing process. The sterilized samples include rigid endoscopes, flexible endoscopes, endoscopic instruments, medical scissors (Fig. 6).

Fig. 6. *Samples are cleaned and wrapped before being sterilized and being evaluated by SCBIs.*

○**Results and discussion:**

For the best sterilization effect, it is required to clean the samples before carrying out the sterilization process. The samples were cleaned and packaged together with the VH2O2 SCBIs in a bag made of medical paper specialized for sterilization. The sterilizing process lasted 60 minutes. After that, the SCBIs were incubated within 24 hours at the incubation temperature of 60^0C. The efficacy of the sterilization was evaluated by observing the indicators of the SCBIs (Fig. 7).

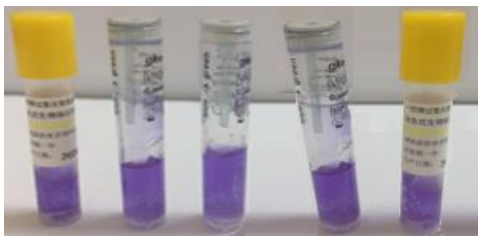

a) SCBIs before being incubated (3 items were packaged and sterilized together with the samples, 2 items were unsterilized and used as the reference).

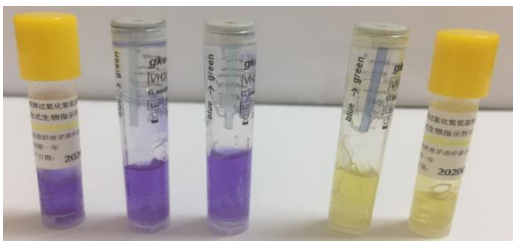

b) SCBIs after being incubated (3 items that were sterilized together with the samples unchanged the color, 2 referent items changed to yellow color).

Fig. 7. *The efficacy of the H_2O_2 sterilization process is monitored by SCBI indicators.*

The final visual of the spore growth was recorded. The obtained results show that all samples were sterilized: the original purple color of the indicators that the SCBIs were packaged together with sterilized samples remains unchanged while the referent indicators changed to yellow color.

IV. CONCLUSION

A low-temperature hydrogen peroxide plasma sterilizer has been made on the principle of using a 13.56 MHz RF generator to create H_2O_2 gas plasma. Many free radicals including O_2•-, HO•, HO_2•, and UV light are produced to interact with essential

 ISBN:

cell components, disrupt the metabolism of microorganisms, sterilize medical devices. The sterilization process includes three steps: Sample cleaning, Sample wrapping, and Sample sterilization. The sterilizing cycle process undergoes four basic steps: Vacuum pumping, Pre-plasma, Diffuse, and Venting with the pressure inside the chamber changing from 600 Pa to 108000 Pa. The obtained result with the sterilized samples shows the efficacy of the H_2O_2 gas plasma sterilization, laying the foundation for developing a H_2O_2 gas plasma sterilizer in the future.

REFERENCES

[1] William A. Rutala, David J. Weber, Robert A. Weinstein, Jane D. Siegel, Michele L. Pearson, Raymond Y.W. Chinn, Alfred DeMaria, Jr, James T. Lee, William A. Rutala, W. E. Scheckler, B. H. Stover, M. A. Underwood, Guideline for Disinfection and Sterilization in Healthcare Facilities 2008, Updated 2019, https://www.researchgate.net/publication/301684049.

[2] Fabrice Collin, Chemical basis of reactive oxygen species reactivity and iInvolvement in neurodegenerative diseases, *Int. J. Mol. Sci., 2019,* **20(**10), 1-17.

[3] Danil Dobrynin1, Gregory Fridman, Gary Friedman1, and Alexander Fridman, Physical and biological mechanisms of direct plasma interaction with living tissue, *New Journal of Physics,* 2009, **11**, 115020.

DEVELOPMENT OF AN EXTRACORPOREAL SHOCK WAVE THERAPY MODULE USING PNEUMATIC TECHNIQUE

Doan Thi Thu Thuy*, Chu Thi Minh Hoa, Pham Trung Kien, Nguyen Minh Tan, Nguyen Tuan Anh

Center of Laser Technology, National Centre for Technological Progress, C6 Thanh Xuan Bac, Thanh Xuan, Hanoi, Vietnam

*E-mail: doanthuthuy.xuantung2013@gmail.com

Abstract. Shock waves have been used in medical applications since the 1980s. The effect of the shock waves on different tissues (lung, fat, kidney, muscle, bone, kidney stone,...) has also been recorded in three broad categories: Destruction of tissue, Healing the wound, and Decrease of pain, depends on the energy content: energy at low, medium, and high levels. Overall, there are two fundamentally different types of shock waves: (i) Non-Focused also called Radial, Dispersive, or Soft Shock Waves; (ii) Focused or Hard Shock Waves. Soft Shock Waves are related to Extracorporeal Shock Wave Therapy (ESWT) using in orthopedics, while Hard Shock Waves are often referred to as Extracorporeal Shock Wave Lithotripsy (ESWL) using in urology. In both techniques, the shock waves are generated outside the patient's body and focused on the target indicated: the urolith with ESWL and the orthopedic with ESWT. This paper presents the research and development of an Extracorporeal Shock Wave Therapy Module using air-compressed techniques to create shock waves. The energy levels of 0.5 - 8 Bar, stepping at 0.5 Bar and the pulse frequencies of 2 - 21 Hz are recorded.

Keywords: *Extracorporeal shock wave therapy, Pneumatic shock wave*

I. INTRODUCTION

Shock waves have been used in medicine for a long time: in 1985, the first extracorporeal shock wave lithotripsy treatment of a gallbladder stone was carried out. In the 1990s, the application of extracorporeal shock wave therapy in orthopedic and traumatology was developed (therapy on calcific tendinitis, the nonoperative treatment on epicondylitis, tendons, ligaments, bone alterations). Today with the technological advancements in medical shock waves, the shock waves clinical applications become popular not only in the field of destruction of tissue, but also in healing the wound, decrease of pain, tissue regeneration, functional restoration. The effect of the shock waves on different tissues (lung, fat, muscle, bone, kidney stone,...) has been recorded [1-4].

Theoretically, shock waves are the result of a sudden release of chemical, electrical, nuclear, or mechanical energy, characterized by an abrupt change in pressure, temperature, and density of the medium. In medical applications, shock waves are sudden changes in pressure generated outside the patient's body, rapidly propagated in 3-dimensional space and focused on the target indicated. There are two fundamentally different types of shock waves [4]:

 ISBN:

i) Non-Focused also called Radial, Dispersive or Soft shock waves are used in orthopedics with the related techniques are known as Extracorporeal Shock Wave Therapy (ESWT);

ii) Focused or Hard shock waves are referred to as Extracorporeal Shock Wave Lithotripsy (ESWL) using in urology.

A typical shock wave is illustrated in Fig. 1.

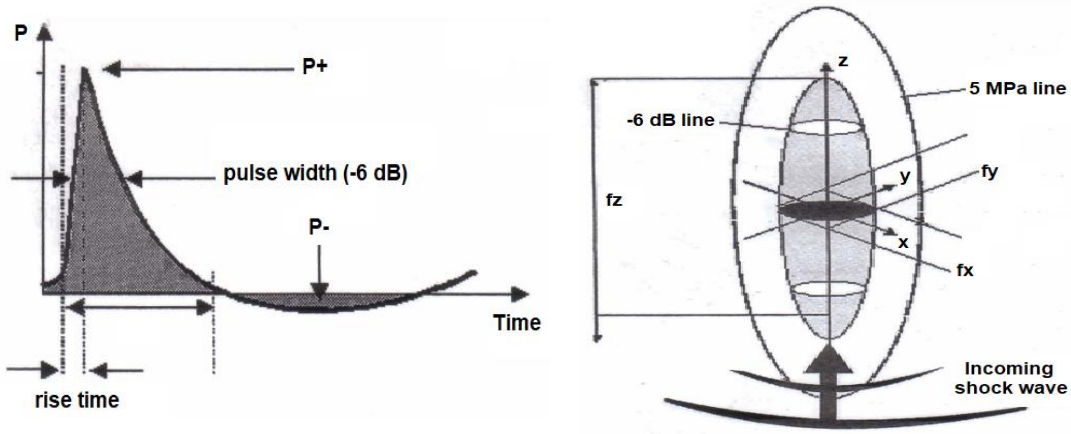

a) Profile of a typical shock wave. b) 3-dimentional pressure front.

Fig. 1. *Illustration of a typical shock wave [4].*

Technically, shock waves are characterized by: (i) a positive pressure (denoted as P+ in Fig. 1a) with a short rise time (a few nanoseconds) and a peak pressure of up to 100 megapascals (MPa); (ii) a negative pressure (denoted as P- in Fig. 1a) with the pressure value of 10% of the maximum positive pressure. The -6 dB pulse width is the duration at the point of the pressure higher than 50% of maximum positive pressure. After the rapid increase of pressure is a long period of decreasing pressure. Negative pressure is one of the specialized characters of a shock wave.

The energy of the shock wave (E) is measured in millijoules (mJ). The total energy contained in a shock wave is determined by the following formula:

$$E = [A\text{-}\rho c]\int p^2(t)dt$$

where p is the wave curve; A is the area of the wave surface; ρ is the density of the medium; c is the propagation speed in the medium; t is time.

There are three factors deciding a shock wave (Fig. 1b):

- -6 dB area (measured in mm along the x, y, z axes): is the boundary around the focus where the pressure has decreased to half of its peak value.
- 5 MPa area (measured in mm along the x, y, z axes): is the boundaries of the focus where the pressure has decreased to 5 MPa.
- 5 mm area: The 5 mm spherical area around the focus.

The focal size (f_x, f_y, f_z) presents the focal zone at the -6 dB area or 5 Mpa area. The 5 Mpa area is the area where the pressure exceeds 5 MPa. The -6 dB zone is the volume of tissue, where the pressure is at least one-half of the peak pressure.

A common parameter to describe shock waves is the energy flux density EFD, also called the energy density - the amount of energy in one square millimeter of the focal point field and is measured in mJ/mm^2.

Energy and EFD can be calculated for the positive pressure part (E_+, EFD_+) or the sum of the positive and negative pressure parts (E_{tot}, EFD_{tot}). The total energy applied during therapy is the total energy per pulse multiplied by the number of pulses.

II. DEVELOPMENT OF THE MODULE

In general, there are two technical solutions to generate shock waves in Extracorporeal Shock Wave Therapy [5]:

i) Using a compressed air system: using compressed air to accelerate a bullet in a barrel, then the bullet strikes an endplate to generate shock waves.

ii) Using an electromagnetic system: using alternating magnetic fields to accelerate a bullet, causing it to strike an endplate creating shock waves.

In our research, we have developed the ESWT module using a compressed air system (Fig. 2).

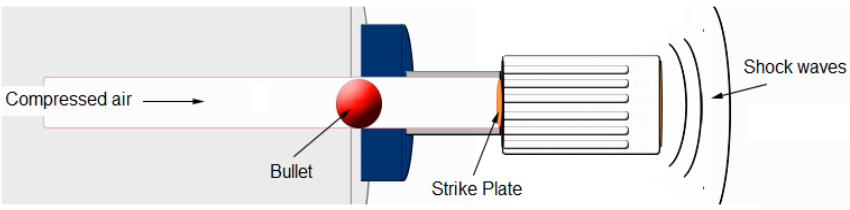

Fig. 2. *Blog diagram of the ESWT module using a compressed air system.*

The blog diagram of the ESWT module using the pneumatic technique is shown in Fig. 3.

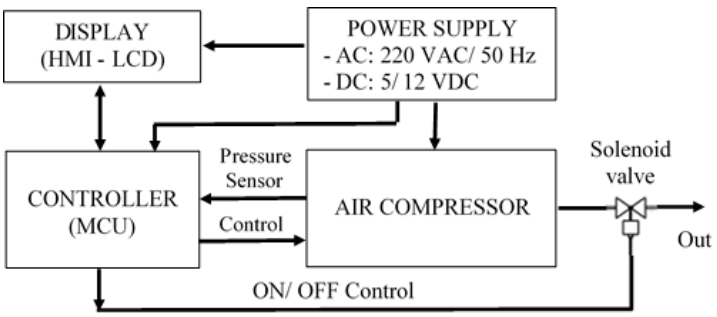

Fig. 3. *Blog diagram of the extracorporeal shock wave therapy module.*

The Controller based on the ATmega16A microcontroller generates pulses at the frequencies of 1 to 21 Hz which are later sent to the Air Compressor. The Compressor and the Solenoid valve are controlled by ON/OFF control signals corresponding to the

 ISBN:

programmed treatment modes. The compressed air, then being used to accelerate the bullet in the barrel, causing it to strike the endplate, generating shock waves.

The module has three features: relieve pain, ED treatment, and lose weight with different treatment modes such as Elbow Therapy, Back Therapy, Knee Therapy, Shoulder Therapy, Hip Therapy, Spine Therapy, Hand Therapy, Frame Feet Therapy,... All modes of therapy and frequencies, treatment pressure are indicated in LCD.

III. RESULTS AND DISCUSSION

The ESWT module using the pneumatic technique is designed and developed by the Center for Laser Technology, National Centre for Technological Progress has the same functionality as the SW21 system manufactured by Skalet Mechanical and Electrical Equipment Co., Ltd, China with function keys arranged on the front of the device.

Fig. 4 shows the image of the completed ESWT module with the ports as follows:

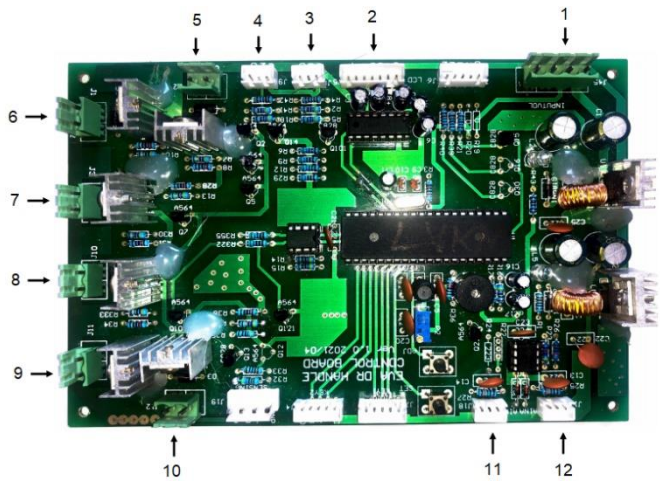

Fig. 4. *Image of the ESWT module developed by Center for Laser Technology.*

- Port #1: Power supply 24 VDC
- Port #2: RS 232 port
- Port #3: Digital input 1
- Port #4: Digital input 2
- Port #5: Countrol signal output 1
- Port #6: Countrol signal output 2
- Port #7: Countrol signal output 3
- Port #8: Countrol signal output 4
- Port #9: Countrol signal output 5
- Port #10: Countrol signal output 6
- Port #11: Analog input 1
- Port #12: Analog input 2

The images of the main interface are illustrated in Fig. 5.

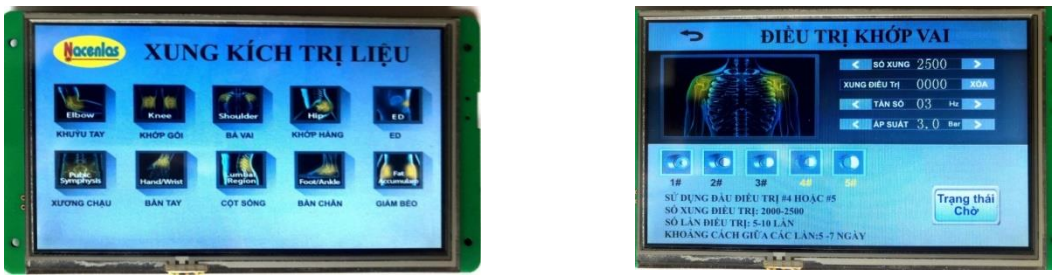

a) Mode therapy interface. b) Parameter setting interface.

Fig. 5. *Images of the main interface.*

In any ESWT system, there are two most important parameters that must be considered: treatment frequency and treatment pressure. In our module, the treatment frequency is controlled in the range of 1 to 21 Hz, step of 1 Hz. The treatment pressure is in the range of 1 to 8 Bar at a step of 0.5 Bar. Parameters of the developed module are measured and compared with that of the SW21 system.

- **Treatment frequency measurement:**

Treatment frequencies are generated by the ATmega16A microcontroller and sent to the module driver via the control signal output (PB7 - pin 8 of ATmega16A). However, it is required to be evaluated by measurement equipment. In our experiment, the measurement is carried out using the Oscilloscope TBS 1102 (Fig. 6).

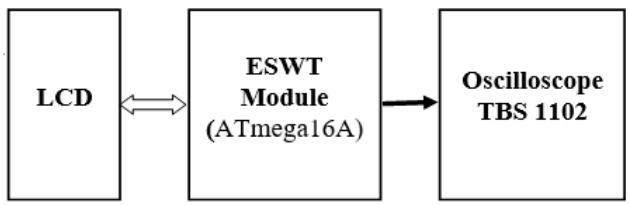

a) Diagram of the frequency measurement.

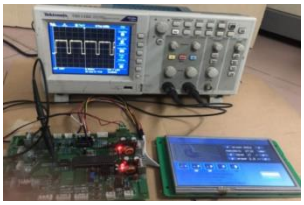

b) Image of the measurement.

Fig. 6. *The treatment frequency measurement.*

Results of the treatment frequency measurement are shown in Table 1.

Table 1. *Treatment frequencies of the module are compared with the SW21 system.*

SW21 frequencies (Hz)	1	2	3	4	5	6	7	8	9	10	11
The module frequencies (Hz)	1.0	2.0	2.8	3.7	4.9	5.8	6.8	7.6	8.7	10	10.8
SW21 frequencies (Hz)	12	13	14	15	16	17	18	19	20	21	
The module frequencies (Hz)	11.8	12.6	13.6	14.7	15.4	16.8	17.5	18.6	19.5	20.2	

The obtained results show that the deviation of the treatment frequencies between the developed module and SW21 system is around ± 0.4 Hz.

- **Output pressure measurement:**

The treatment pressure of the air compressor is detected by a pressure sensor MPX5999D, Motorola, and is feedbacked to the ATmega16A for control.

The pressure range of MPX5999D is from 0 to 1000 kPa (0-10 Bar) corresponding to the voltage from 0.2 to 4.7 V. The output voltage of MPX5999D is sent to the ADC of the ATmega16A (PA0 - pin 40 of ATmega16A). The control signals include PB2 (pin 4) to PB6 (pin 7) of ATmega16A.

The voltage values are measured by multimeter VC890C+ and the pressure values are measured by pressure gauge HNT-341A-0.5MPA, DAICHI KEIKI SEISAKUSHO (Fig. 7).

 ISBN:

Fig. 7. *The pressure measured by HNT-341A-0.5MPA and the voltage measured by VC890C+.*

The obtained output pressure measurement on the developed module and the SW21 system is shown in Table 2.

Table 2. *Sensor output voltages according to the pressure of the Oxygen Tank.*

SW21 pressure values (Bar)	1	2	3	4	5	6	7	8
The module pressure values (Bar)	0.92	1.88	2.95	4.05	4.95	6.08	6.98	8.05
Sensor output voltage (V)	0.57	0.94	1.42	1.98	2.46	2.86	3.23	3.60

The obtained results show that the deviation of the pressure values measured on the developed module and the SW21 system is around ± 0.12 Bar and that the treatment pressure in the range from 0 to 8 Bar is rather linear, corresponds to the output voltage from 0.56 to 3.60 V (Fig. 8).

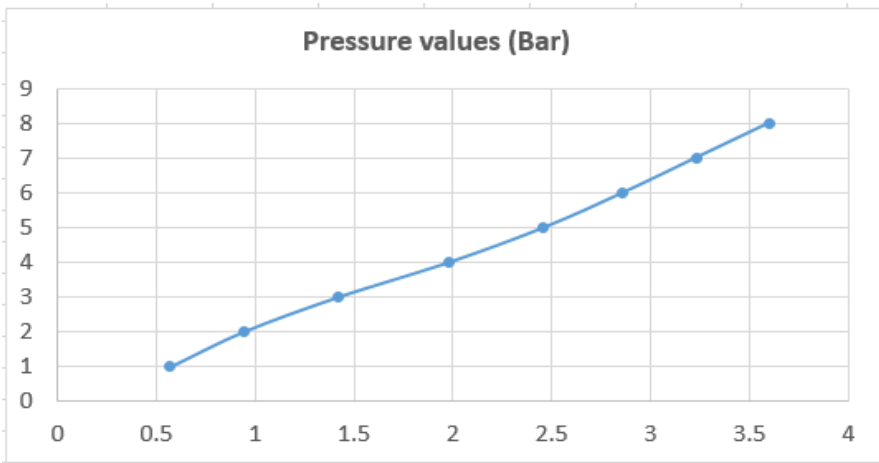

Fig. 8. *The treatment pressures correspond to the output voltages of the sensor.*

IV. CONCLUSION

An extracorporeal shock wave therapy module has been made on the principle of using the pneumatic technique to generate shock waves. As the result, treatment frequency in the range 1 to 21 Hz and treatment pressure in the range 0 to 8 Bar are obtained. The module is designed with the functionality similar to model SW21 of the Skalet Mechanical and Electrical Equipment Co., Ltd, China, including the functions: Relieve Pain, ED Treatment, Lose Weight, and the treatment modes: Elbow Therapy, Back Therapy, Knee Therapy, Shoulder Therapy, Hip Therapy, Spine Therapy, Hand Therapy, Frame Feet Therapy. The deviation of the treatment frequencies and the treatment pressures between the developed module and SW21 system is around ± 0.4 Hz and ± 0.12 Bar, respectively.

These are the important results for developing an Extracorporeal Shock Wave Therapy system using pneumatic technique in the future.

REFERENCES

[1] Wang C. J, Schaden W., Ko J. Y., History of shockwave treatment and its basic principles, *Shockwave Medicine. Transl. Res. Biomed. Basel, Karger*, 2018, **6**, 1-16.

[2] S. K. Shrivastava, et al., Shock wave treatment in medicine, *Journal of Biosciences*, 2005, **30**, 269-275.

[3] Michael Thiel, Application of Shock Waves in Medicine, *Clinical Orthopaedics and Related Research*, 2001, **387**, 18-21.

[4] Scott McClure, et al., Extracorporeal shock wave therapy: Theory and equipment, *Clinical Techniques in Equine Practice*, 2003, **2**(4), 348-357.

[5] https://www.shockwavetherapy.education/index.php/theory/types-of-shockwave.

 ISBN:

INTERPRETING THE GRAVITY ANOMALY OF THE SOUTHERN VIETNAM USING DERIVATIVE METHOD

Nguyen Hong Hai*

Experimental - Practical Area, An Giang University, An Giang, Vietnam

Faculty of Physics and Engineering Physics, University of Science, Ho Chi Minh City, Vietnam

Vietnam National University, Ho Chi Minh City, Vietnam

*E-mail: *honghaiatn@gmail.com; nhhai@agu.edu.vn*

Abstract. In the gravity survey, there are many methods to delineate the boundaries of structure and the most common method is to determine the maxima of the total horizontal derivative of the Bouguer anomaly map. This article mentions using the derivative calculations for interpreting the Bouguer data in the Southern Viet Nam (between latitudes 8.52^{o}N and 11.76^{o}N, and longitudes 104.45^{o}E and 107.50^{o}E). The maxima of total horizontal derivative, the maxima of normalized enhanced analytic signal and tilt angle method is used and compared. For the first two methods (the total horizontal derivative and the normalized enhanced analytic signal), the maxima are usually discrete so linking them up manually is difficult. Therefore, we have used the propose of Blakely and Simpson for determining these maxima automatically. The tilt angle, which is expressed as the arctan value of the ratio of the vertical derivative of the potential field to its horizontal derivative, skips the step of determining the maxima. In the tilt angle map, the boundaries of structure are investigated from the 0° contours. So, a combined Euler deconvolution and tilt angle method is applied to build the Euler_Tilt map based on the depth results along the 0 value of the tilt angle for computing the positions and the depth to the top of the faults. All calculations are done with code written in Matlab and are done based on Oasis software. The analysis results are consistent with previous publications and add some new information about the geology of the region.

I. INTRODUCTION

Determination of potential fields' anomaly borders is useful for their interpretation. Bouguer gravity anomalies are frequently used to delineate geologic contacts and borders of geological formation. In recent years, with the rapid development of information technology, information technology is applied to analyze gravity data fastly and accurately. Most existing boundary detection algorithms locate source edges through characteristic values which are from potential derivatives. The most common is the total horizontal derivative (THD) (Cordell and Grauch, 1982) [1]. In addition, the group of analytical signal methods is also used to directly determine the boundaries, but they cannot display the strong and weak amplitude anomalies simultaneously (Nabighian, 1972, 1974, 1984; Roest et al., 1992; Hsu et al., 1996) [2]. In recent years, many methods based on calculus of derivatives have been used to overcome this problem such as the tilt angle method (Miller and Singh, 1994; Verduzco and Fairhead, 2004) [3]; group of methods to normalize the analytical signal or total horizontal derivative (Wijns et al., 2005; Cooper and Cowan, 2008; Cooper, 2009; Ma and Li, 2012). In Vietnam, the THD method is also applied by

many authors on gravity data or magnetic data to determine faults (Le Huy Minh et al., 2001; Le Huy Minh et al., 2002; Cao Dinh Trieu, 2005; Lai Hop Phong et al., 2011; Pham Thanh Luan, 2019; Pham Thanh Luan, 2021) [4-6].

In this article, we are limited to the methods of using derivatives to analyze gravity data. The analysis of gravity data using derivatives methods is to provide an indirect means of seeing the subsurface by sensing various rocks below. However, if the data set contains features with a large variation in amplitude, then the features with small amplitudes may be difficult to outline. In addition, because most boundary detection is derivative-based filters, they also amplify high-frequency noise content in the data. This article aims at estimating depths and boundaries of gravity anomalies by using some derivative methods such as: the total horizontal derivative (THD) [1], the normalized enhanced analytic signal (NAS) [2] and tilt angle (TA) method [3]. These methods are tested on models and applied on real data in Southern Vietnam. In addition, this article also mentions the use of the combined Euler deconvolution and tilt angle method [4] is applied to build the Euler-Tilt map based on the depth results along the 0 value of the tilt angle for computing the positions and the depth to the top of the faults. All analysis contributes to provide an indirect insight into subsurface geologic features within Southern Vietnam.

II. SUMMARY OF METHODS

2.1. The total-horizontal derivative (THD)

To detect and enhance the boundaries of the anomalies, Cordell and Grauch (1982) [1] used the value of total horizontal derivative, as follow:

$$\mathrm{THD} = \sqrt{\left(\frac{\partial\phi}{\partial x}\right)^2 + \left(\frac{\partial\phi}{\partial y}\right)^2} \tag{1}$$

where, $\frac{\partial\phi}{\partial x}$ and $\frac{\partial\phi}{\partial y}$ is the derivative in x and y direction respectively.

2.2. Normalized enhance analytic signal (NAS)

The normalized enhanced analytic signal is presented by Yao et al. in 2015 [2]. The normalized enhanced analytic signal uses different orders vertical derivatives of the potential field data to normalize different orders enhanced analytic signals. These methods avoid the influence of the nearby points and balance the boundaries of large and small amplitude anomalies simultaneously. Cooper and Cowan (2006) [7] use the first order vertical derivative to normalize the total horizontal gradient. Here, the total horizontal gradient is replaced with the analytic signal amplitude to define a new boundary detector NAS. The expression of NAS is:

$$\mathrm{NAS} = \tan^{-1}\left(\frac{\mathrm{AS}}{\left|\frac{\partial\phi}{\partial z}\right| + \mathrm{p.max(AS)}}\right) \tag{2}$$

where, $\frac{\partial\phi}{\partial z}$ is the derivative in z, p is a nonnegative constant value. In general, the value of p is between 0 and 0.5 and AS is analytic signal amplitude.

 ISBN:

$$AS = \sqrt{\left(\frac{\partial\phi}{\partial x}\right)^2 + \left(\frac{\partial\phi}{\partial y}\right)^2 + \left(\frac{\partial\phi}{\partial z}\right)^2} \quad (3)$$

Normally, the Blakely-Simpson method [8] is used to identify the maxima of THD and the maxima of NAS automatically.

2.3. The tilt angle (TA)

Tilt angle is one of the conventional local phase filters for enhancing features and causative body boundary detection in potential field images. This filter was first developed by Miller and Singh (1994), developed by Verduzco et al. (2004); then Ansari and Anasari (2011). Tilt angle is the ratio of the vertical derivative to the absolute amplitude of the total horizontal derivative, which is defined as [3]:

$$TA = \tan^{-1}\left(\frac{\partial\phi}{\partial z}\Big/ THD\right) \quad (4)$$

2.4. The Euler - Tilt method

To compute the positions and the depth to the top of the faults, a combining the 3D Euler deconvolution and tilt angle method was proposed by Nguyen Hong Hai et al. in 2019 [4]. Based on the Oasis Montaj software, the tilt angle method was used to delineate the faults (0 contours); then, the Euler deconvolution was applied along the 0 contour of tilt to determine the depth of the faults. This one was intended to overcome the shortcomings of each method. Here, the Euler deconvolution was proposed by Thompson in 1982 [9] and Reid et al. (1990) [10] developed the equivalent method (3D Euler deconvolution) operating on gridded magnetic data. It uses the equation:

$$(x - x_0).\Delta g_x + (y - y_0).\Delta g_y + (z - z_0).\Delta g_z = N.(B_z - \Delta g) \quad (5)$$

where, x_0, y_0, z_0 are the unknown coordinates of the source body center (or edge to be estimated) whose gravity anomaly vertical component Δg_z detected at (x, y, z) - the known coordinates of the observation point of the gravity and the gradients; B_z is base level (regional anomalies value) of the gravity to be estimated and N is a value that describes the anomaly attenuation rate commonly known as the structural index (degree of homogeneity).

III. RESULTS AND DISCUSSION

3.1. Detecting the boundary of models

a) Model 1

Fig. 1 shows the synthetic gravity data from a rectangular prism with the parameters of the model described in Table 1. Contour lines of gravity anomalies of the model do not describe the boundaries of the sources clearly.

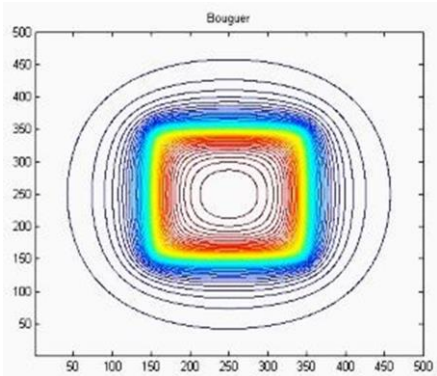

Fig. 1. *The synthetic gravity anomaly map of model 1.*

Fig. 2 shows the application of the boundary detection filters of the gravity data in Fig. 1.

Table 1. *The parameters of the models.*

	Model 1		**Model 2**			
	Prism		**Prism 1**		**Prism 2**	
Observed grid (km)	x = 1:1:500; y = 1:1:500; z_0 = 0		x = 1:1:200; y = 1:1:200; z_0 = 0			
Coordinate border	x_1= 150 x_2= 350	y_1= 150 y_2=350	x_1= 85 x_2= 115	y_1= 80 y_2=110	x_1= 85 x_2= 115	y_1= 115 y_2 = 135
Depth of the top and the below surface	z_1=10;	z_2=30.	z_1=5;	z_2=15.	z_1=5	z_2=20
Density	100kg/m^3		100kg/m^3			

The THD map (Fig. 2a) describes the prism's top surface exactly, contour lines are symmetry and the noise is not found. The AS map (Fig. 2b) has a diagnostic interpretation of the model boundaries difficulty. Meanwhile, the NAS map and the TA map identify the position of the prism quite exactly, but there are some disadvantages such as the noise appearing so much (Fig. 2c) or the boundaries are not straight (Fig. 2d).

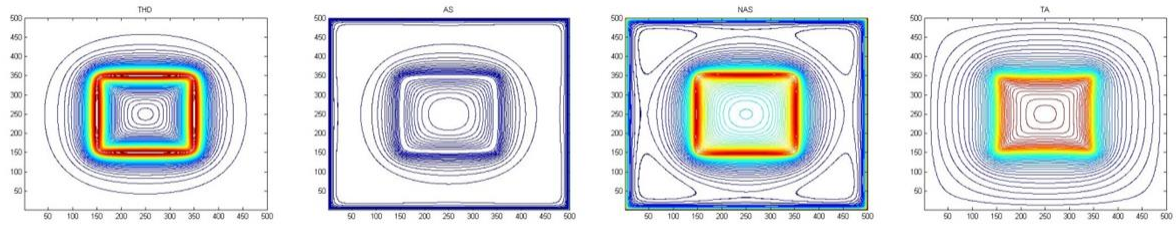

(a) *(b)* *(c)* *(d)*

Fig. 2. *The boundary detection of model 1 by: a) THD; b) AS; c) NAS and d) TA.*

b) Model 2

The model 2 has two rectangular prisms, has shown in Fig. 3. Two boundaries of two prisms are not separated. Fig. 4 shows the effect of boundary detection methods of the gravity data in Fig. 3, showing that their maximum and zero values lay on the model boundary.

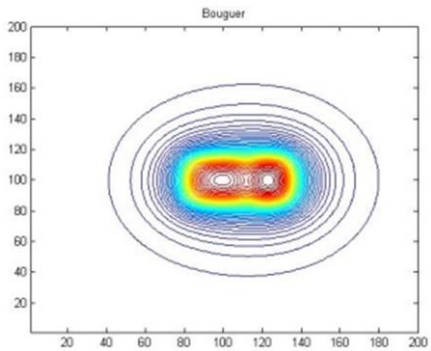

Fig. 3. *The synthetic gravity anomaly map of model 2.*

In this case, the THD map (Fig. 4a) shows the position of the two prisms is located quite exactly and two boundaries of two prisms are separated, but not clearly. The AS map (Fig. 4b) has much noise, but expresses nearly the shape of the model. Meanwhile, the NAS map (Fig. 4c) shows almost full of the boundary of two prisms' top surfaces; the positions of two prisms are located exactly. And the TA map (Fig. 4d) is, too.

In conclusion, each method of boundary separation has different advantages and disadvantages. The AS method shows that the boundary shape of the models is not really clear. While the THD method is suitable for single anomalies; then the two remaining methods (NAS and TA) are suitable for adjacent anomalies; margin is enhanced; however,

 ISBN:

noise is a big problem if the method uses many partial derivatives and the prism's top surface is not entirely rectangular.

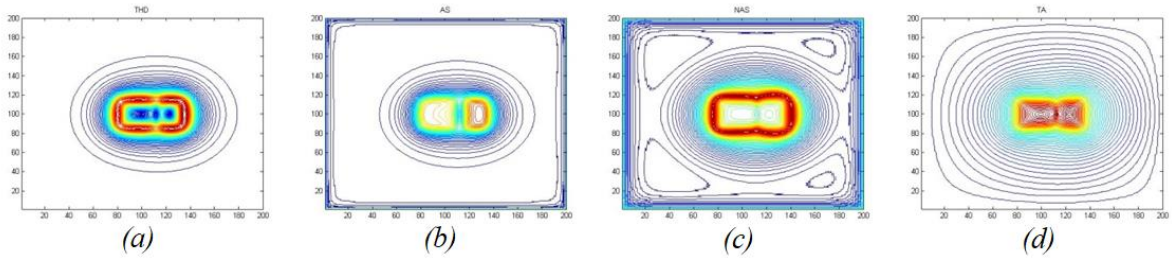

Fig. 4. *The boundary detection of model 2 by (a) THD; (b) AS; (c) NAS and (d) TA.*

3. 2. Interpreting the gravity anomaly of the Southern Vietnam

The data of this article is the Bouguer gravity anomaly map (1:500,000 scale) in Southern Vietnam which was collected at Southern Vietnam of South Vietnam Geological Mapping Division (Lai Manh Giau et al., 2011) and supplemented with the gravity measurement points (1:50,000 scale) of Tan Bien sheet [11,12]. The data were interpolated to grid data sized 178×178, spacing 2 km and then smoothed by moving average filter with window size 3×3 (Fig. 5).

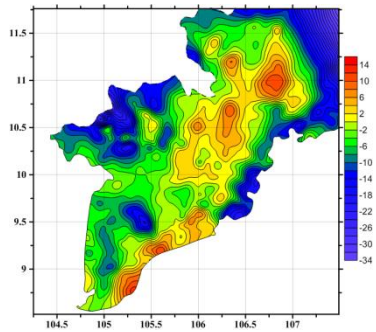

Fig. 5. *The Bouguer gravity anomalies map of the Southern Vietnam (contour interval: 2 mgal).*

a) The structural boundaries of the Southern Vietnam from some derivative map

Applying the THD, NAS and TA method on this map, the result has shown in Fig. 6.

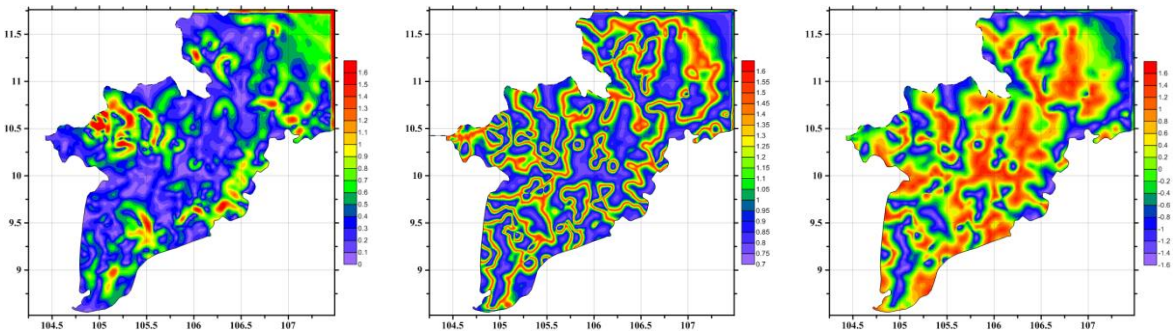

(a) The THD map (c.i.: 0.1 mgal/km) *(b) The NAS map (c.i.: 0.1 mgal/km)* *(c) The TA map (c.i.: 0.2 radian)*

Fig. 6. *The derivative maps of Southern Vietnam's gravity data: a) THD; b) NAS and (c) TA.*

The THD map (Fig. 6a) shows the boundaries of the research area, but is complicated and not sharp, so it is necessary to calculate the maximum values of THD to show the boundaries more clearly. The NAS map (Fig. 6b) with p = 0.0001, the maximum values (red zone) tend to lie along boundaries of anomalies and along the longitudinal direction, NW-SE direction and NE-SW direction; so, the NAS can be used to delineate faults of the research area. While, the TA map (Fig. 6c) is valid from -π/2 to +π/2. Therefore, in the contour map, boundaries are in the middle of extreme (green zone). In

Fig. 8, the green region is rather wide, so the shape of faults and boundaries is recognized, but it is hard to determine the exact position.

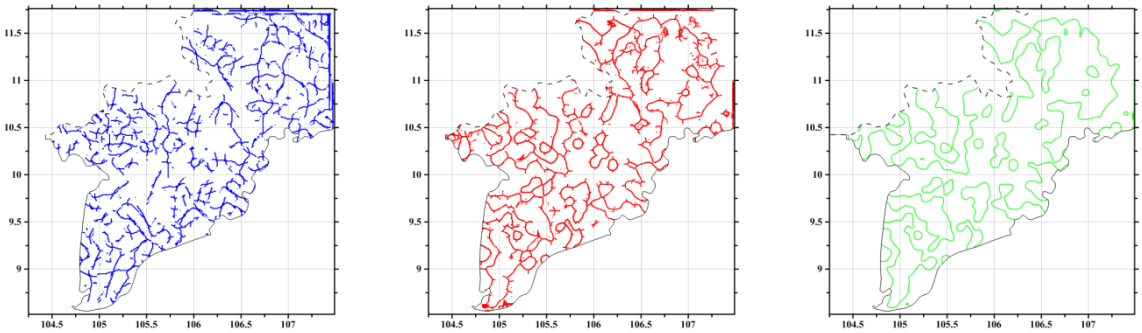

a) The MTHD map *b) The MNAS map* *c) The ZeroTA map*

Fig. 7. *The boundary maps of Southern Vietnam's gravity data: a) MTHD; b) MNAS and c) ZeroTA.*

For delineating the structural boundaries of the Southern Vietnam, the maxima of total horizontal derivative - MTHD, the maxima of normalized enhanced analytic signal - MNAS (the maxima was determined by Blakely and Simpson method) and the zero of tilt derivative map (ZeroTA) are calculated and overplayed them. Fig. 8a is the overplay map of MNAS (red line) and ZeroTA (green line), shows that all zero values of tilt derivative coincide with the maxima of the NAS, some other MNAS values may be noise. Fig. 8b is the overlay map of MNAS (red line) and MTHD (blue line). Where the MNAS coincides with MTHD, they represent the true contact locations. In case MTHD was isolated, it represents the best available contact location. And the overplay map (Fig. 8c) of MTHD (blue line) and ZeroTA (green line) shows the same results in the Fig. 8b. These show that MNAS and ZeroTA results are reliable, can be used to determine the faults and MTHD can be used to check the existence and elongation of faults.

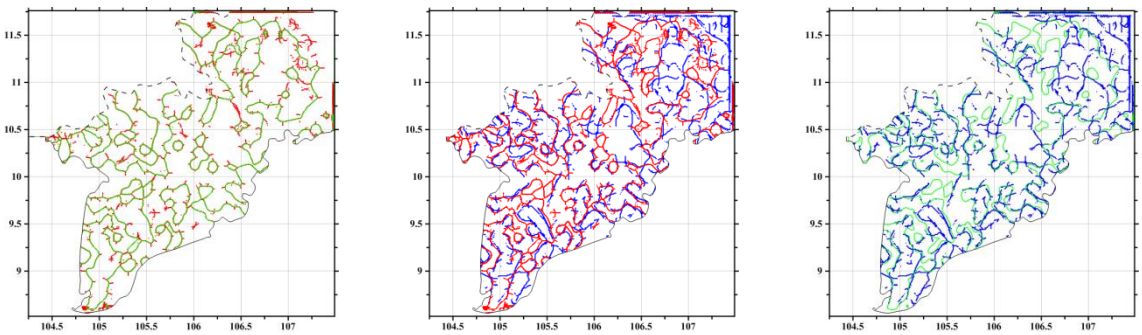

a) MNAS (red) – ZeroTA (green) *b) MNAS (red) – MTHD (blue)* *c) MTHD (blue)– ZeroTA (green)*

Fig. 8. *The overlay maps of Southern Vietnam's gravity data: a) MNAS (red) – ZeroTA (green); b) MNAS and c) ZeroTA.*

b) Interpreting the gravity anomaly of the Southern Vietnam

As mentioned in the introduction, the 3D Euler Deconvolution method is used to estimate the depth of the field source with the Bouguer anomaly map, 20×20 window size, 15% maximum depth error. The zero-structural index is used to estimate the position and depth of the source. The maximum depth to the top of the anomaly boundary is about 4000 m. The result (Fig. 9) shows that the zero contour of tilt angle tends to lie along boundaries

 ISBN:

of anomalies and along the faults (Fig. 10). In which, the faults of the Northwest - Southeast direction and the faults of the Longitude and Sub-longitudinal direction are clearly visible.

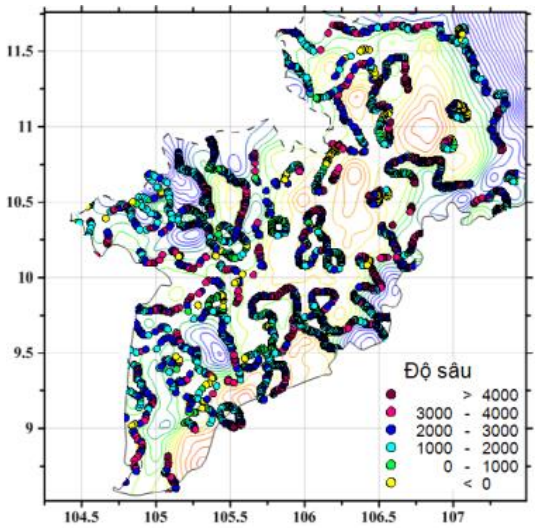

Fig. 9. *The Euler_Tilt map of Southern Vietnam from the gravity data.*

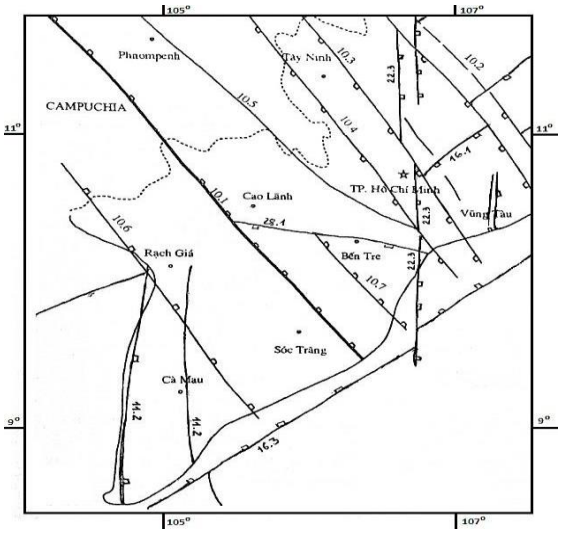

Fig. 10. *An outline of faults in the Southern Vietnam from the publication of Cao Dinh Trieu and Pham Huy Long [13].*

Fig. 10 is an outline of faults in the Southern Vietnam from the publication of Cao Dinh Trieu and Pham Huy Long in 2002 [13] ("Kiến tạo đứt gãy lãnh thổ Việt Nam" -a publication that comprehensively addresses tectonic faults in Vietnam on the basis of a consistent ideology and methodology). In comparison with Fig. 10, the faults of the Southern Vietnam from Fig. 9 can be divided into 4 groups as follow:

- The faults of Northwest - Southeast direction (NWSE), including: Hau River $^{(10.1)}$, Dinh Quan - Chua Chan $^{(10.2)}$, Sai Gon River $^{(10.3)}$, Vam Co Dong $^{(10.4)}$, Moc Hoa - Go Cong$^{(10.5)}$, Gia Ray - Rach Gia $^{(10.6)}$, Co Chien River$^{(10.7)}$ and a new fault not mentioned in Fig.10 is Ham Luong. In which, the Co Chien River fault extends to Hong Ngu. And, the Moc Hoa - Go Cong fault is not clearly visible in Fig. 9, but there are identifiable signs in Fig. 8.

- The faults of Northeast - Southwest direction (NESW), Hon Dat - Tay Ninh, Ca Mau - Go Cong Dong which Fig. 10 does not mention.

- The faults of Longitudinal and Sub-longitudinal direction (LONG), including: Vung Tau fault, Loc Ninh - Thu Dau Mot$^{(22.3)}$ and Ca Mau - Phu Quoc$^{(11.2)}$ fault system (Dat Mui - Southern Rach Gia and Ganh Hao - Rach Gia). In which, the Ca Mau - Phu Quoc fault system extends to the Cambodian border. In addition, a new fault appears along the border of Bien Hoa zone and Soc Trang sub-zone from Tay Ninh to Bac Lieu.

- The fault of Latitudinal and Sub-latitudinal direction (LAT): Sa Dec - Cho Gao$^{(28.1)}$ extends along the Tien River.

IV. CONCLUSION

In this research, the gravity anomalies of modes maps were built for the initial evaluation of the efficiency of the total horizontal derivative, the normalized enhanced analytic signal and tilt angle method. After that, applying on the real data. The results show that the tilt angle is quite suitable for detecting boundaries of Bouguer anomalies of Southern Vietnam, but should still be combined with other methods for the best effect. When overplaying THD, NAS, TA map to clarify fault directions; the following criteria were used to interpret the final contact locations:

- The NAS and TA map were almost the same, the NAS had more noise.
- Where the TA contacts were isolated and not aligned with the flight lines or other known noise directions, they provided reliable contact locations.
- Where the TA were parallel to and slightly offset from the THD contacts, the TA contacts represented the true contact locations.
- Where the THD contacts were isolated, they represented the best available contact locations.

Based on the Oasis Montaj and Matlab software, the Euler-Tilt map was built for locating and estimating the depth of the faults. Applying to interpret the Bouguer data of the Southern Vietnam, 16 faults (8 faults of the Northwest - Southeast direction (the direction commonly found in gravity data analysis), 2 faults of Northeast - Southwest direction, 5 faults of the Longitudinal and Sub-longitudinal direction and 1 faults of the Latitudinal and Sub-latitudinal direction (rarely found in gravity data analysis)). There are 3 new faults (Hon Dat - Tay Ninh, Ca Mau - Go Cong Dong, Tay Ninh - Bac Lieu) identified in this study (only using gravity data) that Cao Dinh Trieu and Pham Huy Long [13] has not mentioned. In addition, Dat Mui - Southern Rach Gia, Ganh Hao - Rach Gia and Co Chien River fault are extended to the Southwest border.

In summary, this method is effective in analyzing gravity data and can be applied to magnetic data; together with another filtering techniques (such as upward and downward continuation) to identify geological structures in depth and confirm new results.

ACKNOWLEDGMENTS. The author would like to thank Assoc. Prof. Dang Van Liet (University of Science, VNU-HCM, Vietnam) for his helpful advice on various technical issues.

REFERENCES

[1] Cordell L. & Grauch, V. J. S., Mapping basement magnetization zones from aeromagnetic data in the San Juan Basin, New Mexico, *Presented at the 52nd Ann. Internat. Mtg., Soc. Explor. Geophys*., Dallas, 1985.

[2] Yao Y., Huang D., Yu X. & Chai B., Edge interpretation of potential field data with the normalized enhanced analytic signal, *Acta Geodaetica et Geophysica*, 2016, **51**(1), 125-136.

 ISBN:

[3] Miller H. G. & Singh V., Potential field tilt-a new concept for location of potential field sources, *Journal of applied Geophysics*, 1994, **32**(2-3), 213-217.

[4] Nguyen H. H., Van Dang L. & Van Vo V., A combined Euler deconvolution and tilt angle method for interpretation of magnetic data in the South region, *Science and Technology Development Journal*, 2019, **22**(2), 219-227.

[5] Pham L. T., Oksum E. & Do T. D., Edge enhancement of potential field data using the logistic function and the total horizontal gradient, *Acta Geodaetica et Geophysica*, 2019, **54**(1), 143-155.

[6] Pham T. L., Nghiên cứu phát triển một số phương pháp mới trong công tác xử lý, phân tích số liệu trường thế, Doctoral dissertation, Vietnam National University, Hanoi, 2020.

[7] Cooper G. R. J. & Cowan D. R., Enhancing potential field data using filters based on the local phase, *Computers & Geosciences*, 2006, **32**(10), 1585-1591.

[8] Blakely R. J., & Simpson R. W., Approximating edges of source bodies from magnetic or gravity anomalies, *Geophysics*, 1986, **51**(7), 1494-1498.

[9] Thompson D. T., EULDPH: A new technique for making computer-assisted depth estimates from magnetic data, *Geophysics*, 1982, **47**(1), 31-37.

[10] Reid A. B., Allsop J. M., Granser H., Millett A. T. & Somerton, I. W., Magnetic interpretation in three dimensions using Euler deconvolution, *Geophysics*, 1990, **55**(1), 80-91.

[11] Giau L. M., et al., Bản đồ các trường dị thường trọng lực Việt Nam (Phần đất liền) tỷ lệ 1:500.000, niên đại 2011, *Journal of Geology - Series A*, 2011, **333**, 34-37.

[12] An T. D. et al., Báo cáo kết quả công tác đo trọng lực thuộc đề án lập bản đồ địa chất và điều tra khoáng sản, tỷ lệ 1:50.000 nhóm tờ Tân Biên, Department of Geology and Minerals of Vietnam, Hanoi, Vietnam, 2011.

[13] Trieu C. D. & Long P. H., Kiến tạo đứt gãy lãnh thổ Việt Nam, Science and Technics Publishing House, Hanoi, 2002.

MAGNETIC DATA INVERSION FOR 3D GEOMETRY OF THE SHALLOW SOURCES IN THE SOUTHERN VIETNAM

Nguyen Hong Hai*

Experimental - Practical Area, An Giang University, An Giang, Vietnam

Faculty of Physics and Engineering Physics, University of Science, Ho Chi Minh City, Vietnam

Vietnam National University, Ho Chi Minh City, Vietnam

*E-mail: *honghaiatn@gmail.com; nhhai@agu.edu.vn*

Abstract. To investigate 3D geometry of the Earth's crust based on gravity data, the Bouguer gravity anomaly value is often used; the magnetic data is rarely done in the 3D inversion, but it is usually applied to calculate the depth of the source corresponding to the geological boundaries or faults. Based on the Parker - Oldenburg algorithm, David G.O built the 3DINVER program in 2005, using Matlab software and allowing it to be widely used. This paper mentions the new approach of Prutkin in 2017 is to identify 3D geometry of the Earth's crust corresponding to the high frequency of the magnetic fields (local anomalous sources) in the Southern Vietnam. Because the Parker-Oldenburg iterative method computed 3D geometry of a horizontal density interface from gridded gravity anomaly, the transformation of magnetic data to the pseudo-gravity is applied to compute 3D geometry from magnetic data. The high frequency component corresponding to the shallow source is separated by the Bidimensional Empirical Mode Decomposition method and the source's depth is determined by the Radially Averaged Power Spectrum method.

I. INTRODUCTION

In recent years, the method of analyzing the correlation between magnetic and gravity anomalies to study the structure of the Earth's crust has been widely applied; not only survey the geological structure - especially the interface survey - from the measured values of gravity/magnetic fields on the ground (observed fields), but also survey the geological structure for gravity/magnetic fields of high, medium and low frequencies. This survey provides topography of the shallow, medium and deep interfaces of the Earth's crust, thus explains the geological structure better. For potential field data inversion, many methods have been proposed, such as the method of Cordell and Henderson (1968) [1]; Parker (1972) [2], Bhaskara Rao and Ramesh Babu (1990) [3]; Oldenburg based on Parker's algorithm to give a method to determine the topography surface from the gravity data called Parker - Oldenburg algorithm in 1974 [4]. In the Southern Vietnam and adjacent areas, there have been a number of studies on interfaces (crystalline basement, Moho discontinuity surface) of the Earth's crust using gravity and magnetic data materials such as Ton Tich Ai and Do Duc Thanh (1989) [5]; Dang Van Liet et al. (2005, 2008) [6-7]; Nguyen Ngoc Thanh Son et al. (2012) [8]; Nguyen Hong Hai (2015) [9]; Phung Van Phach et al. (2011) [10]; Bui Cong Que (1982, 1992) [11-12]; Cao Dinh Trieu et al. (1995, 1999, 2005, 2017) [13-16].

This work provides a new approach to identify interfaces of the Earth's crust corresponding to the high frequency of the magnetic fields (local anomalous sources -

 ISBN:

about 5 km) in the Southern Vietnam by the Parker-Oldenburg iterative method and the Bidimensional Empirical Mode Decomposition method.

II. SUMMARY OF METHODS

2.1. Pseudogravity transform

As described in the summary, the Parker-Oldenburg method is used. Therefore, in order to compute 3D geometry from magnetic data, it is necessary to apply the transformation of aeromagnetic data to pseudogravity. Poisson's theorem relates linearly the derivative of the gravity taken along the total magnetization vector direction and the magnetic potential due to a common, isolated source with constant density and magnetization distributions.

$$\Delta T = \frac{J}{G.\rho}\frac{\partial g}{\partial z}$$

Pseudogravity anomalies from magnetic surveys or pseudomagnetic anomalies from observed (or computed) gravitational gradients can be used to enhance geologic interpretations of subsurface structures, such as their depth determination. The pseudogravity transform is more easily understood and more easily undertaken in the Fourier domain. It is derived by an integration of the total magnetic intensity grid data using conventional Fast Fourier Transform tools.

2.2. Gravity Anomaly Separation

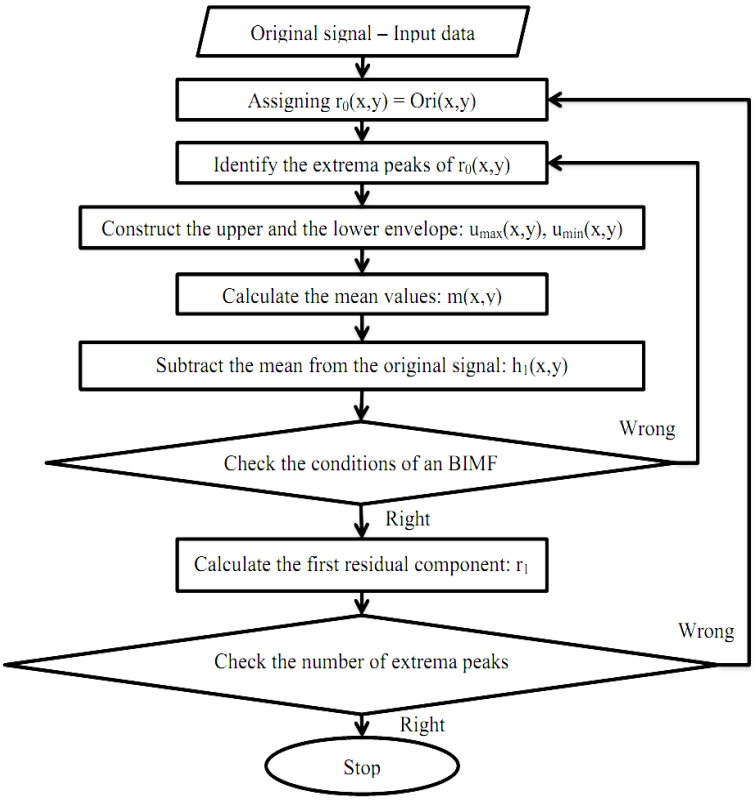

Fig. 1. *BEMD algorithm diagram.*

This paper mentions the 3D geometry of the Earth's crust corresponding to the high frequency of the magnetic fields (local anomalous sources) in the Southern Vietnam. After the pseudogravity transform step, the Bidimensional Empirical Mode Decomposition method (BEMD) which was developed by Nunes et al. in 2003 [17], is applied to separating the high frequency component (local anomalous sources) from the observed anomaly. The steps of method are summarized in Fig. 1. The result is:

$$Ori(x,y) = \sum_{i=1}^{n} h_{ik} + r_n$$

where, r_n is the residual; h_{1k}, h_{2k}, h_{3k} …are BIMF components, they correspond with decreasing frequency ranges.

<u>Note</u>: Two Stoppage Criteria: S and SD. i) **The S number**: S is defined as the consecutive number of siftings, in which the numbers of zero crossing and extrema are the same for these S siftings. Ii) **Standard Deviation (SD)** is smaller than a pre-set value.

2.3. Paker - Oldenburg method.

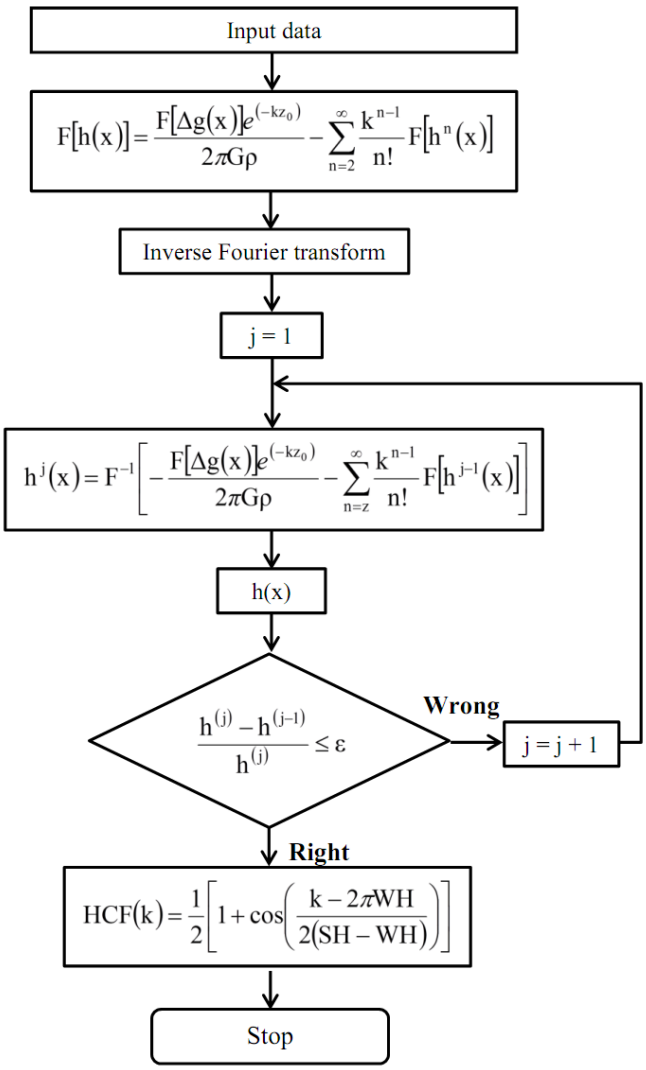

Fig. 2. *Parker – Oldenburg algorithm diagram.*

 ISBN:

Based on many geophysical studies, the three-dimensional thickness determination of the density variation interface using the gravity anomaly is a common method. Parker - Oldenburg method is perhaps the most commonly used technique to estimate the depth of density interface from gravity data. Parker - Oldenburg method is suitable for local studies, given that a functional relationship between gravity data and interface geometry is derived for Earth's planar approximation. Based on the Parker - Oldenburg algorithm, David G.O built the 3DINVER program in 2005 [18], using Matlab software and allowing it to be widely used. The steps of method are summarized in Fig. 2. In which, F(Δg) is the Fourier transform of the gravity anomaly, G is the gravitational constant, ρ is the density contrast across the interface, K is the wave number, h(x) is the depth to the interface (positive downwards) and z_0 is the mean depth of the horizontal interface. The iterative process is terminated when either the RMS error between two successive approximations is lower than a pre-assigned value - used as convergence criterion, or until a pre-assigned maximum number of iterations are reached. A high-cut filter in the frequency domain has been incorporated to enhance the convergence in the iterative process.

III. RESULTS AND DISCUSSION

The research area is the interior of the Southern Vietnam including Eastern region and Mekong Delta. The terrain of this area is relatively flat. The data of this paper is the aeromagnetic map in 1985's of Department of Geology and Minerals of Vietnam, 1:200,000 in Southern Vietnam. For convenient analysis, we perform the following pre-processing steps: *(i)* interpolating data to grid 178×178, spacing 2 km and then smooth by moving average filter 3×3 (Fig. 3), *(ii)* calculating the geomagnetic main field by the formula of Nguyen Thi Kim Thoa (2007) [19], then calculating the total magnetic anomalies (Fig. 4) and *(iii)* computing the Pseudogravity by our program based on function *pse* of Arisoy and Dikmen (2011) [20] and *coefficient of variation* of Blakely [21]. The result of the pseudogravity transform with I = 5°, D = - 0.2^o is represented in Fig. 5 (The inclination and declination values are averages for the whole region (same as Reduction to pole at low latitudes [22]).

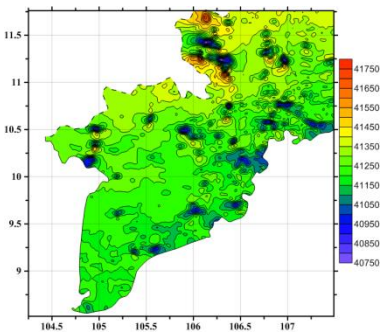

Fig. 3. *The total magnetic intensity map of the Southern Vietnam (contour interval: 50 nT).*

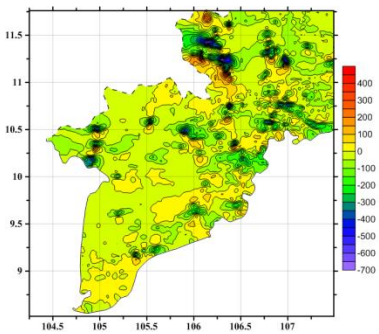

Fig. 4. *The total magnetic anomalies map of the Southern Vietnam (contour interval: 50 nT).*

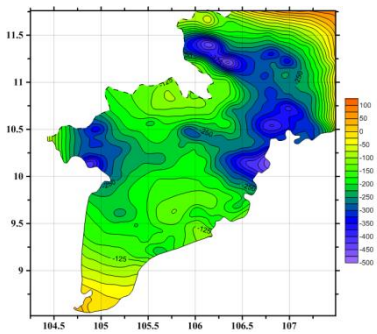

Fig. 5. *The pseudogravity anomalies map of the Southern Vietnam (contour interval: 25 nT).*

The anomalies of the pseudogravity map are relatively stable, symmetric and clear. The map clearly shows the large negative anomalies concentrated in the mountainous areas of Ha Tien, Tay Ninh, Bien Hoa and Ba Ria - Vung Tau. The intensity is limited in the

range -500nT to +100nT. The BEMD is applied to the pseudogravity map to decompose it into four components ($BIMF_{P1}$, $BIMF_{P2}$, $BIMF_{P3}$ and $BIMF_{P4}$) which have different frequencies from high to low in Fig. 6. The power spectrum shows that the average depth of these sources is 4.9 km, 11.5 km, 14.6 km, 20.2 km; respectively.

The $BIMF_{P1}$ component (Fig. 6a) has high frequency so the sources are shallow; thus the anomalies are the local anomalies and more detailed than the observed anomalies map (pseudogravity map). The anomalies of $BIMF_{P1}$ appear along boundaries between positive anomalies and negative anomalies of observed anomalies map; they appear along boundaries of zones such as South Central, Bien Hoa swell zone, Can Tho basin zone and Ha Tien swell bead. Because it is the highest frequency component of the pseudogravity field and has a depth of 4.9 km, it is used as an input data to define the 3D shallow surface corresponding to the high frequency field. Applying the Parker - Oldenburg method with input parameters: the initial depth is 5 km, the density contrast ρ is 0.36 g/cm^3 and the parameters for a high-cut filter in the frequency domain are WH = 0.019 and SH = 0.023.

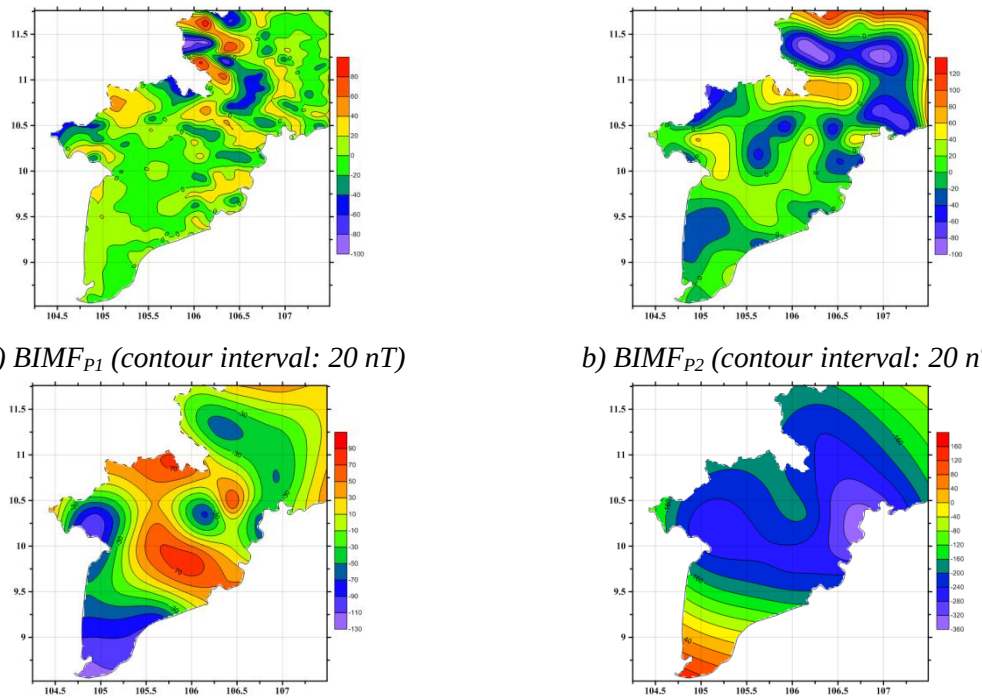

a) $BIMF_{P1}$ (contour interval: 20 nT) *b) $BIMF_{P2}$ (contour interval: 20 nT)*

c) $BIMF_{P3}$ (contour interval: 20 nT) *d) $BIMF_{P4}$ (contour interval: 40 nT)*

Fig. 6. *The pseudogravity anomalies map of BIMF components of the Southern Vietnam*

The results of the 3D geometry of the shallow sources (with high frequency) in the Southern Vietnam are shown in Fig 7, the contour interval is 1 km, rms error is 0.0044. The depth value of the topography surface of the high-frequency varies quite complexly, from upwelling near the ground (Northern Saigon River, Vam Co River and Bay Nui (An Giang)), to sink to the depth of 5 - 6 km (the lower pool of Tien River - Hau River and Ca Mau Region); and even down to the depth of over 10 km (in the area of Ho Chi Minh City and Vinh Hung). In the study area, existing some fault systems along the NE-SW direction (along Kien Giang to Tay Ninh) and along the NW-SE fault system (Tien - Hau River fault system), Binh Phuoc - Ba Ria fault, Sai Gon River - Vam Co fault system which show clearly and play the role of structural subdivision:

 ISBN:

- Uplifted fault block (Tay Ninh - Bien Hoa) is located in the Northeast.
- The slight structural depressions (Moc Hoa - Tan An, Ben Tre - Tra Vinh) are weak differentiation.
- The strong and quiet homogeneity structural depressions (Chau Thanh, Vinh Hung and Ho Chi Minh City) have the largest subsidence amplitude which down to the depth of over 10 km.
- The differential subsidence (Ca Mau - Soc Trang) consists of interwoven weak structural depressions.

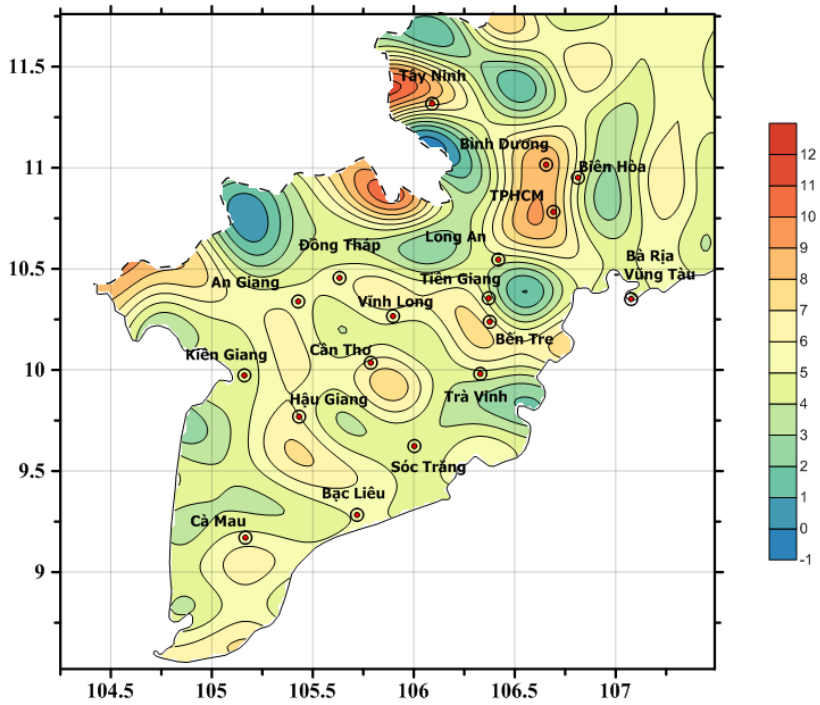

(a) Contour map

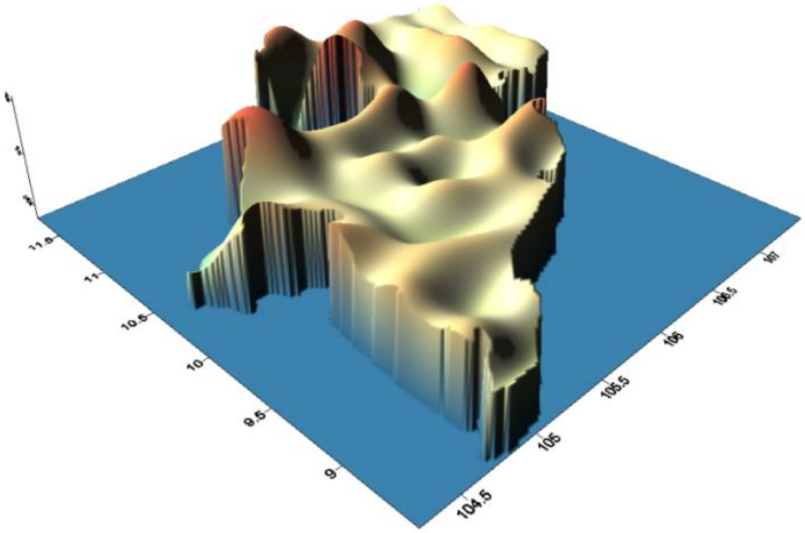

(b) 3D Surf map

Fig. 7. *3D geometry of the shallow sources in the Southern Vietnam.*

IV. CONCLUSION

To identify 3D geometry of the shallow sources in the Southern Vietnam, the Parker-Oldenburg iterative method is applied on the high frequency of the pseudogravity (the transformation of magnetic data), which is separated by the the Bidimensional Empirical Mode Decomposition method.

The results show that the pseudogravity interface (with the nature of magnetic data) should be directed to Ha Tien uplift, mountainous areas (where granite is exposed on the ground). With the high frequency component of pseudogravity, the shape of the 3D geometry - possibly close to the crystalline basement - is folded, showing the substructure of the study area.

ACKNOWLEDGMENTS. The author would like to thank Assoc. Prof. Dang Van Liet (University of Science, VNU-HCM, Vietnam) for his helpful advice on various technical issues.

REFERENCES

[1] Cordell L., & Henderson R. G., Iterative three-dimensional solution of gravity anomaly data using a digital computer, *Geophysics*, 1968, **33**(4), 596-601.

[2] Parker R. L., The rapid calculation of potential anomalies, *Geophysical Journal International*, 1973, **31**(4), 447-455.

[3] Rao D. B., Prakash M. J., & Babu N. R., 3D and 2½ D modelling of gravity anomalies with variable density contrast, *Geophysical Prospecting*, 1990, **38**(4), 411-422.

[4] Oldenburg, D. W., The inversion and interpretation of gravity anomalies, *Geophysics*, 1974, **39**(4), 526-536.

[5] Ai T. T., & Thanh D. D., Xác định độ sâu mặt móng kết tinh trước Kainozoi tại đồng bằng sông Cửu Long bằng phương pháp trọng lực, *Journal of Geology*, 1989, **194-195**, 34-37.

[6] Van Liet D., Determination of the crystal-basement from gravity data using genetic algorithms, *Science and Technology Development Journal*, 2005, **8**(12), 21-26.

[7] Van Liet D., Quyet P. Q., & Phuoc N. H., The model of the tertiary basement rock beneath the interior of the Mekong Delta using gravity data, Final Report, Salamander Energy Vietnam, Ho Chi Minh City, 2008.

[8] Son N. N. T., Hai N. H., Toan L. P, & Liet D. V., Determination of the crystal basement of some gravity anomalies in Mekong delta area by using the forced neural network, Proceedings of the International Scientific Conference Geophysics - Cooperation and Sustainable Development, 2012, 371-379.

[9] Hai N. H., The application of perceptron networks to determine the crystal basement of local gravity anomaly in An Giang, *An Giang University Journal of Science*, 2015, **4**(4), 86-95.

[10] Phach P. V., et al., Báo cáo tổng kết Nghiên cứu cấu trúc - kiến tạo và địa động lực hiện đại khu vực đồng bằng sông Cửu Long nhằm nâng cao khả năng thích ứng và giảm thiểu thiệt hại trong bối cảnh mực nước biển dâng cao, Vietnam Academy of Science and Technology, 2011.

[11] Que B. C., Về một số đặc điểm cấu trúc sâu vỏ trái đất ở Việt Nam theo các tài liệu địa vật lý. *Journal of Geology*, 1982, **154**, 9-12.

 ISBN:

[12] Que B. C., & Lap N. K., Cấu trúc sâu vỏ Trái đất và tính địa chấn lãnh thổ Việt Nam, Vietnam Academy of Science and Technology, 1992.

[13] Trieu, C. D., Mô hình mật độ vỏ trái đất lãnh thổ Việt Nam, *Journal of Computer Science and Cybernetics*, 1995, **11**(3), 56-64.

[14] Trieu C. D., & Toan D. V., Main structural feature of the crust in Vietnam and adjacent area on the basic of gravity data, Proc. of the 4th National Conference on Marine Sciences and Technology in Vietnam, 1999, 854-863.

[15] Trieu C. D., Trường địa vật lý và cấu trúc thạch quyển lãnh thổ Việt Nam, Science and Technics Publishing House, Hanoi, 2005.

[16] Trieu, C. D. et al., Thạch quyển và Manti Đông Nam Á, Science and Technics Publishing House, Hanoi, 2017.

[17] Nunes, J. C., Bouaoune, Y., Delechelle, E., Niang, O., & Bunel, P., Image analysis by bidimensional empirical mode decomposition, *Image and Vision Computing*, 2003, **21**(12), 1019-1026.

[18] Gómez-Ortiz D., & Agarwal B. N., 3DINVER. M: a MATLAB program to invert the gravity anomaly over a 3D horizontal density interface by Parker-Oldenburg's algorithm, *Computers & Geosciences*, 2005, **31**(4), 513-520.

[19] Thoa, N. T. K., Trường địa từ và kết quả khảo sát tại Việt Nam, Science and Technics Publishing House, Hanoi, 2007.

[20] Arısoy M. Ö., & Dikmen Ü., Potensoft: MATLAB-based software for potential field data processing, modeling and mapping, *Computers & Geosciences*, 2011, **37**(7), 935-942.

[21] Blakely R. J., Potential theory in gravity and magnetic applications, Cambridge University Press, 1996.

[22] Nguyen H. H., Van Dang L. & Van Vo V., A combined Euler deconvolution and tilt angle method for interpretation of magnetic data in the South region, *Science and Technology Development Journal*, 2019, **22**(2), 219-227.

ISOMERIC RATIOS IN INVERSE (γ, n) AND (n,γ) REACTIONS ON Ce, Cd, Pd AND Se TARGETS

Bui Minh Hue[1,2*] and Tran Duc Thiep[1,2]

[1]*Graduate University of Science and Technology, VAST, 18 Hoang Quoc Viet, Hanoi, Vietnam*

[2]*Institute of Physics, VAST, 10 Dao Tan St., Ba Dinh, Hanoi, Vietnam*

*E-mail: *bmhue@iop.vast.ac.vn*

Abstract. The isomeric ratios of isomeric pairs produced from inverse (γ,n) and (n,γ) reactions on Ce, Cd, Pd and Se targets induced by bremsstrahlung end-point energy of 25 MeV and thermal neutrons were investigated. The experiments were taken place by the activation method combining with off-line gamma-ray spectroscopy. The data analysis and necessary corrections as the self-absorption and summing cascade effects were made in gamma rays radioactivity measurements to improve the accuracy of the isomeric ratio determination. The results were discussed and compared with those in the existing literature. The obtained results in the (γ,n) reactions were validated by comparison with the theoretical predictions using TALYS 1.95 code.

Keywords: *Inverse reaction, Isomeric ratio, Offline gamma spectroscopy – Talys 1.95.*

I. INTRODUCTION

When the projectile of one reaction is the ejectile of another reaction, these two nuclear reactions are so-called inverse reactions, for examples (γ,p) and (p,γ); (γ,n) and (n,γ); (γ,α) and (α,γ). The first studies of inverse reactions can be found in refs. [1,2] since the 1960s. Mohr [3] studied the relation between the $^{16}O(\alpha,\gamma)^{20}Ne$ reaction and its reverse $^{20}Ne(\gamma, \alpha)^{16}O$ reaction in stars and in the laboratory. The authors show that whereas the stellar reaction rates of the $^{16}O(\alpha,\gamma)^{20}Ne$ reaction are identical to the laboratory rates, this is not the case for the photo-disintegration rates under stellar and under laboratory conditions. Although the thermal population of the first excited state in ^{20}Ne remains extremely small at typical temperatures of neon burning, it nevertheless provides an important contribution to the reaction rate under stellar conditions. Inverse reactions, including photonuclear and thermal neutron capture reactions, namely (γ,n) and (n,γ) reactions play an important role in astrophysics and the study of nuclear structure and nuclear reaction mechanisms [2-4]. Until now, most investigations about thermal neutron capture reactions have focused on the determination of reaction cross section or reaction rate, but the studies on isomeric ratio (IR) have been still limited. The IR, defined as the ratio of the probability for forming isomeric and ground states, provides diverse information about the nuclear structure and nuclear reaction mechanism [5-8]. This ratio connects with many problems of modern nuclear physics and can be used to test different models of nuclear reactions induced by various projectiles.

In this work, we investigate IRs in some (γ, n) and (n, γ) reactions, which lead to the same residual nucleus with near the same excitation energy by activation method using off-line gamma spectroscopy. Namely, they are $^{138}Ce(\gamma,n)^{137m,g}Ce$ and $^{136}Ce\ (n,\gamma)^{137m,g}Ce$; $^{116}Cd(\gamma,n)^{115m,g}Cd$ and $^{114}Cd(n,\gamma)^{115m,g}Cd^{116}$;$^{110}Pd(\gamma,n)^{109m,g}Pd$ and $^{108}Pd(n,\gamma)^{109m,g}Pd$;

 ISBN:

$^{82}Se(\gamma,n)^{81m,g}Se$ and $^{80}Se(n,\gamma)^{81m,g}Se$. The experimental results are expected to to examine the role of the reaction channel effect, intake momentum and impulse effect on the IRs. Moreover, the obtained results in the (γ,n) reactions were compared with the theoretical predictions using TALYS 1.95 code.

II. EXPERIMENTS

The bremsstrahlung source is obtained by interaction of 25 MeV electron beam produced from MT-25 Microtron accelerator [10] and a 3 mm thickness W disk and cooled by the water demonstrated in Fig. 1. The end-point energy of bremsstrahlung is 25 MeV. The bremsstrahlung spectra, which were simulated by GEANT4 toolkit [11], are shown on Fig. 2.

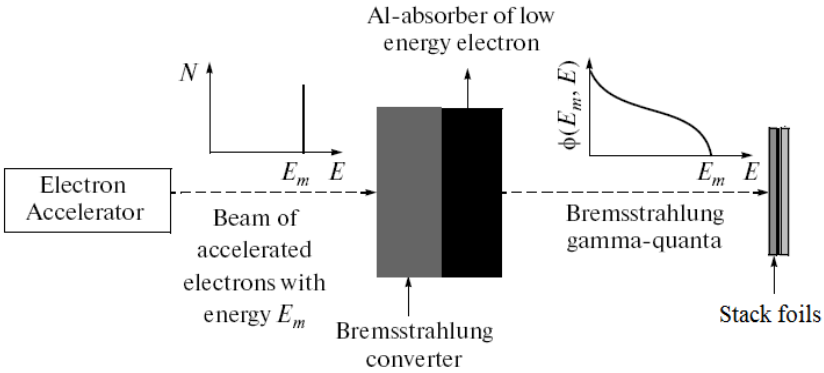

Fig. 1. *The scheme for production of bremsstrahlung source.*

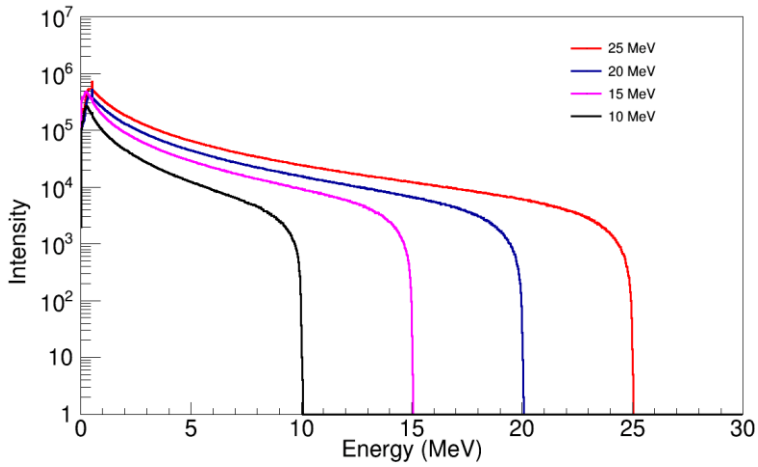

Fig. 2. *Calculated bremsstrahlung spectra with different energies using GEANT4 toolkit*.

The thermal neutron source was also created at Microtron MT-25 and shown in Fig. 3. The bremsstrahlung photon flux was obtained when the electron beam impinged on a uranium electron-photon converter with cylinder form (diameter and length of 10 mm) surrounded by beryllium. The neutron beam was produced by (γ,n) photonuclear and (γ,f) fission reactions of uranium with high energy part and by (γ,n) photonuclear reaction of beryllium with low energy part of the bremsstrahlung photon flux. This uranium-beryllium converter was placed within a 120×120×120 cm^3 graphite cube, which served as a main neutron moderator to thermal and epithermal neutrons.

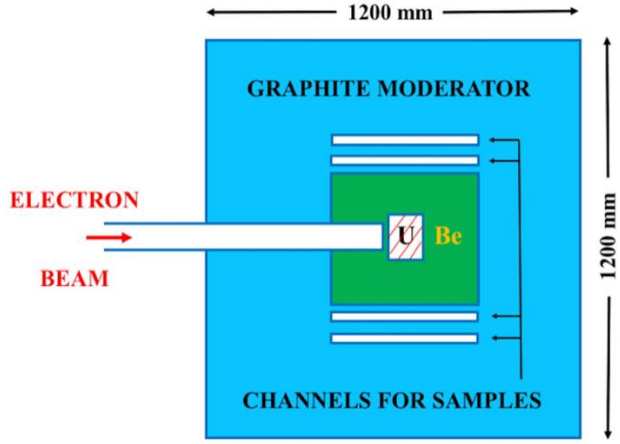

Fig. 3. *The scheme for production of thermal and epithermal neutrons*.

The high-purity natural Ce_2O_3, PdO, SeO_2 and Cd samples with the mass and diameter of 0.8 g; 0.323 g; 0.2484 g; 0.7143 g and 1.6 cm; 1.0 cm; 1.0 cm; 1.0 cm; respectively were irradiated in the photon and neutron sources with the definite time, which was preliminarily estimated by the activation method so that the interested gamma rays have good count statistics. Afterwards, the gamma-ray activities were measured for proper time of cooling and measurement by using the high-resolution gamma-ray spectroscopy consisting of the high-energy resolution HPGe detector (1.80 keV at γ - ray 1332 keV of ^{60}Co), the PC based 8192 channel analyzers for the data processing, the GENIE 2000 and Gamma Vision software used for the data acquisition and γ-ray spectra analysis.

III. DATA ANALYSIS

The simplified decay schemes of the isomeric pairs ^{137m,g}Ce (a), ^{115m,g}Cd (b), ^{109m,g}Pd (c) and ^{81m,g}Se (d) are presented in Fig. 4. The selection of gamma rays for the IR calculations is very important as it is related to the gamma ray processing and count statistics. This issue was performed based on the conditions that a selected gamma ray to have high intensity and separated from interfering gamma rays. As a result, the selected gamma rays and spectroscopic characteristic data used for the IR calculation were determined and shown in Table 1. The data in this table were taken from refs. [12,13].

The losses of the interested gamma ray count due to the self-absorption and summing coincidence effects, which contribute to the IR determination error were corrected by formulas (1) and (2) below taken in refs. [8,9,14].

$$F_g = \frac{\mu}{1 - e^{-\mu}} \tag{1}$$

$$C_c = \frac{1}{1 - \sum_{i=1}^{i=j} f_i \times \varepsilon_t(i)} \tag{2}$$

 ISBN:

where f_i - the fraction of coincidence photons of energy i in coincidence with the gamma ray of interest and ε_t (i) - the total efficiency of the coincidence photon of energy i and C_c - the correction factor; μ - the linear attenuation coefficient, t - the sample thickness and F_g is defined as the ratio of the true and measured counts of the interested gamma rays. The linear attenuation coefficients were taken from ref. [15].

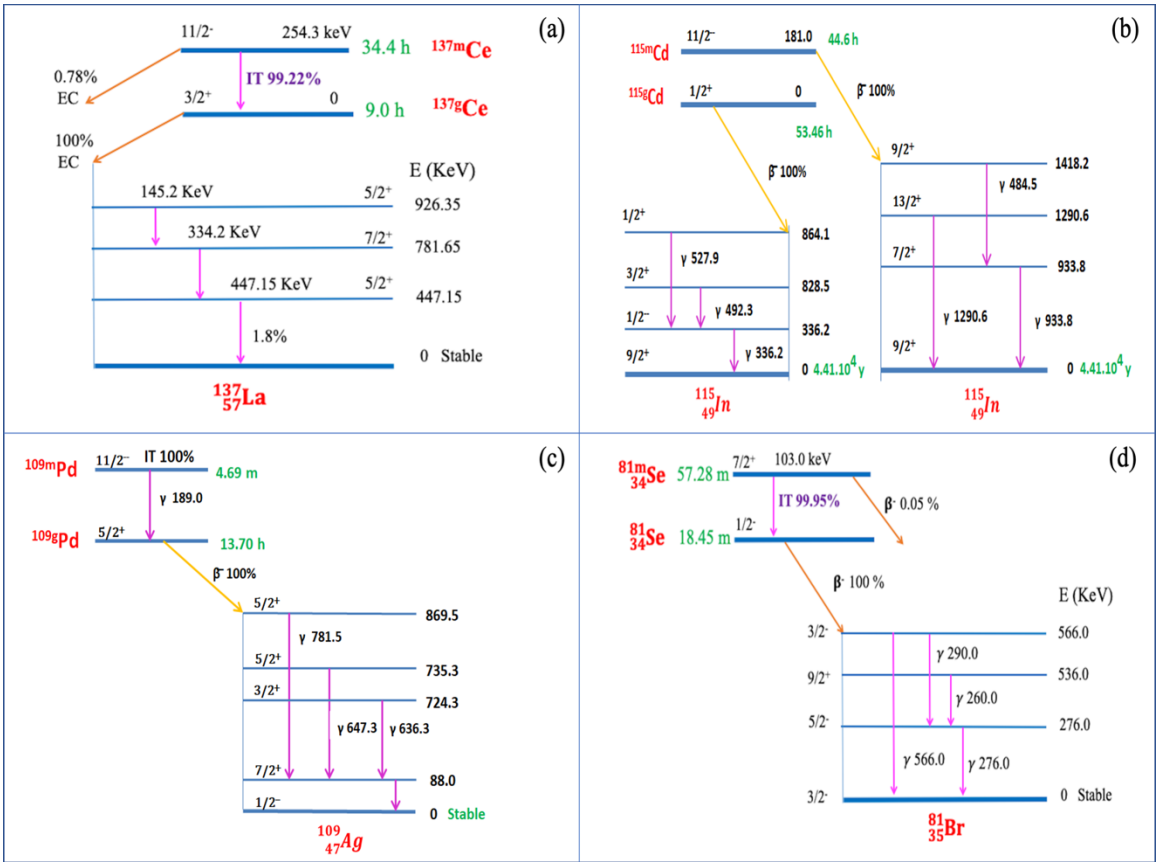

Fig. 4. *The simplified decay schemes of the isomeric and ground states of ^{137m,g}Ce (a), ^{115m,g}Cd (b), ^{109m,g}Pd (c) and ^{81m,g}Se (d).*

Table 1. *Gamma rays and spectroscopic characteristic data of the isomeric and ground states used for the isomeric calculations.*

Nuclear Reaction	Target Spin, Parity, [J^π]	Nuclear state	Spin Parity [J^π]	Decay Mode [%]	Half Life	γ-ray Energy [keV]	Intensity [%]
^{138}Ce(γ, n)^{137}Ce ^{136}Ce(n, γ)^{137}Ce	0^+	^{137m}Ce	$11/2^-$	IT: 99.2 EC: 0.78	34.4 h	254.3	99.2
^{138}Ce(γ, n)^{137}Ce ^{136}Ce (n, γ)^{137}Ce	0^+	^{137g}Ce	$3/2^+$	EC: 100	9.0 h	447.1	1.8
^{116}Cd(γ, n)^{115}Cd ^{114}Cd(n, γ)^{115}Cd	0^+	^{115m}Cd	$11/2^-$	β^- : 100	44.6 d	933.8	2.0
^{116}Cd(γ, n)^{115}Cd ^{114}Cd(n, γ)^{115}Cd	0^+	^{115g}Cd	$1/2^+$	β^- : 100	2.23 d	336.2 527.9	45.9 27.45
^{110}Pd(γ, n)^{109,}Pd ^{108}Pd(n, γ)^{109}Pd	0^+	^{109m}Pd	$11/2^-$	IT: 100	4.69 m	189.0	55.9
^{110}Pd(γ, n)^{109}Pd ^{108}Pd(n, γ)^{109}Pd	0^+	^{109g}Pd	$5/2^+$	β^- : 100	13.7 h	88.04	3.6
^{82}Se(γ, n)^{81}Se ^{82}Se(n, γ)^{81}Se	0^+	^{81m,}Se	$7/2^+$	IT: 99.95 β^- : 0.05	57.28 m	103.0	13.0
^{82}Se(γ, n)^{81}Se ^{80}Se(n, γ)^{81}Se	0^+	^{81g,}Se	$1/2^-$	β^- : 100	18.45 m	276.0 290.0	0.7 0.55

The gamma spectrum of the natural samples of Ce (as one example of analyzed spectra) is shown in Fig. 5 irradiated in the bremsstrahlung and neutron sources for the respective time of irradiation, cooling and measurement. One can see very well the gamma rays of the investigated reaction products.

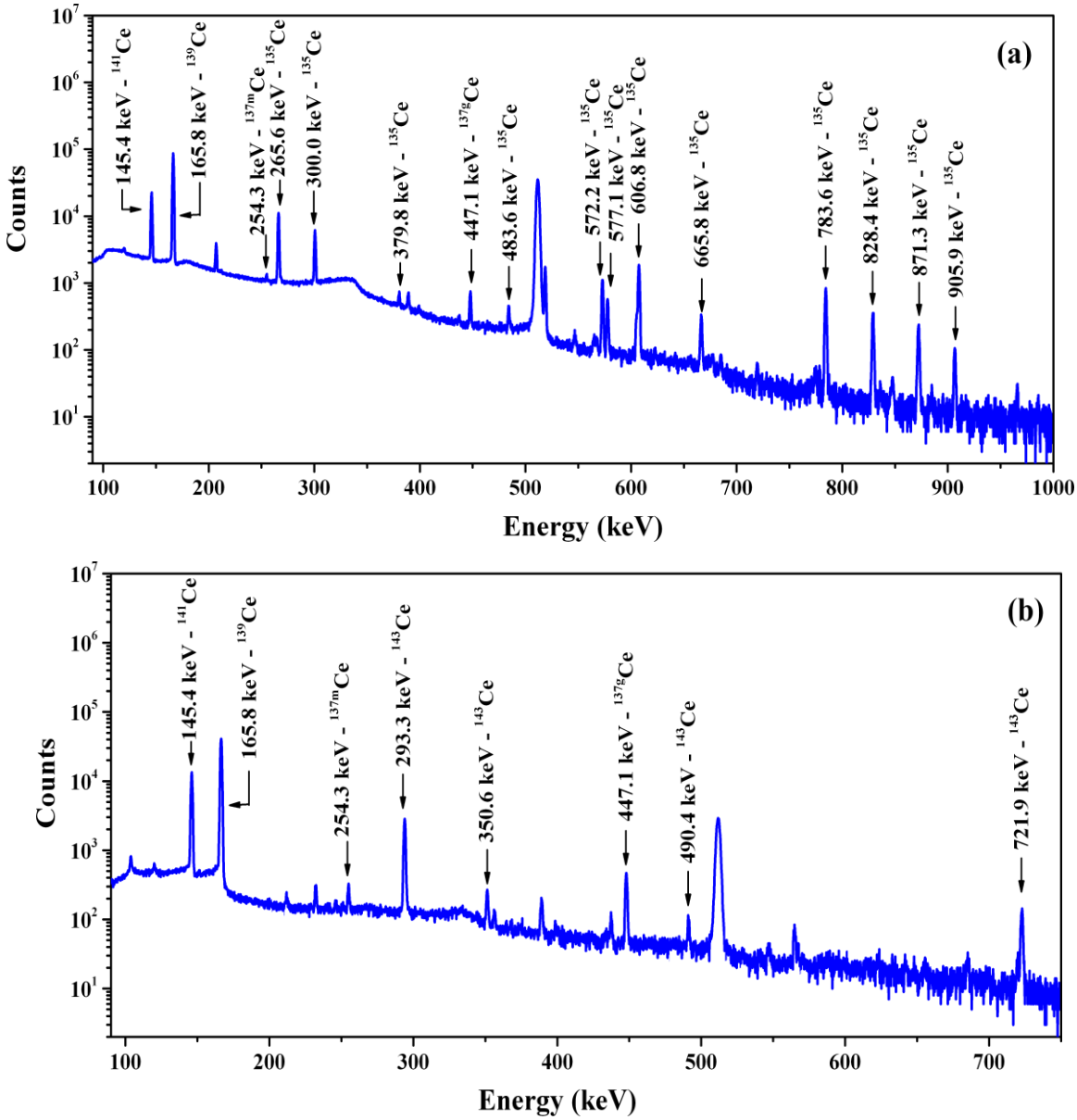

Fig. 5. *Typical spectra of natural Ce-sample irradiated by 25 MeV bremsstrahlung for 60 min. with cooling and measurement time of 60 and 20 min. respectively at a distance of 5 cm from the detector (a) and irradiated in the neutron source for 90 min. with cooling and measurement times of 35 and 60 min. respectively at a distance of 0 cm from the detector (b).*

The IR was calculated by formula (3) below as in refs. [8,9]:

$$\frac{1}{IR} = \frac{\frac{S_g e_m I_m}{S_m e_g I_g} L_3 L_6 L_9 - L_1 L_5 L_8 - L_3 L_4 L_8 - L_3 L_6 L_7}{L_2 L_5 L_8} \quad (3)$$

 ISBN:

where m and g - the isomeric and ground states; S, ε and I - the counts, the efficiencies and the intensities of the gamma rays of interest and Λ_i (i = 1 ~ 9) are expressions related to the irradiation, cooling and measurement time.

IV. RESULTS AND DISCUSSION

Table 2 presents the results of this work together with the existing data, which were taken from refs. [8,16-25].

Table 2. *The isomeric ratio of the investigated (γ,n) and (n,γ) inverse reactions.*

Nuclear Reaction and Product	Type of projectile	Product Exc. Energy [MeV]	Isomeric Ratio *IR*
^{138}Ce(γ, n)^{137m,g}Ce	25 MeV Bremsstrahlung	5.5	0.221(22) (This work) 0.19(2) [18]
^{136}Ce (n, γ)^{137m,g}Ce	Thermal neutron	7.4	0.112(11) (This work) 0.109(10) [8] 0.15(1) [19] 0.088(6) [20]
^{116}Cd(γ, n)^{115m,g}Cd	25 MeV Bremsstrahlung	5.8	0.165(16) (This work) 0.168(20) [21]
^{114}Cd(n, γ)^{115m,g}Cd	Thermal neutron	6.1	0.116(12) (This work) 0.099(33) [22]
^{110}Pd(γ, n)^{109m,g}Pd	25 MeV Bremsstrahlung	6.3	0.069(7) (This work) 0.065(3) [17]
^{108}Pd(n, γ)^{109m,g}Pd	Thermal neutron	6.1	0.023(2) (This work) 0.018(5) [23], 0.028(5) [16]
^{82}Se(γ, n)^{81m,g}Se	25 MeV Bremsstrahlung	6.9	0.556(55) (This work) 0,56(2) [24]
^{80}Se(n, γ)^{81m,g}Se	Thermal neutron	6.7	0.114 ± 0.014 (This work) 0.204(24) [20] 0.136(0.011) [16] 0.096(9) [25]

From the obtained data, one can make the following notes:

- The experimental IRs in inverse (γ,n) and (n,γ) reactions, which lead to the same isomeric pairs ^{137m,g}Ce, ^{115m,g}Cd, ^{109m,g}Pd, and ^{81m,g}Se are different due to the reaction channel effect. The IRs in (γ,n) reactions are significantly higher than that in (n,γ) reactions. This trend can be explained by the intaken angular momentum and impulse, transferred to the target nuclei from the projectiles, namely the higher the intake angular momentum and impulse the higher the isomeric ratio.
- The IRs in this work for the (γ,n) reactions, and that of refs. [17,18,21,24] in the error limit are in good agreement. Likewise, for the (n,γ) reactions, our results and the data from the references are in an agreement except for ^{81m,g}Se to be an agreement with refs. [16,25] and being considerably less than that from ref. [20].

Theoretical IR calculation of ^{137m,g}Ce, ^{115m,g}Cd, ^{109m,g}Pd, and ^{81m,g}Se produced from (γ,n) reaction used Talys 1.95 code [26] and Geant4 simulation tool. In case of bremsstrahlung induced nuclear reactions, the isomeric ratios could be analytically calculated by the expression below:

$$IR = \frac{Y_m}{Y_g} = \frac{N_0 \int_{E_{th}^m}^{E_\gamma^m} \sigma_m(E)\phi(E)dE}{N_0 \int_{E_{th}^g}^{E_\gamma^m} \sigma_g(E)\phi(E)dE} \quad (4)$$

where E_g^m - the bremsstrahlung end-point energy, ϕ (E) – the bremsstrahlung photon flux simulated by GEANT4 (Fig. 2), N_0 - the number of the target nuclei; $\sigma_m(E)$ and $\sigma_g(E)$ - the cross sections of the isomeric and ground states obtained by TALYS 1.95 code; E_{th}^m and E_{th}^g - the threshold reaction energies for the isomeric and ground state respectively.

The theoretical IR results were obtained by the calculation using six level density models of TALYS 1.95 as: Constant temperature + Fermi gas model; Back-shifted Fermi gas model; Generalised superfluid model; Microscopic level densities (Skyrme force) from Goriely's tables; Microscopic level densities (Skyrme force) from Hilaire's combinatorial tables and Microscopic level densities (temperature dependent HFB, Gogny force) from Hilaire's combinatorial tables. For demonstration, Table 3 are shown the theoretical results, calculated using the six models with the Goriely T-dependent HFB model of the strength function for (γ, n) reactions, induced by 25 MeV bremsstrahlung.

Table 3. *The IRs calculated by the six models of TALYS code 1.95 with the Goriely T-dependent HFB model strength function for (γ, n) reactions, induced by 25 MeV bremsstrahlung.*

No	Isomeric Pair	Model 1	Model 2	Model 3	Model 4	Model 5	Model 6	Exp. results
1	^{137m,g}Ce	0.063	0.071	0.061	0.087	0.077	0.058	0.221(22)
2	^{115m,g}Cd	0.167	0.190	0.161	0.201	0.193	0.154	0.165(16)
3	^{109m,g}Pd	0.058	0.072	0.056	0.068	0.083	0.070	0.069(07)
4	^{81m,g}Se	0.531	0.544	0.454	0.710	0.636	0.549	0.556(55)

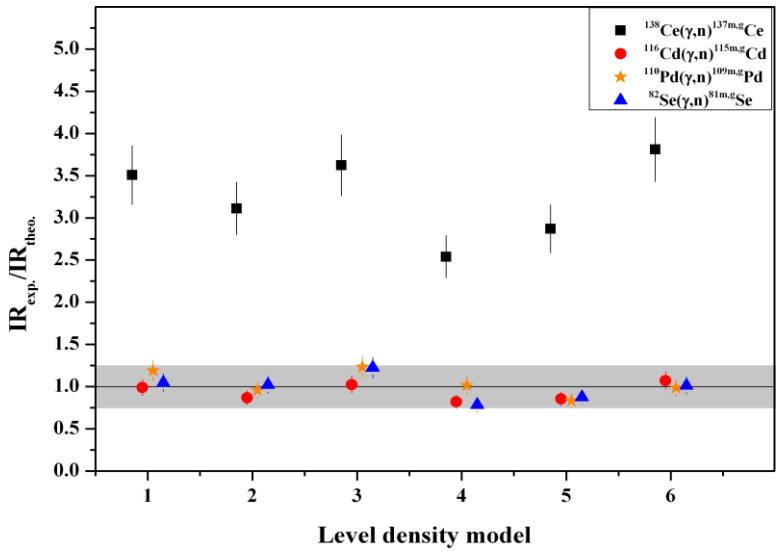

Fig. 6. *Measured ($IR_{exp.}$) and calculated ($IR_{theo.}$) isomeric ratios of $^{138}Ce(\gamma,n)^{137m,g}Ce$, $^{116}Cd(\gamma,n)^{115m,g}Cd$, $^{110}Pd(\gamma,n)^{109m,g}Pd$ and $^{82}Se(\gamma,n)^{81m,g}Se$ induced by 25 MeV bremsstrahlung.*

The present experimental results are best suited to the predictions using the 6th level density model. The deviations between the experimental and calculated data using 6 level density models are less than 23% (see Fig. 6) except for ^{137m,g}Ce. The difference in the case of ^{137m,g}Ce requires the level density and strength function models to be more detailed.

 ISBN:

V. CONCLUSIONS

The IRs of isomeric pairs ^{137m,g}Ce, ^{115m,g}Cd, ^{109m,g}Pd and ^{81m,g}Se produced in inverse (γ,n) and (n,γ) reactions have been measured by the activation method. The experimental results show that the IRs in (γ,n) reactions are higher than that in (n,γ) reactions. This trend can be explained by the intaken momentum and impulse, transferred to the target nuclei from the projectiles. These are the effects of momentum and impulse in nuclear reactions.

The theoretical IR calculations for (γ,n) reactions based on TALYS 1.95 code are consistent with the experimental results, except in the case of ^{138}Ce(γ,n)^{137m,g}Ce reaction.

ACKNOWLEDGMENTS. The authors would like to express sincere thanks to the MT-25 Microtron group for operating the irradiation facility and the Chemical Department of the Flerov Laboratory of Nuclear Reaction for providing the measurement system. Bui Minh Hue was funded by Vingroup Joint Stock Company and supported by the Domestic PhD Scholarship Program of Vingroup Innovation Foundation (VINIF), Vingroup Big Data Institute (VINBIGDATA), code VINIF.2020.TS.18.

REFERENCES

[1] Cohen S. G., Fisher P. S. and Warburton E. K., Inverse photonuclear reactions ^{14}N(p,γ)^{14}O and ^{15}N(p,γ)^{16}O in the giant resonance region, *Phys. Rev.*, 1961, **121**(3), 858-865.

[2] Wahsweiler H. G. and Greiner W., Angular distributions for the inverse photonuclear process in Si^{28} in the eigenchannel reaction theory, *Phys. Rev. Lett. V*, 1967, **19**(3), 131-134.

[3] Mohr P., Angulo C., Descouvemont P. and H., Relation between the ^{16}O(α,γ)^{20}Ne reaction and its reverse ^{20}Ne(γ,α)^{16}O reaction in stars and in the laboratory, *Eur. Phys. J. A*, 2006, **27**(1), 75-78.

[4] Beard M., Frauendorf S., Kampfer B., Schwengner R. and Wiescher M., Photonuclear and radiative-capture reaction rates for nuclear astrophysics and transmutation: 92-100Mo, 88Sr, 90Zr, and 139La, *Phys. Rev. C*, 2012, **85**, 065808.

[5] Huizenga J. R. and Vandenbosch R., Isomeric cross-section ratios for reactions producing the isomeric pair ^{197m,g}Hg, *Phys. Rev.*, 1960, **120**(4), 1313-1318.

[6] Huizenga J. R and Vandenbosch R., Interpretation of isomeric cross section ratios for (n,g) and (g,n) reactions, *Phys. Rev.*, 1960, **120**(4), 1305-1312.

[7] Do N. V., Luan N. T., Xuan N. T., Khue P. D, Hien N. T, Kim G., Kim K., Shin S. G, Kye Y., Cho M. H., Measurement of yield ratios for the isomeric pair ^{137m,g}Ce in the ^{141}Pr(γ,x)^{137m,g}Ce reactions with bremsstrahlung end-point energies of 50-, 60-, and 70-MeV, *Radiation Physics and Chemistry*, 2020, **176**, 1-9, 10901.

[8] Thiep T. D., An T. T., Cuong P. V., Vinh N. T., Hue B. M., Belov A. G, Maslov O. D, Channel effect in isomeric ratio of ^{137m,g}Ce produced in different nuclear reactions, *J. Radioanal. Nucl. Chem.*, 2017, **314**, 1777-1784.

[9] Hue B. M., Thiep T. D., An T. T., Cuong P. V., Lukyanov S. M, Belov A. G., Mitrofanov S., The isomeric ratios in (n,γ) neutron capture reactions on ^{108}Pd and ^{110}Pd nuclei, *J. Radioanal Nucl. Chem.*, 2020, **326**(1), 503-509.

[10] Belov A. G., Bondarenko P. G., Teteriev Yu. G., Preprint of JINR, D15-93-80, Dubna, Russia, 1993.

[11] Geant4 Collaboration, Physics Reference Manual, Release 10.4, 2017.

[12] Firestone R. B., Table of Isotopes, CD ROM Edn., Version 1.0, Wiley-Interscience, New York, 1996.

[12] Radiation Search, http://ie.lbl.gov/toi/radSearch.asp53.

[13] Montgomery D. M. and Montgomery G. A., A method for assessing and correcting coincidence summing effects for germanium detector efficiency calibration, *J. Radioanal. Nucl. Chem.*, 1995, **l93**(1), 71-79.

[14] https://physics.nist.gov/PhysRefData/XrayMassCoef/tab3.html

[15] Bishop C. T., Vonach H. K. and Vandenbosch R., Isomer ratio for some (n,γ) reactions, *Nucl. Phys. A*, 1964, **60**, 241-249.

[16] Palvanov S. R., Bozorov E. K., Mamajusupova M. I, Palvanova G. S., Saidimov Y. A., Excitation of isomeric states in reactions (γ,n) and (n,2n) on ^{110}Pd, *Nucleus. World Journal of Research and Review*, 2017, **5**(5), 28-31.

[17] Gangrsky Yu. P, Zuzaan P., Kolesnikov N. N., Lukashek V. G., Tonchev A. P., Isomeric ratios in crossing (n,γ) and (γ,n) reactions, *Bull. Rus. Acad. Sci. Phys*., 2001, **65**, 121-126.

[18] Bernard K., Yield ratios of isomers produced by neutron activation, *Phys. Rev.*, 1963, **129**(2), 769-775.

[19] Torrel S. and Krane K. S., Neutron capture cross sections of ^{136,138,140,142} Ce and the decays of ^{137}Ce, *Phys. Rev. C*, 2012, **86**, 034340.

[20] Kyryjenko A. V, Osipenko A. P, Parlag A. M., Pylypchenko V. A., Sabolchiy N. T., Sokolyuk I. V., Khimich I.V., Investigation of the cadmium nuclei isomers state excitation in the photonuclear reactions, Uzhgorod University Scientific Herald, *Series Physics*, 2006, **19**, 85-89.

[21] Gicking A. M., Takahashi K., Krane K. S., Neutron capture cross sections of stable Cd isotopes, *Eur. Phys. J. A*, 2019, **55**, 52-62.

[22] Sehgal M. L., Hans H. S, Gill P. S., Thermal neutron cross-sections for producing some isomers, *Nucl. Phys.*, 1959, **12**(3), 261-268.

[23] Palvanov S., Cross section of excitation of isomer states ^{81m,g}Se in the reaction (γ,n) and (n,2n), *Journal of Scientific and Engineering Research*, 2018, **5**(1), 41-45.

[24] Nakamura S., Furutaka K., Harada H., Katoh T., Thermal-neutron capture cross sections and resonance integrals of the ^{80}Se(n,γ)^{81m,g}Se reaction, *Journal of Nuclear Science and Technology*, 2008, **45**(2), 116-122.

[25] www.talys.eu.

 ISBN:

OPTIMAL STRUCTURE OF PHOTONIC CRYSTAL FIBER WITH INFILTRATED BENZENE CORE FOR APPLICATION SUPERCONTINUUM GENERATION

Ngoc Vo Thi Minh[1], Bao Tran Le Tran[1], Trong Dang Van[1], Bao Le Xuan[1], Thao Tran Ngoc[1], Long Vu Dinh[1], Thanh Tran Viet[1], Oanh Truong Thi Chuyen[1], Thu Ho Thi Anh[1], Thuy Nguyen Thi[2], Vu Tran Quoc[1], Lanh Chu Van[1*]

[1]*Department of Physics, Vinh University, 182 Le Duan, Vinh City, Viet Nam*

[2]*University of Education, Hue University, 34 Le Loi Street - Hue City, Viet Nam*

*E-mail: *chuvanlanh@vinhuni.edu.vn*

Abstract. In this paper, we investigate photonic crystal fibers (PCFs) with hollow-core infiltrated by Benzene. Characteristic quantities of PCF including the effective refractive index, chromatic dispersion, effective mode area, and confinement loss have been calculated according to numerical simulation and analyzed in detail. The obtained results are compared with other publications. The flat all-normal and anomalous dispersion are achieved in the studied wavelength region, in which two structures with the lattice constant $\Lambda = 1.5$ μm, the filling factors $d/\Lambda = 0.45$, and $\Lambda = 2.0$ μm, $d/\Lambda = 0.3$ can be chosen as the optimal structure with the flattest dispersion. The values of effective mode area and confinement loss are as small as acceptable. These advantages of PCF are favorable for application in supercontinuum generation.

Keywords: *Photonic crystal fibers; Flat all-normal and anomalous dispersion; Optimal structure, Effective mode area, Confinement loss.*

I. INTRODUCTION

Over the past decades, PCFs have attracted the research of many scientists who have achieved outstanding achievements in optical communication and other applications. The PCF which contains a silica core bordered with a silica-air photonic crystal material with a hexagonal symmetry [1] or a micrometer-spaced hexagonal array [2,3] has been described. PCFs can direct the light by total internal reflection phenomenon for solid core fiber [3] and photonic bandgap effect for hollow-core fiber [4]. Light is confined inside the fiber in ways not previously likely or even conceivable by a photonic crystal-like microstructure arrangement of capillaries [5] that is obtained some great properties of PCF as endlessly single-mode [6], ultra-high birefringence of the PCF with ultralow confinement loss [7], ultra-flattened dispersion [8], low confinement loss [9] and high intrinsic nonlinearity of the SF57 glass material [10]. This micro-structured arrangement has a low refractive index than the core material of fiber which ensures great confinement of light [11]. The structure of PCFs can provide flexibility in its design by changing types of the different lattice, air hole diameter (d), lattice constant (Λ), filling factor (d/Λ), and refractive index (n) of the glass material [12,13].

Researchers are significantly interested in the very important characteristics of PCF as the effective mode area, chromatic dispersion, zero wavelength dispersion, and

confinement loss [14,15]. They were originally introduced as a measure of nonlinearities [16], confinement loss [17], micro-bending loss [18], macro-bending loss [19], splicing loss [20], and numerical aperture [21]. Most of these works have been studied in detail these each quantity, but they have not yet been considered about each other. In addition, PCFs containing air-holes in the cladding or the core will have difficulty in tuning the characteristic quantities. To overcome that, recently a series of publications have infiltrated liquid into the core of PCFs. These infiltration liquids have been used for supercontinuum (SC) generation [22], make effect to dispersion properties of PCFs [23-25]. In the paper [22], the ones used Toluene to penetrate the core of the PCF and have shown two optimal structures for supercontinuum generation with lattice constant 2 μm filling factors 0.3 and 0.35, respectively. However, the limitation of the structures with Toluene core is the confinement loss remains high value at the value of zero wavelength dispersion.

Both Benzene and Toluene have unsaturated ring structures, Toluene is a derivative of benzene and this is the suggestion that Benzene can be penetrated the core to replace Toluene as work [22]. Benzene is also a toxic substance as toluene that affects human health so when used, we must use the protection of labor. In this paper, we designed a PCF which is made of fused silica glass with a hollow core is infiltrated with Benzene. We analyze characteristics quantities of PCF as effective refractive index, effective mode area, chromatic dispersion, zero wavelength dispersion, and confinement loss. Moreover, the relations between them are also considered. In these analyzes, PCF with benzene core owns a lower confinement loss, flatter dispersion curves in comparison to the Toluene. This result is indeed good to apply for supercontinuum generation.

II. DESIGN AND THEORY

The geometrical structure with a hexagonal lattice of PCFs is shown in Fig. 1. They are designed by Lumerical mode solutions software [26], where the background material is fused silica and the core is infiltrated by Benzene liquid. In simulations, the lattice constants are 1.5 μm and 2.0 μm with the filling factors of 0.3-0.8. The core of PCF is infiltrated by Benzene liquid. The diameter of core PCF is defined $D = 2\Lambda - 1.1d$. We simulated 22 structures for these PCFs. The real parts of the refractive index of Benzene and fused silica are shown in Fig. 2. The data of refractive index as the wavelength is used in the simulation for Benzene by Cauchy's equation (1) [27] and for Fused Silica by Sellmeier's equation (2) [28], where the wavelength λ has dimensions of micrometers (μm):

$$n^2(\lambda) = A_0 + A_1\lambda^2 + \frac{A_2}{\lambda^2} + \frac{A_3}{\lambda^4} + \frac{A_4}{\lambda^6}, \quad (1)$$

where A_0=2.170184597; A_1=0.00059399 μm^{-2}; A_2=0.02303464 μm^2; A_3=0.000499485 μm^4; A_4=0.000178796 μm^6 and

$$n^2(\lambda) = B_0 + \frac{B_1\lambda^2}{\lambda^2 - C_1} + \frac{B_2\lambda^2}{\lambda^2 - C_2} + \frac{B_3\lambda^2}{\lambda^2 - C_3}, \quad (2)$$

 ISBN:

with B_0 = 1; B_1 = 0.6694226; B_2 = 0.4345839; B_3 = 0.8716947; C_1 = 4.4801×10^{-3} µm^2; C_2 = 1.3285×10^{-2} µm^2, C_3 = 95.341482 µm^2.

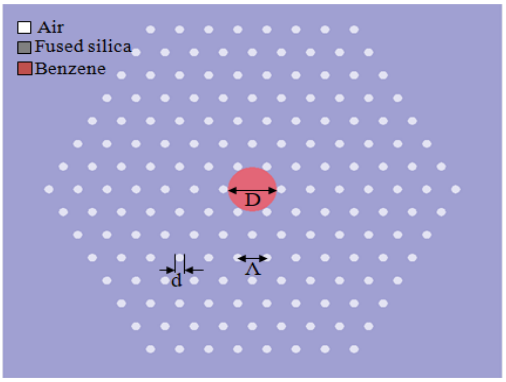

Fig. 1. *The geometrical structure of PCF infiltrated with Benzene in the core.*

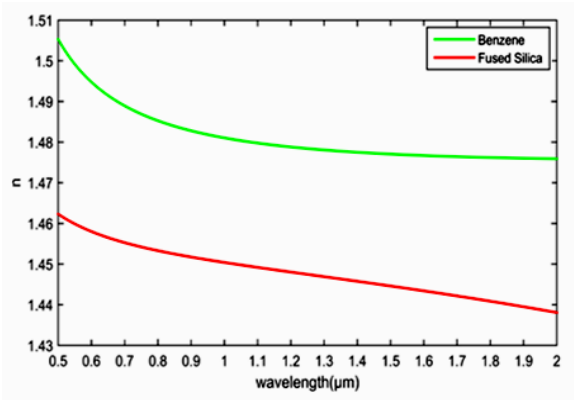

Fig. 2. *Real parts of the refractive index of Benzene [27] and Fused Silica [28].*

The main characteristics of PCFs such as effective refractive index (n_{eff}), effective mode area (A_{eff}), chromatic dispersion (D), and confinement loss (L_c) are described by the following equations [9,12,14,29]:

$$n_{\text{eff}} = \frac{\beta(\lambda, n_m(\lambda))}{k_0}, \tag{3}$$

with the phase constant β and wave number $k_0 = \frac{2\pi}{\lambda}$

$$A_{eff} = \frac{\left(\int_{-\infty}^{\infty}\int_{-\infty}^{\infty} |E|^2 \, dxdy\right)^2}{\int_{-\infty}^{\infty}\int_{-\infty}^{\infty} |E|^4 \, dxdy}, \tag{4}$$

$$D = -\frac{\lambda}{c}\frac{d^2 \operatorname{Re}\left[n_{eff}\right]}{d\lambda^2}, \tag{5},$$

and

$$L_c = 8.686 k_0 \operatorname{Im}\left[n_{eff}\right](dB/m), \tag{6}$$

where Im[n_{eff}] is the imaginary part of the n_{eff}.

III. RESULTS AND DISCUSSION

3.1. Effective refraction index

Fig. 3 presents the real part of the effective refractive index n_{eff} of fundamental modes for PCFs with d/Λ that varies from 0.3 to 0.8 and different lattice constants, Λ = 1.5 µm and 2.0 µm. The results have shown that the real part of the effective refractive index decreases when the wavelength increases.

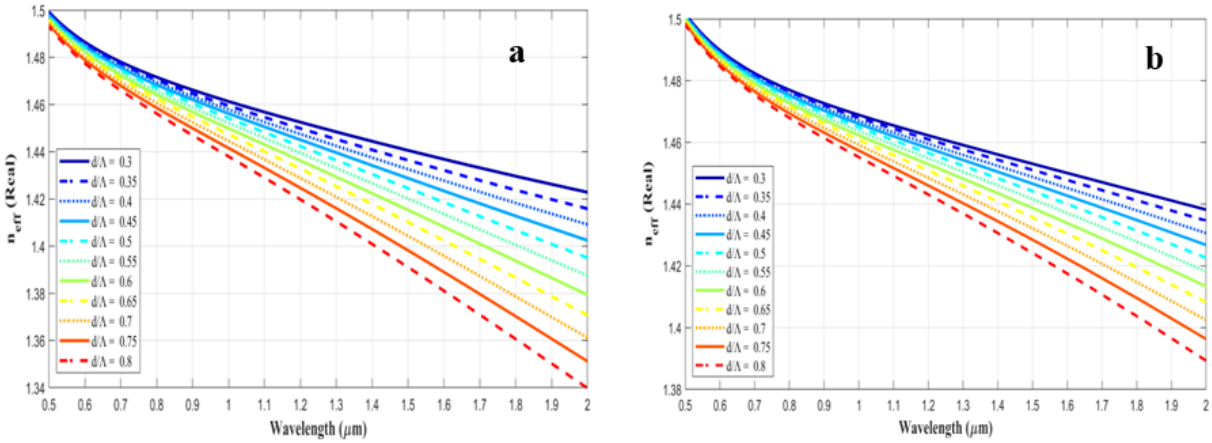

Fig. 3. *The dependence of the effective refractive index on the wavelength of PCFs with various d/Λ and a) Λ = 1.5 μm, b) Λ = 2.0 μm.*

Furthermore, an increase in d/Λ causes the effective refractive index to decrease monotonically. That means effective refractive index curves have the smallest slope with d/Λ equals 0.3 and the largest slope with d/Λ = 0.8. These results are similar to the results for PCF that is infiltrated with Toluene in the publication [22]. The maximum and minimum values of the effective refractive index are 1.4522 and 1.388 corresponding to structures with d/Λ = 0.3, Λ= 2.0 μm and d/Λ = 0.8, Λ =1.5 μm. The effective refractive index grows up as the lattice constant is lifted (Table 1)

Table 1. *The value of the effective refractive index of PCFs at the 1.55 μm wavelength.*

	Λ = 1.5 (μm)										
d/Λ	0.3	0.35	0.4	0.45	0.5	0.55	0.6	0.65	0.7	0.75	0.8
n_{eff}	1.440	1.435	1.431	1.427	1.423	1.418	1.413	1.408	1.402	1.396	1.388
	Λ = 2.0 (μm)										
d/Λ	0.3	0.35	0.4	0.45	0.5	0.55	0.6	0.65	0.7	0.75	0.8
n_{eff}	1.452	1.450	1.448	1.446	1.443	1.440	1.437	1.434	1.431	1.427	1.422

3.2. Chromatic dispersion

The chromatic dispersion of the PCFs as a function of wavelength is quoted in Fig. 4. An increase in dispersion values with increasing the wavelength is observed over the entire investigated wavelength while these values decrease with increasing the filling factor. Interestingly, the zero-dispersion wavelength (ZDW) shifts towards longer wavelengths as d/Λ decreases. The properties of the dispersion are strongly influenced by the variation of the filling factors and the lattice constants. When Λ = 1.5 μm, the all-normal and anomalous dispersions with one and two ZDWs are obtained, PCF with d/Λ = 0.3-0.45 possess the all-normal dispersion, dispersion with two ZDWs is obtained when d/Λ = 0.5-0.75, and only PCF with d/Λ = 0.8 has one ZDW (Fig. 5a). When Λ increases (Λ = 2.0 μm), we have obtained the ultra-flattened dispersion in range wavelength from 1 μm to 2 μm (Fig. 5b). Namely, the dispersion with d/Λ = 0.3 is all-normal while the other dispersion curves exist one ZDW. Both all-normal and anomalous dispersion are favorable factors to be able for generating SC with a broader output spectrum. In comparison with Toluene-infiltrating PCFs in work [22], the chromatic dispersion curves of these PCFs are

 ISBN:

flatter. This result is due to the higher molecular density of Toluene and the larger effective refractive index of the PCFs infiltrated with Benzene.

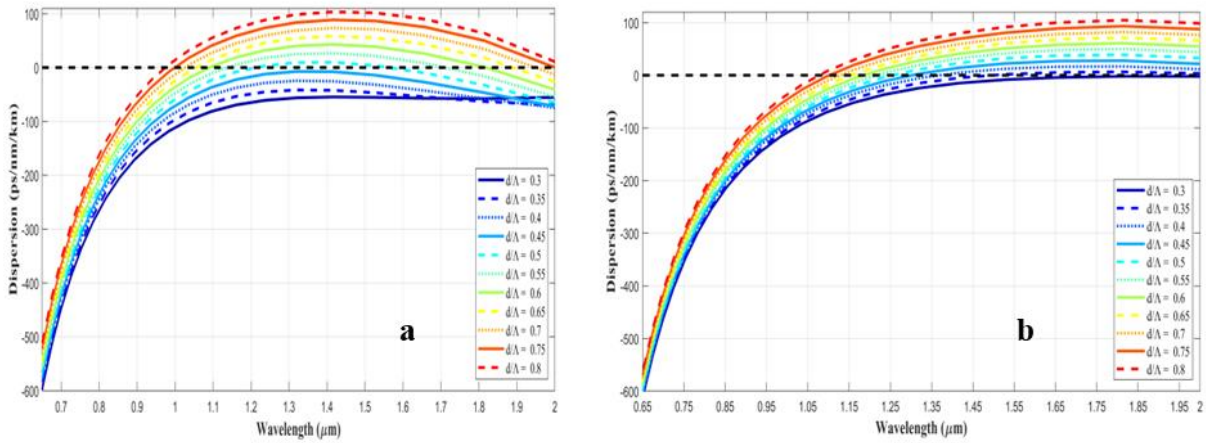

Fig. 4. *The dependence of chromatic dispersion on the wavelength of PCFs with various d/Λ and a) Λ = 1.5 μm, b) Λ = 2.0 μm.*

The values of chromatic dispersion calculated at wavelength 1.55 μm are defined in Table 2. For structures with anomalous dispersion, the value of the dispersion increases with the increase of the filling factor, and this value rises when the lattice constant increases for the same value of d/Λ.

Table 2. *The value of the chromatic dispersion of PCFs at the 1.55 μm wavelength.*

	Λ = 1.5 (μm)										
d/Λ	0.3	0.35	0.4	0.45	0.5	0.55	0.6	0.65	0.7	0.75	0.8
D	-55.274	-46.766	-31.651	-14.144	3.785	21.613	38.830	55.214	71.093	86.597	01.585
	Λ = 2.0 (μm)										
d/Λ	0.3	0.35	0.4	0.45	0.5	0.55	0.6	0.65	0.7	0.75	0.8
D	-8.329	1.731	12.353	22.290	32.071	41.635	51.007	60.643	70.233	80.626	91.533

D: ps/nm/km.

From all the above analysis, two all-normal dispersion curves which are the flattest and the closest to zero dispersion curves corresponding to two cases Λ = 1.5 μm, d/Λ = 0.45 and Λ = 2.0 μm, d/Λ = 0.3 are selected as two optimal structures, which can be considered in SC generation.

3.3. Effective mode area

Fig. 5 shows that the effective mode area increases with wavelength, for the case of lattice constant is unchanged, the effective mode area decreases when the filling factor increases. When the lattice constant increases the effective mode area changes less and less for the same values of d/Λ, because of the tight field confinement in the core with a decrease of the wavelength and increase of the lattice constant. This result is quite similar to that of PCFs in [22]. It can be seen clearly that, the effective mode area rapidly increases for the case Λ = 1.5 μm while the effective mode area is almost increasing linearly according to the wavelength with Λ = 2.0 μm. This result is similar to the result of core-PCF that is infiltrated Toluene in [22].

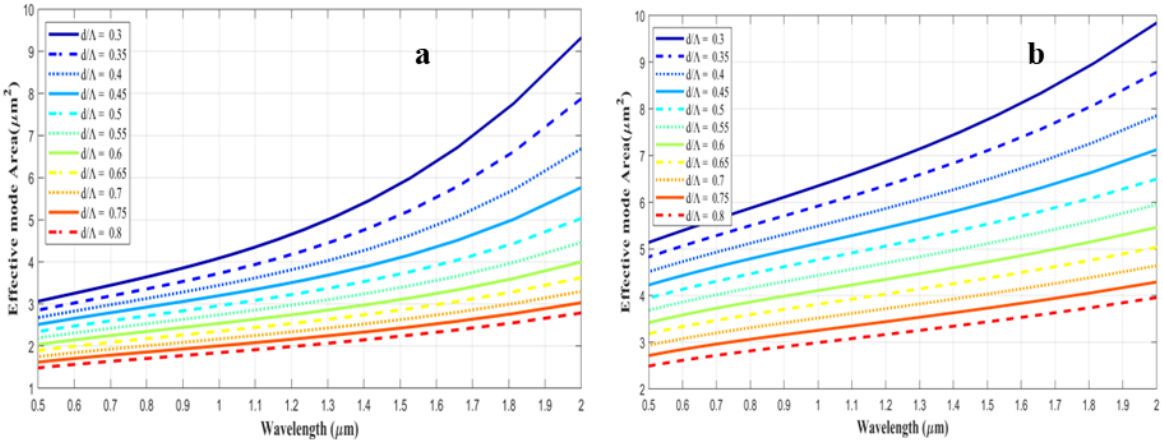

Fig. 5. *The dependence of effective mode area on the wavelength of PCFs with various d/Λ and a) Λ = 1.5 μm, b) Λ = 2.0 μm.*

Table 3 manifests values of effective mode area at 1.55 m of wavelength. The obtained values are quite small as expectation which means that the nonlinear coefficient can be large because it is inversely proportional to the effective mode area. The PCFs with Λ = 1.5 μm, d/Λ = 0.8 have the smallest effective mode area value, which is 2.261 μm^2. The maximum value of the effective mode area is 7.860 μm^2 corresponding to the structure Λ = 2.0 μm, d/Λ = 0.3. Two optimal structures that have a relatively small effective mode area, are 4.166 μm^2 and 7.860 μm^2 that can be acceptable in SC generation.

Table 3. *The value of the effective mode area of PCFs at the 1.55 μm wavelength.*

	Λ = 1.5 (μm)										
d/Λ	0.3	0.35	0.4	0.45	0.5	0.55	0.6	0.65	0.7	0.75	0.8
A_{eff}	5.989	5.219	4.632	4.166	3.765	3.434	3.143	2.891	2.656	2.454	2.261
	Λ = 2.0 (μm)										
d/Λ	0.3	0.35	0.4	0.45	0.5	0.55	0.6	0.65	0.7	0.75	0.8
A_{eff}	7.860	7.179	6.550	6.040	5.576	5.153	4.758	4.405	4.063	3.759	3.463

A_{eff}: μm^2.

3.4. Confinement loss

The small confinement loss is obtained in the PCFs and they decrease under the probation of the filling factor d/Λ. Fig. 6 demonstrates the dependence of the confinement loss on the wavelength with various d/Λ and Λ. An increase of the lattice constant causes L_c to reduce significantly. The values of L_c of the two proposed PCFs are 30.383 dB/m and 21.750 dB/m, respectively (Table 4).

Table 4. *The value of the confinement loss of PCFs at the 1.55 μm wavelength.*

	Λ = 1.5 (μm)										
d/Λ	0.3	0.35	0.4	0.45	0.5	0.55	0.6	0.65	0.7	0.75	0.8
L_c	44.702	38.502	33.783	30.383	27.503	25.568	24.346	23.451	22.944	23.157	23.545
	Λ = 2.0 (μm)										
L_c	21.750	19.685	17.766	16.707	15.937	15.377	15.009	15.014	14.964	15.344	15.892

L_c: dB/m

 ISBN:

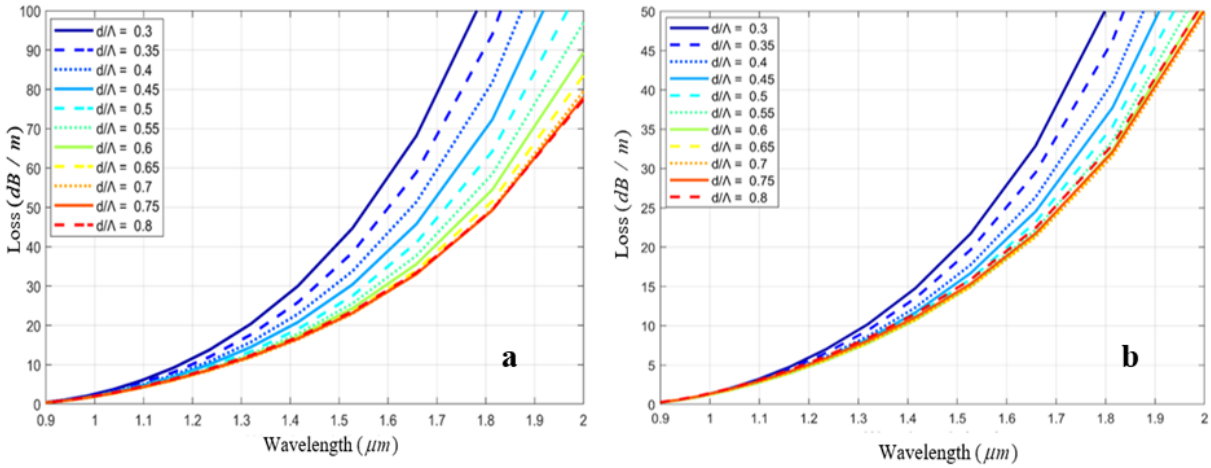

Fig. 6. *The dependence of confinement loss on the wavelength of PCFs with various d/Λ and a) Λ = 1.5 μm, b) Λ = 2.0 μm.*

IV. CONCLUSION

In this work, we have analyzed the characteristic of PCF with hollow-core infiltrated by Benzene with the lattice constant Λ of 1.5 μm and 2.0 μm, the filling factor varies from 0.3 to 0.8. Both flat all-normal and anomalous dispersions are obtained, the effective mode area and the confinement loss are small as expected, which are important factors of our simulation. In comparison with the publication [22], our designed PCFs show more advantages. Furthermore, two structures with the flattest dispersion have been proposed for consideration for SC generation.

ACKNOWLEDGMENTS. This research is funded by Vietnam National Foundation for Science and Technology Development (NAFOSTED) under grant number 103.03-2020.03 and Vietnam's Ministry of Education and Training (B2021- DHH-08).

REFERENCES

[1] J. C. Knight, T. A. Birks, P. St. J. Russell, and D. M. Atkin, All-silica single-mode optical fiber with photonic crystal cladding, *Opt. Lett.*, 1996, **21**, 1547-1549.

[2] I. M. Nascimento, G. Chesini, Marco Sousa, Jonas H. Osório, J.M. Baptista, Cristiano M. B. Cordeiro, Pedro A.S. Jorge, Application of a photonic crystal fiber LPG for vibration monitoring, *Proc. of SPIE*, 2013, **8794**, 87941L-1.

[3] T. A. Birks, J. C. Knight, and P. S. J. Russell, Endlessly single-mode photonic crystal fiber, *Opt. Lett.*, 1997, **22**, 961-963.

[4] R. F. Cregan, B. J. Mangan, J. C. Knight, T. A. Birks, P. S. J. Russell, P. J. Roberts, and D. C. Allan, Single-mode photonic band gap guidance of light in air, *Science*, 1999, **285**, 1537-1539.

[5] J. C. Knight, Photonic crystal fibers, *Nature*, 2003, **424**, 847.

[6] P. Russell, Photonic crystal fibers, *Science*, 2003, **299**, 358-362.

[7] D. Chen, L. Shen, Ultrahigh birefringent photonic crystal fiber with ultralow confinement loss, *IEEE Photonics Technology Letters*, 2007, **19**, 185-187.

[8] W. H. Reeves, J. Knight, P. S. J. Russell, P. Roberts, Demonstration of ultra-flattened dispersion in photonic crystal fibers, *Optics Express*, 2002, **10**, 609-613.

[9] S. Olyaee, F. Taghipour, A new design of photonic crystal fiber with ultra-flattened dispersion to simultaneously minimize the dispersion and confinement loss, *Journal of Physics, Conference Series*, 2011, **276**, 012080.

[10] T. M. Monro, K. M. Kiang, J. H. Lee, K. Frampton, Z. Yusoff, R. Moore, J. Tucknott, D. W. Hewak, H. N. Rutt, D. J. Richardson, High nonlinearity extruded single-mode holey optical fibers, *Optical Fiber Communication Conference and Exhibit, IEEE*, 2002, FA1-FA1-3.

[11] K. Tajima, J. Zhou, K. Nakajima, K. Sato, Ultralow loss and long length photonic crystal fiber, *Journal of Light wave Technology*, 2004, **22**, 7.

[12] R. Buczyński, Photonic crystal fibers, *Acta Physica Polonica Series A*, 2004, **106**, 141-168.

[13] J. Knight, T. Birks, P. S. J. Russell, J. De Sandro, Properties of photonic crystal fiber and the effective index model, *J. Opt. Soc. Am. A*, 1998, **15**, 7480752.

[14] N. A. Mortensen, Effective area of photonic crystal fibers, *Optics Express*, 2002, **10**, 341-348.

[15] B. Dabas, R. K. Sinha, Dispersion characteristic of hexagonal and square lattice chalcogenide As_2Se3 glass photonic crystal fiber, *Opt. Commu*., 2010, **283**, 1331-1337.

[16] G. P. Agrawal, Nonlinear Fiber Optics, Academic Press, San Diego, 2001.

[17] T. P. White, R. C. McPhedran, C. M. de Sterke, L. C. Botton, and M. J. Steel, Confinement losses in microstructured optical fibers, *Opt. Lett.*, 2001, **26**, 1660-1662.

[18] K. Petermann, Fundamental mode microbending loss in graded index and w fibers, *Opt. Quant. Electron.*, 1977, **9**, 167-175.

[19] T. Sorensen, N. A. Mortensen, J. Broeng, A. Bjarklev, T. P. Hansen, E. Knudsen, S. E. B. Libori, H. R. Simonsen, and J. R. Jensen, Spectral macro-bending loss considerations on photonic crystal fibres, *IEE Proc.-Optoelectron*., 2002, **149**, 206-210.

[20] D. Marcuse, Loss analysis of sigle-mode fiber splices, *The Bell System Technical Journal*, 1977, **56**, 703-718.

[21] N. A. Mortensen, J. R. Jensen, P. M. W. Skovgaard, and J. Broeng, Numerical aperture of single-mode photonic crystal fibers, *IEEE Photonics Technology Letters*, 2002, **14**, 1094-1096.

[22] L. Chu Van, A. Anuszkiewicz, A. Ramaniuk, R. Kasztelanic, K. Xuan Dinh, M. Trippenbach, R. Buczyński, Supercontinuum generation in photonic crystal fibres with core filled with toluene, *Journal of Optics*, 2017, **19**, 125604.

[23] N. Karasawa, Dispersion properties of liquid-core photonic crystal fibers, *Applied Optics*, 2012, **51**, 5259-5265.

[24] J. Pniewski, T. Stefaniuk, H. Le Van, V. Cao Long, L. Chu Van, R. Kasztelanic, G. Stępniewski, A. Ramaniuk, M. Trippenbach, and R. Buczyński, Dispersion engineering in nonlinear soft glass photonic crystal fibers infiltrated with liquids, *Applied Optics*, 2016, **55**, 5033-5040.

[25] K. Dinh Xuan, L. Chu Van, V. Cao Long, Q. Ho Dinh, L. Van Mai, M. Trippenbach, R. Buczyński, Influence of temperature on dispersion properties of photonic crystal fibers infiltrated with water, *Opt. Quant. Electron*., 2017, **49**, 87.

 ISBN:

[26] Lumerical Eigenmode Expansion (EME) Solver, https://www.lumerical.com/tcad-products/mode/EME, 2016.

[27] K. Moutzouris, M. Papamichael, S. C. Betsis, I. Stavrakas, G. Hloupis, D. Triantis, Refractive, dispersive and thermo-optic properties of twelve organic solvents in the visible and near-infrared, *Appl. Phys. B*, 2014, **116**, 617-622.

[28] I. H. Malitson, Interspecimen comparison of the refractive index of fused silica, *J. Opt. Soc. Am.*, 1965, **55**, 1205-1209.

[29] N. Naddi, E. Mahammed, K. L. N. Ksihore, Dispersion and effective area of air hole containing photonic crystal fibres, *J. Electron. Commun. Engine.*, 2017, **12**, 09-12.

[30] X. Li, Z. Xu, W. Ling, P. Liu, Design of high nonlinear photonic crystal fibers with flattened chromatic dispersion, *Appl. Opt.*, 2014, **53**(29), 6682.

CHEMICAL COMPOSITION OF ESSENTIAL OILS OF *Litsea elongata* (Nees) Benth. & Hook.f. IN PU HOAT NATURE RESERVE, NGHE AN PROVINCE

Nguyen Tien Cuong*, Pham Hong Ban, Mai Van Chung

Department of Biology, Vinh University

*E-mail: *tiencuong1907@gmail.com*

Abstract. Chemical composition of essential oils obtained from the leaf, bark stem and fruits of *Litsea elongata* were reported, corresponding oil content 0.21%, 0.17% and 0.18% (w/w), respectively. The analysis was performed by means of gas chromatography-flame ionization detector (GC-FID) and gas chromatography coupled with mass spectrometry (GC-MS). Total 39 components were identified in leaves (28 compounds), stem bark (22 compounds) and fruits (28 compounds), which represented about 57.34%, 38.04 % and 35.01% of the total, respectively. Germacrene D is a dominant sesquiterpene hydrocarbons compound recorded in all oils.

Keywords: *Essential oil, Litsea elongata, Nghe An, Pu Hoat.*

I. INTRODUCTION

Litsea, a genus belonging to family Lauraceae, consists of 400 species distributed throughout the tropical and subtropical Asia, the Pacific, and Australia [1]. Essential oils from several *Litsea* species have been traditionally and/or commercially used for human need due to their antioxidant, antibacterial, antifungal, and insecticidal activities. It has been recorded 45 *Litsea* species in Vietnam [2], of which several species have been used as medical material or essential oils, e.g., *L. cubeba*, *L. glutinosa*, *L. helferi*, *L. ferruginea*, *L. verticillata* [3], *L. acutivena* [4], *L. umbellata* and *L. khasyana* [5], *L. euosma* [6].

*Litsea elongata (*Nees) Benth. & Hook.f. is an evergreen, small or/and medium tree with the height of 10-12 meters, stem diameter of 0.4 meters. This species plant is commonly recognized in Pu Hoat Natural Reserve (Nghe An Province, Viet Nam). To date, lack of documents regarding *L. elongata* plants was reported there; therefore, it is necessary to investigate the chemical composition of essential oil for the first time from Pu Hoat Natural Reserve.

II. MATERIALS AND METHODS

2.1. Materials

Fresh leaves, stem bark and fruits of *L. elongata* were collected from plants at an altitude of 750-850 m in Pu Hoat Nature Reserve (Nghe An Province, Vietnam) in December 2019. Voucher specimen (numbered as NTC.NN 06.01, NTC.NN 06.02 and NTC.NN 06.03, respectively) were identified by the botanically taxonomical specialist (Assoc. Prof. Dr. Pham Hong Ban from Vinh University) and deposited in the herbarium of Vinh University.

2.2. Essential oil extraction

 ISBN:

Essential oils (1.0 kg/each type of material) were extracted by hydrodistillation for 6 hours using the Clevenger-type apparatus, and then was stored in a sealed amber glass at -18 °C for analyses. The yield calculation was performed in g of essential oil per 100 g of fresh material (%, w/w).

2.3. Analytical method

Gas Chromatography (GC) analysis: The essential oil was analysed by using an Agilent Technologies HP 6890 Plus Gas chromatograph which was equipped with a flame ionization detector (FID). The analysis was carried out on an HP-5MS column (Agilent Technologies, Santa Clara, CA 95051, USA) measuring 30 m × 0.25 mm i.d., film thickness 0.25 µm. The carrier gas as hydrogen was at a flow rate of 1 ml/min. The injector and detector temperatures were maintained at 250 °C and 260 °C, respectively. The column temperature was programmed from 40 °C with a 2 min hold to 220 °C with 10 min at 4 °C/min. A volume of 1.0 ml of each oil sample was injected into the GC by splitting method with the split ratio of 10:1. The inlet pressure was maintained at 6.1 kPa. The relative amounts of each component were calculated based on the GC peak area percentage that was performed on basis of the FID signal using the GC HP-Chemstation software (Agilent Technologies, Santa Clara, CA, USA).

Gas Chromatography-Mass Spectrometry (GC-MS) analysis: GC-MS analysis of the essential oil was performed on an HP 6890N Plus Chromatograph (Agilent Technologies) which was fitted with a HP-5MS column (30 m × 0.25 mm i.d., film thickness 0.25 µm) and interfaced with a mass spectrometer HP 5973 MSD. The analytical conditions were the same as used for GC analysis, except that helium (1 ml/min) was used as the carrier gas. The ionization voltage was 70 eV with the emission current of 40 mA. The acquisitions scan mass range of MS was 35-350 amu with the sampling rate of 1.0 scan/s.

Identification of components: Components of essential oil was identified by comparison of their retention indices and mass spectra with data generated under identical experimental conditions. The retention time was in relation to a homologous series of *n*-alkanes (C_4-C_{32}) and authentic compounds under the same chromatographic conditions. Further identification was used for processing and interpretation of mass spectra with several commercially available libraries included: NIST/EPA/NIH Mass Spectral Library [7] and Wiley Registry of Mass Spectral Data [8], as well as by comparing with literature data [9,10].

III. RESULTS AND DISCUSSION

Hydrodistillation of fresh leaves, bark stem and fruits of *L. elongata* plants gave light or naple yellow oils in 0.21%, 0.17% and 0.18% (w/w), respectively. It was verified the major presence of monoterpene hydrocarbons (33.42% in leaves; 6.25% in stem bark and 14.64% in fruits), sesquiterpene hydrocarbons (21.81% in leaves; 28.39% in stem bark and 17.40% in fruits); whereas oxygenated monoterpenes and oxygenated sesquiterpenes was in low content (Table 1). The non-terpenes in leaves, stem bark and fruits of *L. elongata* plants present in high content (42.66%, 61.96% and 64.99% of total, respectively).

Table 1. *Chemical composition of essential oil of Litsea elongata plants from Pu Hoat Natural Reserve.*

No	Compound	RI[a]	RI[b]	Content (%)		
				Leaf	Stem bark	Fruit
1	α-Pinene	939	934.5	4.98	1.69	0.97
2	β-Myrcene	989	983.1	3.68	1.25	1.21
3	Carene	1002	997.7	0.05	-	-
4	α-Phellandrene	1006	999.1	-	-	0.27
5	Pyridine	1108	1003	16.61	-	-
6	D-Limonene	1028	1023.7	6.86	2.57	2.61
7	β-Ocimene, (Z)-	1032	1028.9	1.11	0.71	2.52
8	Eucalyptol	1035	1031.5	1.03	0.07	0.25
9	β-Ocimene, (E)-	1042	1038.4	-	-	0.07
10	γ-Terpinene	1054	1050.3	0.13	0.03	0.12
11	Linalool	1089	1086.3	0.43	-	0.1
12	1,6-Cyclodecadiene	1105	1108	-	-	6.87
13	(+)-2-Bornanone	1144	1141	0.25	-	-
14	Isoborneol	1150	1147.8	0.05	-	-
15	α-Cubebene	1357	1352.2	0.24	3.01	2.95
16	α-Copaene	1371	1375.5	0.59	-	-
17	β-Bourbonene	1385	1381.7	1.95	3.89	2.27
18	γ-Elemene	1391	1388	0.43	0.29	0.24
19	β-Gurjunene	1409	1405.6	-	0.23	-
20	Caryophyllene	1422	1419.3	6.49	0.66	2.67
21	α-Bergamotene	1434	1431.1	0.09	0.2	0.4
22	Aromandendrene	1441	1439	0.05	0.97	0.22
23	γ-Farnesene	1451	1449.3	0.51	0.45	-
24	cis-Muurola-3,5-diene	1451	1450	0.1	-	-
25	α-Humulene	1452	1453	0.64	2.0	1.82
26	γ-Muurolene	1478	1473	0.29	1.42	0.67
27	Germacrene D	1479	1475.9	8.09	14.55	5.64
28	α-Farnesene	1481	1480.6	-	-	0.04
29	Epizonarene	1484	1478	-	-	0.1
30	Viridiflorene	1492	1488.9	0.26	-	-
31	Bicyclogermacrene	1495	1489	2.01	-	-
32	Bicyclosesquiphellandrene	1514	1511.7	0.07	0.72	0.19

 ISBN:

33	β-Panasinsene	1515	1518	-	-	0.19
34	Isoaromadendrene epoxide	1628	1625.6	-	0.02	-
35	τ-Cadinol	1631	1626.4	0.17	-	0.43
36	α-Cadinol	1644	1640.2	-	-	1.13
37	τ-Muurolol	1646	1642.2	0.18	3.21	0.97
38	Isolongifolol	1731	1740	-	0.1	-
39	Cubenol	1922	1919.9	-	-	0.09
Monoterpene hydrocarbons				33.42	6.25	14.64
Oxygenated monoterpenes				1.76	0.09	0.35
Sesquiterpene hydrocarbons				21.81	28.39	17.4
Oxygenated sesquiterpenes				0.35	3.31	2.62
Total of terpenes				**57.34**	**38.04**	**35.01**
Others				**42.66**	**61.96**	**64.99**

RI^a: Calculated from retention indices on HP-5MS capillary column; RI^b: Retention indices on literatures [7-10]; (%): percentage of compound's content in total oil; (-) no information.

Essential oil from leaf of *L. elongata* consists of 28 terpenes (accounting for 57.34% of the chromatographical components), of which Pyridine (16.61%) and Germacrene D (8.09%) were main constituents. The essential oil from stem bark contains 22 terpene compounds (made up 38.04% of total) with major component as Germacrene D (14.55%). The essential oil from *L. elongata* fruits consists of 28 terpenes (accounting for 35.01% of the chromatographical components), of which 1,6-Cyclodecadiene (6.87%), Germacrene D (5.64%) were dominant constituents.

Being partly different from previous studies introduced monoterpenes as the major fraction in essential oils of some *Litsea* species in Vietnam [3-6], our results recorded basic components of oils from stem bark and fruit of *L. elonggata* plants as sesquiterpene hydrocarbons, whereas monoterpenes as the dominant fraction in essential oils of leaves.

It is interesting that Germacrene D is one of the most abundant components in all *L. elongata* oils. Germacrene D has been known to express antibacterial and antifungal activities; that sesquiterpene hydrocarbons can be used as an adjuvant agent in the application of aminoglycosides and azoles [11]. A high content of Germacrene D obtained in the essential oil from *L. elongate* plants may ascribe to its biological activities.

IV. CONCLUSION

Chemical composition of the essential oil in leaves, bark stem and fruits of *L. elongata* plants were investigated for the first time from Pu Hoat Natural Reserve. Essential oils were extracted by hydrodistillation, then analyzed by GC/GC-MS methods and accounted for 57.34%, 35.01% and 38.04% of the total, respectively, with Germacrene D as a dominant sesquiterpene hydrocarbons compound obtained in all oils.

REFERENCES

[1] W. M. N. H. W. Salleh, F. Ahmad, K. H. Yen, and R. M. Zulkifli, Essential oil compositions of Malaysian Lauraceae: A mini review, *Pharm. Sci.*, 2016, **22**, 60-67.

[2] K. D. Nguyen, Flora of Vietnam, Lauraceae family, *Sci. & Techn.*, Ha Noi, 2010, **20**, 65-112.

[4] C. S. Le, N. D. Do, D. T. Tran, et al., Analysis of the essential oils from five Vietnamese Litsea species (Lauraceae), *J. Essent. Oil-Bear. Plants*, 2014, **17**(5), 960-971.

[4] N. D. Do, T. T. L. Nguyen, A. D. Nguyen, T. H. Le, et al., Composition of essential oils from Litsea acutivena Hayata, *Am. J. Plant Sci.*, 2019, **10**, 615-621.

[5] T. C. Nguyen, H. B. Pham, and V. C. Mai, Chemical composition and antioxidant activity of leaf essential oil two Litsea species from Viet Nam, *Chem. Nat. Compd.*, 2021, **57**(4), 776-778.

[6] D. T. Tran, H. H. Hoang, X. T. Trinh, and X. D. Nguyen, Volatile constituents of the leaf oil of *Litsea euosma* J. J. Sm. from Vietnam, *J. Essent. Oil-Bear. Plants*, 2006, **9**(2), 122-125.

[7] NIST, Data from NIST Standard Reference Database 69, 2018.

[8] F. W. McLafferty, Wiley Registry of Mass Spectral Library, 9th Ed., Wiley, 2009.

[9] R. P. Adams, Identification of essential oil components by gas chromatography/mass spectrometry, 4th Allured Publishing Corporation, Carol Stream, 2007.

[10] V. I. Babushok, P. J. Linstrom, and I. G. Zenkevich, Retention indices for frequently reported compounds of plant essential oils, *J. Phys. Chem. Ref. Data*, 2011, **40**(4), 043101.

[11] K. Noge, and J. X. Becerra, A common sesquiterpene in the genus *Bursera* (Burseraceae), *Mol.*, 2009, **14**(12), 5289-5297.

 ISBN:

AUTHORS INDEX

A

Anusara Srisrual 23

B

Bao Anh Phung Ngoc 144

Bao Le Xuan 397

Bao Tran Le Tran 293, 301, 309, 317, 397

Bien Chu Van 37

Bijeesh Kozhikkodan Veettil 112, 260

Bui Dinh Bao 204

Bui Dinh Thuan 239

Bui Minh Hue 388

C

Co Ngoc Duong 152

Cong Vu Tien 152

Cuong H. Le 119

Chi K. Hoang 119

Chin Hoang Van 37

Chu Thi Minh Hoa 357, 364

Chung Anh Do 45

D

Dang Hai Ninh 193

Danh Thuong Sy 222

Dau Duong Hieu 161

Dinh Xuan Khoa 239,246

Do Thanh Thuy 239

Doan Hoai Son 83

Doan Minh Khai 324

Doan The Ngo Vinh 193

Doan Thi Thu Thuy 357, 364

Duc Hoang Trong 293, 301, 309, 317

Duong Anh Nguyen 45

Duong Chi Tong 254

Duong Duc La 152

Duy Hoang Dang 187

E

Elsa Dieudonné 144

Eun Kyu Kim 31

H

Ha Minh Quan 239

Ha T. H. Tran 119

Hai Van Bui 93, 144

Hang T. N. Tran 119

Hervé Delbarre 144

Hiep Hoang Phu 222

Hieu Van Le 37

Ho Xuan Huy 280

Hoang Minh Dong 246

Hung Dao Van 309, 317

Hung Le Trinh 93

Huong M. Le 119

Huong Thi Le 332

Huu Hoang Trung 67

Huu Tu Nguyen 78

Huynh Quang Linh 351

K

Karine Deboudt 144

Kieu Thi Van Anh 337

Kieu-Anh Thi Doan 15

Kudryashov Sergey Ivanovich 83

L

Lanh Chu Van 293, 301, 309, 317, 397

Le Canh Trung 239

Le Dinh Vi 193, 210

Le Thi Giang 179

Le Thi Huong 217

Le Thi Minh Phuong 246

Le Thi Ngoc Linh 337

Le Thi Thu Huong 217

Le Van Doai 246

Le Van Hieu 239
Linh Phan-Thuy Tran 15
Long Vu Dinh 397
Luong Thi Yen Nga 246
M
Mai Huong Thi Nguyen 332
Mai Van Chung 406
Marilou Cadatal-Raduban 15
Marzuki Sinambela 62
Minh Duc Vu 45
Minh Hong Pham 15, 62
Minh Lam Thuy 161
Mui Viet Luong 15
My Tran Diem 161
N
Nghia Huu Pham 187
Ngo Dinh Hong Le 239
Ngo Thi Lien 193
Ngoc Vo Thi Minh 37, 293, 301, 397
Nguyen Dac Dien 286
Nguyen Dang Nguyen 37
Nguyen Dieu Linh 337
Nguyen Duc Tri 351
Nguyen Duy Tuan 324
Nguyen Hong Giang 254
Nguyen Hong Hai 280, 371, 380
Nguyen Huy Bang 246
Nguyen Kim Thanh 210
Nguyen Minh Tan 357, 364
Nguyen Minh Tuan 324
Nguyen Nang Binh 254
Nguyen Quang Hiep 233
Nguyen Quoc Long 93
Nguyen Tien Cuong 406
Nguyen Tien Dung 239
Nguyen Tuan Anh 246, 324, 357, 364
Nguyen Thanh Binh 217
Nguyen Thanh Cong 193
Nguyen Thanh Lam 254
Nguyen The Thuong 139, 346, 351
Nguyen Thi Bich Ngoc 127
Nguyen Thi Dung 179
Nguyen Thi Hang Nga 127
Nguyen Thi Huyen Trang 83
Nguyen Thi Linh 239
Nguyen Thi Mai Huong 217
Nguyen Thi Thu Hien 246, 254
Nguyen Trong Tinh 217
Nguyen Trung Thanh 105
Nguyen Van Hao 337
Nguyen Vu Tung 198, 210
Nhan Duong Trong 161
Nhat-Duc Hoang 112, 260
O
Oanh Truong Thi Chuyen 397
P
Phakkhaphum Lethaisong 23
Pham Hong Ban 406
Pham Quang Hieu 268, 274
Pham Trung Kien 357, 364
Pham Van Thin 193, 210
Phan Duc Nhan 324
Phan Nguyen Nhue 204
Phan Thi Thuy 217
Phan Trung Vinh 254
Phan Van Cuong 89
Phu Van Le 93
Phuong Nguyen Le Hoai 161
Q
Quang H. Tran 119
Quang Ho Dinh 37
Quang Minh Ngo 7, 78

 ISBN:

Quoc Khanh Doan 168

S

Son Bach 332

T

Tan Tran Duy 293, 301

Tien Minh Pham 93

Tin Duong Quoc Chanh 161

Titipa Zunsuwan 23

Toai Pham Van 152

Toan Nguyen Trung 67, 152

Tuan Minh Vu 45

Tuong Nguyen Manh 152

Thai Doan Thanh 246

Thanh Hai Do 168

Thanh Son Pham 7, 78

Thanh Tran Viet 397

Thanh Vinh Nguyen 37

Thao Nguyen Thi 37

Thao Thi Phuong Cao 222

Thao Tran Ngoc 397

Thi Dung Nguyen 133

Thi Thanh Nhan Pham 222

Thi Thao Nguyen 133

Thu Ho Thi Anh 397

Thu Trang Hoang 7, 78

Thuan Nguyen Van 161

Thuy Nguyen Thi 293, 301, 309, 317, 397

Thuy Thi Phan 332

Tran Duc Thiep 388

Tran Quang Dat 193, 210

Tran Thi Thanh Huyen 239

Trong Dang Van 293, 301, 309, 317, 397

Trung Le Canh 37

Truong Dinh Tuan 105

Truong Thi Thao 337

V

Van An Nguyen 7

Van Dai Pham 7

Van Nguyen Thanh 161

Van Nhu Le 168

Van Sang Doan 168

Viengthong Xayavong 45

Vo Quang Sang 54

Vo Thi Anh Tuyet 346

Vu Ba Dung 173

Vu Duong 127

Vu Thi Kim Oanh 31

Vu Tran Quoc 397

Vu Van Thu 286

Xuan Bach Nguyen 78

Xuan-Linh Tran 112

Xuan-Linh Tran 260

Y

Yiting Duan 54